NASA/TM–2012-218950

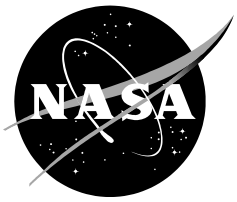

Advanced Model for Extreme Lift and Improved Aeroacoustics (AMELIA)

Jonathan Lichtwardt
California Polytechnic State University, San Luis Obispo

Eric Paciano
California Polytechnic State University, San Luis Obispo

Dr. Tina Jameson
California Polytechnic State University, San Luis Obispo

Robert Fong
NASA Ames Research Center, Moffett Field, CA

Dr. David Marshall
California Polytechnic State University, San Luis Obispo

Prepared in accordance with the requirements outlined by NASA Aeronautics Subsonic Fixed Wing Program Contract #NNL07AA55C fulfilled by California Polytechnic State University in collaboration with Georgia Tech Research Institute

Table of Contents

List of Figures

1. NRA Objective

With the very recent advent of NASA's Environmentally Responsible Aviation Project (ERA), which is dedicated to designing aircraft that will reduce the impact of aviation on the environment, there is a need for research and development of methodologies to minimize fuel burn, emissions, and reduce community noise produced by regional airliners. ERA tackles airframe technology, propulsion technology, and vehicle systems integration to meet performance objectives in the time frame for the aircraft to be at a Technology Readiness Level (TRL) of 4-6 by the year of 2020 (deemed N+2). The proceeding project that investigated similar goals to ERA was NASA's Subsonic Fixed Wing (SFW). SFW focused on conducting research to improve prediction methods and technologies that will produce lower noise, lower emissions, and higher performing subsonic aircraft for the Next Generation Air Transportation System.

The work provided in this investigation was a NASA Research Announcement (NRA) contract #NNL07AA55C funded by Subsonic Fixed Wing. The project started in 2007 with a specific goal of conducting a large-scale wind tunnel test along with the development of new and improved predictive codes for the advanced powered-lift concepts. Many of the predictive codes were incorporated to refine the wind tunnel model outer mold line design. The large scale wind tunnel test goal was to investigate powered lift technologies and provide an experimental database to validate current and future modeling techniques. Powered-lift concepts investigated were Circulation Control (CC) wing in conjunction with over-the-wing mounted engines to entrain the exhaust to further increase the lift generated by CC technologies alone. The NRA was a five-year effort; during the first year the objective was to select and refine CESTOL concepts and then to complete a preliminary design of a large-scale wind tunnel model for the large scale test. During the second, third, and fourth years the large-scale wind tunnel model design would be completed, manufactured, and calibrated. During the fifth year the large scale wind tunnel test was conducted.

This technical memo will describe all phases of the Advanced Model for Extreme Lift and Improved Aeroacoustics (AMELIA) project and provide a brief summary of the background and modeling efforts involved in the NRA. The conceptual designs considered for this project and the decision process for the selected configuration adapted for a wind tunnel model will be briefly discussed. The internal configuration of AMELIA, and the internal measurements chosen in order to satisfy the requirements of obtaining a database of experimental data to be used for future computational model validations. The external experimental techniques that were employed during the test, along with the large-scale wind tunnel test facility are covered in great detail. Experimental measurements in the database include forces and moments, and surface pressure distributions, local skin friction measurements, boundary and shear layer velocity profiles, far-field acoustic data and noise signatures from turbofan propulsion simulators. Results and discussion of the circulation control performance, over-the-wing mounted engines, and the combined performance are also discussed in great detail.

The wind tunnel test was conducted at the National Full Scale Aerodynamic Complex (NFAC) starting in November of 2011 concluding in March of 2012. All wind tunnel test objectives were met or exceeded.

2. AMELIA Background

NASA is committed to identifying solutions that meet improvement goals for noise, emissions, and fuel burn. Subsonic Fixed Wing has classified the N+2 design metrics as a 40% reduction in fuel consumption, progress towards -42 dB lower noise levels and a 70% decrease in emissions over current generation aircraft, and a takeoff and landing field length of less than 3,000 ft. Theoretically the aircraft should reach a Technology Readiness Level (TRL) of 4-6 by the year 2020. Cal Poly contracted with DHC Engineering to create conceptual designs of four separate configurations to address the N+2 goals with a down selection by Cal Poly to one favorable configuration.

2.1. Phase 1: AMELIA Conceptual Design Considerations

Four CESTOL configurations were developed for consideration for the large-scale wind tunnel test. The first design, Configuration 1, utilizes a Hybrid blended-Wing-Body (HWB). Upper surface blowing coupled with leading and trailing edge blowing for circulation control provides powered lift system. The aft fuselage terminates in a beaver tail, where a structural dorsal provides additional structural support. An isometric view of Configuration 1 is provided in Figure 2.1 and shows the V-tail in conjunction with aft fuselage strakes to aid in flow attachment.

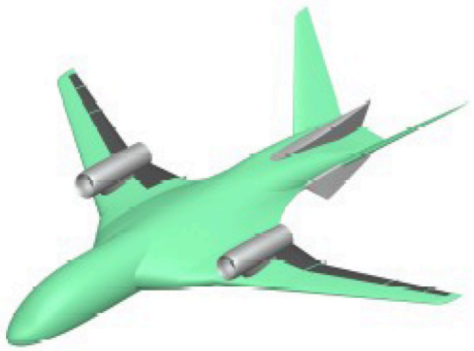

Figure 2.1. Configuration 1 utilizes a hybrid blended-wing-body, over-the-wing mounted engines, a V-tail and circulation control at the leading and trailing edge of the wings.

Drastically different from the first, the second configuration is a more conventional design. This configuration utilizes a high aspect ratio wing along with a cruciform tail. Utilizing over-the-wing mounted engines upper surface blowing is provided, which when combined with circulation control at the trailing edge, creates the powered lift necessary for short takeoff and landing. The inboard section of the wing was specifically designed to enhance flow turning ability during these flight segments. Configuration 2 is shown in Figure 2.2.

Figure 2.2. Configuration 2 is comprised of a high aspect ratio wing, over the wing engines, circulation control at the trailing edge and a cruciform tail.

The third configuration was inspired by recent interest in an aircraft utilizing a true Blended-Wing-Body (BWB). This aircraft concept is a significant departure from the first two aircraft designs in that the two turbofan engines are embedded within the very thick wing root; this can be seen in Figure 2.3. The exhaust discharges through a high aspect ratio 2-D nozzle at the trailing edge of the vehicle. The intent is not only to produce thrust through this nozzle throughout the flight but also to create increased flow circulation around the aircraft generating additional lift during takeoff and landing.

The final and most complex design is shown in Figure 2.4, termed the Diamond-Wing-Body (DWB). It may be thought of as a Joined-Wing with a vertical structural member joining the fore and aft wings at the outer span points. The intent is to improve local airflow and mitigate shock formation at high subsonic Mach numbers. These vertical members are more like wingtip sails than winglets and act structurally as struts. The forward wing sweeps aft, and the aft wing sweeps forward forming a

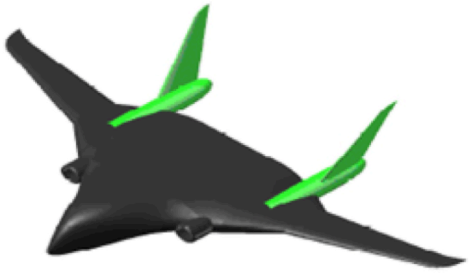

Figure 2.3. Configuration 3 is a complete blended wing body with embedded engines.

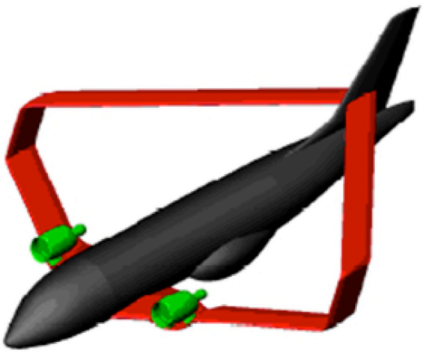

Figure 2.4. Configuration 4 utilizes a high aspect ratio wing, in a diamond wing configuration.

diamond planform shape in the top view. Both wings have a high aspect ratio. The propulsion system is a medium-sized geared turbofan engine mounted within a channel wing.

2.2. Phase 1: Large Scale Wind Tunnel Model Conceptual Design Decision

All conceptual designs were carefully considered prior to the decision for a final configuration. Cal Poly wanted to address the NRA edict to truly choose a design that would be technically challenging as well as fit the N+2 time frame. Configuration 2 was deemed to be too conventional given its standard tube and wing configuration. The NRA was seeking out technology that would be challenging for computational modeling, specifically aerodynamics and aeroacoustics, as well as provide new experimental information to the CESTOL community. Configuration 1, although technically challenging for CFD, more closely fit the N+1 time frame compared to the other possible candidates. Configuration 4 was deemed to be an N+3 design with the channel wing and diamond wing design components, and Cal Poly determined that it would be out of the scope for this NRA project. Configurations 1 and 3, both fit the N+2 time frame and were both technically challenging for the experimental community as well as for CFD. Configuration 1 became the front-runner to become the large scale wind tunnel model, largely because of the difficulty in laying out passenger seats to meet FAA regulations, and the significant unknowns associated with the imbedded engines (especially the internal ducting of hot exhaust and the performance of the exhaust nozzle). Cal Poly made the decision that Configuration 1 could be realized as a large scale wind tunnel model given the NRA schedule constraints and available funding; the model was designated as the Advanced Model for Extreme Lift and Improved Aeroacoustics (AMELIA). Figure 2.5 shows a rendering of AMELIA.

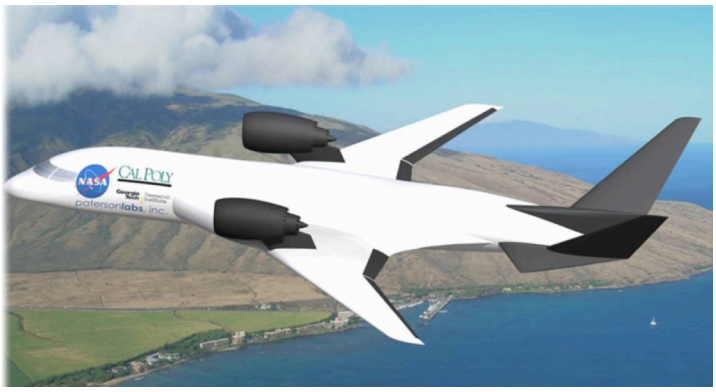

Figure 2.5. An image of AMELIA flying over Hawaii.

2.3. Phase 2: Final Wind Tunnel Selection

The NRA specified the model to be at least 8 feet full-span. This constraint, along with the size of available wind tunnels, AMELIA's final design lead to a 10ft wing span in order to meet all objectives specified in the NRA. Initial trade studies were performed for the 8ft span model, and it quickly became clear that a 10ft span was necessary to allow for enough room for the model to hold all the desired instrumentation. The following two sections describe the wind tunnel and model manufacture selection process based on the 10ft span.

A comparison matrix was constructed that consisted of all the domestic tunnels with all required and optional capabilities that might be used for the proposed testing. This comparison is shown below in Table 2.1, with only the most pertinent features listed. The information provided in Table 2.1 Table 2.1 Initial wind tunnel selection trade study from Phase 1 of the AMELIA project. is outdated with respect to schedule and cost, as the trade study was performed in 2008. However, this initial trade was accurate at the time and valuable in decision-making process for the AMELIA project.

The top two choices that immediately stood out, both in cost and capabilities, were the NFAC 40 by 80 which is operated by Arnold Engineering Development Center and the 14 by 22 at Langley, operated by NASA. The 14 by 22 is approximately the minimum size for a model of the scale being proposed. For the proposed test, the 14 by 22 would need to be operated in the open jet configuration for the acoustic

measurements, with the model mounted with the wings vertical. This posed two issues that are non-trivial. For the estimated maximum lift coefficient and the smallest proposed model size, the expected static loads generated at the maximum test speed of 100 kts are within 10% of the allowable maximum without taking any dynamic loading conditions into account. This test constraint could have resulted in a wind tunnel test that may not be able to complete the full range of desired test conditions. Taking the model span to tunnel span in the vertical configuration, the resulting ratio is approximately 0.6 for the Langley tunnel, which is beyond the recommended range. Although the results may be correctable, the goal of the project is to provide data to validate CFD and the only realistic way to correct the data from such a novel configuration is to use CFD. This would result in data that may be fundamentally flawed with no way to provide concrete correction factors. Another key factor that affected the decision was the tunnel availability in calendar year 2010. However, as the project progressed the 2010 test schedule was pushed into the 2011/2012 calendar year. This schedule conflict would have been a nonissue, except the technical reasons for deciding against the 14 by 22 were technically sound for AMELIA.

Table 2.1 Initial wind tunnel selection trade study from Phase 1 of the AMELIA project.

Name	Size	Speed	Air Supply	Model Support	Test Section	Notes	Cost
NFAC 40 by 80	40ft by 80ft	300 kts 0.45 M	3000 psi 40 lb/sec	Sting, capacity +/- 6800 lb lift, +/-4000 ft-lb pitch moment	Elliptic rectangle	**42 in acoustic lining 500 Hz**, JP-5, hydraulic fluid, electric power	$ 494,000
Langley 14 by 22	14ft by 22ft	200 kts 0.3 M	4000 psi 30 lb/sec	Sting, capacity 4000 lb vertical plane and 3500 lb horizontal plane	Rectangular closed, slotted, or 3/4 open jet	**July 2010 ONLY Available Test Dates**, floor boundary layer removal, moving ground belt, acoustic testing	$ 304,503
Lockheed Martin Low Speed	16ft by 23ft	180 kts 0.27 M	330 psi 20 lb/sec	Struts, capacity +/-10000 lb	Rectangular	Floor blowing, ground planes	$ 400,000
Boeing VSTOL	20ft by 20ft	215 kts 0.32 M	1000 psi 20 lb/sec	Strut or movable sting, 360000 in-lb capacity	Rectangular closed, slotted, 3/4 open, or open jet	Moving ground belt, 500 kva, hydraulic fluid, ground planes	$ 700,000
Boeing LSAF	9ft by 12ft	165 kts 0.25 M	30 lb/sec	Single strut, capacity 6000 lb	Rectangular open jet	**Anechoic Chamber**, smoke wand, laser flow visualization	$ 800,000

The final wind tunnel selection resulted in the 40 by 80 at the NFAC being the venue for the proposed test for several key reasons. The 40 by 80 also provides seamless testing of both aerodynamic and acoustic information simultaneously. The test section of the 40 by 80 is large enough that the amount of flow turning created by the circulation control wing and the over-the-wing mounted engines will not impinge directly on the tunnel walls or support system, thereby minimizing wind tunnel wall effects on the experimental data.

An additional benefit is the location of the 40 by 80, which is no more than a three hour drive from Cal Poly. This factor did not play a role in the decision, but provides a direct benefit in reducing travel costs and improved communications with respect to test planning and execution. The convenient NFAC location to Cal Poly ended up playing a much larger role in the success of AMELIA project than anticipated. The Cal Poly test team ended up moving the model to the Fluid Mechanics Laboratory (FML) at the Ames Research Center approximately four months earlier than initially scheduled in order to calibrate the circulation control system. Cal Poly did not have the facilities to support the calibration and the FML testing was instrumental in the Cal Poly test team's understanding of the response and performance of the circulation control system. During the wind tunnel testing phase, this understanding

led to efficient execution of circulation controls.

2.4. Phase 2: Model Manufacturing

Wind tunnel model fabrication posed the greatest technical risk, since the model directly affects the test data. Much research was devoted to finding credible manufacturers that would produce a model capable of meeting all of the testing priorities previously stated. Along with finding the best-fit manufacturer, the model was adjusted to incorporate achievable tolerances and geometries. A total of eight different model manufacturers were contacted, requesting estimates on both a cost and schedule for the model design. Table 2.2 shows the trade study performed in 2008 comparing the 8 leading manufacturing choices, however it lead the Cal Poly team to a great working relationship with the manufacturer of the wind tunnel model.

2.4.1. Model Manufacturing Considerations

The primary wind tunnel test speed of 100 kts was the main contributing factor to the material selection for the model. Both machined stainless steel and aluminum were chosen for their strength and ease of manufacturability, respectively. With the chosen material properties, the detailed structural integrity of the model was defined. Since the model design incorporated leading- and trailing-edge blowing slots, tolerance became one of the more important manufacturing considerations. After researching the smallest allowable tolerance for the slot geometry, it was found that the smallest slot could be at a height of 0.0115 in. This did not affect the existing trailing edge slot geometry, but increased the leading edge slot heights by 15% from the original designed slot. Another manufacturing consideration was the design and material of the low-pressure wing plenums for the circulation control wings. The plenum design must allow adequate space for instrumentation while being small enough to have enough wall thickness to meet the appropriate safety factors.

2.4.2. Model Manufacturer Selection

The model manufacturers were first contacted and introduced to the initial model design. All of the manufacturers responded with varying levels of interest. The manufacturers were then updated throughout the development of the model, to keep them up-to-date and to answer any of their questions. Table 2.2 shows the rough cost and schedule estimates from each of the manufacturers.

As shown in Table 2.2, the model manufacturer was eventually down selected to Patersonlabs Incorporated (Table 2.2 and more information on the down select process can be found at end of year 1 final review). They provided the most competitive cost and schedule, and were the most responsive during the proposal period. Patersonlabs also had prior experience building many complex models, including recently completing a model tested at NASA Ames Research Center's 11 ft by 11 ft Transonic Wind Tunnel (11 by 11).

Table 2.2. Phase 1 model manufacturer trade study.

Model Manufacturer	Cost	Schedule
Patersonlabs Incorporated	$458,000	16-18 Weeks
Triumph Aerospace Systems	$2,000,000	52 Weeks
Tri Model Incorporated	$906,890	34 Weeks
Advanced Technologies Incorporated (ATI)	$865,000	27 Weeks
Aeronautical Testing Service Incorporated (ATS)	Coming	Coming
Lockheed Martin	Model Exceeds Capabilities	N/A
Dynetics Incorporated	Coming	Coming
Alliant Techsystems Incorporated (Formerly ATK GASL)	$602,761	20 weeks

During the time of the trade study, the final model geometry had not been defined. Patersonlabs, once chosen, played a large role in the detailed and internal design of AMELIA. A PDR and a CDR was presented to NASA by Cal Poly with Patersonlabs to refine the model to meet NASA's and the NFAC's manufacturing requirements. The final manufacturing cost billed by Patersonlabs was approximately $750,000. Adding the parts and labor combined with the charged amount to Cal Poly lead the final AMELIA cost of approximately $1M. Although the initial quoted price of AMELIA increased by 50%, Patersonlabs was instrumental in the success of the AMELIA project. After the PDR there was a large effort to redesign the internal high- and low-pressure flow paths to accommodate an 8 inch flow through balance. The initial design utilized a single flow path through a 6 inch balance; this design did not support the two separate flow paths for the circulation control wings or the engine simulators which require different pressure and mass flow settings during operation (see Sections 10.0 and 11.0 for more detail on the design of these two subsystems). The aforementioned redesign was a significant driver in the cost increase from the initial quote from Patersonlabs.

2.5. Computational Fluid Dynamics and the need for an experimental Data Base

There are several papers in the past few years presenting computational studies of circulation control technologies[28]. Most of them have focus on 2D studies. While there are a number of excellent 2D experimental datasets available for such CFD validation, the same is not true for 3D experimental data. This effort aims to address this short fall by creating a comprehensive and relevant 3D database for current and future 3D simulations.

3. Wind Tunnel Test Overview

3.1. AMELIA Design

In order to convert the Configuration 1 geometry (as defined in Section 2.1) into AMELIA and use the geometry in a large-scale wind tunnel test setting, many design modifications to the concept design were needed. The most significant alteration to the geometry came in the mounting system of the wind tunnel model. A sting was chosen as the ideal method to measure aerodynamic forces and moments, mainly for its ability to take measurements non-intrusively. Direct mounting of the model to the sting through the aft end raised concerns with disturbing the flow around the beaver tail. An underbody mount was designed to

provide an attachment location with minimal flow disturbance. The mount was faired with a clamshell blade that extends vertically from the sting tip. The blade mount also serves to extend the negative angle of attack limit. Figure 3.1 shows a three view drawing of the model mounted to the blade attachment with empennage removed and relevant dimensions shown. The tail empennage is not shown in the three-view because it was not attached to the model during testing in order to reduce the complexity of the tunnel model for computational modeling. The strakes, structural rudder and V-tail as seen in Figure 3.2 were manufactured in order to supplement subsequent research and testing. These surfaces attach to the model via off blocks.

The selected configuration utilizes an optimized supercritical airfoil with a dual radius flap at the trailing edge. In order to minimize cost and complexity of the model, dual radius flaps of 0º, 30º, 60º and 90º deflections were proposed, as opposed to a mechanical flap where the deflection angle can be varied. The 90º flap deflection was later changed to 80º due to issues with the manufacturing of the flap with the appropriate blowing slot height. The flaps of the Configuration 1 design were also modified to be a single continuous flap for each wing, in order to reduce the amount of flow disturbance from discontinuities of the flap surface as well as allowing for less complicated configuration changes while the model is mounted on the sting. A cut away view of the model, with the 0° and 80° flap, is shown in Figure 3.2. Figure 3.2 also highlights many of AMELIA's unique features, such as the internal flow control systems, the balance block, and the support structure for the over the wing mounted engines. Sections 10.0 and 11.0 will go into greater detail in the internal design, the low- and high-pressure systems, and the instrumentation of AMELIA.

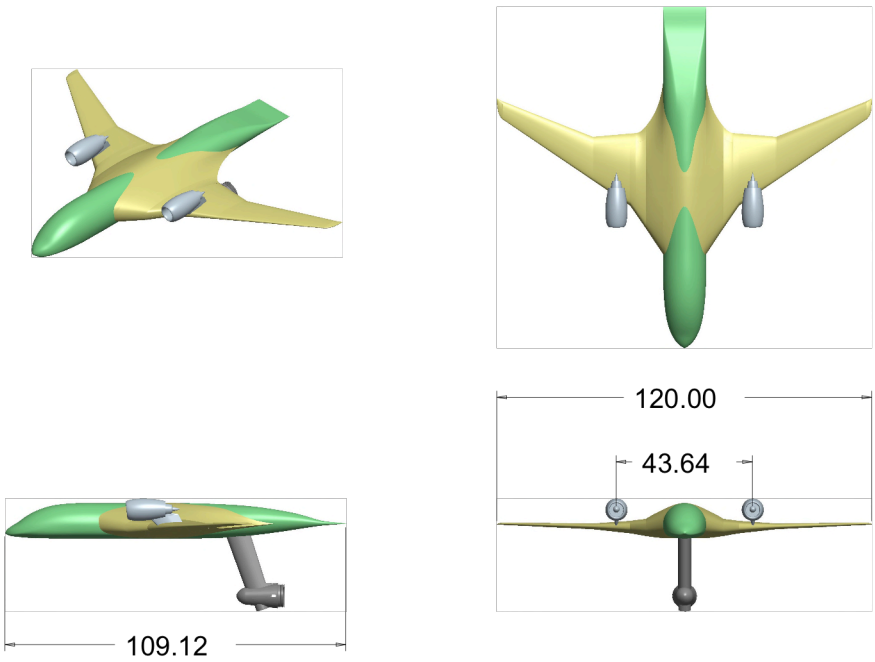

*Note: All Dimensions In Inches

Figure 3.1. A three-view drawing of AMELIA with sting-blade attachment and tail surfaces removed.

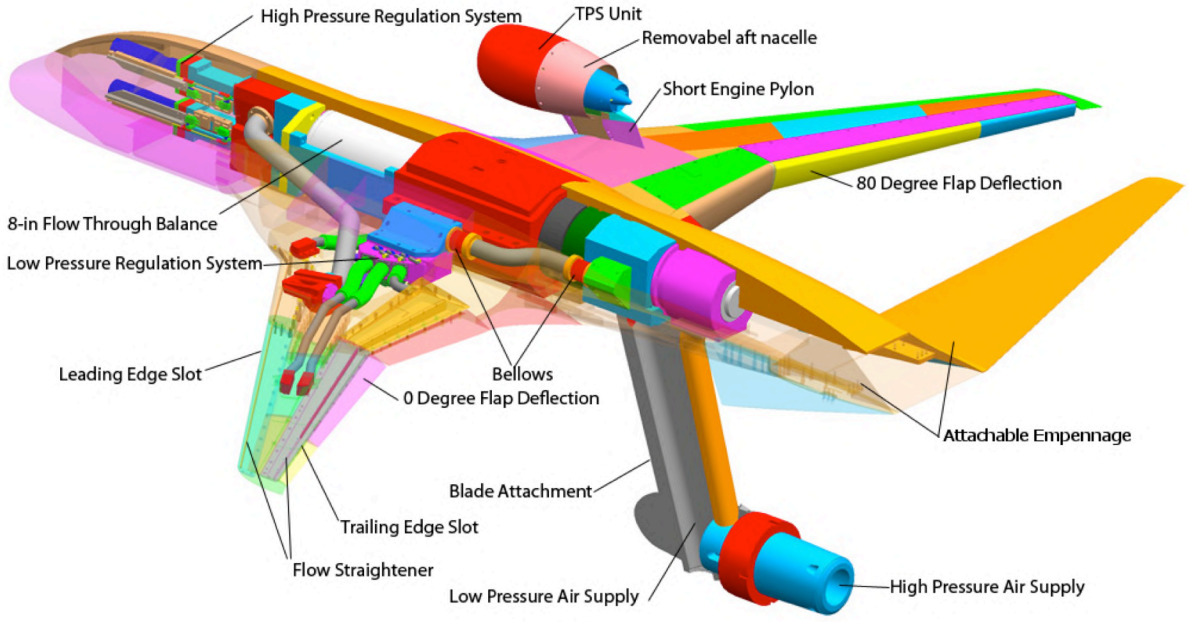

Figure 3.2. A section view of AMELIA revealing the complex internal components and highlighting the flow system for the powered lift system and the flow-through balance.

3.2. Wind Tunnel Test Facility

The National Full-Scale Aerodynamic Complex (NFAC) 40 ft by 80 ft wind tunnel was chosen to perform the 8-10 week long wind tunnel test. The NFAC offered several benefits over other large wind tunnels across the country, with the most significant being: the 10 foot model could be mounted on a sting which allows for cleaner measurements of the produced aerodynamic forces and moments, the tunnel could supply the high pressure air at the mass flow rate necessary to operate the CCW slots and the turbofan simulators, the tunnel is large enough such that the downwash created by the CCW wings would not impinge on the floor of the tunnel thus creating cleaner far-field acoustic measurements, the tunnel was acoustically treated such that aerodynamic and acoustic measurements could be performed simultaneously, and the NFAC's cost and schedule fit within Cal Poly's time frame and budget. Figure 3.3 shows a scale schematic of the model mounted on the sting in the 40 ft by 80 ft NFAC wind tunnel with an early concept of the associated acoustic measurement devices mounted on the tunnel floor relative to the wind tunnel model placed in the center of the tunnel. Also depicted in Figure 3.3 is a preliminary CFD result of the flow features expected from the interaction of the upper surface blowing and the circulation control powered lift system. The downwash of the powered lift system is estimated to be approximately a full span down from the model. Using a smoke wand and capturing the streamlines at several vertical locations, the wake created by the circulation control wing were observed.

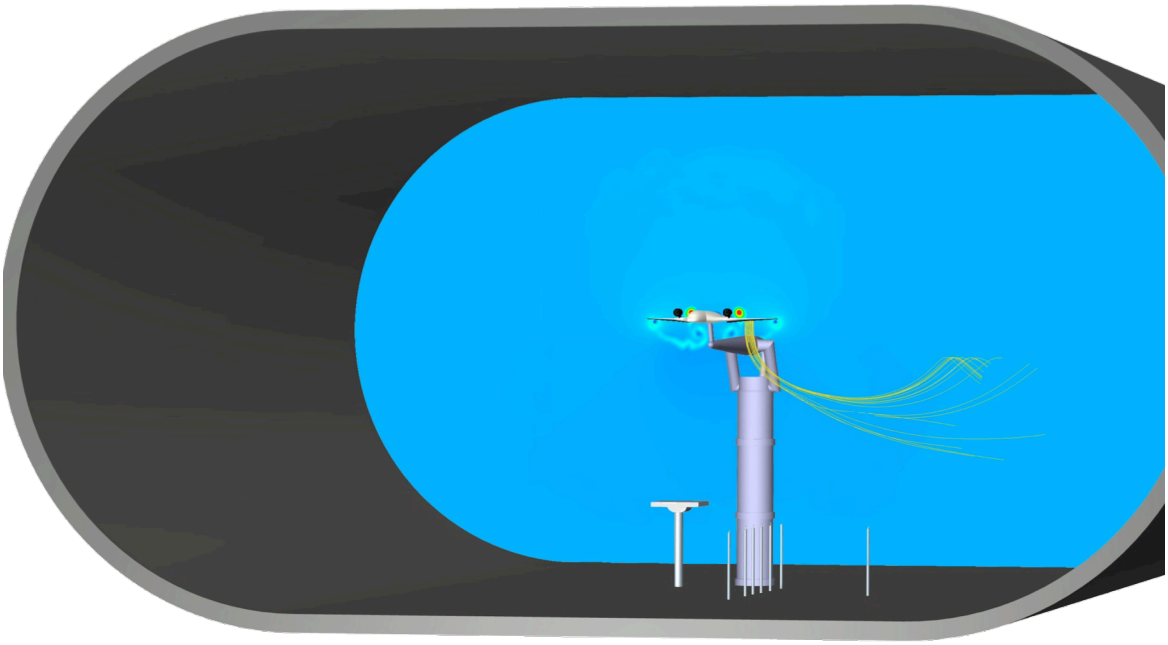

Figure 3.3. Early schematic of the model mounted on a sting in the NFAC 40 ft by 80 ft wind tunnel along with the far-field microphones and the stationary array mounted on the tunnel floor.

3.3. AMELIA Personnel

This project was a collaborative effort between educational intuitions, professional organizations, as well as individuals from NASA Ames Research Center and NASA Langley Research Center. Cal Poly lead the project while Georgia Tech Research Institute (GTRI), DHC Engineering, ES Aero, and Paterson Labs were subcontractors. Several students also worked on the project leading to a number of master's theses and senior projects. Table 3.1 is a complete list of students and professional who contributed to the AMELIA project along with their affiliation.

Table 3.1. List of AMELIA Participants

Name	Affiliation
Greg Altmann Cassy Anthony Richard Balatbat Tyler Ball Brett Behrends Rob Bulmahn Bryan Costanza Jason Daniel Michael Green Fletcher Hartshorn Joun Kim Greg McKenzie Elaine Schreiber Scott Turner Dustin Quint	Cal Poly Students

Bryan Blessing Bobby Ehrmann Rory Golden Jay Marcos Kevin Lane Jon Lichtwardt Eric Paciano John Pham Travis Storm Andrew Welborn	Cal Poly Graduate Students
Tina Jameson David Marshall Mark Waters	Cal Poly Professors
Dave Hall	DHC Engineering
Phil Johnson Dave Mason Jay Paterson	Patersonlabs
Rob Fong Ted Garbeff Craig Hange Clif Horne Kevin James Greg Jones Rabindra Mehta Bob Lockyer Barry Porter Mike Rogers Joe Posey Jim Ross Greg Zilliac Nate Burnside	NASA
Bob Englar Rick Gaeta Warren Lee Don Nance	Georgia Tech Research Institute
Trevor Foster Andy Gibson	ES Aero
Chris Hartley Charlie Rogers Joe Sacco Jeff Johnson Dave Dustenhauser	AEDC / NASA 40 ft x 80 ft Wind Tunnel Management

The wind tunnel test team consisted of Project PI Dr. David Marshall, test lead Dr. Tina Jameson, and graduate students Jonathan Lichtwardt and Eric Paciano from Cal Poly. Rob Fong, Nate Burnside, Clif Horne were the designated test team from NASA while Ted Garbeff, Batty Porter, and Kevin James were test support from NASA Ames Research Center.

4. Model Description

4.1. Design Considerations

The AMELIA wind tunnel model design stemmed from the larger body of research conducted during the first year of the grant aimed at developing a concept for a cruise efficient short take-off and landing aircraft. Four very different concepts were traded, including a traditional tube and wing design, hybrid and full blended wing body configurations, and a diamond box wing design. These concepts are shown in

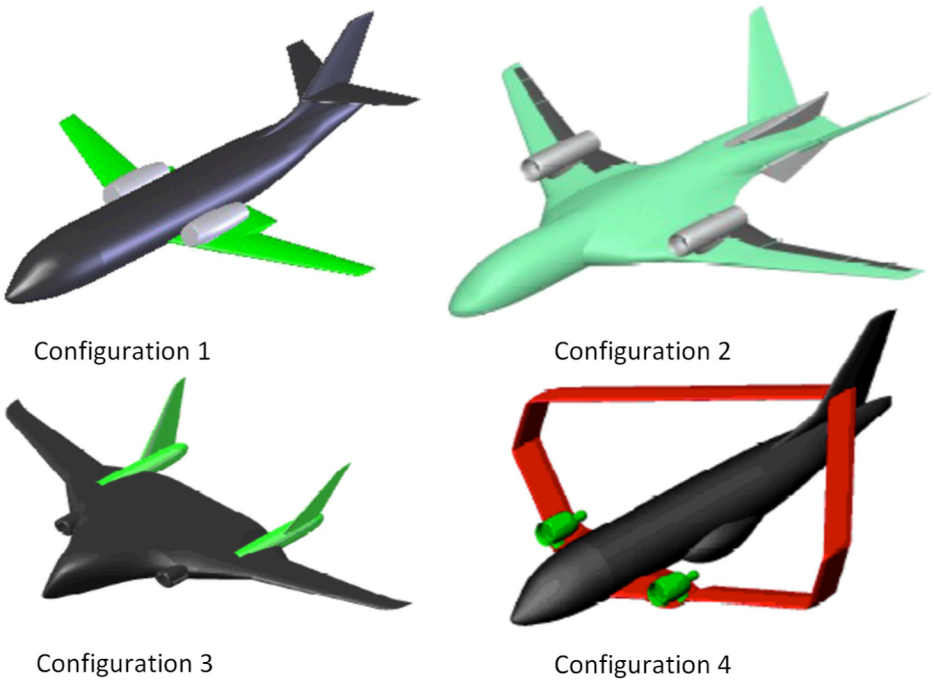

Figure 4.1. The results of the year 1 conceptual design study.

Figure 4.1.

After close consideration of each design, it was apparent that Configuration 1 was too conventional to be an N+2 design. Configuration 4 on the other hand was too advanced to be considered within an N+2 time frame. A large scale wind tunnel test, being conducted by a competing NRA utilized a model that was similar to Configuration 3 in that it was a blended wing body with circulation control wings[3].

Configuration 2 was considered to be at the appropriate level for the N+2 time frame. Further investigations into this design also showed that a 10 ft span model based on Configuration 2 would not exceed the load limits of all our perspective test locations. After consulting all involved in the project, it was decided that Configuration 2—the hybrid blended wing body—was best suited for the AMELIA test[2,3]. Figure 4.2 shows the final concept model for AMELIA. Not clearly apparent in the rendering are this configuration's circulation control slots, which allow this concept to be considered "high lift".

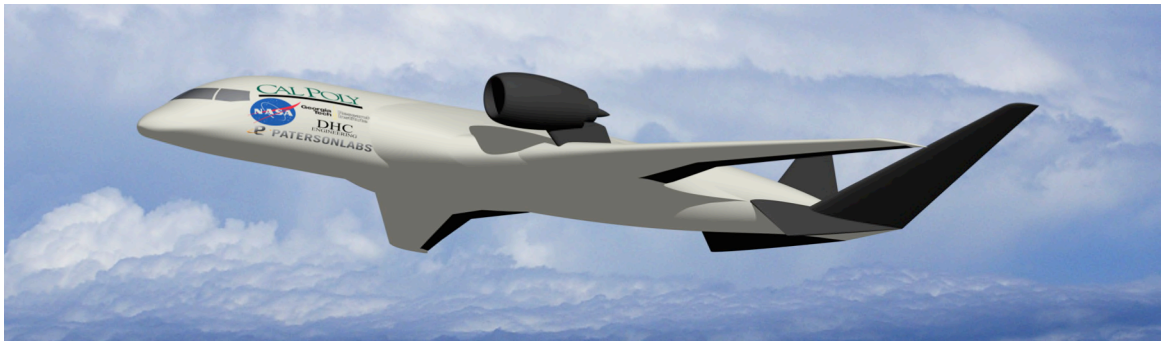

Figure 4.2. Final AMELIA concept rendering.

In order to utilize the concept geometry in a large scale wind tunnel test setting, many design modifications were needed. The most significant alteration to the geometry came in the mounting system of the wind tunnel model. A sting was chosen as the ideal method of support, mainly because of its ability to non-intrusively support the model. Direct mounting of the model to the sting through the aft end raised concerns with disturbing the flow around the tail. An underbody mount was designed to provide an attachment location with minimal flow disturbance.

The physical size of the wind tunnel model was largely influenced by section 4.14 of the contract's statement of work, *"The size of the wind tunnel model shall be at least 8-foot span (4 foot half span), but may be larger if required for the associated wind tunnel in which the model will be tested"*[1]. Another primary driver of the wind tunnel model's overall size was consideration for the manufacturability of the circulation control slots. A $1/11^{th}$ scale wind tunnel model was determined sufficient with a span of 10ft and minimum slot height of 0.012 inches.

The wind tunnel model was originally intended to be manufactured solely out of stainless steel, in order to permit the utilization of this model across a large range of dynamic pressures. During manufacturing, however, the decision was made to make many of the larger sections from aluminum as a means to minimize fabrication cost.

AMELIA was designed to be as modular as possible. For instance, the tail surfaces can be removed from the model and be replaced by off-blocks that follow the tail contour, allowing tail-on and tail-off testing. Testing with different engine heights can also be achieved through the use of different sized pylons. Testing without engines is also an option on AMELIA, however this requires some work to cover the footprint of the pylon in the skin. Figure 4.3 shows the many components of the AMELIA wind tunnel model.

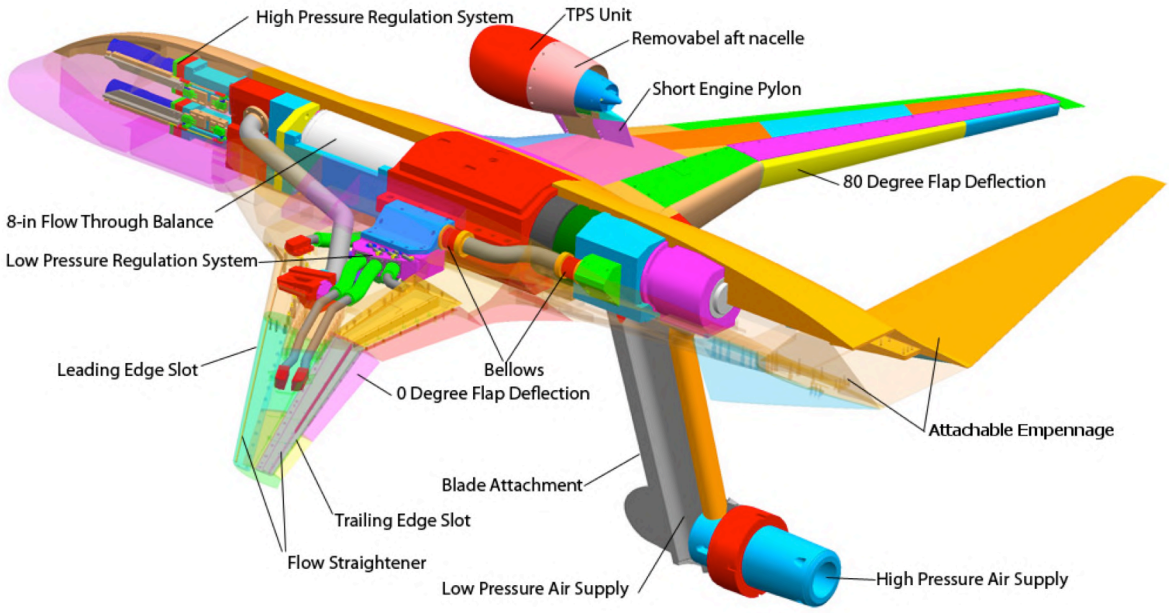

Figure 4.3. Internals of AMELIA model.

4.2. Balance

The aerodynamic loads were measured using a MC-130 8.0 inch diameter Air Balance manufactured by Triumph Aerospace, Force Measurement Systems. The six-component force balance has two internal air flow paths and one external flow path which utilizes a system of welded bellows to isolate forces. The load limits of the balance can be seen in Table 4.1. (For a detailed discussion of the internal balance and its calibration see Reference 4).

Table 4.1. Load limits of the 8" flow through balance.

Force Component	Balance Limits
Normal Force	11,000 lb_f
Axial Force	900 lb_f
Side Force	2000 lb_f
Rolling Moment	1667 ft-lb_f
Pitching Moment	7563 ft-lb_f
Yawing Moment	1375 ft-lb_f

AMELIA was originally designed to accommodate a smaller 6-inch flow through balance; however the force isolation of the flow paths came into question during the critical design review. The 8-inch balance was incorporated into the design in late 2009 to address the issues identified in the Critical Design Review(papers and reports prior to 2009 still show the 6-inch balance).

4.3. Engine Simulators

With the inclusion of circulation control technology on AMELIA, Cal Poly consulted their partners at Georgia Tech Research Institute for advice on potential areas of research. A wind tunnel test at GTRI suggested further research was needed in the interaction between engine exhaust and over-the-wing

circulation control flow. In order to simulate engine flow on the AMELIA model, various methods were researched including injectors, flow-through nacelles, and turbine propulsion simulators (TPS units). TPS units were selected for their ability to most accurately simulate the inlet flow and the exit flow of both the fan and core.

Tech Development Inc. Model 441 simulators were selected for use on the AMELIA model. On loan from NASA Langley Research Center, these units were manufactured in the 1960's and have been used on many prior wind tunnel tests. The TPS units are powered by compressed air delivered to the wind tunnel model by the tunnel's supply. The maximum mass flow rate each unit can accept is 2.1 lbs/sec at 425 psig, under these conditions the units operate at 45,000 RPM. The units were calibrated in 2011 by GTRI (more information on this can be seen in the *Turbofan Propulsion Simulator* section of this report). The aft and forward ends of the TPS units can be seen in Figure 4.4 and Figure 4.5.

Figure 4.4. Aft end of a Model 441 showing core and fan exits.

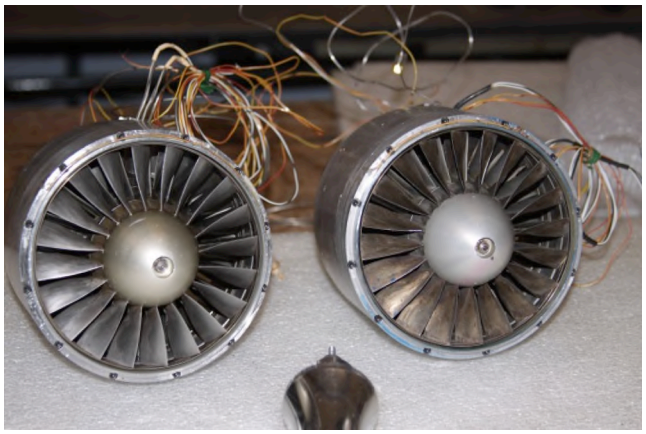

Figure 4.5. Fan inlet of the Model 441 simulators.

4.4. Slot Blowing

One of the more unique aspects of the AMELIA model is the design's utilization of circulation control to achieve high lift. The process of actively controlling the circulation around the wing is achieved by ejecting high momentum air from slots running nearly the entire span of the wing. These slots are located near the trailing edge just above the flaps. The AMELIA model also has slots at the leading edge of the wing, which are primarily used to maintain flow attachment. Figure 4.6 shows a cut view of AMELIA's airfoil, plenums inside the model at the leading- and trailing-edge distribute air to the circulation control slots. Each plenum contains a barrier of metal foam and rigimesh which acts as a flow straightener (for more information on the circulation control flow quality see the *Slot Blowing Performance and Calibration* section).

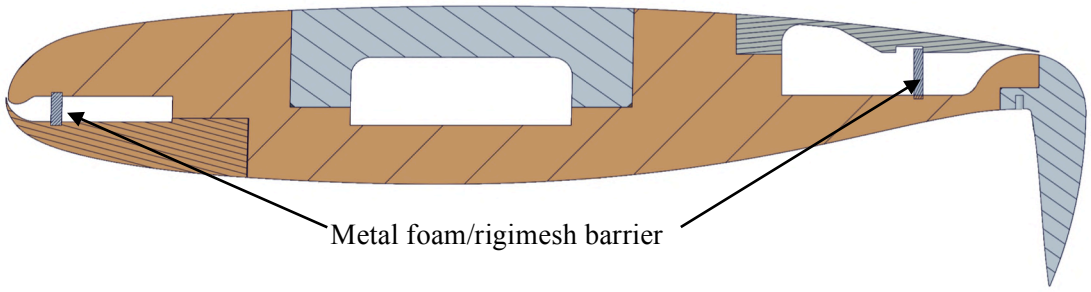

Figure 4.6. Cut view of an inboard section of AMELIA's wing with an 80 degree flap deflection.

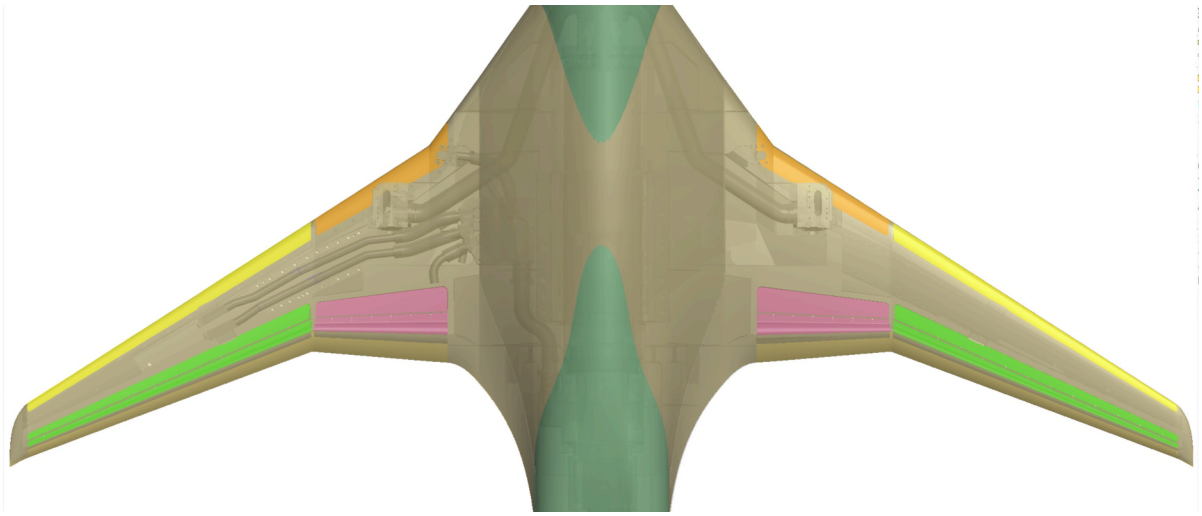

Figure 4.7. AMELIA's eight circulation control plenums as seen from above.

Figure 4.7 highlights the location of each of the eight circulation control plenums. As shown, circulation control acts on the majority of the wing, however a break in the plenums creates a small un-blown region. The slot height is a significant variable in calculating the discharge coefficient (C_μ), which is often considered a critical parameter in circulation control and powered lift discussion. Given this variables importance[22], the trailing edge slot was manufactured with a set-screw/tie-down system that permits adjustment of the slot height at multiple locations along the span of the model. Figure 4.8 shows a cut view of AMELIA's set-screw/tied-down system, with the set-screw in black and the tie-down shown in grey. The set-screw is screwed in through the lower surface panel until it touches the underside of the upper surface panel. With the set-screw resisting any compression of the plenum, the tie down (a flat head cap screw) is threaded into the underside of the upper surface, securing the plenum from expanding. Once

the appropriate slot height was set, and verified, the set-screw and tie-down were permanently secured using Loctite.

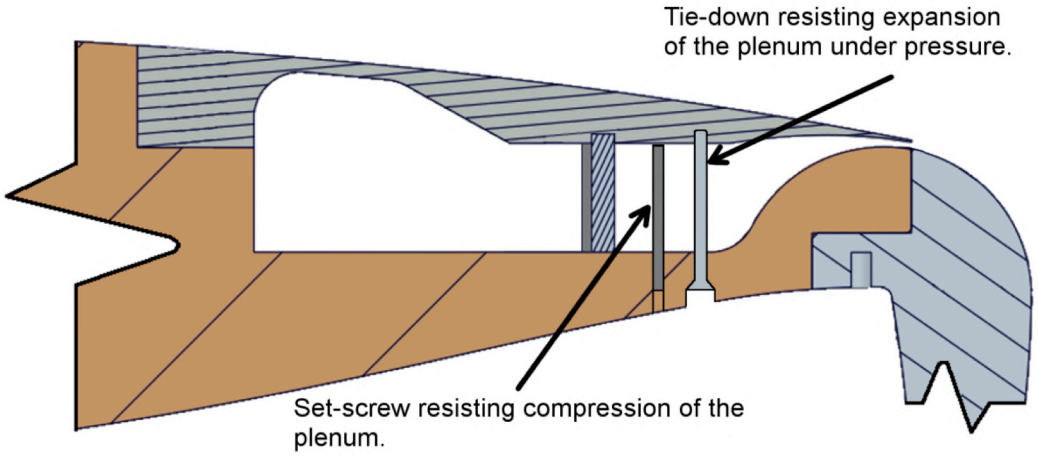

Figure 4.8. Set-screw/Tie-down system for setting slot height.

The leading edge slot however, as a result of the thickness of material required in the lower panel, does not have the set-screw/tie-down system. The leading edge slot height (or more appropriately *width* in this case) was fixed throughout the entirety of the wind tunnel test.

4.5. Physical Layout

The model is supplied using two separate air systems for the propulsion simulators and the blown slots. Figure 4.3 shows a complete cut-away schematic of the model revealing the internal piping for both the high- and low-pressure systems.

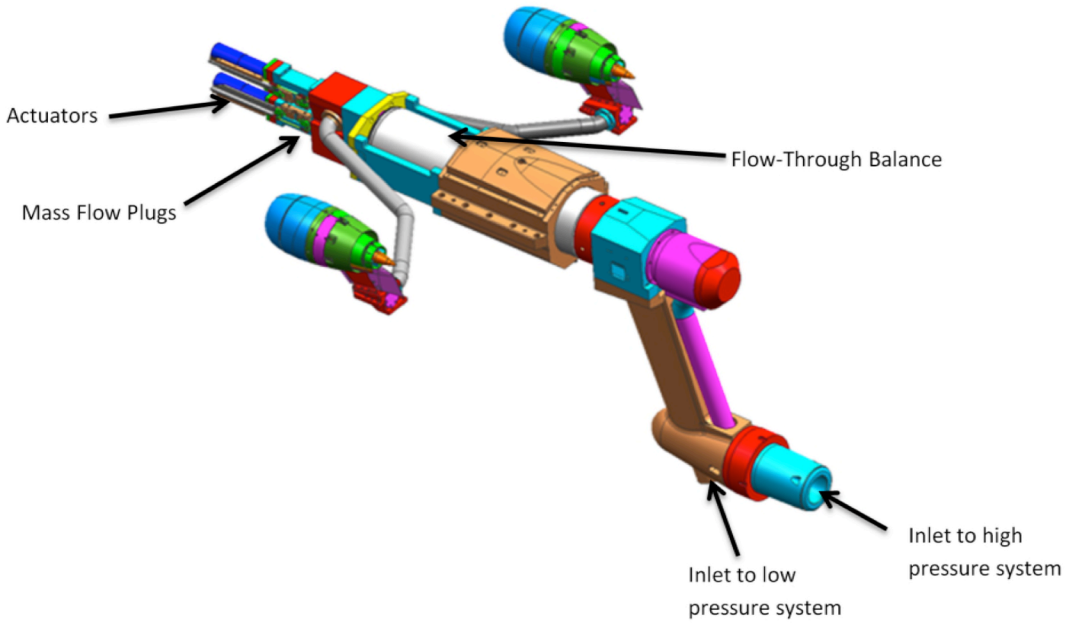

Figure 4.9. AMELIA's high pressure air supply system.

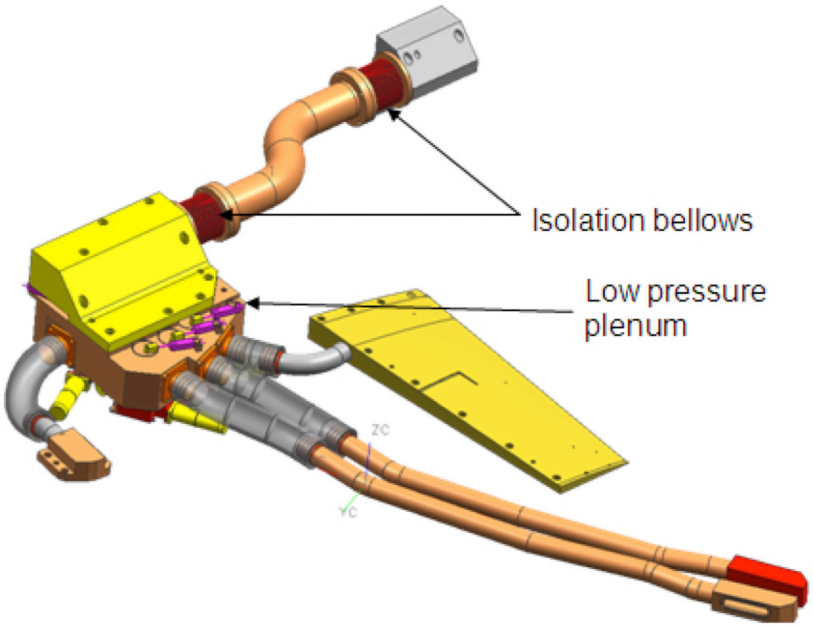

Figure 4.10. AMELIA's low pressure air supply system.

The high pressure air system (600 psi maximum determined by the limits of the flow through balance) is supplied through the sting and into the fabricated strut. The air passes up the strut and through the 8in flow thru balance. Forward of the balance is a mass flow plug system that controls the air flow to the left and right TPS units. The conical plugs are driven using MMP 24vdc gear motors, and use linear potentiometers for position feedback. The plugs can be positioned to provide from 0-100% mass flow. The TPS units are supplied through stainless steel pipes that attach to wing mounted pylons. Figure 4.9 shows the complete piping and flow control assembly for the high pressure air system along with the sting-blade attachment.

The low pressure system (approximately 100 psi) supplies air to the eight plenums that feed the circulation control slots at the leading and trialing edges of the wing. The low pressure system is controlled using 24vdc gear motors driving 4 butterfly valves per wing, with rotary potentiometers for feedback. The flow to each plenum can be controlled individually via butterfly valve from the control room. To isolate and minimize adverse effects on the balance the low pressure plenums are each fed by a pipe that has bellows at both ends of the pipe, as shown in Figure 4.10.

4.6. Wing Design

A NASA SC(2)-0414 airfoil, modified to accommodate the circulation control slots, and dual radius flaps is used throughout AMELIA's 10ft span. This super critical airfoil was selected for its large leading edge radius, and the ease of circulation control integration. The original airfoil (shown in blue) with the modified (pink) airfoil can be seen in Figure 4.11[5].

Figure 4.11. AMELIA's modified airfoil (pink) over the original NASA SC(2)-0414.

In order to obtain the unconventional "hybrid blended wing body" status, the wing root is nearly as thick as the fuselage—this fact along with a few other unique aspects of the wing make characterizing typical values like reference area and mean aerodynamic chord difficult to define. A list and figure (Figure 4.12 and Table 4.2) show the values used for reference.

Table 4.2. Significant wing dimensions.

C_{tip}	5.7 in
C_{root}	32.7 in
S_{ref}	15.8 ft^2
$C_{wing\ break}$	14.1 in
b (span)	10 ft
AR	6.33
MAC	22.4 in
Taper Ratio	0.174

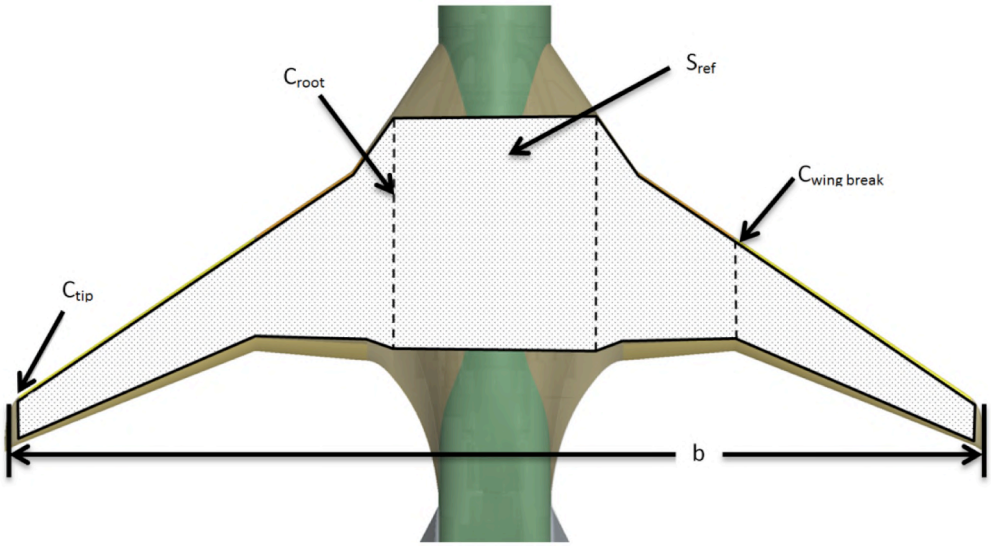

Figure 4.12. AMELIA's wing reference area and a few important dimensions.

4.7. Dual Radius Flaps

One of the critical aspects of AMELIA's high lift generation is the model's dual radius flaps, which can be seen to some extent in Figure 4.3 and Figure 4.6. These flaps are designed to take advantage of the Coanda effect at the exit of the trailing edge slot. In order to minimize the complexity of the mechanics required within the wind tunnel model, fixed flaps of 0, 30, 60 and 80 degree deflections were manufactured. The flaps on each wing are broken down into inboard, midboard, and outboard sections, as can be seen in Figure 4.3. (For detailed discussion on the design of AMELIA's dual radius flaps see Reference 6).

4.8. Surface Finish

Early in the planning of the wind tunnel test, it was decided that obtaining a data set of global skin friction values was of primary importance. The chosen method of obtaining these values was the Fringe-Imaging Skin Friction (FISF) technique. One of the requirements of the FISF technique is that the model have a #2 surface finish (mirror like) or better[7], which lead the first design of AMELIA to have a nickel plated surface. A FISF test article representing a simplified version of AMELIA's blended wing can be seen in Figure 4.13 with a nickel plated surface.

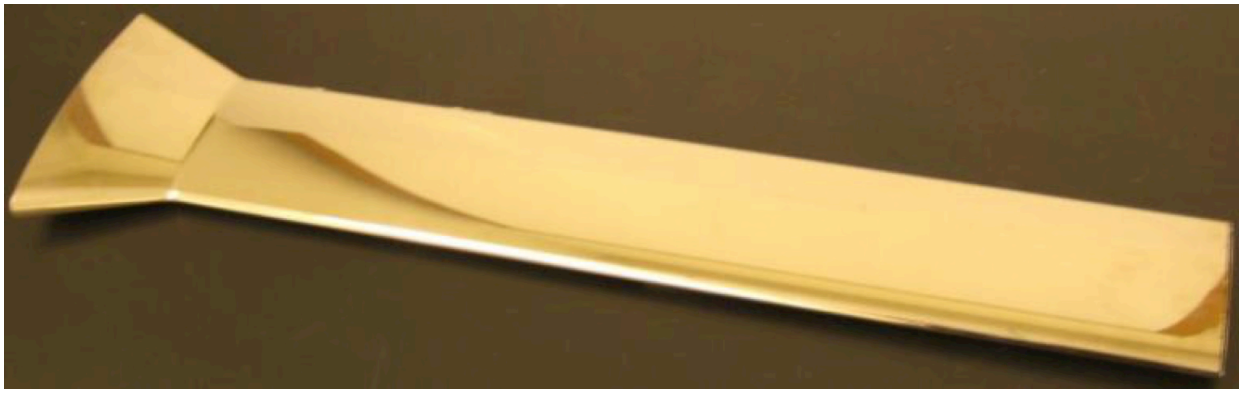

Figure 4.13. FISF test article with nickel plated surface.

Although the nickel plated surface produced excellent fringes during preliminary FISF testing, it was determined that many portions of the AMELIA model were too large to fit in available nickel plating baths. Patersonlabs instead suggested the use of DuPont Imron polyurethane enamel with black pigment. After many successful FISF tests with an Imron sample, the surface treatment was chosen to be applied to the AMELIA model. The Imron also had the added benefit of being extremely durable, and maintaining its reflectivity despite frequent cleaning. Figure 4.14 shows the final surface treatment of the wind tunnel model.

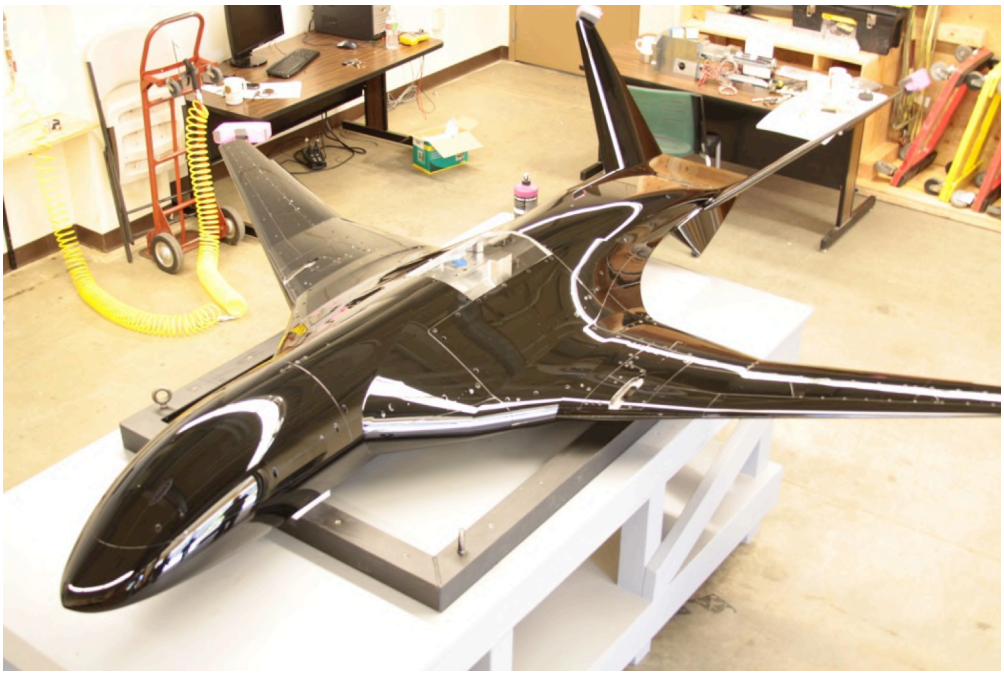

Figure 4.14. AMELIA's highly reflective Imron enamel surface treatment.

4.9. Empennage

The tail surface of the wind tunnel model can be seen in Figure 4.14. As previously mentioned, these surfaces can be removed and replaced with covers that follow the aft end contours. In an effort to minimize complexity and bring the focus of the wind tunnel data on the effects of circulation control and the other design features of AMELIA, all wind tunnel testing was conducted without the tail surfaces. Figure 4.15 shows the wind tunnel model as tested—without tail surfaces.

Figure 4.15. AMELIA installed in the tunnel with empennage removed.

4.10. Blade Attachment

In order to facilitate clean aerodynamic flow at the aft end of the model, a blade attachment was used at the model/sting interface. The blade has no angular offset and thus does not affect the models angle of attack, it does however offset the model vertically 24.5", and forward 9.10". The blade also serves as the passage for the high and low pressure air supplies, as shown in Figure 4.16. The low pressure air is delivered to the model through the main portion of the blade, while the high pressure air is routed externally on the aft end of the blade. A sheet metal cover was designed to fare the aft end of the blade, however the fairing could not safely accommodate the instrumentation bundles. Wind tunnel tape was applied to the blade as a replacement for the fairing.

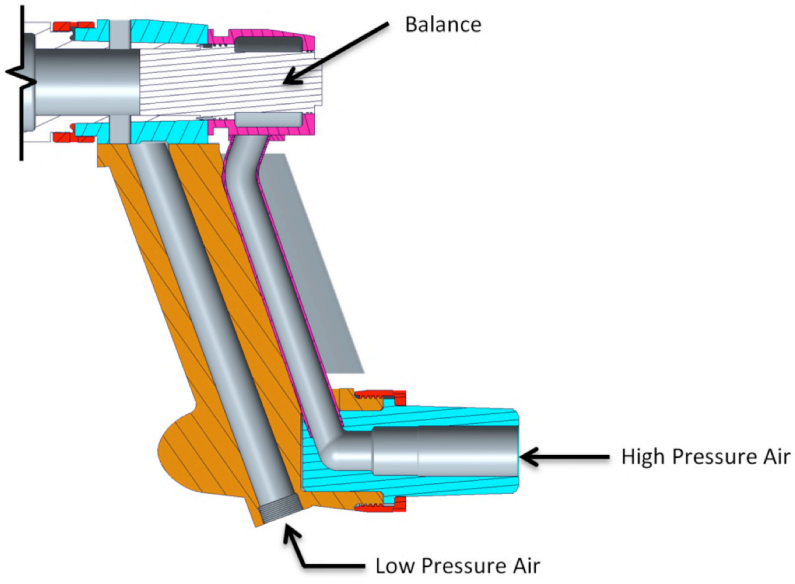

Figure 4.16. Section view of the blade supporting the model.

5. Test Facility Description

5.1. Wind tunnel

Figure 5.1. Aerial View of the National Full-Scale Aerodynamics Complex (image courtesy of the NFAC).

The AMELIA Model was tested in the 40- by 80-Foot Wind Tunnel. Despite the relatively small 10 ft span of AMELIA, the large test section was required in order to accommodate the downwash created by AMELIA's circulation control wings, which can persist for several spans below the model. As the overall goal of this effort was to gather a dataset for CFD validation, the complex flow associated with jet impingement on a tunnel wall was highly undesirable.

The National Full-Scale Aerodynamics Complex (NFAC), Figure 1, is a unique facility primarily used for determining aerodynamic characteristics of large-scale and full-scale rotorcraft, fixed wing and powered-lift V/STOL aircraft, as well as testing of wind turbines, parachutes, trucks, and other non-traditional types of testing. The facility is located at Ames Research Center, Moffett Field, CA, and is managed and operated by the U.S. Air Force's Arnold Engineering Development Center (AEDC).

The NFAC is comprised of the largest wind tunnels in the world, the 40- by 80- Foot Wind Tunnel and the 80- by 120-Foot Wind Tunnel. The 40- by 80-Foot Wind Tunnel has a closed test section with semicircular sides and a closed-circuit air return passage. The 80-by 120-Foot Wind Tunnel is an non-return tunnel with a closed test section that is rectangular in cross-section. The two test sections share a common fan drive system. By adjusting the position of vane sets, the airflow can be directed through one test section or the other (40x80 or 80x120). The air in the tunnel is driven by six 40-foot diameter, 15-

bladed, variable-pitch fans, each powered by a 22,500-hp motor. The maximum speed in the 40- by 80-Foot Wind Tunnel test section is 300 knots, while the maximum speed in the 80- by 120-Foot Wind Tunnel test section is 100 knots.

Actual test section dimensions for the 40- by 80-Foot Wind Tunnel are 39 feet high, 79 feet wide (at the horizontal center line), and 80 feet long. The test section dimensions for the 80- by 120-Foot Wind Tunnel are 79 feet high, 119 feet wide, and 170 feet long. Both the 40- by 80- and 80- by 120-Foot Wind Tunnel test sections are lined with sound absorbing material to permit acoustic and aerodynamic data to be acquired simultaneously[8] although the 40- by 80- has more extensive treatment.

5.2. Model Support (sting mount)

AMELIA was mounted to the NFAC sting mechanism using the 13' sting, as shown in Figure 2. The model is connected to the sting through a load path which includes the eight component balance (three forces, three moments, two air pressures) and blade with tapered mating attachment points at both ends. The blade is an offset height adapter between the sting and the non-metric side of the balance, raising the model centerline 24.5" above the sting's centerline. The balance bolts directly onto the model center body, so the model is cantilevered off the end of the sting/blade/balance assembly with a series of tapered mates between.

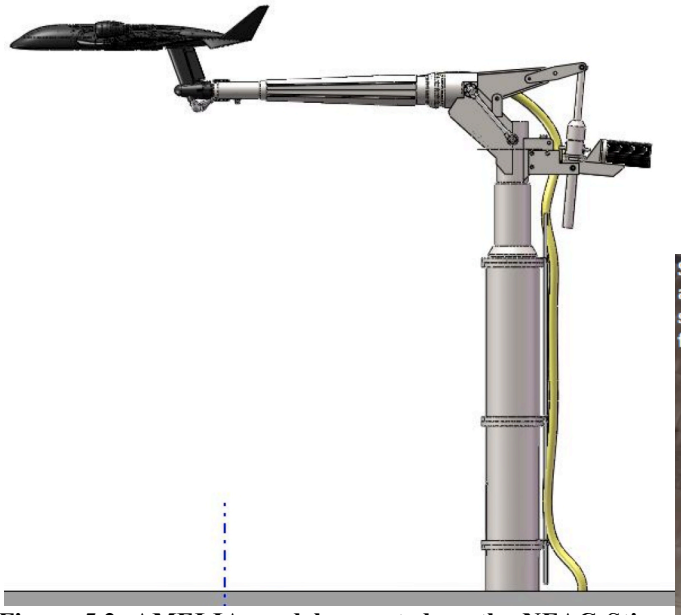

Figure 5.2. AMELIA model mounted on the NFAC Sting Model Support System using 13' Sting Arm

The NFAC sting mechanism is designed to flow high pressure air thru the sting model support. Prior to testing, all of the internal sting tubing was hydro-tested to 1.5 x max working load. The working load limit of the sting air delivery system is 1000 psig as configured for the AMELIA test.

Figure 5.3. Photo showing model support system and slot blowing air routing.

5.3. High Pressure Air

The AMELIA test utilized the NFAC's High Pressure Air System (HPAS). In the 40x80 HPAS, dry, heated air was delivered to AMELIA in two separate lines, each controlled by a 14-poppet digital valve assembly. The digital valves are controlled independently to control for pressure or flow rate. HPA was supplied to the model in two paths, one terminating at the engine simulator units and the other at the slot-blowing plenums. Each path was split inside the model to supply air to the left and right slot blowing plenums or engine simulators. The engine simulators were provided air at conditions ranging up to 190 psig and 2 lbm/s (total) at 110°F, while the slot-blowing system was fed up to 210 psig and 2.8 lbm/s (total) at 110°F. The HPA paths through the model are shown in Figure 3. Air for slot blowing is routed externally up the sting pitch support through a 3" diameter, 50' long steel braided flex hose. The flex hose connects to a three foot straight section of rigid pipe and an orifice plate flow-meter. The orifice plate allows the system to run at a higher upstream pressure, which reduces the flow speed to meet the rating of the flex hose. It also served as a redundant mass flow measurement device. Air for the engine simulators was routed through the internal flow path of the sting model support.

6. Test Parameters

6.1. Test Parameters

The test parameters for the large-scale wind tunnel test included several different physical model changes as well as varying several operational set points for certain model components. Described in Table 6.1 is each variable parameter, mechanism, range, and the justification for each component and how it was manipulated. The engine height and circulation control flaps were physical model changes. The model changes were scheduled to have the least amount of impact to the schedule. With the exception of the critical test points (as explained in Section 6.2), the flaps were changed at the end of a day while facility walk-throughs, maintenance, and general daily shut down operations were performed. The engine pylon height changes were significantly more involved and were performed only twice to minimize tunnel down time.

Wind tunnel speed, model attitude, engine simulator RPM, and circulation control mass flow were NFAC facility managed parameter changes. NFAC staff physically made the manipulations with oversight from the Cal Poly test team. Both the engine simulator set points and the circulation control set points were manipulated by increasing or decreasing the mass flow in the low and high pressure systems (see Sections 10.0 and 11.0 for more detail). The engine simulator RPM was directly related to the mass flow; the tunnel operator would adjust the mass flow and temperature of the high pressure system in order to set the RPM condition of the engine simulator.

Table 6.1 AMELIA Test Parameters

Parameter	Mechanism	Range	Justification
Engine Height	Mechanical: model pylon change	Low: 2.75 in High: 4.75 in	Investigate aerodynamic and aeroacoustic impacts to performance
Engine Simulator RPM	Pneumatic: Tunnel mass flow	0 % to 77% 0 RPM to	Investigate system performance
Model Attitude	Mechanical: sting pitch	-5 degrees to +25 degrees	Investigate system performance
Circulation Control Mass Flow	Pneumatic: Tunnel mass flow	0% to 100% 0 lbm to 2.8 lbm	Investigate system performance
Circulation Control Flaps	Mechanical: model flap change	0 degrees 30 degrees 60 degrees 80 degrees	Investigate circulation control performance
Wind Tunnel Speed	Mechanical: fan drive change	0 kts 40 kts 60 kts 100 kts	Investigate system performance

The wind tunnel speeds for the AMELIA test were chosen based on the engine simulator performance and model size. Figure 6.1 shows graph of the engine simulator thrust coefficient as function of tunnel speed and engine RPM. It was determined that the AMELIA test would investigate the model performance at a thrust coefficient of approximately 2.5. The largest portion of the test will focus on this thrust coefficient which leads to a tunnel speed of 40 kts. Two other tunnel speeds, 60 kts and 100 kts were also investigated to expand the experimental database.

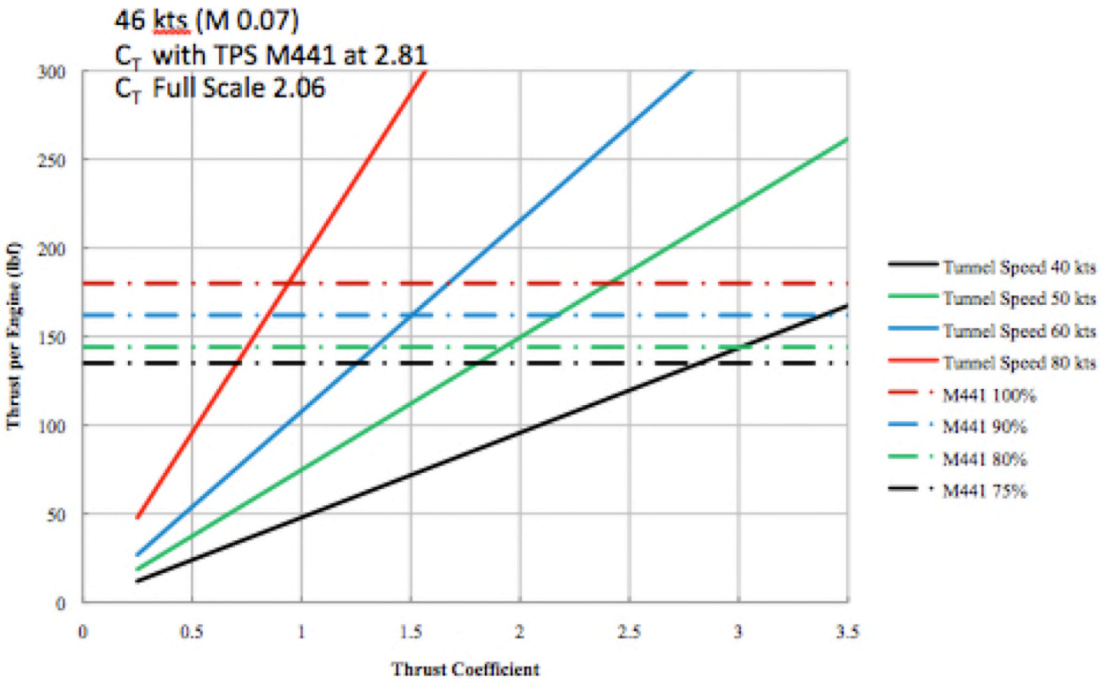

Figure 6.1. Engine simulator thrust coefficient as function of tunnel speed and RPM.

6.2. Test Matrix

The tunnel time for the AMELIA test was scheduled to be 8-10 weeks permitting the final schedule and cost. The final time at the NFAC was approximately 8 weeks of wind on time not including an additional 5 weeks of model preparation in the test section. Table 6.2 through Table 6.9, go into detail of the AMELIA test priorities, critical test points, test matrix runs, and the complete as-run test matrix.

The AMELIA test team wanted to maximize the number of runs for a given model geometry and test priority. Table 6.2 states the final order in which the test was conducted, calling out the phases of the test from low engine pylon height, height engine pylon height, and the clean wing. The testing order described in Table 6.2 may not seem intuitive, however, based on the complexity of the model it was most efficient to start with the TPS units installed and then move to the clean wing configuration once all runs were conducted with the TPS. Due to the internal model design of the test equipment, once the TPS units were removed they could not easily be reintegrated back into the model.

Table 6.2. AMELIA Testing phases with associated engine heights.

Phase	Mile Stones
I - Low Engine Height	Baseline Runs
I	6 Critical Test Points
II	Test Matrix Conditions
III – High Engine Height	3 Critical Test Points
III	Test Matrix Conditions
IV – Clean Wing	1 Critical Test Point
IV	Test Matrix Conditions

During the test planning phase, taking into account all the test parameters and the test variables (schedule, cost, complexity) the test was going to be deemed a success if all 10 critical test points were obtained. The critical test points obtained the most diverse amount of experimental data (aerodynamic forces and moments, external surface pressures, skin friction, far-field acoustic data, local noise, and on-body dynamic measurements) giving the numerical modeling community a limited but in-depth experimental data set. However, as stated above, it was not practical to change engine heights during the critical test point phase, so the critical test points were split and taken with their respective engine height. The general test matrix runs were also important to develop a broader database with a subset of the experimental measurements. The critical test points are shown in Table 6.3 (note: OEI in the Table is "One Engine Inoperative").

Table 6.3. AMELIA Critical Test Points.

#	TS (kt)	alpha	beta	Cμ	Engine Setting	flap	Eng.	Reason
1	100	0	0	0	0%	0	Low	Simple
2	40	0	0	0.36	77%	80	Low	Diverted Landing
3	60	5	0	0.36	20%	80	Low	Landing
4	60	5	0	0.18	77%	60	Low	Takeoff
5	40	5	0	0.10	77%/30%	60	Low	OEI (1)
6	40	5	0	0.10	30%/77%	60	Low	OEI (2)
7	100	0	0	0	0%	0	High	Simple
8	40	0	0	0.36	77%	80	High	Diverted Landing
9	60	5	0	0.36	20%	80	High	Landing
10	60	5	0	0.18	0%	60	Clean	Baseline

Once the model had been mounted into the test section, checked out, and calibrated several pre-runs were taken to insure the quality of data obtained during the test would be satisfactory as well as setting a baseline for data comparison. The AMELIA steps were as follows (not necessary in order):

1. Static tests of all blown features on the model
2. Reynolds number sweep
3. Dynamic pressure sweep
4. Turbofan propulsion simulator sweep
5. Circulation control mass flow sweep
6. Repeat test points

After the completion of the preliminary and baseline sweeps, the critical test points were obtained (as shown in Table 6.2), and then the test matrix points were obtained. Table 6.4, Table 6.5, and Table 6.6 show the text matrix runs for the low engine height, high engine height, and the clean wing, respectively. The test matrix runs were designed to change one model parameter at a time, starting with the parameter that needed the least amount of time to physically modify. Not shown in Table 6.4 through Table 6.6 are (1) the sideslip sweeps were taken for only one tunnel speed and one flap deflection at each engine configuration, as it was projected that the difference in the sideslip would not be significant for each engine configuration (see Section 13.0 for the results). (2) Circulation control mass flow sweeps were taken at each engine configuration for a constant angle of attack of -5^{o}, 0^{o} and $+10^{o}$. Table 6.4 also shows measurements taken at the 30^{o} flap configuration. Only a limited data set was taken at the 30^{o} flap configuration, as it was not the main focus of the test, however it does provide additional data and allows for a more detailed comparison of flap setting and system performance at the 40 kt condition.

Table 6.4. Phase II: Low engine height test matrix.

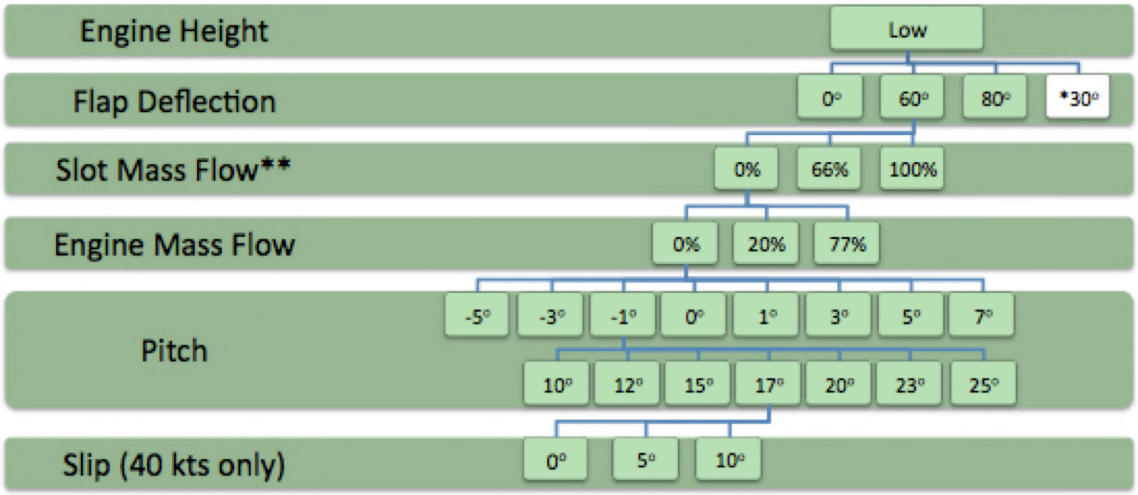

Table 6.5. Phase III: High engine height test matrix.

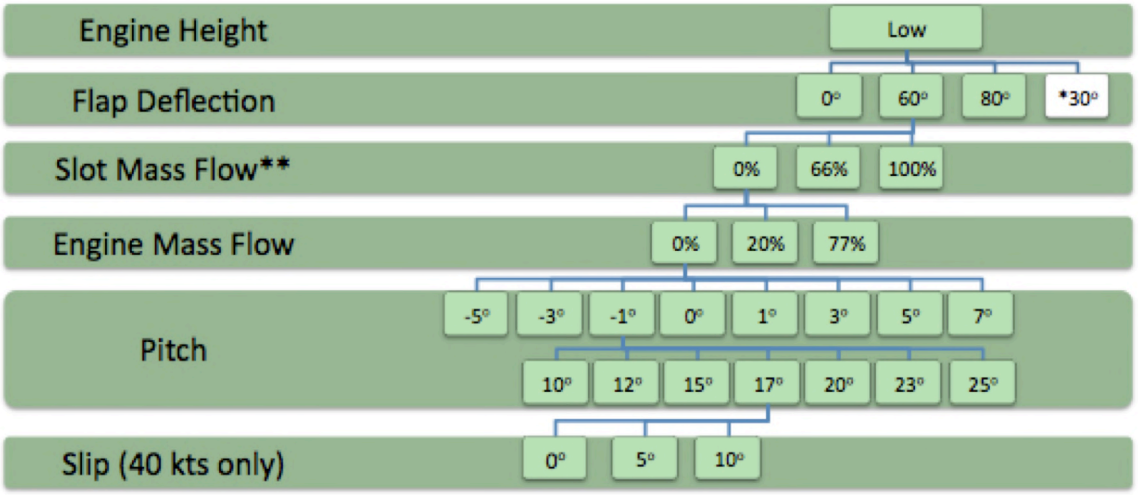

Table 6.6. Phase II: Clean wing test matrix.

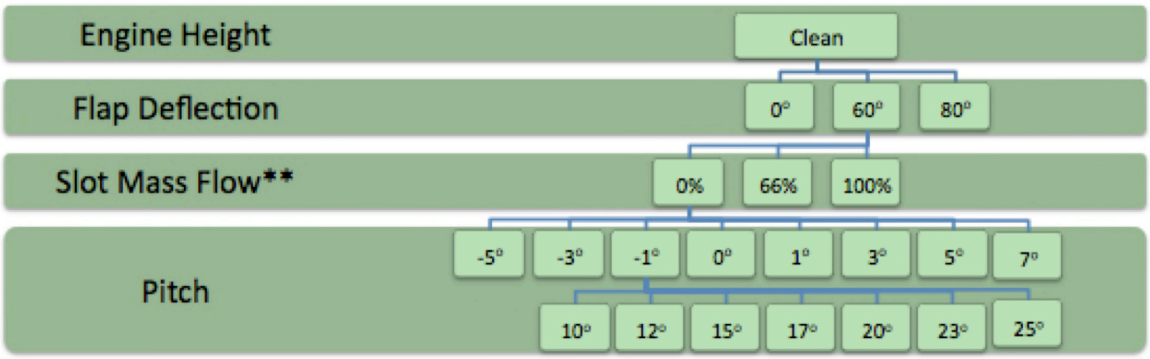

The AMELIA test over all was able to meet its entire set of objectives stated in Table 6.2. Table 6.7 and Table 6.8 give summaries of the AMELIA test, where Table 6.7 summarizes the number of days spent in model preparation, model installation, test execution, and model removal and Table 6.8 summarizes the wind-on portion, highlighting the number of useful data runs achieved at each engine height. Additional funds were requested from Subsonic Fixed Wing Project to support additional tasks during the wind-on portion of the test. These additional funds allowed Cal Poly to obtain additional test matrix data points, specifically the high engine height and all data at the clean wing configurations.

Table 6.7. AMELIA Test summary.

Task	Planned Duration (days)	Actual Duration (days)
Model Support Installation	10	9
Sting-Only Runs	2	1
Model/Instrumentation Installation	2	9
Instrumentation Checkout	7	9.5
HPA Checkout	5	2.5
Holiday Stand-Down	0	5
Wind-On Testing	30	30.5
Removal	5	5
Total	61	71.5

Table 6.8. AMELIA Wind-on test summary.

Model Configuration	Runs	Useful Data Runs	Calendar Days	Wind-on Days
Low Pylon	18 - 171	151	12/21/2011 – 1/27/2012	20
High Pylon	172 - 203	29	1/30/2012 – 2/3/2012	5
Clean Wing	204 - 270	64	2/6/2012 – 2/10/2012	5
TE-only Blowing	271 - 312	41	2/14/2012 – 2/15/2012	2
Total User Occupancy Hours	617.5			
Total Wind-On Calendar Time	12/21/2011 – 2/15/2012			

As a part of any test, there are unforeseen facility issues that can cause delays during the test execution phase. However, the facility down time was very minimal (approximately 13.5% of test execution) and significantly added to the efficiency of the AMELIA test. During the wind-on portion of the test, Cal Poly was able to record all 10 critical test points, over 280 useful data runs in the test matrix phases, and add in successful oil flow and smoke flow visualization runs. Table 6.9 is the as-run test matrix in the NFAC for the readers' reference.

Table 6.9. AMELIA as-run test matrix.

	Objective	Run Number	Tunnel speed (knots)	Model Attitude	Slot Flow (lbm/s)	C_MU	TPS L / R (PSI)	TPS L / R RPM	Engine Height	Flaps
As Run										
	Baseline acoustics *(sting only)*	1	40,80,100,110,120	0	OFF	OFF	OFF	OFF	Low	0
	Alpha Calibration	2,3,4,15,16	0	A1	OFF	OFF	OFF	OFF	Low	0
	LW Load Point	5	0	0	OFF	OFF	OFF	OFF	Low	0
	RW Load Point	6	0	0	OFF	OFF	OFF	OFF	Low	0
	Centerline Fwd Load Point	7	0	0	OFF	OFF	OFF	OFF	Low	0
	Centerline Aft Load Point	8	0	0	OFF	OFF	OFF	OFF	Low	0
	Combined Load (Fwd & LW)	9	0	0	OFF	OFF	OFF	OFF	Low	0
	Weight Tare/Sting Deflect	10,11	0	A1	OFF	OFF	OFF	OFF	Low	0
HPA Run 12/16/11	Slot and TPS Checkout	12	0	0	SLOT SWEEP A		TPS SWEEP		Low	0
	Microphones	various	0	0	OFF	OFF	OFF	OFF	Low	0
12/21/11	Reynolds sweep	18	40,80,100,110,120	0	OFF	OFF	OFF	OFF	Low	0
12/22/11	Baseline 1	19	40	A1	OFF	OFF	OFF	OFF	Low	0
	BETA CUT	20	40	**B1 A1=0**	OFF	OFF	OFF	OFF	Low	0
		21	100	A1	OFF	OFF	OFF	OFF	Low	0
	Critical Test Point 1	22,23-25	100	0	OFF	OFF	OFF	OFF	Low	0
	Model Change - Install 60 deg flap									
12/23/11		26	80	A1	OFF	OFF	OFF	OFF	Low	60
	Model Change - Install 0 deg flap									
1/3/12	Slots only	27,28	0	0	SLOT SWEEP A		OFF	OFF	Low	0
	TPS simulators	28	0	0	OFF	OFF	TPS SWEEP		Low	0
1/4/12	Oil Viscosity Investigation	29	0	0	Full, 1/3, 2/3, Full		OFF	OFF	Low	0
	TPS simulator sweep	30	0	0	OFF	OFF	TPS SWEEP		Low	0
	Power lift	31	0	0	SLOT SWEEP A		TPS SWEEP		Low	0
	One Engine Out Checkout	32	0	0	OFF	OFF	190 / 0	34K / 0	Low	0
1/5/12	Slot flow sweep / TPS Sweep	33	40	0	SLOT SWEEP A		TPS SWEEP		Low	0
	Powered Lift	34,35	40	0	SLOT SWEEP A		TPS SWEEP		Low	0
1/6/12	Baseline 2	36	40	A1	2.8	0.36	190	34,000	Low	0
	Model Change - Install 80 deg flap									
	Critical Test Point 2	37	40	0	2.8	0.36	190	34,000	Low	80
	Critical Test Point 3	38	80	5	2.8	0.36	10	9,000	Low	80
	Baseline 3	39	40	A1	2.8	0.36	190	34,000	Low	80
1/9/12	*Model Change - Install 60 deg flap*									
	Critical Test Point 5	40	40	5	0.933	0.10	0 / 180	13,500 / 34,000	Low	60
	Critical Test Point 6	41	40	5	0.933	0.10	180 / 0	34,000 / 13,500	Low	60
1/10/12	No HPA Alpha Sweep	42	40	A1	OFF	OFF	OFF	OFF	Low	60
	Critical Test Point 4	43	80	5	1.867	0.18	190	34,000	Low	80
	Repeat - Critical Test Point 5	44	40	5	0.933	0.10	0 / 180	13,500 / 34,000	Low	80
	Oil Flow Vis #1 - No TPS	45	30	2	2.8	0.36	OFF	OFF		
1/11/12	Low Pylon - Matrix Runs	46	40	A1	2.8	0.36	190	34,000	Low	60
	BETA Alpha Sweeps	47	40	**B=-5 A3**	2.8	0.36	190	34,000	Low	60
	BETA Alpha Sweeps	48	40	**B=-10 A3**	2.8	0.36	190	34,000	Low	60
	BETA Alpha Sweeps	49	40	**B=+5 A3**	2.8	0.36	190	34,000	Low	60
	BETA Alpha Sweeps	50	40	**B=+10 A3**	2.8	0.36	190	34,000	Low	60
	Low Pylon - Matrix Runs	51	60	A3	2.8	0.36	OFF	OFF	Low	60
	Low Pylon - Matrix Runs	52	60	A3	1.867	0.18	190	34,000	Low	60
	Low Pylon - Matrix Runs	54	60	A3	2.8	0.36	190	34,000	Low	60
	Low Pylon - Matrix Runs	55	100	A3	2.8	0.36	OFF	OFF	Low	60
1/12/12	Low Pylon - Matrix Runs	56	40	A3	2.8	0.36	190	34,000	Low	60
	Low Pylon - Matrix Runs	57	100	A3	OFF	OFF	OFF	OFF	Low	60
	Low Pylon - Matrix Runs	58	100	A3	2.8	0.36	190	34,000	Low	60
	Low Pylon - Matrix Runs	59	100	A3	OFF	OFF	190	34,000	Low	60
	Low Pylon - Matrix Runs	60	60	A3	OFF	OFF	OFF	OFF	Low	60
	Low Pylon - Matrix Runs	61	60	A3	1.867	0.18	OFF	OFF	Low	60
	Low Pylon - Matrix Runs	62	60	A3	OFF	OFF	190	34,000	Low	60
	Low Pylon - Matrix Runs	63	0	A3	2.8	0.36	OFF	OFF	Low	60
	Low Pylon - Matrix Runs	64	0	A3	1.867	0.18	OFF	OFF	Low	60
	Low Pylon - Matrix Runs	65	0	A3	OFF	OFF	190	34,000	Low	60
	Low Pylon - Matrix Runs	66	40	A3	2.8	0.36	OFF	OFF	Low	60
	Low Pylon - Matrix Runs	67	40	A3	OFF	OFF	190	34,000	Low	60
	Model Change - Install 80 deg flap									
1/13/12	Low Pylon - Matrix Runs	68	40	A3	2.8	0.36	OFF	OFF	Low	80
	Low Pylon - Matrix Runs	69	40	A3	2.8	0.36	190	34,000	Low	80
	Low Pylon - Matrix Runs	70	40	A3	OFF	OFF	190	34,000	Low	80
	Low Pylon - Matrix Runs	71	40	A3	1.867	0.18	OFF	OFF	Low	80
	Low Pylon - Matrix Runs	72	40	A3	OFF	OFF	OFF	OFF	Low	80
	Low Pylon - Matrix Runs	73	0	A3	OFF	OFF	190	34,000	Low	80
	Low Pylon - Matrix Runs	74	0	A3	OFF	OFF	10	9,000	Low	80
	Low Pylon - Matrix Runs	75	0	A3	2.8	0.36	OFF	OFF	Low	80
	Low Pylon - Matrix Runs	76	0	A3	1.867	0.18	OFF	OFF	Low	80
	Low Pylon - Matrix Runs	77	100	A3	2.8	0.36	OFF	OFF	Low	80
	Low Pylon - Matrix Runs	78,79	100	A3	2.8	0.36	190	34,000	Low	80
	Low Pylon - Matrix Runs	80	100	A3	OFF	OFF	190	34,000	Low	80
	Low Pylon - Matrix Runs	81	40	A3	2.8	0.36	190	34,000	Low	80

1/11/12	Low Pylon - Matrix Runs	46	40	A1	2.8	0.36	190	34,000	Low	60
	BETA Alpha Sweeps	47	40	**B=-5 A3**	2.8	0.36	190	34,000	Low	60
	BETA Alpha Sweeps	48	40	**B=-10 A3**	2.8	0.36	190	34,000	Low	60
	BETA Alpha Sweeps	49	40	**B=+5 A3**	2.8	0.36	190	34,000	Low	60
	BETA Alpha Sweeps	50	40	**B=+10 A3**	2.8	0.36	190	34,000	Low	60
	Low Pylon - Matrix Runs	51	60	A3	2.8	0.36	OFF	OFF	Low	60
	Low Pylon - Matrix Runs	52	60	A3	1.867	0.18	190	34,000	Low	60
	Low Pylon - Matrix Runs	54	60	A3	2.8	0.36	190	34,000	Low	60
	Low Pylon - Matrix Runs	55	100	A3	2.8	0.36	OFF	OFF	Low	60
1/12/12	Low Pylon - Matrix Runs	56	40	A3	2.8	0.36	190	34,000	Low	60
	Low Pylon - Matrix Runs	57	100	A3	OFF	OFF	OFF	OFF	Low	60
	Low Pylon - Matrix Runs	58	100	A3	2.8	0.36	190	34,000	Low	60
	Low Pylon - Matrix Runs	59	100	A3	OFF	OFF	190	34,000	Low	60
	Low Pylon - Matrix Runs	60	60	A3	OFF	OFF	OFF	OFF	Low	60
	Low Pylon - Matrix Runs	61	60	A3	1.867	0.18	OFF	OFF	Low	60
	Low Pylon - Matrix Runs	62	60	A3	OFF	OFF	190	34,000	Low	60
	Low Pylon - Matrix Runs	63	0	A3	2.8	0.36	OFF	OFF	Low	60
	Low Pylon - Matrix Runs	64	0	A3	1.867	0.18	OFF	OFF	Low	60
	Low Pylon - Matrix Runs	65	0	A3	OFF	OFF	190	34,000	Low	60
	Low Pylon - Matrix Runs	66	40	A3	2.8	0.36	OFF	OFF	Low	60
	Low Pylon - Matrix Runs	67	40	A3	OFF	OFF	190	34,000	Low	60
	Model Change - Install 80 deg flap									
1/13/12	Low Pylon - Matrix Runs	68	40	A3	2.8	0.36	OFF	OFF	Low	80
	Low Pylon - Matrix Runs	69	40	A3	2.8	0.36	190	34,000	Low	80
	Low Pylon - Matrix Runs	70	40	A3	OFF	OFF	190	34,000	Low	80
	Low Pylon - Matrix Runs	71	40	A3	1.867	0.18	OFF	OFF	Low	80
	Low Pylon - Matrix Runs	72	40	A3	OFF	OFF	OFF	OFF	Low	80
	Low Pylon - Matrix Runs	73	0	A3	OFF	OFF	190	34,000	Low	80
	Low Pylon - Matrix Runs	74	0	A3	OFF	OFF	10	9,000	Low	80
	Low Pylon - Matrix Runs	75	0	A3	2.8	0.36	OFF	OFF	Low	80
	Low Pylon - Matrix Runs	76	0	A3	1.867	0.18	OFF	OFF	Low	80
	Low Pylon - Matrix Runs	77	100	A3	2.8	0.36	OFF	OFF	Low	80
	Low Pylon - Matrix Runs	78,79	100	A3	2.8	0.36	190	34,000	Low	80
	Low Pylon - Matrix Runs	80	100	A3	OFF	OFF	190	34,000	Low	80
	Low Pylon - Matrix Runs	81	40	A3	2.8	0.36	190	34,000	Low	80
1/23/12	Low Pylon - Matrix Runs	118	0	A3	2.8	0.36	OFF	OFF	Low	80
	Low Pylon - Matrix Runs	119	0	A3	1.867	0.18	OFF	OFF	Low	80
	Low Pylon - Matrix Runs	120	0	0	SLOT SWEEP B	-	OFF	OFF	Low	80
	Low Pylon - Matrix Runs	121	0	-5	SLOT SWEEP B	-	OFF	OFF	Low	80
	Low Pylon - Matrix Runs	122	0	10	SLOT SWEEP B	-	OFF	OFF	Low	80
	Low Pylon - Matrix Runs	123	0	0	SLOT SWEEP B	-	190	34,000	Low	80
	Low Pylon - Matrix Runs	124	40	0	SLOT SWEEP B	-	OFF	OFF	Low	80
	Low Pylon - Matrix Runs	125	40	-5	SLOT SWEEP B	-	OFF	OFF	Low	80
	Low Pylon - Matrix Runs	126	40	10	SLOT SWEEP B	-	OFF	OFF	Low	80
	Low Pylon - Matrix Runs	127	40	0	SLOT SWEEP B	-	190	34,000	Low	80
	Low Pylon - Matrix Runs	128	40	A3	2.8	0.36	190	34,000	Low	80
	Low Pylon - Matrix Runs	129	60	0	SLOT SWEEP B	-	OFF	OFF	Low	80
1/24/12	Low Pylon - Matrix Runs	130	100	A3	1.867	0.18	OFF	OFF	Low	80
	Low Pylon - Matrix Runs	131	100	A3	1.867	0.18	190	34,000	Low	80
	Low Pylon - Matrix Runs	132	100	0	SLOT SWEEP C	-	OFF	OFF	Low	80
	Model Change - Install 60 deg flap									
	Low Pylon - Matrix Runs	133	40	A3	2.8	0.36	190	34,000	Low	60
	Low Pylon - Matrix Runs	134	40	A3	1.867	0.18	OFF	OFF	Low	60
	Low Pylon - Matrix Runs	135	40	A3	1.867	0.18	190	34,000	Low	60
	Low Pylon - Matrix Runs	136	40	0	SLOT SWEEP C	-	OFF	OFF	Low	60
	Low Pylon - Matrix Runs	137	40	-5	SLOT SWEEP C	-	OFF	OFF	Low	60
	Low Pylon - Matrix Runs	138	40	10	SLOT SWEEP C	-	OFF	OFF	Low	60
	Low Pylon - Matrix Runs	139	0	A3	2.8	0.36	OFF	OFF	Low	60
	Low Pylon - Matrix Runs	140	0	0	SLOT SWEEP C	-	OFF	OFF	Low	60
1/25/12	Low Pylon - Matrix Runs	141	0	-5	SLOT SWEEP C	-	OFF	OFF	Low	80
	Low Pylon - Matrix Runs	142	0	10	SLOT SWEEP C	-	OFF	OFF	Low	80
	Low Pylon - Matrix Runs	143	60	0	SLOT SWEEP C	-	OFF	OFF	Low	80
	Low Pylon - Matrix Runs	144	100	0	SLOT SWEEP C	-	OFF	OFF	Low	80
	Low Pylon - Matrix Runs	145	100	A3	1.867	0.18	OFF	OFF	Low	80
	Low Pylon - Matrix Runs	146	100	A3	1.867	0.18	190	34,000	Low	80
	Low Pylon - Matrix Runs	147	0	0	SLOT SWEEP C	-	OFF	OFF	Low	80
	Model Change - Install 30 deg flap									
	Low Pylon - Matrix Runs	148	0	A3	2.8	0.36	OFF	OFF	Low	30
	Low Pylon - Matrix Runs	149	0	A3	OFF	OFF	190	34,000	Low	30
	Low Pylon - Matrix Runs	150	40	A3	OFF	OFF	OFF	OFF	Low	30
	Low Pylon - Matrix Runs	151	40	A3	2.8	0.36	OFF	OFF	Low	30
	Low Pylon - Matrix Runs	152	40	A3	2.8	0.36	190	34,000	Low	30
1/26/12	Low Pylon - Matrix Runs	153	40	A3	2.8	0.36	190	34,000	Low	30
	Low Pylon - Matrix Runs	154	40	A3	OFF	OFF	190	34,000	Low	30
	Low Pylon - Matrix Runs	155	60	A3	OFF	OFF	OFF	OFF	Low	30
	Low Pylon - Matrix Runs	156	60	A3	2.8	0.36	OFF	OFF	Low	30
	Low Pylon - Matrix Runs	157	60	A3	OFF	OFF	190	34,000	Low	30
	Low Pylon - Matrix Runs	158	60	A3	2.8	0.36	190	34,000	Low	30
	Low Pylon - Matrix Runs	159	100	A3	2.8	0.36	OFF	OFF	Low	30
	Low Pylon - Matrix Runs	160	100	A3	OFF	OFF	OFF	OFF	Low	30
	Model Change - Install 0 deg flap									
	Low Pylon - Matrix Runs	161	0	0	SLOT SWEEP C	-	OFF	OFF	Low	0
	Low Pylon - Matrix Runs	162	0	-5	SLOT SWEEP C	-	OFF	OFF	Low	0
	Low Pylon - Matrix Runs	163	0	10	SLOT SWEEP C	-	OFF	OFF	Low	0
1/27/12	Low Pylon - Matrix Runs	164	0	0	SLOT SWEEP C	-	OFF	OFF	Low	0
	Low Pylon - Matrix Runs	165	40	0	SLOT SWEEP C	-	OFF	OFF	Low	0
	Low Pylon - Matrix Runs	166	40	-5	SLOT SWEEP C	-	OFF	OFF	Low	0
	Low Pylon - Matrix Runs	167	40	10	SLOT SWEEP C	-	OFF	OFF	Low	0
	Low Pylon - Matrix Runs	168	60	0	SLOT SWEEP C	-	OFF	OFF	Low	0
	Low Pylon - Matrix Runs	169	100	0	SLOT SWEEP C	-	OFF	OFF	Low	0
	Model Change - Install 80 deg flap									
	Smoke Vis #1	170	40	0 / 10	SLOT SWEEP D	-	OFF	OFF	Low	80
	Smoke Vis #2	171	40	10	2.8 / 1.87 / .93 / 0	-	OFF	OFF	Low	80
1/28/12	***Model Change - Install High TPS***									
1/30/12	TPS Checkout	172	0	0	OFF	OFF	TPS Sweep	TPS Sweep	High	80
	Weight Tare	173	0	A3	OFF	OFF	OFF	OFF	High	80
	High Pylon - Matrix Runs	174	0	A3	2.8	0.36	OFF	OFF	High	80
	High Pylon - Matrix Runs	175	0	A3	OFF	OFF	190	34,000	High	80
	High Pylon - Matrix Runs	176	40	A3	2.8	0.36	190	34,000	High	80
	High Pylon - Matrix Runs	177	40	A3	2.8	0.36	OFF	OFF	High	80
	High Pylon - Matrix Runs	178	40	A3	OFF	OFF	OFF	OFF	High	80
1/31/12	High Pylon - Matrix Runs	179	0	A3	OFF	OFF	10	9,000	High	80
	High Pylon - Matrix Runs	180	40	A3	OFF	OFF	190	34,000	High	80
	High Pylon - Matrix Runs	181	100	A3	2.8	0.36	10	9,000	High	80
	High Pylon - Matrix Runs	182	60	A3	2.8	0.36	10	9,000	High	80
	Critical Test Point 9	183	60	5	2.8	0.36	10	9,000	High	80
	Critical Test Point 8	184	40	0	2.8	0.36	190	34,000	High	80
	Model Change - Install 0 deg flap									

2/1/12	High Pylon - Matrix Runs	185	40	A3	2.8	0.36	OFF	OFF	High	0
	High Pylon - Matrix Runs	186	40	A3	2.8	0.36	190	34,000	High	0
	High Pylon - Matrix Runs	187	40	A3	OFF	OFF	190	34,000	High	0
	High Pylon - Matrix Runs	188	40	A3	OFF	OFF	OFF	OFF	High	0
	High Pylon - Matrix Runs	189	100	A3	OFF	OFF	OFF	OFF	High	0
	Critical Test Point 7	190	100	0	OFF	OFF	OFF	OFF	High	0
	High Pylon - Matrix Runs	191	40	A3	1.867	0.18	OFF	OFF	High	0
	High Pylon - Matrix Runs	192	40	A3	1.867	0.18	190	34,000	High	0
	High Pylon - Matrix Runs	193	0	A3	2.8	0.36	OFF	OFF	High	0
	High Pylon - Matrix Runs	194	0	A3	1.867	0.18	OFF	OFF	High	0
	High Pylon - Matrix Runs	195	0	A3	OFF	OFF	190	34,000	High	0
	Model Change - Install 60 deg flap									
2/2/12	High Pylon - Matrix Runs	196	40	A3	2.8	0.36	OFF	OFF	High	60
	High Pylon - Matrix Runs	197	40	A3	2.8	0.36	190	34,000	High	60
	High Pylon - Matrix Runs	198	40	A3	OFF	OFF	190	34,000	High	60
	High Pylon - Matrix Runs	200	0	A3	2.8	0.36	OFF	OFF	High	60
	High Pylon - Matrix Runs	201	0	A3	1.867	0.18	OFF	OFF	High	60
	High Pylon - Matrix Runs	202	0	A3	OFF	OFF	190	34,000	High	60
2/3/12	High Pylon - Matrix Runs	203	100	A3	2.8	0.36	190	34,000	High	60
2/4/12	*Model Change - remove TPS*									
2/6/12	Weight Tare	204	0	A3	OFF	OFF	OFF	OFF	clean	60
	Weight Tare Verification	205	0	A3	OFF	OFF	OFF	OFF	clean	60
	Clean Wing - Matrix Runs	206	0	A3	2.8	0.36	OFF	OFF	clean	60
	Clean Wing - Matrix Runs	207	0	A3	1.867	0.18	OFF	OFF	clean	60
	Clean Wing - Matrix Runs	208	0	0	SLOT SWEEP C	-	OFF	OFF	clean	60
	Clean Wing - Matrix Runs	209	0	-5	SLOT SWEEP C	-	OFF	OFF	clean	60
	Clean Wing - Matrix Runs	210	0	10	SLOT SWEEP C	-	OFF	OFF	clean	60
	Clean Wing - Matrix Runs	211	40	A3	OFF	OFF	OFF	OFF	clean	60
	Clean Wing - Matrix Runs	212	40	A3	1.867	0.18	OFF	OFF	clean	60
	Clean Wing - Matrix Runs	213	40	A3	2.8	0.36	OFF	OFF	clean	60
	Clean Wing - Matrix Runs	214	40	0	SLOT SWEEP C	-	OFF	OFF	clean	60
	Clean Wing - Matrix Runs	215	40	-5	SLOT SWEEP C	-	OFF	OFF	clean	60
	Clean Wing - Matrix Runs	216	40	10	SLOT SWEEP C	-	OFF	OFF	clean	60
	BETA Alpha Sweeps	217	40	**B=-5 A3**	2.8	0.36	OFF	OFF	clean	60
2/7/12	Clean Wing - Matrix Runs	218	40	A3	2.8	0.36	OFF	OFF	clean	60
	BETA Alpha Sweeps	219	40	**B=-10 A3**	2.8	0.36	OFF	OFF	clean	60
	BETA Alpha Sweeps	220	40	**B=+5 A3**	2.8	0.36	OFF	OFF	clean	60

7. Test Measurements

With the overall goal of obtaining a variety of datasets thorough enough to be used for CFD validation, AMELIA was designed to include as much instrumentation as possible. Some of this instrumentation was installed as early as manufacturing, while other instrumentation was added in the weeks prior to the beginning of the test. AMELIA's instrumentation measured quantities associated with the following:

1) Wing Surface Pressures
2) Various Circulation Control Related Pressures
3) Wing Surface Temperature
4) Circulation Control Flow Temperature
5) TPS
6) Aero Loads
7) Other Measurements

In the following sections, the importance of each measurement will be discussed, along with a thorough discussion of the instrumentation used to record each measurement.

7.1. Wing Surface Pressures

Accounting for a large portion of the instrumentation on AMELIA, 232 static pressure ports are embedded into the surface of the model's wings. All ports are located on the left wing in five chordwise and one spanwise group—barring five ports reserved for the right wing. Figure 7.1 shows each of the chordwise group's location on the model, while Figure 7.2 shows each group in detail with pressure port names (the port names shown in red in Figure 7.2 indicate malfunctioning ports). Ports were clustered in areas of interest—near the slots on both the leading edge and above the flap. Buttlines 240, 500 and 638 included ports on the upper surface of the dual radius flap for all flap deflections. A custom "quick disconnect" exists to bridge the connection between flap and wing in order to reduce the time required to change flaps.

Five upper surface ports from the left wing were mirrored to the right wing. These right wing ports provided indication of the upper surface flow symmetry.

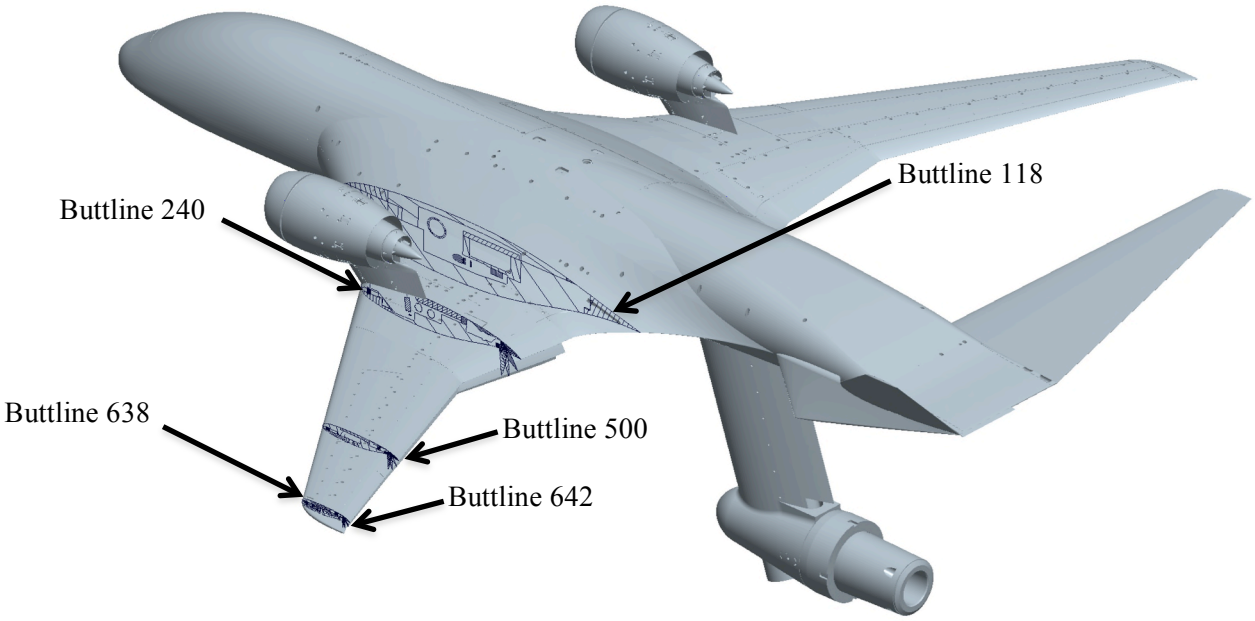

Figure 7.1. Chordwise groups of surface pressure ports.

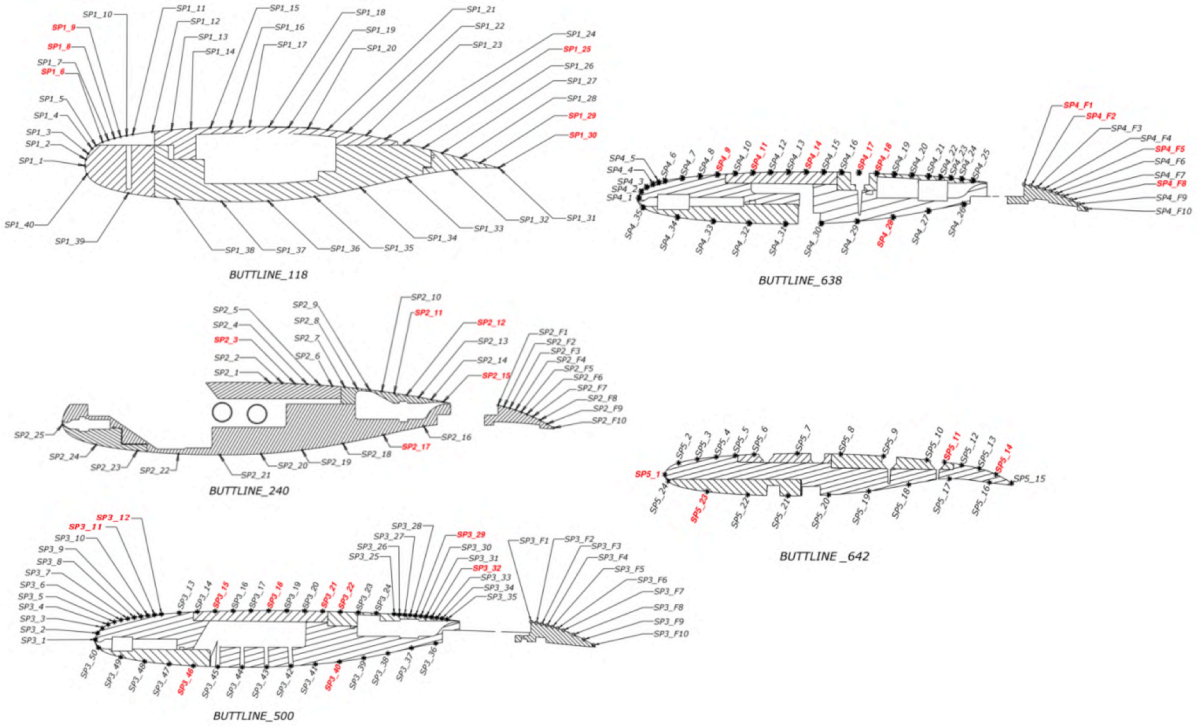

Figure 7.2. Pressure port distribution of each group.

Not shown in the figures is the spanwise wing surface pressure group which runs from the wing root to tip on the upper and lower surface at roughly 30% chord. This group accounts for 24 surface pressure ports,

the layout of this group can be found in the model's manufacturing drawings in the appendix of this report.
The wing surface pressure ports were manufactured prior to the application of the Imron surface treatment. Each port was pressurized during the surface treatment application process to prevent Imron from clogging the ports—special care was also taken to prevent material build-up around the 0.020" (ID) ports. Internal to the model, each port lead to a short length of stainless steel tubing, usually only 4 to 8 inches in length. Urethane tubing (0.032") bridged the gap from the stainless steel tubes to the pressure module's top plate.

All the wing pressures were routed and connected to the NFAC's PSI- Initium system. The system is comprised of pressure modules, which convert pressure into a digital signal and the Digital Temperature Compensated (DTC) Initium which interfaces with the NFAC's Standard Data System (SDAS) via Ethernet.

Figure 7.3. Pressure Systems Inc.'s DTC Initium system, shown with two pressure modules (image courtesy of Measurement Specialties Inc).

AMELIA required three 2.5 psi, and three 15 psi pressure modules, which were located in the nose of the model in order to provide adequate space for cable routing. Pressure ports near the leading edge and slot were connected to the 15 psi modules, while lower surface ports and ports in some mild regions of the upper surface were left on the 2.5 psi modules. Each module was capable of accommodating 64 ports (however, every 16th port was used as a reference pressure). The Initium mainframe was located at the base of the sting arm—approximately 25 feet from the modules and connected via a PSCB cable. Also connected to each module were reference pressure tubing, calibration pressure tubing and purge tubing. Figure 7.3 shows Pressure Systems Inc.'s Digital Temperature Controlled Initium system with two sample pressure modules[9].

Prior to entering the tunnel, each of the 232 wing surface pressures were checked for leaks and plugs using a Druck Portable Low Pressure Calibrator provided by the NFAC. The leak/plug check was done initially when connecting the pressure port's tubing to the module, and a second time after the model had been installed in the tunnel and the modules became active. The active modules also provided an opportunity to verify the identity of each port on the control room's computer systems. After the initial installation, leak/plug checks and identity verification were repeated when skin panels (with ports) were removed or flaps were changed.

7.2. Circulation Control Pressures

Also occupying ports on the six pressure modules were 24 total pressure measurements at three locations inside each circulation control plenum. The locations of these total pressure probes can be seen in Figure 7.4.

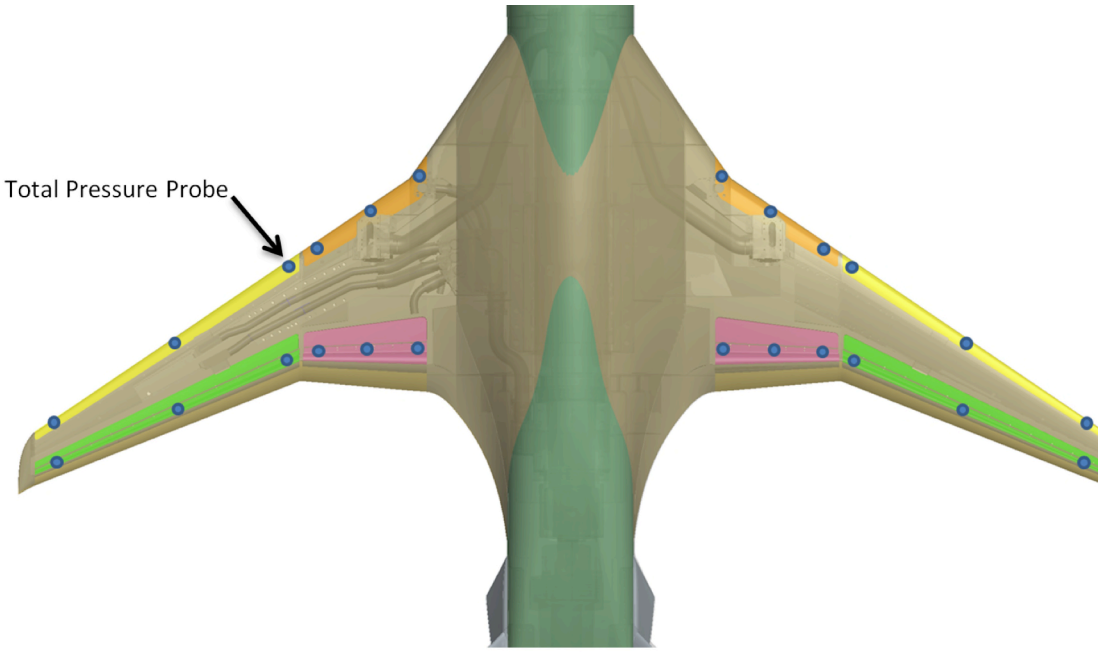

Figure 7.4. Circulation control plenum total pressure probe distribution.

These total pressure values were used to indicate the distribution of pressure inside each plenum and between right and left wings. An imbalance in pressure across wings resulted in a (manual) adjustment to the butterfly valves controlling the amount of mass flow directed to each plenum. Pressure distribution within each plenum was a function of the plenums metal foam/rigimesh treatment, and thus is not easily changed (for more information on the metal foam/rigimesh treatment see the circulation control flow calibration section).

During the circulation control flow calibration a pressure sensor was added to the low pressure distribution plenum on each wing (in order to comply with high pressure air safety requirements at the calibration facility). For the sake of verifying the conditions within the model during the calibration were repeated in the wind tunnel test, Kulite pressure transducers were added to the low pressure distribution plenum.

7.3. Wing Surface Temperature

One of the primary sources of uncertainty in the Fringe Imaging Skin Friction method is contributed by the determination of the oil viscosity[10] . In order to minimize this uncertainty, the oil's viscosity should be calibrated as close to its working temperature as possible. To determine the temperature of the upper surface of the wing during FISF testing, AMELIA's right wing contains 12 J-type thermocouples. The location of each of these thermocouples can be seen in Figure 7.5.

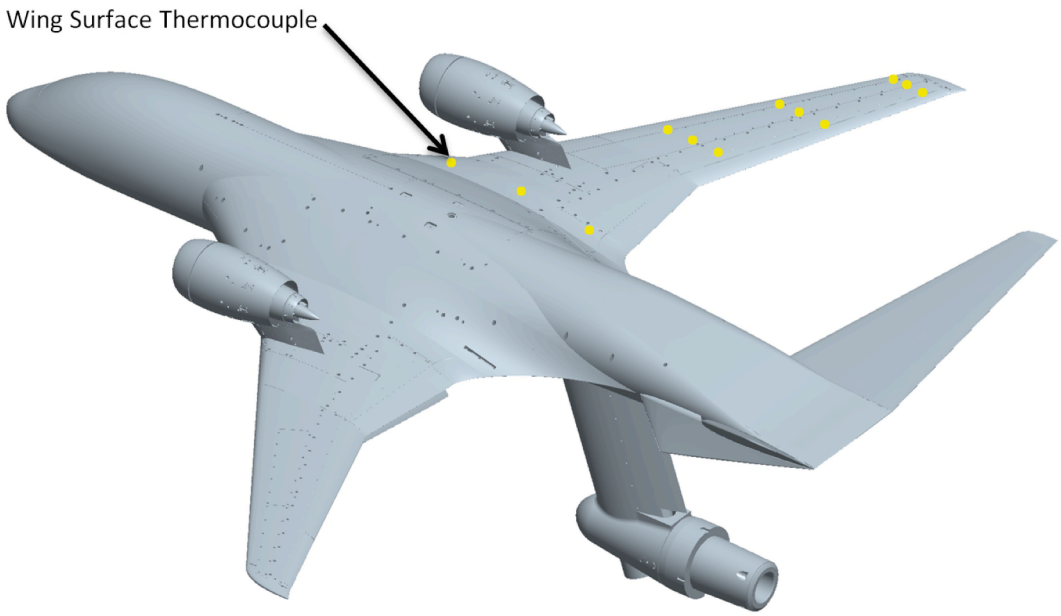

Figure 7.5. Thermocouple layout on AMELIA's right wing.

A few of the surface thermocouples failed during the test, most likely due to the wear and tear on the wiring from repeated panel removal and reinstallation. (These non-functioning thermocouples are listed in the instrumentation list found in the appendix of this report).

Part of the NFAC's LXI system, the wires from these J-type thermocouples terminated in mini-connectors at the aft end of the model, where extensions traversed down the blade and into the T-frame below the tunnel. Similar to the wing surface pressures, each thermocouple's identity was verified using a heat gun, once the model was in place in the tunnel.

7.4. Circulation Control Flow Temperature

Similar to the late addition of the circulation control pressure sensors, J-type thermocouples were also added to the low pressure distribution plenums. These thermocouples were the only flow temperature measurement in the circulation control flow system (besides the orifice plate upstream of the model). Readings from these thermocouples were used in the calculation of the circulation control discharge coefficient, C_{μ}. Figure 7.6 shows the added thermocouple (red) and pressure transducer (red) at both the low pressure distribution plenum and the TPS mounting block(discussed in the subsequent section).

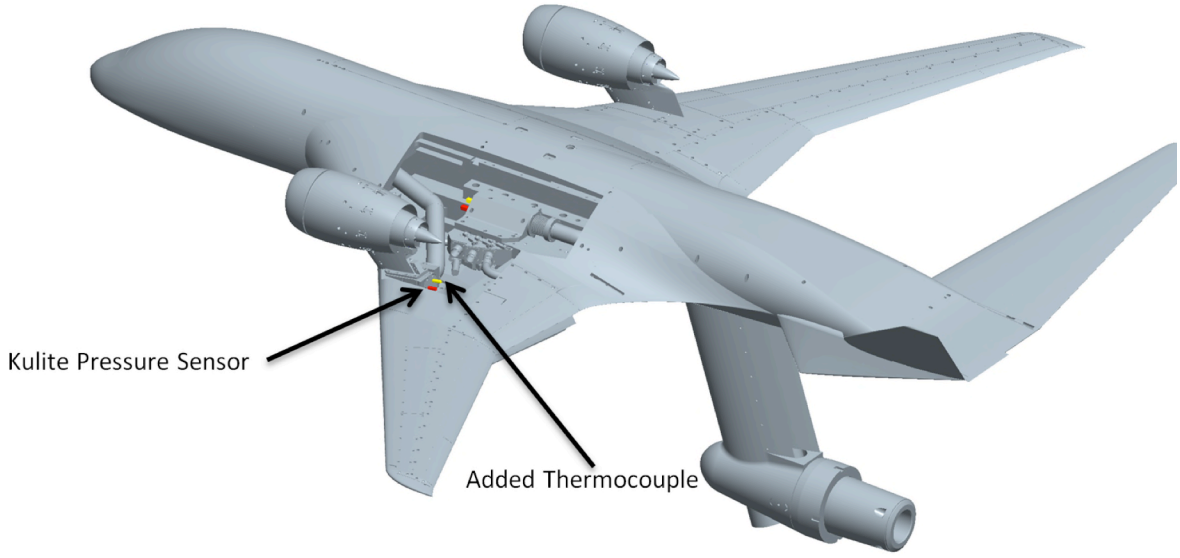

Figure 7.6. Thermocouple(yellow) and pressure transducers(red) added to AMELIA.

7.5. TPS Measurements

TPS units are known to be delicate systems prone to catastrophic failures; much effort was devoted to adequately monitoring TPS health, as a malfunctioning TPS unit would certainly delay testing progress. The turbine propulsion simulators were thus the highest risk component onboard the AMELIA model. In order to mitigate the TPS unit risk, each unit was heavily instrumented with pressure ports/probes, thermocouples, RPM sensors, and accelerometers.

The core of each unit contains a forward and aft bearing, each instrumented with two redundant J-Type thermocouples and two RPM sensors. Magnetic pick-ups at the bearings detect revolutions per minute—the signal is transmitted to the control room computers via a wired connection. Aft and forward bearing temperature served as the primary indicator of the health of the unit.

Driving the TPS units, the high pressure air supply line required a few additional measurements. At the base of each TPS pylon high pressure Kulites and thermocouples were added a few months prior to the wind tunnel test (seen in Figure 7.6). Measurements from these instruments helped to indicate the symmetry of each wing's supply conditions from the common high pressure air supply line at the model entrance (see the high pressure air system section of the Model Description for more information).

With the pressure sensor and thermocouple measuring the inlet conditions of the core flow, conditions at the exit of the core were measured by two total pressure probes, two J-type thermocouples and two static pressure ports. Figure 7.7 shows the aft end of the TPS unit with each of the total pressure ports highlighted. The static pressure ports lay at the base of the probe, in-line with the probe face. The thermocouples are located 90° from each port with respect to the unit's central axis.

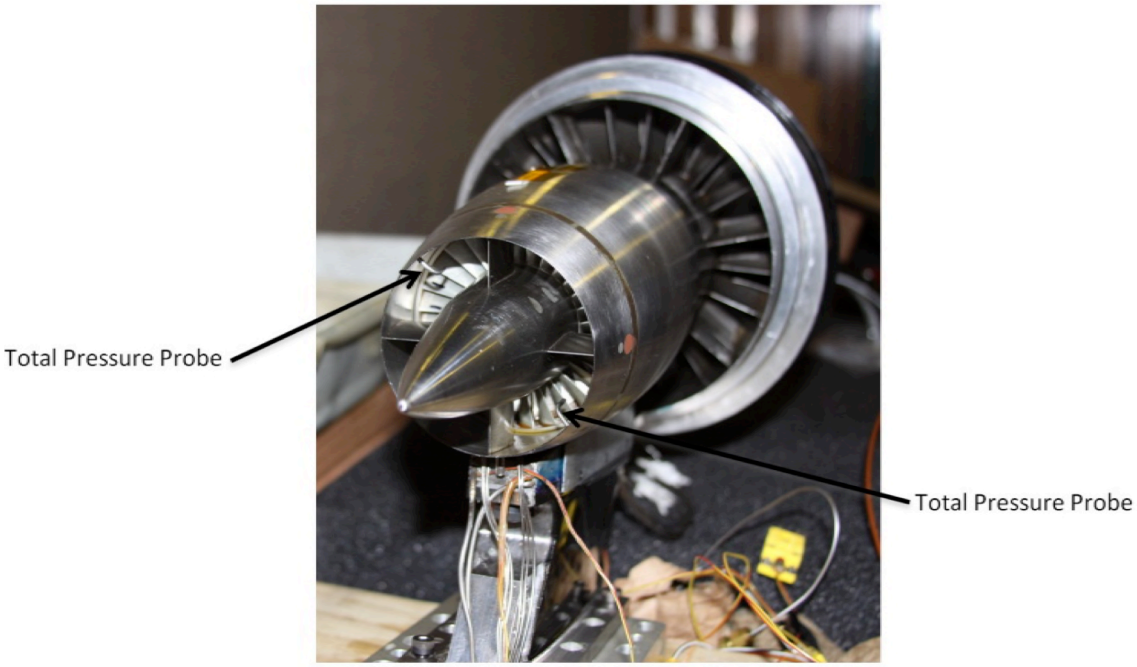

Figure 7.7. Instrumentation in the core of the TPS unit.

The fan inlet is instrumented with eight static pressure ports spaced about 1.5 inches from the fan face. Figure 7.8 shows the location of the inlet static pressure ports(red) from a front view and side view. Also shown in Figure 7.8 is one of seven instrumentation rakes in the fan exit. Each rake consists of four total pressure probes (cyan), one J-type thermocouple (yellow) and a static pressure port (at the base of the rake aligned with the probe face. The rakes are organized in a radial array similar to the inlet—the pylon prevents the bottom location from being used. Figure 7.9 shows a fan duct rake in detail. Each rake fit into a slot in the fan exit fairing such that the base of the rake was flush with the inner wall of the duct.
The pressures coming from each rake were also 0.032" urethane tubes. Once these tubes were routed out of the TPS unit, they terminated in a circular 50-pin quick disconnect. From the QD to the pressure modules in the nose 0.040" urethane tubing was used.

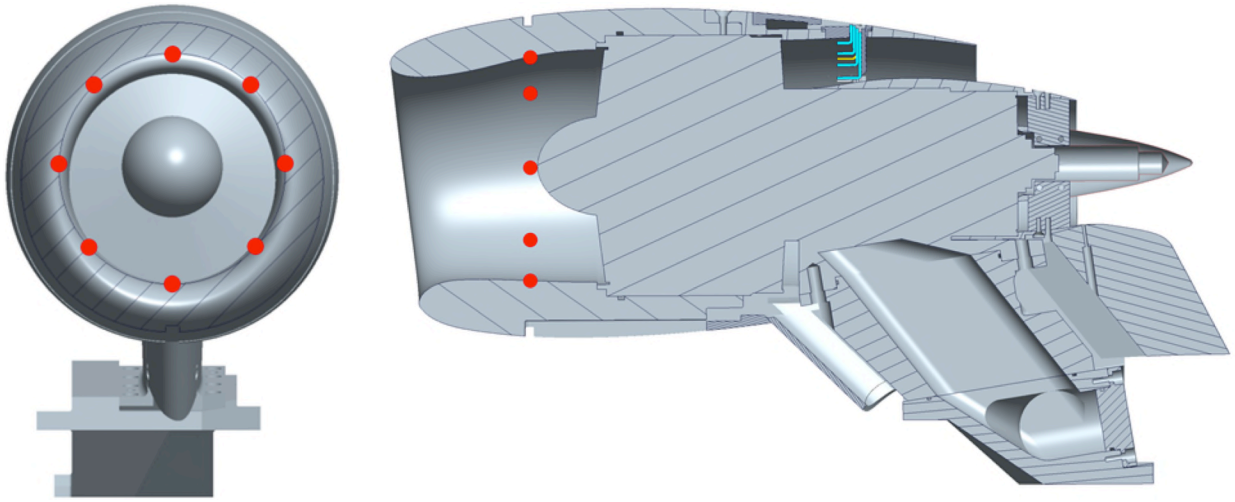

Figure 7.8. Front and side view of the TPS, each red dot represents the location of a static pressure tap.

Throughout the test, the vibration of each unit was monitored closely using a single BMA180 three-axis accelerometer per unit. These accelerometers were mounted to the base of each pylon, under the upper surface skin of the wing—this location allowed for the detection of both issues with the TPS unit as well as problems in the low pressure distribution plenum. "An embedded microcontroller translated the short-distance I^2C protocol of the accelerometer, to a serial signal which was then boosted and sent to the control room. A Labview interface (Appendix C) read the serial stream, graphically displayed the RMS of each three axis accelerometer, and provided an on-demand data logging ability for the user"[11].

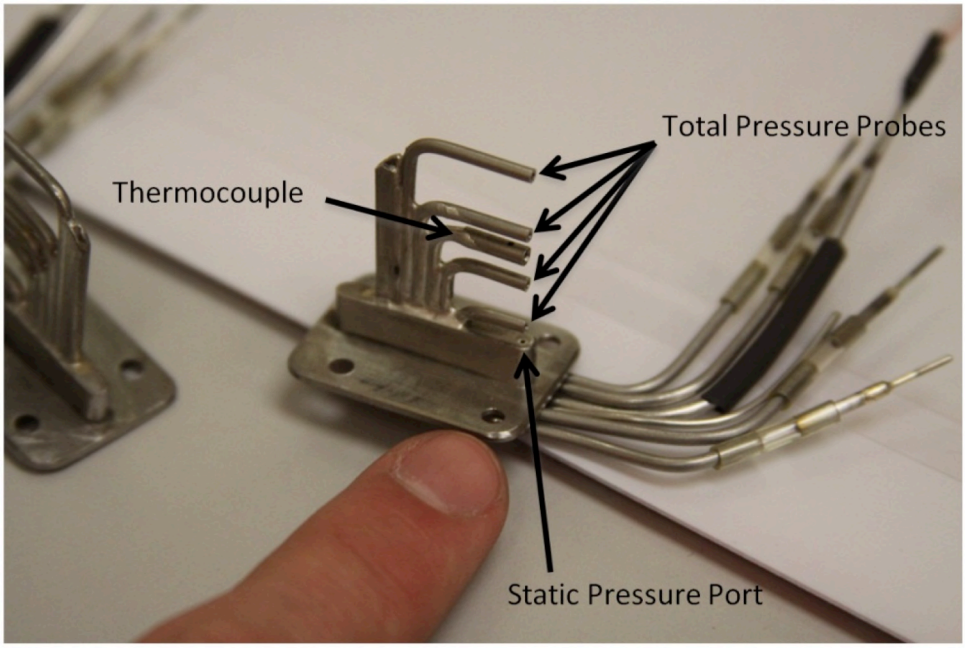

Figure 7.9. Fan duct instrumentation rake (one of seven).

7.6. Aerodynamic Loads

The 8-inch flow-through balance discussed in the Model Description section was used to measure AMELIA's aerodynamic loads. The force balance was manufactured by Triumph Aerospace (Force Measurement Systems) in 1990 for an unrelated test program, and was selected for application to AMELIA based on its high load limits and its internally isolated flow paths. An external flow path was added specifically for use on AMELIA. Although this external air delivery system utilizes four welded bellows with precision flanges, pressurization of the system (during the balance calibration) revealed an additional force on the axial force component. The balance load envelope was adjusted to accommodate the increase in axial force from the original 500 lbs to the redefined load of 1200 lbs (which is reflected in Table 1 of the Model Description). For more information on the balance or the balance calibration conducted by Triumph see Reference 12.

7.7. Other Measurements

A redundant set of inclinometers were mounted in the nose of the model, one analog (Q-Flex) and one digital (Schaevitz). The Q-Flex model QA-2000 is a high performance, internally temperature compensated accelerometer provided by NASA Ames Unitary Plan Wind Tunnel. The UPWT also provided a Schaevitz high precision gravity referenced tilt sensor.

Eight unsteady pressure Kulites are located in the upper surface of the models wing, wing blend and TPS unit. Figure 7.10 shows the Kulites (in magenta) on the upper surface of the wing (the TPS Kulite is located on the inner wall of the fan duct). The location of each Kulite was determined in order to provide an estimate of local noise levels on the full scale aircraft (for more information on the Kulites see the acoustics section of this report).

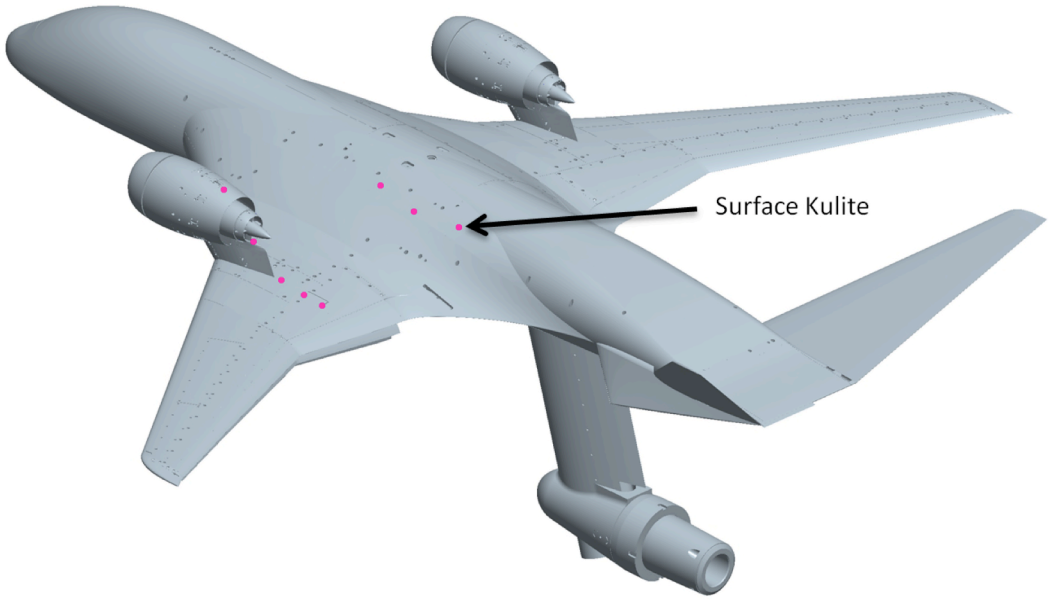

Figure 7.10. Unsteady pressure Kulites on the left wing.

In order to monitor cavity temperature within the model, a single thermocouple was placed inside the nose near the pressure modules. This helped ease concerns of thermal damage to the pressure tubing and modules from heat given off by the TPS supply air. In the case that the thermocouple showed excessive temperatures a small air supply line could be turned on to deliver cool air to the modules. Figure 7.12 shows the pressure modules and cooling line in the nose of the model. Another thermocouple was placed within the left wing to monitor cavity temperature. Figure 7.11 shows the approximate location of these thermocouples.

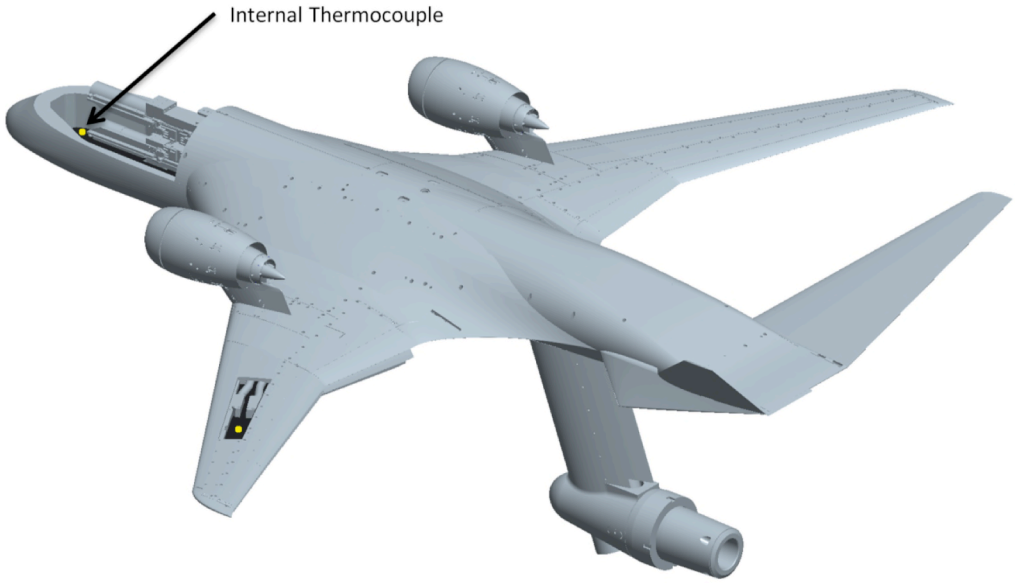

Figure 7.11. Thermocouples monitoring cavity temperature in the model.

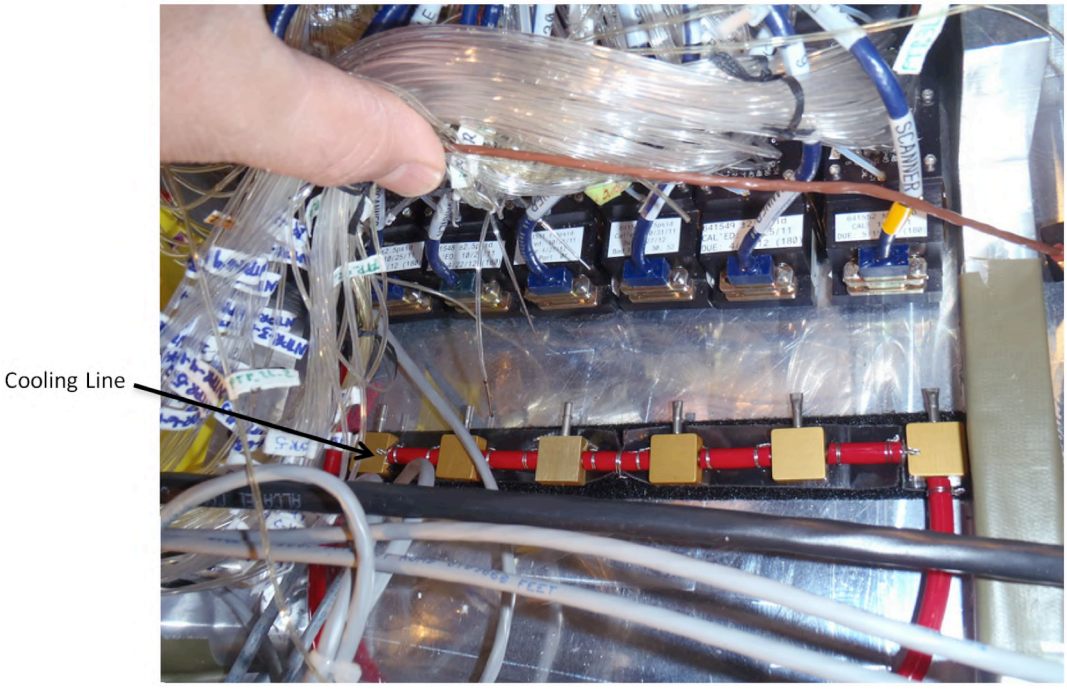

Figure 7.12. The pressure modules and cooling line housed in the nose.

8. Data Acquisition

This section provides a description of the NFAC data acquisition system (DAS) and its configuration for the AMELIA test. Real time calculation requirements and post-point analysis routines are described. Cal Poly derived equation sets and reduction routines are provided for computations different from the standard NFAC listing.

8.1. System Description

The data system at both wind tunnels at the NFAC has been in place since 2007; capabilities of the data system were driven by the requirements of tests scheduled in 2007-2008 and anticipated future tests. The data system runs on a distributed computing system with nineteen high-end PCs running Microsoft Windows XP, and two server PCs connected by a Reflective Memory real time network and a switched Ethernet, Local Area Network. This system currently allows for processing of over 500 low-speed digital measurements, 240 mid- and 256 high-speed analog measurements, in addition to 96 mid-speed analog measurements for Safety-of-Flight (SOF) operations. This data is streamed to ten dual core PCs at control and user stations for wind tunnel operation and monitoring. There are four different data acquisition subsystems for measurements of different acquisition rates and signal type. They are: steady DAS (SDAS), basic DAS (BDAS), dynamic DAS (DDAS), and safety-of-flight DAS (SOFDAS). The steady data system, SDAS, is a low-speed time-based data system capable of sampling rates between 4 and 10 Hz. SDAS interfaces with digital instruments including model pressures (PSI-Initium system), thermocouple measurements, tunnel-wall pressures, and NFAC-external balance measurements. High pressure air controller measurements interface with SDAS. BDAS is a mid-speed N/rev-pulse based data system capable of 240 analog channels at a 8.5 kHz sampling rate. SOFDAS is a time-based data system capable of sampling 96 analog channels at up to 2000 Hz. For more information on the NFAC DAS, see van Aken[13].

The 40-by-80-foot wind tunnel is equipped with 192 wall pressure ports. The ports are sunk below the acoustic treatment of the 4-foot by 4-foot by 42-inch cavities that line the tunnel walls. There are twelve streamwise rows of pressure ports, spaced around the perimeter of the test section. Each row contains 15 to 17 pressure ports in streamwise direction. Fourteen PSI 9116 16-channel Intelligent Pressure Scanning modules electronically scan and send mean data to the SDAS at 10 Hz via Ethernet.

Cal Poly used a total of 365 channels on SDAS acquired at 10 Hz, 143 channels on BDAS acquired at 1,000 Hz, and 96 channels on SOFDAS acquired at 1000 Hz. Wind-on data points were acquired for 32 seconds, and wind-off data points (typically) for 4 seconds. A data point duration study was conducted at the beginning of the test to determine how sampling length affected data quality. The results are contained in Run 14. Zero and resistor calibration points were acquired at the beginning and end of each run. After the initial points are acquired, a report is generated to make sure measured zero and resistor-calibration voltages are within tolerance. At the end of each test day, Cal Poly was provided with tab-delimited text files containing averaged engineering units (EU) summary data from the day's runs. The summary files were used to make presentations for NASA management, and for additional post processing and data review.

In addition to the data acquired from model and tunnel sensors, content from the 4 HD cameras mounted in the test section was transferred to Cal Poly. The video feed, which is originally intended for incident recording, was used for flow visualization during both the smoke and oil runs. The videos are made available with the data sets.

8.2. Real Time Calculations

Real time processing is handled by a dedicated PC, which computes the average, minimum, maximum, half peak-to-peak, and standard deviation for voltage data at 0.25 second intervals. Voltages are converted

to engineering units and any required real-time derived computations are then performed on the averaged data. Except for SOFDAS, data is only stored when a data point is being acquired.

In addition to the standard tunnel conditions and model pressure and temperature measurements, Cal Poly required real time computations for TPS thrust from a calibration look-up table, angle of attack measurement from two sensors, and mass flow rate from orifice plate instrumentation. Real time computations was also required for the two 14-poppet Emco Digital Valves, providing flow control to the TPS and redundant mass flow rate measurement on the low pressure side. The reduction routine for the orifice plate was provided by the manufacturer, Wyatt Engineering. The Schaevitz and Qflex clinometers followed the standard equation sets from the Ames Unitary Plan Wind Tunnel. Thrust was calculated real time from a 5 by 8 look-up table where corrected gross thrust was bi-linearly interpolated as functions of test section velocity and TPS RPM from calibration data. The calibration matrix and thrust calculation are presented in a later section. Equation sets for the clinometers and orifice plate are provided in an appendix.

8.3. Post-Point Processing

Following each data point the post-point computations are performed giving time history data in engineering units. Upon completion, the data is made available for data review. The standard NFAC data analysis toolbox is used to plot and review runs near real time.

As balance forces and moments are reduced to coefficients in real time, the only additional post-point processing was the calculation of slot blowing and TPS performance coefficients, C_μ and C_T; the computation steps are as follows.

The thrust coefficient, C_T, is calculated based on the combined gross thrust of the TPS.

$$C_T \equiv \frac{Thrust}{q_\infty S_{ref}} \tag{1.1}$$

Thrust is calculated based on the look up table, described above.

The momentum coefficient, C_μ, defines the performance of a circulation control wing. It is also referred to as the blowing coefficient, discharge coefficient, or jet momentum coefficient. It is defined the same way as the thrust coefficient.

$$C_\mu \equiv \frac{Thrust}{q_\infty S_{ref}} = \frac{\int \left(\rho_J \vec{V_j} \cdot \vec{n}\right)\left(\vec{V_j} \cdot \vec{n}\right) dA}{q_\infty S_{ref}} \tag{1.2}$$

The subscript j denotes properties with respect to the jet flow (i.e. in the slot). The integral in the numerator of Eq. (8.2) is approximated as

$$C_\mu = \frac{\dot{m}_J u_J}{q_\infty S_{ref}} \tag{1.3}$$

Mass flow rate measurements from the digital poppet valve and the orifice plate are accounted for in the jet mass flow rate, $\dot{m}_j$. The small slot height makes direct measurement of the jet velocity difficult, so it is standard to approximate using isentropic relations. For isentropic flow, the jet velocity is

$$u_j = \left(\frac{2}{\gamma - 1} \gamma R T_{t,J} \left(1 - \left(\frac{P_J}{P_{t,J}} \right)^{\frac{\gamma-1}{\gamma}} \right) \right)^{1/2} \tag{1.4}$$

The specific heat ratio, γ, is 1.4, and the gas constant, R, for dry air is 1716.59 ft-lb_f/slug-R. It is also common practice to substitute the freestream static pressure, in lieu of the jet static pressure, P_j. From a technical standpoint, this will yield a lower jet velocity than actual, and for CFD, should be calculated from expansion to the local static pressure using, say, the static pressure taps located at the leading edge and on the flaps. The reason C_μ is reported using expansion to the freestream static pressure is because the local static pressure will change with angle of attack or any geometry change in the CCW surface (i.e. flap deflection), thus making comparison between model configurations and alpha sweeps not meaningful. As measuring the mass flow rate into each of the 8 individual plenums was not possible, the reflected C_μ is a combined momentum coefficient for the system. The total pressure, $P_{t,j}$, substituted in Eq. (8.4) is then the average of all 24 plenum total pressure measurements. The data files reflect averaging of only the 12 trailing edge pressures when the leading edge slots were blocked during runs 271-312. Momentum coefficient values are bookkept in the data files corresponding to calculations based on 3 different temperature measurements ($T_{t,j}$ in Eq. (8.4)) and 2 mass flow rate measurements. Jet velocity is calculated 4 ways using the orifice plate thermocouple, left low pressure plenum thermocouple, right low pressure plenum thermocouple, and the average of the left and right low pressure plenum temperature measurement. Additional calculations for both mass flow rate measurements yields 8 total variations in C_μ. C_μ values presented in this report are with respect to the average of the low pressure plenum thermocouples and the digital poppet valve mass flow rate measurement.

9. Acoustics

Acoustic data was acquired for the AMELIA wind tunnel test in support of NASA's Subsonic Fixed Wing Project's milestone (SFW.45.01.A.4.018) to "Acquire experimental acoustics data, including phased array measurements, for a large-scale, full-span model of an advanced hybrid wing body CESTOL vehicle with above-wing podded propulsion, which includes leading-edge and trailing-edge circulation control blowing for high lift". This effort was funded by NASA's Sub-sonic Fixed Wing project. A detailed description of the AMELIA acoustic effort can be found in AIAA 2012-2231, Burnside, N. and Horne, C., *Acoustic Surveys of a Scaled-Model CESTOL Transport Aircraft in Static and Forward Speed Conditions* (presented at 18th AIAA/CEAS Aeroacoustics Conference (33rd AIAA Aeroacoustics Conference) 04 - 06 June 2012, Colorado Springs, CO). The following descriptions in this section are excerpted from that report.

Acoustic instrumentation included fixed microphones, a phased microphone-array, and surface-mounted unsteady pressure sensors. All microphones were G.R.A.S free-field condenser type. The unsteady pressure measurements were made using a mix of 5 psi and 15 psi Kulite transducers type XCS-062. All acoustic signals were acquired simultaneously using a National Instruments 24-bit PXI data system. Data were sampled at 102.4 kHz yielding a 40 kHz bandwidth. Eight unsteady surface pressure transducers were mounted on the model at locations near the TPS nacelle and along the mid-fuselage as shown in Fig. 2. Seven fixed microphones were installed outboard of the left wing and a phased microphone array was outboard of the right wing as shown in Fig. 1. The microphones were staggered so that their turbulence would not impinge on downstream microphones. Emission angles to each microphone are relative to the acoustic center of the model, defined as the point on the stream-wise centerline of the model on a line between the points of sweep change in the wing trailing edges. Figure 9.1 and Figure 9.2 show the location of the acoustic center.

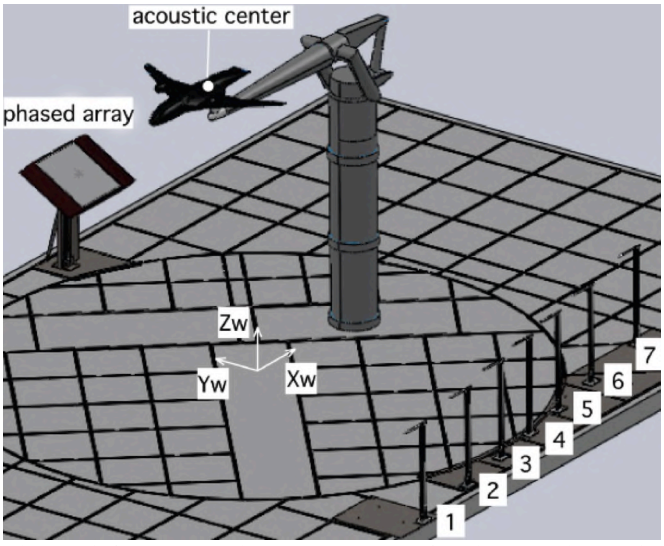

Figure 9.1. Test section layout used for AMELIA test in the 40x80ft wind tunnel.

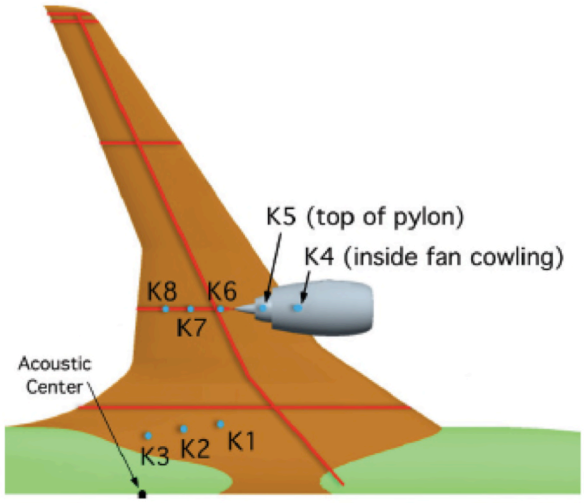

Figure 9.2. Test section layout used for AMELIA test in the 40x80ft wind tunnel.

The 48-channel, 40-inch diameter array (shown in Figure 9.1) was mounted in an aerodynamic fairing and recessed behind a porous Kevlar screen. The array pattern and processing software were purchased from Optinav, Inc. In addition to conventional beamforming, the software provides deconvolutional post-processing with CLEAN-SC, DAMAS2, TIDY, and other algorithms, however conventional and TIDY processing were used exclusively for this test.

9.1. Experimental Results

Selected results from the measurements are presented in the following sections to convey a sense of the scope of test conditions, and quality of data with regard to signal-to-noise levels. The data are presented at model scale and physical measurement distances in the wind tunnel. The microphone and array data have not been corrected for directional nosecone or array fairing treatment effects, which can vary from 0 to 10 dB, but more typically around 2dB.

9.1.1. Turbo Fan Propulsion Simulator (TPS) Measurements

The TPS units were not acoustically representative of the full-scale turbo propulsion system, but provided the desired aerodynamic effect on the wing flow. They did provide an intense wide-band acoustic source above the wing for comparative measurements of wing shielding effects, as discussed below. Referring to the overhead view of the wing and TPS in Figure 9.2, it can be seen that forward TPS radiation should experience little shielding in the forward arc, but the wing should significantly shield aft TPS radiation. Local pressure sensors K4, K5, and K6 were placed on along the axis TPS to help distinguish forward-from aft-radiated noise, however several of the Kulites failed at the start of the test (K2, K4, K6).

The placement of the propulsion unit above the wing was chosen to allow the wing to obstruct some of noise propagating towards the ground, and to determine the aerodynamic effects of this configuration. During the test, the TPS height above the wing was varied with pylons of two different heights (Z/D = 0.84 and 1.25), but the span- and chord-wise placements were not varied. Comparisons of the high- and low-pylon directivities of OASPL at 40 kts for flap angles of 0º and 80º are shown in Figure 9.3 and Figure 9.4, respectively. The low pylon configuration was expected to provide greater wing shielding, and this trend is observed in the range of 70º to 130º for the three flap angles, with a 2 dB to 3 dB difference in shielding effect for the two pylon heights. The TPS units are expected to generate a complex source distribution, with forward- and aft-radiated fan/turbine and jet noise.

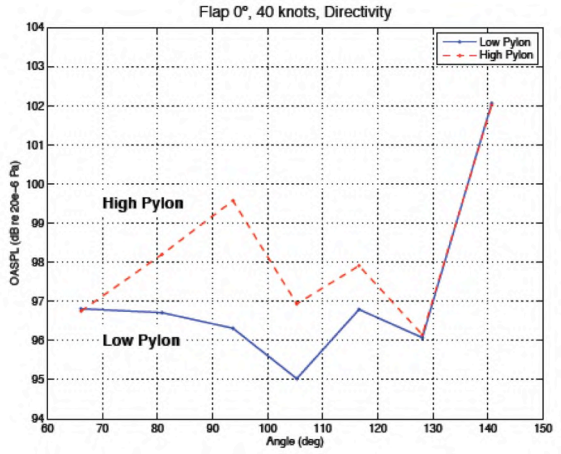

Figure 9.3. OASPL comparison of low vs high pylon directivity at 40 kts, flap 0°.

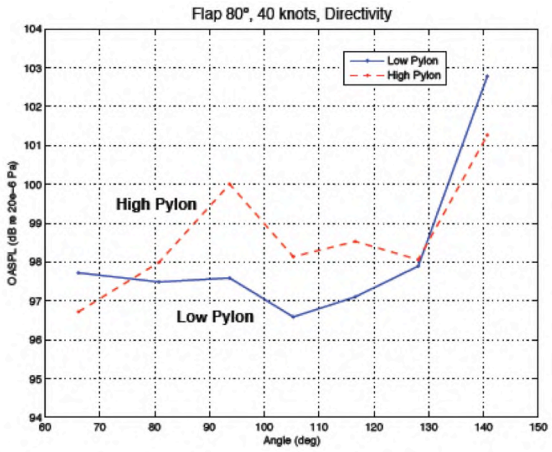

Figure 9.4. OASPL comparison of low vs high pylon dectivity at 40 kts, flap 60°.

9.1.2. Slot-Blowing Active Lift Noise

The AMELIA test provided an excellent opportunity to document the noise associated with blown trailing- and leading-edge (TE and LE) slots. A cross-section of the wing at 80º flap is shown in Figure 9.5, which depicts the separate TE and LE plenums as well as the slot nozzle exits. Measurements were acquired with both TE and LE slots active, as well as with TE only active. The AMELIA test provided a new and unique set of aerodynamic and acoustic measurements to help improve the understanding of active lift on a realistic flight configuration. Figure 9.6 shows a set of 1/3-octave spectra for each of the 7 fixed microphones for the 40 kt, 60º flap configuration. Both TE and LE slots are active from minimum to maximum slot flow rate, corresponding to 0.002 " Cμ " 0.88. The plots show that the slot noise increases across all frequencies as the mass flow increases, with the highest rate of increase with Cμ at the lowest flow rates. At the lowest and highest Cμ values, the spectra are smooth, however several tones are present up to 10 kHz at moderately low Cμ. A preliminary comparison of the variations in model lift coefficient and 110º microphone OASPL level is shown in Figure 9.7. The trend of increasing CL with blowing rate is non-linear as is the case with OASPL, but the rate of increase at the lowest Cμ values is more moderate.

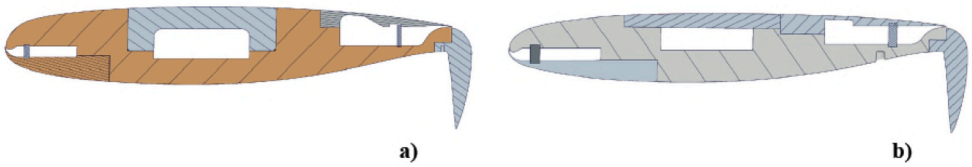

Figure 9.5. Wing cross section of slot plenums and exits, flap 80°, a) inboard cut 26 in from model center, b) outboard cut 50 in from model center.

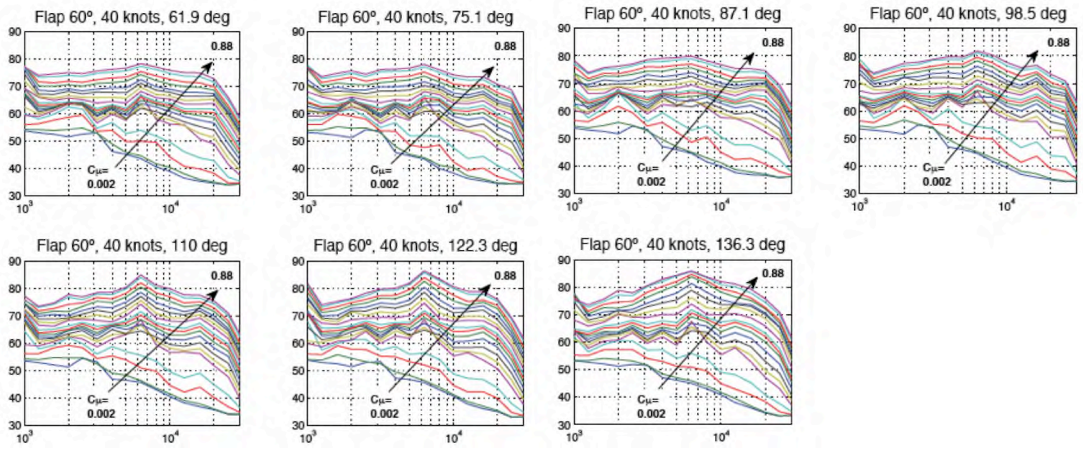

Figure 9.6. Effect of slot mass flow rate on 1/3-octive spectra for 7 microphones, 40 kts, flap 60°, Cμ 0.002.

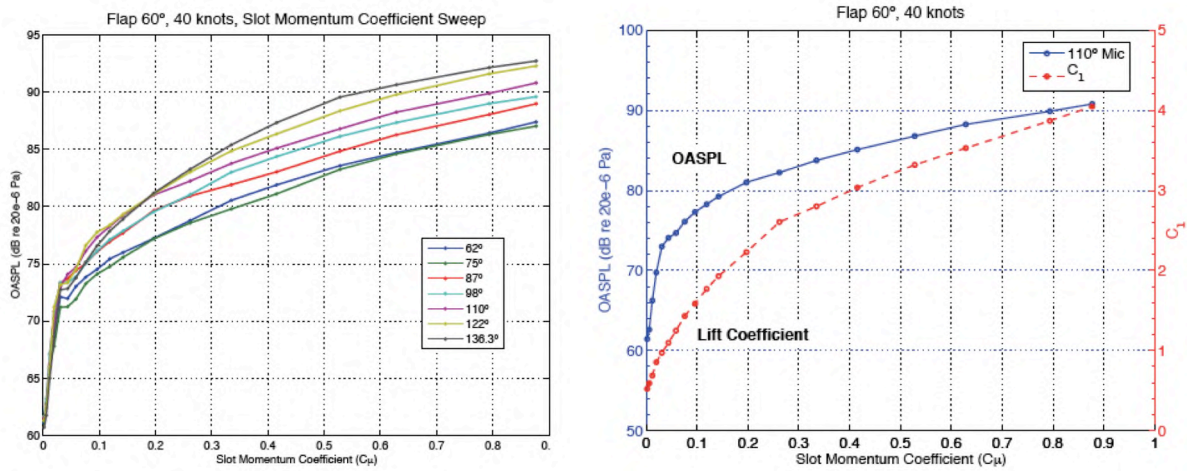

Figure 9.7. Left plot shows variation of OASPL with slot mass flow rate for 7 microphones, 40 kts, flap 60; Right plot shows variation of OASPL and model lift coefficient with slot momentum coefficient, 110° microphone, 40 kts, flap 60°.

9.1.3. TPS and slot blowing relative source strength

An indication of the relative strengths of the noise sources may be gleaned from combined plots of slot blowing and TPS OASPL directivity, as is seen in Figure 9.8 for the 40 kt, 60º flap condition. The lowest level curve is for TPS removed, slots off, and represents a combination of noise from the model airframe, sting, and pylon support with relatively small variation in directional level. The curves associated with slot blowing as Cμ varies from 0.06 to 0.88 range from roughly 12 to 26 dB higher. Operating the TPS units at full power adds 5-10 dB to the highest slot blowing level. This suggests that that the TPS dominates the OASPL field when it is running, and that slot-blowing noise overwhelms the airframe noise over most of the full range of Cμ.

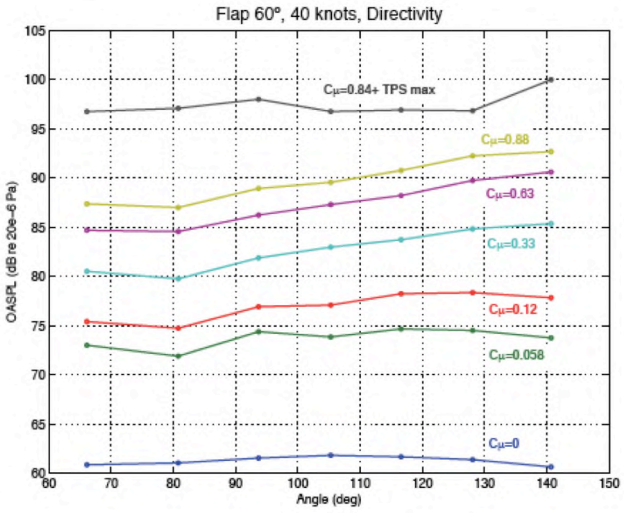

Figure 9.8. Comparison of directional OASPL levels for three configurations: a) clean wing (Cμ =0, TPS removed), b) slow blowing (Cμ 0.058 to 0.88), c) max Cμ, TPS max (33,400 RPM), 40 kts, flap 60º).

9.1.4. Phased Microphone Array Results

Contamination of the slot noise source by the high-pressure air ducting and valves is a concern that can be addressed by examining array source location plots. Two coiled hoses external to the sting delivered the slot air. Figure 9.9 shows no evidence of sidelobes at frequencies ranging from 1 kHz to 16 kHz suggesting that contamination is minimal. A separate high-pressure air flow-path was used to drive the TPS units; air flowed through the sting, then through a model support blade at the end of the sting, and finally through an 6-inch flow through balance inside the model.

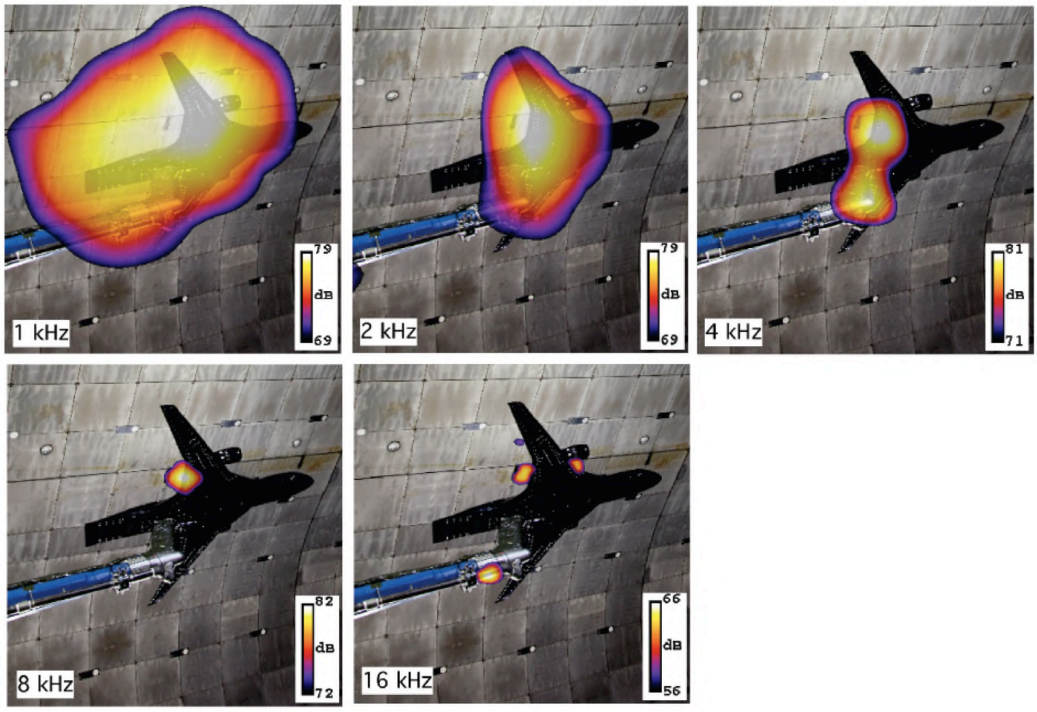

Figure 9.9. Phased array images at 1 kHz, 2 kHz, 4 kHz, 8 kHz, 16 kHz, 40 kts, flap 60º, clean wing, max slot blowing.

Figure 9.10 shows that most of the acoustic energy from the TPS units was due only to the TPS. The lack of high-pressure air contamination to the TPS and slot-blowing model noise is consistent with the flow control metering systems located internally within the solid metal skin model.

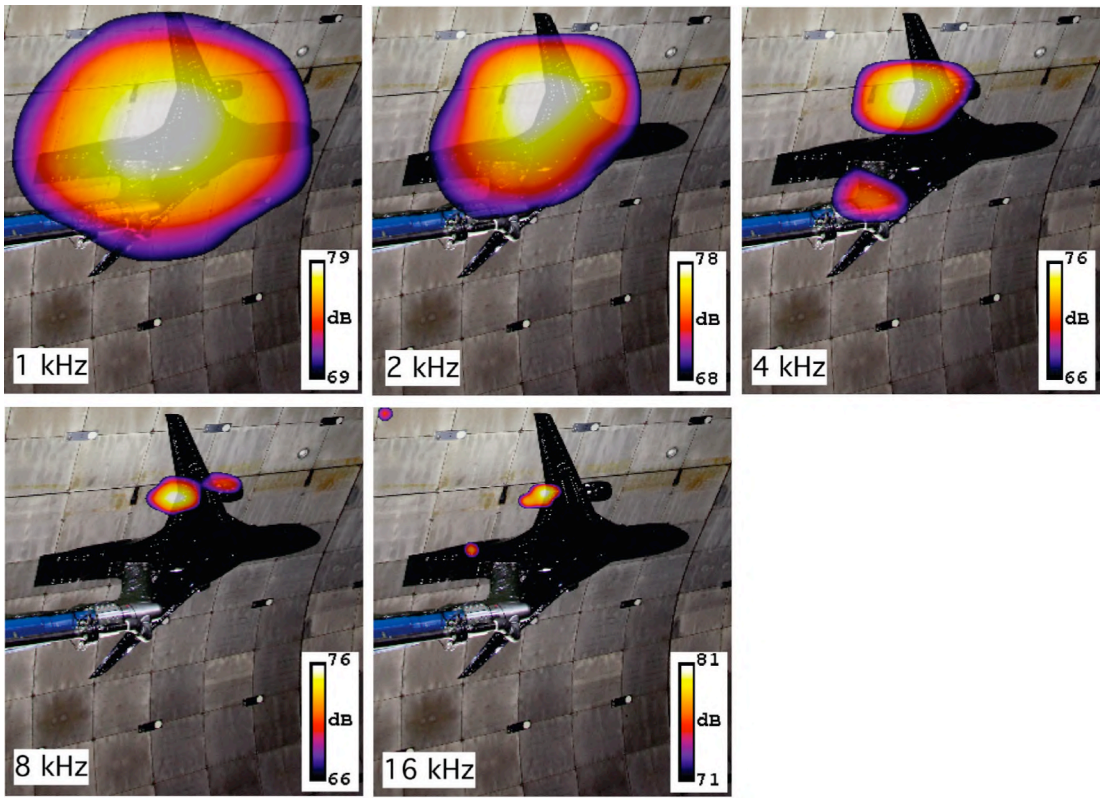

Figure 9.10. Phased array images at 1 kHz, 2 kHz, 4 kHz, 8 kHz, and 16 kHz, 40 kts, flap 60º, high-pylon, max TPS, no slot blowing.

Preliminary analyses indicate signal-to-noise of the 40-inch, 48-element phased array was excellent over the full range of test conditions. The seven single microphones showed a good signal-to noise ratio for the 40 kt case but at higher speeds the wind tunnel background noise exceeded the noise produced by the lowest slot blowing rates.

10.Slot Blowing Performance and Calibration

10.1. Slot Design Considerations

Circulation control plenums have evolved drastically from the cumbersome, bolt on additions used in static tests on the QSRA in the 80's, to the advanced plenum designs with internal slot height sensors used recently by Jones[14,15]. Many of the past circulation control wind tunnel experiments have been conducted using an elliptical airfoil with a circular trailing edge[16,17,18,19,20]. Over the years this geometry and slight variations of it have provided a thorough foundation of circulation control data. An example of an elliptical airfoil configuration can be seen in Figure 10.1 and Figure 10.2. While this configuration continues to be relevant in many areas of research, recently circulation control airfoils have changed shape to reflect the state of the art in next generation commercial transport wing design.

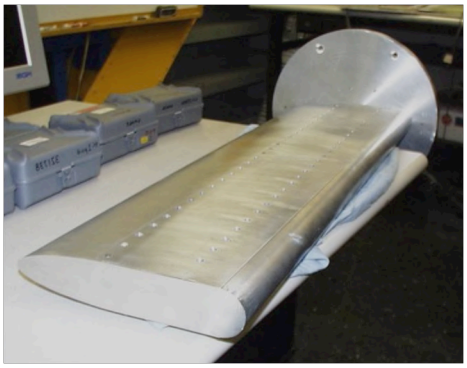

Figure 10.1. Elliptical circulation control airfoil model with rounded trailing edge.

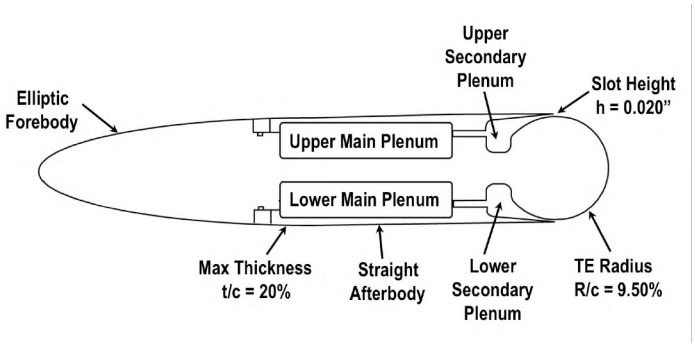

Figure 10.2. Cross section of the elliptical airfoil.

Many of the recently manufactured circulation control wind tunnel test articles depart from the circular trailing edge in favor of a dual radius flap design.[21] In principal the dual radius flap enables the preservation of plenum geometry despite an adjustable flap deflection. The cross section of a circulation control wing using a dual radius plain flap can be seen in Figure 10.3[21]. AMELIA employs a simplified version of the dual radius flap shown in the figure, wherein flap deflection is fixed for a given set of flaps.

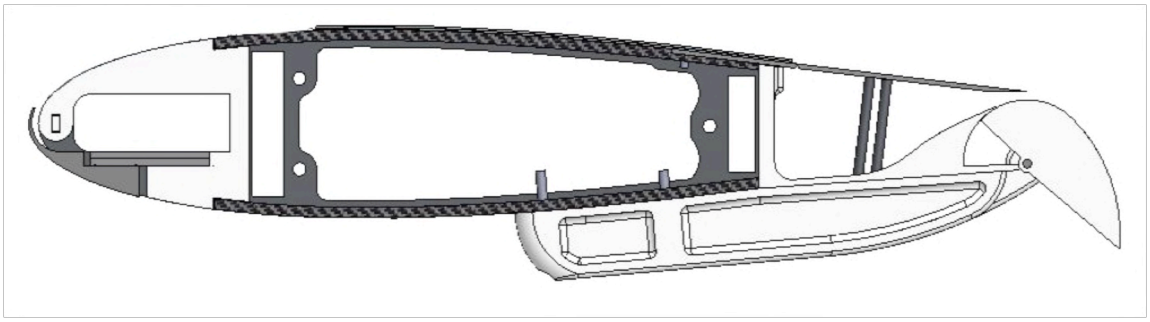

Figure 10.3. Cross section of a circulation control wing using a dual radius flap[21].

One of the major considerations influencing the design of the circulation control plenum was the plenum/flap attachment. With slot height on the order of 0.012" at the wingtip a continuous surface was desired that would allow the boundary layer to grow from the plenum inlet, throughout the slot, and onto the flap surface. In order to achieve a continuous surface, each flap would need to extend into the plenum

where it would attach near the start of the nozzle converging section. This design, although ideal with respect to the circulation control flow quality, proved problematic in that the slot height (a critical value in the determination of the discharge coefficient) would need to be re-measured after each flap change. Alternatively, the flap could be manufactured to attach outside of the circulation control plenum, however the transition from flap to plenum would remain the primary concern.

Other significant design considerations include the resistance of the plenum structure in expansion under the force of pressurization and local temperature gradients. Accurate knowledge of the slot height throughout the wind tunnel test was a top priority, as even an expansion of a few thousandths of an inch could be a large increase relative to the small ideal height. Two methods were considered to maintain the true slot height. The first used a pair of set-screws and tie-downs placed at close intervals along the length of the plenum. This method would allow the restricting structural device to be placed within the plenum at a distance sufficient to not disturb the slot flow. It would also allow for local adjustability of the slot height, permitting precision control on-the-fly (when the system is under pressure). The set-screw/tie-down method had prior success in wind tunnel tests executed by Englar and Cattafesta[21,22]. The second method involved placing rigid supports within the plenum at regular intervals along the span of the slot[15]. These thin supports would reside within the slot itself, and would be secured to both the lower (nozzle) surface and the upper skin. Later versions of this method included supports only in the nozzle section of the plenum—terminating before they reach the slot. The primary concern with these supports is their close proximity to the slot itself, and the resulting influence on the circulation control flow.

The flow straightening treatment within each plenum was also a consideration when formulating the design of the circulation control plenums. With the instrumentation and structure within AMELIA's wings, only a limited amount of volume could be allocated to the plenums. Similar circumstances had been seen in previous wind tunnel tests[15], where the plenum volume was insufficient to establish a true stagnant condition. In these previous tests choke plates were employed to act as a flow restriction device and unify the conditions along the length of the plenum. The design of the air supply system to the circulation control plenums within AMELIA would only serve to intensify the need for flow treatment—as each narrow plenum was fed by only a single source at one end. Figure 10.4 and Figure 10.5 show the internals of the FAST-MAC model with multiple plenum supply locations and choke plate in contrast to the AMELIA model configuration with a single plenum supply[15]. The type of plenum treatment to use on the AMELIA model was the subject of lengthy debate. Choke plates seemed to offer the most promise, and were successfully applied in similar cases, however acousticians worried the small orifices in the plates would emit high frequency noise that could be indistinguishable from the slot noise. Other options for flow treatment included a metal foam product manufactured by ERG Aerospace. The foam could be manufactured to appropriate tolerances, and was available in many porosities, the manufacturer also provided data showing its ability to provide a pressure reduction in fluid flow.

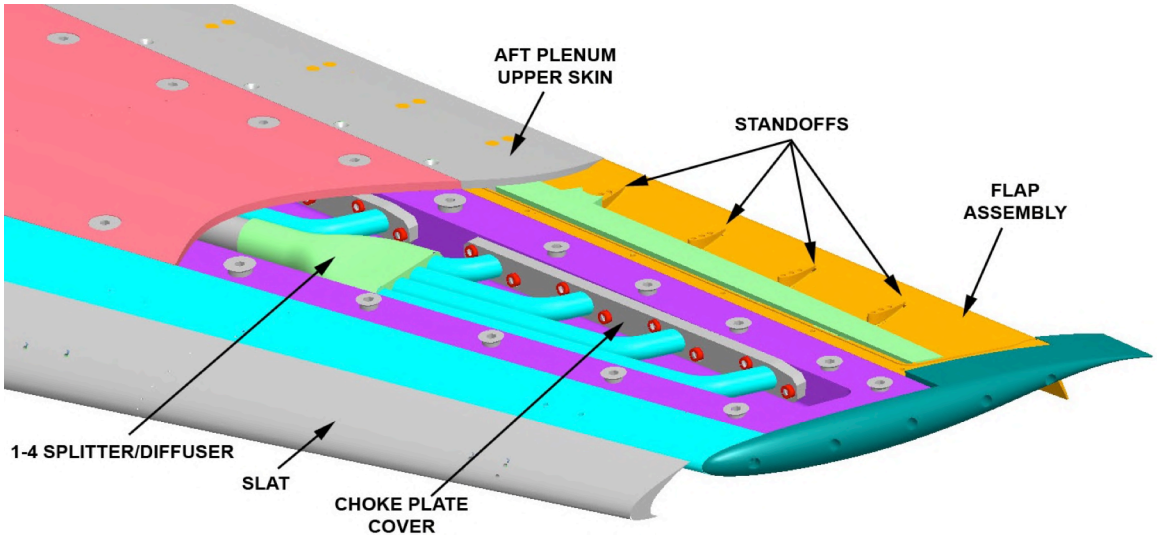

Figure 10.4. The internals of the FAST-MAC wind tunnel model, with multiple plenum supply locations and a choke plate[15].

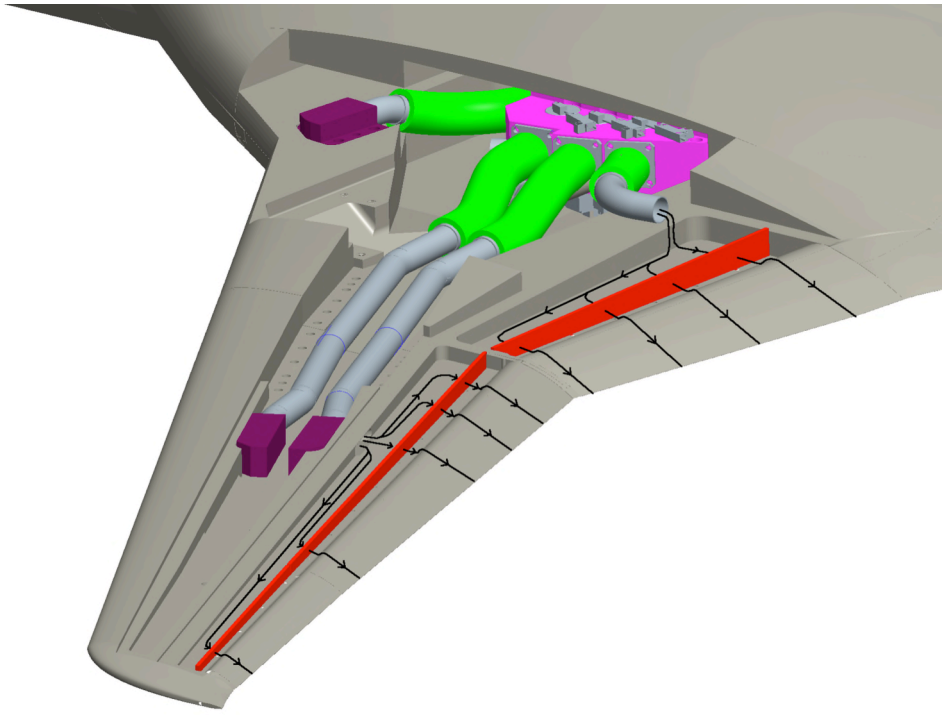

Figure 10.5. Circulation control supply system inside the AMELIA model, each plenum supplied by a single source.

Minimizing breaks in the slot caused by plenum intersections was a high priority in terms of providing clean circulation control flow across the upper surface of the wing and flaps. In order to achieve this, many plenum layout designs were considered, including a design that allowed air to pass freely from inboard to outboard plenum. Other designs (like the one shown in Figure 10.5) included separate inboard and outboard plenums, allowing for independent pressure control. The separating structure, at both the leading and trailing edge in this design, tapered as it approached the slot face in order to minimize

unblown regions. Although the unblown region at the wing break was minimized, it could not be completely eliminated.

The majority of the plenum design characteristics (nozzle contraction ratio, plenum aspect ratio, slot height to chord ratio) were based on values used in previous models and suggestions from Englar and Jones.

10.2. Slot Calibration

Figure 10.6. The trailing edge slot on an (unpainted) AMELIA.

AMELIA's final slot configuration can be viewed in Figure 10.6 for the trailing edge of the left wing. The model is shown with a zero degree flap, and no surface treatment (this image was captured during model construction at PatersonLabs). The flap joins to the model just aft of the circulation control slot, which allows for the preservation of the slot height despite flap changes. Adjustments to the slot height are enabled through the set-screw/tie down method discussed in the previous section and seen in Figure 10.7.

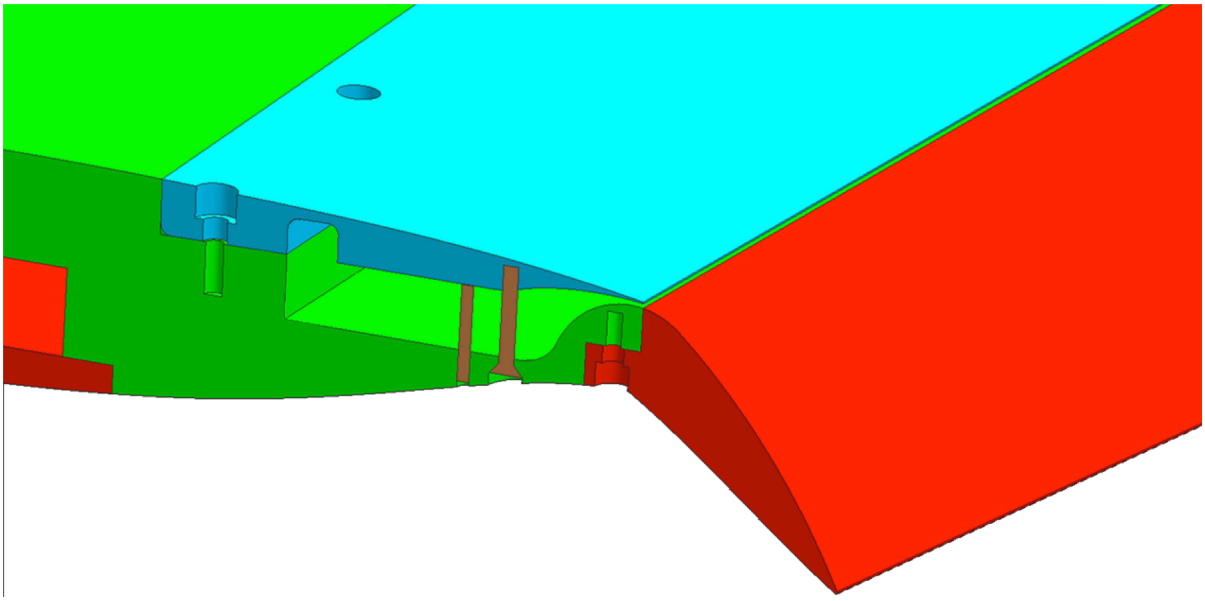

Figure 10.7. Cut-view of AMELIA's wing showing trailing edge plenum shape and flap attachment.

The final plenum layout can be seen in Figure 10.8. Each of AMELIA's wings uses four plenums (two leading edge and two trailing edge). The trailing edge plenum covers are incorporated into the skin of the upper surface, while the leading edge covers make up the lower surface. Each inboard plenum terminates at the wing break (approx. 29.5" from model centerline), the outboard plenums terminate at the wingtip (roughly 58.5" from the model centerline). A detailed view of the plenum is shown in Figure 10.9, data associated with the figure is presented in Table 10.1.

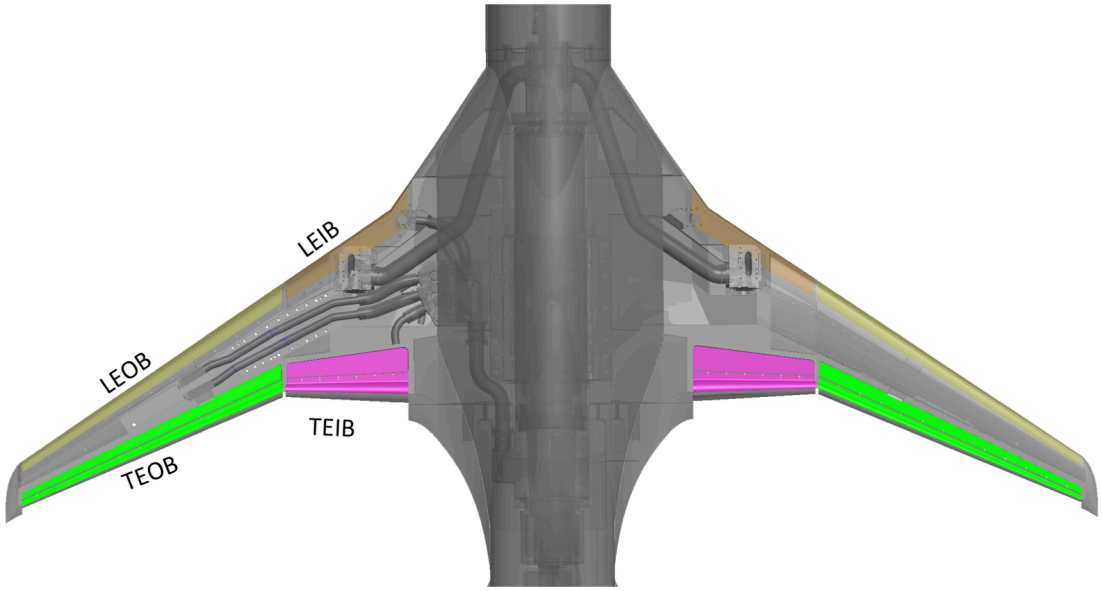

Figure 10.8. Circulation control plenum layout.

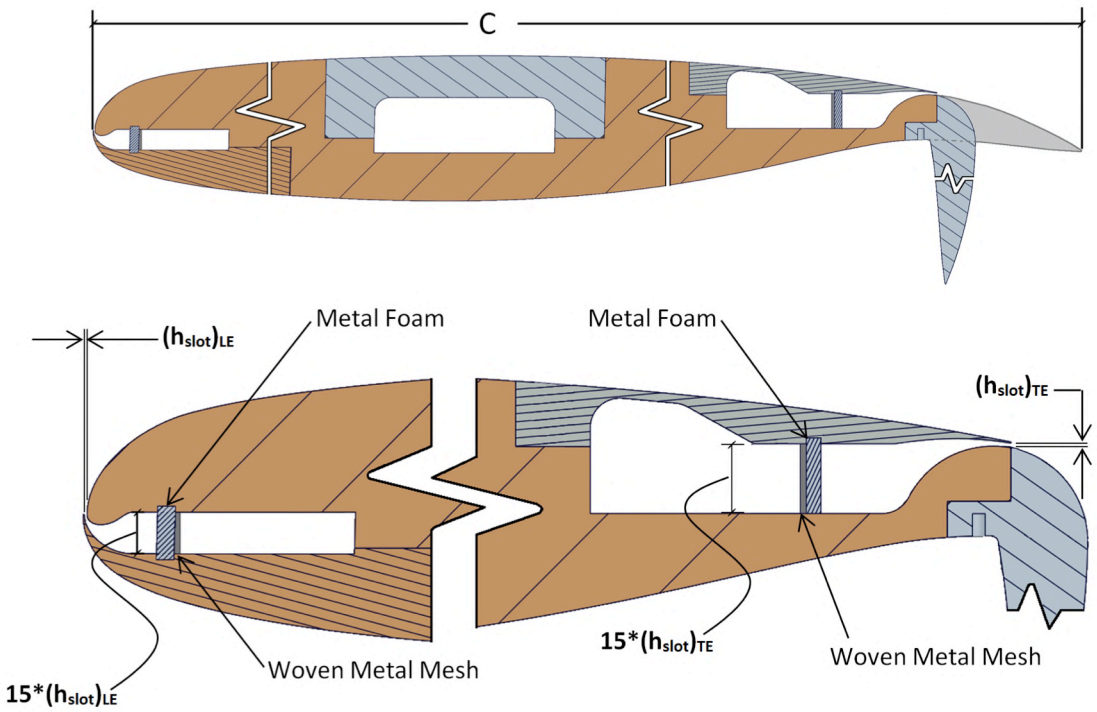

Figure 10.9. Detailed view of the circulation control plenums.

Table 10.1. Leading and trailing edge plenum design details.

	Leading Edge	Trailing Edge
h_{slot}/c	0.001428*	0.00238
Contraction Ratio	15:1	15:1
Minimum Lip Thickness	0.01”	0.01”
***this ratio held true until $(h_{slot})_{LE}$ =0.012” (BL_540→End of slot)**		

The information presented in the above table and figure, define the design parameters used in the manufacturing of AMELIA. The slot height was adjusted to the *ideal* values (shown above) through use of the set-screw/tie down pairs (for more information on the actual slot height compared to the ideal see the slot height section). In order to condition the circulation control flow, each plenum contains a barrier of a woven metal mesh and metal foam.

10.2.1. Metal Foam

Slot flow condition was achieved using a metal foam product manufactured by ERG Aerospace. During the slot flow calibration effort, metal foam with 12-15% density and 6-8% density were tested (both sets of foam contained 40 pores per inch). The foam density value is a ratio of the mass of the foam divided by its original mass of aluminum (prior to undergoing the chemical process that creates the cavities). The higher density foam was found to be more effective in resisting flow (thus providing more straightening), and its rigidity made it more easily manipulated. Although each piece of foam was custom manufactured for each plenum, a small degree of hand work was required to ensure proper fitment. Furthermore room

temperature vulcanizing silicone (RTV) was used at either end of the foam as a means to ensure a proper air seal. The metal foam and woven metal mesh (Rigimesh) are shown in Figure 10.10.

Figure 10.10. Samples of metal foam and woven metal mesh used in the circulation control plenums (images courtesy of ERG Aerospace and the Pall Corporation).

10.2.2. Rigimesh

The woven metal mesh in Figure 10.10 is a product manufactured by Pall Corporation known as Rigimesh. Rigimesh is available in many values of porosity and is used widely in the aerospace industry for screening material in wind tunnels. This product was recommended for use in AMELIA's plenums based on its ability to resist flow. Pressure loss calculations based on a simplified version of AMELIA's low pressure system supply geometry, indicated a large difference in pressure being delivered to the inboard and outboard plenums. It was suspected that Rigimesh could be employed to accommodate for the uneven pressure loss created by the differing geometry leading to the inboard and outboard plenums.

10.3. Slot Flow Calibration Set-Up

The wind tunnel model was transported to the FML six months prior to the scheduled wind-on date, in order to provide an assisted check-out and build-up of AMELIA's critical systems. Calibration of AMELIA's slots occurred over a three month period at NASA Ames Research Center's Fluid Mechanics Lab(FML). The calibration was a considerable effort requiring an air source capable of delivering 300 CFM at 80 psi. In order to achieve the requirements of the model's air supply system, an instrument quality air compressor capable of 1600 CFM at 150 psi was rented. The compressor was placed outside the FML's Test Cell 1, as shown in Figure 10.11.

A Flow-Dyne critical flow nozzle, with a 1.004" throat diameter, was installed between the compressor and the wind tunnel model as a means of making mass flow rate measurements. The nozzle included an approach tube with taps for upstream temperature and pressure measurements. A second pressure tap (located downstream of the diffuser section) allowed for the verification of the pressure ratio required for critical flow.

In order to choke the flow at the throat, an upstream to downstream pressure ratio of 1.2 was required across the nozzle. The slot flow calibration would require a mass flow rate of 1.4 lbm/s, as each wing was calibrated independently. At the typical air supply temperature, this mass flow rate corresponds to an upstream pressure of approximately 77 psig. However, due to the flow resistance properties of the treatment being tested in the circulation control plenums, the upstream pressure needed to be raised to nearly 87 psig to maintain the required pressure ratio. This higher upstream pressure forced the calibration

Figure 10.11. Air compressor used for the slot flow calibration effort.

mass flow rate to be slightly higher than required (approximately 1.58 lbm/s). The goal of the calibration—to achieve uniform slot flow—would be minimally effected by the difference in mass flow rate.

Many components, besides the critical flow nozzle, were required including reducers, multiple safety relief valves, and globe valves for flow control. The calibration system schematic can be seen in Figure 10.12.

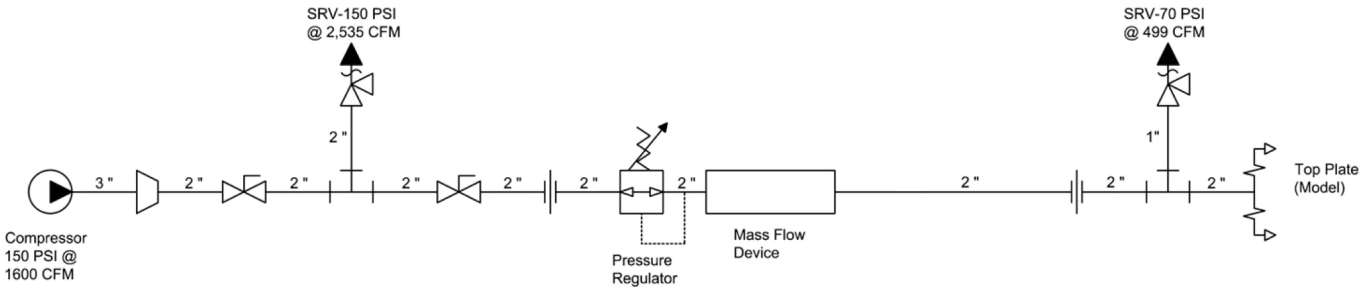

Figure 10.12. Schematic of the slot flow calibration air delivery system.

In order to produce realistic flow conditions in the circulation control plenums, air was delivered to the model's low pressure distribution plenum (see the Model Description Section for further details on this plenum). From the low pressure distribution plenum, AMELIA's internal butterfly valves could be used to control the mass flow delivered to each circulation control plenum (this would also provide a check-out of the gear motors used to adjust the butterfly valves). Figure 10.13 shows the model in Test Cell 1, with the air supply attached to the right wing low pressure distribution plenum. The model was secured to a work table through a metal frame bolted to the model's underside.

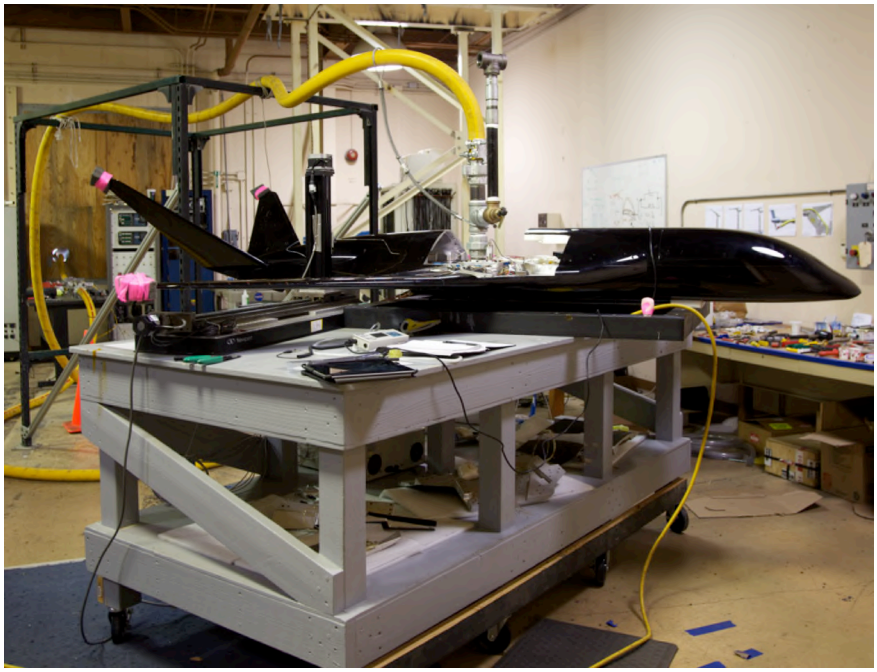

Figure 10.13. Slot flow calibration set-up with air supply attached at the LPDP.

10.4. Oil Flow Results

Initial slot flow calibration runs were treated as a means to qualitatively evaluate the safety and performance of the test set-up and model. In regards to the slot flow, these qualitative evaluations typically involved a certain degree of "feeling" the flow, after which it was apparent that there was serious non-uniformity coming from the leading edge slots. Fluorescent tufts were used to further explore the poor flow coming from the slots, however after a few runs it was determined that the tufts lacked the resolution needed to fully visualize the upper surface flow. Pigmented gear oil was later used on the upper surface of the wing as the primary indicator of flow uniformity. The slot flow calibration was performed on the right wing (as shown in Figure 10.13), as the left wing was instrumented with numerous surface pressure ports that could be compromised by the oil. Once acceptable flow uniformity was achieved on the right wing, the plenum treatment would be duplicated on the left wing and checked for symmetry.

10.4.1. No Treatment

As a baseline case, oil flow visualization was performed on the right wing with no flow treatment in the plenums. The effects of the leading edge outboard plenum inlet were clearly present, and extended as far as the trailing edge inboard plenum (as shown in Figure 10.14). In the absence of flow treatment the plenum does little to create static conditions, allowing the flow to rush out of the slot in the region near the inlet. This was also apparent in the drastically varying readings from the three total pressure probes spanning the plenum chamber (see the Model Description Section for the location of the total probes). Not shown by the oil is the three dimensionality of the flow. Although the flow remains attached to the upper surface of the wing, swirl and vorticity (presumably created by the pathway to the inlet of the plenum) exist well above the wings upper surface.

Figure 10.14. Slot Flow Calibration Oil Flow Visualization: No Plenum Treatment.

10.4.2. 6% Dense Metal Foam

The first attempt at treating the flow in the plenum began with the lighter of the two metal foam densities. The foam was lightly glued into the pre-manufactured grooves just upstream (with respect to the circulation control flow direction inside the plenum) of the total pressure probes. The effect of the 6% dense metal foam can be seen in Figure 10.15. The region affected by the inlet is clearly diminished, however it remains present. The plenum treatment does create some regions of promise, primarily the areas unaffected by the inlet flow where streamlines remain relatively perpendicular to the leading edge slot. Similarities to the "No Treatment" case were present, in the variance in total pressure probe measurements and three dimensionality of the flow.

Figure 10.15. Slot Flow Calibration Oil Flow Visualization: 6% Dense Metal Foam.

10.4.3. 12% Dense Metal Foam

With the few regions of acceptable flow created by the 6% dense metal foam, there was much anticipation for the success of the 12% dense metal foam. This foam was installed in the same manner as the 6%, and tested at the same conditions. The oil flow visualization results for the 12% dense metal foam can be seen in Figure 10.16. Although the areas of acceptable flow quality have grown slightly, the inlet effects still dominate the flow over the wing. Many of the undesirable pressure qualities remained present with this plenum treatment.

Figure 10.16. Slot Flow Calibration Oil Flow Visualization: 12% Dense Metal Foam.

The failure of the 12% metal foam inspired further investigation of the flow within the plenums. The same pigmented oil applied to the wing upper surface, was then applied inside the LEOB plenum (this was also done during the 6% dense metal foam runs). The oil flow visualization of the flow within the plenum can be seen in Figure 10.17. The location of the plenum inlet is near the center of the top figure. The visible oil streaks in the plenum are the attachment lines of the vortices, and serve as further evidence of the existence of highly directional flow in the plenum. As a result of the internal oil flow runs, the focus of the slot flow calibration effort shifted to eliminating the swirled flow in the plenums.

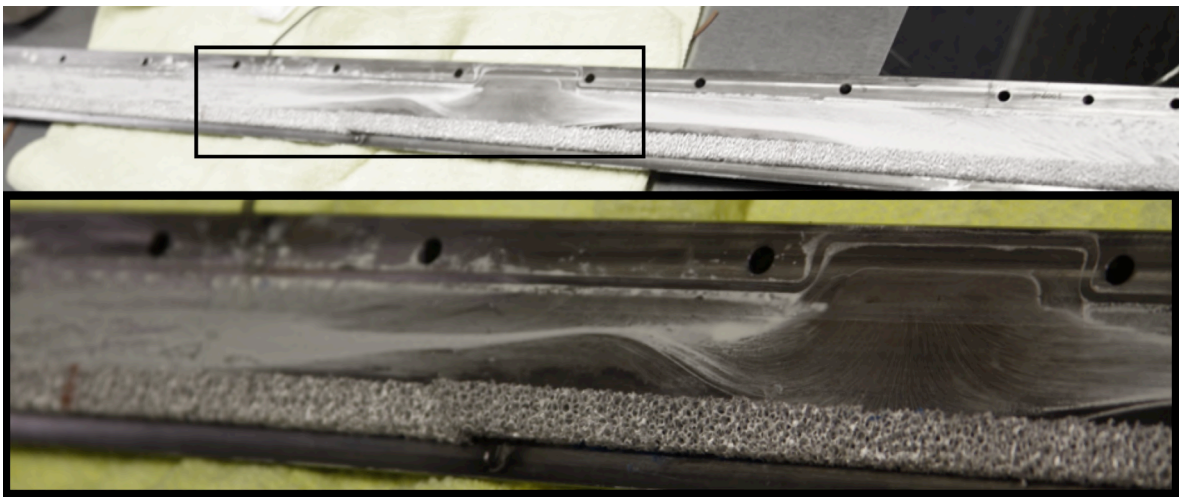

Figure 10.17. Plenum Internal Oil Flow Visualization.

10.4.4. Other Plenum Treatments

The metal foam did succeed in straightening the flow in the regions on either side of the inlet, for this reason many other plenum treatments were testing in combination with the foam. Secondary treatments were tested for the sole purpose of mitigating the vortical flow at the inlet, and thus were implemented only at the plenum inlet (as opposed to the metal foam which spanned the entire plenum length). The first action in mitigating the swirled flow was to smooth the sharp edges of the inlet to each plenum. Additional metal foam, shaped in the form of a wedge, was added to the plenum inlet as one of the first secondary treatments to be tested. The wedge shape and density were altered multiple times before it was ruled out as a treatment. A perforated plate, made from shim stock, was the next test subject. After many iterations of the amount of perforation and layout within the plenum, this treatment was rejected. A rudimentary turning vane was also implemented at the inlet, although (like the other treatments) it altered the flow, the turning vane did little to improve the uniformity. Combinations and variations of these treatments all proved to lessen the effect of the inlet, but not eliminate it.

It wasn't until a small strip of Rigimesh was added to the upstream side of the foam (near the inlet), that the flow began to behave as desired. Until that time, the Rigimesh had not been considered, as it was intended to be implemented near the low pressure distribution plenum to reduce the pressure of the flow being delivered to the inboard plenums.

A summary of the attempts to obtain uniform flow in the leading edge outboard plenum can be seen in Figure 10.18.

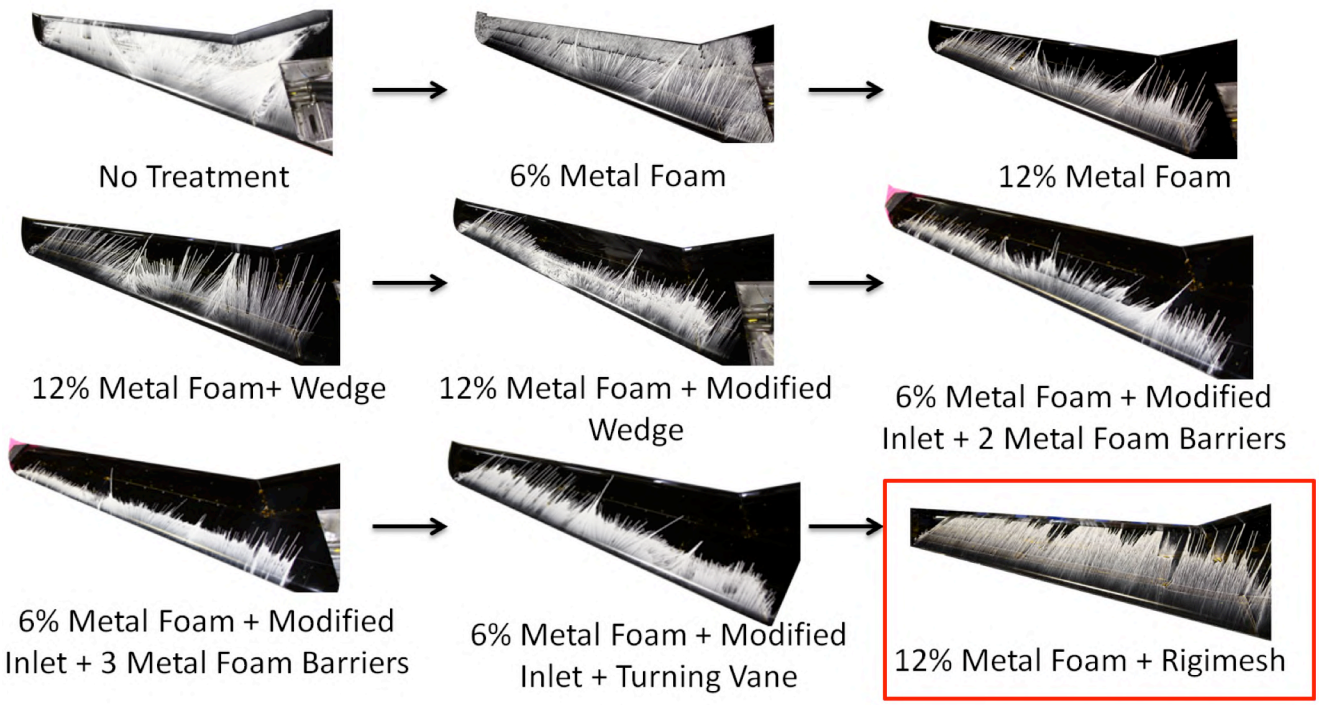

Figure 10.18. Slot Flow Calibration Oil Flow Visualization: Summary.

10.4.5. 12% Metal Foam + Rigimesh

The 12% dense metal foam lined with Rigimesh produced uniform slot flow with an acceptable pressure distribution inside the plenum, shown in more detail in Figure 10.19. Further tuning of the slot flow was accomplished by adjusting the grade, and number of layers of Rigimesh inside each plenum. As mentioned previously, the Rigimesh was intended to be used in the supply pipes branching from the low

Figure 10.19. Slot Flow Calibration Oil Flow Visualization: 12% Dense Metal Foam + Rigimesh.

pressure distribution plenum. In that application, only a small amount of Rigimesh would be needed, therefore only two sheets (9”x9”) were purchased. Fortunately, the facility provided an additional roll of Rigimesh of an unknown porosity. Although its exact porosity could not be identified, its performance very nearly matched the grade J and grade K being tested. Table 10.2 outlines the Rigimesh used in the final configuration of each plenum. Both the outboard plenums required a second layer only in the vicinity of the plenum inlet, while the foam in the inboard plenums received two layers over their entirety. The final configuration of both the trailing edge inboard and outboard plenums can be seen in Figure 10.20.

Table 10.2. Rigimesh treatment in each plenum.

Plenum	Rigimesh Type
LEIB	K,K
LEOB	K,K
TEOB	J,?*
TEIB	J,?*
*** ? represents the unidentified Rigimesh type**	

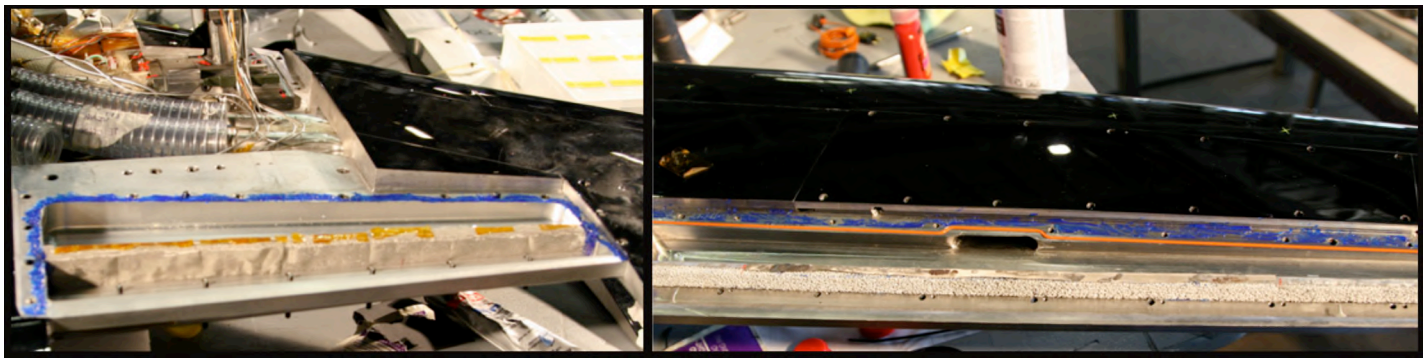

Figure 10.20. 12% dense metal foam + Rigimesh in the trailing edge inboard and outboard plenums.

10.5. Slot Height Setting and Verification

As mentioned previously the design slot height-to-chord ratio differed greatly from the actual slot height-to-chord ratio. With the appropriate plenum treatment in place, and the plenum cover secured, the slot height could be measured and adjusted through the use of the tie-down/set-screw system. Precision measurement of the slot height was of primary importance.

10.5.1. Slot Height Measurement

A hand-held capacitance based gap measurement device was used to obtain values for AMELIA's slot height. The device (borrowed from NASA Langley Research Center) is formally known as the Capacitec Gapmaster3 and when used with the flat-tip, double sided measurement wand has an accuracy of ±0.5 mils. The flexible probe was outfitted with a "probe-stop" that ensured the measurement was taken at a constant depth throughout the survey. Some regions of the slot were inaccessible with the probe due to nozzle curvature, in these regions feeler gauges were employed.

The slot height measurement survey consisted of documenting the slot height in each plenum prior to the wind tunnel test, during the test, and after the test. It also includes a limited dataset of pressurized (circulation control *on*) versus static (circulation control *off*) slot height measurements.

10.5.2. Slot Setting Accuracy

The trailing edge slot height was set according to the slot height-to-chord ratio mentioned previously. Although the tie-down/set-screw system worked well overall, some regions— primarily near the ends of the plenum—proved more stubborn than others. A comparison of the actual slot height to the ideal slot height for each wing is shown in Figure 10.21. The edges of the outboard plenum depart from the ideal curve by nearly 8 mils in some places, however effects from this departure can be considered extremely local. The difference was caused by the inability of the tie-down to overcome the local stiffness of the plenum cover. In one case (as shown at the inboard-most measurement of the left wing's outboard plenum) attempts to further tighten the cover resulted in a permanent tie-down failure.

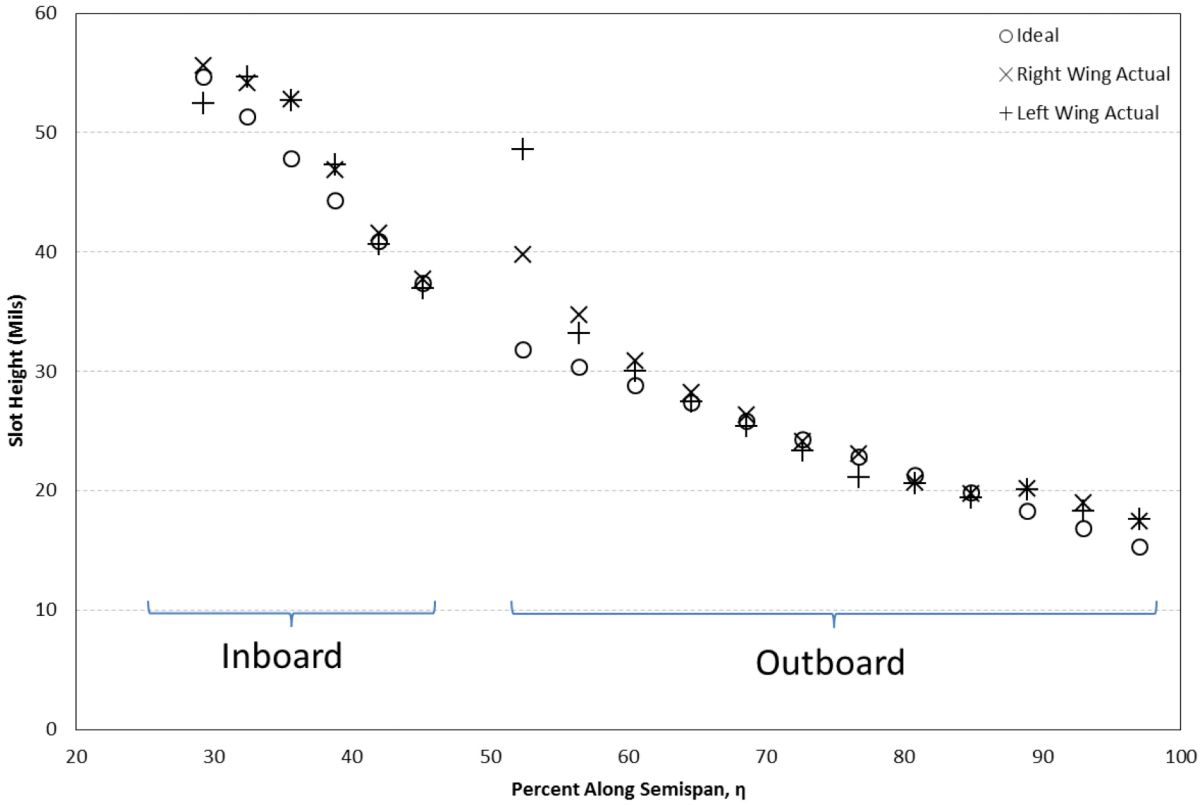

Figure 10.21. Actual Slot Height vs Ideal Slot Height.

The actual slot height values were used to calculate a new slot height-to-chord ratio, as well as a new slot height to radius ratio. These values are shown in Table 10.3, and were used to verify agreement between the test configuration and the original (ideal) design configuration from Year 1 of the NRA. The 6% difference in actual vs. ideal slot height to chord ratio was deemed acceptable.

Table 10.3. Design parameters-as measured.

Design Parameters		
	Ideal	**Actual**
$\mathbf{h_{slot}/c}$	0.00238	0.00252
$\mathbf{h_{slot}/r}$	0.049	0.052

10.5.3. Pressurization Effects

Past circulation control experiments have outlined the importance of documenting the behavior of the slot height under pressure. During pressurization, a small change in the slot height could have serious consequences in the uncertainty associated with the calculation of the discharge coefficient. An investigation into the effect of pressurizing—or flowing circulation control air through—the plenum was conducted using the trailing edge of the right wing. The experiment was performed prior to the wind tunnel test, using the existing setup from the slot flow uniformity work. The comparison between static and pressurized slot height for the right wing trailing edge can be seen in Figure 10.22.

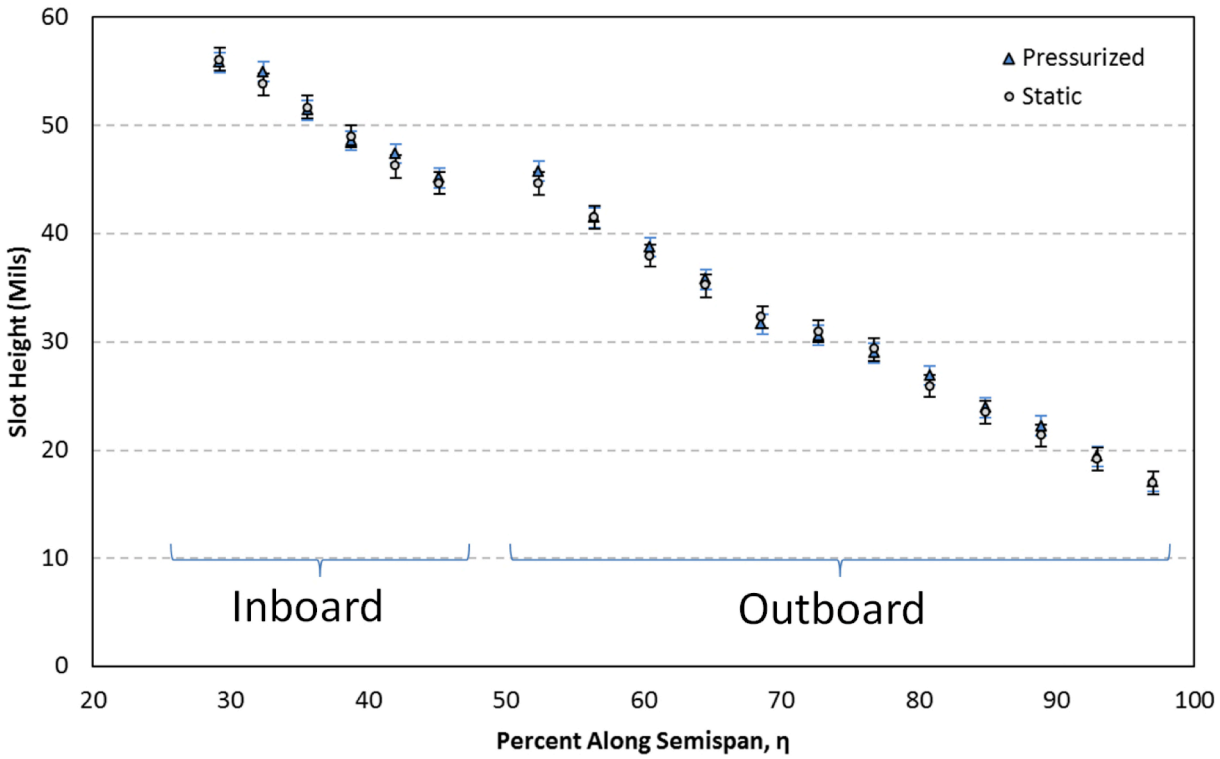

Figure 10.22. Pressurized vs Static Slot Height.

The 95% confidence interval for the static slot height measurements is ±1.1 mils, and for the pressurized slot height measurements is ±0.9 mils. Of primary significance is the scatter of the data falls within the error of the measurement. This verifies the success in setting and securing the slot height using the set-screw/tie-down system. The success of the system in restraining expansion during pressurization severely reduces the time required to take slot height measurements, as the measurements could instead be made statically. Static slot height measurements were preferred as they greatly reduced the risk of damaging the delicate Gapmaster Probe. Further measurements including those for the left wing, and the pretest, during test, and posttest slot height datasets were obtained under static conditions.

10.5.4. Slot Height Symmetry

Establishing symmetric circulation control flow was a primary concern during the slot flow calibration. Although the plenum treatment plays a significant role in establishing symmetric flow, the slot height setting is considered just as (if not more) important for its ability to locally effect the flow. Every effort was expended in adjusting the slot height to match across wings, however in some locations slight differences exist due to local material strength differences, or lack of resolution in the set-screw/tie-down adjustment method. A comparison between the wings at the leading edge is presented in Figure 10.24 and Figure 10.23, where uncertainty for a 95% confidence interval is ±1.1 mils for each wing.

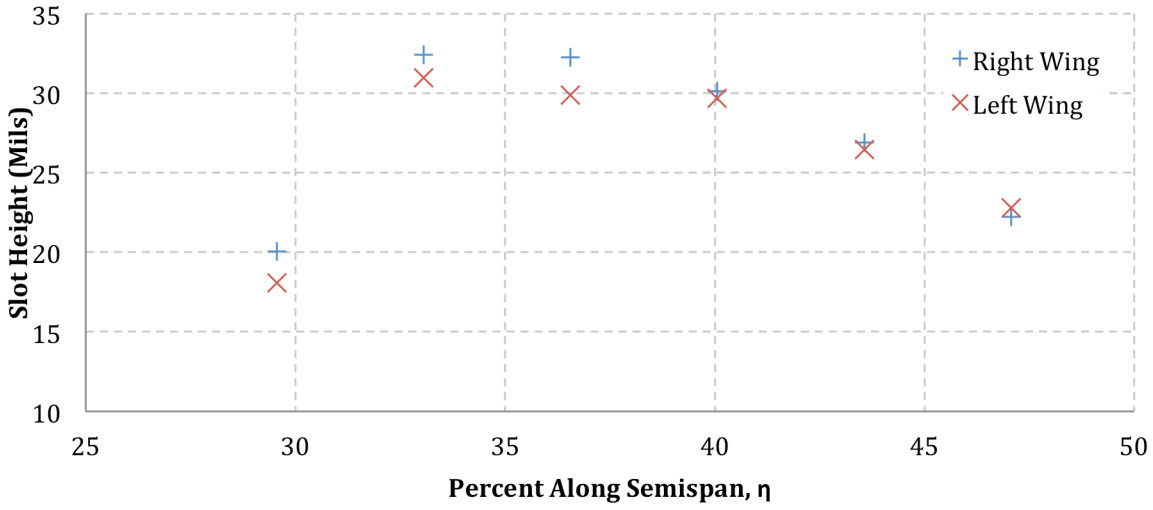

Figure 10.24. Leading Edge Inboard Plenum left and right wing slot height comparison.

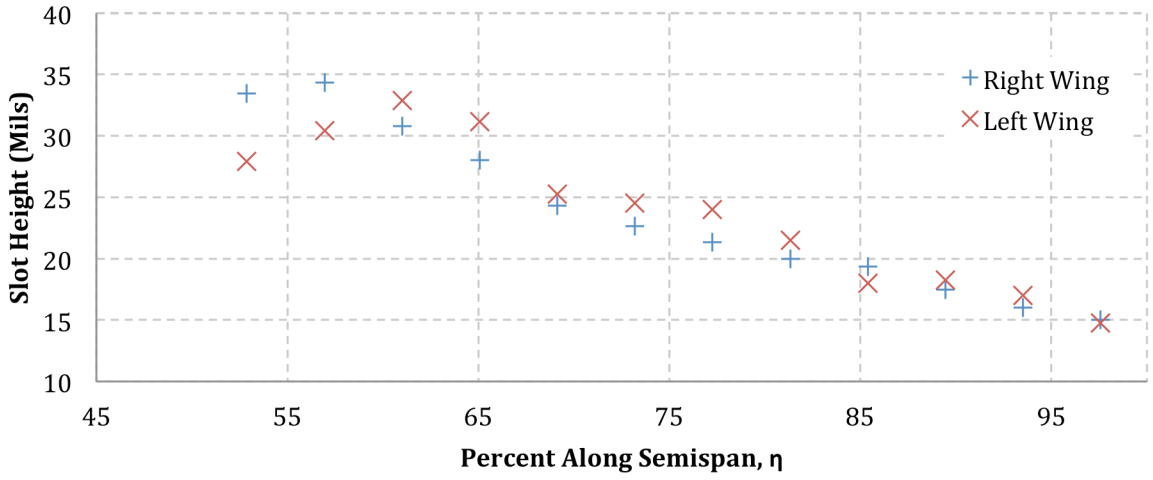

Figure 10.23. Leading Edge Outboard Plenum left and right wing slot height comparison.

The leading edge inboard plenum matched well with only a few locations on the left wing a few mils different from the right wing. The outboard plenum, however, differs by as much as 5 mils in some places. Although this difference is undesired, little could be done as the leading edge plenums are not adjustable.

A comparison of the trailing edge slot heights between the left and right wings can be seen in Figure 10.25 and Figure 10.26, where the 95% confidence interval uncertainty is ±1.1 mils for each wing.

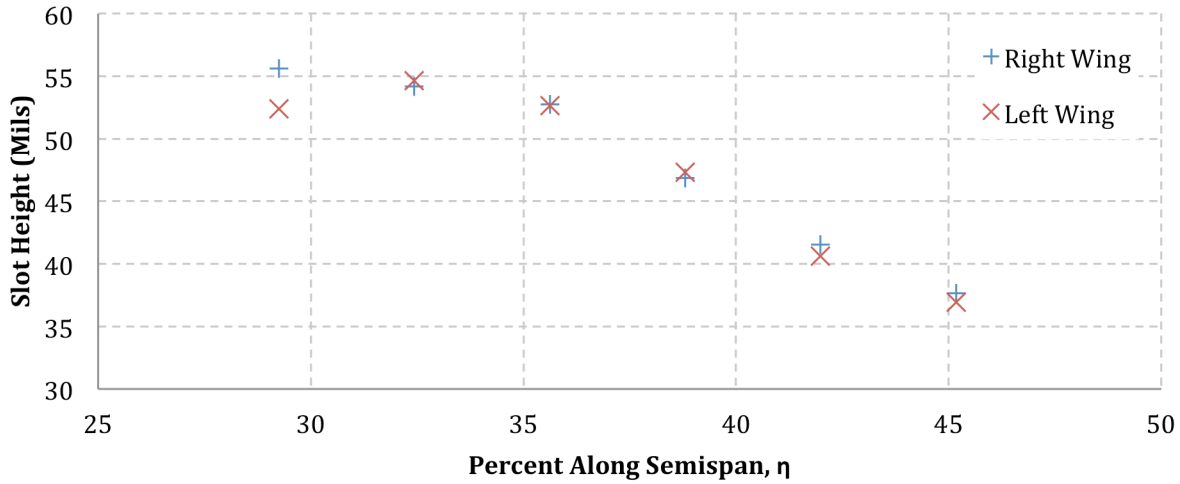

Figure 10.25. Trailing Edge Inboard Plenum left and right wing slot height comparison.

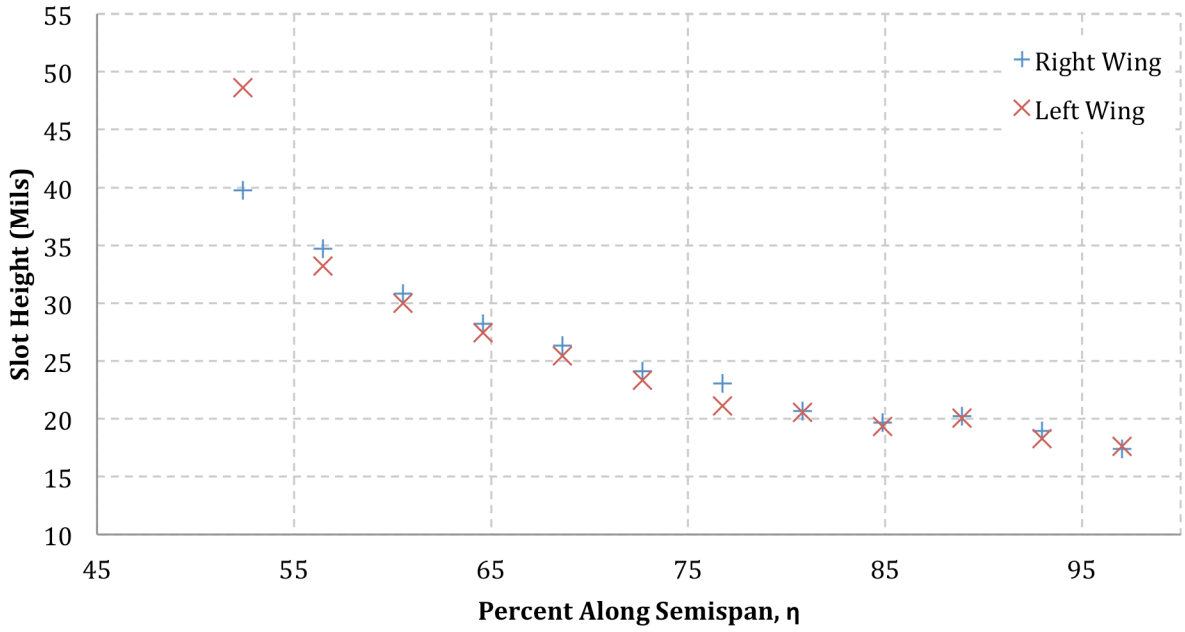

Figure 10.26. Trailing Edge Outboard Plenum left and right wing slot height comparison.

Adjustment through the set-screw/tie-down system allowed for much better agreement between the left and right wing trailing edge slot heights. One difference of 3 mils exists at the inboard most station on the inboard plenum. At this location the cover material is at its thickest and adjustments are difficult. At the same location on the outboard plenum of the left wing a tie-down was tightened beyond its ability and permanent damage to the system at this station occurred. The effect of the broken tie-down was deemed minimal and very localized as an adjacent station was only 1" away.

The success in establishing slot height symmetry permitted the permanent fastening of each plenum and set-screw/tie-down station.

10.6. Total Pressure Survey

The pigmented oil provided a qualitative means to verify flow uniformity and flow symmetry across wings, however a quantitative comparison was also desired. The small scale of the measurements limited the type of instrumentation to hot wires or total pressure probe. The total pressure probe was the selected measurement device as it was widely available and robust enough to withstand the harsh measurement environment.

10.6.1. Survey Set-Up

A total pressure probe with a 0.020" diameter tip was mounted on a Labview controlled 2-axis traverse. The traverse was fixed to a table which was oriented parallel to the slot to be scanned. In order to fully capture the slot flow total pressure profile with as much accuracy as possible the probe was brought to within 3 probe diameters to the slot exit (in the case of the trailing edge only). The flaps were removed to permit the full range of motion of the traverse. The leading edge inboard plenum could not be traversed due to the calibration set-up—the connection at the low pressure distribution plenum prevented the upper surface skin from being attached. At the leading edge outboard slot a total pressure survey was conducted. The measurement could not be made at the slot face, but was instead made on the upper surface of the wing at roughly 20% chord. The total pressure survey set-up is shown in Figure 10.27.

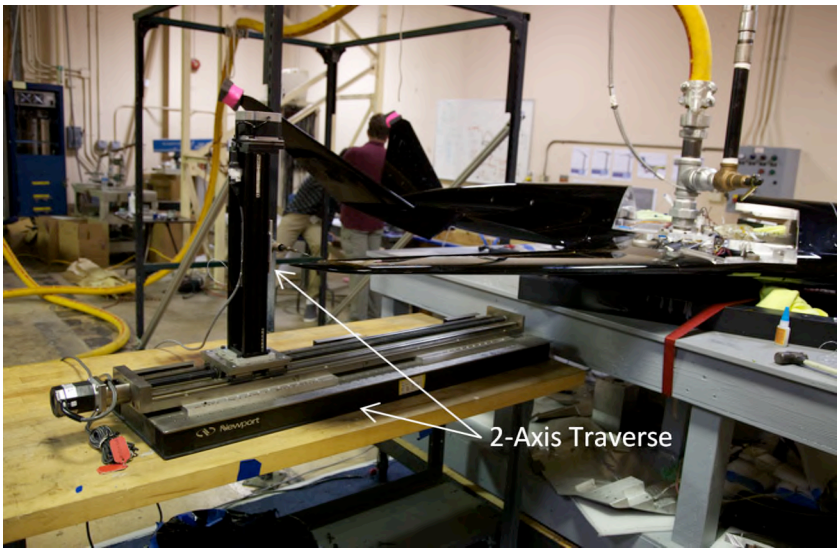

Figure 10.27. Total pressure survey set-up at the right wing trailing edge slot.

10.6.2. Survey Results

The total pressure profiles for the right wing's trailing edge inboard plenum are presented in Figure 10.28. The profiles were recorded at various locations along the span of the plenum, these are indicated by the station number shown in the legend. (Table 10.4 provides a quantification of the station number as a percentage along the span of the *individual plenum*.) The vertical axis represents jet width and is presented in inches from the jet centerline. Total pressure can be read from the horizontal axis in psid. The measurements presented in the figure were taken roughly 0.060" from the slot face. As expected the highest total pressure occurs at the inboard most station where the slot height is greatest. The pressure continues to decrease as the probe travels outboard and the slot height tapers. The traverse grid was not sufficiently able to capture the total pressure at the bottom portion of the jet for the two most inboard stations, however the trend of the outboard stations indicates the expected behavior of the pressure returning to zero. These profiles correlate well with the internal pressure probes, and indicate that there are no problem areas in the TEIB plenum.

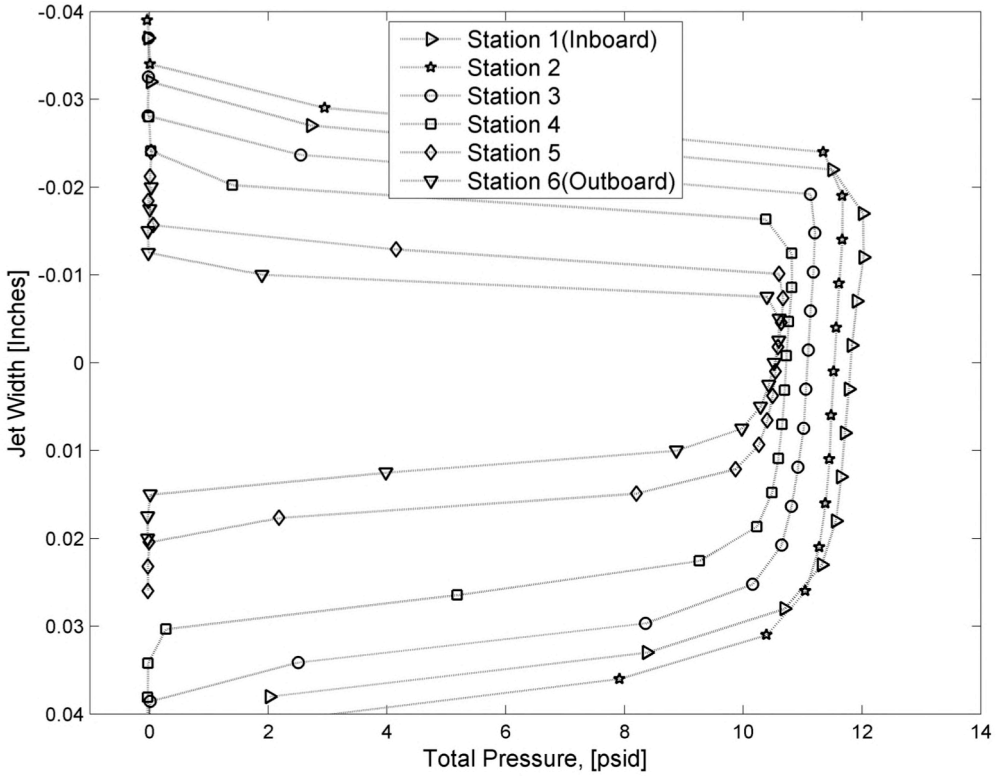

Figure 10.28 . Right wing trailing edge inboard total pressure.

Table 10.4. Station as percent plenum span(TEIB).

Station Number	Percent Along Span
Station 1	2%
Station 2	23%
Station 3	45%
Station 4	68%
Station 5	90%
Station 6	99%

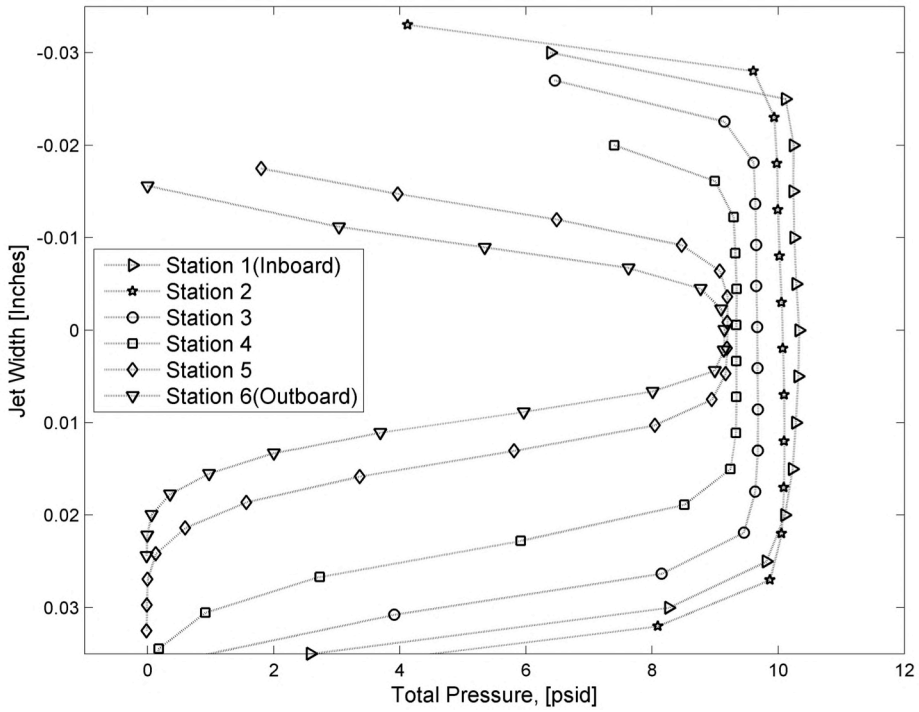

Figure 10.29. Left wing trailing edge inboard total pressure.

The corresponding total pressure survey for the left wing is shown in Figure 10.29 (the legend corresponds to the same values in Table 10.4). The maximum total pressure is achieved at the inboard most station as expecected, however it is nearly 2 psi less than the maximum of the right wing. This is most likely due to a difference in the alignment of the traverse. It was very difficult to align the traverse on the left wing precisely how it had been on the right, primarily due to the traverse/model frame interference. It is suspected that as the probe head traveled outboard, it also traveled slightly away from the slot face, causing the decayed profiles shown at the outboard stations. The profile shape and pressure readings are consistent with jet decay theory. Unfortunately, this survey did not capture the upper portion of the jet, however the trend indicates the total pressure returns to zero.

Table 10.5. Station as percent plenum span (TEOB).

Station Number	Percent Along Span
Station 1	3%
Station 2	23%
Station 3	42%
Station 4	61%
Station 5	80%
Station 6	98%

A survey of the right wing trailing edge outboard plenum (shown in Figure 10.30) shows rounded total pressure profiles similar to those previously discussed. These decayed profiles were expected as the probe was traversed roughly 5 probe diameters from the jet exit, and the average internal pressure of the outboard plenum was less than that used for the inboard surveys. There is greater total pressure variation along the span of this plenum due to plenum length and sensitivity to the decreasing nominal slot height.

The profiles at stations 3 and 4 have the least total pressure, which is likely due to the additional plenum treatment required to diffuse vorticity associated with the plenum inlet. Although ideally these profiles would align as well as those from the trailing edge inboard plenum, these were found to be sufficient given that the flow directionality issues had been solved. Total pressure profiles for the corresponding plenum on the left wing were recorded and verified against these measurements. The left wing data trends matched well with those shown here.

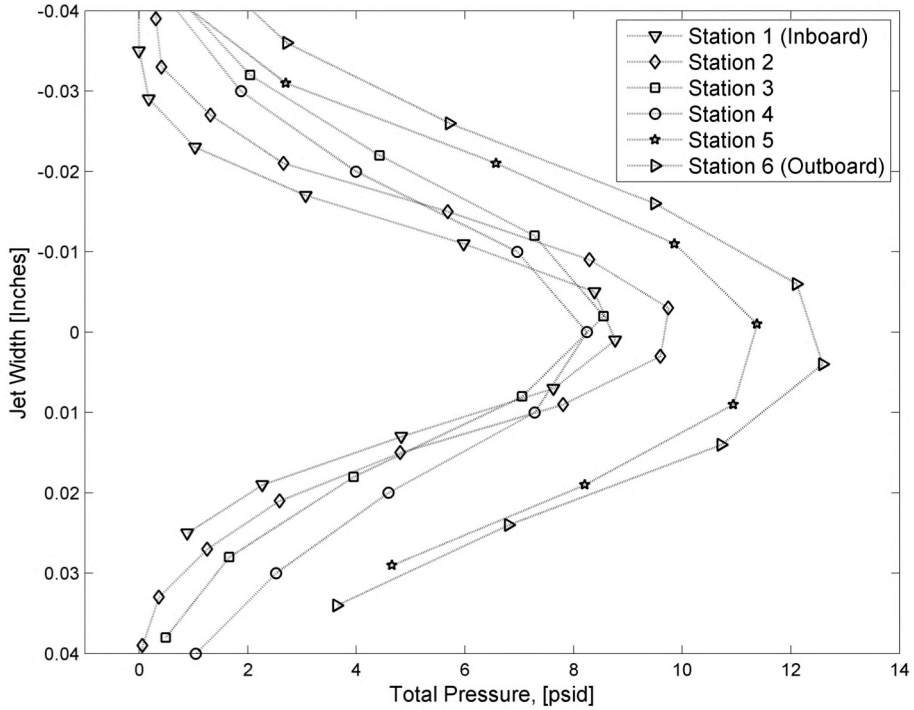

Figure 10.30. Right wing trailing edge outboard total pressure.

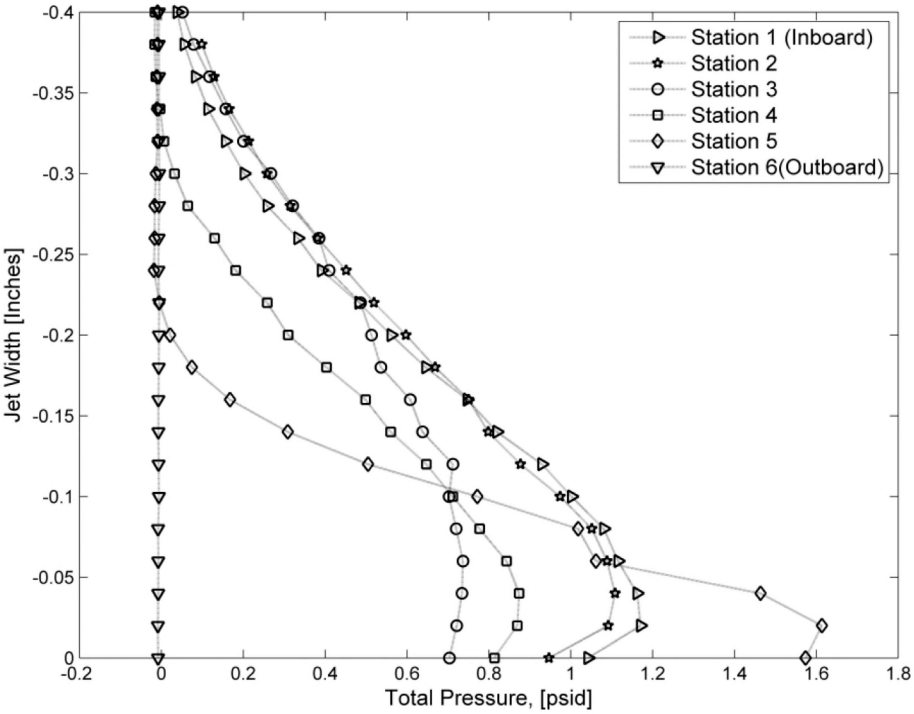

Figure 10.31. Right wing leading edge outboard total pressure.

An upper surface survey, showing the jet decay from the leading edge slot, is presented in Figure 10.31. As mentioned in the previous section, surveys of this type were taken along the 20% chord line, and relied on the Coanda effect of the leading edge curvature to deliver each jet profile. The 20 thousandths (od) diameter probe was unable to resolve total pressure close to the wall, however the profiles show good agreement along the span, given the distance from the jet. Similar to the behavior of the trailing edge outboard plenum, at the leading edge mid span region (stations 3 and 4), there is a slight loss of pressure due to the second layer of Rigimesh required near the plenum inlet. The profile at station 5 has the greatest maximum total pressure this is most likely a result of the orientation of the traverse and slightly higher pressure at the end of the plenum (similar to that at the trailing edge outboard plenum). Station 6 captured no profile and was beyond (outboard) the influence of the leading edge plenum. When repeated on the left wing, the survey showed good agreement.

Table 10.6. Station as percent plenum span (TEOB).

Station Number	Percent Along Span
Station 1	1%
Station 2	14%
Station 3	28%
Station 4	57%
Station 5	86%
Station 6	101%

10.7. Slot Blowing Calibration Conclusion

The work conducted at the Fluid Mechanics Lab in preparation for the wind tunnel test was invaluable to the success of the test. Figure 10.32 shows the results of an oil flow visualization run at the NFAC during the experiment. The circulation control flow streamlines show the successful application of the final plenum treatment configuration. The treatment was evaluated periodically throughout the test and proved to remain effective despite the many wind-on hours. Having achieved directionally uniform slot flow streamlines, the wind tunnel test data can be relied upon as a valid representation of the circulation control concept.

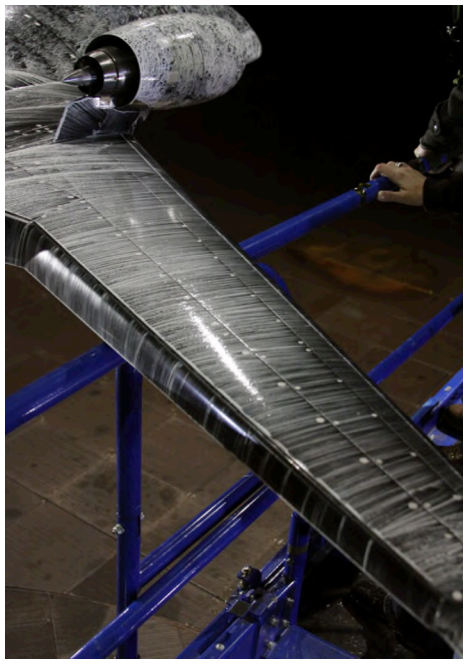

Figure 10.32. Uniform slot flow during wind tunnel test.

11. Turbofan Propulsion Simulators

This section provides a description of the pre-test characterization and operational control of the TDI Model 441 turbofan propulsion simulators (TPS). Cal Poly had three TPS units on loan from NASA Langley Research Center for testing on AMELIA; serial numbers 1, 3, and 4. For the duration of the powered testing, S/N 3 was mounted in the right-handed nacelle and S/N 4 was mounted in the left-handed nacelle.

11.1. Calibration Effort

Georgia Tech Research Institute (GTRI) was contracted to characterize the aerodynamic, propulsive, and acoustic performance of the TPS units. Since no load cells exist on the propulsion units, it is customary to calibrate the units so force and moments measurements in the wind tunnel can be corrected for the powered effects. It was also desired to have a real time indication of thrust in the wind tunnel so discrepancies in performance between left and right sides can be corrected if needed. The units were calibrated in their fully-installed configuration, i.e. assembled in the nacelle and pylon mounted. Serial Numbers 3 and 4 were successfully calibrated, while calibration was not completed on S/N 1 due to mechanical failures. Prior to model installation at the NFAC, the unit was repaired and was on stand-by in case of a failure in the other units during testing. The testing at GTRI took place between June 20 and June 24, 2011. Details of their effort are summarized here and are taken from their unpublished calibration report entitled "TPS/Nacelle/Pylon Characterization Testing Final Data Report."

11.1.1. Test Set-up

The calibrated simulators were tested in both the left- and right-handed nacelles mounted on the long pylon. Note the long pylon is used for the TPS mounted in the high engine height, and the short pylon is used to mount the TPS in the low engine height. Drag differences for the long and short pylons were measured and are discussed later. Forces and moments were measured using a 2.5 inch flow-thru air balance from Triumph. Flow rate was regulated using a digital poppet valve controlled via Labview through a National Instruments Compact FieldPoint programmable automation controller, both borrowed from NASA Langley. During testing, the TPS unit was installed in a single nacelle and mounted on the corresponding long pylon. The installed unit was then mounted sideways on the test fixture and attached to the flow-thru balance whose air supply was regulated by the digital valve. Facility air, rated at 310 psig, was supplied to the digital valve. The freestream flow was generated by a GTRI-owned centrifugal blower and supplied via a duct with an exit diameter of 18 inches (the maximum nacelle diameter is approximately 7.3 inches). The test set-up is shown in Figure 11.2 and Figure 11.1.

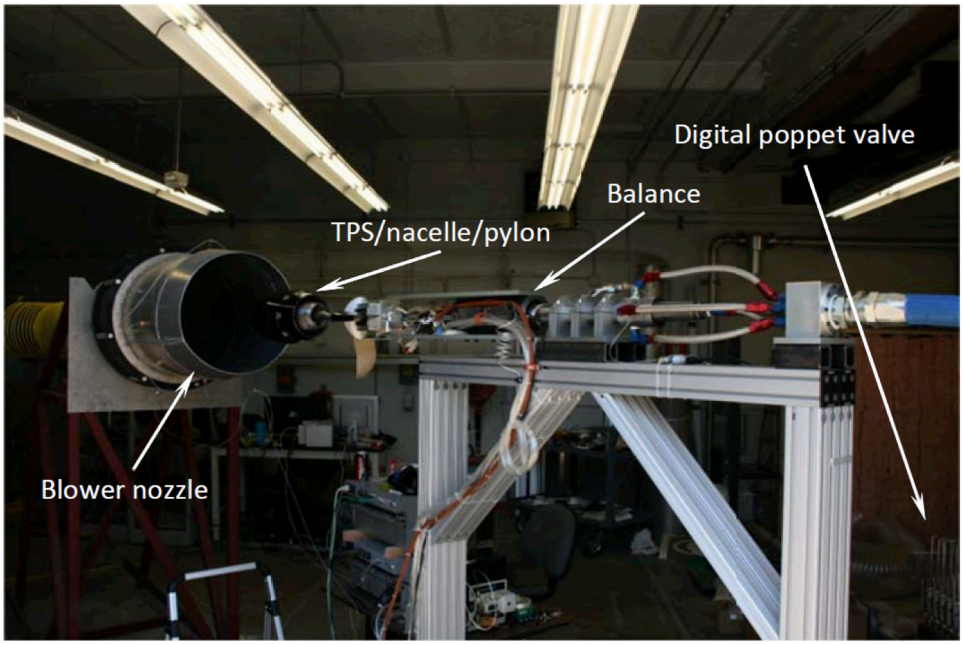

Figure 11.2. Calibration test set-up.

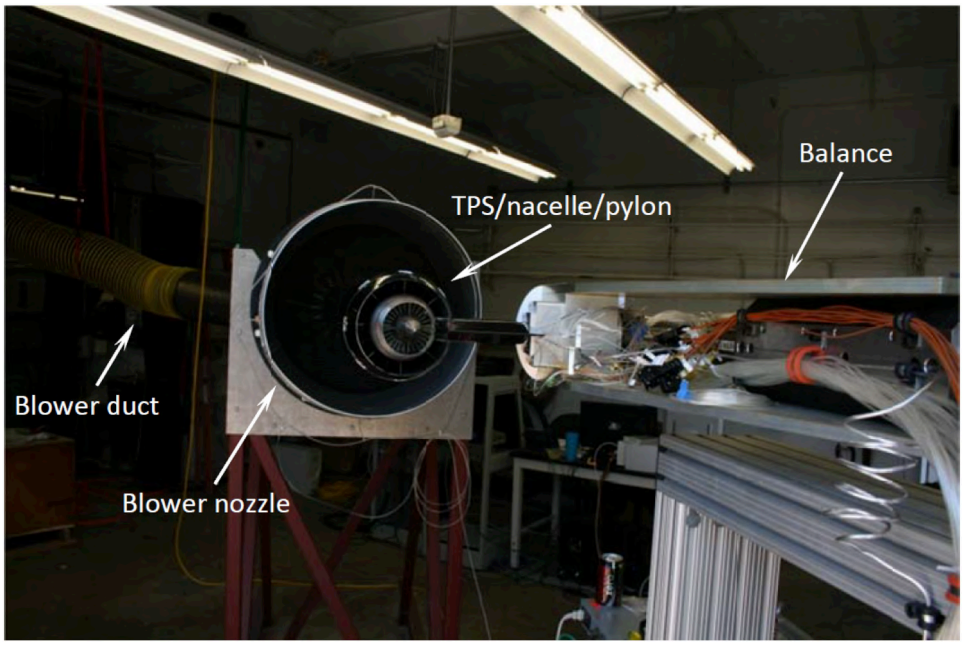

Figure 11.1. Calibration test set-up, rear view.

Three TPS and nacelle configurations were tested – S/N 3 mounted in the left-handed nacelle, S/N 4 mounted in the left-handed nacelle, and S/N 3 mounted in the right handed nacelle – at freestream velocities ranging from 0 to 100 KTS. Two run schedules – nominal RPM settings of 38250, 36000, 33750, 29250, 23850, 20250, and 0 (noted as A1) and nominal RPM settings of 36000, 29250, 23850, and 0 (noted as A2) – were evaluated. The as-tested test matrix is shown in Table 11.1. The testing for the long and short pylon drag differences was conducted at each freestream velocity listed below.

Table 11.1. As-tested TPS characterization test matrix.

Configuration (nacelle/S.N.)	Freestream Velocity [KTS]							
	0	40	50	60	70	80	90	100
LH/3	A1	A1	--	A1	--	A1	--	A1
LH/4	A1	A1	--	A1	--	A1	--	A1
RH/3	A1	A1	A2	A1	A2	A1	A2	A1

11.1.2. Data Acquisition

Aerodynamic data were acquired for all TPS/nacelle-mounted models, including balance data and total and static pressures plus thermocouple measurements. The TPS instrumentation was the same for the calibration as for when tested on AMELIA. Blower/duct (freestream) and ambient temperature and pressure data were also acquired. All pressure data were acquired with a Pressure Systems Inc. NetScanner Model 98RK System and gathered and recorded in Labview. All thermocouple data were acquired with a National Instruments SCXI-1102 Thermocouple/Voltage Input Module and gathered and recorded in Labview. Both the pressure and thermocouple data were continuously sampled at a rate of 1 kHz and 100 samples were averaged during the acquisition at each test point. The TPS instrumentation was the same for the calibration as for when tested on the model (recall the inlet has 8 static pressure taps, the fan has 7 rakes each fitted with 4 total pressure probes, 1 temperature probe, and 1 static pressure tap, and the core is instrumented with 2 total pressure probes, 2 static pressure taps, and 2 temperature probes). Pressure tubing and thermocouple wires were replaced prior to testing on AMELIA.

Propulsive data was acquired with the Triumph Force Measurement Systems MC-15-2.5-Bi flow-thru air balance. Data from the six balance strain gauges and the front and aft bellows pressure transducers were acquired with a National Instruments SCXI-1520 Universal Strain Gage Input Module, gathered in Labview, and converted to directional forces using high-quality calibration matrices provided by Triumph. The data were continuously sampled at a rate of 1 kHz and 100 samples were averaged during acquisition at each test point.

11.2. Calibration Results

The results from the characterization of the TPS units in their as-tested configuration – S/N 3 in right-handed nacelle and S/N 4 in left-handed nacelle – are provided in the figures and tables below. In the figures, the solid lines were generated with an interpolation routine that allowed for the determination of thrust per unit RPM for constant freestream velocities based on the experimental data points (shown with open markers). The data and accompanying calibration report are provided in addition to the data sets from the full-scale test.

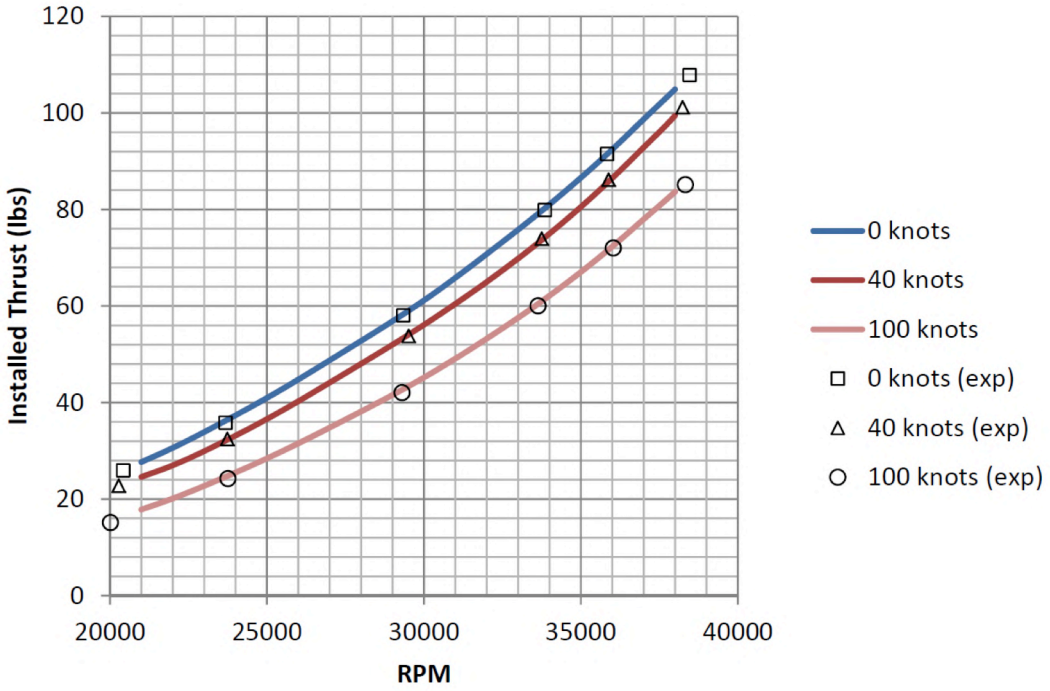

Figure 11.4. Numerically generated calibration curves overlaid on experimental data for S/N 4 in left-handed nacelle.

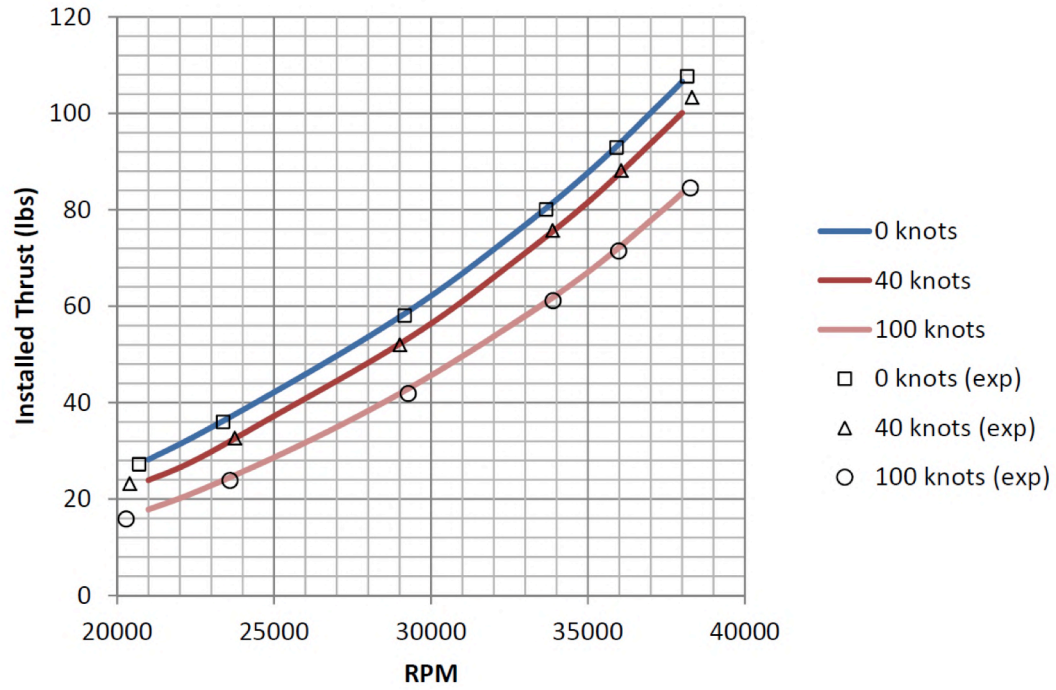

Figure 11.3. Numerically generated calibration curves overlaid on experimental data for S/N 3 in right-handed nacelle.

Table 11.2. Tabulated installed propulsive calibration results for the TPS in the left-handed nacelle.

Installed thrust from calibration of TPS S/N 4 in LH Nacelle [lb_f]								
RPM [-]	Freestream Velocity [KTS]							
	0	**40**	**50**	**60**	**70**	**80**	**90**	**100**
21,000	27.7	24.6	23.7	22.6	21.4	20.2	19.0	17.8
22,500	32.2	28.4	27.2	26.1	24.9	23.8	22.6	21.4
25,000	41.0	36.6	35.5	34.4	33.2	31.8	30.0	28.4
27,500	50.8	46.1	44.7	43.4	41.9	40.0	38.2	36.5
30,000	61.2	56.1	54.1	52.5	50.8	49.1	47.2	45.2
32,500	73.3	67.4	65.8	63.7	61.4	59.1	57.2	55.4
35,000	86.5	80.5	78.8	77.0	74.5	72.1	69.6	67.0
37,500	101.8	96.0	94.0	91.4	88.8	86.2	83.6	80.8
38,000	104.9	99.4	97.0	94.4	91.8	89.2	86.4	83.7

Table 11.3. Tabulated installed propulsive calibration results for the TPS in the right-handed nacelle.

Installed thrust from calibration of TPS S/N 3 in RH Nacelle [lb_f]								
RPM [-]	Freestream Velocity [KTS]							
	0	**40**	**50**	**60**	**70**	**80**	**90**	**100**
21,000	28.2	23.9	22.9	21.9	20.9	19.9	18.8	17.8
22,500	33.1	28.1	26.8	25.6	24.5	23.5	22.5	21.5
25,000	42.1	37.2	35.8	34.5	33.2	31.9	30.1	28.6
27,500	51.7	46.4	45.1	43.5	41.8	40.1	38.3	36.6
30,000	62.1	56.4	54.9	53.3	51.5	49.6	47.7	45.6
32,500	74.3	68.5	67.0	65.4	63.6	61.7	58.9	55.9
35,000	87.6	81.6	79.9	78.2	75.9	73.5	70.8	67.0
37,500	103.3	96.9	95.3	93.6	92.0	89.1	84.6	80.6
38,000	106.6	100.1	98.5	96.8	95.2	92.5	88.0	83.5

Figure 11.5 presents the drag force as a function of freestream velocity for the long and short pylon. The maximum drag difference between the long and short pylons is 0.07 lb_f. This is within the limits of the balance, and it is thus concluded that pylon heights have negligible differences in drag at all tested freestream velocities. These results also indicate that pylon height differences during the AMELIA test, where an 8-inch balance is used, should be negligible.

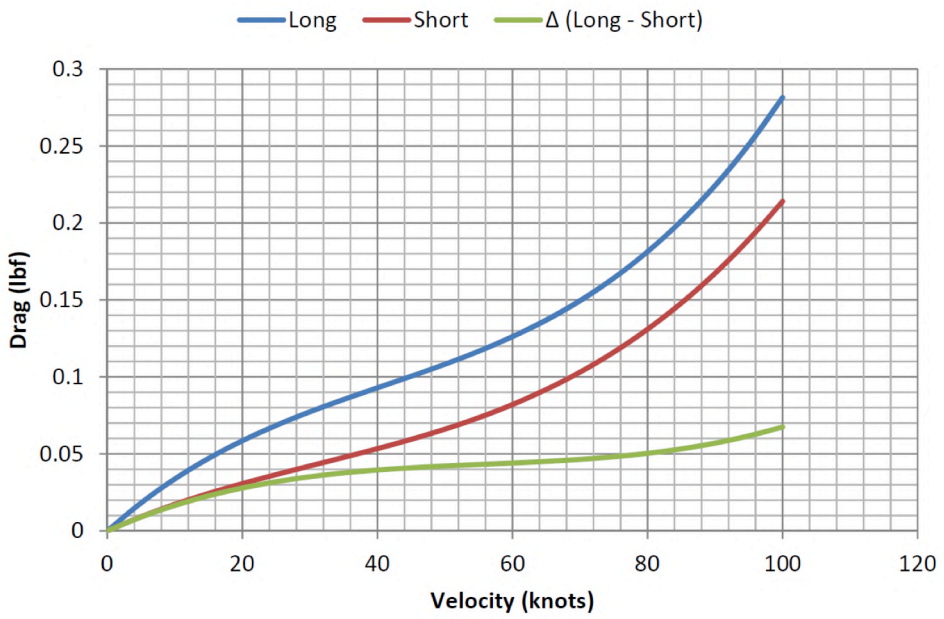

Figure 11.5. Drag as a function of freestream velocity for the long and short pylon height.

11.2.1. Thrust Correction

The isolated nacelle thrust calibration provided balance-measured forces which were corrected and delivered to the NFAC in the form of a look-up table in which the TPS contribution could be subtracted from the full configuration and the thrust can be monitored in real time. Differences in atmospheric conditions between the calibration and wind tunnel test environments required corrections of measurements to sea-level standard conditions. It is because changes in atmospheric pressure create thrust differences that, for a constant flight speed, need to be corrected. Humidity is not corrected for as it is a second order effect. The delivered calibration data correlates sea-level corrected thrust as a function of corrected freestream velocity and RPM; each isolated nacelle and TPS has a corresponding calibration table. The raw TPS RPM is corrected to standard day as

$$RPM_{corrected} = \frac{RPM}{\sqrt{\theta}} \tag{11.1}$$

Where θ, the temperature ratio, is defined as

$$\theta = \frac{T_{T,\infty}}{T_{STD}} \tag{11.2}$$

The standard temperature, T_{STD}, depends on the units of the measured freestream total temperature, $T_{T,\infty}$; for English units, T_{STD} = 518.67°R (a constant). Stagnation quantities are used for both the pressure and temperature corrections. In a similar manner, the freestream tunnel velocity, V_∞ (in knots), is corrected to standard day by

$$V_{corrected} = \frac{V_\infty}{\sqrt{\sigma}} \tag{11.3}$$

Sigma is the density ratio, computed as

$$\sigma = \frac{\delta}{\theta} \tag{11.4}$$

Where δ is the pressure ratio

$$\delta = \frac{P_{T,\infty}}{P_{STD}} \tag{11.5}$$

For English units, the standard pressure is 14.6968 psia; $P_{T,\infty}$ is the freestream total pressure. The thrust is corrected as

$$F_{corrected} = \frac{F_N}{\delta} \tag{11.6}$$

F_N is the net thrust, presented in Table 11.2 and Table 11.3. The net thrust is equal to the gross thrust minus ram drag; in other words, the ram drag component is in the measured thrust value. Ram drag is a function of the fan mass flow rate; it is temperature dependent and is the primary reason for the shift in thrust lines at different wind speeds (see Figure 11.4 and Figure 11.3). For these reasons, the calibration matrix is a function of corrected tunnel speed and RPM instead of traditionally fan pressure ratio (FPR) and RPM. A post-test nacelle calibration of mass flow rate would allow the calibration and full-scale data to be re-reduced to correct for ram drag but at present there are no plans to do so.

Starting with the data presented in Table 11.2 and Table 11.3, it was corrected following the outlined method and the resulting corrected calibration matrices are presented in Table 11.4 and Table 11.5. A bi-linear interpolation algorithm is implemented for navigating within the matrix real time.

It is also important to note that since the thrust axis of the TPS is not perfectly aligned with the body axis of the model, there are components in all 6 of the balance force and moment measurements. The data files are uncorrected, and the TPS net thrust is only subtracted from the drag data where noted in this report.

Table 11.4. Tabulated calibration matrix outputting corrected net thrust as a function of wind speed and TPS RPM.

Corrected Net thrust from calibration of TPS S/N 4 in LH Nacelle [lb_f]					
Corrected RPM [-]	Corrected Freestream Velocity [KTS]				
	0	**43.17**	**60.58**	**87.51**	**111.1**
20,000	27.95	25.30	23.20	19.99	19.06
22,500	36.01	32.55	30.04	26.41	26.11
25,000	45.52	41.45	38.49	34.36	34.70
27,500	56.47	52.00	48.55	43.84	44.82
30,000	68.87	64.21	60.23	54.84	56.48
32,500	82.71	78.08	73.52	67.37	69.68
35,000	97.99	93.59	88.43	81.43	84.41
36,000	104.51	100.26	94.84	87.48	90.73

Table 11.5. Tabulated calibration matrix outputting corrected net thrust as a function of wind speed and TPS RPM.

Corrected Net thrust from calibration of TPS S/N 3 in RH Nacelle [lb_f]					
Corrected RPM [-]	Corrected Freestream Velocity [KTS]				
	0	**42.94**	**59.68**	**82.88**	**106.31**
20,000	28.11	25.44	23.13	21.62	17.29
22,500	35.79	32.67	30.20	28.80	23.12
25,000	44.99	41.62	38.97	37.81	30.39

27,500	55.71	52.31	49.43	48.65	39.09
30,000	67.96	64.73	61.60	61.31	49.23
32,500	81.73	78.88	75.45	75.80	60.81
35,000	97.02	94.77	91.01	92.12	73.82
36,000	103.56	101.61	97.71	99.16	79.43

A good indication of the uncertainty in the drag data is how well the balance measured drag correlates with the computed drag from the calibration data for a wind-off TPS sweep. Figure 11.6 shows the comparison between wind tunnel balance measured drag and drag computed using the TPS thrust calibration matrix. The data were acquired during run 65, a wind-off alpha-sweep. The calibration thrust data are corrected for angle of attack and converted to drag by multiplying the thrust by the cosine of the angle of attack. Drag values are negative due to the orientation of thrust in the body axis system. The TPS were held at the maximum RPM set point of ~34,500 for the duration of the alpha sweep. The model is in the low engine height configuration with 60° flaps. As seen in the plot, the largest difference is 5.9 lb_f or 3.2%.

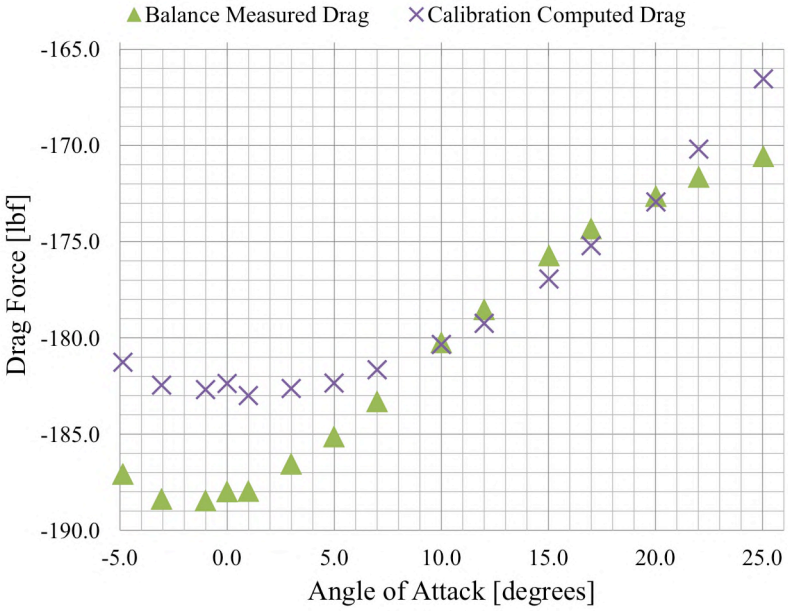

Figure 11.6. Measured and computed drag force for run 65: wind-off, angle of attack sweep.

11.3. TPS Controls

Control to the TPS units came from two controllers being operated on separate systems. The two controllers provided the gross high pressure line air (pressure, temperature, and thus mass flow rate), via the digital valves, and the individual TPS model control, via the needle valves (or mass flow plugs). Details of the controllers and how they interface with the operation of the TPS units during testing are discussed in this section.

11.3.1. Model Internal Control

Model internal control was provided by a separate Cal Poly operated Labview controller. The controller operated the two independent flow paths, controlling the 8 butterfly valves on the low pressure side and the 2 needle valves on the high pressure side. The butterfly valves controlled the flow split between the

slot blowing plenums and the needle vales controlled the flow split between left and right TPS units. The needle valves supplement the wind tunnel HPA controller. Wind tunnel HPA provided closed-loop "coarse" control of the air entering the model; inside the model, the needle valves provided fine control to match left and right TPS performance. During testing, it was found that the coarse control of the wind tunnel HPA controller was enough to match TPS performance within tolerance. As such, the needle valves were left in the fully open configuration unless closed for one engine inoperative (OEI) points or for safety reasons. Figure 11.7 shows a schematic of the internal model controller. The instrumentation and connections from the model to the wind tunnel control room are shown in the figure.

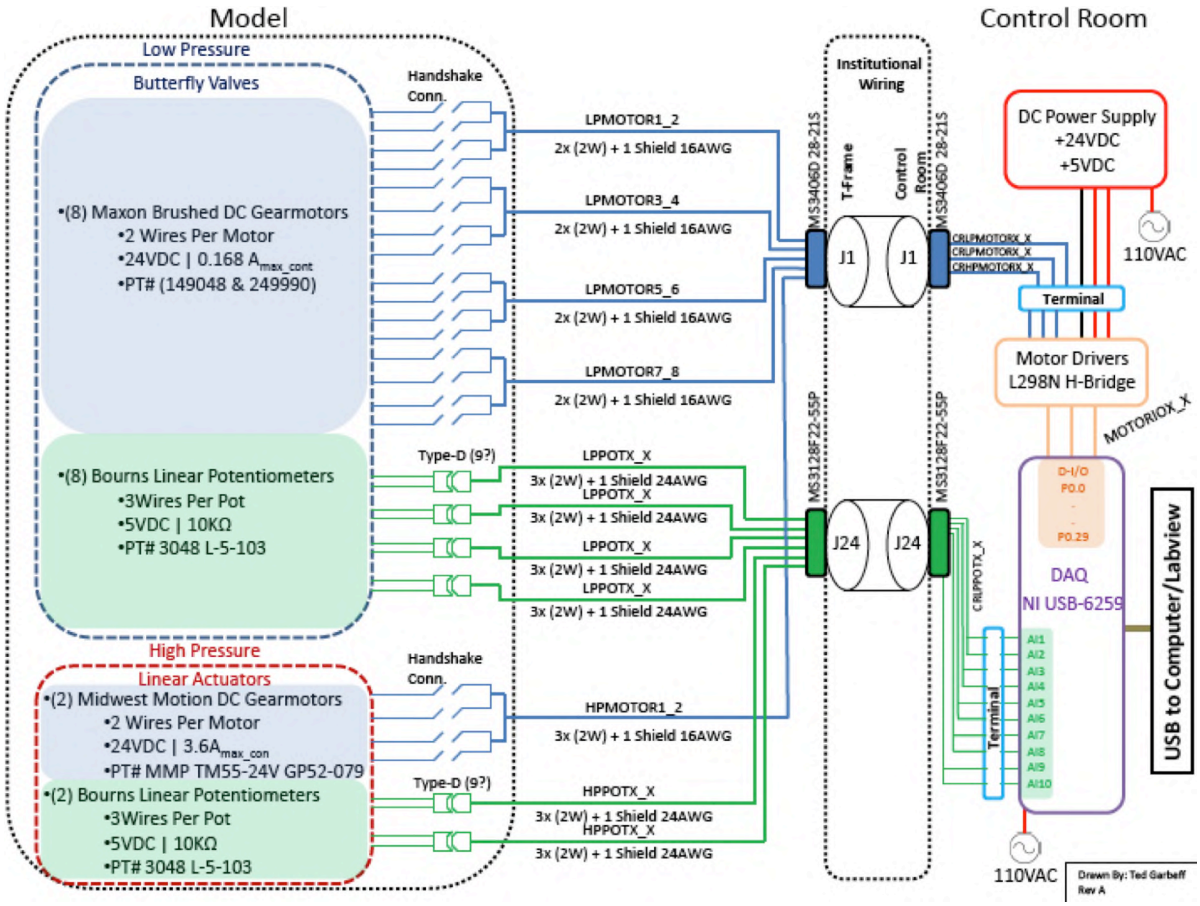

Figure 11.7. Internal model controller schematic.

During model build-up, it was discovered that the thermal expansion of the brass needle valves restricted the 24 VDC motors ability to actuate the valves in the internal HPA block. As the delivered wind tunnel HPA temperature was warmer than those experienced during build-up, the outer diameter of each needle valve was shaved 2-3 thousandths of an inch to relieve the motors. This had no operational effect on the TPS units during the test, unless testing in an OEI configuration. In the OEI configuration, one needle valve is fully closed to simulate the lost engine and the point is repeated for the other side to get a full data set. Initial HPA check-out showed that a portion of flow was able to bypass the closed needle valve and spin up the TPS to ~16,500 RPM. Maintaining operation of the valves at temperature allowed the needle position to be adjusted to compensate for the RPM differences between left and right sides that existed after the valves were machined down.

11.3.2. Operational Control

Wind tunnel high pressure air control has two modes of operation: flow control mode and pressure control mode. Flow control mode sets and maintains a constant mass flow rate, and pressure control mode

holds a constant line pressure. RPM values hold truer in flow control mode because it is driven by the mass flow rate being delivered, whereas the delivered pressure dictates the thrust produced. However, as line temperature increases, the pressure rises to maintain a constant mass flow rate thereby requiring more frequent adjustment in flow control mode during a run. In pressure control mode, as line temperature increases, the mass flow rate changes, however temperature is a second order effect on the sensitivity of mass flow rate. Accordingly, pressure control mode was used for the majority of the test. HPA control was run on BDAS providing safety-of-flight monitoring in addition to set point control for data acquisition.

Traditionally, the drive air supplied to TPS units is heated to preclude exposure of the aft bearing to excessively low temperatures, resulting from the expansion through the turbine, causing a failure. Upon operation of the model 441 units, however, an increase in drive air temperature resulted in increased aft bearing temperatures despite the nearly -110°F flow temperature exiting the last turbine stage. Regulating the drive air temperature to 150°F resulted in aft bearing temperatures nearly reaching the SOF limit at 125°F. This necessitated the change to lower the maximum operating condition from 80% to 77%, or 36,000 RPM to 34,500 RPM, respectively. Drive air temperature was regulated at 110°F. At 40 KTS, this represents a reduction in thrust of 9.9 lb_f, ~10%. Other SOF TPS instrumentation did not approach their limits. The forward bearing temperature tracked the aft bearing and stayed below the SOF limit of 225°F. The full TPS set point was well below their maximum rated RPM to preserve the lifetime of the units and was never allowed to approach the SOF limit of 46,000 RPM.

Due to the relative humidity in the tunnel circuit (as high as 80%) and high pressure line temperature, small amounts of icing did occur on the back end of the TPS core. At points where appreciable ice accumulation was observed, ice was shed. (Ice crystals extending ~1-2 inches off the core are considered appreciable ice build-up). The TPS units were brought down to idle (~9000 RPM) to let the accumulated ice melt and then brought back up on-condition for a repeat point. This procedure could have been repeated as much as 4 times during a run. There were a small number of occurrences where the repeat point was not taken; run sheets are annotated to reflect this. To avoid any non-linear aerodynamic interactions, deicing points were avoided whenever possible at higher angles of attack. There are no evident performance differences caused by the icing on the back end of the TPS.

12. Test Matrix

The as-run test matrix is presented in Table 12.1. The TPS units were running for a total of 43.5 hours accumulated over 65 separate runs.

Table 12.1. The "As-Run" Test Matrix with Run Notes.

Date	Run	Velocity (KTS)	α (deg)	β (deg)	Flap Defl. (deg)	Pylon Height	CCW Config.	m_dot (lbm/sec)	TPS Config.	RPM (L/R)	Run Notes
	18	40,60,100,110	0	0	0	Low	Off	0	Off	windmill	Re Sweep
22-Dec	19	40	Sweep	0	0	Low	Off	0	Off	windmill	Baseline #1
	20	40	0	Sweep	0	Low	Off	0	Off	windmill	
	21	100	Sweep	0	0	Low	Off	0	Off	windmill	
	22	100	0	0	0	Low	Off	0	Off	windmill	CTP #1
	23	100	0	0	0	Low	Off	0	Off	windmill	CTP #1
	24	100	0	0	0	Low	Off	0	Off	windmill	CTP #1
22-Dec	25	100	0	0	0	Low	Off	0	Off	windmill	CTP #1
23-Dec	26	60	Sweep	0	60	Low	Off	0	Off	windmill	
3-Jan	27	0	0	0	Unknown	Low	Sweep	vary	Off	0	Slot Sweep
	28	0	0	0	Unknown	Low	Sweep	vary	Off	0	Slot Sweep
	29	0	0	0	Unknown	Low	Sweep	vary	Off	0	Oil Viscosity Investigation
	30	0	0	0	Unknown	Low	On	vary	Sweep	vary	TPS Sweep
	31	0	0	0	Unknown	Low	On	vary	Sweep	vary	Powered Lift Sweep
3-Jan	32	0	0	0	Unknown	Low	Full	2.8	OEI (77%/36%)	34,500/16,5	OEI Check-out
4-Jan	33	40	0	0	Unknown	Low	Sweep	vary	Sweep	vary	Slot only, TPS only
	34	40	0	0	Unknown	Low	Sweep	vary	Sweep	vary	Powered Lift Matrix
4-Jan	35	40	0	0	Unknown	Low	Sweep	vary	Sweep	vary	Powered Lift Matrix
6-Jan	36	40	Sweep	0	0	Low	Full	2.8	Full	34,500	Baseline #2
	37	40	0	0	80	Low	Full	2.8	Full	34,500	CTP #2
	38	60	5	0	80	Low	Full	2.8	20%		CTP #3
6-Jan	39	40	Sweep	0	80	Low	Full	2.8	Full	34,500	BAD RUN
9-Jan	40	40	5	0	60	Low	1/3		OEI (Left Engine)	36%/77%	CTP #5 (1st Attempt)
9-Jan	41	40	5	0	60	Low	1/3		OEI (Right Engine)	77%/36%	CTP #6
10-Jan	42	40	Sweep	0	60	Low	Off	0	Off	windmill	
	43	60	5	0	60	Low	2/3	1.87	Full	34,500	CTP #4
	44	40	5	0	60	Low	1/3		OEI (Left Engine)	36%/77%	CTP #5 (2nd Attempt)
10-Jan	45	30	0	0	60	Low	Full	2.8	Off	windmill	Oil Flow Vis. # 1
11-Jan	46	40	Sweep	0	60	Low	Full	2.8	Full	34,500	
	47	40	Sweep	-5	60	Low	Full	2.8	Full	34,500	
	48	40	Sweep	-10	60	Low	Full	2.8	Full	34,500	
	49	40	Sweep	5	60	Low	Full	2.8	Full	34,500	
	50	40	Sweep	10	60	Low	Full	2.8	Full	34,500	
	51	60	Sweep	0	60	Low	Full	2.8	Off	windmill	
	52	60	Sweep	0	60	Low	2/3	1.87	Full	34,500	
	53					Run Number Skipped					
	54	60	Sweep	0	60	Low	Full	2.8	Full	34,500	
11-Jan	55	100	Sweep	0	60	Low	Full	2.8	Off	windmill	
12-Jan	56	40	Sweep	0	60	Low	Full	2.8	Sweep	vary	
	57	100	Sweep	0	60	Low	Off	0	Off	windmill	
	58	100	Sweep	0	60	Low	Full	2.8	Full	34,500	
	59	100	Sweep	0	60	Low	Off	0	Full	34,500	
	60	60	Sweep	0	60	Low	Off	0	Off	windmill	
	61	60	Sweep	0	60	Low	2/3	1.87	Off	windmill	
	62	60	Sweep	0	60	Low	Off	0	Full	34,500	
	63	0	Sweep	0	60	Low	Full	2.8	Off	0	
	64	0	Sweep	0	60	Low	2/3	1.87	Off	0	
	65	0	Sweep	0	60	Low	Off	0	Full	34,500	1/3 slot and OEI points
	66	40	Sweep	0	60	Low	Full	2.8	Off	windmill	
12-Jan	67	40	Sweep	0	60	Low	Off	0	Full	34,500	
13-Jan	68	40	Sweep	0	80	Low	Full	2.8	Off	windmill	
	69	40	Sweep	0	80	Low	Full	2.8	Full	34500	Baseline #3 (also R81/82)
	70	40	Sweep	0	80	Low	Off	0	Full	34,500	
	71	40	Sweep	0	80	Low	2/3	1.87	Off	windmill	
	72	40	Sweep	0	80	Low	Off	0	Off	windmill	
	73	0	Sweep	0	80	Low	Off	0	Full	34,500	
	74	0	Sweep	0	80	Low	Off	0	20%		
	75	0	Sweep	0	80	Low	Full	2.8	Off	0	
	76	0	Sweep	0	80	Low	2/3	1.87	Off	0	
	77	100	Sweep	0	80	Low	Full	2.8	Off	0	

Date	Run	Velocity (KTS)	α (deg)	β (deg)	Flap Defl. (deg)	Pylon Height	CCW Config.	m_dot (lbm/sec)	TPS Config.	RPM (L/R)	Run Notes
	78	100	Sweep	0	80	Low	Full	2.8	Full	34,500	
	79	100	Sweep	0	80	Low	Full	2.8	Full	34,500	Repeat of Run 78
	80	100	Sweep	0	80	Low	Off	0	Full	34,500	
13-Jan	81	40	Sweep	0	80	Low	Full	2.8	Full	34,500	
17-Jan	82	40	Sweep	0	80	Low	Full	2.8	Full	34,500	
	83	40	Sweep	0	80	Low	2/3	1.87	Full	34,500	
	84	60	Sweep	0	80	Low	Full	2.8	20%		
	85	60	Sweep	0	80	Low	Full	2.8	Off	windmill	
	86	60	Sweep	0	80	Low	Full	2.8	Full	34,500	
	87	60	Sweep	0	80	Low	Off	0	Off	windmill	
	88	60	Sweep	0	80	Low	Off	0	Full	34,500	
	89	60	Sweep	0	80	Low	2/3	1.87	Off	windmill	
	90	60	Sweep	0	80	Low	2/3	1.87	Full	34,500	
17-Jan	91	100	Sweep	0	80	Low	Off	0	Off	windmill	
18-Jan	92	40	Sweep	0	0	Low	Full	2.8	Full	34,500	
	93	40	Sweep	0	0	Low	Full	2.8	Off	windmill	
	94	40	Sweep	0	0	Low	Off	0	Full	34,500	
	95	40	Sweep	0	0	Low	Off	0	Off	windmill	
	96	40	Sweep	0	0	Low	2/3	1.87	Full	34,500	
	97	40	Sweep	0	0	Low	2/3	1.87	Off	windmill	
	98	60	Sweep	0	0	Low	Full	2.8	Full	34,500	
	99	60	Sweep	0	0	Low	Full	2.8	Off	windmill	
	100	60	Sweep	0	0	Low	Off	0	Full	34,500	
18-Jan	101	60	Sweep	0	0	Low	Off	0	Off	windmill	
19-Jan	102	40	Sweep	0	0	Low	Full	2.8	Full	34,500	
	103	60	Sweep	0	0	Low	2/3	1.87	Full	34,500	
	104	60	Sweep	0	0	Low	2/3	1.87	Off	windmill	
	105	100	Sweep	0	0	Low	Off	0	Off	windmill	
	106	100	Sweep	0	0	Low	Full	2.8	Full	34,500	
	107	100	Sweep	0	0	Low	Full	2.8	Off	windmill	
	108	100	Sweep	0	0	Low	Off	0	Full	34,500	
	109	100	Sweep	0	0	Low	2/3	1.87	Off	windmill	
19-Jan	110	100	Sweep	0	0	Low	2/3	1.87	Full	34,500	
20-Jan	111	0	Sweep	0	0	Low	Full	2.8	Off	0	
	112	0	Sweep	0	0	Low	2/3	1.87	Off	0	
	113	0	Sweep	0	0	Low	Off	0	Full	34,500	
	114	30	5	0	Unknown	Low	Full	2.8	Off	windmill	Oil Flow Vis. #2
	115	60	10	0	Unknown	Low	Full	2.8	Full	34,500	Oil Flow Vis. #3
	116	30	10	0	Unknown	Low	Full	2.8	Off	windmill	Oil Flow Vis. #4
20-Jan	117	30	5,10,15	0	Unknown	Low	Full	2.8	Off	windmill	Oil Flow Vis. #5
23-Jan	118	0	Sweep	0	80	Low	Full	2.8	Off	0	
	119	0	Sweep	0	80	Low	2/3	1.87	Off	0	
	120	0	0	0	80	Low	Sweep	vary	Off	0	
	121	0	-5	0	80	Low	Sweep	vary	Off	0	
	122	0	10	0	80	Low	Sweep	vary	Off	0	
	123	0	0	0	80	Low	Sweep	vary	Full	34,500	
	124	40	0	0	80	Low	Sweep	vary	Off	windmill	
	125	40	-5	0	80	Low	Sweep	vary	Off	windmill	
	126	40	10	0	80	Low	Sweep	vary	Off	windmill	
	127	40	0	0	80	Low	Sweep	vary	Full	34,500	
	128	40	Sweep	0	80	Low	Full	2.8	Full	34,500	
23-Jan	129	60	0	0	80	Low	Sweep	vary	Off	windmill	
24-Jan	130	100	Sweep	0	80	Low	2/3	1.87	Off	windmill	
	131	100	Sweep	0	80	Low	2/3	1.87	Full	34,500	
	132	100	0	0	80	Low	Sweep	vary	Off	windmill	
	133	40	Sweep	0	60	Low	Full	2.8	Full	34,500	
	134	40	Sweep	0	60	Low	2/3	1.87	Off	windmill	
	135	40	Sweep	0	60	Low	2/3	1.87	Full	34,500	
	136	40	0	0	60	Low	Sweep	vary	Off	windmill	
	137	40	-5	0	60	Low	Sweep	vary	Off	windmill	
	138	40	10	0	60	Low	Sweep	vary	Off	windmill	

Date	Run	Velocity (KTS)	α (deg)	β (deg)	Flap Defl. (deg)	Pylon Height	CCW Config.	m_dot (lbm/sec)	TPS Config.	RPM (L/R)	Run Notes
	139	0	Sweep	0	60	Low	Full	2.8	Off	0	
24-Jan	140	0	0	0	60	Low	Sweep	vary	Off	0	
25-Jan	141	0	-5	0	60	Low	Sweep	vary	Off	0	
	142	0	10	0	60	Low	Sweep	vary	Off	0	
	143	60	0	0	60	Low	Sweep	vary	Off	windmill	
	144	100	0	0	60	Low	Sweep	vary	Off	windmill	
	145	100	Sweep	0	60	Low	2/3	1.87	Off	windmill	
	146	100	Sweep	0	60	Low	2/3	1.87	Full	34,500	
	147	0	0	0	60	Low	Sweep	vary	Off	0	
	148	0	Sweep	0	30	Low	Full	2.8	Off	0	
	149	0	Sweep	0	30	Low	Off	0	Full	34,500	
	150	40	Sweep	0	30	Low	Off	0	Off	windmill	
	151	40	Sweep	0	30	Low	Full	2.8	Off	windmill	
25-Jan	152	40	Sweep	0	30	Low	Full	2.8	Full	34,500	
26-Jan	153	40	Sweep	0	30	Low	Full	2.8	Full	34,500	
	154	40	Sweep	0	30	Low	Off	0	Full	34,500	
	155	60	Sweep	0	30	Low	Off	0	Off	windmill	
	156	60	Sweep	0	30	Low	Full	2.8	Off	windmill	
	157	60	Sweep	0	30	Low	Off	0	Full	34,500	
	158	60	Sweep	0	30	Low	Full	2.8	Full	34,500	
	159	100	Sweep	0	30	Low	Full	2.8	Off	windmill	
	160	100	Sweep	0	30	Low	Off	0	Off	windmill	
	161	0	0	0	0	Low	Sweep	vary	Off	0	
	162	0	-5	0	0	Low	Sweep	vary	Off	0	
26-Jan	163	0	10	0	0	Low	Sweep	vary	Off	0	
27-Jan	164	0	0	0	0	Low	Sweep	vary	Off	0	
	165	40	0	0	0	Low	Sweep	vary	Off	windmill	
	166	40	-5	0	0	Low	Sweep	vary	Off	windmill	
	167	40	10	0	0	Low	Sweep	vary	Off	windmill	
	168	60	0	0	0	Low	Sweep	vary	Off	windmill	
	169	100	0	0	0	Low	Sweep	vary	Off	windmill	
	170	40	10	0	80	Low	Full	2.8	Off	windmill	Smoke Wand Vis. #1
27-Jan	171	40	0	0	80	Low	Full	2.8	Off	windmill	Smoke Wand Vis. #2
30-Jan	172	0	0	0	80	High	Off	0	Sweep	vary	TPS Check-out
	173	0	Sweep	0	80	High	Off	0	Off	0	Weight Tare
	174	0	Sweep	0	80	High	Full	2.8	Off	0	
	175	0	Sweep	0	80	High	Off	0	Full	34,500	
	176	40	Sweep	0	80	High	Full	2.8	Full	34,500	
	177	40	Sweep	0	80	High	Full	2.8	Off	windmill	
30-Jan	178	40	Sweep	0	80	High	Off	0	Off	windmill	
31-Jan	179	0	Sweep	0	80	High	Off	0	20%		
	180	40	Sweep	0	80	High	Off	0	Full	34,500	
	181	100	Sweep	0	80	High	Full	2.8	20%		
	182	60	Sweep	0	80	High	Full	2.8	20%		
	183	60	5	0	80	High	Full	2.8	20%		CTP #9
31-Jan	184	40	0	0	80	High	Full	2.8	Full	34,500	CTP #8
1-Feb	185	40	Sweep	0	0	High	Full	2.8	Off	windmill	
	186	40	Sweep	0	0	High	Full	2.8	Full	34,500	
	187	40	Sweep	0	0	High	Off	0	Full	34,500	
	188	40	Sweep	0	0	High	Off	0	Off	windmill	
	189	100	Sweep	0	0	High	Off	0	Off	windmill	
	190	100	0	0	0	High	Off	0	Off	windmill	CTP #7
	191	40	Sweep	0	0	High	2/3	1.87	Off	windmill	
	192	40	Sweep	0	0	High	2/3	1.87	Full	34,500	
	193	0	Sweep	0	0	High	Full	2.8	Off	0	
	194	0	Sweep	0	0	High	2/3	1.87	Off	0	
1-Feb	195	0	Sweep	0	0	High	Off	0	Full	34,500	
2-Feb	196	40	Sweep	0	60	High	Full	2.8	Off	windmill	
	197	40	Sweep	0	60	High	Full	2.8	Full	34,500	
	198	40	Sweep	0	60	High	Off	0	Full	34,500	
	199	Run Number Skipped									

Date	Run	Velocity (KTS)	α (deg)	β (deg)	Flap Defl. (deg)	Pylon Height	CCW Config.	m_dot (lbm/sec)	TPS Config.	RPM (L/R)	Run Notes
	199					Run Number Skipped					
	200	0	Sweep	0	60	High	Full	2.8	Off	0	
	201	0	Sweep	0	60	High	2/3	1.87	Off	0	
2-Feb	202	0	Sweep	0	60	High	Off	0	Full	34,500	
3-Feb	203	100	Sweep	0	60	High	Full	2.8	Full	34,500	
6-Feb	204	0	Sweep	0	60	Clean	Off	0	N/A	N/A	Weight Tare
	205	0	Sweep	0	60	Clean	Off	0	N/A	N/A	Weight Tare
	206	0	Sweep	0	60	Clean	Full	2.8	N/A	N/A	
	207	0	Sweep	0	60	Clean	2/3	1.87	N/A	N/A	
	208	0	0	0	60	Clean	Sweep	vary	N/A	N/A	
	209	0	-5	0	60	Clean	Sweep	vary	N/A	N/A	
	210	0	10	0	60	Clean	Sweep	vary	N/A	N/A	
	211	40	Sweep	0	60	Clean	Off	0	N/A	N/A	
	212	40	Sweep	0	60	Clean	2/3	1.87	N/A	N/A	
	213	40	Sweep	0	60	Clean	Full	2.8	N/A	N/A	
	214	40	0	0	60	Clean	Sweep	vary	N/A	N/A	
	215	40	-5	0	60	Clean	Sweep	vary	N/A	N/A	
	216	40	10	0	60	Clean	Sweep	vary	N/A	N/A	
6-Feb	217	40	Sweep	-5	60	Clean	Full	2.8	N/A	N/A	
7-Feb	218	40	Sweep	0	60	Clean	Full	2.8	N/A	N/A	
	219	40	Sweep	-10	60	Clean	Full	2.8	N/A	N/A	
7-Feb	220	40	Sweep	5	60	Clean	Full	2.8	N/A	N/A	
8-Feb	221	40	Sweep	10	60	Clean	Full	2.8	N/A	N/A	
	222	60	Sweep	0	60	Clean	Off	0	N/A	N/A	
	223	60	Sweep	0	60	Clean	2/3	1.87	N/A	N/A	
	224	60	Sweep	0	60	Clean	Full	2.8	N/A	N/A	
	225	60	0	0	60	Clean	Sweep	vary	N/A	N/A	
	226	100	Sweep	0	60	Clean	Off	0	N/A	N/A	
	227	100	Sweep	0	60	Clean	2/3	1.87	N/A	N/A	
	228	100	Sweep	0	60	Clean	Full	2.8	N/A	N/A	
	229	100	0	0	60	Clean	Sweep	vary	N/A	N/A	
	230	60	5	0	60	Clean	2/3	1.87	N/A	N/A	CTP #10
8-Feb	231	60	20	0	60	Clean	Full	2.8	N/A	N/A	Oil Flow Vis. # 6
9-Feb	232	0	Sweep	0	0	Clean	Full	2.8	N/A	N/A	
	233	0	Sweep	0	0	Clean	2/3	1.87	N/A	N/A	
	234	0	0	0	0	Clean	Sweep	vary	N/A	N/A	
	235	0	-5	0	0	Clean	Sweep	vary	N/A	N/A	
	236	0	10	0	0	Clean	Sweep	vary	N/A	N/A	
	237	40	Sweep	0	0	Clean	Off	0	N/A	N/A	
	238	40	Sweep	0	0	Clean	2/3	1.87	N/A	N/A	
	239	40	Sweep	0	0	Clean	Full	2.8	N/A	N/A	
	240	40	0	0	0	Clean	Sweep	vary	N/A	N/A	
	241	40	-5	0	0	Clean	Sweep	vary	N/A	N/A	
	242	40	10	0	0	Clean	Sweep	vary	N/A	N/A	
	243	60	Sweep	0	0	Clean	Full	2.8	N/A	N/A	
	244	60	Sweep	0	0	Clean	2/3	1.87	N/A	N/A	
	245	60	Sweep	0	0	Clean	Off	0	N/A	N/A	
	246	60	0	0	0	Clean	Sweep	vary	N/A	N/A	
	247	60	-5	0	0	Clean	Sweep	vary	N/A	N/A	
	248	60	10	0	0	Clean	Sweep	vary	N/A	N/A	
	249	100	0	0	0	Clean	Sweep	vary	N/A	N/A	
	250	100	-5	0	0	Clean	Sweep	vary	N/A	N/A	
9-Feb	251	100	10	0	0	Clean	Sweep	vary	N/A	N/A	
10-Feb	252	100	Sweep	0	0	Clean	Full	2.8	N/A	N/A	
	253	100	Sweep	0	0	Clean	2/3	1.87	N/A	N/A	
	254	100	Sweep	0	0	Clean	Off	0	N/A	N/A	
	255	60	0	0	0	Clean	Sweep	vary	N/A	N/A	
	256	40	Sweep	0	80	Clean	Full	2.8	N/A	N/A	
	257	40	Sweep	0	80	Clean	2/3	1.87	N/A	N/A	
	258	40	Sweep	0	80	Clean	Off	0	N/A	N/A	
	259	40	0	0	80	Clean	Sweep	vary	N/A	N/A	

Date	Run	Velocity (KTS)	α (deg)	β (deg)	Flap Defl. (deg)	Pylon Height	CCW Config.	m_dot (lbm/sec)	TPS Config.	RPM (L/R)	Run Notes
	260	60	Sweep	0	80	Clean	Full	2.8	N/A	N/A	
	261	60	Sweep	0	80	Clean	2/3	1.87	N/A	N/A	
	262	60	Sweep	0	80	Clean	Off	0	N/A	N/A	
	263	60	0	0	80	Clean	Sweep	vary	N/A	N/A	
	264	0	Sweep	0	80	Clean	Full	2.8	N/A	N/A	
	265	0	Sweep	0	80	Clean	2/3	1.87	N/A	N/A	
	266	0	0	0	80	Clean	Sweep	vary	N/A	N/A	
	267	100	Sweep	0	80	Clean	Full	2.8	N/A	N/A	
	268	100	Sweep	0	80	Clean	2/3	1.87	N/A	N/A	
	269	100	0	0	80	Clean	Sweep	vary	N/A	N/A	
10-Feb	270	100	Sweep	0	80	Clean	Off	0	N/A	N/A	
14-Feb	271	0	0	0	60	Clean	Sweep	vary	N/A	N/A	LE slots blocked, valves adjusted to match TE
	272	0	Sweep	0	60	Clean	2/3	1.03	N/A	N/A	LE slots blocked
	273	0	Sweep	0	60	Clean	Full	1.55	N/A	N/A	LE slots blocked
	274	40	Sweep	0	60	Clean	Full	1.55	N/A	N/A	LE slots blocked
	275	40	Sweep	0	60	Clean	2/3	1.03	N/A	N/A	LE slots blocked
	276	40	0	0	60	Clean	Sweep	vary	N/A	N/A	LE slots blocked
	277	40	-5	0	60	Clean	Sweep	vary	N/A	N/A	LE slots blocked
	278	40	10	0	60	Clean	Sweep	vary	N/A	N/A	LE slots blocked
	279	60	Sweep	0	60	Clean	Full	1.55	N/A	N/A	LE slots blocked
	280	60	Sweep	0	60	Clean	2/3	1.03	N/A	N/A	LE slots blocked
	281	60	0	0	60	Clean	Sweep	vary	N/A	N/A	LE slots blocked
	282	60	-5	0	60	Clean	Sweep	vary	N/A	N/A	LE slots blocked
	283	60	10	0	60	Clean	Sweep	vary	N/A	N/A	LE slots blocked
	284	0	0	0	60	Clean	Sweep	vary	N/A	N/A	LE slots blocked
	285	0	-5	0	60	Clean	Sweep	vary	N/A	N/A	LE slots blocked
	286	0	10	0	60	Clean	Sweep	vary	N/A	N/A	LE slots blocked
	287	100	0	0	60	Clean	Sweep	vary	N/A	N/A	LE slots blocked
	288	100	Sweep	0	60	Clean	Full	1.55	N/A	N/A	LE slots blocked
	289	100	Sweep	0	60	Clean	2/3	1.03	N/A	N/A	LE slots blocked
14-Feb	290	40	Sweep	0	60	Clean	Full	1.55	N/A	N/A	LE slots blocked
15-Feb	291	0	0	0	0	Clean	Sweep	vary	N/A	N/A	LE slots blocked
	292	0	Sweep	0	0	Clean	2/3	1.03	N/A	N/A	LE slots blocked
	293	0	Sweep	0	0	Clean	Full	1.55	N/A	N/A	LE slots blocked
	294	40	Sweep	0	0	Clean	Full	1.55	N/A	N/A	LE slots blocked
	295	40	Sweep	0	0	Clean	2/3	1.03	N/A	N/A	LE slots blocked
	296	40	0	0	0	Clean	Sweep	vary	N/A	N/A	LE slots blocked
	297	40	-5	0	0	Clean	Sweep	vary	N/A	N/A	LE slots blocked
	298	40	10	0	0	Clean	Sweep	vary	N/A	N/A	LE slots blocked
	299	60	Sweep	0	0	Clean	Full	1.55	N/A	N/A	LE slots blocked
	300	60	Sweep	0	0	Clean	2/3	1.03	N/A	N/A	LE slots blocked
	301	60	0	0	0	Clean	Sweep	vary	N/A	N/A	LE slots blocked
	302	60	-5	0	0	Clean	Sweep	vary	N/A	N/A	LE slots blocked
	303	60	10	0	0	Clean	Sweep	vary	N/A	N/A	LE slots blocked
	304	0	0	0	0	Clean	Sweep	vary	N/A	N/A	LE slots blocked
	305	0	-5	0	0	Clean	Sweep	vary	N/A	N/A	LE slots blocked
	306	0	10	0	0	Clean	Sweep	vary	N/A	N/A	LE slots blocked
	307	0	0	0	0	Clean	Sweep	vary	N/A	N/A	LE slots blocked, partial repeat of Run 304
	308	100	Sweep	0	0	Clean	Full	1.55	N/A	N/A	LE slots blocked
	309	100	Sweep	0	0	Clean	2/3	1.03	N/A	N/A	LE slots blocked
	310	100	0	0	0	Clean	Sweep	vary	N/A	N/A	LE slots blocked
	311	40	Sweep	0	0	Clean	Full	1.55	N/A	N/A	LE slots blocked
15-Feb	312	40	Sweep	0	0	Clean	Full+	1.87	N/A	N/A	LE slots blocked, valve position adjusted to allow more mass flow (matches 2/3 mdot from full blowing case)

13.Results

13.1. Data Repeatability

This section focuses on the estimation of the repeatability (or precision) error for the AMELIA test data. In order to make such an assessment, multiple sets of identical runs at different model and tunnel configurations were obtained; the runs were distributed as widely as possible to make the most reliable assessment of such uncertainty. Out of a total of 292 data runs, fourteen different repeat run configurations were obtained. A discussion on the statistical analysis of the force and moment coefficient repeatability is first, followed by a discussion on factors that may contribute to non-repeatability in the data. A list of all repeat runs and their respective tunnel and model configuration is given below in Table 13.1. No repeat runs were acquired in the high pylon configuration. For reference, full slots is the maximum slot blowing condition, 2.8 lb_m/sec total through the low pressure side; full TPS is the maximum (or nominal) TPS setting, corresponding to each TPS spinning at ~34,500 RPM and ~1.97 lb_m/sec total air fed to the units.

Table 13.1. Listing of repeated runs and their respective tunnel and model configurations.

	Repeat Run Numbers	Tunnel/Model Configuration
Low Pylon – full slots represents 2.8 lb_m/sec, full TPS represents 34,500 RPM	R19, R95	40 KTS, 0° flap, slots off, TPS off
	R21, R105	100 KTS, 0° flap, slots off, TPS off
	R26, R60	60 KTS, 60° flap, slots off, TPS off
	R36, R92, R102	40 KTS, 0° flap, slots full, TPS full
	R46, R56, R133	40 KTS, 60° flap, slots full, TPS full
	R56, R66	40 KTS, 60° flap, slots full, TPS off
	R69, R81, R82, R128	40 KTS, 80° flap, slots full, TPS full
	R78, R79	100 KTS, 80° flap, slots full, TPS full
	R152, R153	40 KTS, 30° flap, slots full, TPS full
Clean Wing	R213, R218	40 KTS, 60° flap, full slots
	R246, R255	60 KTS, 0° flap, $\alpha = 0°$, slot sweep
Trailing Edge-only Blowing – full slots represents 1.55 lb_m/sec	R274, R290	40 KTS, 60° flap, slots full
	R294, R311	40 KTS, 0° flap, slots full

13.1.1. Uncertainty Analysis

In general, measurements have two sources of error: bias error and precision error. Bias error is generally considered a fixed quantity, with variances in both magnitude and sign. Large biases are believed to be eliminated through a well-controlled experiment; small biases, however, typically remain. Precision error is the random component of the total error that has to do with the difference between a measured value and the population mean of measured values (i.e. the data scatter). Because precision error is the random component of the true error, statistical analysis is used to estimate the data mean and express the data scatter about the estimated mean with a specified level of confidence. The method employed here is referred to as multivariable regression statistical analysis (MRSA); the method is used by Wahls[23] and is consistent with the AIAA standard[24]. In the MRSA method, the data sample mean is estimated by a single least-squares curve fit based on all data from a set of identical runs. This method assumes that the data

scatter is random and can be represented by a normal distribution, and that the dependent variable can be represented as a single function of the independent variable using a polynomial regression equation. For this analysis, the independent variable is either angle of attack (for alpha sweeps) or C_μ (for slot sweeps). The dependent variables are C_L, C_D, and C_m. The data scatter about the mean is quantified with confidence and prediction intervals on the bounds. Herein, the confidence interval is interpreted as the bounds about which the estimated mean encompasses the true mean, and the prediction interval is interpreted as the bounds about which the estimated mean will contain any single future observation. The bound widths are equivalent to the level of confidence in the statistical analysis; here 95% confidence and prediction levels are reported.

13.1.1.1. Repeatability Analysis Method

The polynomial least-squares regression equation of order K takes the general form

$$\hat{Y}(X) = C_0 + C_1X + C_2X^2 + C_3X^3 + \ldots + C_KX^K \tag{1.1}$$

Where X is the independent variable, $\hat{Y}$ is the best estimate of the dependent variable, and C_j are the least-squares constant coefficients. The selection of the order of the curve fit can be subjective, so an algorithm was written to constrain and select the appropriate order of each polynomial regression. The algorithm evaluates the least-squares regression for multiple orders and selects the order that minimizes the standard error while constraining with the following criterion[26]

$$K \leq \sqrt{N} - 1 \tag{1.2}$$

This criterion provides a useful limit for the order of the polynomial regression. N is the total data sample size. The standard error is a measure of the data scatter about the estimated mean; it is an extension of the sample standard deviation accounting for multiple single regression lines in one fit. The standard error is defined as

$$SE = \left[\frac{\sum_{i=1}^{N}\left(Y_i - \hat{Y}_i\right)^2}{N - K - 1}\right]^{1/2} \tag{1.3}$$

Where $\hat{Y}_i$ is the least-squares estimate of Y_i corresponding to X_i at the i^{th} data point (i.e. a single angle of attack or slot set point). The confidence and prediction intervals are defined in terms of the standard error. The confidence interval, CI, is defined as

$$CI(X_0) = \pm t_{95} \cdot SE \cdot Q(X_0) \tag{1.4}$$

The prediction interval, PI, is defined as

$$PI(X_0) = \pm t_{95} \cdot SE \cdot \sqrt{1 + Q(X_0)^2} \tag{1.5}$$

Where t_{95} is the value of the t distribution for 95% confidence. $Q(X_0)$ is a measure of the data density in the area of the independent variable, X_0. The term accounts for the data density such that more populated regions have narrower confidence and prediction intervals than those that are sparser. This effect can be seen in the widening of both prediction and confidence intervals at the ends of the data range, where the mean value is known with less confidence because the data is less concentrated in these regions.

The results of the repeatability analysis are presented in the figures that follow this discussion, Figure 13.1–13.33. Plots are provided for the repeat runs listed in Table 13.1 and repeatability is represented in

terms of the dependent variables: lift coefficient, drag coefficient, and pitching moment coefficient. The regression analyses were based on data acquired over the entire angle of attack range or range of slot set points within a given set of repeat runs. Each figure presents the original polar and the residuals from each curve fit. The residuals, or delta coefficients, are defined as the difference between the least-squares estimation of the data sample mean and the measured value at a given angle of attack.

$$\Delta Y = Y_i - \hat{Y}_i \tag{1.6}$$

The statistical quantities listed in the lower subplot of each figure provide a summary of relevant statistics for each regression. The quantities represented are: the order of the least-squares curve fit, K, the goodness of fit, R^2 (coefficient of determination), and the standard error, S.E., for each regression.

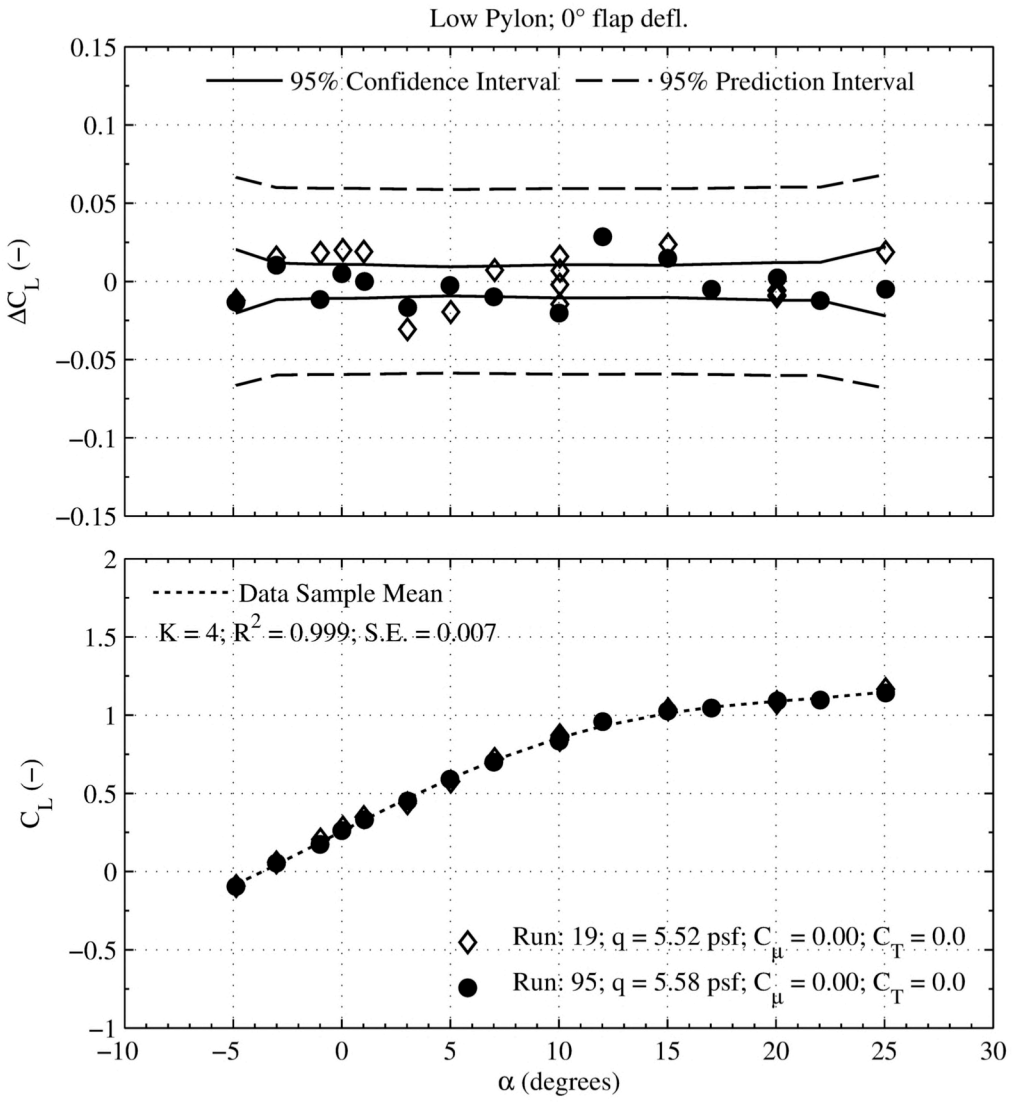

Figure 13.1. Un-powered, long-term repeatability. (a) Lift Coefficient.

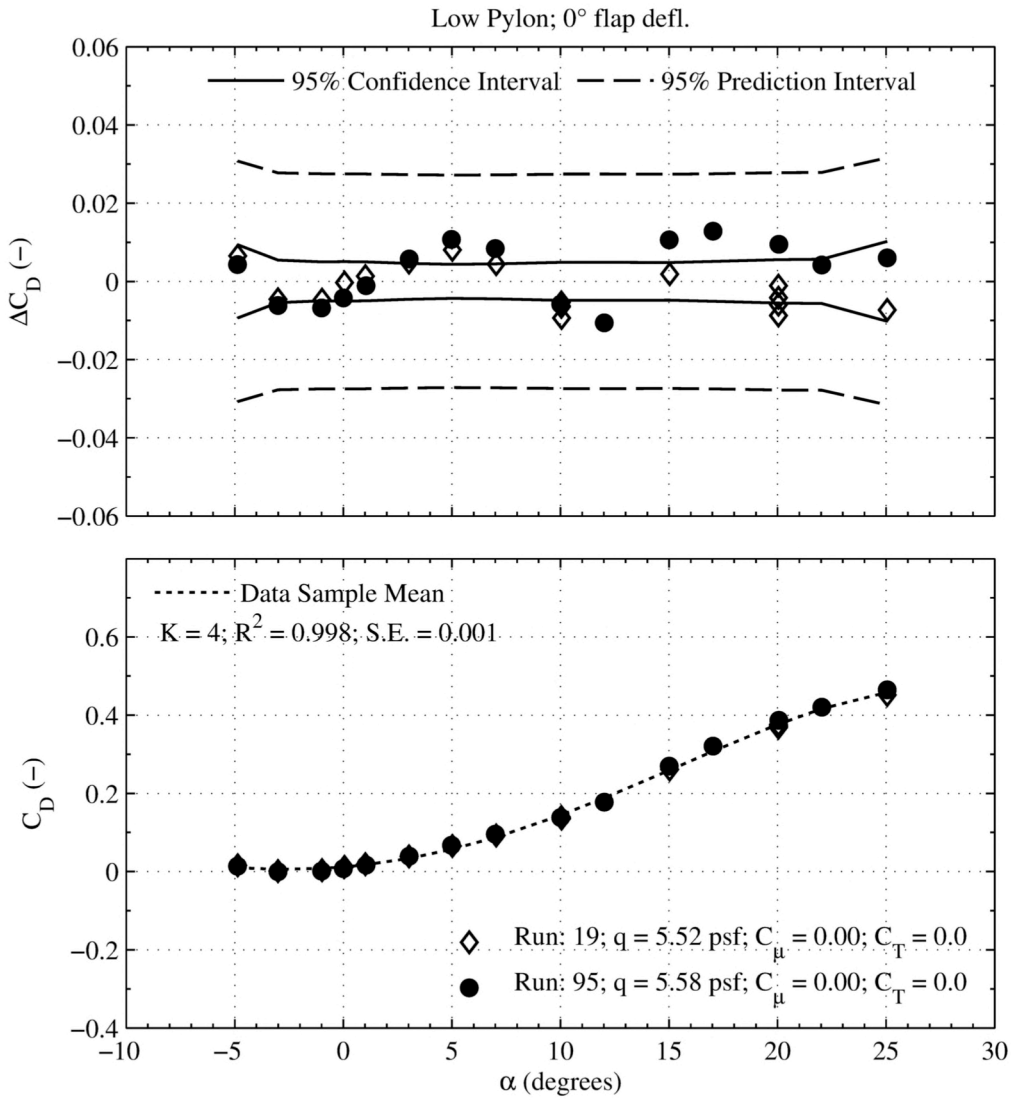

Figure 13.2. Un-powered, long-term repeatability. (b) Drag Coefficient.

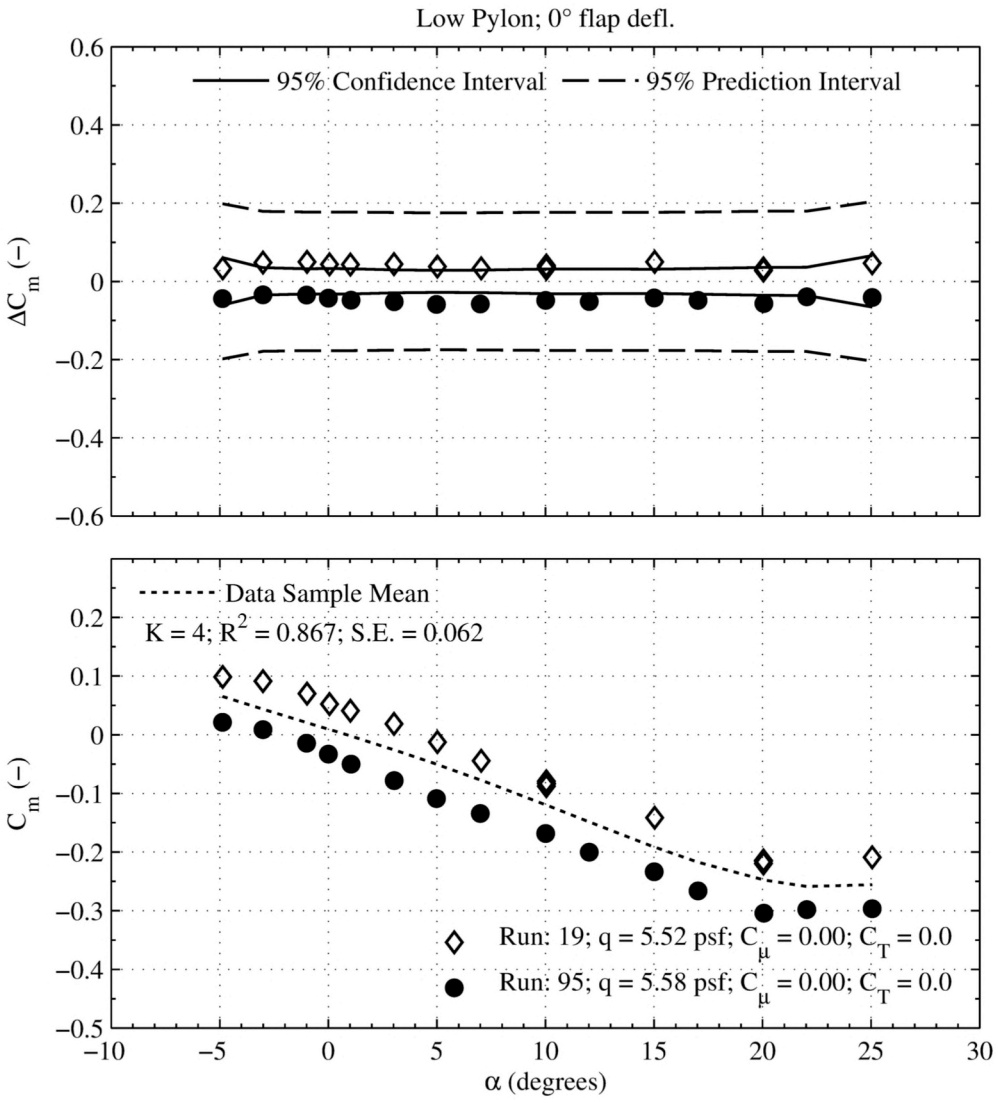

Figure 13.3. Un-powered, long-term repeatability. (c) Pitching Moment Coefficient.

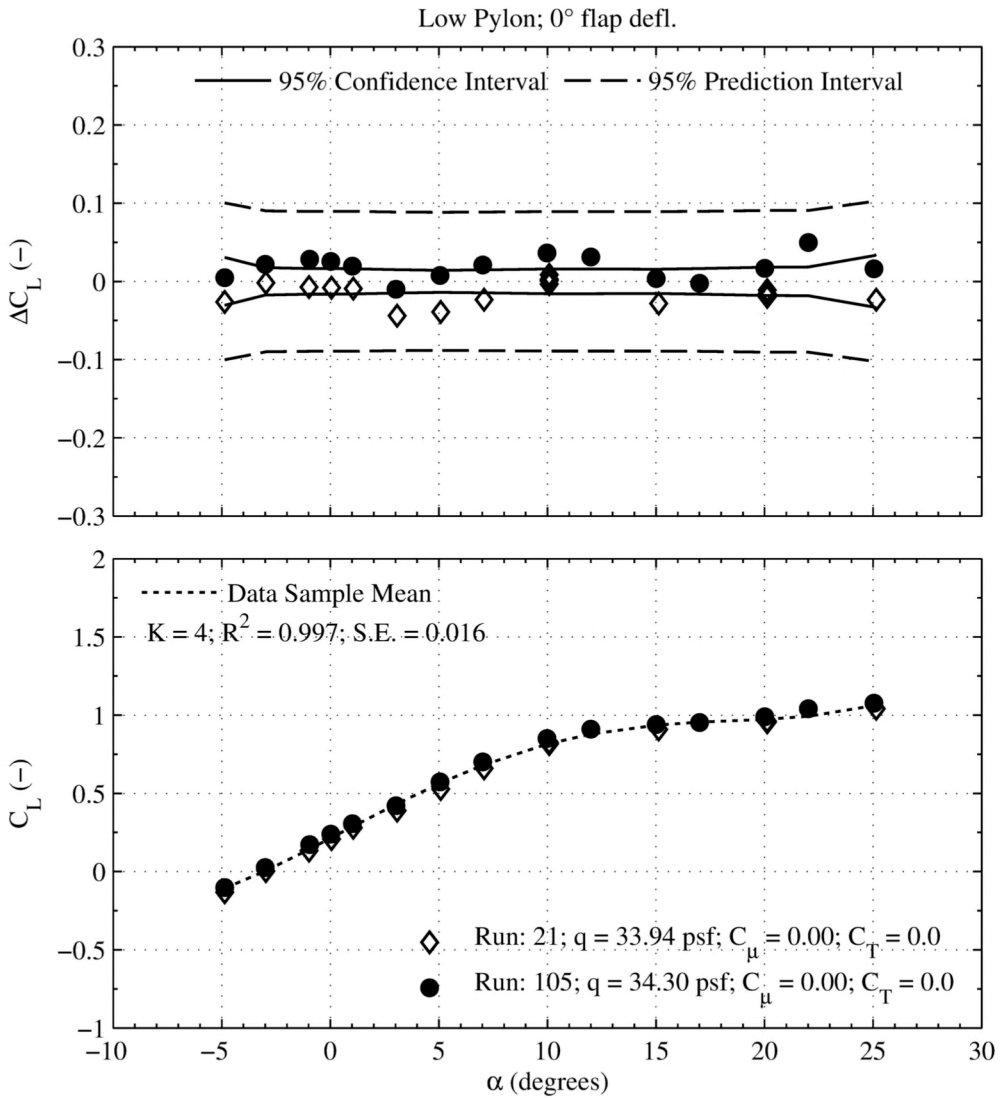

Figure 13.4. Un-powered, long-term repeatability. (a) Lift Coefficient.

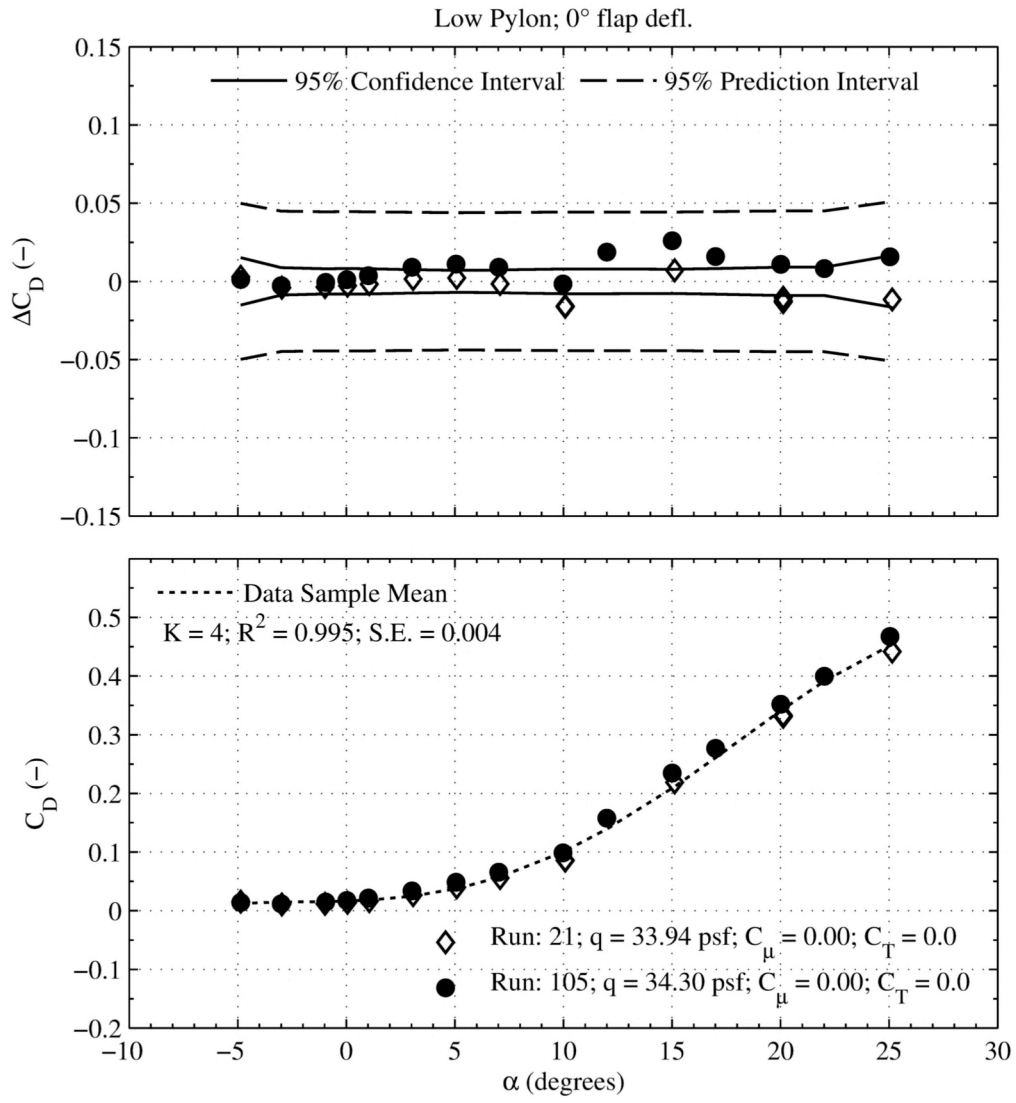

Figure 13.5. Un-powered, long-term repeatability. (b) Drag Coefficient.

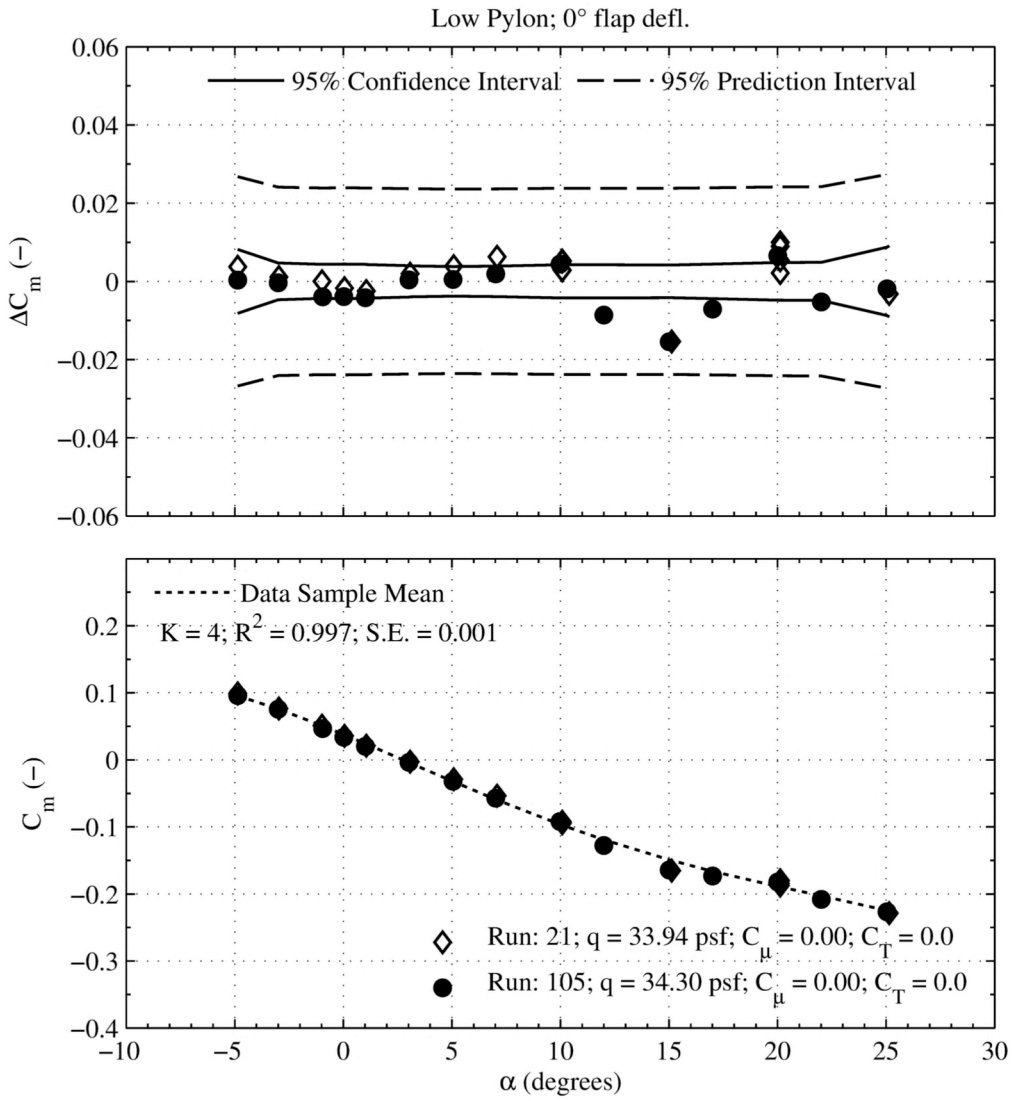

Figure 13.6. Un-powered, long-term repeatability. (c) Pitching Moment Coefficient.

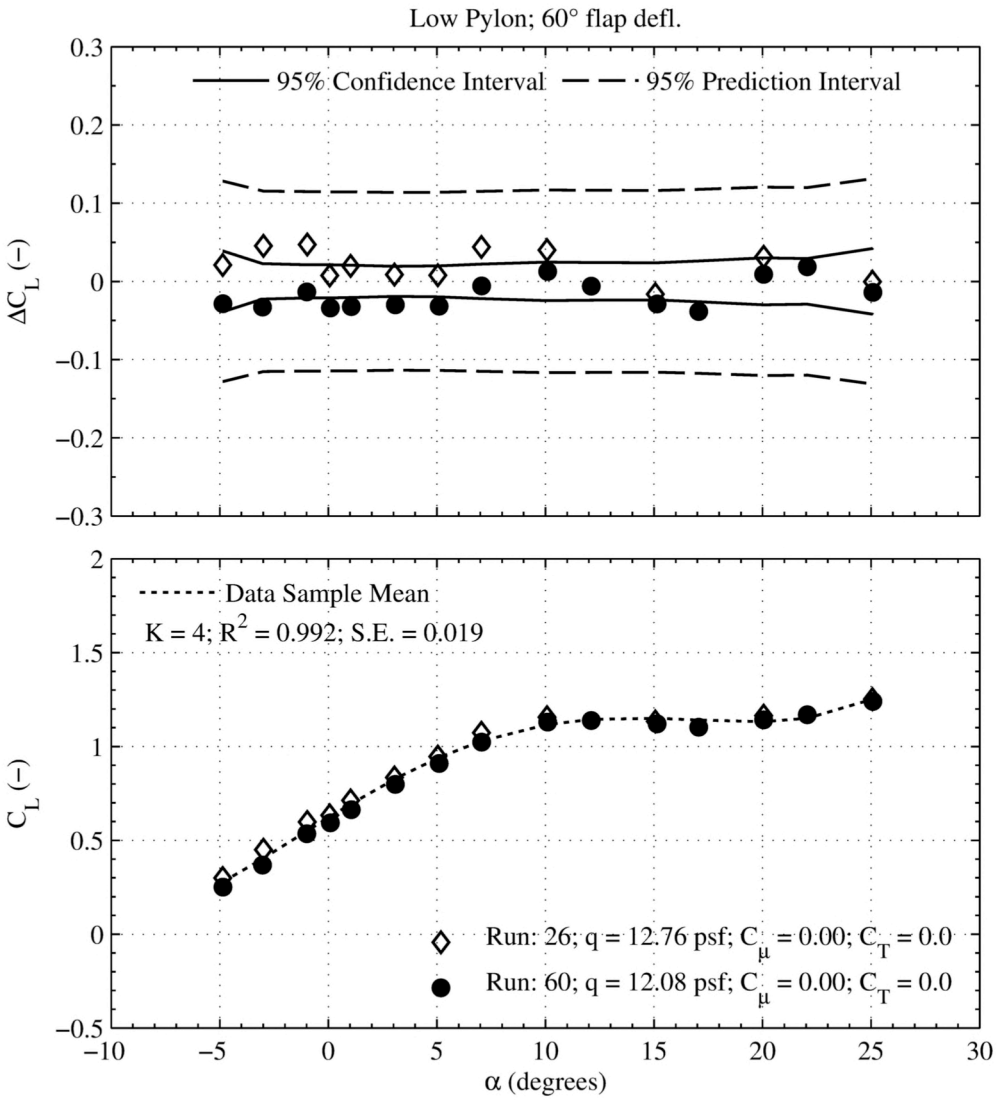

Figure 13.7. Un-powered, long-term repeatability. (a) Lift Coefficient.

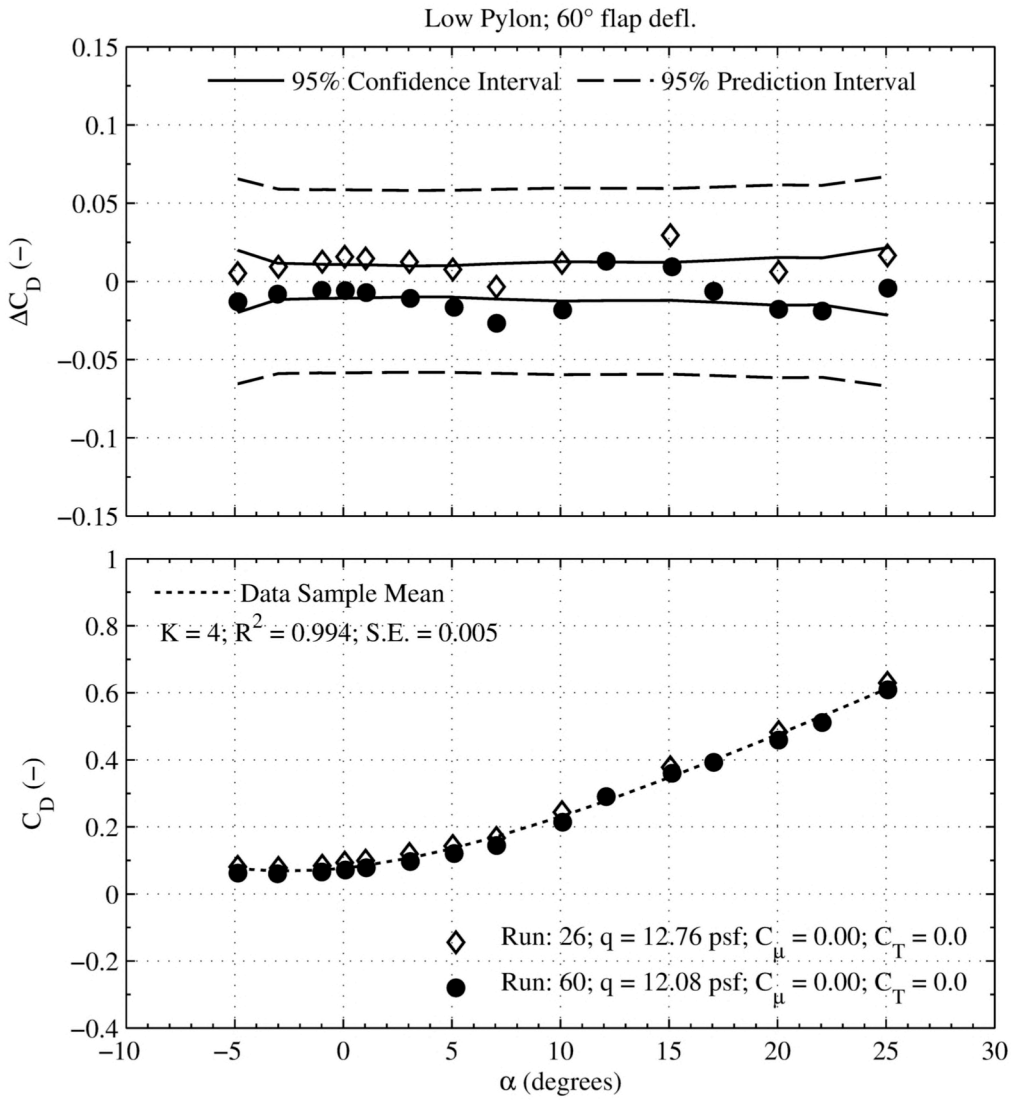

Figure 13.8. Un-powered, long-term repeatability. (b) Drag Coefficient.

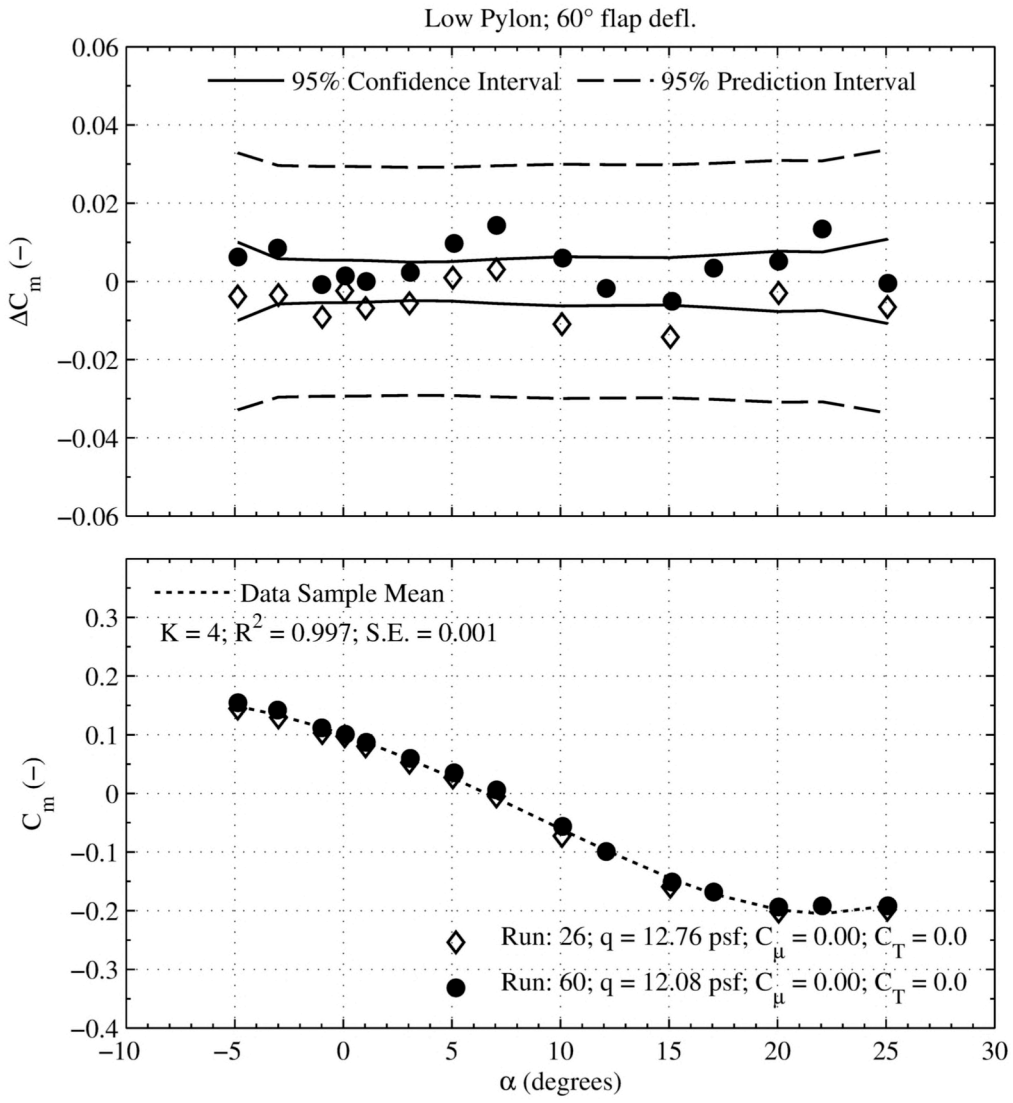

Figure 13.9. Un-powered, long-term repeatability. (c) Pitching Moment Coefficient.

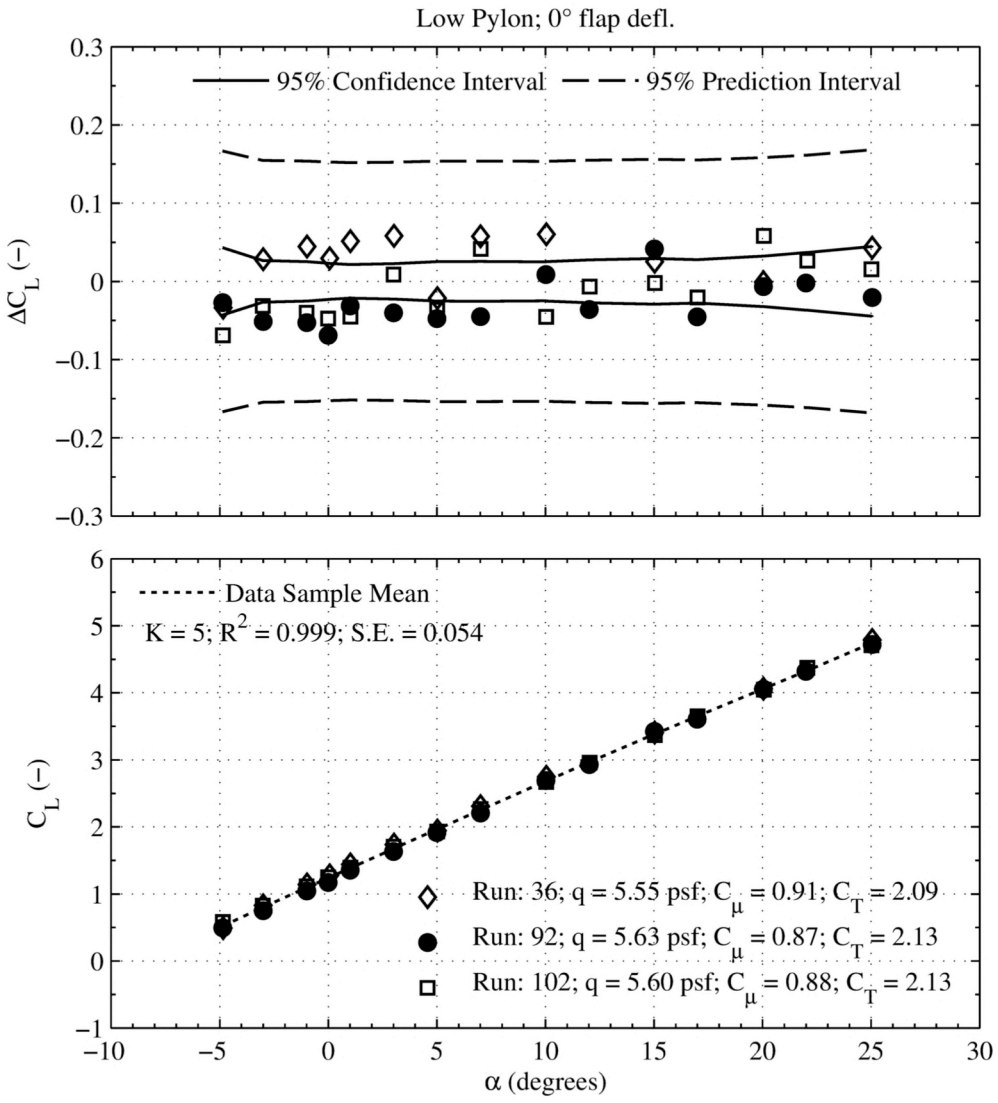

Figure 13.10. Powered, long-term repeatability. (a) Lift Coefficient.

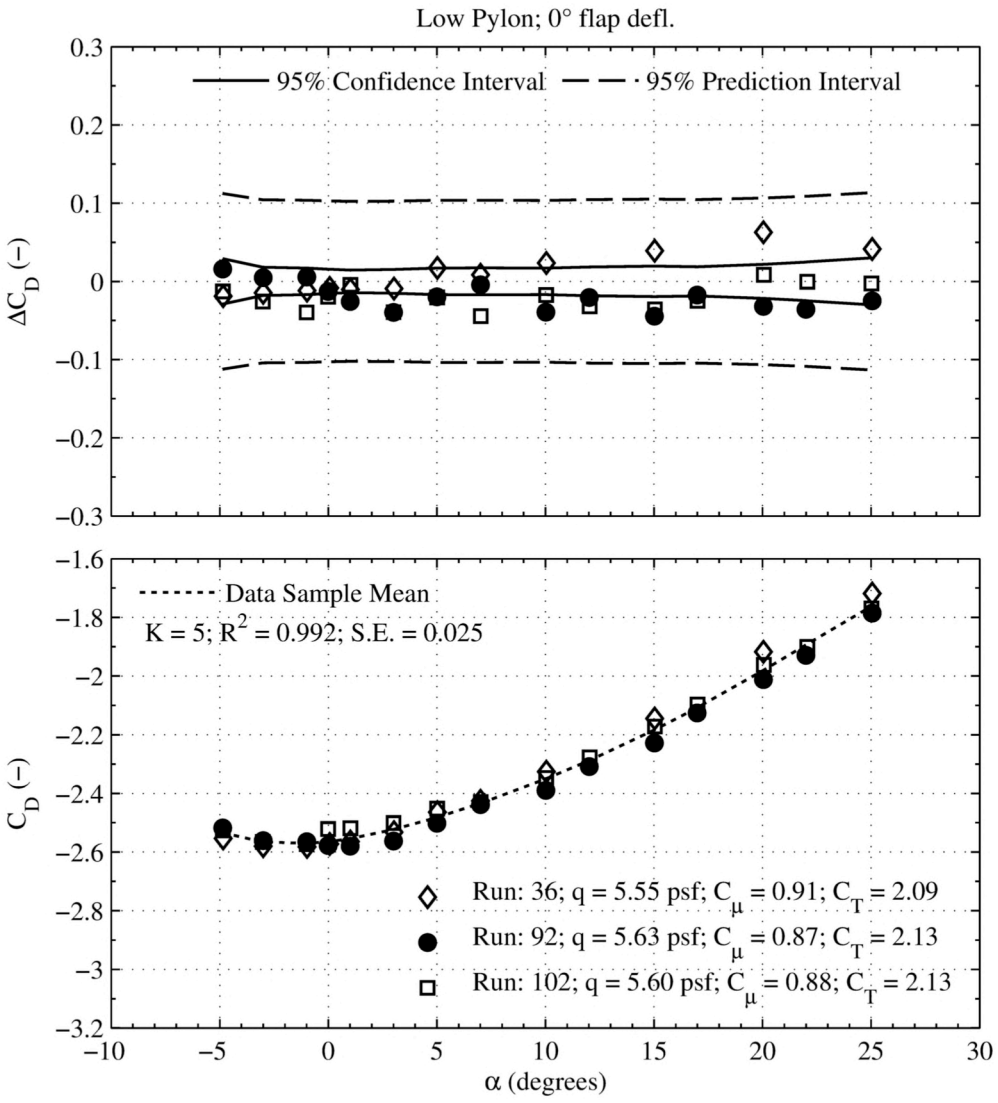

Figure 13.11. Powered, long-term repeatability. (b) Drag Coefficient.

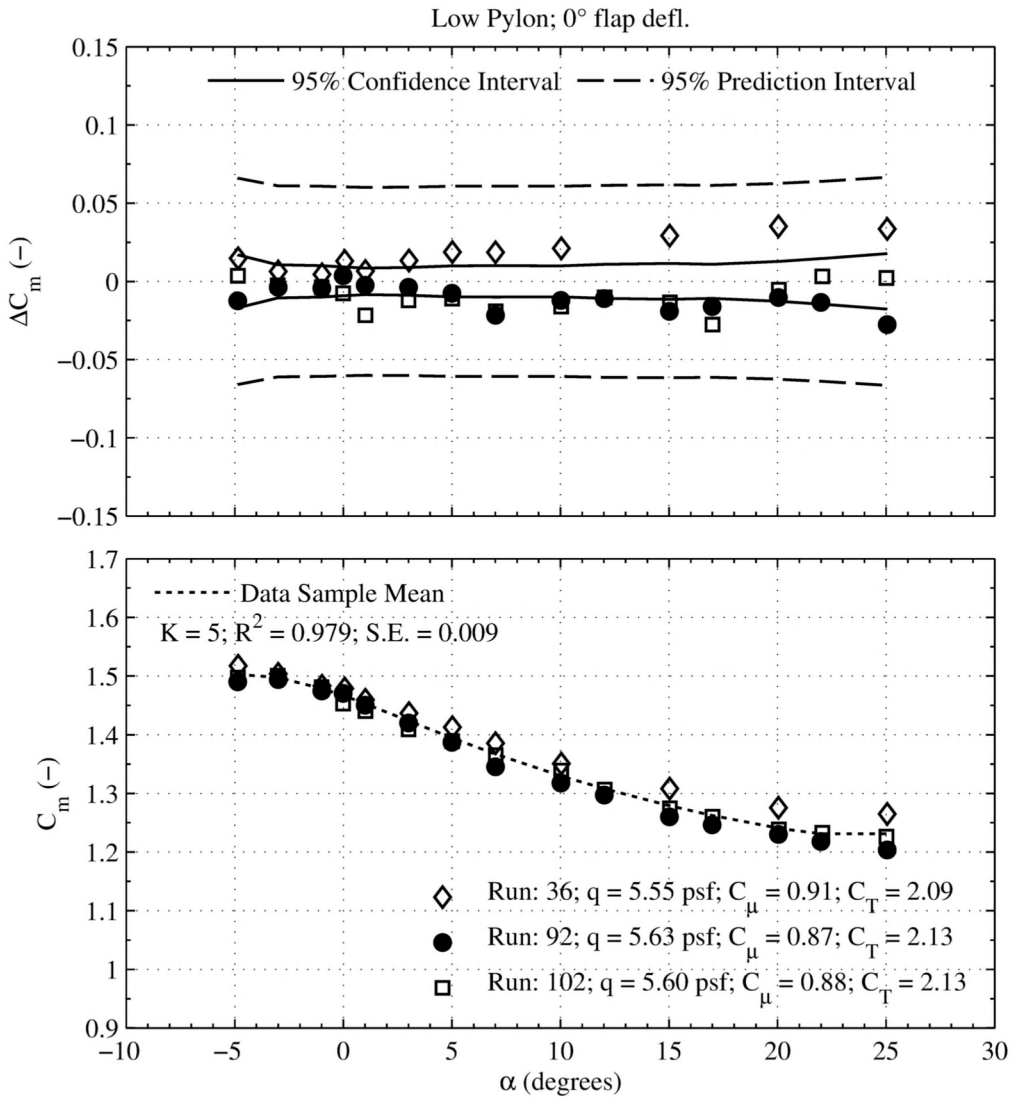

Figure 13.12. Powered, long-term repeatability. (c) Pitching Moment Coefficient.

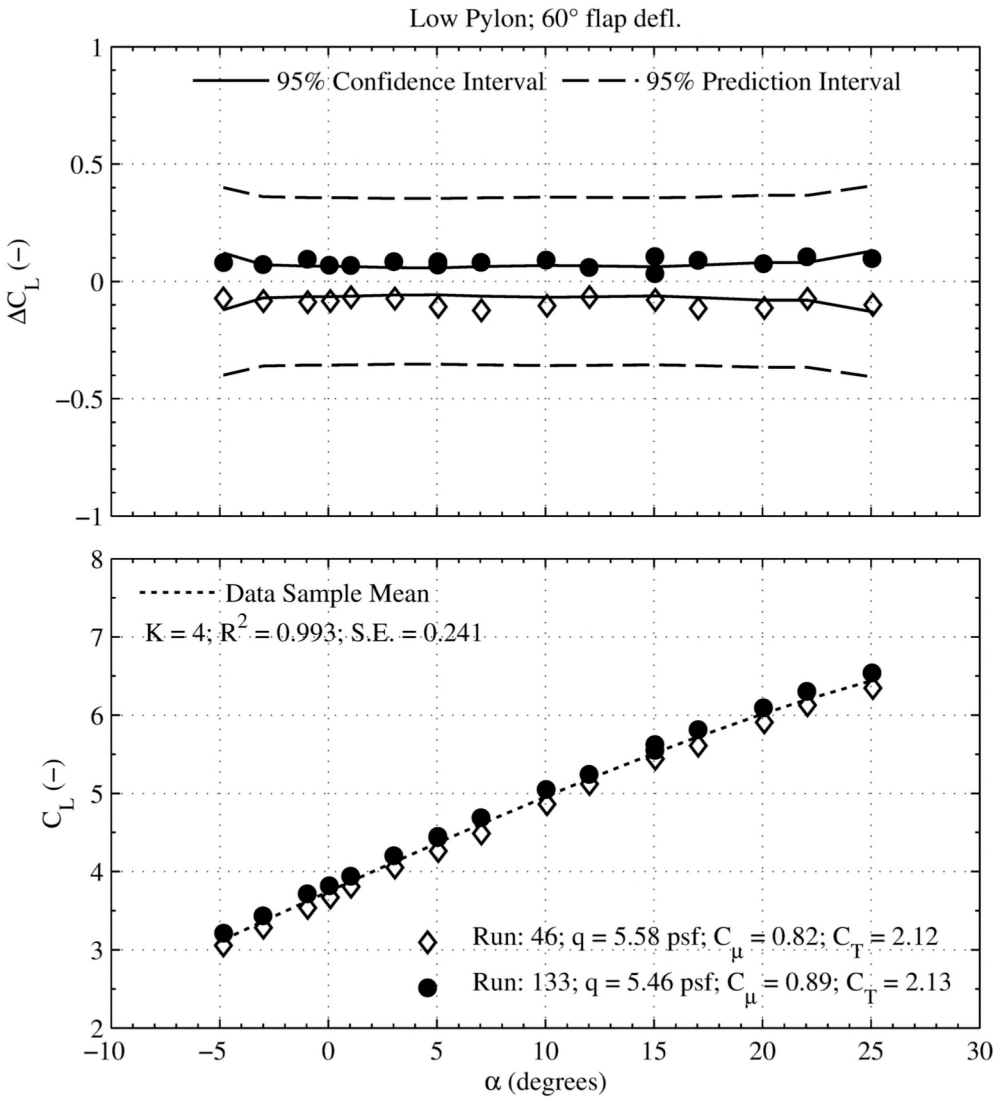

Figure 13.13. Powered, long-term repeatability. (a) Lift Coefficient.

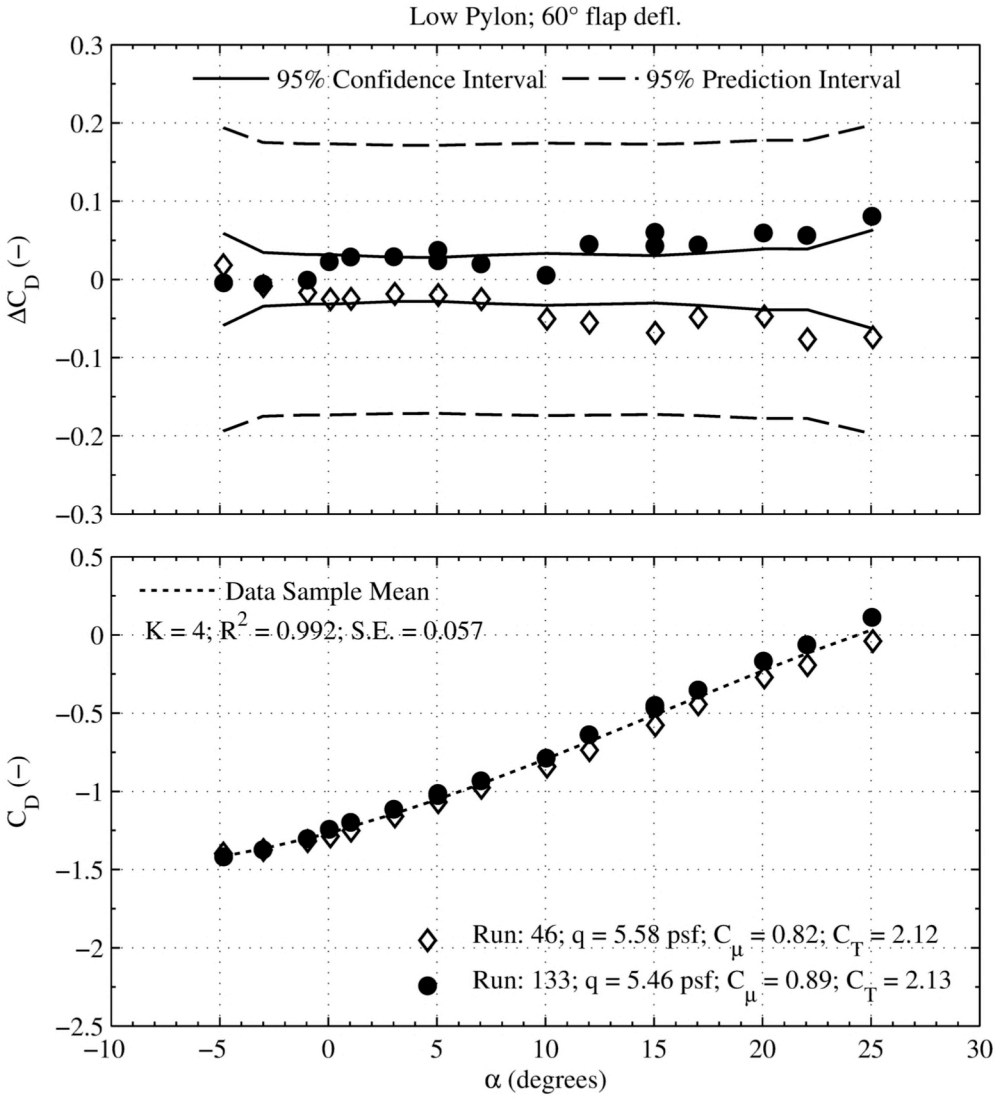

Figure 13.14. Powered, long-term repeatability. (b) Drag Coefficient.

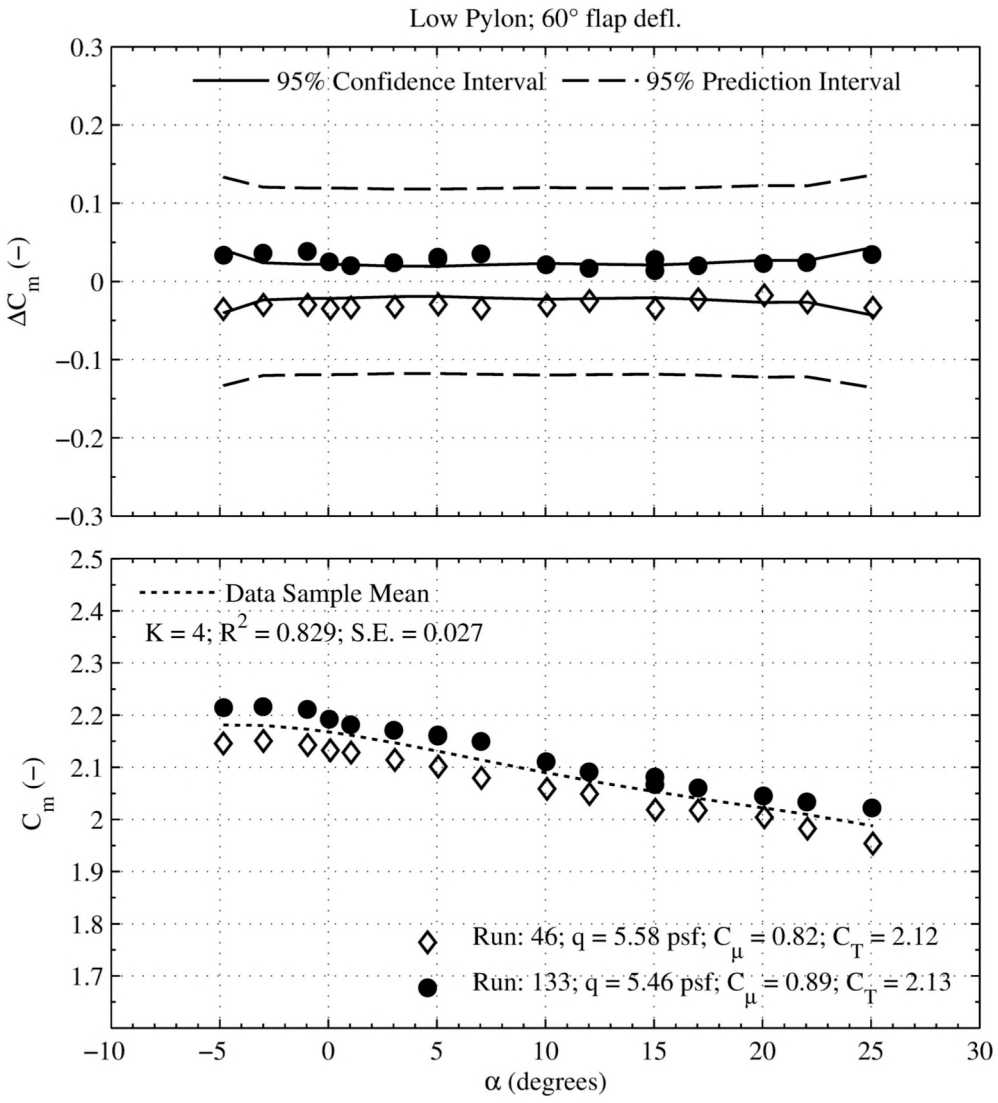

Figure 13.15. Powered, long-term repeatability. (c) Pitching Moment Coefficient.

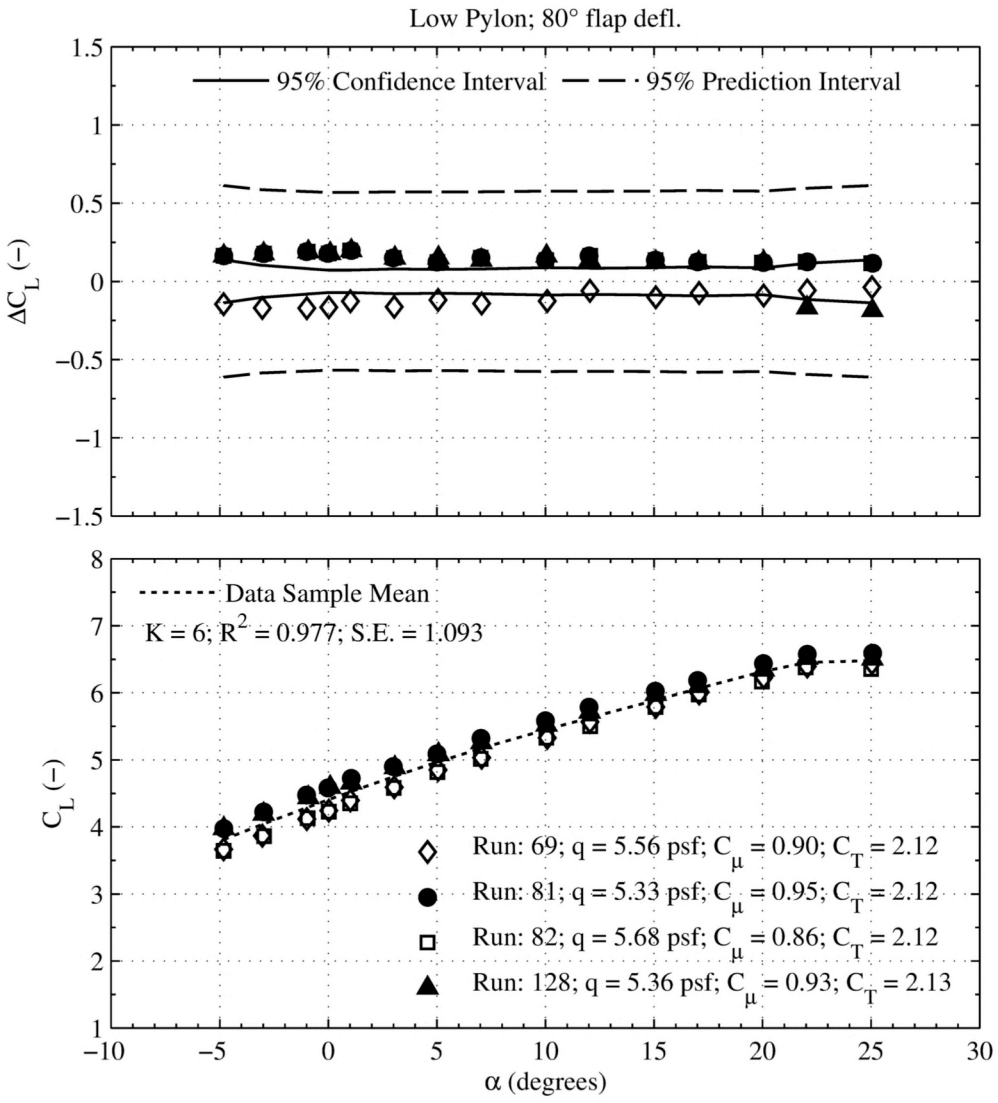

Figure 13.16. Powered, long-term repeatability. (a) Lift Coefficient.

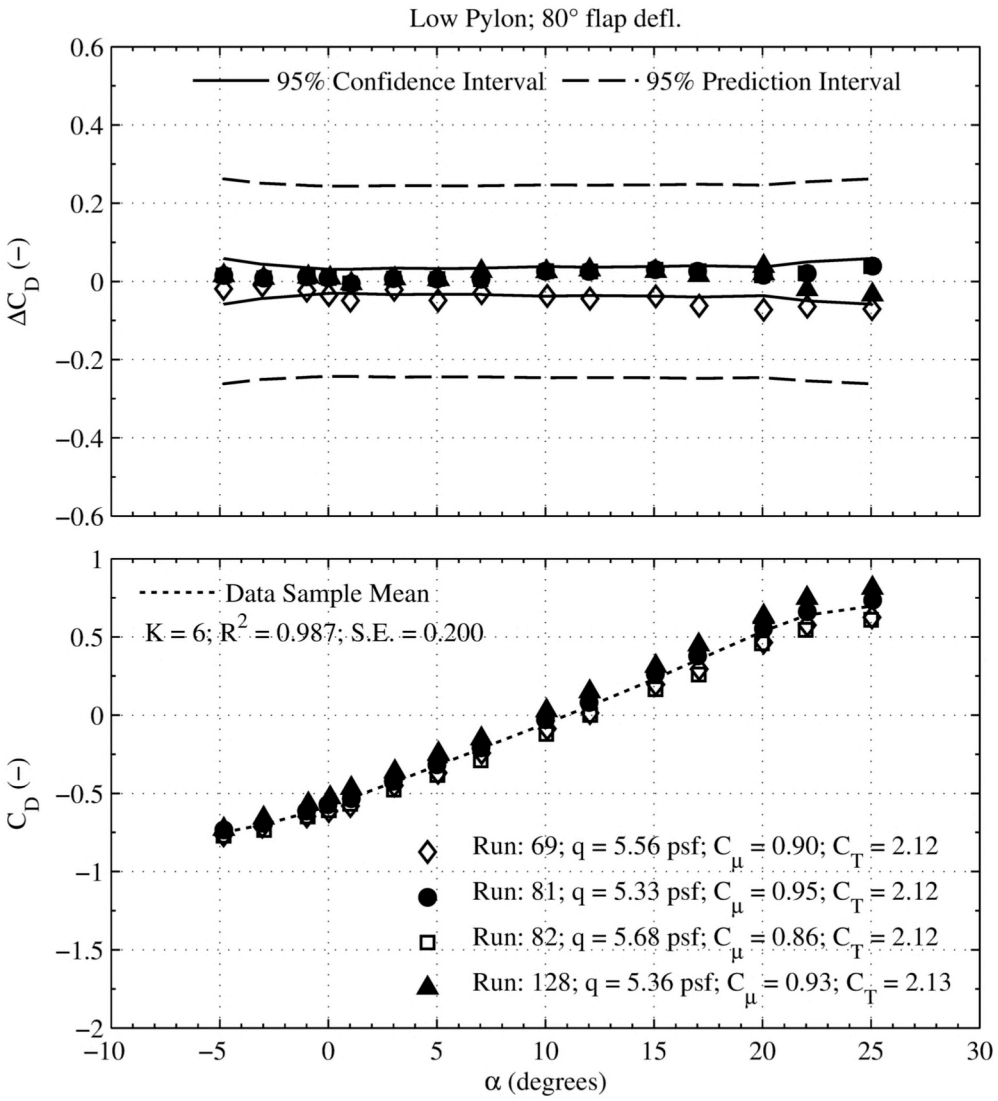

Figure 13.17. Powered, long-term repeatability. (b) Drag Coefficient.

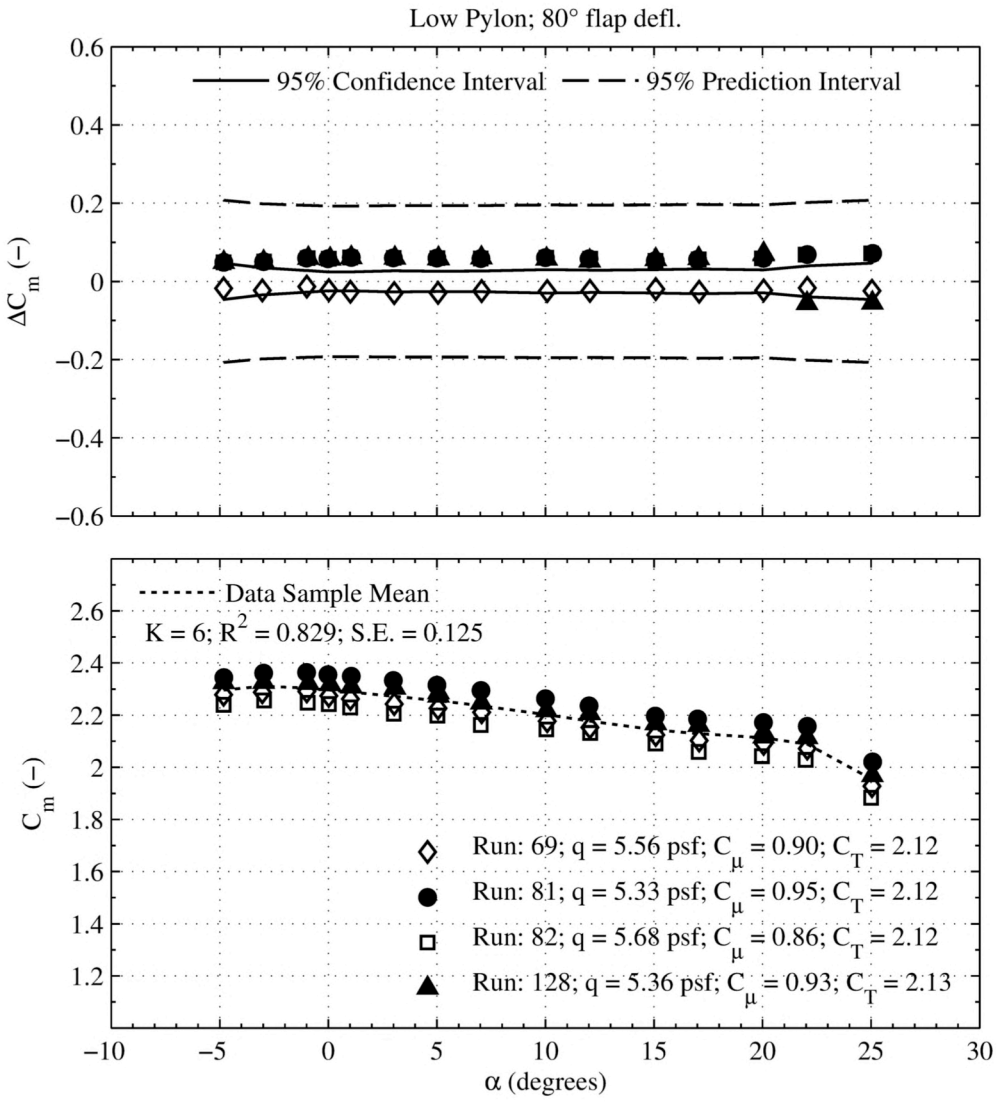

Figure 13.18. Powered, long-term repeatability. (c) Pitching Moment Coefficient.

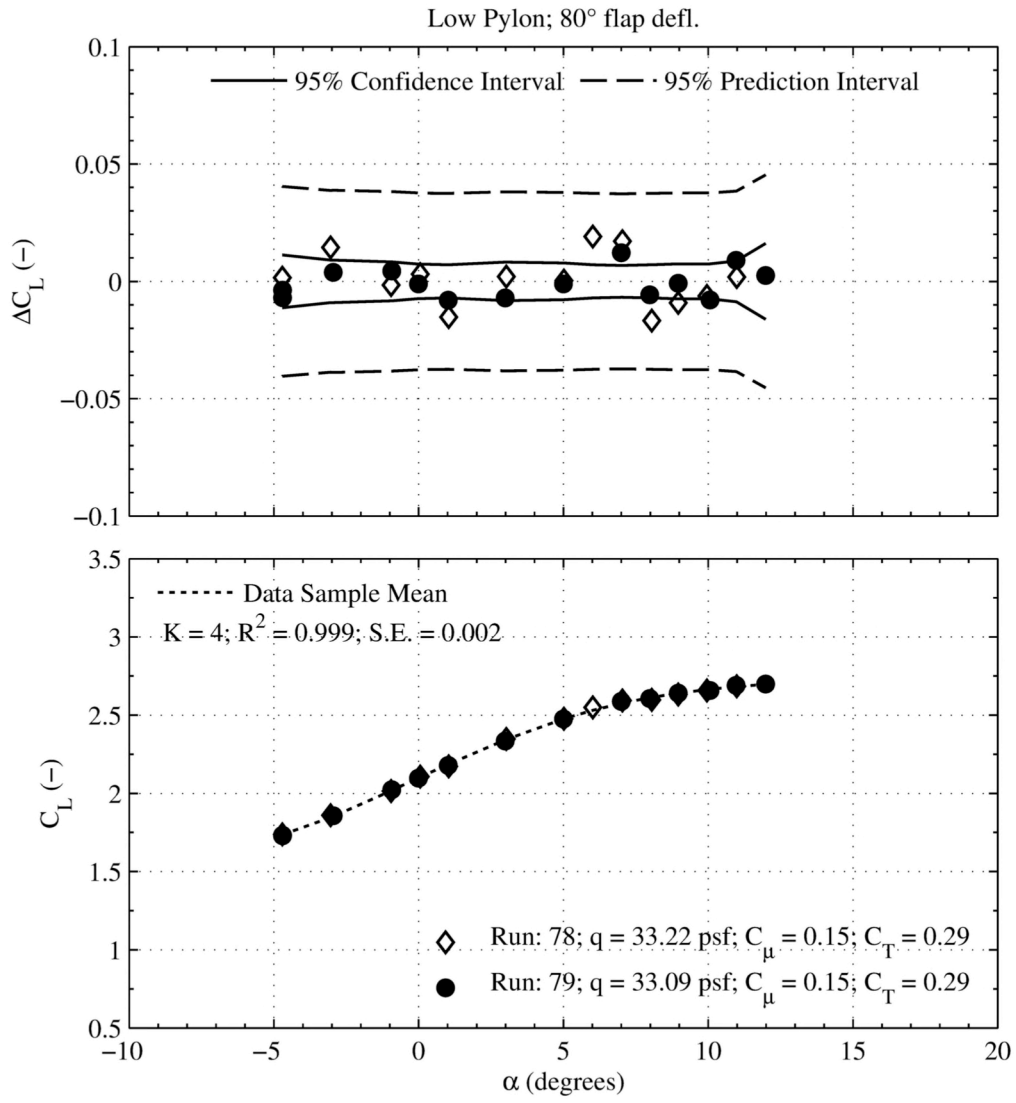

Figure 13.19. Powered, short-term repeatability. (a) Lift Coefficient.

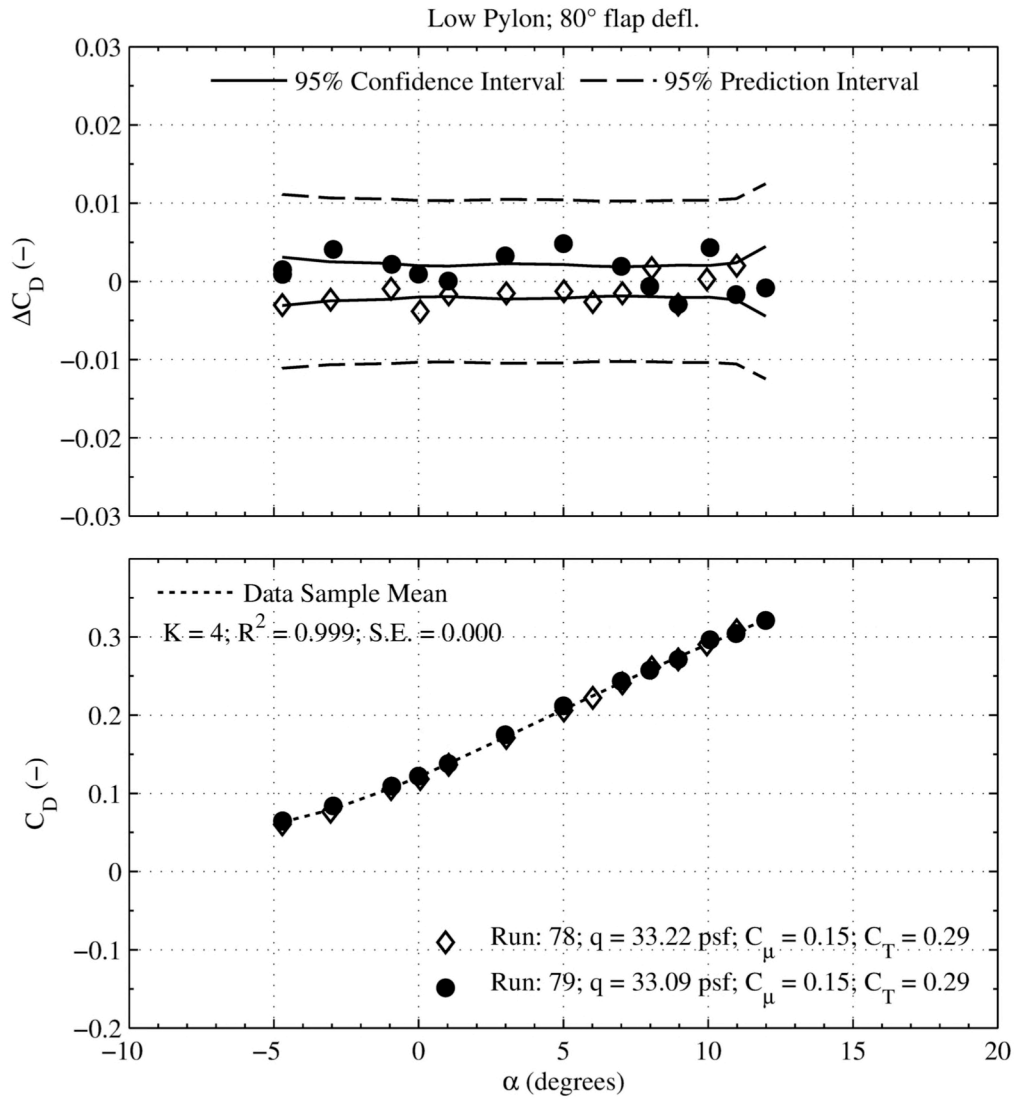

Figure 13.20. Powered, short-term repeatability. (b) Drag Coefficient.

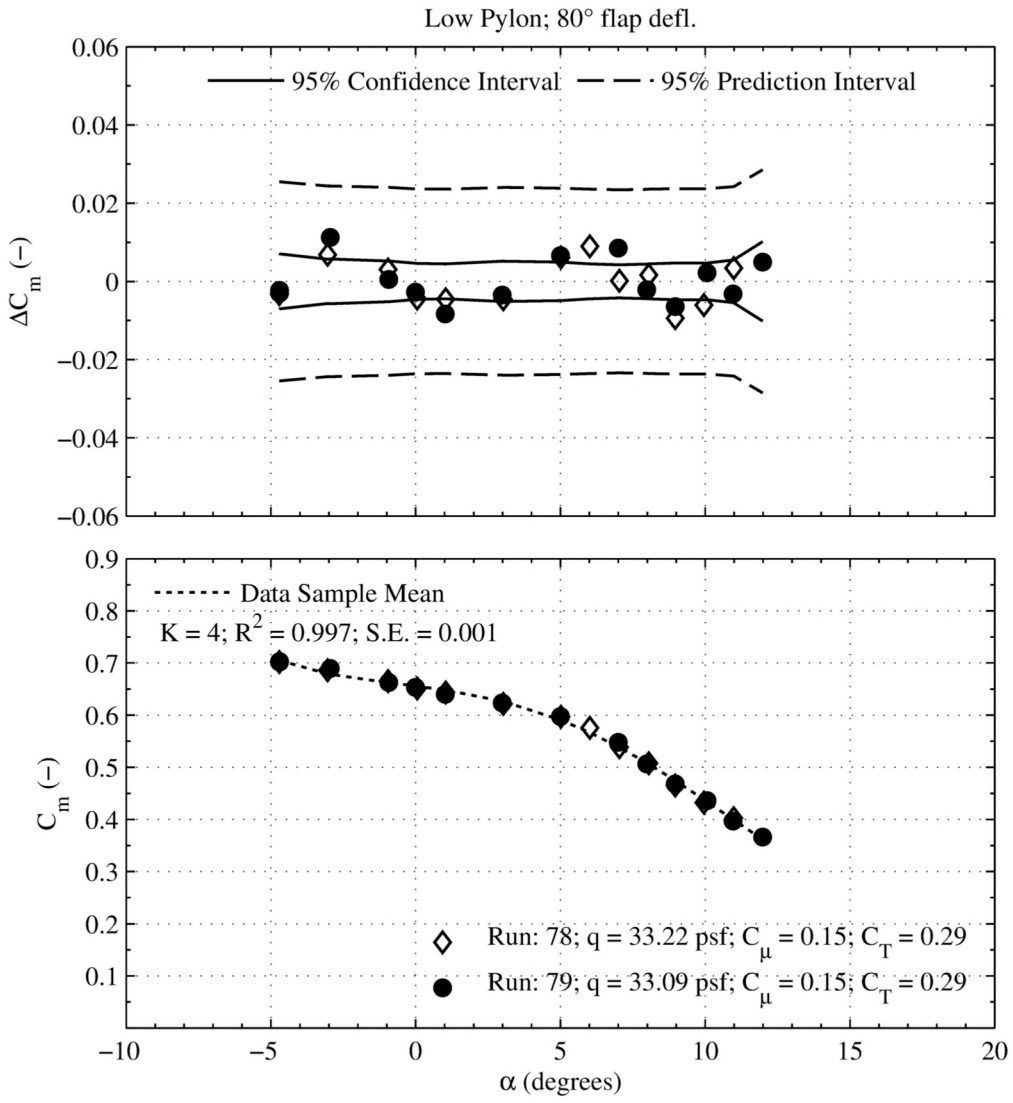

Figure 13.21. Powered, short-term repeatability. (c) Pitching Moment Coefficient.

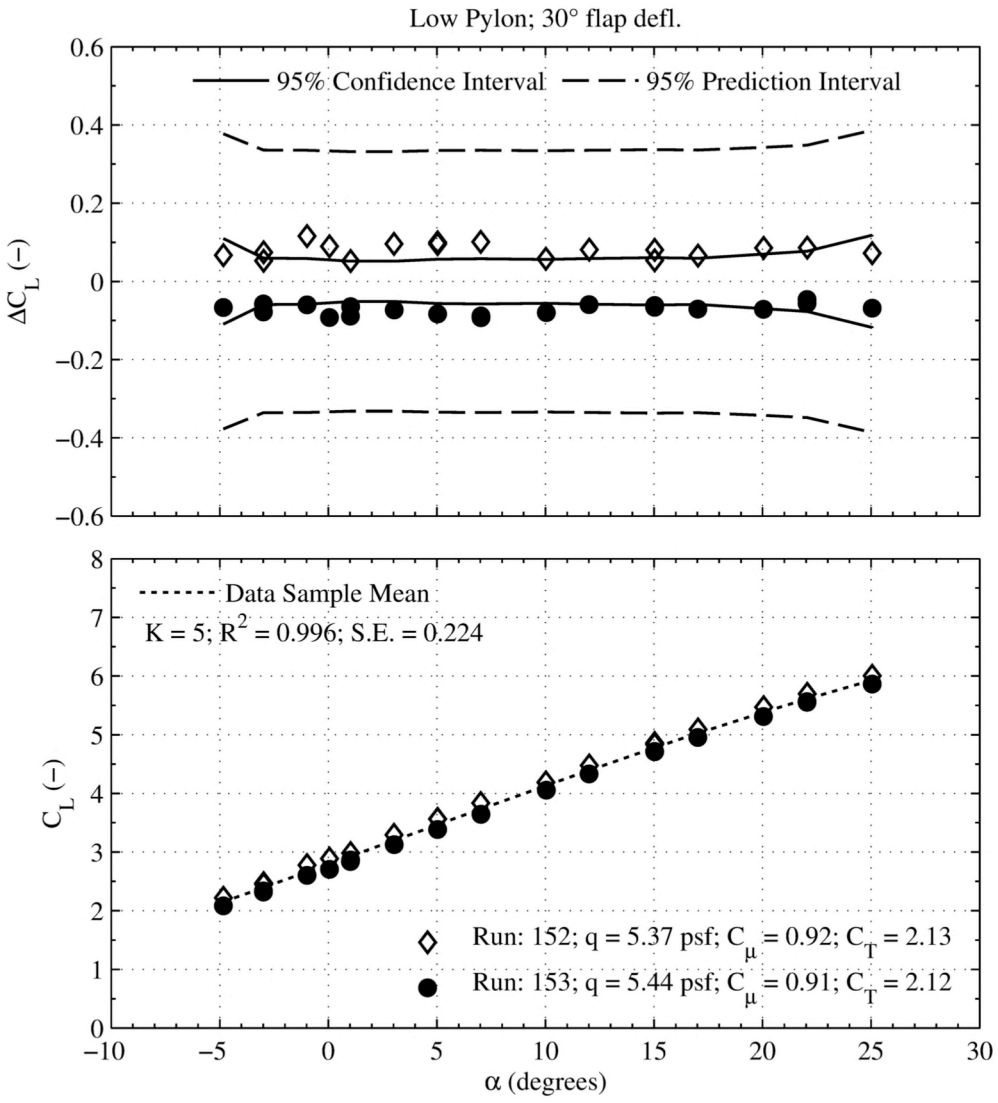

Figure 13.22. Powered, near-term repeatability. (a) Lift Coefficient.

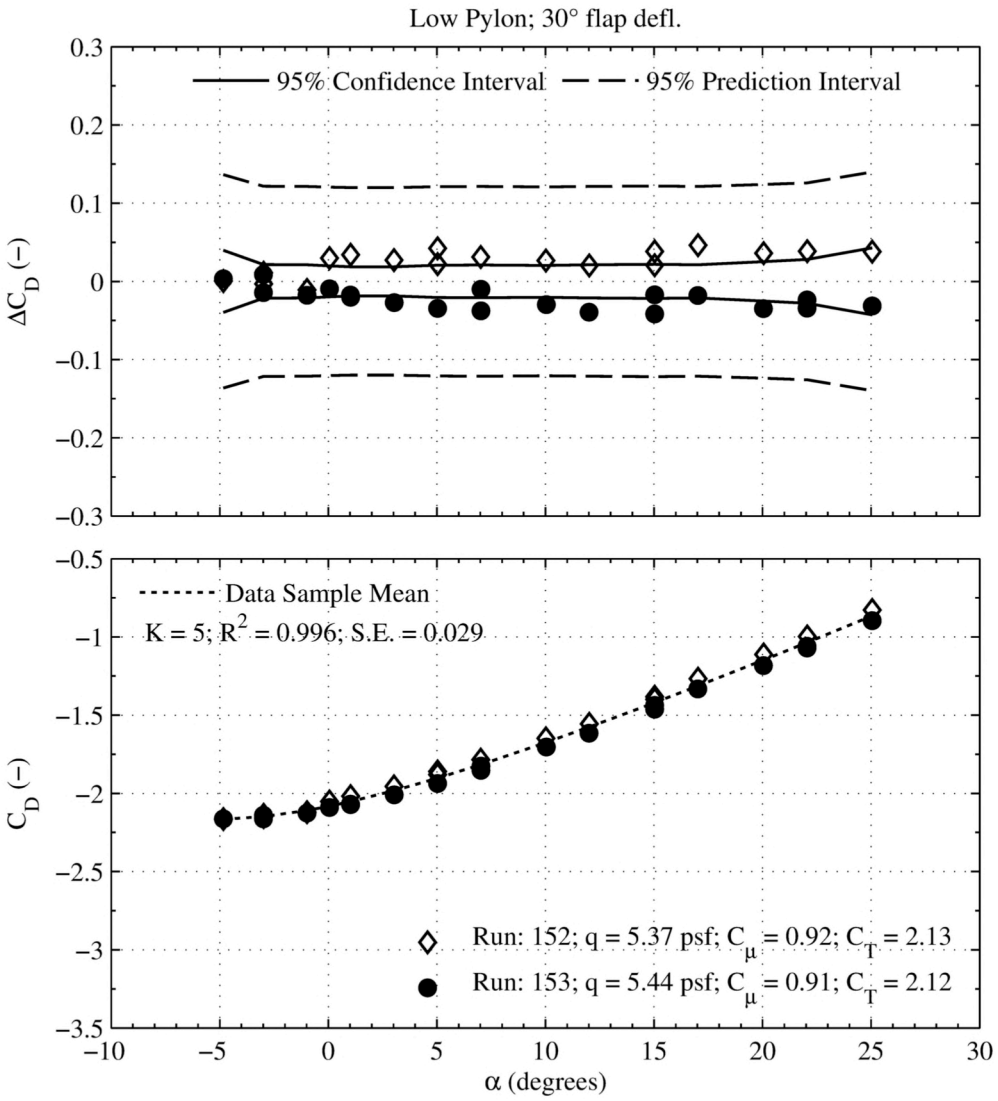

Figure 13.23. Powered, near-term repeatability. (b) Drag Coefficient.

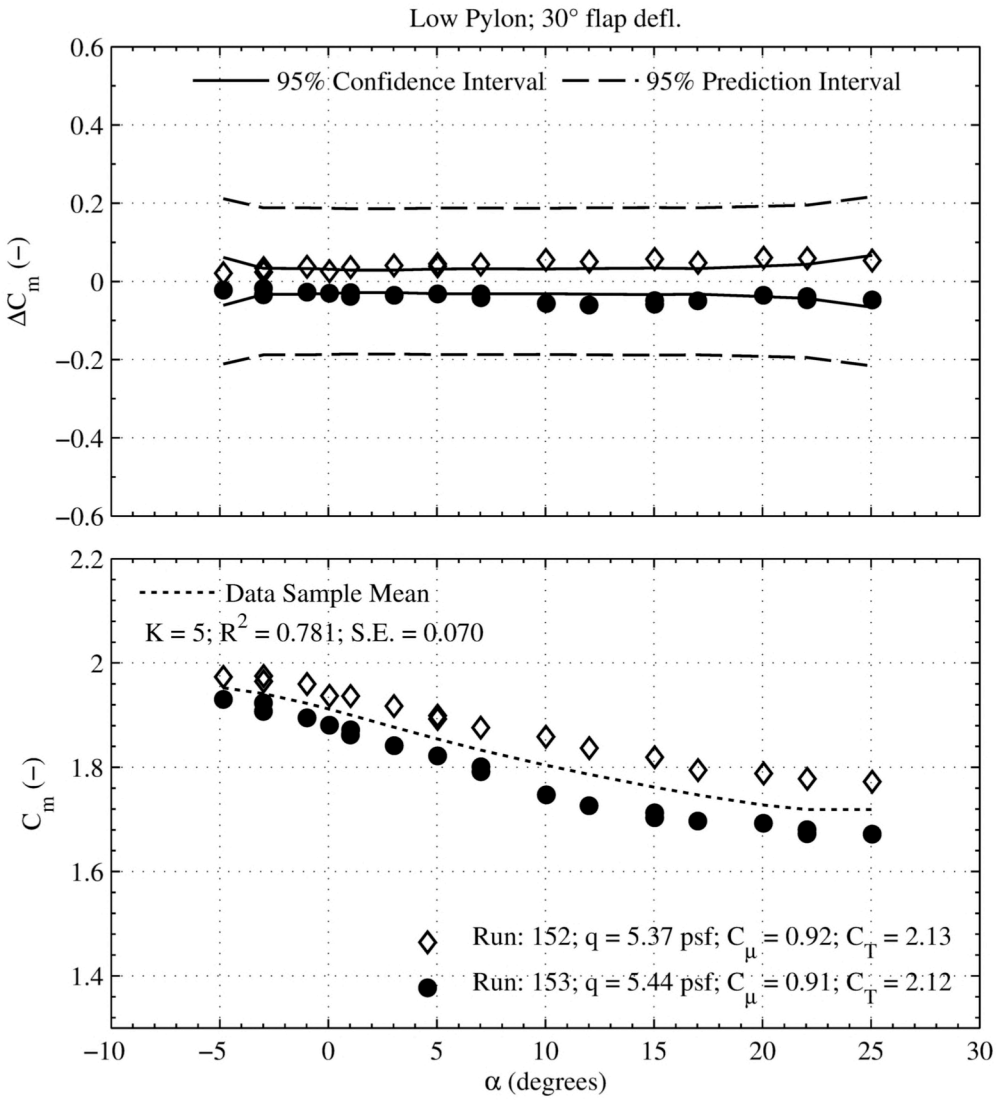

Figure 13.24. Powered, near-term repeatability. (c) Pitching Moment Coefficient.

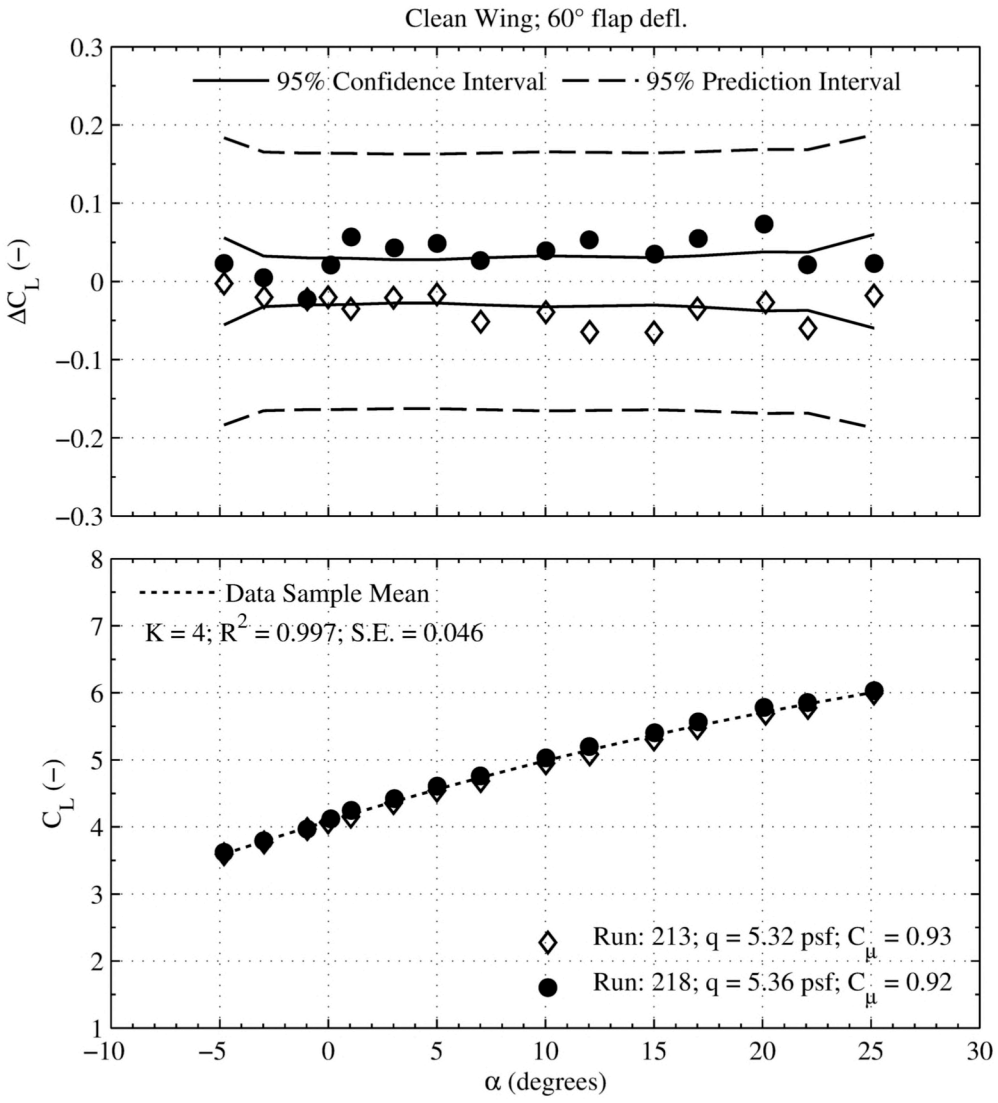

Figure 13.25. Powered, near-term repeatability. (a) Lift Coefficient.

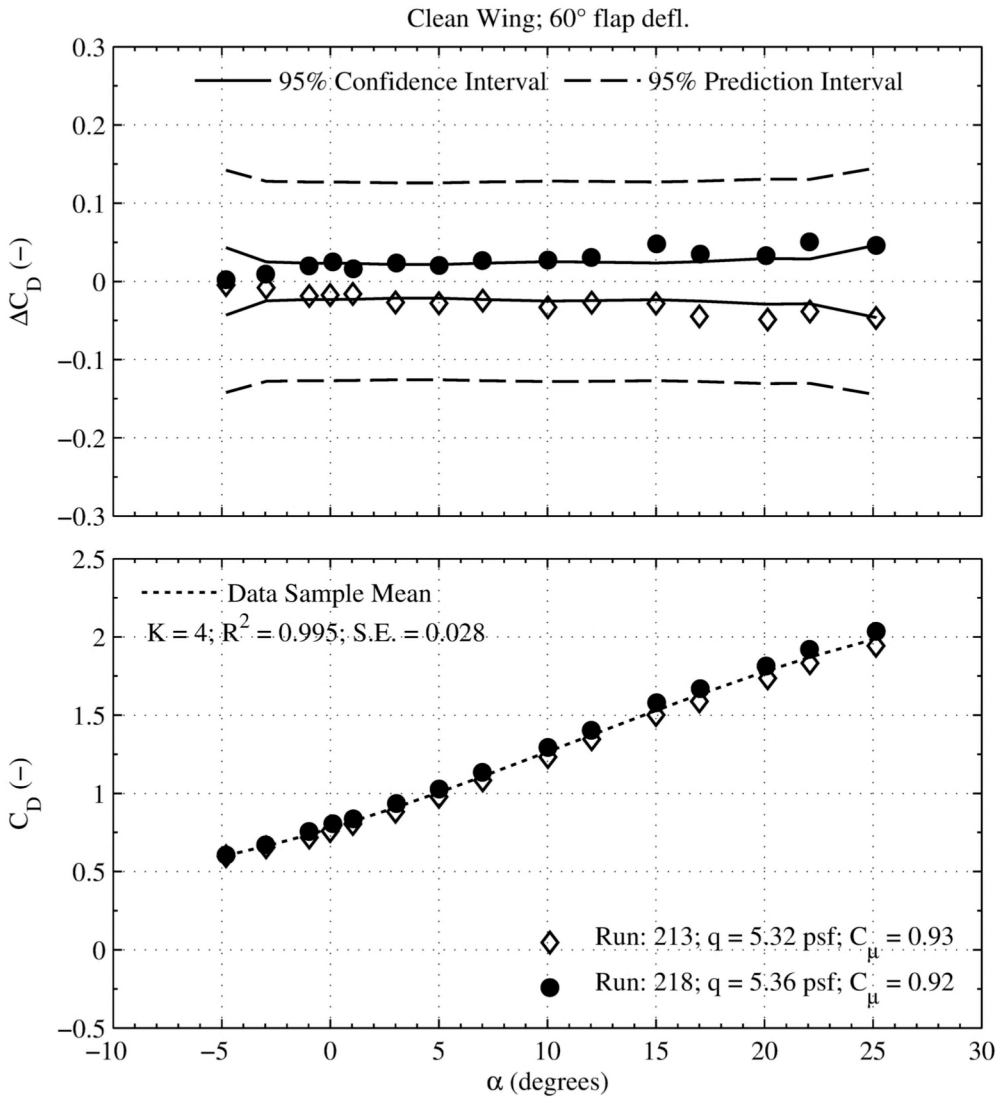

Figure 13.26. Powered, near-term repeatability. (b) Drag Coefficient.

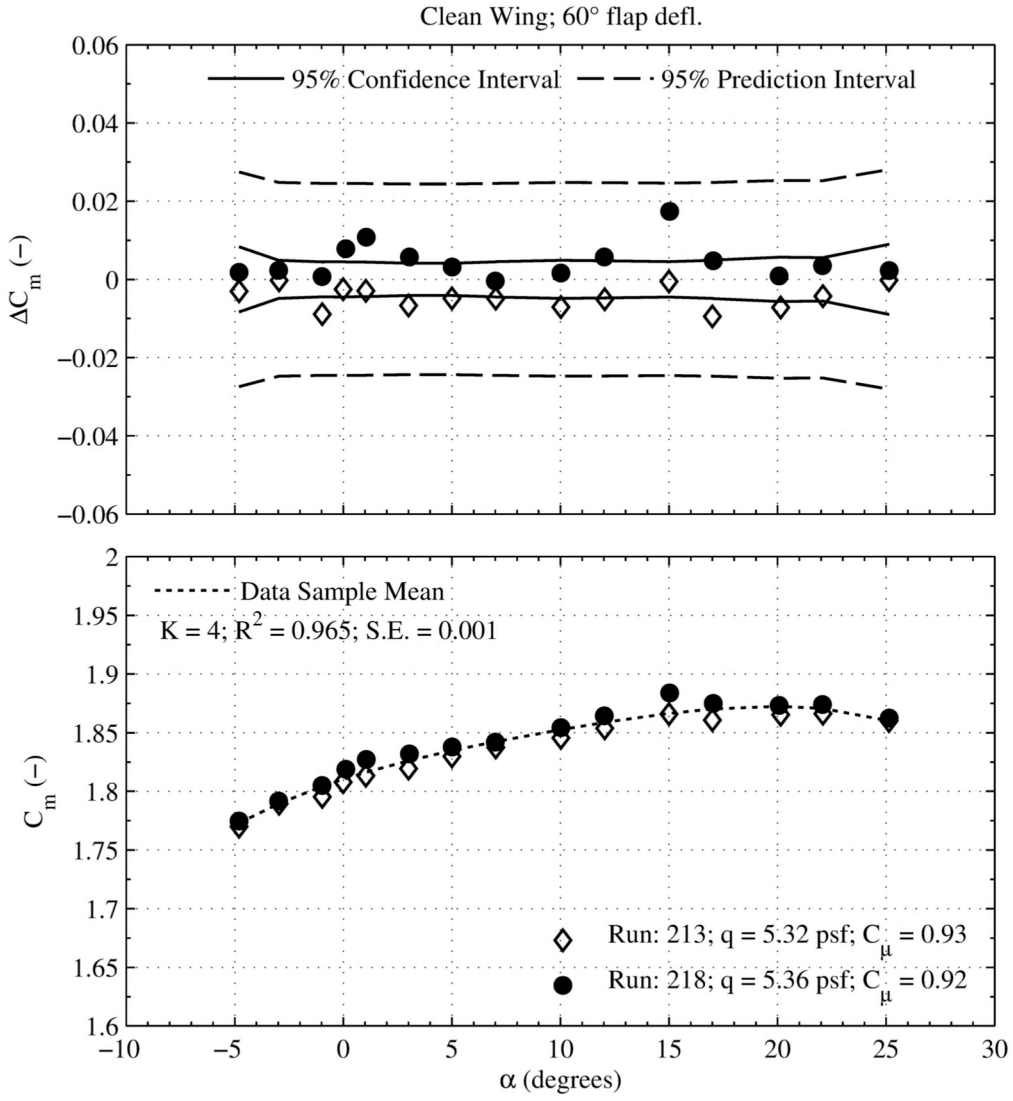

Figure 13.27. Powered, near-term repeatability. (c) Pitching Moment Coefficient.

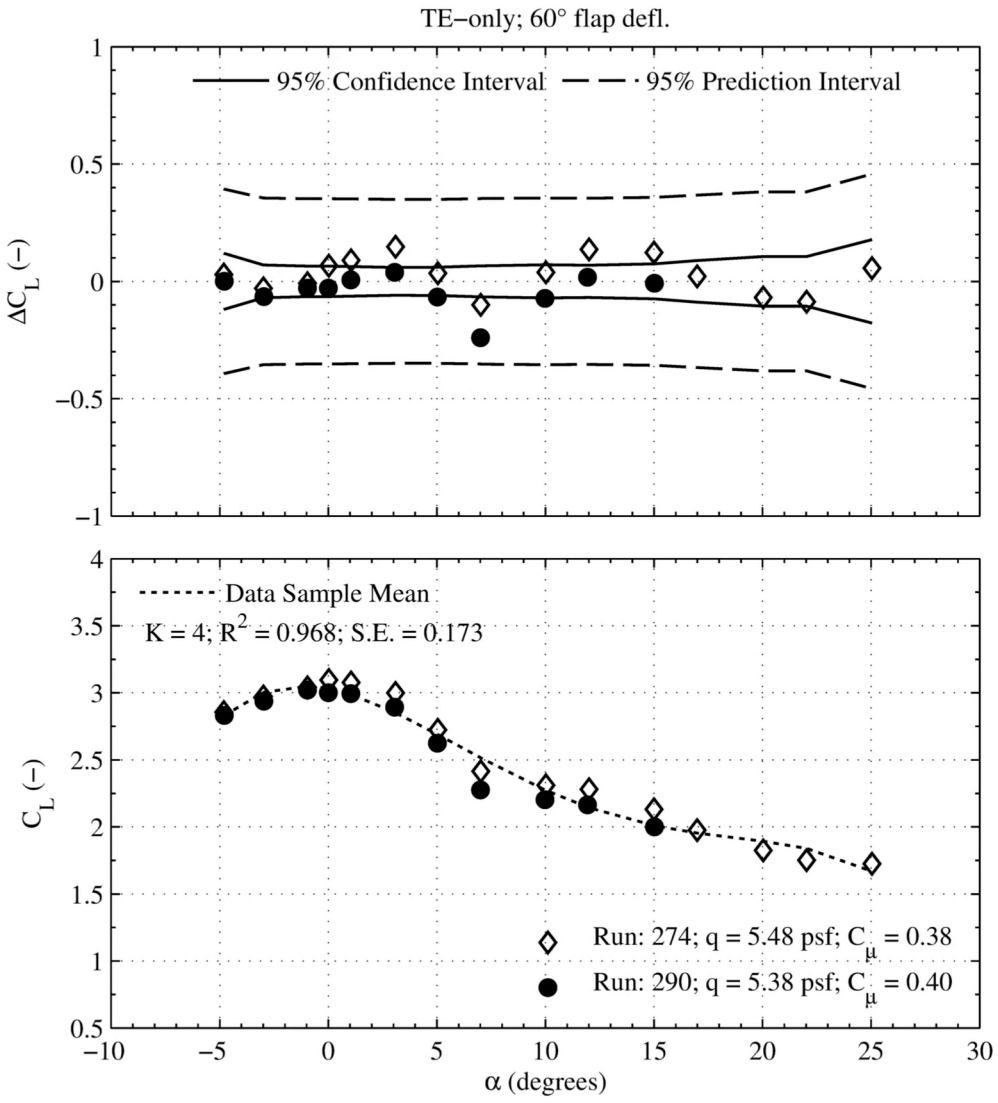

Figure 13.28. Powered, short-term repeatability. (a) Lift Coefficient.

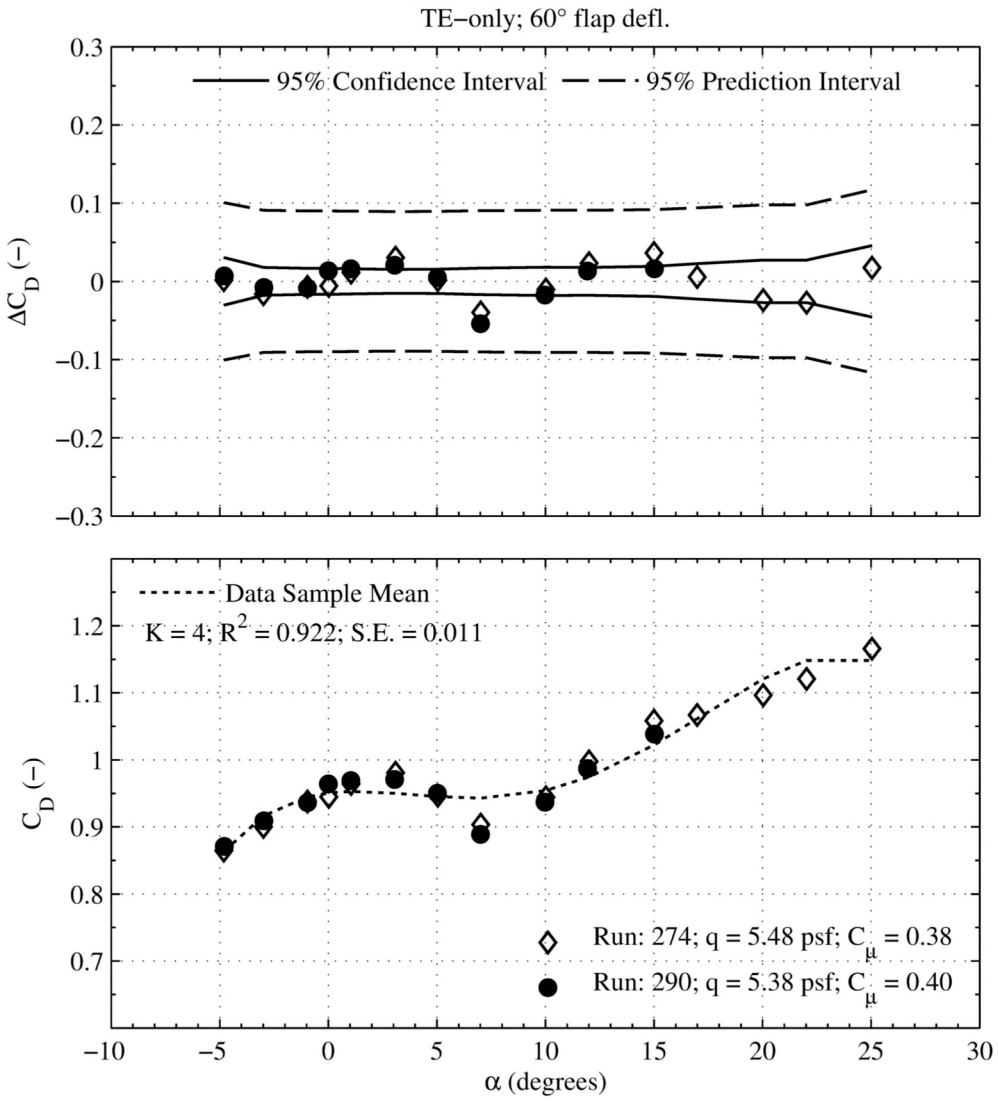

Figure 13.29. Powered, short-term repeatability. (b) Drag Coefficient.

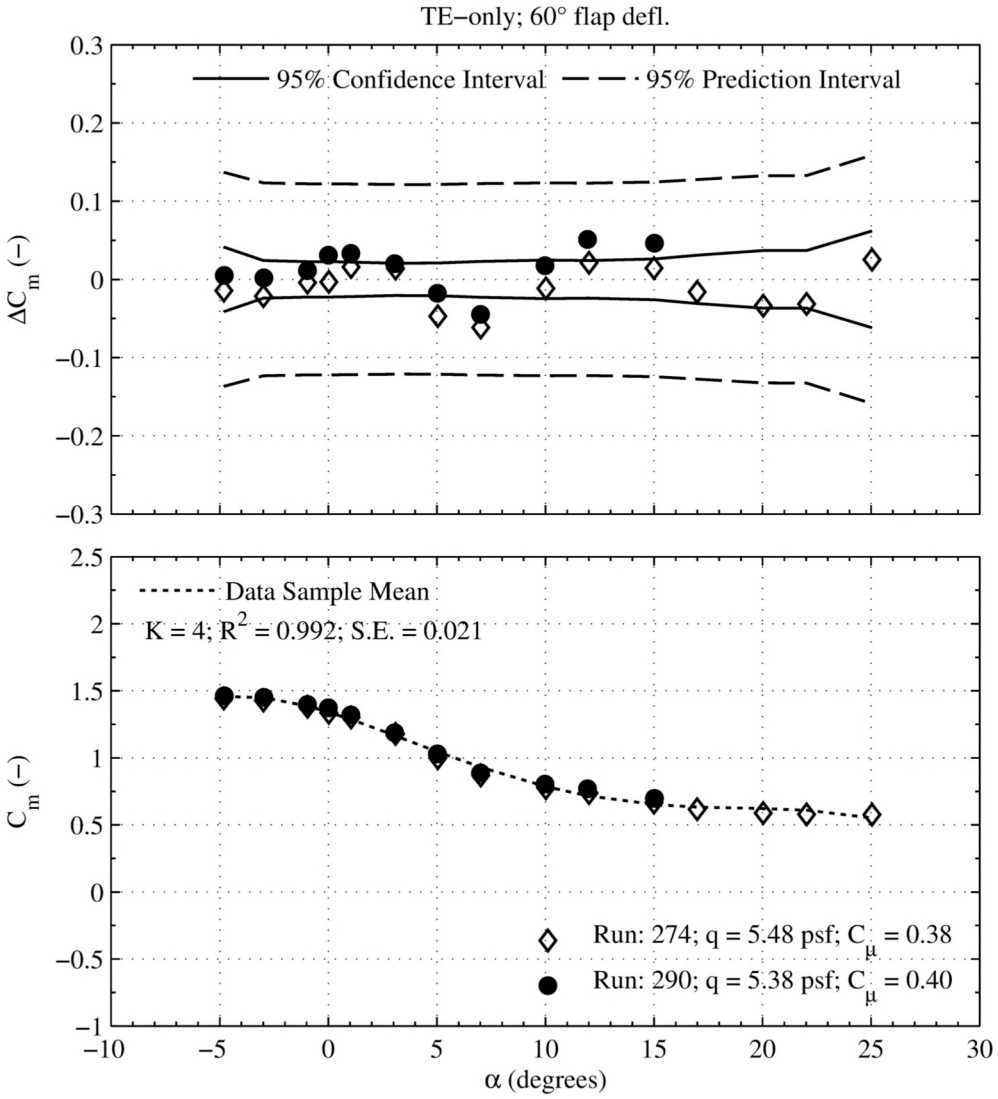

Figure 13.30. Powered, short-term repeatability. (c) Pitching Moment Coefficient.

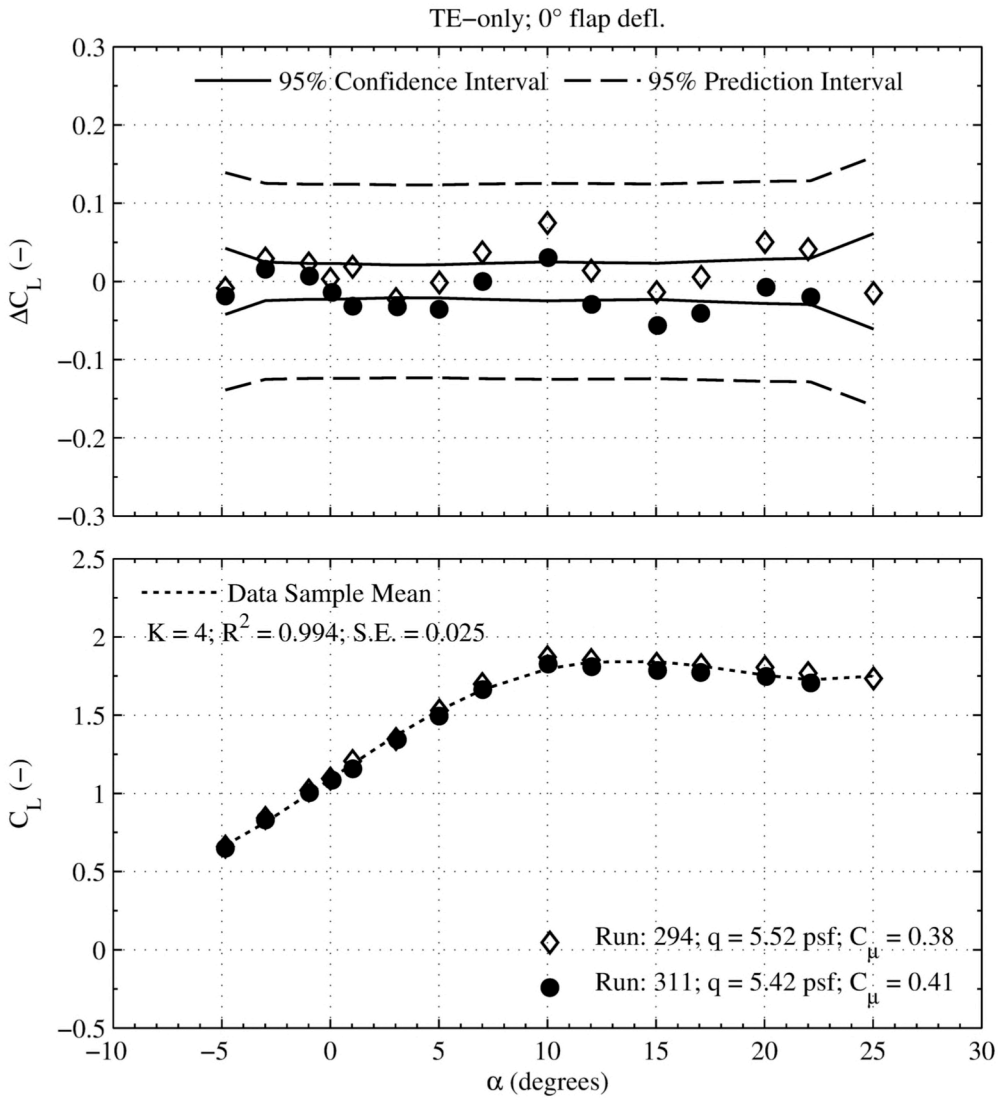

Figure 13.31. Powered, short-term repeatability. (a) Lift Coefficient.

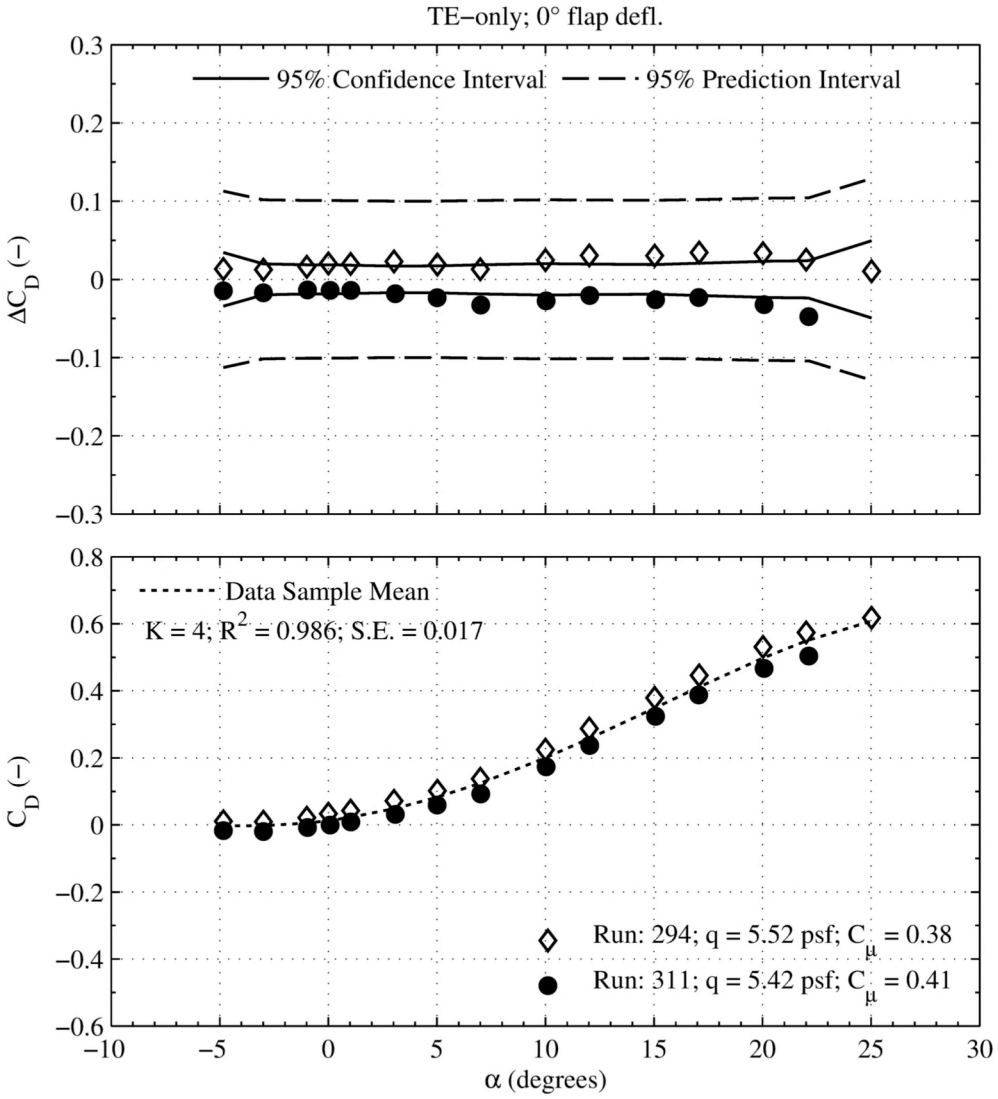

Figure 13.32. Powered, short-term repeatability. (b) Drag Coefficient.

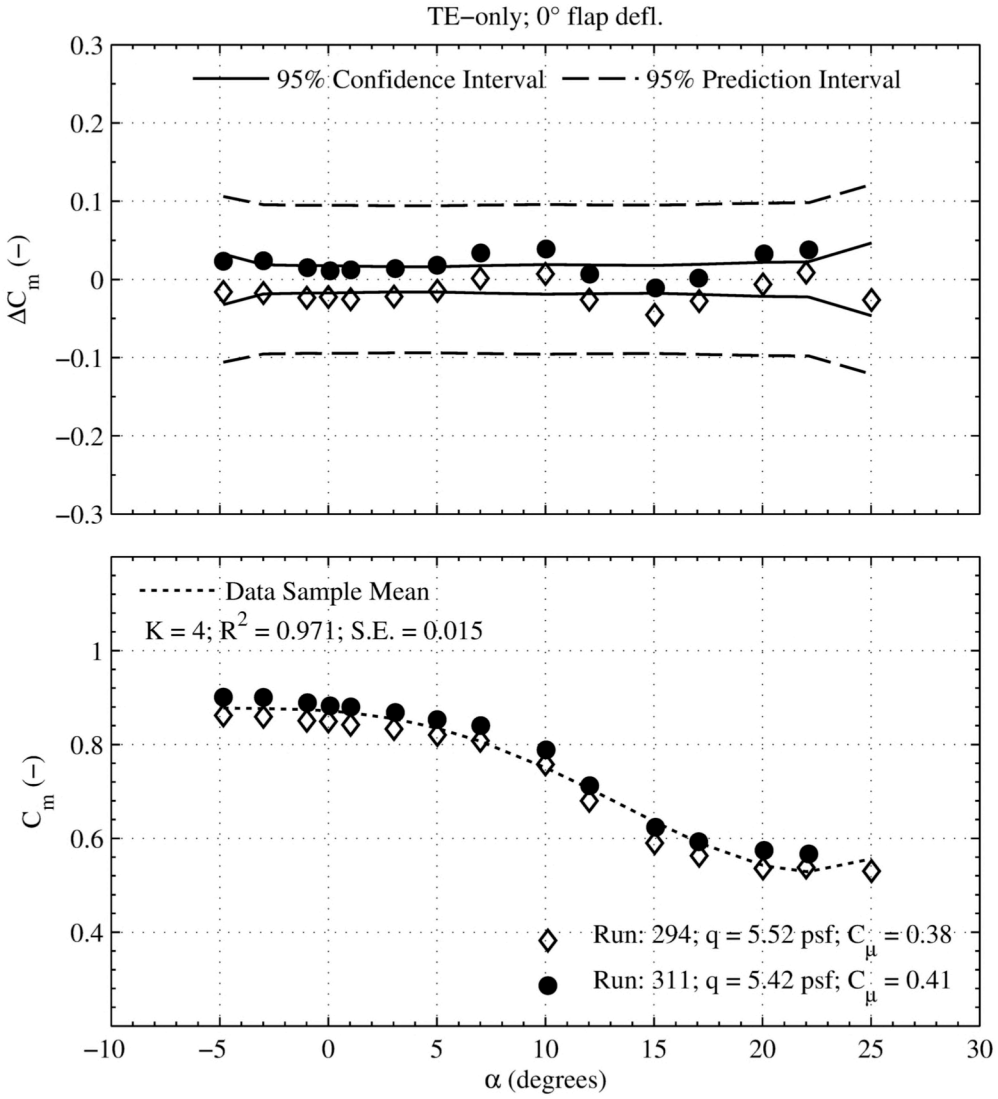

Figure 13.33. Powered, short-term repeatability. (c) Pitching Moment Coefficient.

There are three time scales within which the data repeatability is classified – short term, near term, and long term. These time scales refer to the elapsed time in between repeated runs and the number of model changes (a flap change is considered a model change), if any, between repeated runs. Here, short-term time scale is based on run-to-run repeatability with no model changes, i.e. repeat runs either back-to-back or within the same day. Near-term time scale is based on day-to-day repeatability with no model changes, i.e. runs separated by at least a day with no flap changes in between. Long-term scale is based on week-to-week repeatability with multiple model changes in between. Table 13.2 summarizes the repeatability over the three time scales, separated by powered and un-powered runs. A powered run is considered one where the TPS and/or the slots are blowing. The values presented are simply the averages of the 95%

confidence intervals for all runs in the indicated time scale. The values in the first column indicate repeatability averages for back-to-back runs (i.e. those in succession): R78 and R79. The averages listed in the table are calculated including values from repeated runs of more than two sweeps that may have a combination of two runs that fall into another time scale. I.e. the set of long-term repeats for R69, R81, R82, and R128 contribute to the short-term averages for runs 69 and 81 and also near-term averages for runs 81 and 82.

Table 13.2. Average 95% confidence repeatability as a function of powered and un-powered runs, and time scale..

		Back-to-Back	Short-Term	Near-Term	Long-Term
Load Residuals – un-powered runs	ΔC_L	N/A		N/A	±0.0186
	ΔC_D				±0.0095
	ΔC_m				±0.0158
Load Residuals – powered runs	ΔC_L	±0.0084	±0.0592	±0.0655	±0.0658
	ΔC_D	±0.0022	±0.0186	±0.0231	±0.0275
	ΔC_m	±0.0053	±0.0227	±0.0257	±0.0225

Though there were no pre-test goals set, overall repeatability for coefficients of lift, drag, and pitching moment are good. As is intuitive, the un-powered runs have better repeatability than the powered runs. Repeatability is generally better for more closely spaced runs and is sensitive to the time of day; two primary reasons contribute to this: the tunnel is un-pressurized and the HPA temperature shifts throughout the day as it is heated. These will be discussed in depth, later in this section. It is worth noting that the long-term un-powered runs were separated by a significant amount of downtime. Run 26 was the last run completed before shutting down for the holiday break on December 23, 2011. Running resumed on January 3, 2012. During the 10-day break, periodic balance data were acquired on two separate occasions; one with the balance heater turned off and then with the heater turned on. It was determined that the balance heater should be kept in the on position to avoid temperature dependent trends in the balance data. See *Transient Balance Data* in the Appendix for the data showing the effects of temperature gradients on the balance output.

Repeatability for slot sweeps, and wind-off alpha and slot sweeps was assessed. The wind-on slot sweep, runs 246 and 255, is near-term time scale. The model was in the clean wing configuration, 60 KTS test section velocity, 60° flap deflection, at 0° angle of attack. The slot sweep statistics are not included in the averages in Table 13.2; the repeatability is: $\Delta C_L = \pm 0.0156$, $\Delta C_D = \pm 0.0019$, and $\Delta C_m = \pm 0.0027$. The plots for this set of repeat runs are not provided. Static alpha and slot sweep repeat runs are short-term time scale, repeatable to: $\Delta L = \pm 0.2373$ lb_f, $\Delta D = \pm 0.7848$ lb_f, and $\Delta PM = \pm 1.155$ ft-lb_f. Repeatability plots for the wind-off polars are not provided.

Table 13.3 and Table 13.4 summarize the repeatability for model pressures and wing pressure coefficients, respectively. The tables present averages of 95% confidence intervals separated by PSI module. For 95% confidence, the model pressures are repeatable to ±0.045 psia on the 15 psid modules and ±0.035 psia on the 2.5 psid modules. It is expected that the uncertainty in the lower range PSI

modules is smaller. Repeatability in C_P measurements is ±0.335 for 15 psid modules and ±0.049 for 2.5 psid modules. For 15 psid modules, powered runs are repeatable in pressure and C_P to ±0.043 psia and ±0.436, respectively. Un-powered runs are repeatable in pressure and C_P measurements on the 15 psid modules to ±0.051 psia and ±0.066, respectively. Pressure repeatability for Runs 26 and 60 is the largest across all runs at ±0.102 psia for both modules, thus contributing to the inflated averages on un-powered runs. Module 3 was populated with the plenum pressure tubes; therefore the pressure coefficient analysis is not applicable. The repeatability in the plenum pressure measurements is listed in Table 13.5. Averages between leading- and trailing-edge plenums shows the leading-edge pressures are slightly more repeatable at ±0.061 psia compared to the trailing-edge plenum pressures at ±0.104 psia. These averages are higher than the overall model pressure confidence levels. This is to be expected as the plenum pressures are sensitive to more parameters like line temperature and nozzle exit pressure. Trailing edge-only blowing runs showed confidence levels similar to the combined blowing trailing-edge averages at ±0.106 psia. This is also to be expected because the trailing-edge pressures for the combined blowing runs were used to set on-condition during the trailing edge-only blowing runs. The trailing-edge inboard and leading-edge inboard plenums consistently had the largest confidence levels. These plenums have the highest flow rates and pressure levels. Leading-edge inboard plenum was repeatable to ±0.076 psia and the trailing-edge inboard plenum is repeatable to ±0.135 psia.

Table 13.3. Model pressure repeatability at 95% confidence.

Model Pressures (psia)	Module 1, 15 psid	Module 2, 15 psid	Module 3, 15 psid	AVG 15 psid modules	Module 4, 2.5 psid	Module 5, 2.5 psid	Module 6, 2.5 psid	AVG 2.5 psid modules
R46, R133	±0.0344	±0.1267	±0.0536	±0.0716	±0.0424	±0.0421	±0.0891	±0.0579
R36, R92, R102	±0.0418	±0.0720	±0.0864	±0.0667	±0.0434	±0.0437	±0.1116	±0.0662
R69, R81, R82, R128	±0.0543	±0.0757	±0.1289	±0.0863	±0.0588	±0.0567	±0.0708	±0.0621
R152, R153	±0.0044	±0.0249	±0.0330	±0.0208	±0.0013	±0.0015	±0.0379	±0.0136
R78, R79	±0.0250	±0.0303	±0.0193	±0.0249	±0.0020	±0.0218	±0.0174	±0.0137
R19, R95	±0.0192	±0.0217	±0.0193	±0.0201	±0.0189	±0.0190	±0.0199	±0.0193
R21, R105	±0.0319	±0.0353	±0.0300	±0.0324	±0.0306	±0.0310	±0.0304	±0.0307
R26, R60	±0.1020	±0.1035	±0.0996	±0.1017	±0.1035	±0.1032	±0.0998	±0.1022
R213, R218	±0.0595	±0.0313	±0.0075	±0.0328	±0.0153	±0.0148	±0.0028	±0.0110
R274, R290	±0.0218	±0.0315	±0.0018	±0.0184	±0.0062	±0.0106	±0.0029	±0.0066
R294, R311	±0.0042	±0.0652	±0.0017	±0.0237	±0.0056	±0.0053	±0.0015	±0.0041
Averages	±0.0362	±0.0562	±0.0437	±0.0454	±0.0298	±0.0318	±0.044	±0.0352

Table 13.4. Wing pressure coefficient repeatability at 95% confidence.

C_P (unitless), wing static pressures only	Module 1, 15 psid	Module 2, 15 psid	Module 3, 15 psid	AVG 15 psid modules	Module 4, 2.5 psid	Module 5, 2.5 psid	Module 6, 2.5 psid	AVG 2.5 psid modules
R46, R133	±0.4268	±0.8858	N/A	±0.6563	±0.0148	±0.0697	±0.0316	±0.0387
R36, R92, R102	±0.1013	±0.2036		±0.1525	±0.0112	±0.0246	±0.0361	±0.0240
R69, R81, R82, R128	±0.3746	±0.5773		±0.4760	±0.0178	±0.0751	±0.0501	±0.0477
R152, R153	±0.1214	±0.6127		±0.3671	±0.0101	±0.0246	±0.0162	±0.0170
R78, R79	±0.1103	±0.2959		±0.2031	±0.0056	±0.0930	±0.0337	±0.0441
R19, R95	±0.0335	±0.0922		±0.0629	±0.0199	±0.0169	±0.0522	±0.0230
R21, R105	±0.0277	±0.0690		±0.0484	±0.0164	±0.0170	±0.0274	±0.0203
R26, R60	±0.0399	±0.1350		±0.0875	±0.0250	±0.0200	±0.0572	±0.0341
R213, R218	±1.3002	±0.5490		±0.9246	±0.0239	±0.0635	±0.0819	±0.0564
R274, R290	±0.5464	±0.5715		±0.5590	±0.0727	±0.2150	±0.1737	±0.1538
R294, R311	±0.0669	±0.2264		±0.1467	±0.0537	±0.0492	±0.1000	±0.0676
Averages	±0.2863	±0.3835	N/A	±0.3349	±0.0246	±0.0608	±0.0600	±0.0485

Table 13.5. Plenum pressure repeatability at 95% confidence.

sures (psia)	Left LEIB	Right LEIB	Left LEOB	Right LEOB	LE mean	Left TEIB	Right TEIB	Left TEOB	Right TEOB
	±0.2020	±0.2116	±0.1185	±0.0961	±0.1571	±0.4958	±0.2640	±0.1734	±0.2224
102	±0.0676	±0.0886	±0.0433	±0.0816	±0.0703	±0.2187	±0.0595	±0.1020	±0.1341
32, R128	±0.0531	±0.0574	±0.0312	±0.0334	±0.0438	±0.0935	±0.0470	±0.0385	±0.0601
	±0.0229	±0.0260	±0.0139	±0.0185	±0.0203	±0.1865	±0.0272	±0.0144	±0.0192
	±0.0285	±0.0307	±0.0211	±0.0287	±0.0273	±0.0303	±0.0285	±0.0286	±0.0317
	N/A					N/A			
	N/A					N/A			
	N/A					N/A			
	±0.0393	±0.0787	±0.0406	±0.0393	±0.0495	±0.0604	±0.0620	±0.0329	±0.0436
	N/A					±0.0828	±0.0869	±0.0270	±0.0476
	N/A					±0.2186	±0.2008	±0.0692	±0.1184
	±0.0689	±0.0822	±0.0448	±0.0496	±0.0614	±0.1733	±0.0970	±0.0608	±0.0846

13.1.2. Balance Calibration Uncertainty

The balance calibration uncertainty table is presented below in Table 13.6. The uncertainty statistics listed are given at a 95% confidence level and pertain to how well the calibration matrix fits the calibration, not the overall accuracy of the balance measurements. In the table, load residuals are defined as the difference between the load that was used for the regression analysis of the calibration data and the corresponding fitted value. Statistical quantities are computed using arithmetic mean as population mean. Note this differs from the MRSA approach which uses a least-squares curve fit to estimate the mean. The full-scale accuracy is stated in terms of the largest outlying load residual during calibration.

Table 13.6. Summary of balance calibration accuracies.

	Capacity	Load Residuals – 95% Confidence		FS Accuracy*	
Normal Force	±5000 lbf	±3.8652 lbf	0.0774%	±13.31 lbf	0.2662%
Side Force	±2500 lbf	±4.6674 lbf	0.1866%	±10.49 lbf	0.4197%
Axial Force	±1200 lbf	±2.7080 lbf	0.2256%	±8.25 lbf	0.6873%
Rolling Moment	±27,300 in-lbf	±107.333 in-lbf	0.3932%	±431.89 in-lbf	1.5820%
Pitching Moment	±29,000 in-lbf	±34.4112 in-lbf	0.1186%	±82.27 in-lbf	0.2837%
Yawing Moment	±10,500 in-lbf	±48.7690 in-lbf	0.4644%	±147.78 in-lbf	1.4074%

*Stated in terms of largest outlying load residual

The balance calibration accuracies are plotted in coefficient form and presented as a function of dynamic pressure in Figure 13.34. As seen, the balance yields more accurate coefficients at higher dynamic pressures. The tested dynamic pressure ranges from 5.5 psf at 40 KTS to 33.4 psf at 100 KTS. Figure 13.13 to Figure 13.45, show 95% balance accuracies plotted against 95% data scatter confidence levels. As seen in the plots the data scatter falls outside the bounds of 95% confidence in the balance calibration accuracy for all time scales. This would seem to suggest that confidence in the accuracy of repeatable measurements is due more to the repeatability of the measurement than, say, an unknown measurement bias.

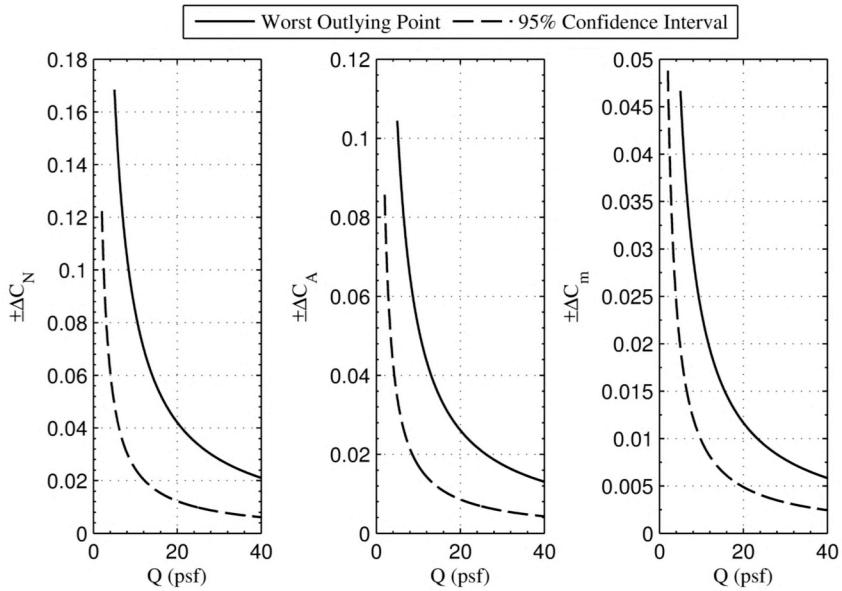

Figure 13.34. Balance accuracy bands in coefficient form, based on the values listed in Table 13.6.

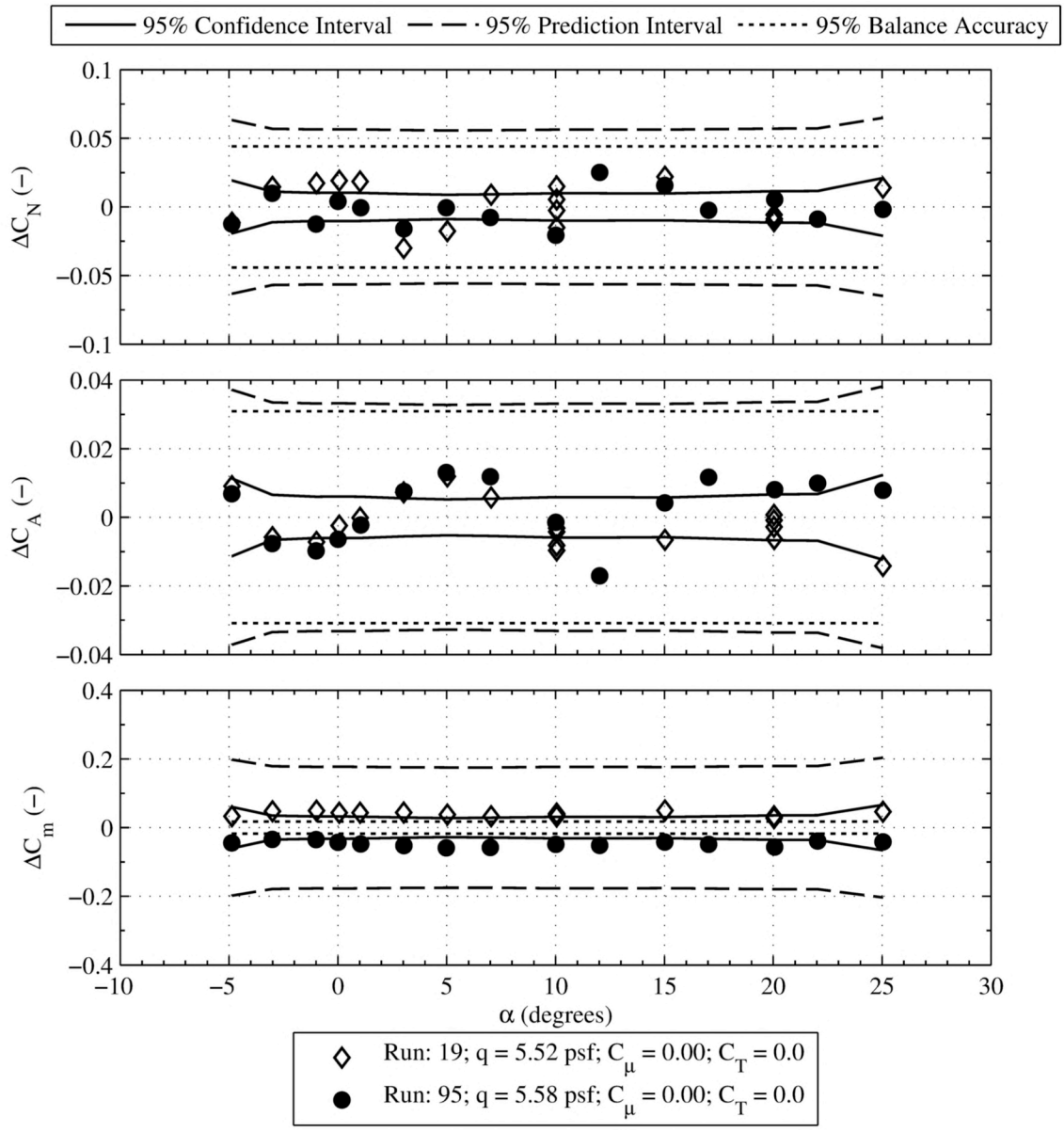

Figure 13.35. Balance calibration accuracies, un-powered repeat runs.

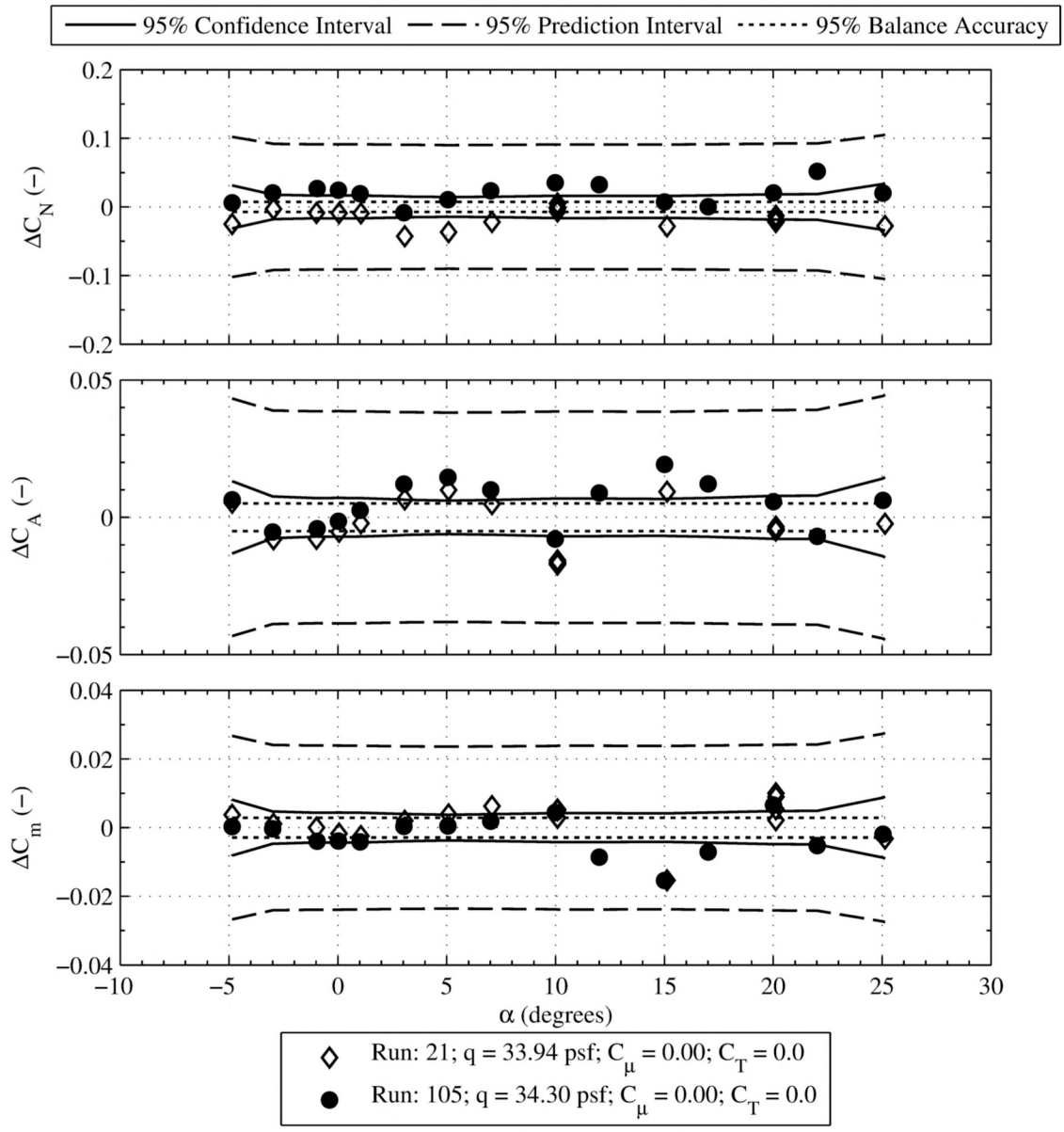

Figure 13.36. Balance calibration accuracies, un-powered repeat runs.

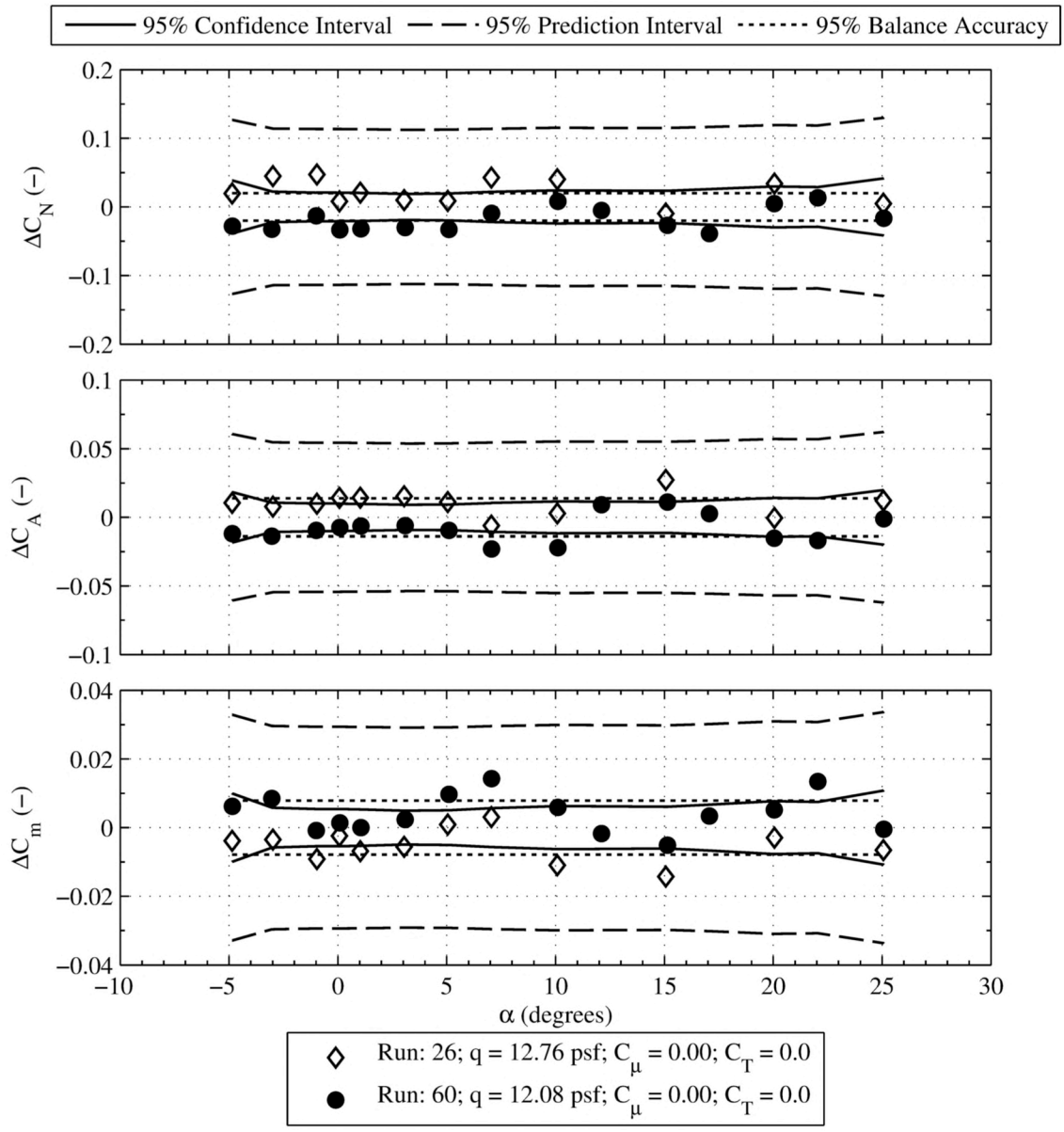

Figure 13.37. Balance calibration accuracies, un-powered repeat runs.

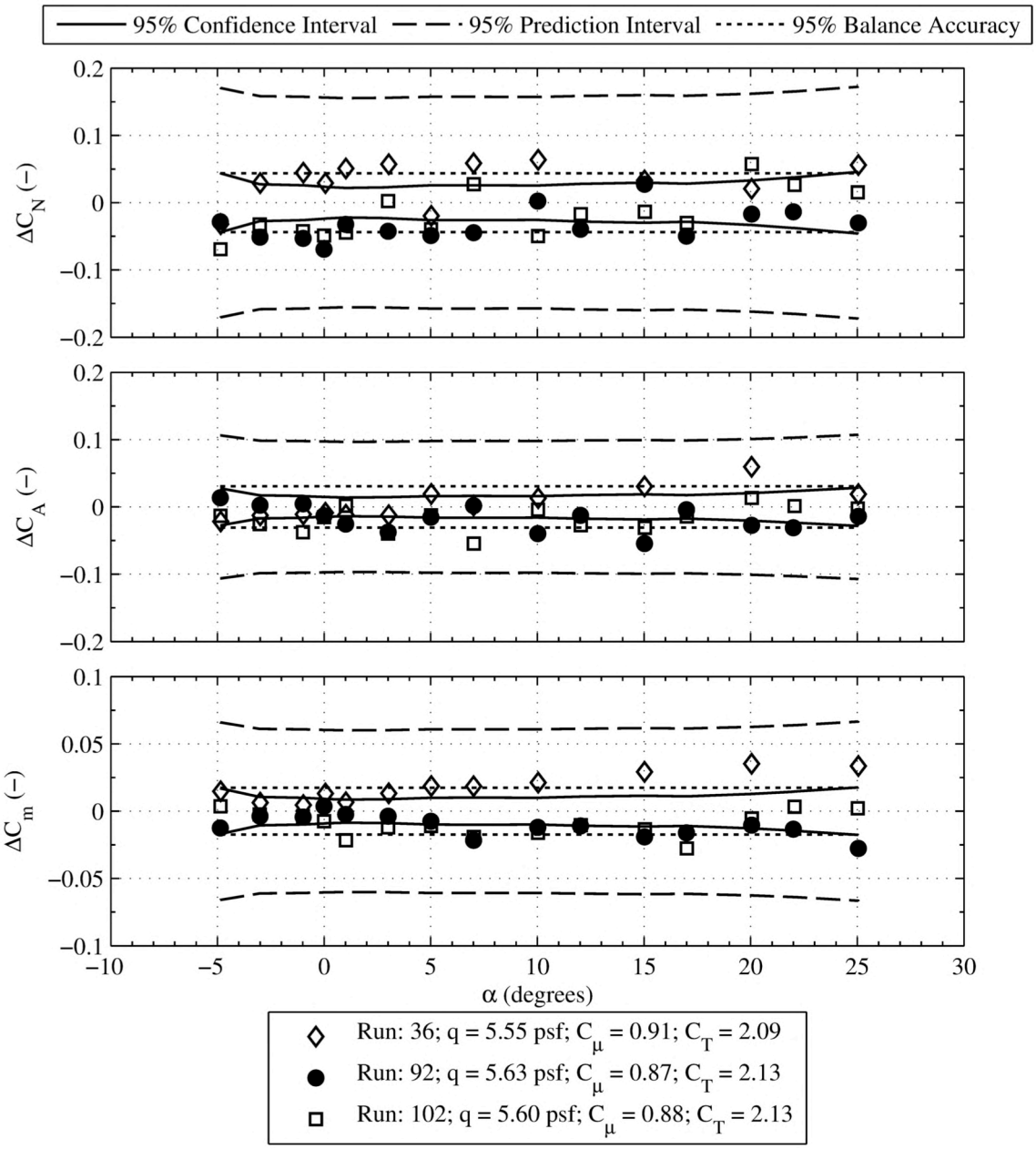

Figure 13.38. Balance calibration accuracies, powered repeat runs.

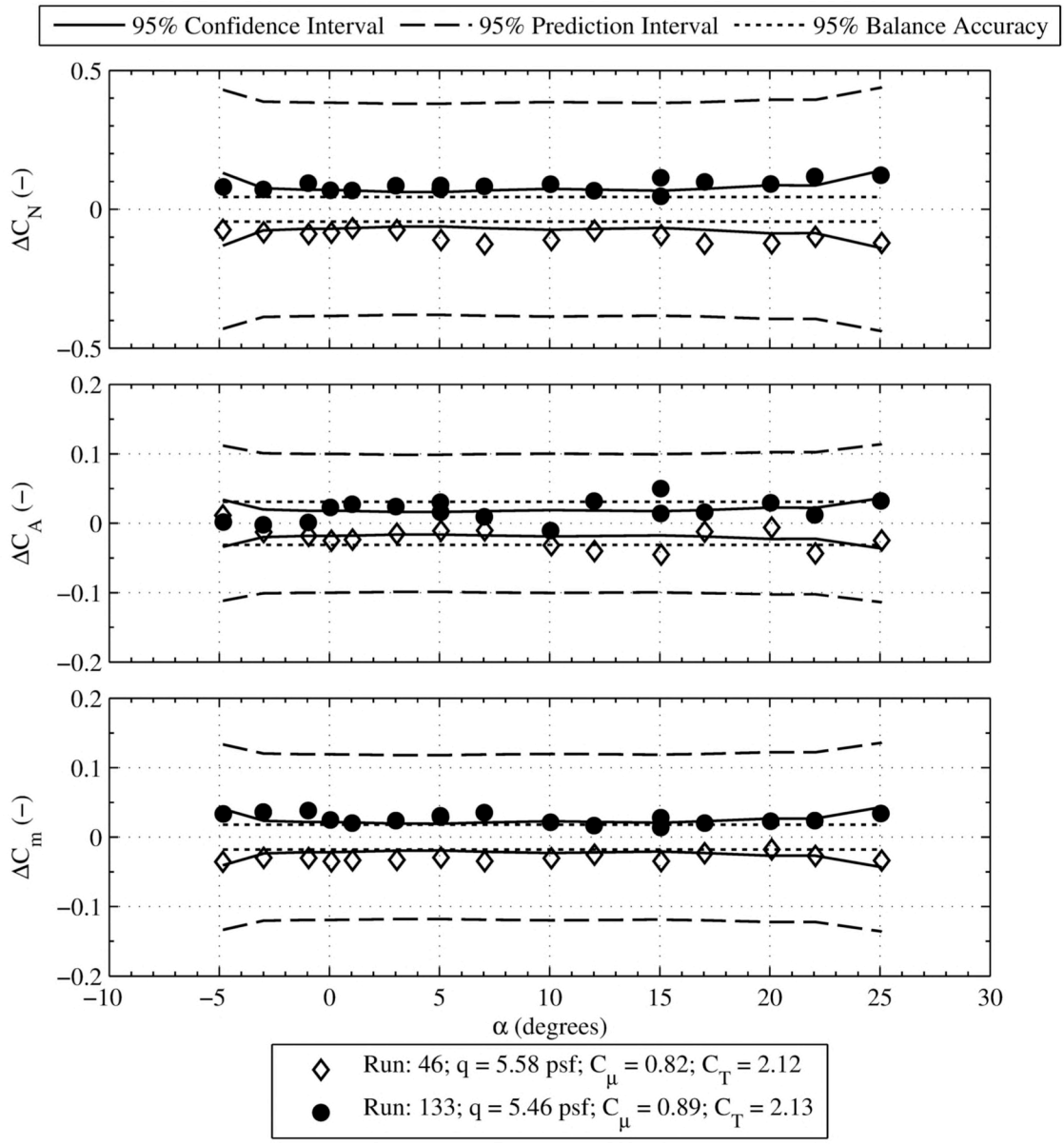

Figure 13.39. Balance calibration accuracies, powered repeat runs.

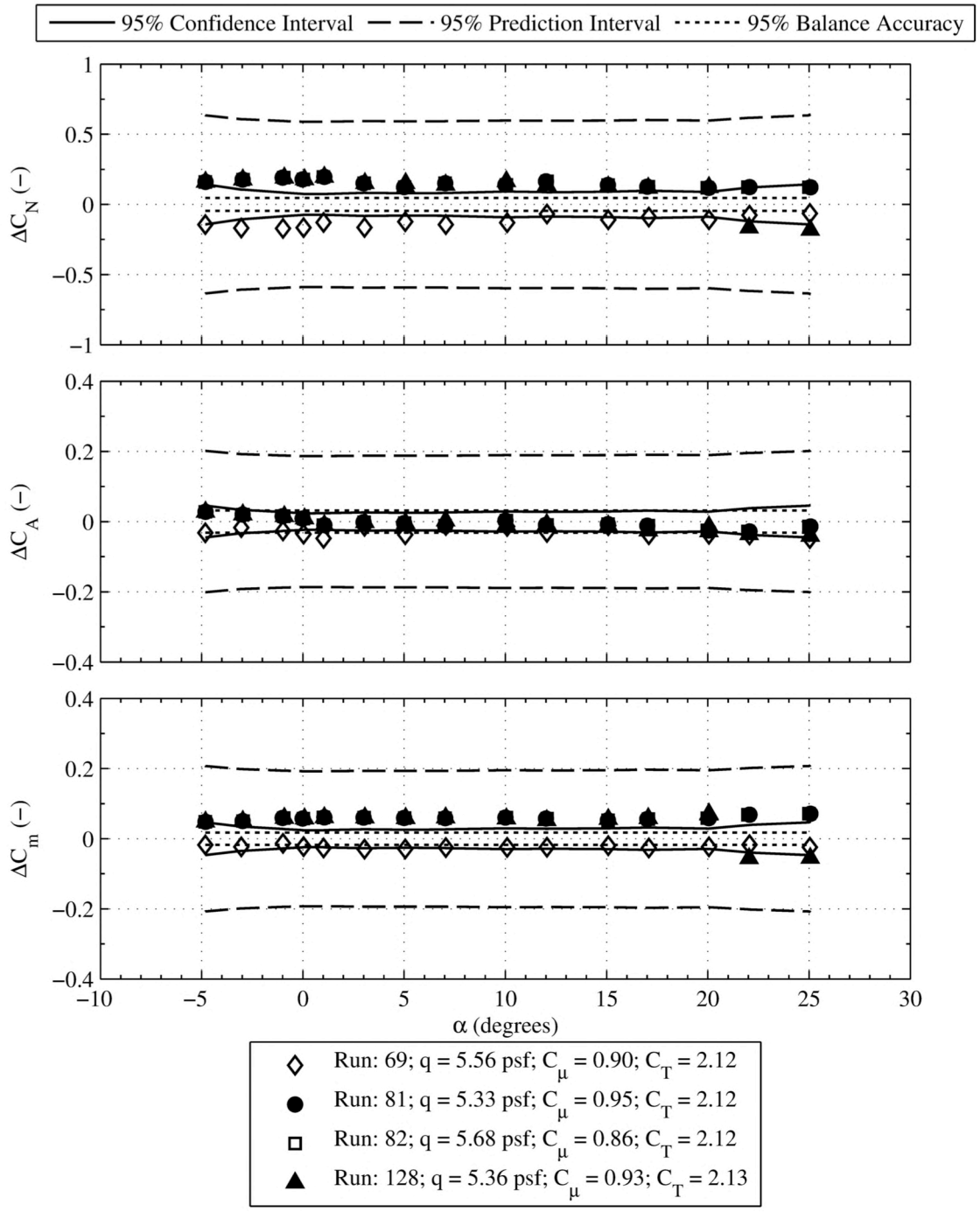

Figure 13.40. Balance calibration accuracies, powered repeat runs.

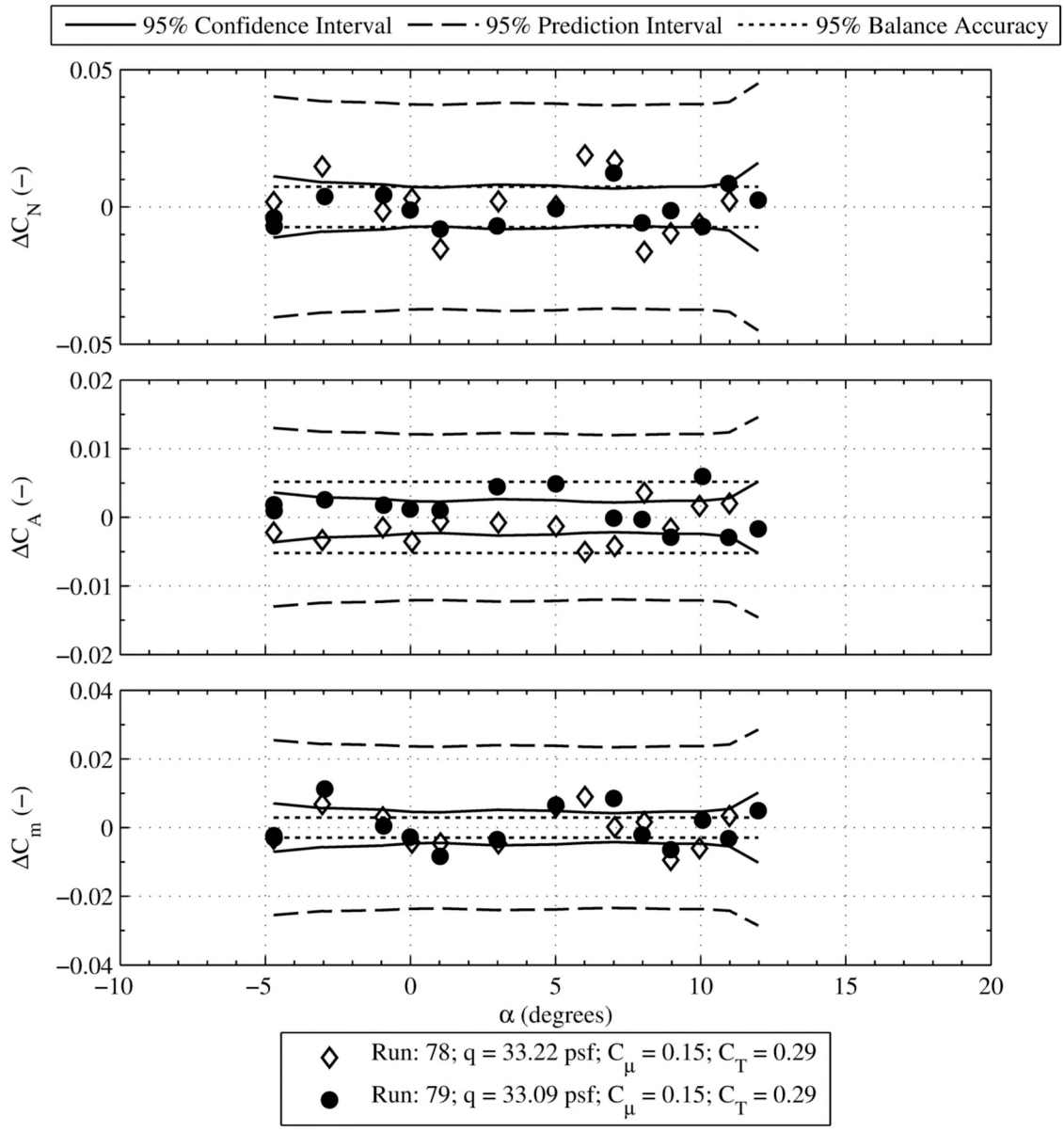

Figure 13.41. Balance calibration accuracies, powered repeat runs.

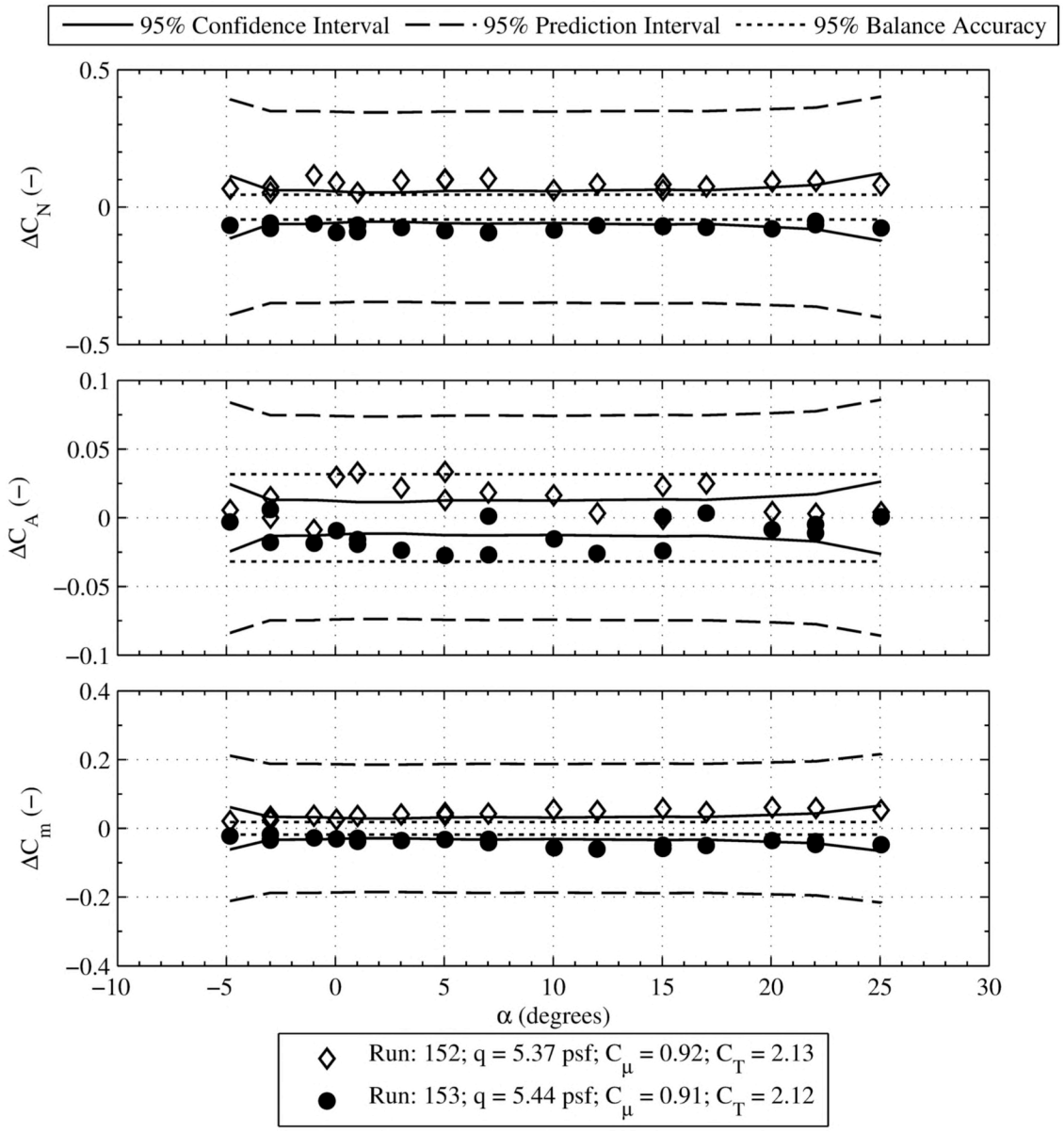

Figure 13.42. Balance calibration accuracies, powered repeat runs.

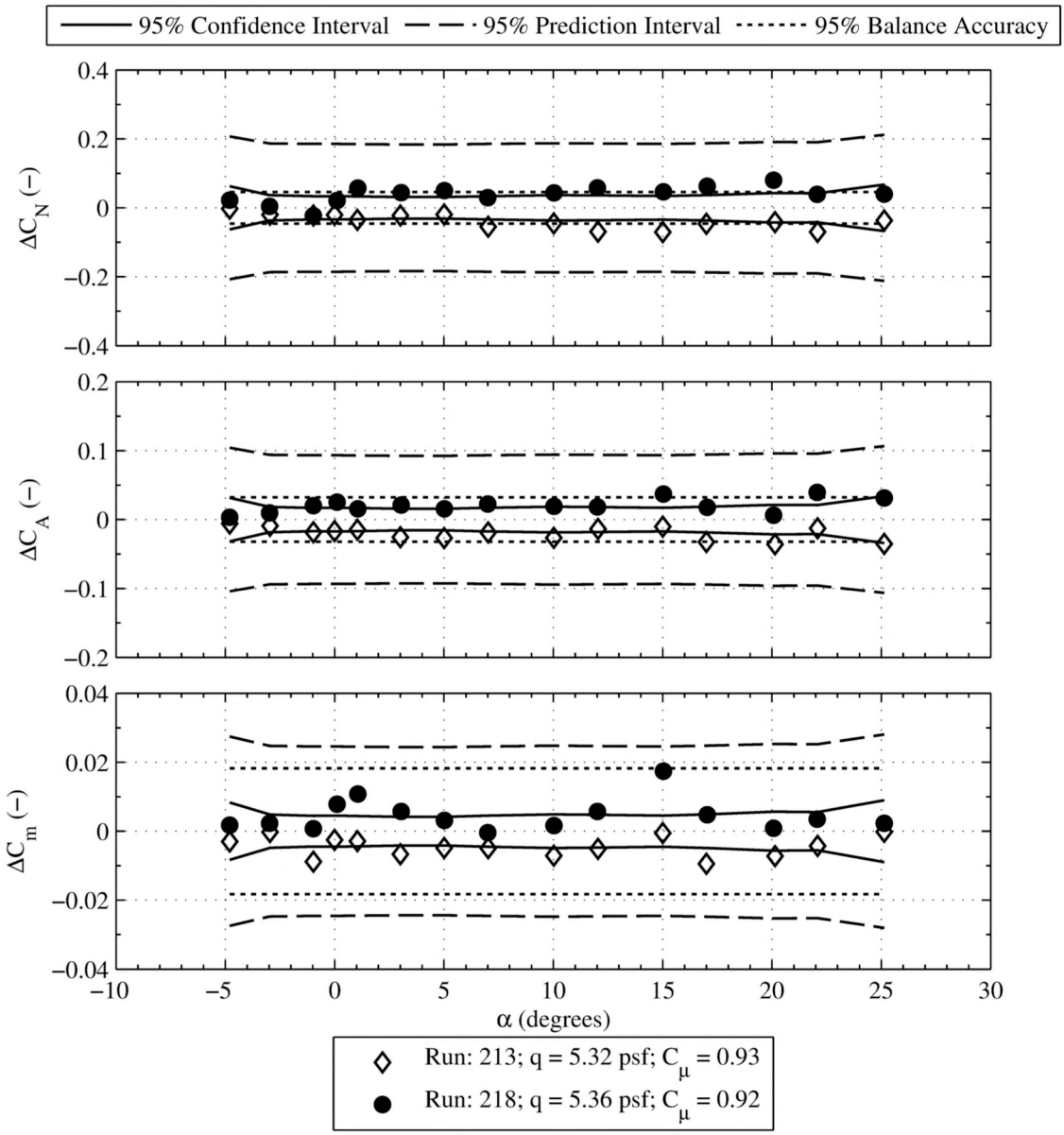

Figure 13.43. Balance calibration accuracies, powered repeat runs.

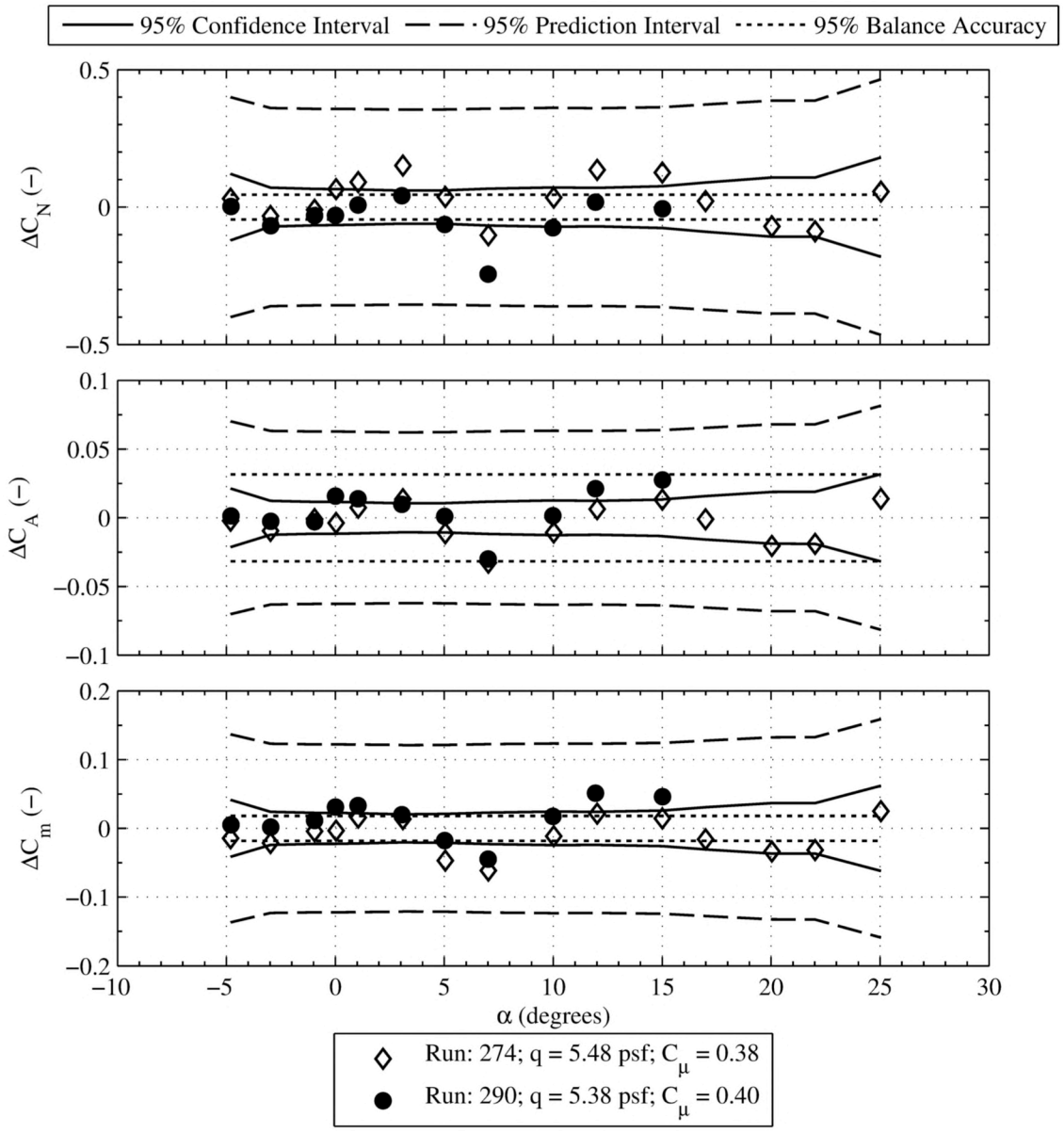

Figure 13.44. Balance calibration accuracies, powered repeat runs.

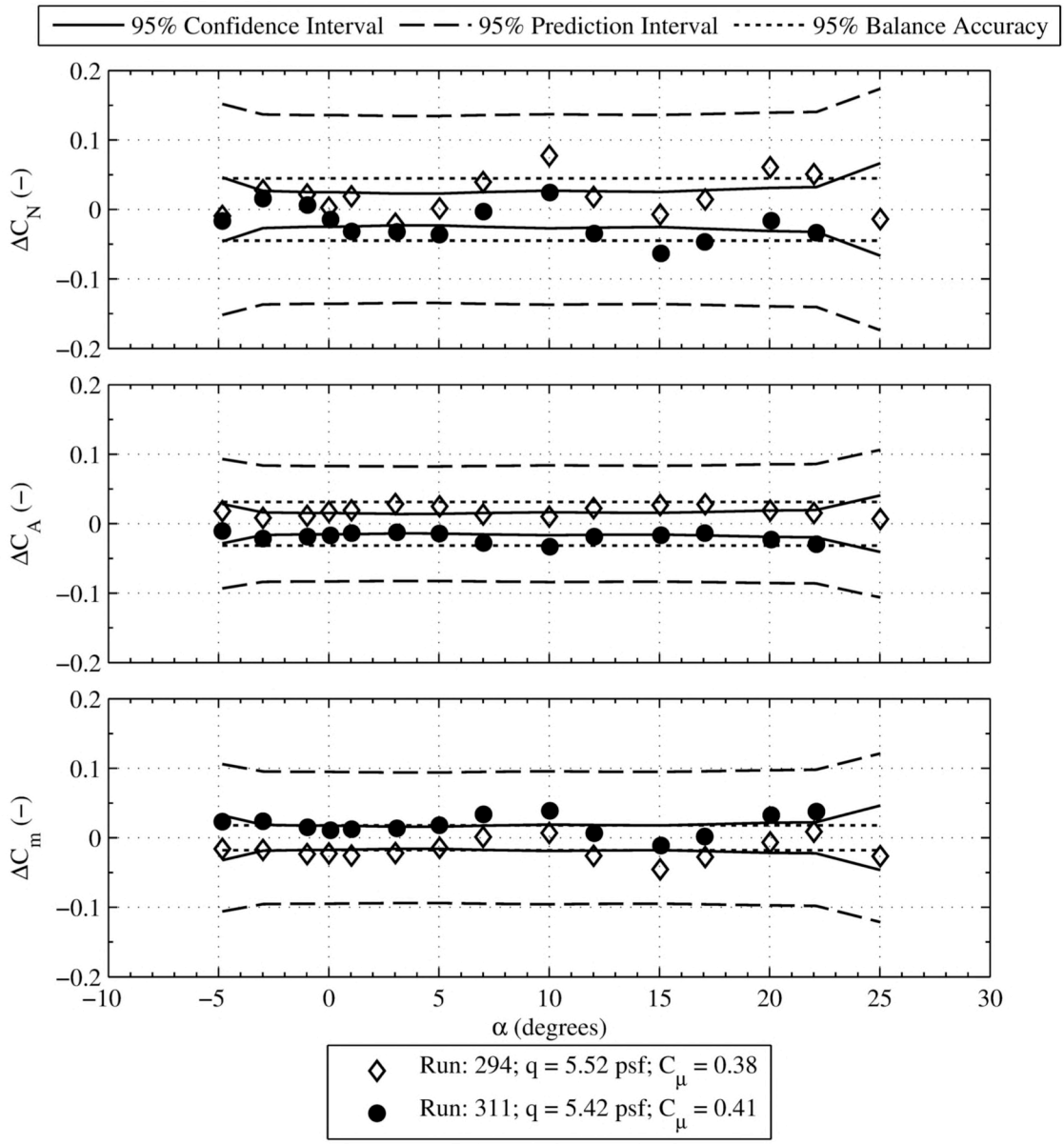

Figure 13.45. Balance calibration accuracies, powered repeat runs.

13.1.3. Factors Degrading Repeatability

There are a large number of possible sources of error that may contribute to non-repeatability in test data, the likely sources are discussed here. The likely sources include (but are not limited to): balance accuracy, balance temperature effects, angle of attack measurement, repeatability of wind tunnel flow conditions, and HPA properties. Balance accuracy and balance temperature effects were addressed earlier in this section. A significant, but un-quantified, potential source of data non-repeatability has to do with pressure tubes and other cables bridging the metric and non-

metric sides of the balance. These cables and tubes can shift and change in size due to temperature fluctuations in a way that may cause fouling to occur.

13.1.3.1. Angle of Attack

The determination of the angle of attack is affected by several parameters including the measurement itself and the test section flow angularity. It is important to quantify, or attempt to quantify these factors because the angle of attack has a direct impact on the calculation of the lift and drag coefficients.

$$C_L = C_N \cos\alpha - C_A \sin\alpha \quad (1.7)$$

$$C_D = C_N \sin\alpha + C_A \cos\alpha \quad (1.8)$$

Using a root-mean-squared estimation of the error, the contribution of angle of attack errors to the lift and drag coefficients is

$$\Delta C_L = -C_D \Delta\alpha(\pi/180) \quad (1.9)$$

$$\Delta C_D = C_L \Delta\alpha(\pi/180) \quad (1.10)$$

The primary measurement of angle of attack came from the onboard Schaevitz and QA-2000 sensors. These sensors were mounted in the nose of the model and were subject to model vibrations. For high-speed, high-lift test points, the model vibrations were sufficiently large to result in variation in the angle of attack sensors as high as 0.3°. For a lift coefficient of 3 (higher than what was seen at highest dynamic pressure), the contribution to the drag coefficient error is 0.016.

Two other factors may contribute to non-repeatability with respect to the model angle of attack. First is the test section flow angularity. The most recent tunnel characterization was completed in 1989[262626] and flow angularity is not considered to be known at this time. Secondly, applying the MRSA over the entire angle of attack range where unsteady aerodynamic effects resulting from the model stalling at high angles of attack could affect repeatability.

13.1.3.2. Flow Conditions

Repeatability in the wind tunnel flow conditions has a direct impact on the aerodynamic data. Table 13.7 lists the repeatability for the relevant flow measurements and calculations. The table lists the mean values and average 95% confidence and prediction intervals across all repeat runs. As the wind tunnel is un-pressurized, velocity is the only directly controlled flow property. As such, the repeatability is the best; the largest 95% prediction interval is ±0.57 KTS. Measurements such as total and static pressures/temperatures are sensitive to the conditions outside the tunnel walls; these measurements affect the calculated quantities Re, M, q. The variation in total and static pressures are generally small, the largest prediction interval is ±0.487 psia in tunnel total pressure and ±0.477 psia in tunnel centerline static pressure. 95% confidence interval in the total temperature is as high as ±9.31°F. Overall, large scatter in the tunnel temperature and pressures should not be as significant to repeatability for this model because the

flow field is dominated by the circulation control wings. Non-repeatability with respect to flow conditions is likely to be driven by the slot flow.

	Quantity	Orifice Plate T/C, °F	Left LPDP T/C, °F	Right LPDP T/C, °F
R36, R92, R102	Mean	80.08	70.55	76.98
	95% CI	±2.95	±3.77	±3.32
	95% PI	±15.95	±20.36	±17.94
R46, R133	Mean	73.55	68.29	74.70
	95% CI	±7.37	±6.18	±6.69
	95% PI	±36.38	±30.47	±32.99
R69, R81, R82, R128	Mean	81.54	74.42	81.88
	95% CI	±1.50	±3.16	±3.37
	95% PI	±9.43	±19.82	±21.17
R78, R79	Mean	81.01	77.48	84.12
	95% CI	±0.29	±1.02	±1.97
	95% PI	±1.34	±4.65	±8.98
R152, R153	Mean	80.89	76.23	81.54
	95% CI	±1.32	±1.05	±1.25
	95% PI	±6.87	±5.46	±6.54
R213, R218	Mean	79.48	71.72	69.67
	95% CI	±1.50	±0.51	±0.54
	95% PI	±7.21	±2.44	±2.58
R274, R290	Mean	70.67	62.21	58.89
	95% CI	±2.51	±2.42	±3.39
	95% PI	±11.61	±11.17	±15.68
R294, R311	Mean	70.15	60.23	57.60
	95% CI	±7.05	±2.81	±4.37
	95% PI	±33.74	±13.43	±20.88

presents mean value and average 95% confidence and prediction intervals for the low pressure line temperature measurements. The measurements are located on the orifice plate assembly, and in the left and right low pressure plenum. Time of day plays a significant role in the repeatability of the temperature measurements. Runs in the morning are significantly colder than those later in the day, as the air is heated throughout the day. The potential effect on repeatability has to do with the mode of operation on the low pressure side and the effect of the temperature gradients on the slots. Though not expected to have an effect[27], changes in plenum temperature may create run-to-run slot height differences; here, the thermal effects have not been quantified. The low pressure side was operated in flow control mode, where the digital valve sets and holds a constant mass flow rate. The implication of operating in this mode is that as the line temperature increases, the pressure rises to maintain a constant mass flow rate. The effect of this is seen in the repeatability of the plenum pressures for runs with higher temperature variations. When comparing between R274/R290 and R294/R311 freestream values are repeatable to

approximately the same magnitude. The confidence and prediction interval in temperature is larger for R294/R311, resulting in pressure intervals that are nearly three times as large. Looking further at these two combinations of repeated runs, it would appear that force and moment coefficients for R274/R290 are less repeatable, see Figure 13.10 and Figure 13.11. Here, however, a flaw in extending the regression for the entire alpha sweep is evident, including the region beyond $\alpha = 1°$ where the flow physics are highly non-linear and the least-squares goodness of fit is poor.

Table 13.7. Flow condition repeatability.

	Quantity	P_t, psia	P_s, psia	T_T, °F	q, psf	V, KTS	M	Re_c, 10^6
R19, R95	Mean	14.876	14.837	49.98	5.55	39.95	0.0609	0.8303
	95% CI	±0.019	±0.019	±0.34	±0.02	±0.08	±0.0001	±0.0017
	P5%PI	±0.096	±0.096	±1.70	±0.12	±0.41	±0.0005	±0.0083
R21, R105	Mean	14.840	14.602	53.58	34.10	100.02	0.1522	2.0342
	95% CI	±0.029	±0.030	±2.30	±0.15	±0.11	±0.0005	±0.0136
	P5%PI	±0.145	±0.150	±11.50	±0.73	±0.57	±0.0024	±0.0681
R26, R60	Mean	14.834	14.748	52.89	12.38	60.00	0.0912	1.2302
	95% CI	±0.106	±0.104	±9.31	±0.32	±0.04	±0.0008	±0.0493
	P5%PI	±0.487	±0.477	±42.86	±1.46	±0.18	±0.0039	±0.2268
R36, R92, R102	Mean	14.835	14.796	43.73	5.60	39.97	0.0613	0.8461
	95% CI	±0.043	±0.043	±0.55	±0.03	±0.04	±0.0001	±0.0038
	P5%PI	±0.235	±0.234	±2.95	±0.15	±0.24	±0.0005	±0.0203
R46, R133	Mean	14.818	14.78	50.89	5.52	39.99	0.0609	0.8244
	95% CI	±0.042	±0.042	±5.18	±0.05	±0.04	±0.0004	±0.0136
	P5%PI	±0.206	±0.208	±25.57	±0.26	±0.18	±0.0018	±0.0673
R69, R81, R82, R128	Mean	14.776	14.738	53.09	5.48	39.97	0.0607	0.8165
	95% CI	±0.061	±0.060	±7.43	±0.10	±0.05	±0.0005	±0.0240
	P5%PI	±0.380	±0.376	±46.64	±0.64	±0.32	±0.0029	±0.1508
R78, R79	Mean	14.780	14.549	65.8	33.15	100.01	0.1504	1.9416
	95% CI	±0.002	±0.001	±0.73	±0.07	±0.06	±0.0002	±0.0055
	P5%PI	±0.008	±0.006	±3.31	±0.33	±0.25	±0.0007	±0.0250
R152, R153	Mean	14.866	14.829	62.09	5.41	39.99	0.0602	0.7942
	95% CI	±0.001	±0.001	±2.44	±0.03	±0.03	±0.0002	±0.0068
	P5%PI	±0.004	±0.005	±12.73	±0.16	±0.17	±0.0009	±0.0356
R213, R218	Mean	14.618	14.581	59.63	5.34	39.96	0.0603	0.7881
	95% CI	±0.015	±0.015	±1.84	±0.02	±0.04	±0.0001	±0.0045
	P5%PI	±0.070	±0.071	±8.83	±0.10	±0.20	±0.0007	±0.0216
R274, R290	Mean	14.741	14.703	55.89	5.43	39.98	0.0606	0.8056
	95% CI	±0.005	±0.005	±4.20	±0.04	±0.02	±0.0002	±0.0118
	P5%PI	±0.022	±0.021	±19.41	±0.20	±0.11	±0.0011	±0.0544

R294, R311	Mean	14.745	14.707	54.57	5.47	40.04	0.0608	0.8117
	95% CI	±0.005	±0.005	±5.18	±0.05	±0.04	±0.0002	±0.0139
	P5%PI	±0.024	±0.023	±24.79	±0.22	±0.20	±0.0012	±0.0664

Table 13.8. Low pressure line temperature repeatability.

	Quantity	Orifice Plate T/C, °F	Left LPDP T/C, °F	Right LPDP T/C, °F
R36, R92, R102	Mean	80.08	70.55	76.98
	95% CI	±2.95	±3.77	±3.32
	95% PI	±15.95	±20.36	±17.94
R46, R133	Mean	73.55	68.29	74.70
	95% CI	±7.37	±6.18	±6.69
	95% PI	±36.38	±30.47	±32.99
R69, R81, R82, R128	Mean	81.54	74.42	81.88
	95% CI	±1.50	±3.16	±3.37
	95% PI	±9.43	±19.82	±21.17
R78, R79	Mean	81.01	77.48	84.12
	95% CI	±0.29	±1.02	±1.97
	95% PI	±1.34	±4.65	±8.98
R152, R153	Mean	80.89	76.23	81.54
	95% CI	±1.32	±1.05	±1.25
	95% PI	±6.87	±5.46	±6.54
R213, R218	Mean	79.48	71.72	69.67
	95% CI	±1.50	±0.51	±0.54
	95% PI	±7.21	±2.44	±2.58
R274, R290	Mean	70.67	62.21	58.89
	95% CI	±2.51	±2.42	±3.39
	95% PI	±11.61	±11.17	±15.68
R294, R311	Mean	70.15	60.23	57.60
	95% CI	±7.05	±2.81	±4.37
	95% PI	±33.74	±13.43	±20.88

13.2. Test Results

This section presents a summary of basic model aerodynamic performance results obtained during the AMELIA wind tunnel test completed in February, 2012. Before the results are discussed, some general comments on the wind tunnel test are in order. The model performed extremely well throughout the test. All test objectives including ten critical test points were successfully completed. Direct measurement of skin friction using the FISF (Fringe Imaging Skin Friction) method was employed for each critical test point. Six different surface oil-flow visualization and two smoke-wand visualization runs were completed. The test matrix incorporated sets of repeat runs at different model configurations and tunnel conditions. The test provided low-speed experimental force and moment data for the N+2 AMELIA model, including surface pressure and acoustic measurements. This is the first wind tunnel test of a full-span model

incorporating leading- and trailing-edge blowing wing circulation control and engine simulators. It is also the first comparison of trailing edge-only blowing aircraft performance versus leading- and trailing-edge blowing aircraft performance. The objective is to utilize the test data to improve CFD tools for modeling N+2 configurations. Table 1 below presents several test statistics regarding relevant run numbers and dates over which AMELIA was tested.

Table 13.9. Test Statistics.

Model Configuration	Runs	Useful Data Runs	Calendar Days	Wind-on Days
Low Pylon	18:171	151	12/21/2011 – 1/27/2012	20
High Pylon	172:203	29	1/30/2012 – 2/3/2012	5
Clean Wing	204:270	64	2/6/2012 – 2/10/2012	5
TE-only blowing	271:312	41	2/14/2012 – 2/15/2012	2
Total User Occupancy Hours	617.5			
Total Wind-on Calendar Time	12/21/2011 – 2/15/2012			

The results that follow will be discussed based on the four basic model configurations, seen in Table 13.9; model performance comparisons between different configurations will be discussed as relevant. The four basic model configurations are: low engine pylon, high engine pylon, clean wing – leading- and trailing-edge blowing, and clean wing – trailing edge-only blowing. The low and high pylon heights were both tested with leading- and trailing-edge blowing, but they will be referred to by their pylon heights, henceforth. The clean-wing combined leading- and trailing-edge blowing will be referred to as the *clean wing* configuration, while the clean-wing trailing edge-only blowing will be referred to as the *trailing edge-only*, or *TE-only* configuration.

The data presented for each model configuration will be further separated into four "blocks" of results. The blocks provide a convenient way to present similar data sets between all four model configurations. Blocks one and two will present results relevant to general aerodynamic performance; blocks three and four will present results more specific to circulation control performance. The figure sets presented in blocks one and two match, as do those in blocks three and four. Operating conditions illustrating different model sensitivities distinguish the like blocks. Table 13.10 provides a summary, and a description follows. It should be noted that this is a basic guideline for the layout of the data that is presented; there are instances when no data are present for a specific block and model configuration. In those cases, the block format is amended and the changes are noted, where applicable.

Table 13.10. Summary of results discussion format.

Block Number	Plot Description	Tunnel Condition	Angle of Attack	Flap Deflection	Slot Configuration	TPS Configuration
One	C_L vs. α C_L vs. C_D C_L vs. C_m C_m vs. α	Fixed	Sweep	Varied	Fixed	Fixed
Two			Sweep	Fixed	Varied	Varied
Three	C_L vs. C_μ C_D vs. C_μ C_m vs. C_μ	Fixed	Fixed	Varied	Sweep	Off*
Four			-5°, 0°, 10°	Fixed	Sweep	Off*

* Slot sweep results are shown with TPS off, unless noted.

Block one and two plots present data from alpha sweeps, as follows:

- C_L vs. α
- C_L vs. C_D
- C_L vs. C_m
- C_m vs. α

Each set of results in block one is shown for a fixed tunnel velocity and point in the powered-lift matrix. Multiple curves are shown to illustrate the effect of flap deflection on model performance for a given powered-lift condition. The points in the powered-lift matrix are: 1) slots off and TPS off, 2) slots off and full TPS, 3) full slots and TPS off, 4) full slots and full TPS. Definition of the term, "full", and how it is used to describe the slot and TPS operating conditions are provided in the next section, *Test Conditions Summary*. Results in block two are shown for a fixed velocity and flap deflection. Multiple curves illustrate the build-up effect that points (1) → (4) in the powered-lift matrix have on model performance, for a fixed configuration.

Block three and four plots present data from slot sweeps, as follows:

- C_L vs. C_μ
- C_D vs. C_μ
- C_m vs. C_μ

Block three presents results at a fixed velocity and angle of attack. Multiple curves for different flap deflection illustrate their effect on blown lift augmentation. Block four results illustrate the sensitivity of model performance to angle of attack as a function of blowing input, at a fixed velocity and flap deflection. Slot sweeps were conducted at -5°, 0°, and 10° angle of attack.
The discussion of experimental results is meant to serve as a summary for both aerodynamic performance and circulation control performance. Results which are of the greatest interest to the high-lift and research communities are favored. Please refer to publications from the following authors, was presented at the 2013 AIAA Aerospace Sciences Meeting: Marshall, Jameson, Paciano, Lichtwardt, and Horne.

13.2.1. Test Condition Summary

A summary of wind tunnel test conditions and performance metrics relevant to slot and TPS data are described here. Testing was conducted at three velocities: 40 KTS, 60 KTS, and 100 KTS. Table 13.11 provides test average and variances on the velocity dependent parameters: dynamic pressure, Mach number, and Reynolds number (based on mean aerodynamic chord). Set-point tolerance on velocity was ±0.1 KTS. Deviation in the remaining column values is primarily due to variation in tunnel atmosphere; intervals are presented with 95% confidence.

Table 13.11. Summary of wind tunnel flow conditions.

Tunnel Velocity, KTS	M	q_∞, psf	Re_c, 10^6
40±0.1	0.061±0.001	5.5±0.2	0.82±0.05
60±0.1	0.091±0.004	12.4±0.3	1.23±0.23
100±0.1	0.151±0.002	33.5±0.5	1.99±0.05

Data acquired during an alpha sweep were generally obtained over a range from -5° to +25°. Runs at high speed and high blowing conditions that saw considerable model vibrations were held to a smaller positive alpha limit; this angle of attack limit was subjective and dependent on the magnitude of the vibrations. During an alpha polar, the model is held at a single slot and TPS power setting and swept through the angle of attack range. Sideslip sweeps were conducted similarly, at a fixed β and swept through the angle of attack range. Slot sweep data were acquired at a fixed angle of attack over a mass flow rate range from 0 lb_m/sec to 2.8 lb_m/sec. The upper limit is 1.55 lb_m/sec for the TE-only blowing configuration.

Several terms will be used to describe the power setting of the TPS and slots and are defined as follows. “Full”, as it pertains to *full* slots or *full* TPS, corresponds to the maximum power setting of the respective system. *Full* slots corresponds to 2.8 lb_m/sec total air fed to the slots. *Full* TPS corresponds to each TPS spinning at 34,500 RPM. The TPS set-point is dependent on the mode of operation; 1.95±0.03 lb_m/sec total mass flow rate in flow control mode and 195±8 psig in pressure control mode. Here, the variance in one parameter is due to the effect of holding the second parameter constant as the line temperature changes. I.e. the variance in pressure is the result of line temperature changes as the digital valve must compensate to hold mass flow rate constant and vice versa. Again, these set-points reflect system totals; the flow split between left- and right-wings/TPS units occurs in the model, downstream of the regulating valves. A reference to “full power” indicates both the slots and TPS are operating at their full settings. Conditions referencing a fraction of full performance reflect that fraction of mass flow rate set for the slots, and RPM for the TPS. I.e. a 2/3 slots condition corresponds to 2/3 of the full set-point, or (2/3)*2.8 lb_m/sec = 1.87 lb_m/sec.

The 2.8 lb_m/sec and 1.87 lb_m/sec references the digital valve set-point; the digital valve is the reference to set on-condition for both the TPS and slots (note there is 1 digital valve per line). Note that this reference is not the *true* value per say, but it serves as a convenient reference. Mass flow rate numbers listed elsewhere (i.e. those used in the calculation of C_μ) are from the calibrated orifice plate and represent the *true* value.

Table 13.12 presents individual plenum nozzle pressure ratio (NPR) and total summed average nozzle pressure ratio as a function of the slot blowing configuration and set-point. Individual plenum NPRs are the average of the three internal total pressure probes. The values listed in the table represent test-wide averages for the specified set-point; though, run-to-run NPR will vary by a few percent due, primarily, to time-of-day and tunnel atmosphere. The NPR calculation uses the freestream static pressure, instead of the jet exit. Although using the jet exit would yield a higher value and truer estimate of the actual NPR, using the freestream pressure allows for meaningful comparison between data at different test conditions. Individual figures are labeled with the average momentum and thrust coefficient as these values are more directly dependent on dynamic pressure. Refer to the *Data Acquisition* section for the reduction routine for calculating the momentum and thrust coefficients.

Table 13.12. Individual plenum and average nozzle pressure ratio summary.

Blowing configuration	Total $\dot{m}^{\ddagger}$, lb_m/sec	Average NPR	Plenum	NPR, $[(P_0)_{plenum}/P_\infty]$
Combined LE- and TE-blowing (R18-R270)	2.80 *(full)*	1.50	LEIB	1.63
			LEOB	1.36
			TEIB	1.67
			TEOB	1.35
	1.87 *(2/3)*	1.22	LEIB	1.27
			LEOB	1.14
			TEIB	1.30
			TEOB	1.15
TE-only blowing (R271-R312)	1.55 *(full)*	1.57	TEIB	1.74
			TEOB	1.39
	1.03 *(2/3)*	1.26	TEIB	1.34
			TEOB	1.17

‡Total mass flow rate references the digital valve set-point

Table 13.13 presents TPS operating conditions at the full set-point. The values listed in the table represent test-wide averages with variances given at 95% confidence levels. The fan and core nozzle pressure ratio, FNPR and CNPR, is calculated by dividing the average of the total pressure probes in each stream by the freestream static pressure.

Table 13.13. Full TPS set-point operating conditions.

	RPM	$\dot{m}$, lb_m/sec	P_{Line}, psig	Thrust‡, lb_f	FNPR	CNPR
Full	34,342±328	1.95±0.03	195±8	187.6±4.4	1.33±0.01	1.12±0.01

‡combined static thrust

13.3. Trailing Edge-Only Blowing

This section discusses model performance in the trailing edge-only blowing configuration. The model is in the clean wing configuration, i.e. the TPS are removed, and the leading edge plenums have been blocked at the downstream side of the butterfly valves. The trailing edge-only (or TE-only) blowing runs were conducted over the final two days of wind-on testing. As a result, only a limited subset of data at the 0° and 60° flap deflections are available. In setting on-condition for the TE-only blowing runs, the goal was to approximately match the same blowing rate through

the trailing edge as was achieved for the combined leading- and trailing-edge blowing runs. To do this, trailing-edge plenum pressures were matched between the two configurations. The result is slightly more than half the mass flow rate, as the split between the leading- and trailing-edges is not half of the total air delivered to the low pressure side of the model. Table 13.12 lists the relevant slot blowing parameters for the full and 2/3 set-points during the TE-only blowing configuration.

Traditionally, circulation control testing has been done with models that are limited to trailing edge blowing. As this wind tunnel test was a first on many fronts, it was important to have this subset of data available to compare against historical data. Results from these experiments have shown large lift augmentation through TE-blowing can be achieved, however performance falls off at positive angles of attack. Stall at the leading edge is the cause., Circulation control can be thought of as *effective* camber; as C_μ is increased, the more effective camber the wing has. At high blowing rates, the effect is manifested at the leading edge, where the stagnation point moves further downstream on the lower surface to a point where it cannot maintain attachment through the increased acceleration around the nose. Previously, a leading-edge device (such as a slat) has been employed in an attempt to delay stall at the leading edge. Although effective at delaying stall to higher angles of attack, the leading-edge article is not entirely sufficient and leading-edge blowing is necessary. It is worth noting that although establishing trends that are consistent with empirical data is important, this report does not serve as a literature review and readers are encouraged to refer to several papers by Englar[1, 2] for a reference on previous circulation control testing. The results that follow not only show the agreement of the AMELIA data to historical circulation control data, but also prove the need for leading-edge blowing.

13.3.1. Block One

Block one plots are presented in Figure 13.46 through Figure 13.53. The plots present trailing edge-only blowing configuration performance as augmented by flap deflection at the full slot condition. It is seen that increasing flap deflection results in increased lift, but at a lower stall angle; at both speeds for the 60° flap deflection, the stall point moves to ~0°. This is expected as the increased flap deflection adds effective camber to the airfoil that, for a constant C_μ, results in earlier separation around the leading edge as the flow cannot maintain attachment due to the high streamline inflow angle. Other trends in the data sets include increased drag and pitch moment with flap deflection. Stall (leading-edge stall) is, in general, more aggressive in the TE-only blowing configuration compared to what is seen with LE- and TE-blowing, and more aggressive at positive flap deflections.

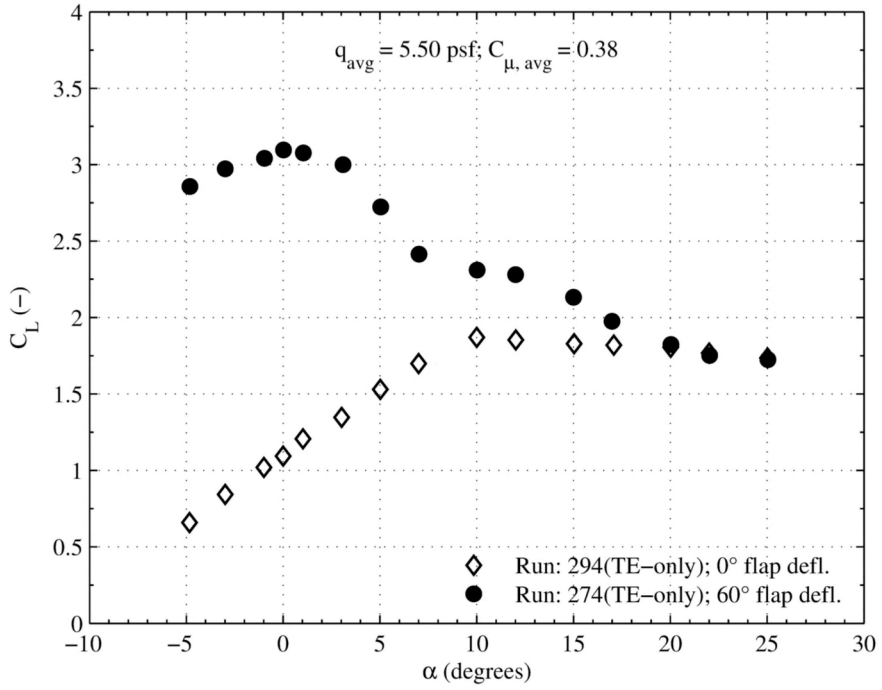

Figure 13.46. TE-only blowing plot set 1. ***(a) 40 KTS, C_L vs. α.***

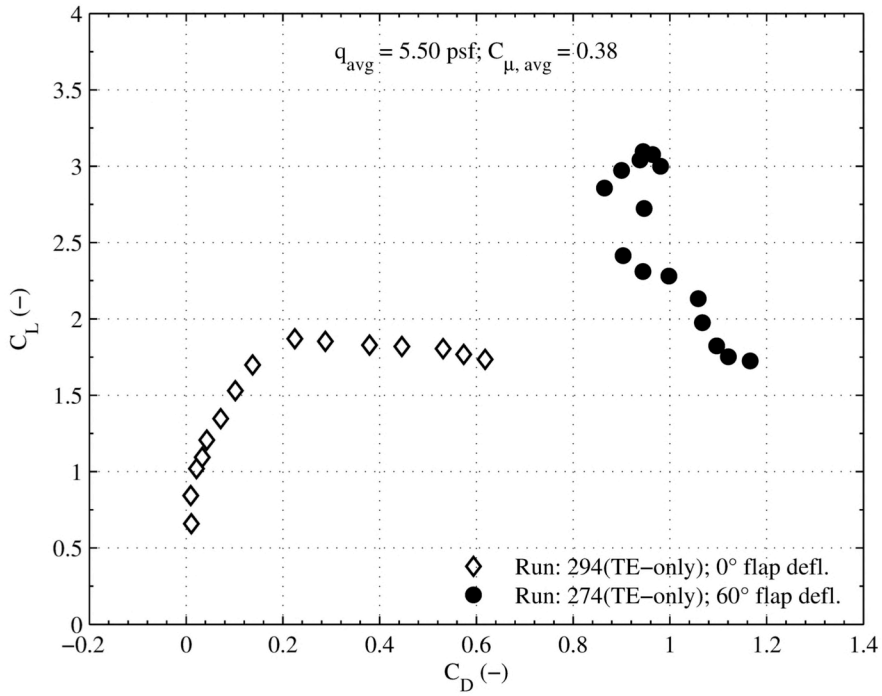

Figure 13.47. TE-only blowing plot set 1. ***(b) 40 KTS, C_L vs. C_D.***

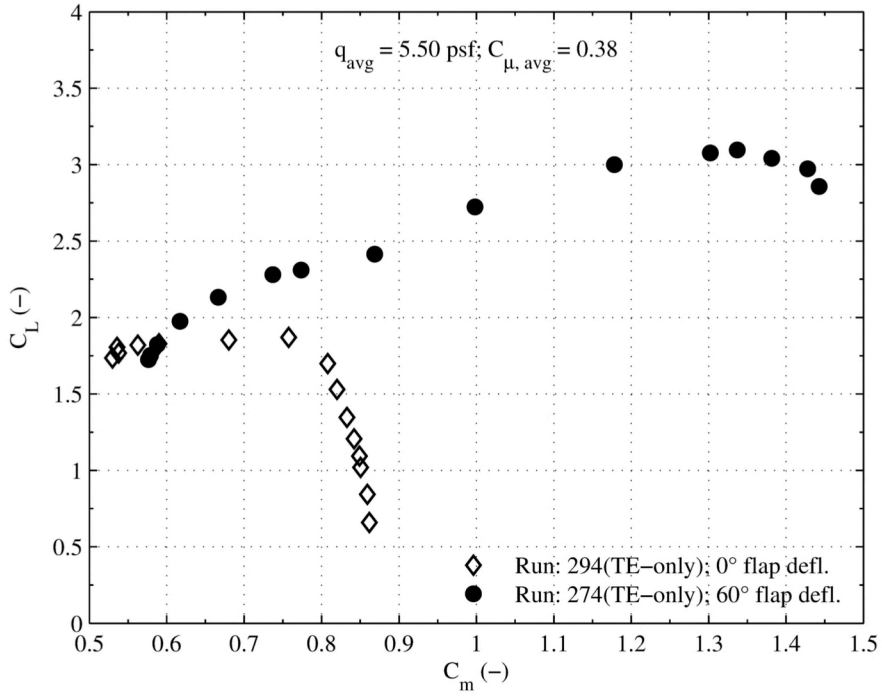

Figure 13.48. TE-only blowing plot set 1. ***(c) 40 KTS, C_L vs. C_m.***

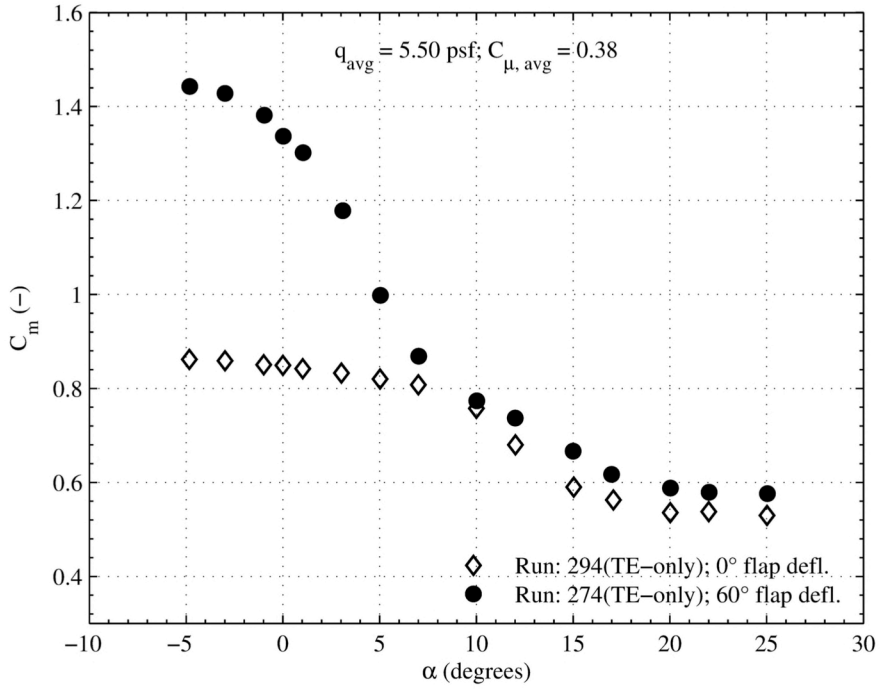

Figure 13.49. TE-only blowing plot set 1. (d) 40 KTS, C_m vs. α.

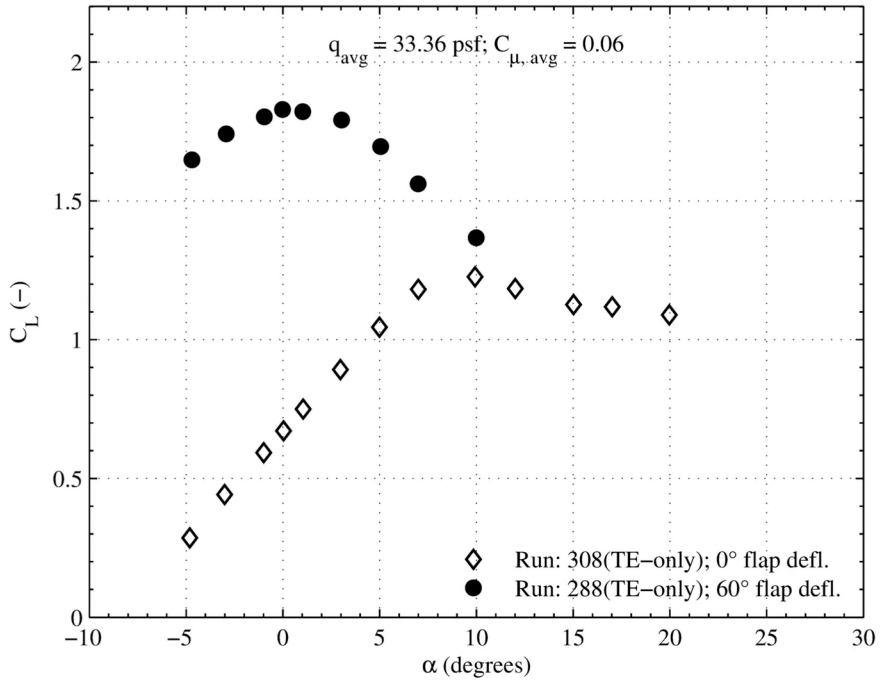

Figure 13.50. TE-only blowing plot set 2. ***(a) 100 KTS, C_L vs. α.***

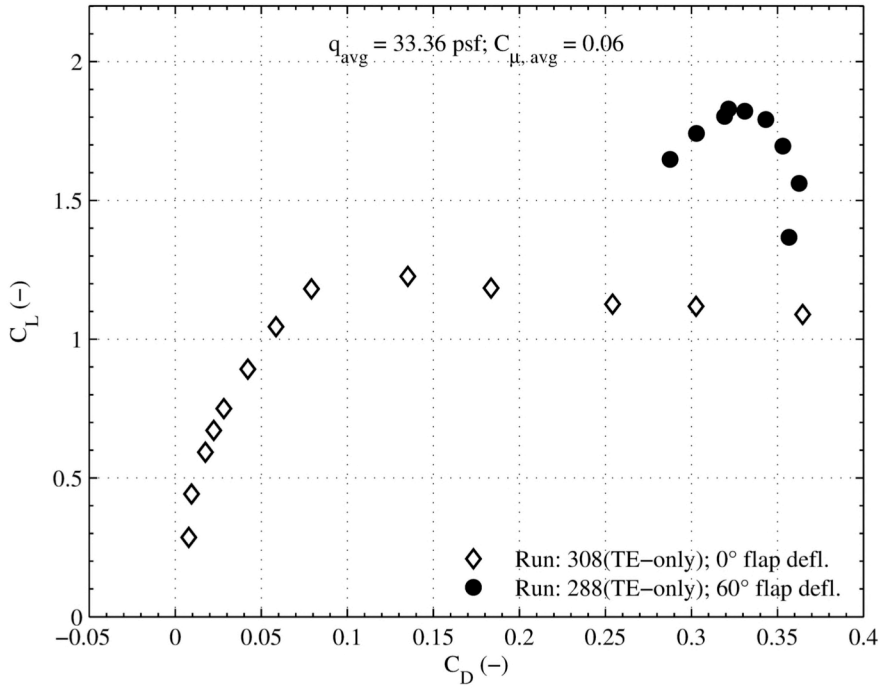

Figure 13.51. TE-only blowing plot set 2. ***(b) 100 KTS, C_L vs. C_D.***

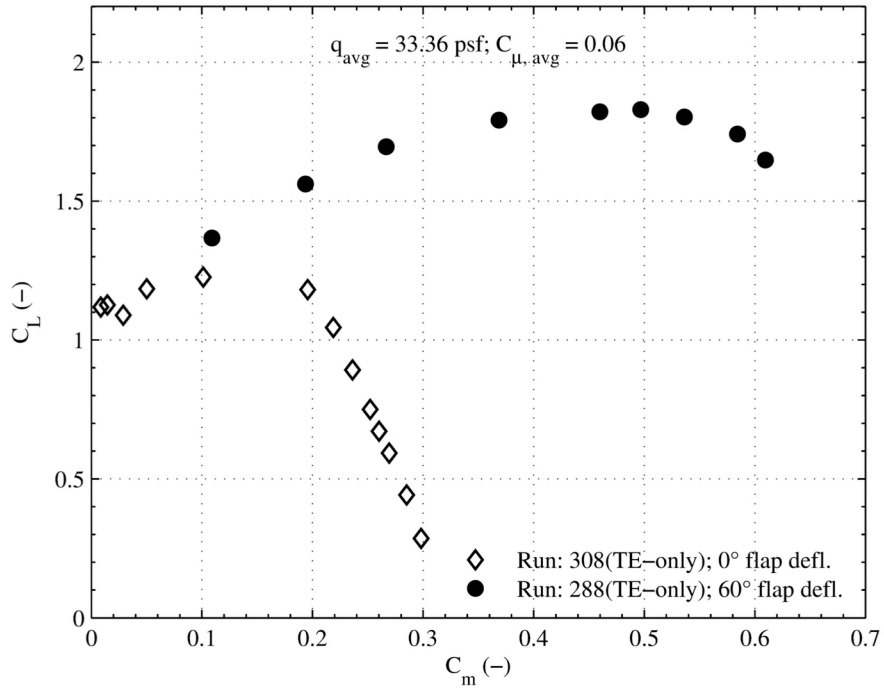

Figure 13.52. TE-only blowing plot set 2. ***(c) 100 KTS, C_L vs. C_m.***

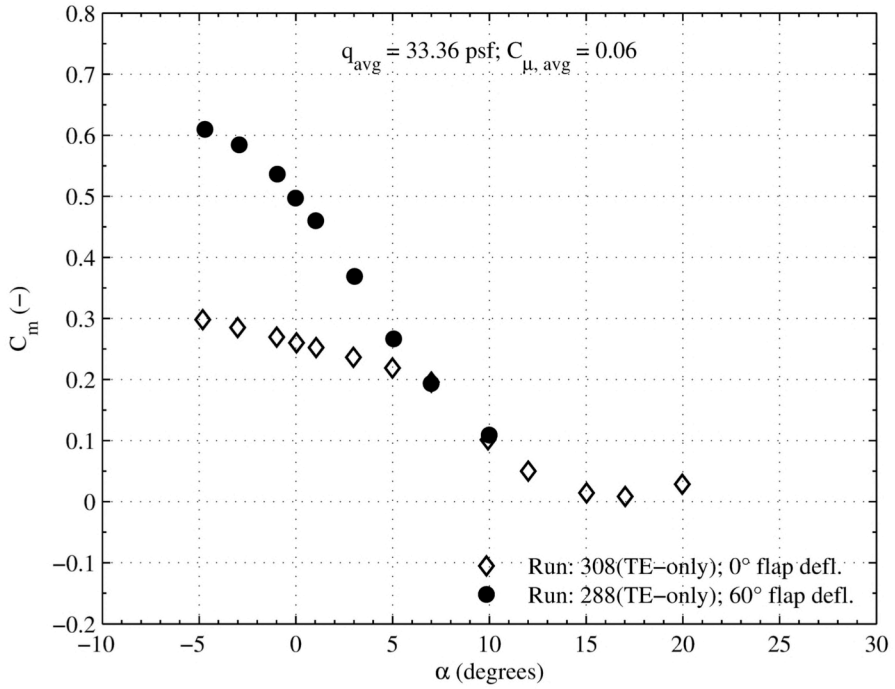

Figure 13.53. TE-only blowing plot set 2. (d) 100 KTS, C_m vs. α.

13.3.2. Block Two

Block two plots are presented in Figure 13.54 through Figure 13.61. The figures show TE-only blowing model performance with multiple curves of data corresponding to alpha sweeps at different slot blowing rates. Figure sets are provided for the 0° and 60° flap deflection at 40 KTS freestream velocity. Across the plot sets, it is seen that lift and pitch moment are increased with blowing. For a fixed flap deflection, the addition of blowing decreases the stall angle due to the inability of the flow to maintain attachment around the leading edge as the up-wash increases due to blowing-induced circulation. For the 0° flap deflection, the stall angle is shifted to ~10° with blowing and remains relatively constant as more blowing is applied. With the 60° flap on, however, the locus of stall points moves to smaller angles as C_μ is increased. For $C_\mu = 0.38$ and $C_L = 3.2$ stall occurs at $\alpha = 0°$. The drag data for the 0° flap show a slot thrust as C_μ is increased; this is not seen with positive flap deflections as the direction of the jet leaving the slot is no longer in line with the drag axis.

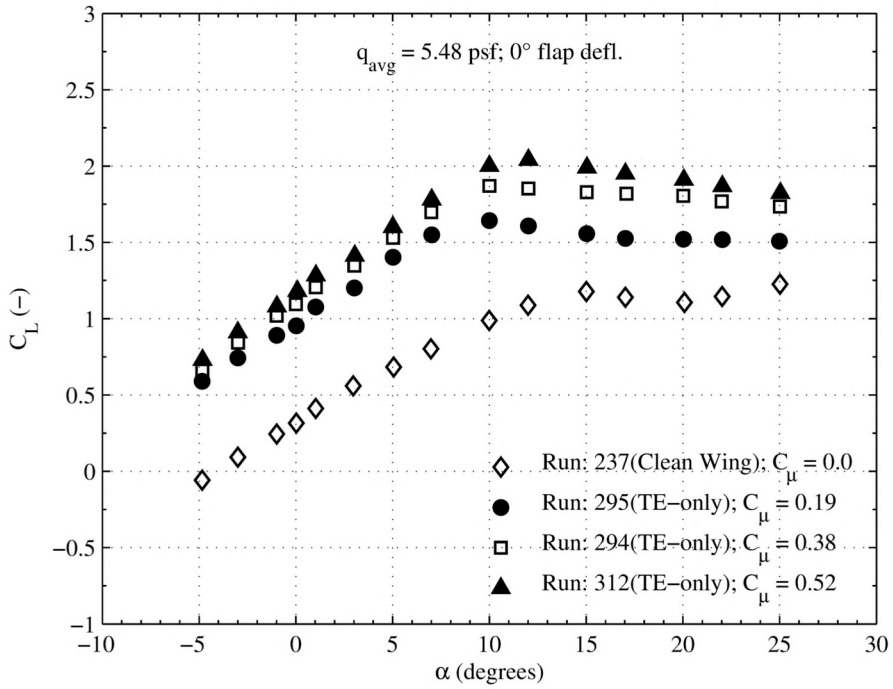

Figure 13.54. TE-only blowing plot set 3. ***(a) 40 KTS, 0° flap deflection, C_L vs. α.***

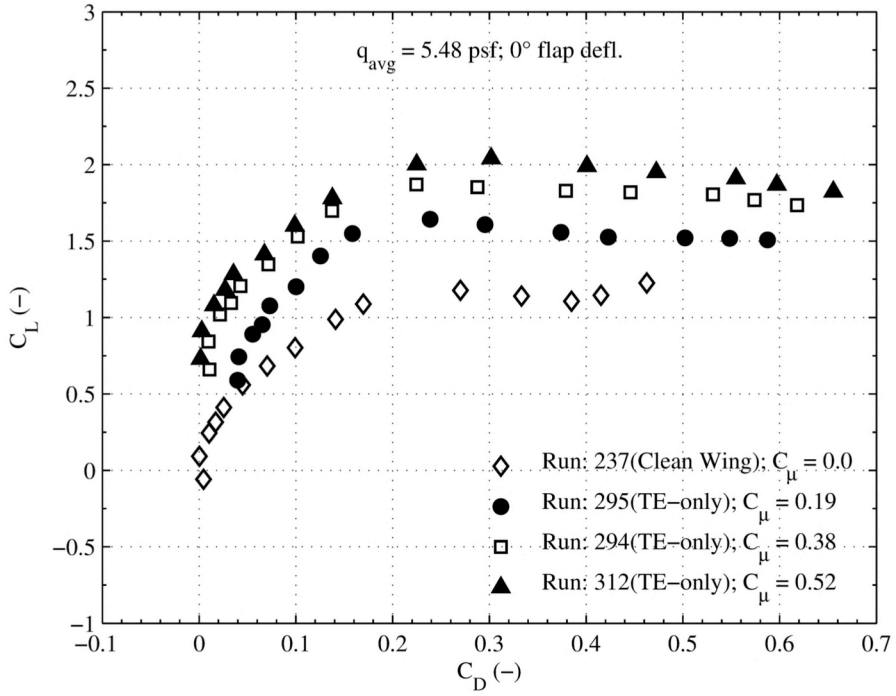

Figure 13.55. TE-only blowing plot set 3. ***(b) 40 KTS, 0° flap deflection, C_L vs. C_D.***

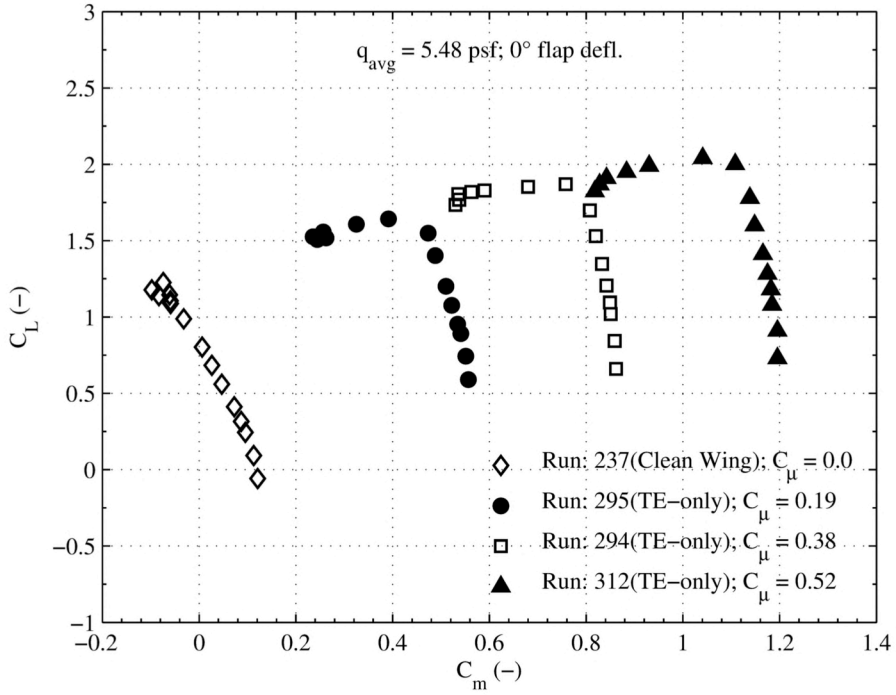

Figure 13.56. TE-only blowing plot set 3. ***(c) 40 KTS, 0° flap deflection, C_L vs. C_m.***

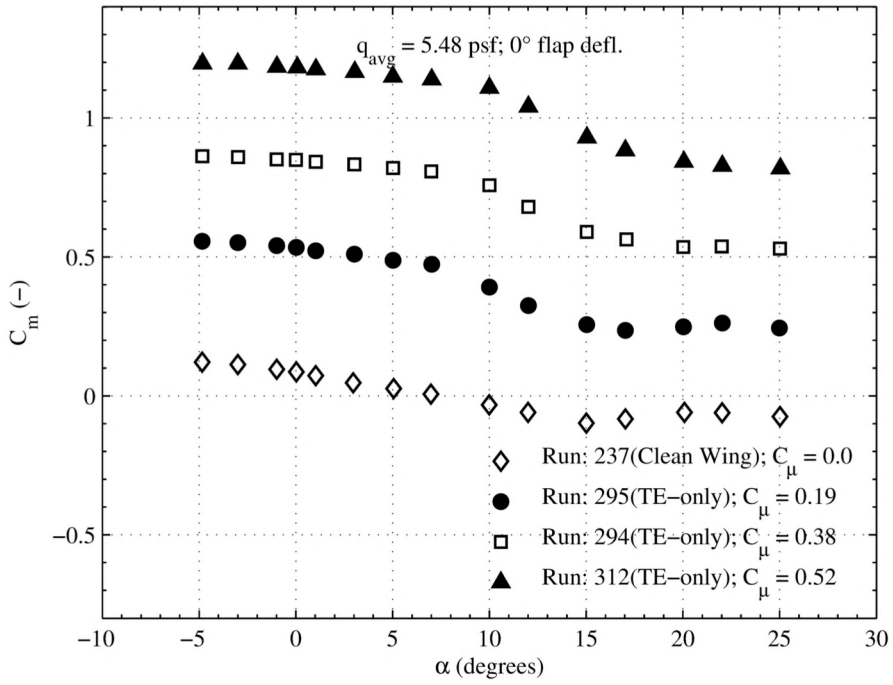

Figure 13.57. TE-only blowing plot set 3. ***(d) 40 KTS, 0° flap deflection, C_m vs. α.***

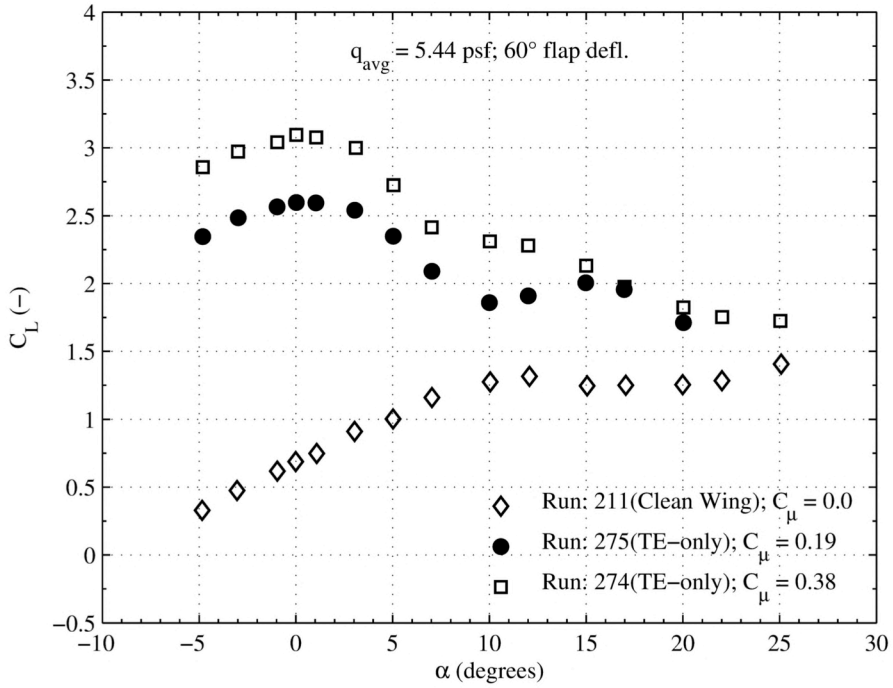

Figure 13.58. TE-only blowing plot set 4. ***(a) 40 KTS, 60° flap deflection, C_L vs. α.***

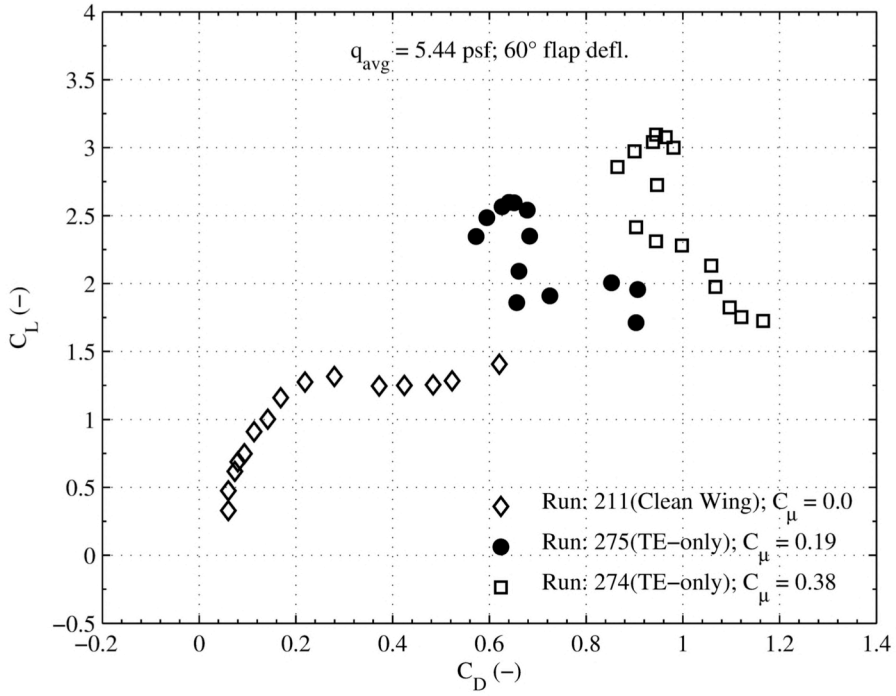

Figure 13.59. TE-only blowing plot set 4. ***(b) 40 KTS, 60° flap deflection, C_L vs. C_D.***

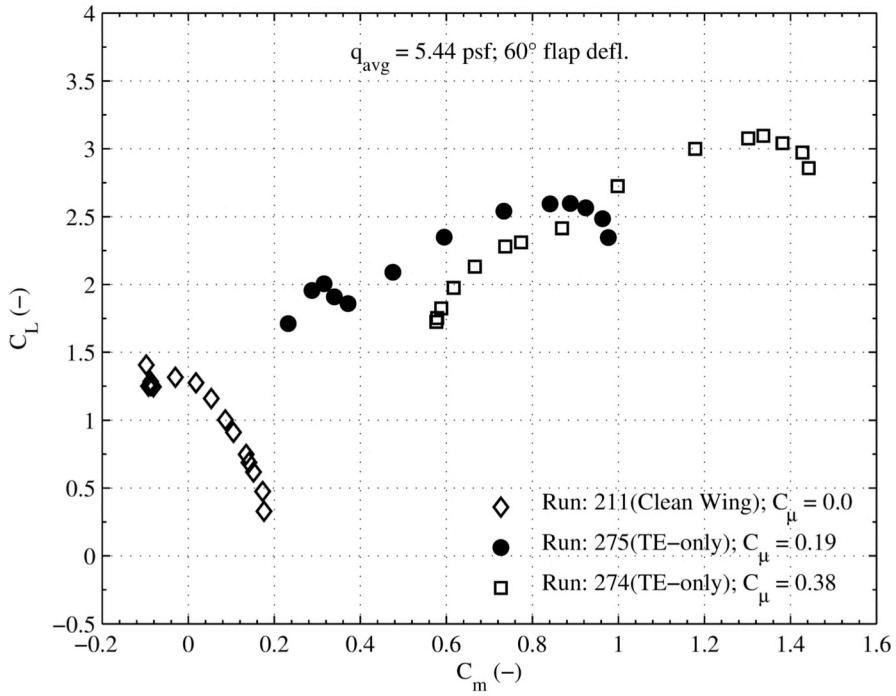

Figure 13.60. TE-only blowing plot set 4. ***(c) 40 KTS, 60° flap deflection, C_L vs. C_m.***

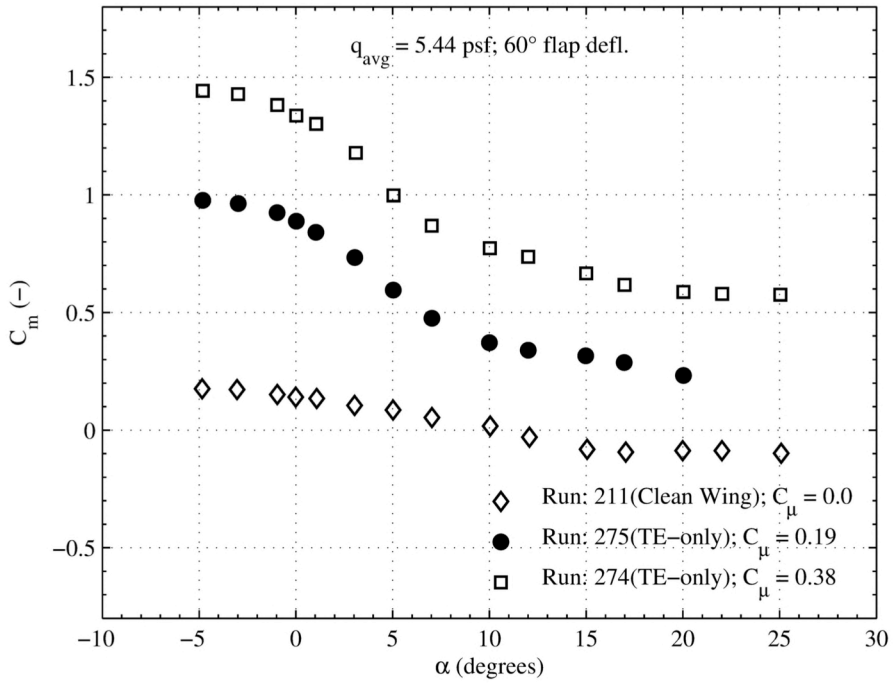

Figure 13.61. TE-only blowing plot set 4. ***(d) 40 KTS, 60° flap deflection, C_m vs. α.***

13.3.3. Block Three

Block three plots are provided below in Figure 13.62 through Figure 13.67. The figure sets present TE-only blowing model performance for slot sweeps at a fixed angle of attack and tunnel speed. Plot sets are provided for α = 0° at 40 KTS and 100 KTS freestream velocity. The region at low C_μ where the increase in C_L with each increment of C_μ is the highest is referred to as the separation control region[3]. For the 60° flap data given in Figure 13.62, $C_\mu < 0.05$ characterizes this region. The separation control region is where the separation point is quickly moved to the trailing edge as blowing is increased. Beyond separation control is the super circulation region. Here, the lift continues to increase but it is not as efficient because the separation point has been fixed at the trailing edge of the flap. Figure 13.63 and Figure 13.66 show the slot thrust, at a fixed angle of attack, provided by the 0° flap.

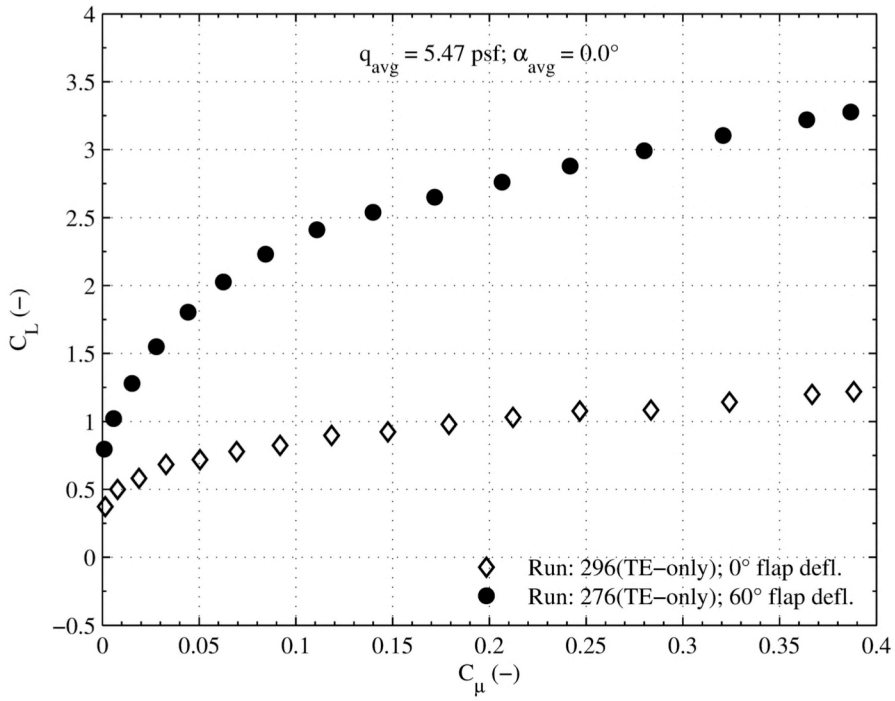

Figure 13.62. TE-only blowing plot set 5. ***(a) 40 KTS, 0° angle of attack, C_L vs. C_μ.***

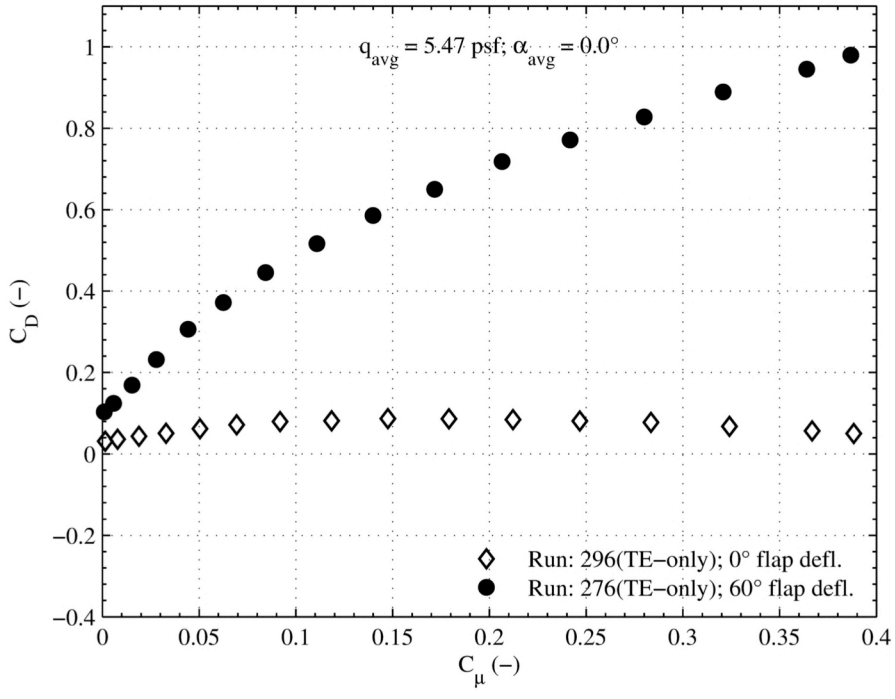

Figure 13.63. TE-only blowing plot set 5. ***(b) 40 KTS, 0° angle of attack, C_D vs. C_μ.***

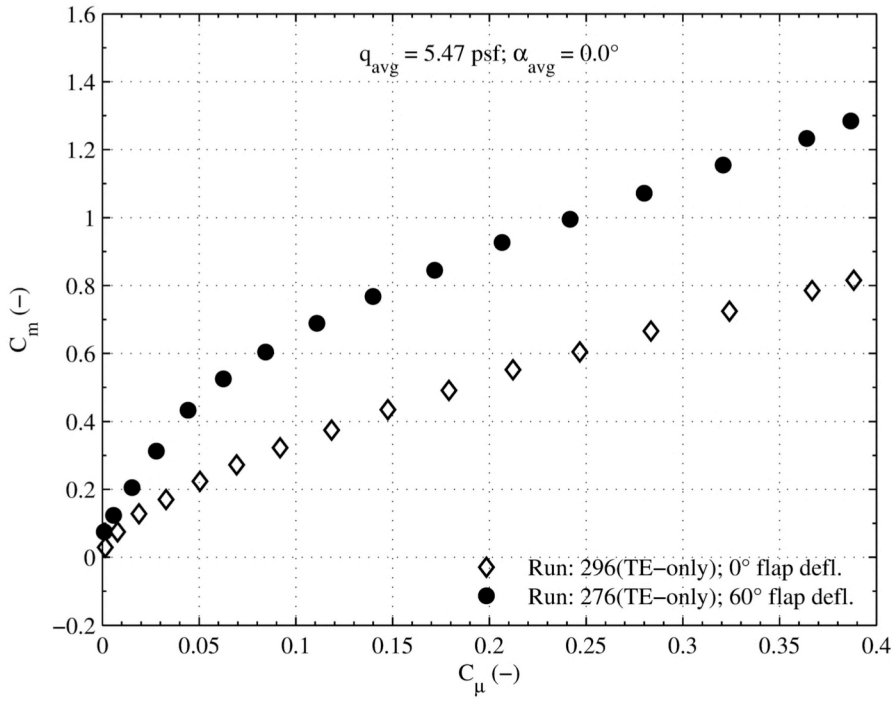

Figure 13.64. TE-only blowing plot set 5. ***(c) 40 KTS, 0° angle of attack, C_m vs. C_μ.***

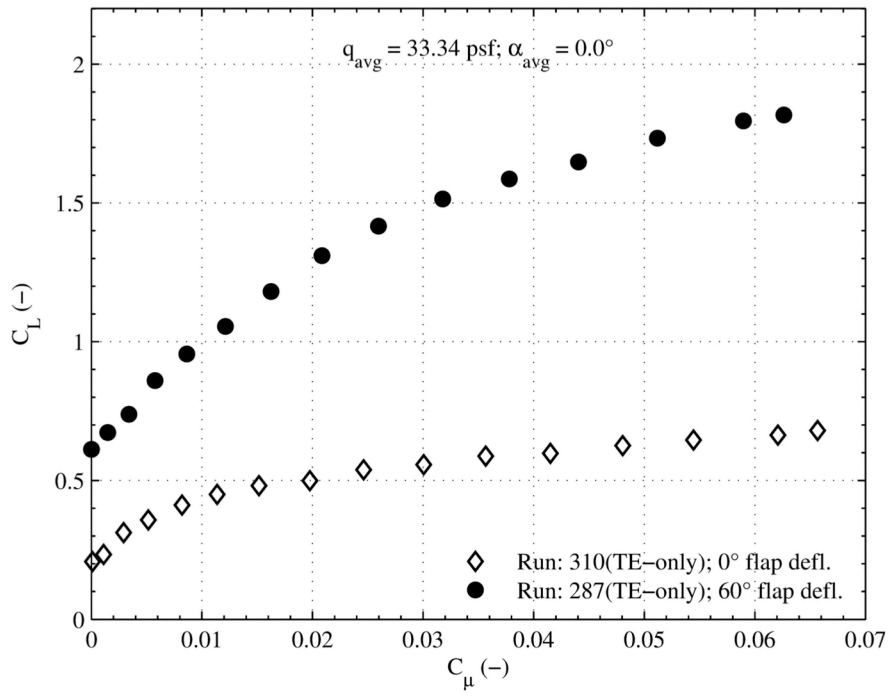

Figure 13.65. TE-only blowing plot set 6. ***(a) 100 KTS, 0° angle of attack, C_L vs. C_μ.***

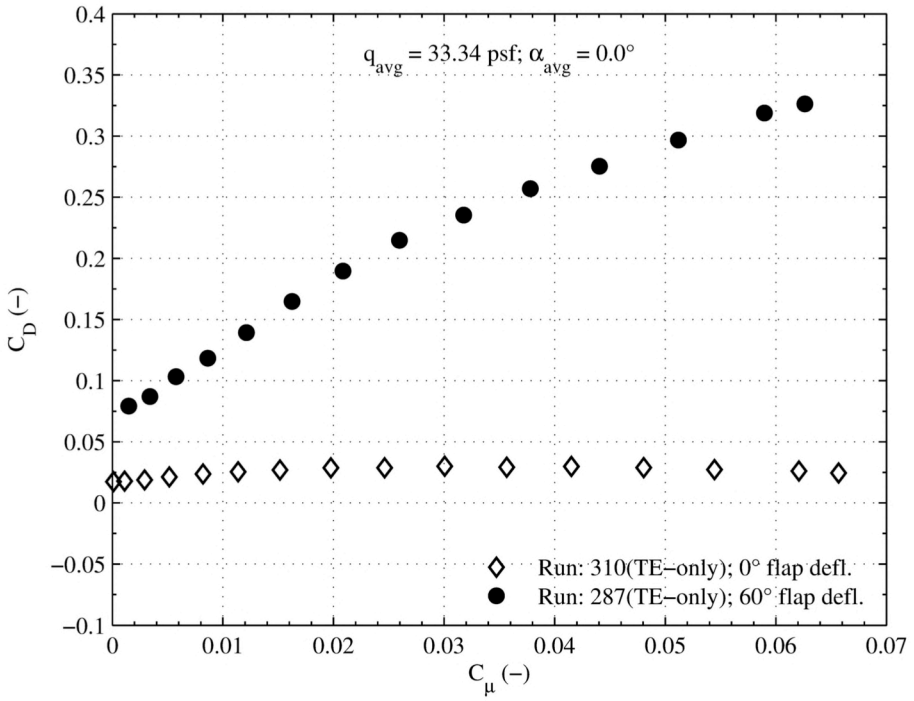

Figure 13.66. TE-only blowing plot set 6. ***(b) 100 KTS, 0° angle of attack, C_D vs. C_μ.***

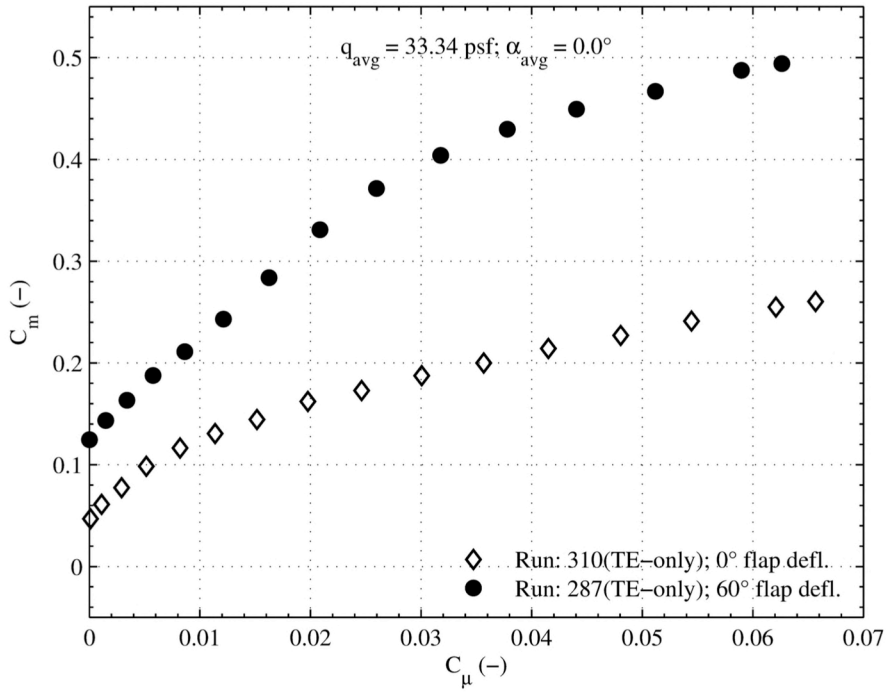

Figure 13.67. TE-only blowing plot set 6. ***(c) 100 KTS, 0° angle of attack, C_m vs. C_μ.***

13.3.4. Block Four

Block four plot sets are presented in Figure 13.68 through Figure 13.73. Data from slot sweeps are presented at 40 KTS for the 0° and 60° flap deflection with multiple curves corresponding to -5°, 0°, and 10° angle of attack. As expected for the 0° flap, C_L increases with angle of attack across the entire slot sweep range. With the 60° flap however, there is a noticeable drop-off in C_L with increasing C_μ at α = 10°. Here, the wing has stalled at the leading edge and becomes ineffective at generating lift through the increased circulation from blowing. Figure 13.69 and Figure 13.72 show the variation in drag coefficient with angle of attack. For the 0° flap, there is increased C_D with C_μ until a point (different for each angle of attack) wherein the slot thrust kicks in and drag begins to decrease with increasing C_μ. This is not seen with the 60° flap, where an increase in α corresponds to an increase in C_D across the slot sweep range. Looking at Figure 13.70 and Figure 13.73, there is a decrease in pitching moment as angle of attack is increased, for both flap deflections.

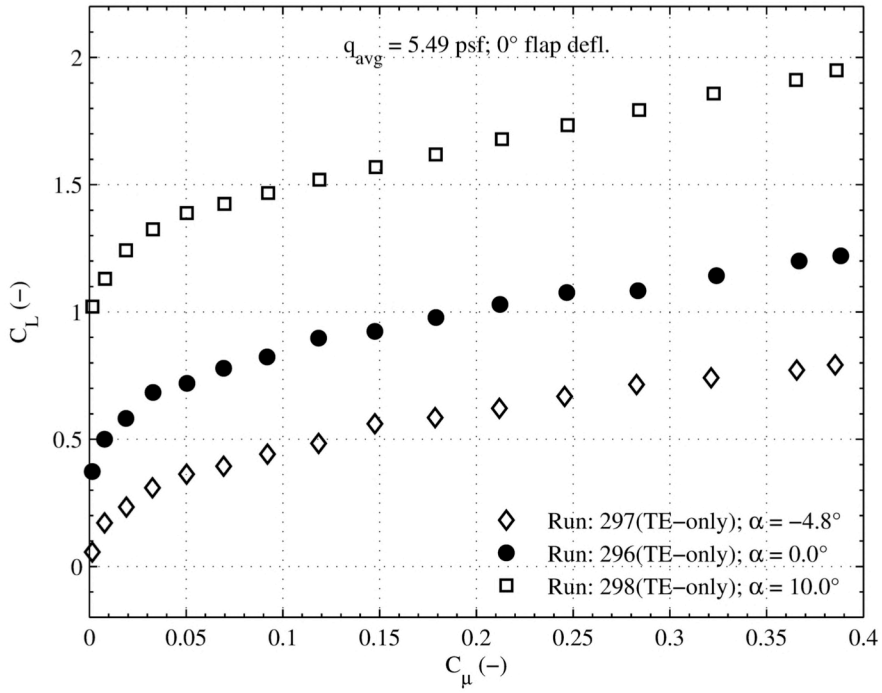

Figure 13.68. TE-only blowing plot set 7. ***(a) 40 KTS, 0° flap deflection, C_L vs. C_μ***

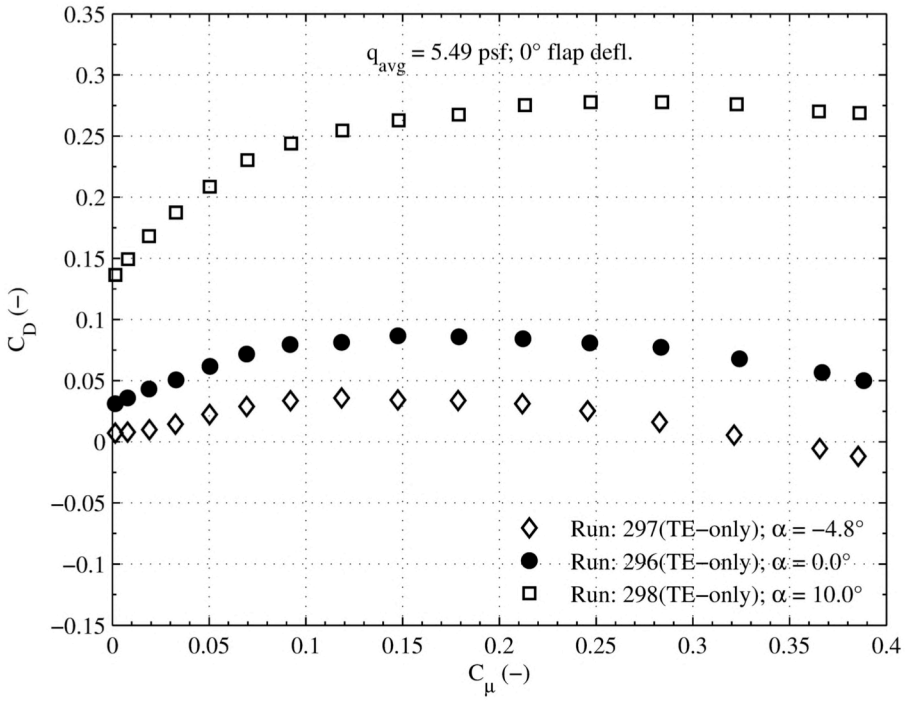

Figure 13.69. TE-only blowing plot set 7. ***(b) 40 KTS, 0° flap deflection, C_D vs. C_μ.***

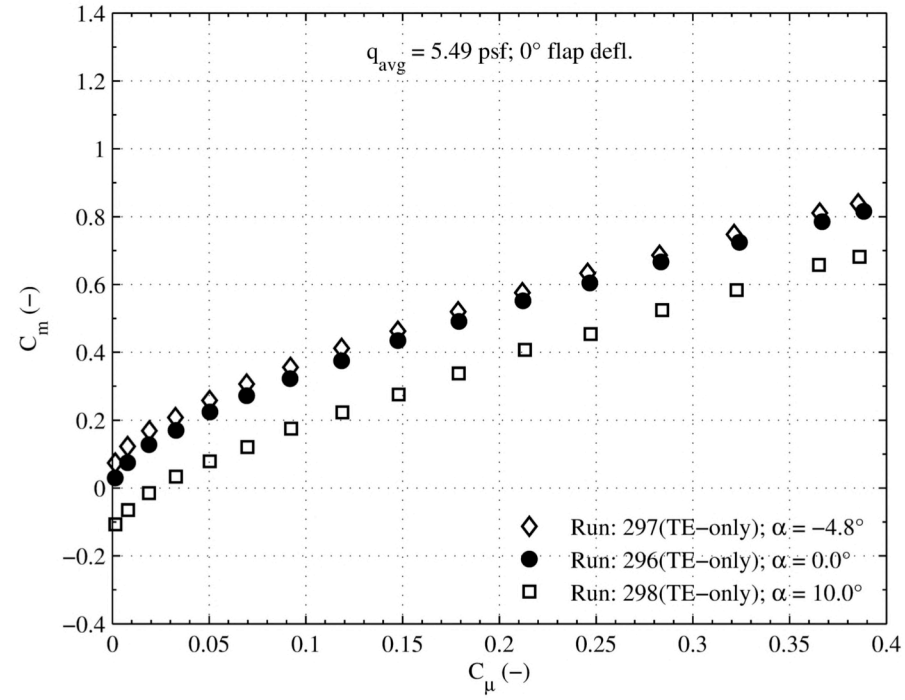

Figure 13.70. TE-only blowing plot set 7. ***(c) 40 KTS, 0° flap deflection, C_m vs. C_μ.***

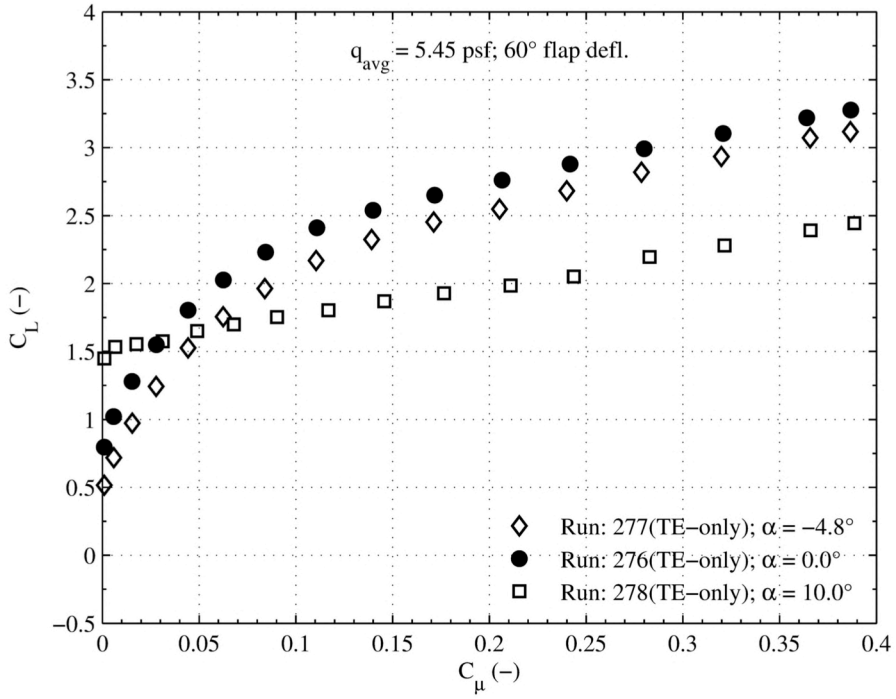

Figure 13.71. TE-only blowing plot set 8. ***(a) 40 KTS, 60° flap deflection, C_L vs. C_μ.***

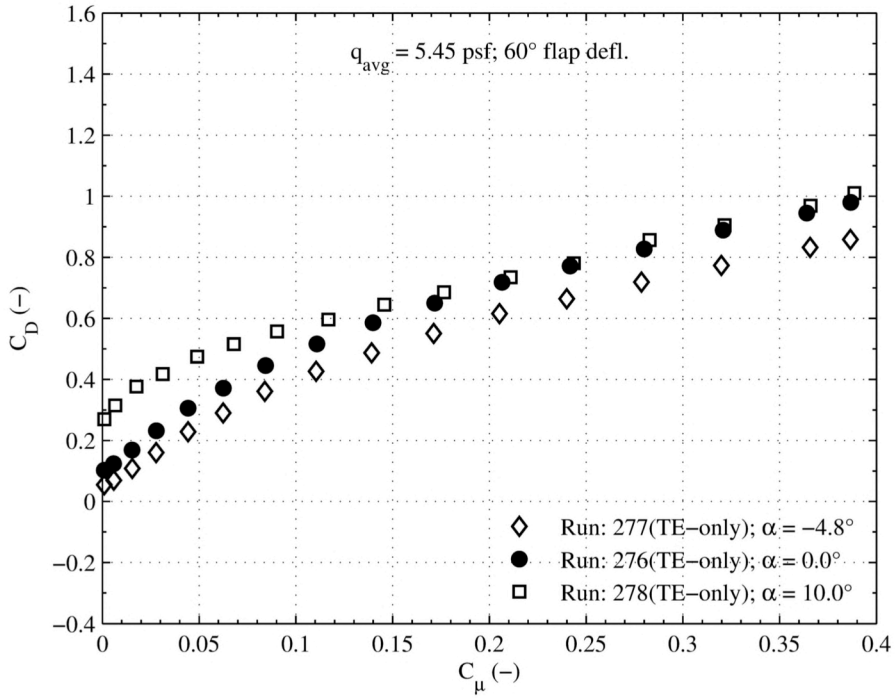

Figure 13.72. TE-only blowing plot set 8. ***(b) 40 KTS, 60° flap deflection, C_D vs. C_μ.***

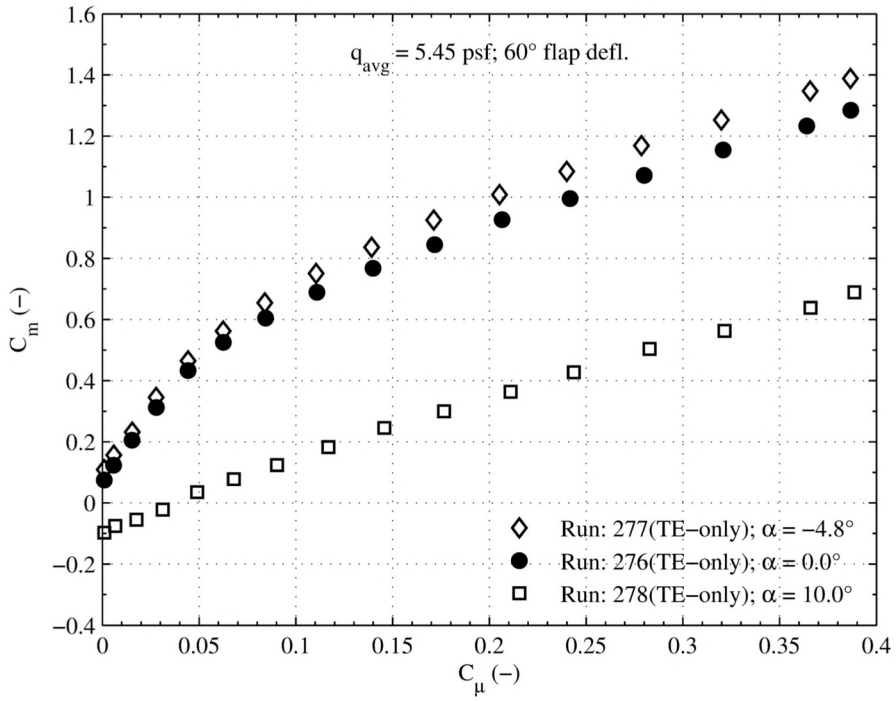

Figure 13.73. TE-only blowing plot set 8. ***(c) 40 KTS, 60° flap deflection, C_m vs. C_μ.***

13.4. Clean Wing

Originally, testing was only planned for the low- and high-pylon heights; clean wing runs were added late in the test planning phase. Low pylon runs at the 30° flap deflection and runs in the high pylon configuration were sacrificed to accommodate the runs in the clean wing configuration. The decision was justified because of the value the clean wing runs present to the CFD community. The removal of the TPS units provides a simpler validation case for CFD; it is likely that a CFD validation will start with this configuration (or the TE-only blowing configuration) before attempting a simulation with the entire model. The addition of the TPS, and the coupling of the CCW and USB, significantly complicates the flow physics. The TPS add a significant burden to building the computational grid and implementing boundary conditions. Cell quality can be quite poor around many of the wing and TPS junction areas.

The model change from the high pylon height to the clean wing configuration was finished over the course of two days. The removal of the TPS units was finished the first day and cosmetic work was finished the second day. An automotive repair product was used to fill the hole in the wing left over from the TPS removal. The Bondo was smoothed to match the wing mold lines and a FARO measuring arm was used to acquire geometric points, post-test, to confirm the mold lines of the wing in relation to the manufactured CAD model. Testing in the clean wing configuration took place over 5 wind-on days and 64 useful data runs were acquired.

13.4.1. Block One

Block one plots for the clean wing configuration are presented in Figure 13.74 through Figure 13.85. The plot sets present full slots model performance at three different tunnel speeds as augmented by flap deflection. Lift coefficient data shows the 80° flap to be ineffective at high angles of attack. At 40 KTS, the 80° flap stalls and has a lower maximum C_L compared to the 60° flap. As speed increases, the 80° flap becomes less effective across the entire angle of attack range. At low speeds this result is not entirely expected as early predictions and previous work suggested a (nearly constant) offset between all flap deflections. At high speeds this is possibly explained by needing a higher C_μ to maintain the offset. Drag data shows increasing drag as flap deflection is increased, with slot thrust from the 0° flap. Pitching moment increases as flap deflection is increased.

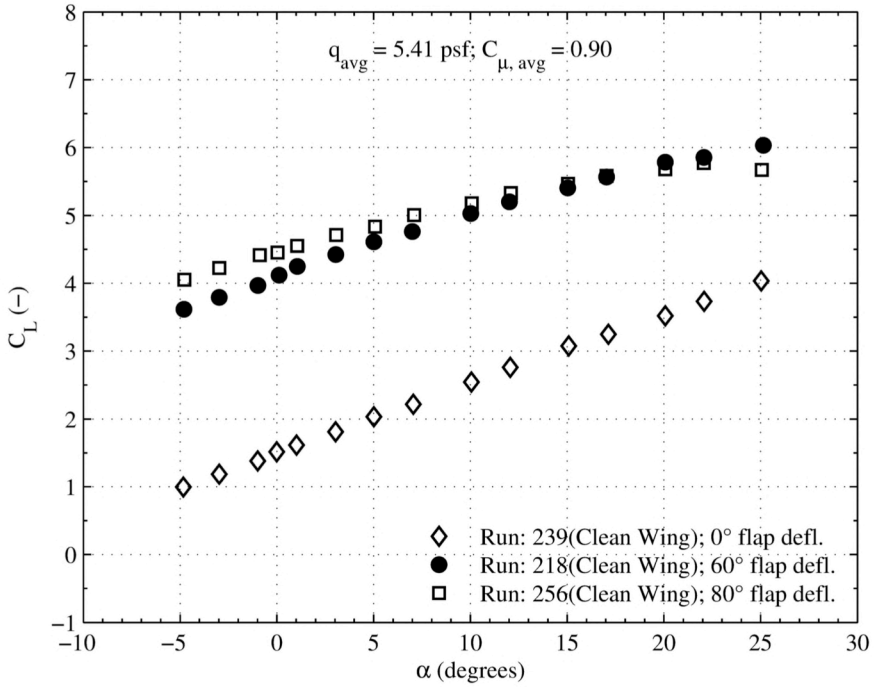

Figure 13.74. Clean wing plot set 1. ***(a) 40 KTS, full slots, C_L vs. α.***

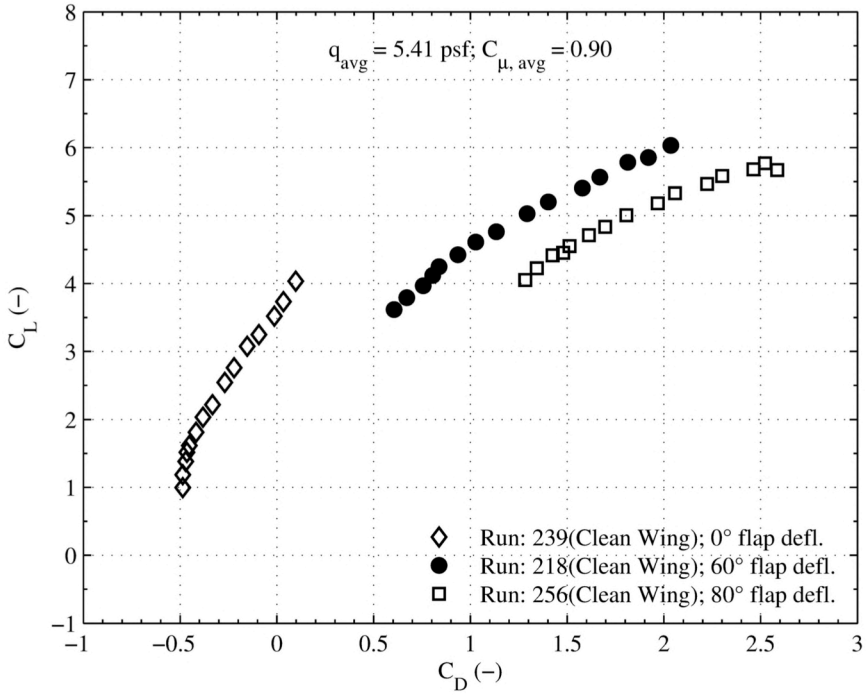

Figure 13.75. Clean wing plot set 1. ***(b) 40 KTS, full slots, C_L vs. C_D.***

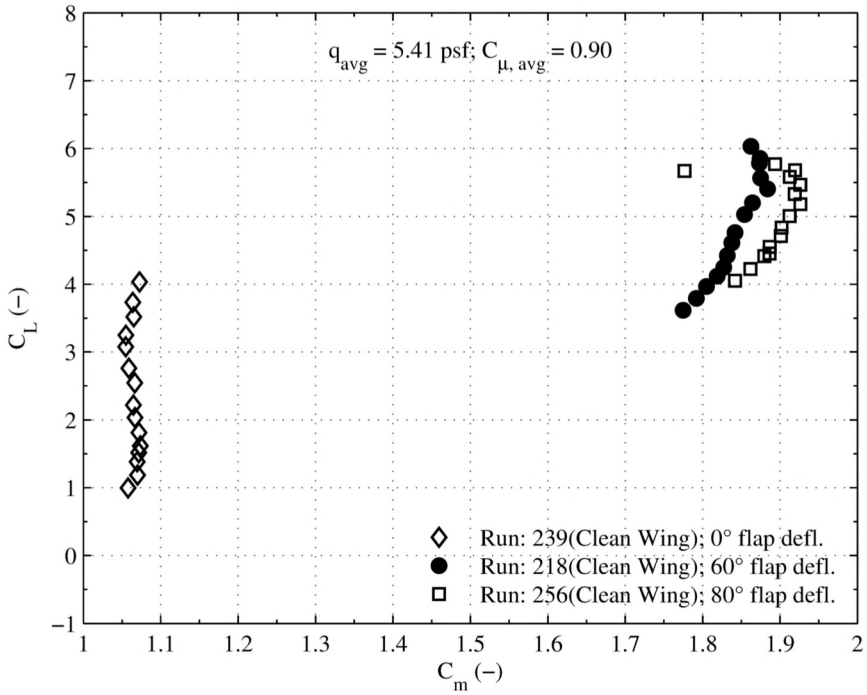

Figure 13.76. Clean wing plot set 1. ***(c) 40 KTS, full slots, C_L vs. C_m.***

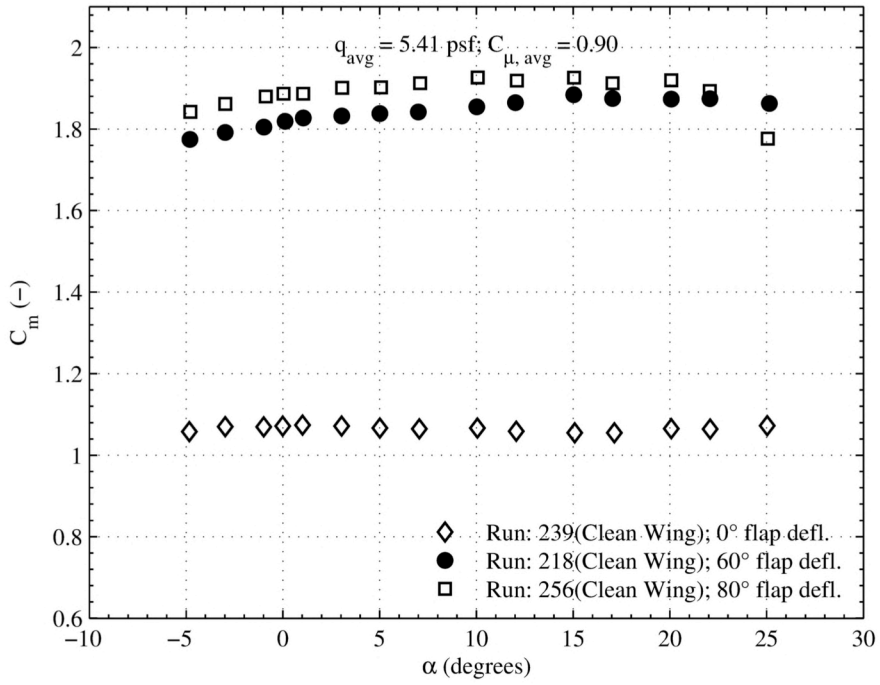

Figure 13.77. Clean wing plot set 1. ***(d) 40 KTS, full slots, C_m vs. α.***

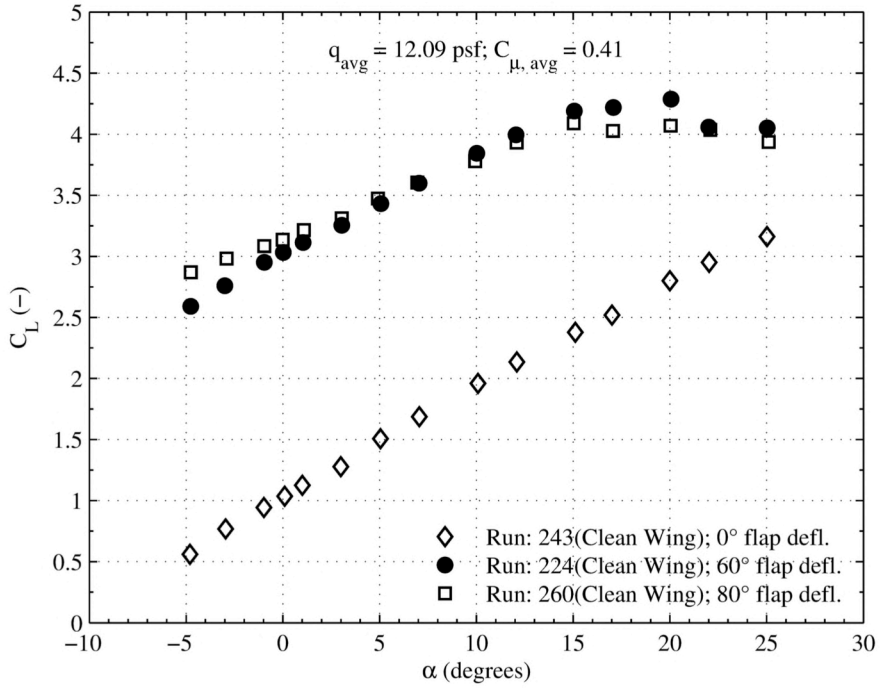

Figure 13.78. Clean wing plot set 2. ***(a) 60 KTS, full slots, C_L vs. α.***

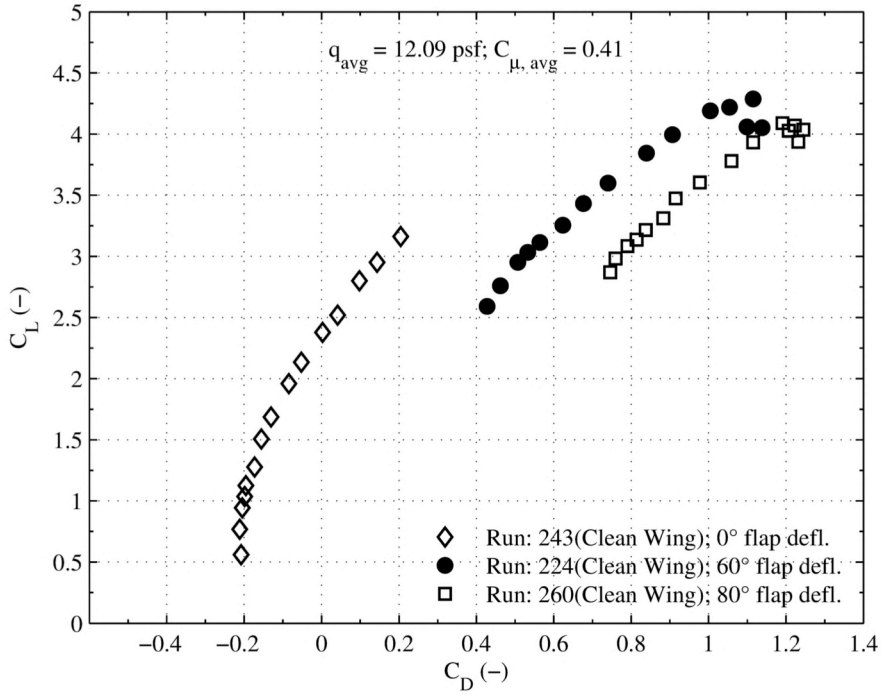

Figure 13.79. Clean wing plot set 2. ***(b) 60 KTS, full slots, C_L vs. C_D.***

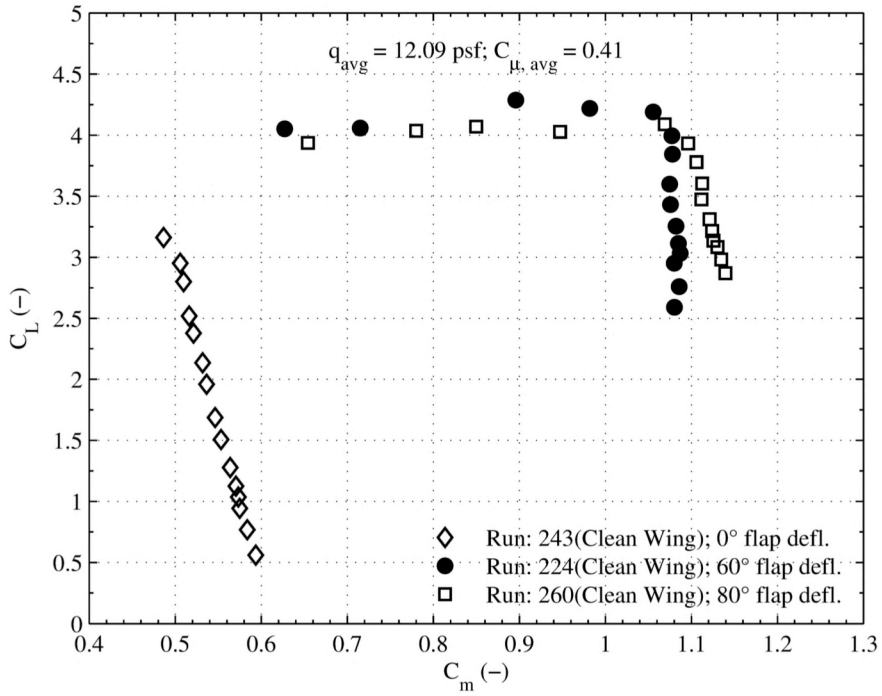

Figure 13.80. Clean wing plot set 2. ***(c) 60 KTS, full slots, C_L vs. C_m.***

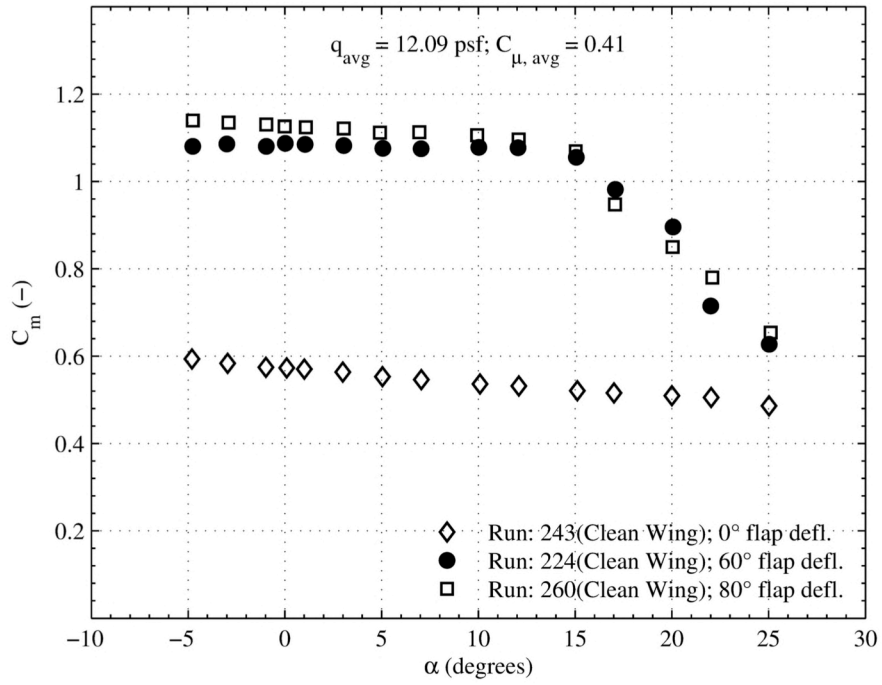

Figure 13.81. Clean wing plot set 2. ***(d) 60 KTS, full slots, C_m vs. α.***

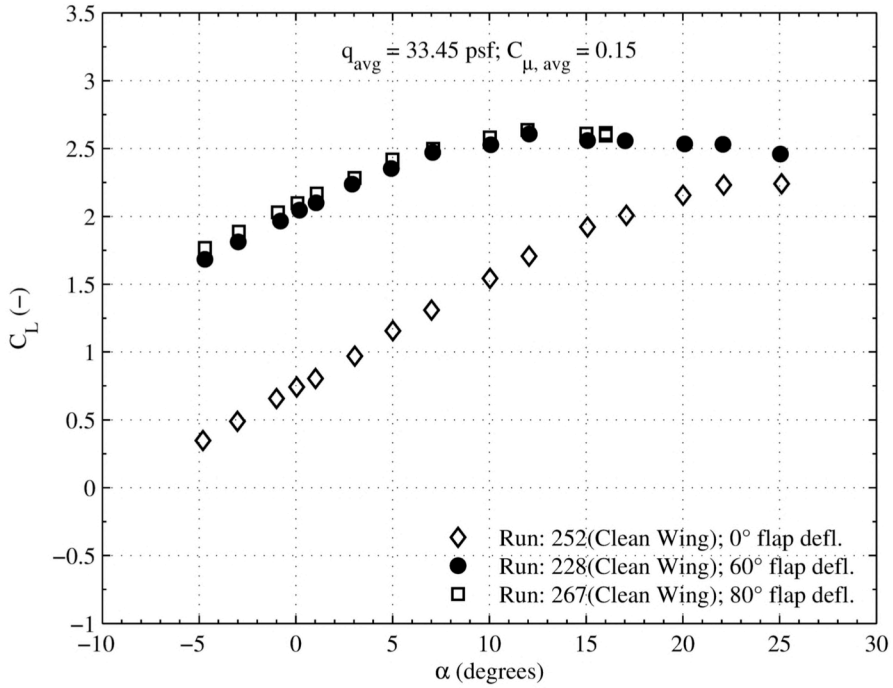

Figure 13.82. Clean wing plot set 3. ***(a) 100 KTS, full slots, C_L vs. α.***

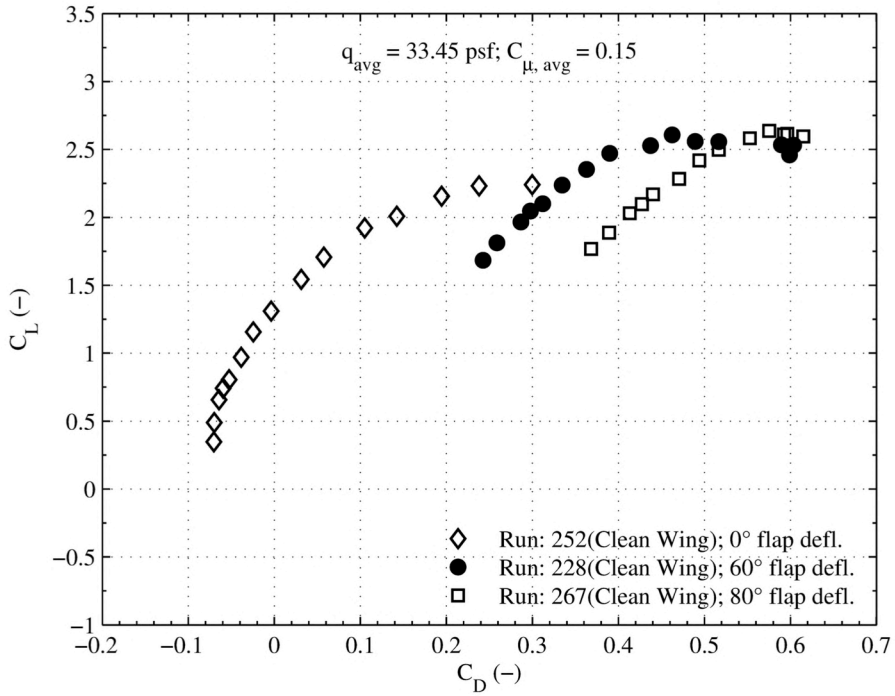

Figure 13.83. Clean wing plot set 3. ***(b) 100 KTS, full slots, C_L vs. C_D.***

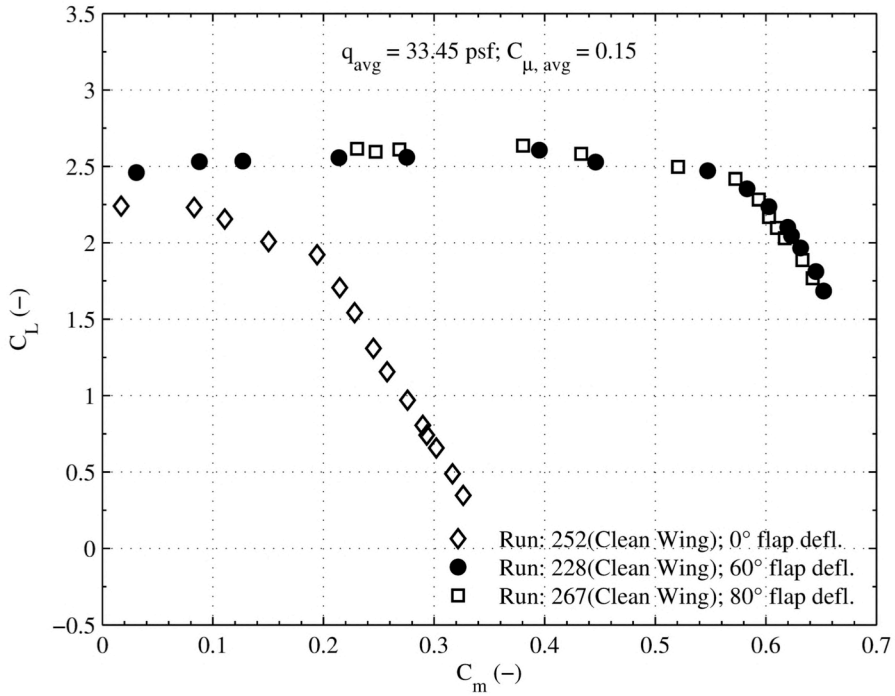

Figure 13.84. Clean wing plot set 3. ***(c) 100 KTS, full slots, C_L vs. C_m.***

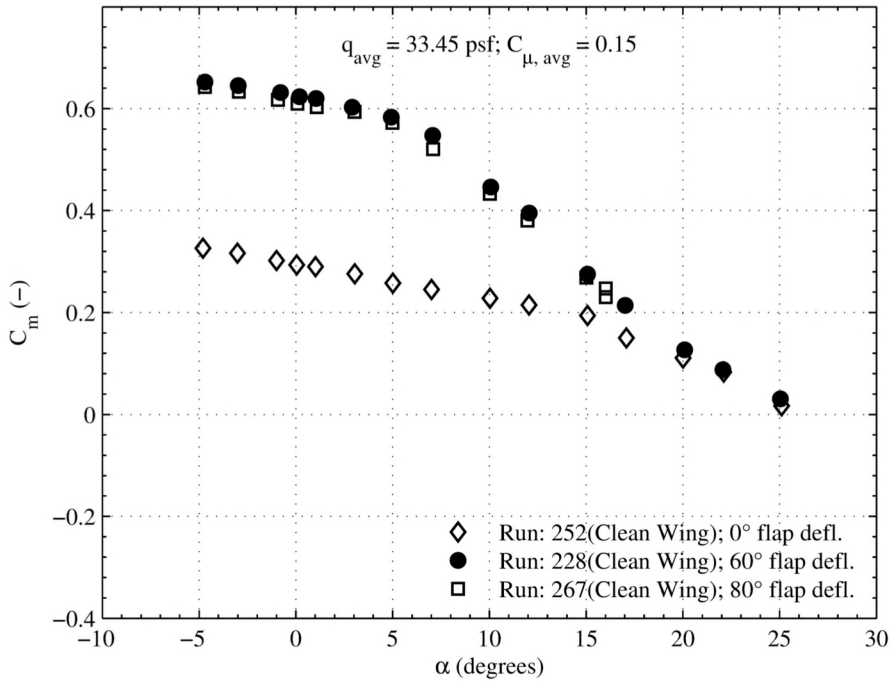

Figure 13.85. Clean wing plot set 3. ***(d) 100 KTS, full slots, C_m vs. α.***

13.4.2. Block Two

Block two plot sets are presented in figures 13.86 – 13.101. The figures show clean wing model performance at several tunnel speeds and flap deflections with data curves corresponding to the off, 2/3, and full slot conditions. Across all plots it is seen that C_L and C_m are increased as C_μ is increased. For positive flap deflections, increasing blowing increases the stall angle. The 0° flap deflection does not show stall before $\alpha = 25°$ for either the 2/3 or full slot runs. Stall happens at a lower angle of attack for higher flap deflections and for increased freestream velocity. 0° flap shows increased slot thrust as C_μ increases. Positive flap deflections show increased drag as C_μ increases. At 100 KTS, the pitching moment polar has a noted negative slope (restoring) that is not shared with the lower speeds.

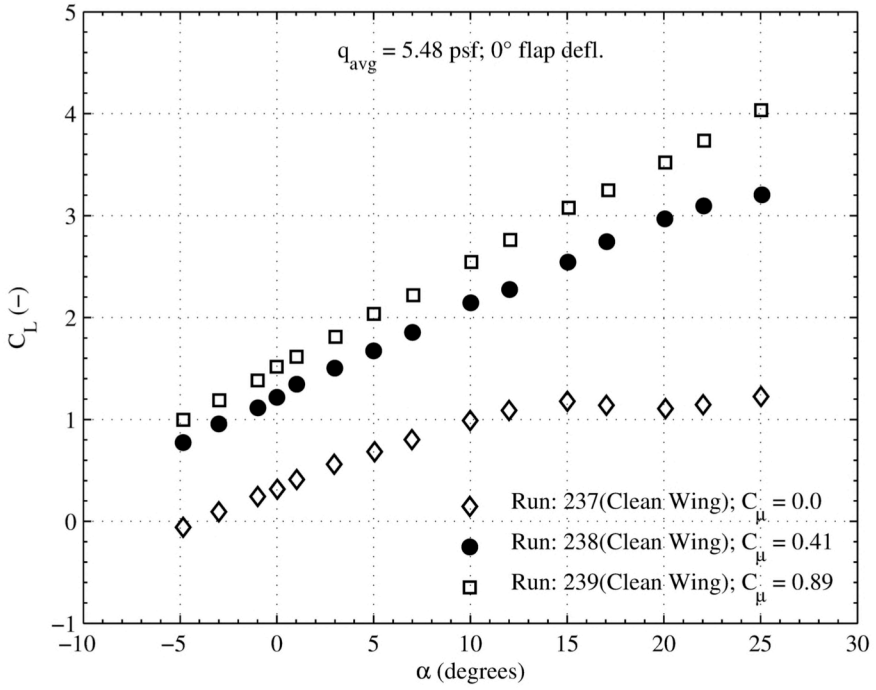

Figure 13.86. Clean wing plot set 4. ***(a) 40 KTS, 0° flap deflection, C_L vs. α.***

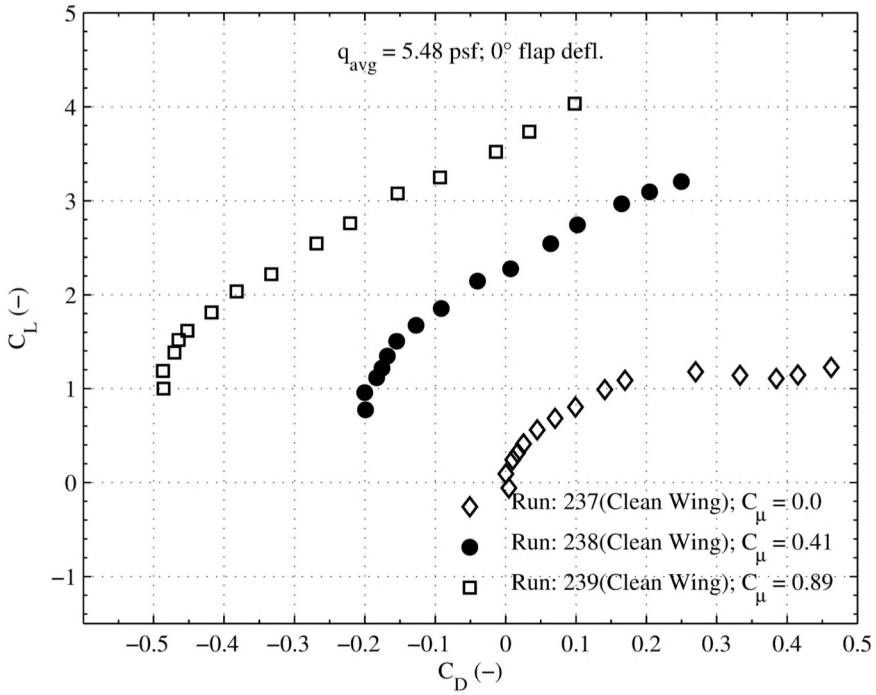

Figure 13.87. Clean wing plot set 4. ***(b) 40 KTS, 0° flap deflection, C_L vs. C_D.***

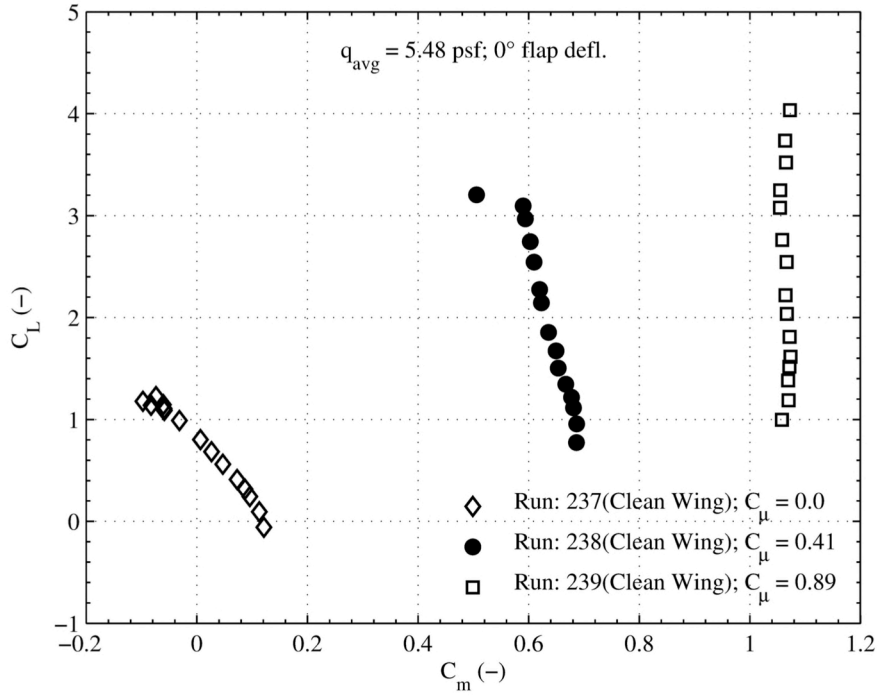

Figure 13.88. Clean wing plot set 4. ***(c) 40 KTS, 0° flap deflection, C_L vs. C_m.***

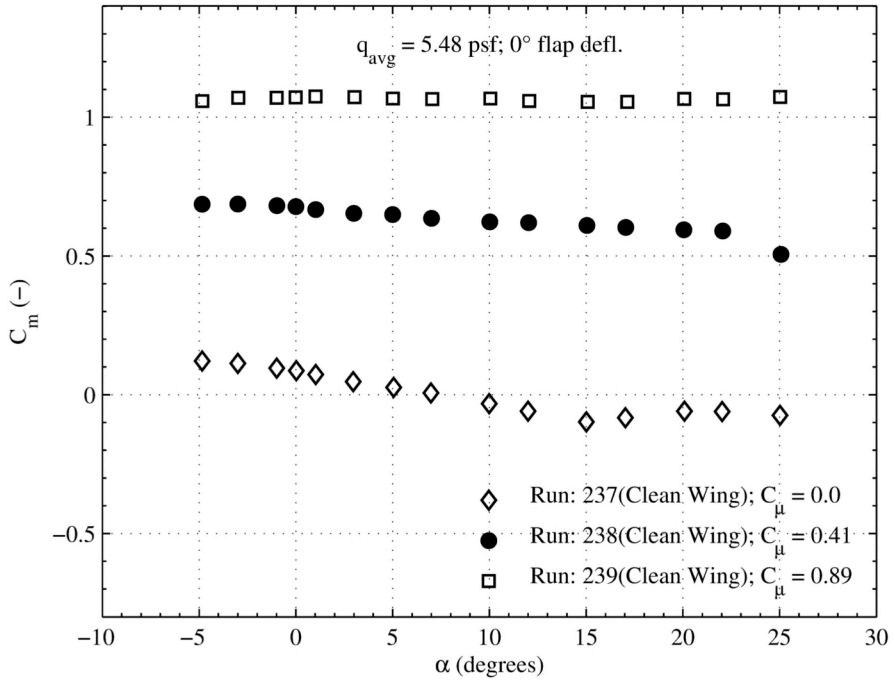

Figure 13.89. Clean wing plot set 4. ***(d) 40 KTS, 0° flap deflection, C_m vs. α.***

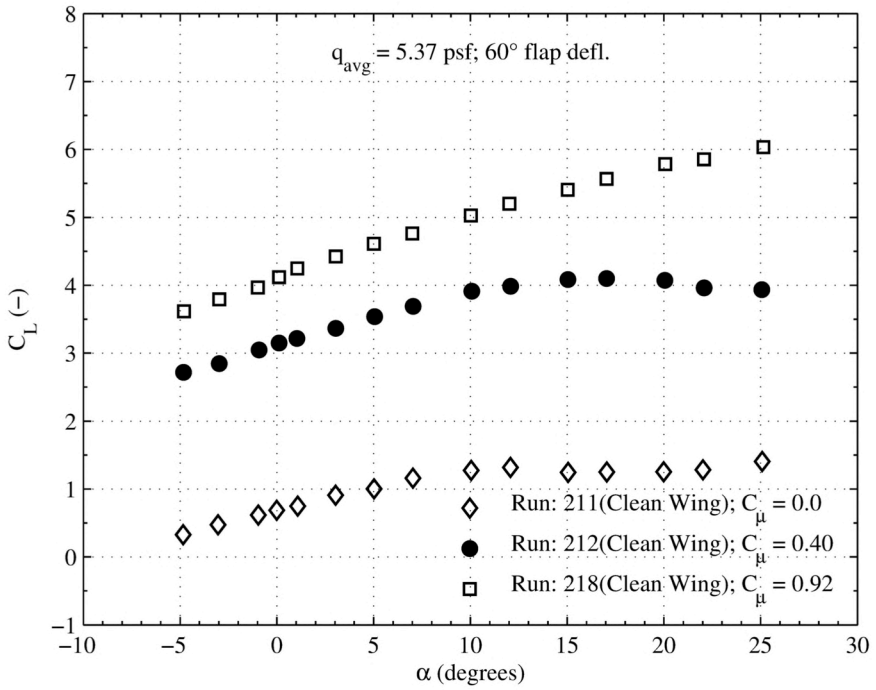

Figure 13.90. Clean wing plot set 5. *(a) 40 KTS, 60° flap deflection, C_L vs. α.*

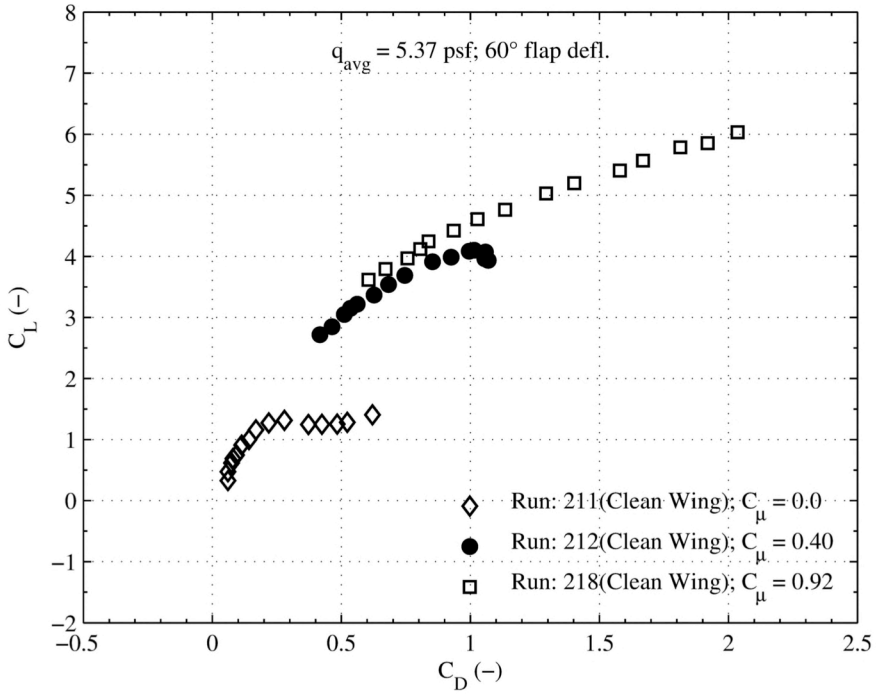

Figure 13.91. Clean wing plot set 5. (b) *40 KTS, 60° flap deflection, C_L vs. C_D.*

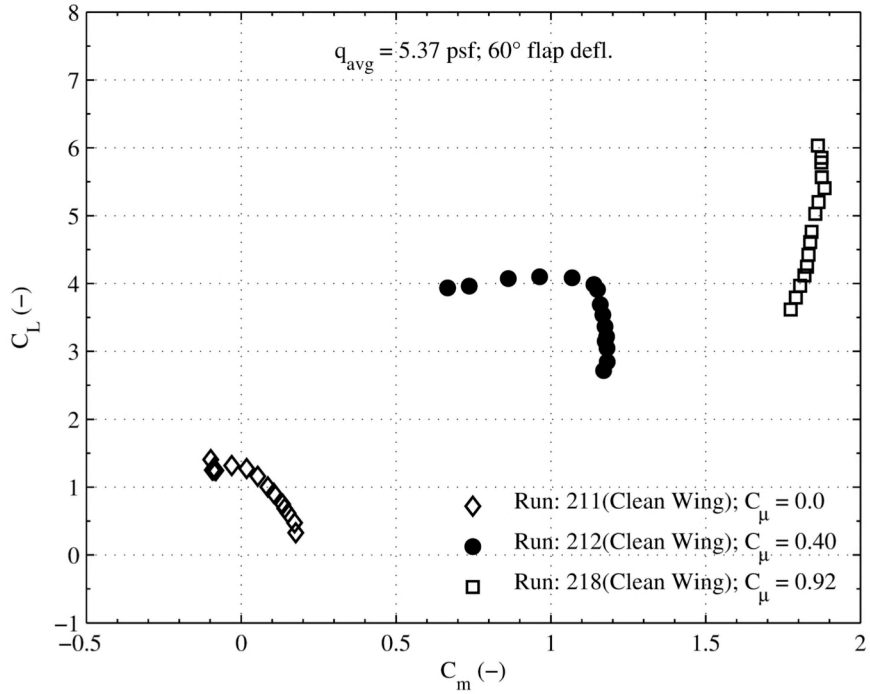

Figure 13.92. Clean wing plot set 5. ***(c) 40 KTS, 60° flap deflection, C_L vs. C_m.***

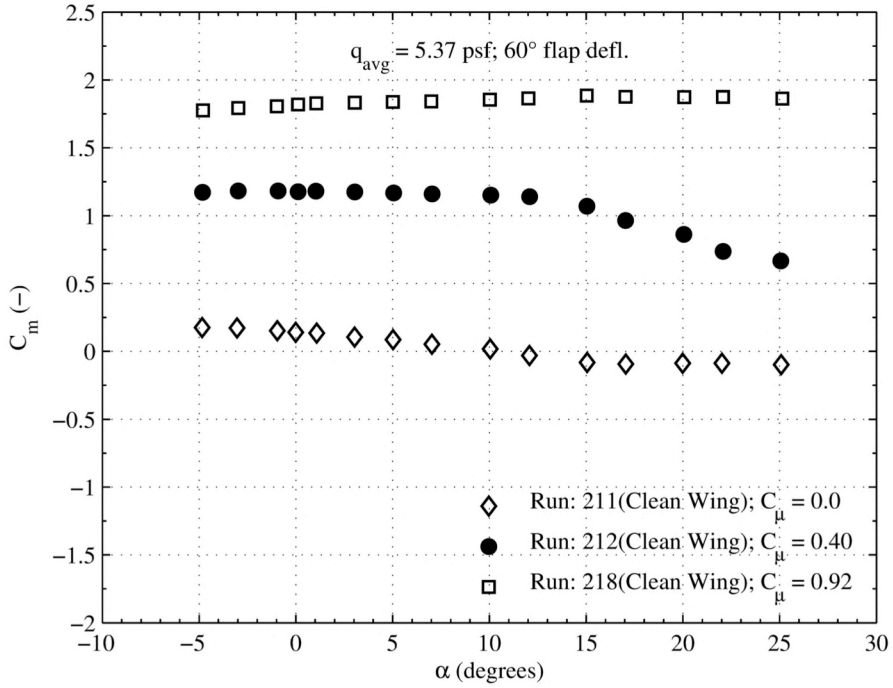

Figure 13.93. Clean wing plot set 5. ***(d) 40 KTS, 60° flap deflection, C_m vs. α.***

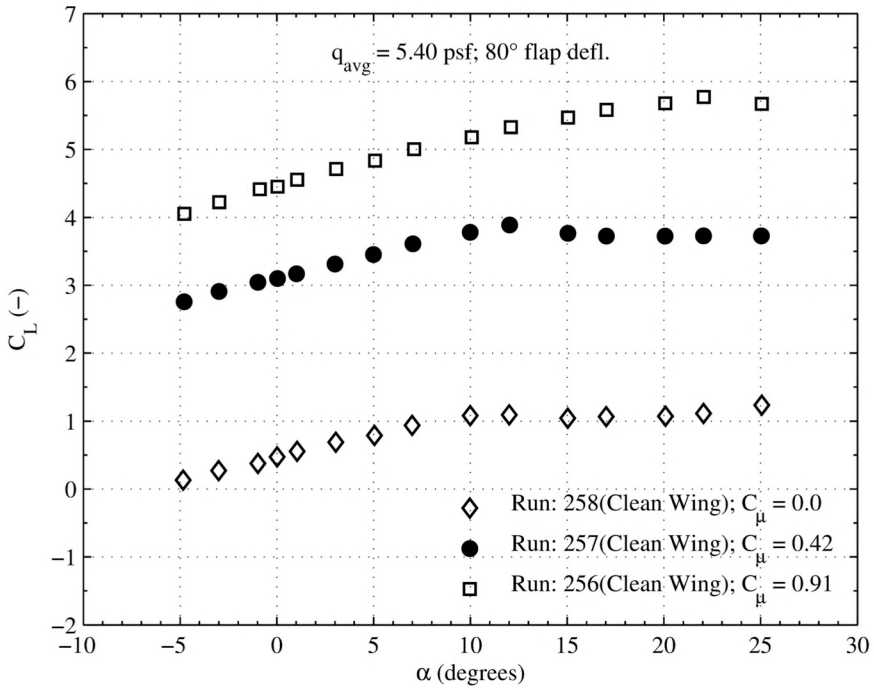

Figure 13.94. Clean wing plot set 6. *(a) 40 KTS, 80° flap deflection, C_L vs. α.*

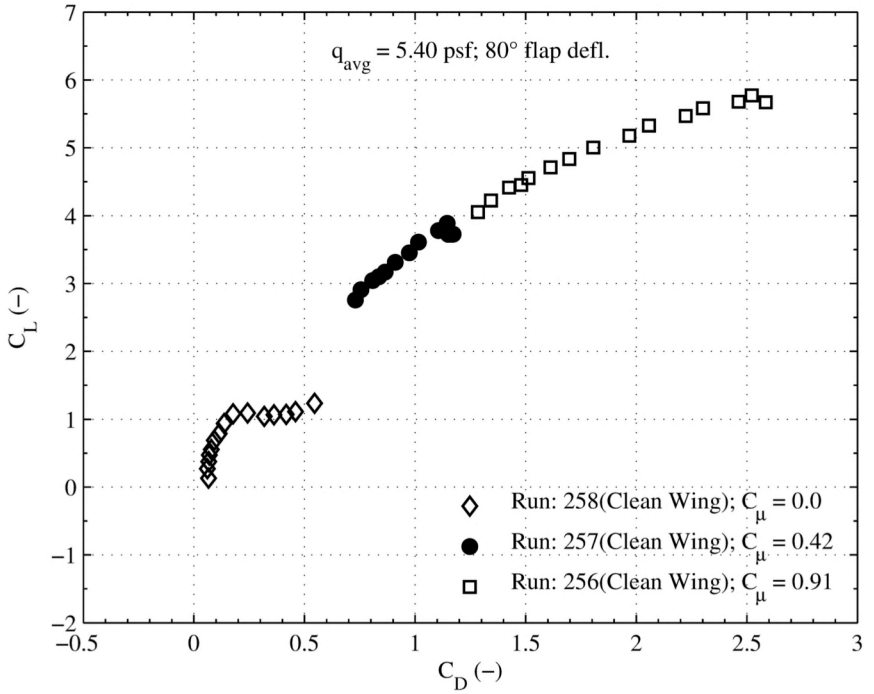

Figure 13.95. Clean wing plot set 6. *(b) 40 KTS, 80° flap deflection, C_L vs. C_D.*

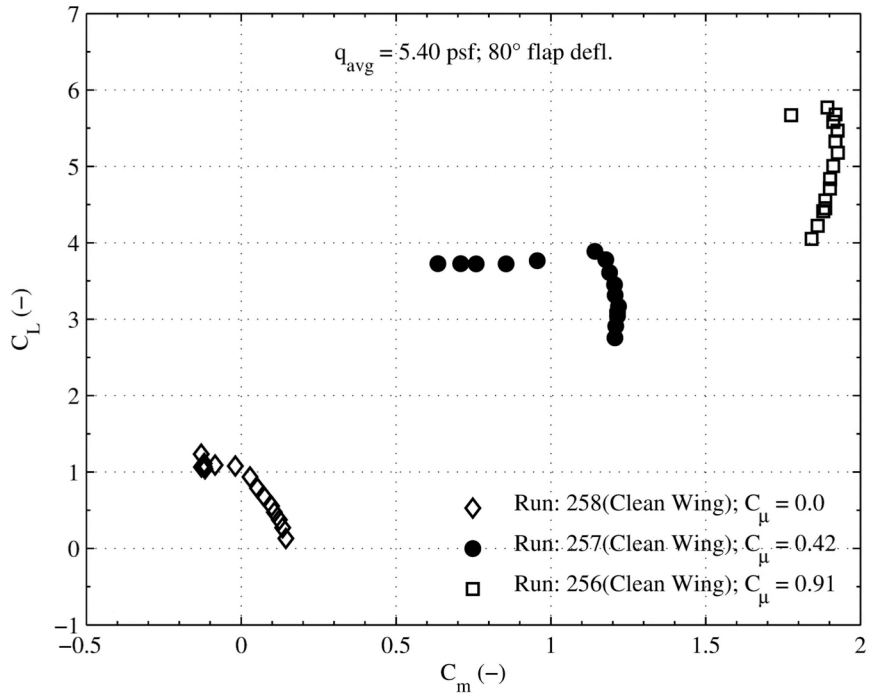

Figure 13.96. Clean wing plot set 6. *(c) 40 KTS, 80° flap deflection, C_L vs. C_m.*

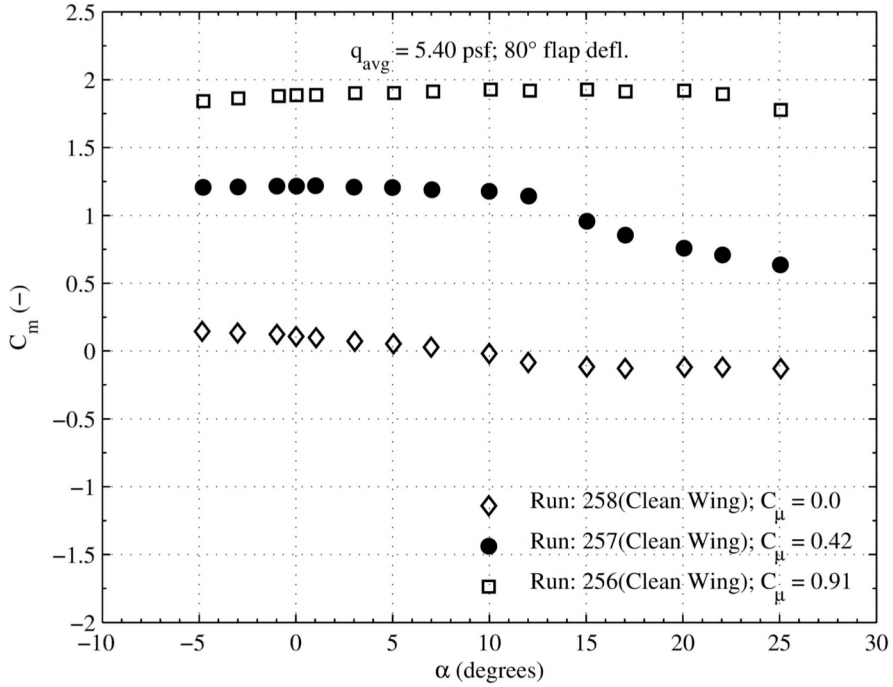

Figure 13.97. Clean wing plot set 6. *(d) 40 KTS, 80° flap deflection, C_m vs. α.*

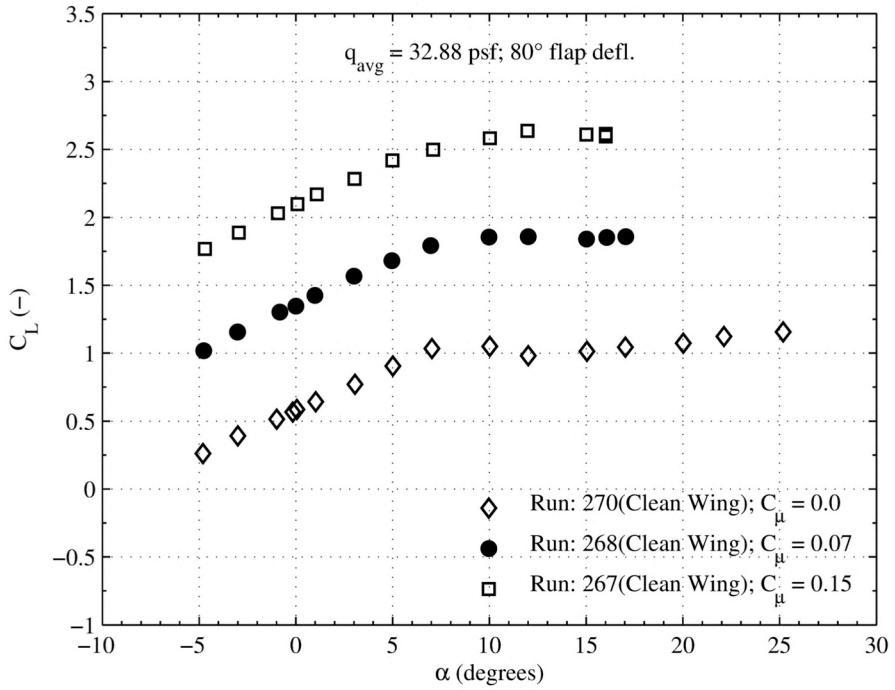

Figure 13.98. Clean wing plot set 7. *(a) 100 KTS, 80° flap deflection, C_L vs. α.*

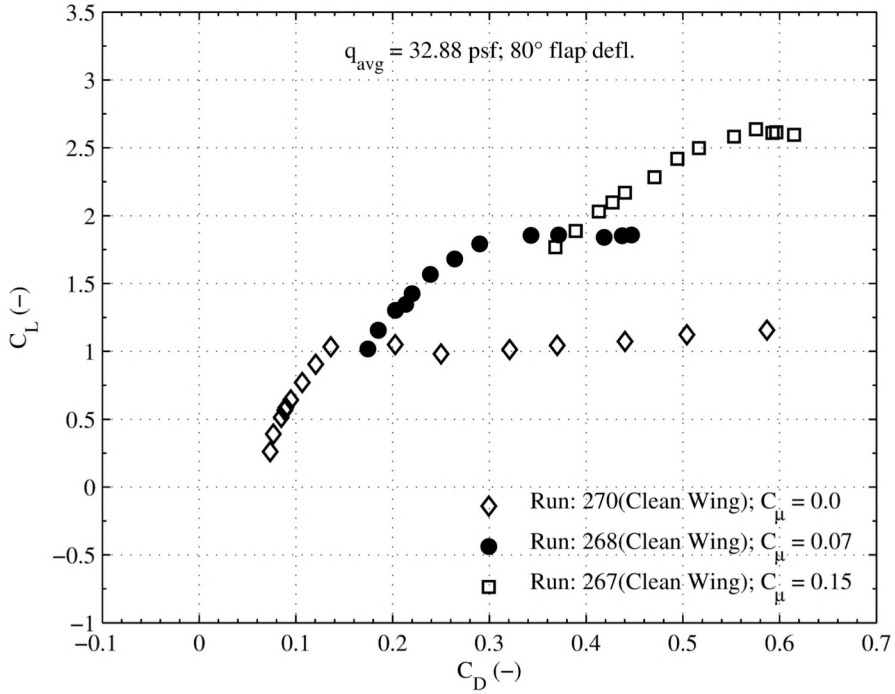

Figure 13.99 Clean wing plot set 7. *(b) 100 KTS, 80° flap deflection, C_L vs. C_D.*

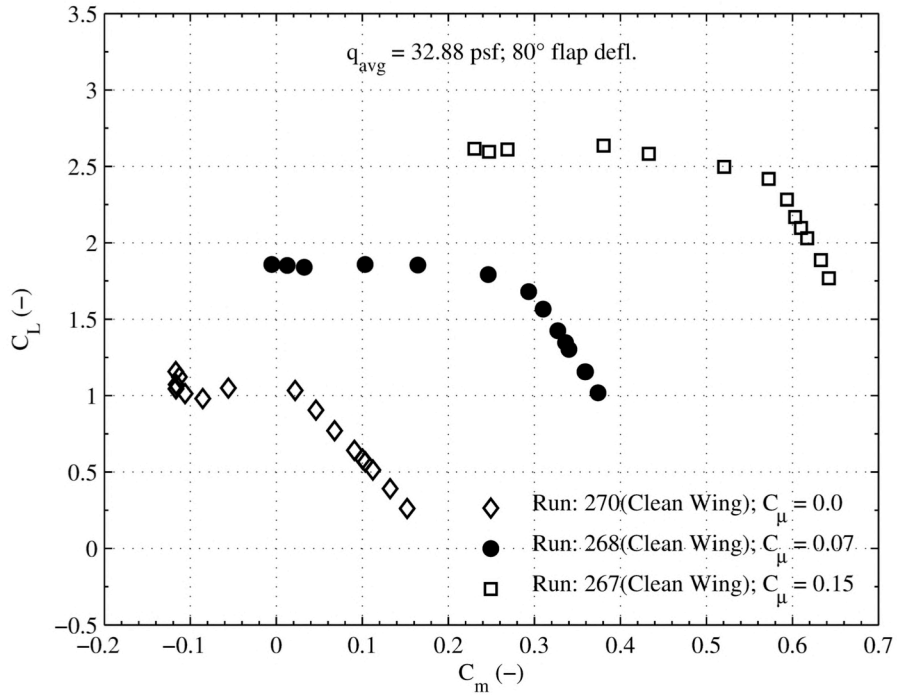

Figure 13.100. Clean wing plot set 7. *(c) 100 KTS, 80° flap deflection, C_L vs. C_m.*

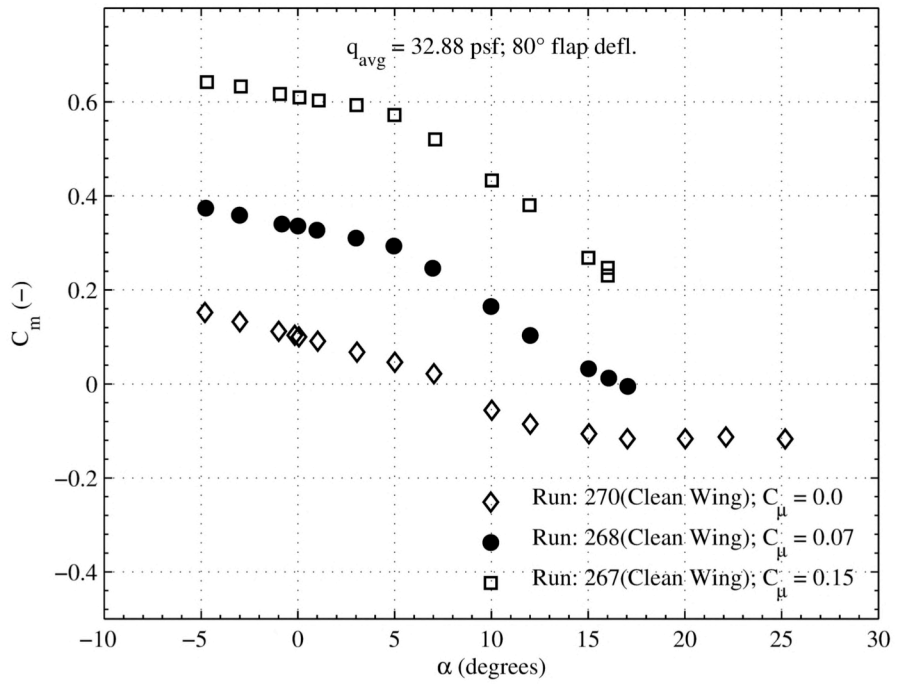

Figure 13.101. Clean wing plot set 7. *(d) 100 KTS, 80° flap deflection, C_m vs. α.*

13.4.3. Block Three

Block three plots are presented in Figure 13.102 through Figure 13.110. The figures provide data from slot sweeps at $\alpha = 0°$ for 40 KTS, 60 KTS, and 100 KTS. At 40 KTS, the 80° flap produces the highest lift as C_μ increases; however, as freestream speed is increased, the 80° flap is unable to maintain the increased lift performance. The 0° flap provides a slot thrust across all freestream speeds; greater slot thrust is achieved as C_μ is increased. For positive flap deflections, drag increases with the flap angle and with increasing C_μ. Looking at the pitching moment plots, increased C_m is seen as C_μ is increased. As expected, the pitching moment trends with respect to the 60° and 80° flap deflections track the trends seen in the lift coefficient plots.

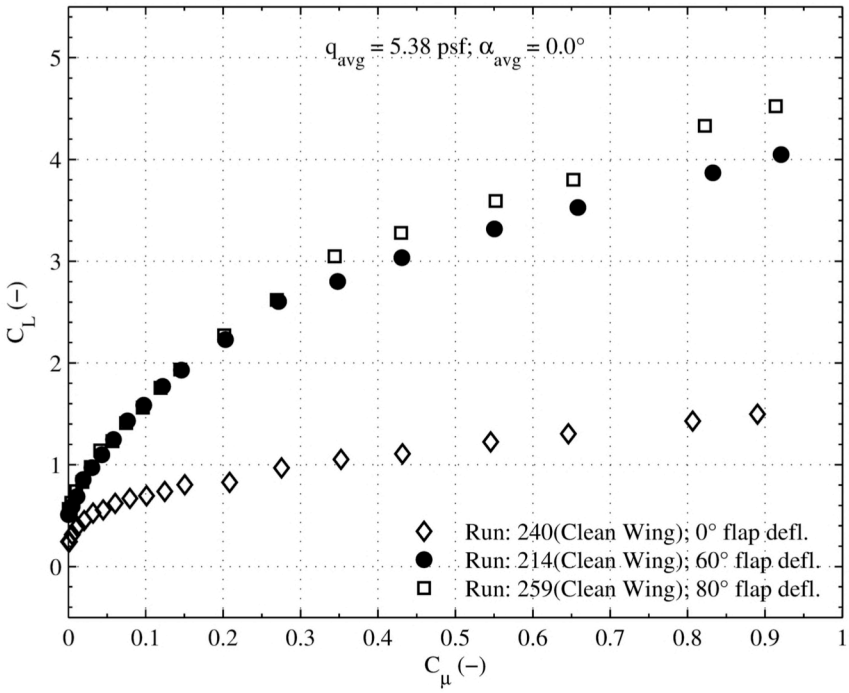

Figure 13.102. Clean wing plot set 8. ***(a) 40 KTS, 0° angle of attack, C_L vs. C_μ.***

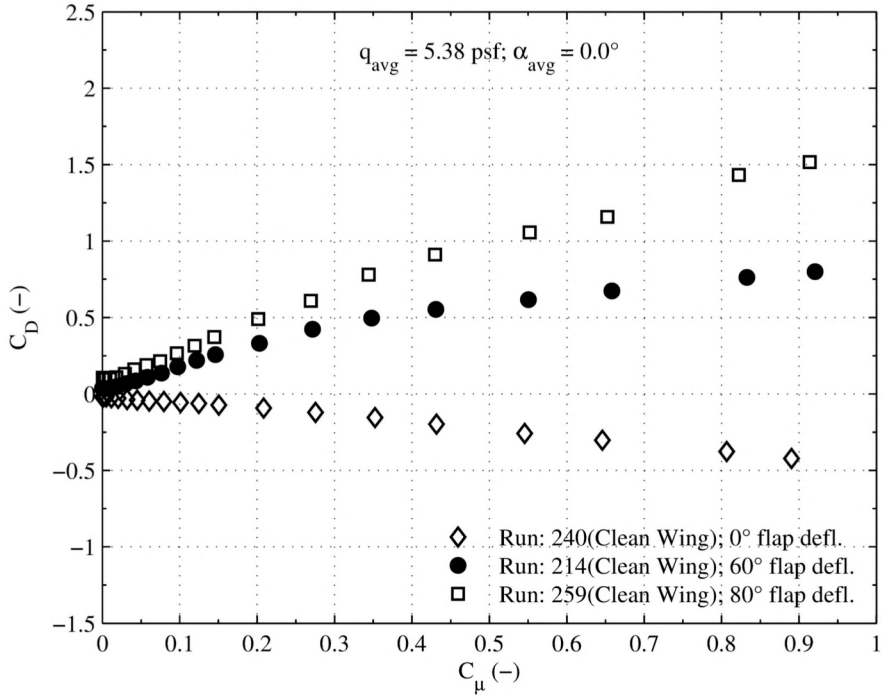

Figure 13.103. Clean wing plot set 8. ***(b) 40 KTS, 0° angle of attack, C_D vs. C_μ.***

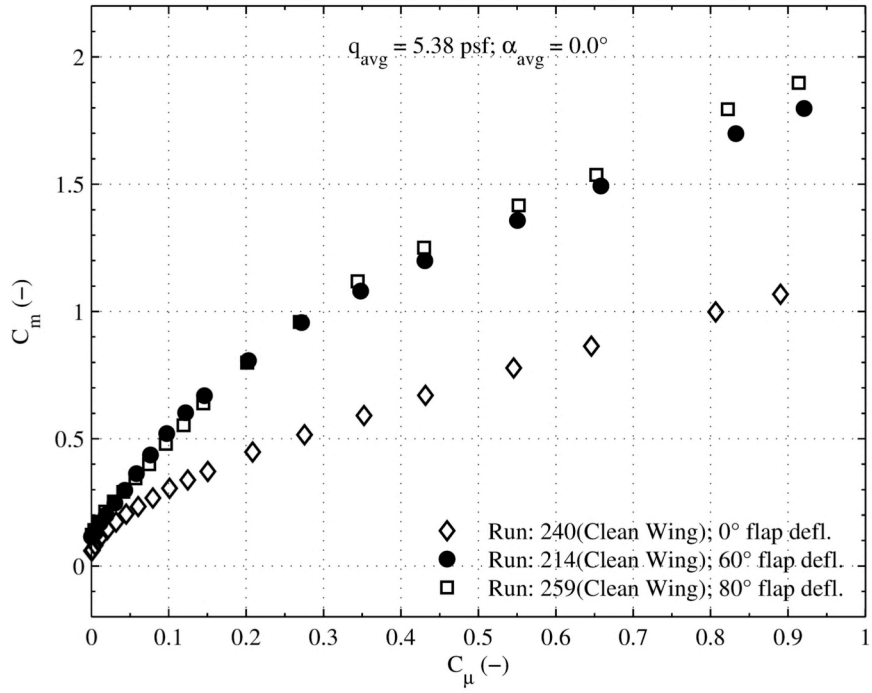

Figure 13.104. Clean wing plot set 8. ***(a) 40 KTS, 0° angle of attack, C_m vs. C_μ.***

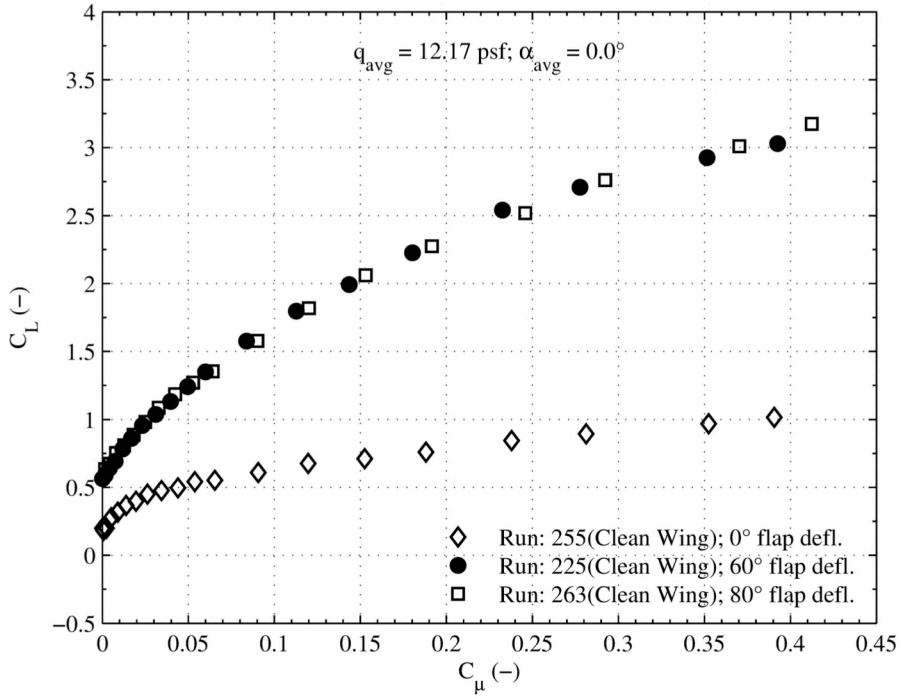

Figure 13.105. Clean wing plot set 9. ***(a) 60 KTS, 0° angle of attack, C_L vs. C_μ.***

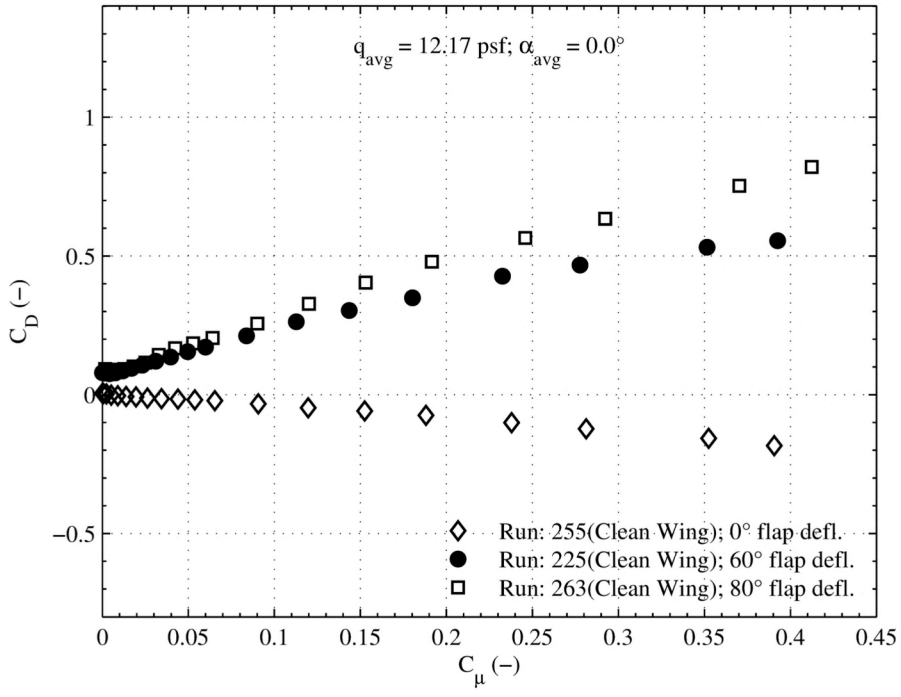

Figure 13.106. Clean wing plot set 9. ***(b) 60 KTS, 0° angle of attack, C_D vs. C_μ.***

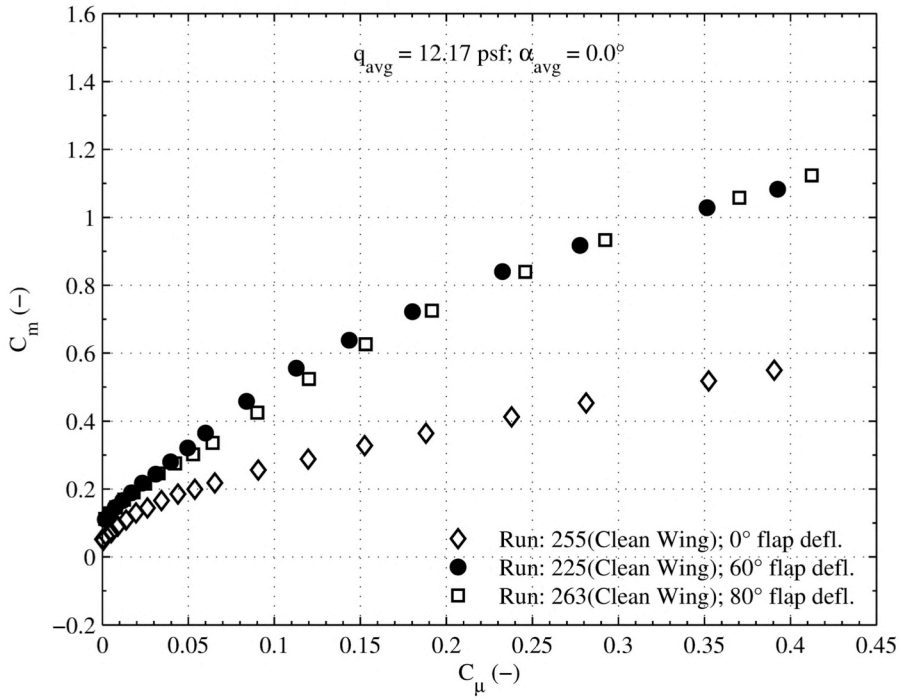

Figure 13.107. Clean wing plot set 9. ***(c) 60 KTS, 0° angle of attack, C_m vs. C_μ.***

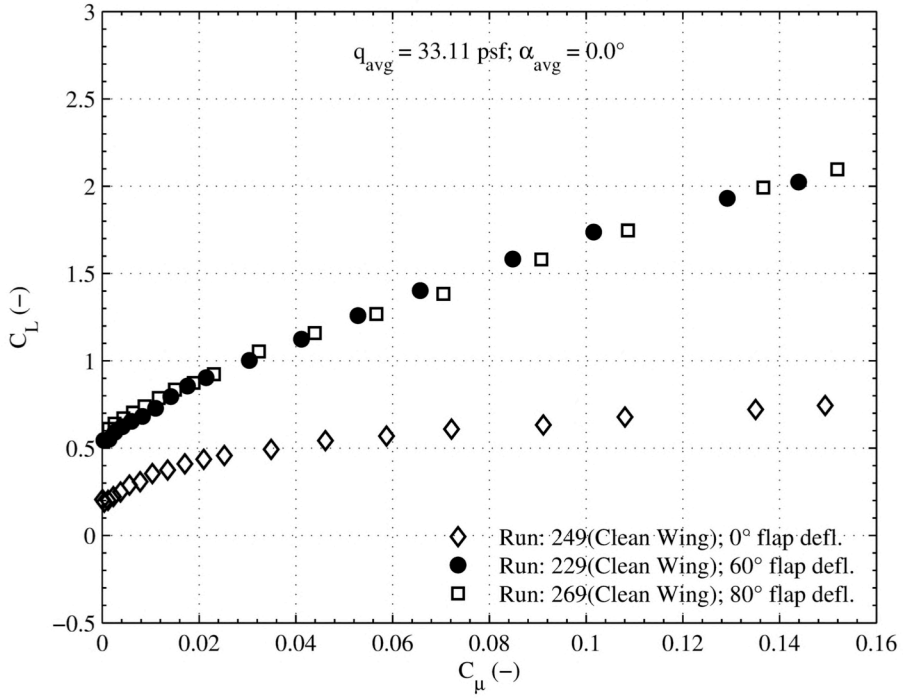

Figure 13.108. Clean wing plot set 10. ***(a) 100 KTS, 0° angle of attack, C_L vs. C_μ.***

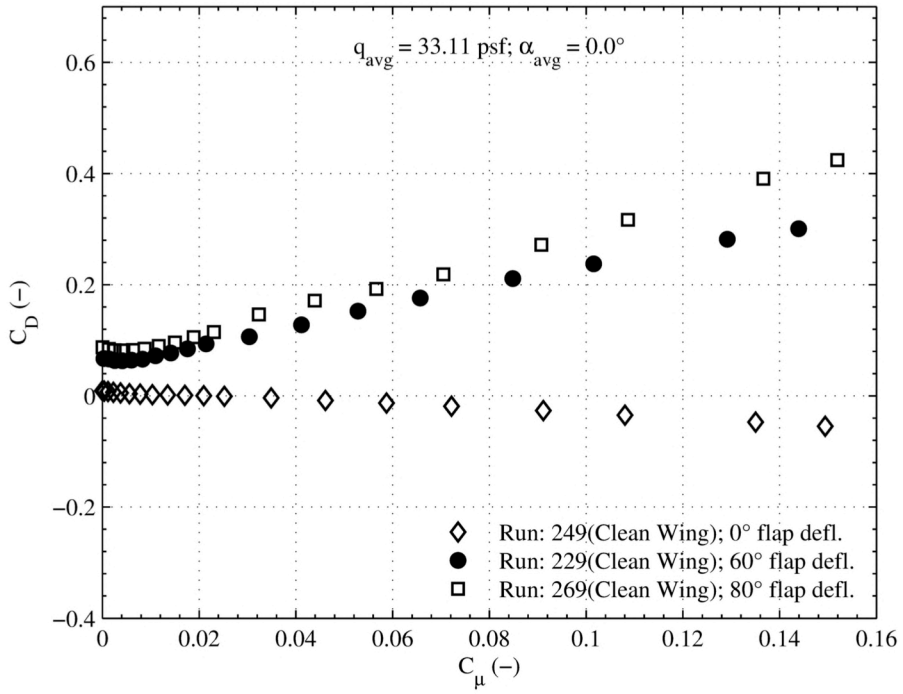

Figure 13.109. Clean wing plot set 10. ***(b) 100 KTS, 0° angle of attack, C_D vs. C_μ.***

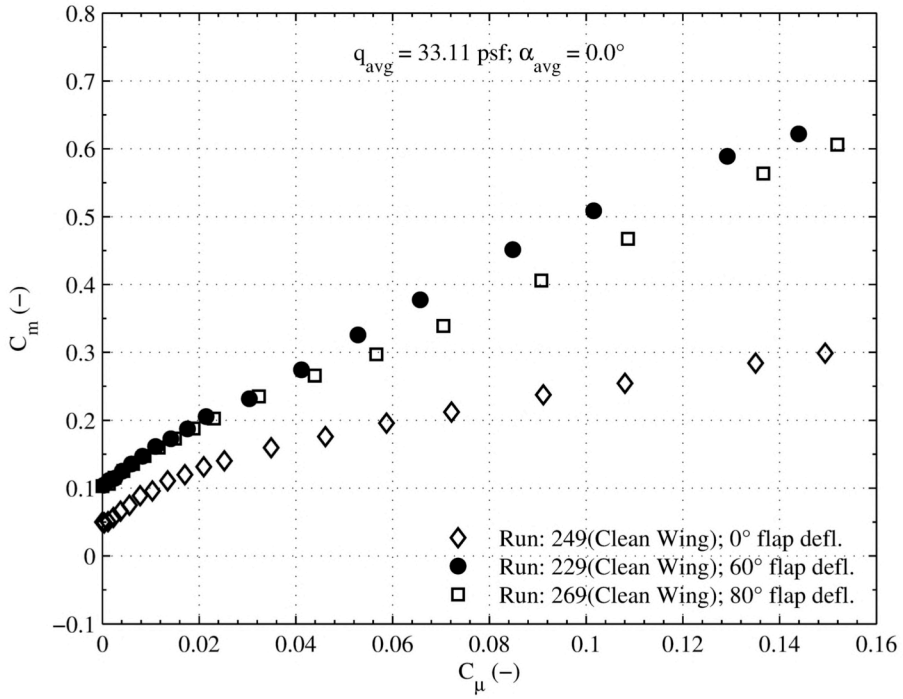

Figure 13.110. Clean wing plot set 10. ***(c) 100 KTS, 0° angle of attack, C_m vs. C_μ.***

13.4.4. Block Four

Figure 13.111 through Figure 13.119 present the plot sets for block four of the clean wing configuration. Data is provided at a fixed freestream speed and flap deflection, with curves for multiple angles of attack. Here, with leading- and trailing-edge blowing, lift continues to increase as angle of attack is increased across all three freestream velocities. The separation control and super circulation regions can be seen in each plot set; at 60 KTS, the separation control region is where $C_\mu < 0.03$ for $\alpha = 0°$. For the 60° flap deflection, drag is positive and increases with C_μ across the three angles of attack. 0° flap data shows trends consistent to what has previously been seen; more slot thrust as C_μ increases and an increase in total drag as angle of attack is increased. Positive drag is seen at $\alpha = 10°$ for the 100 KTS slot sweep. At 40 KTS, pitching moment remains relatively constant across all angle of attack. For the 0° flap, pitching moment decreases with angle of attack and has tends toward $+C_m$ as C_μ increases.

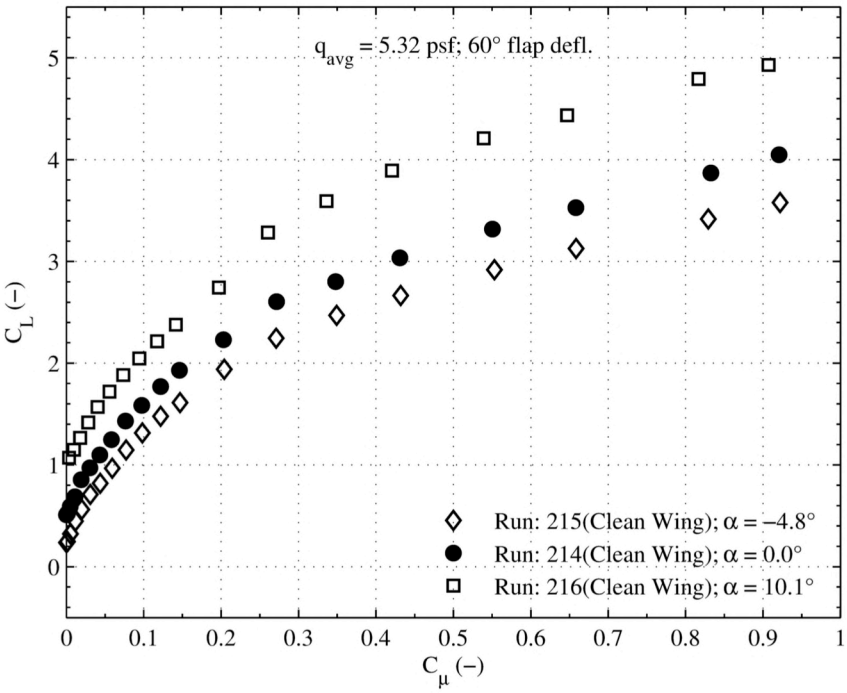

Figure 13.111. Clean wing plot set 11. ***(a) 40 KTS, 60° flap deflection, C_L vs. C_μ.***

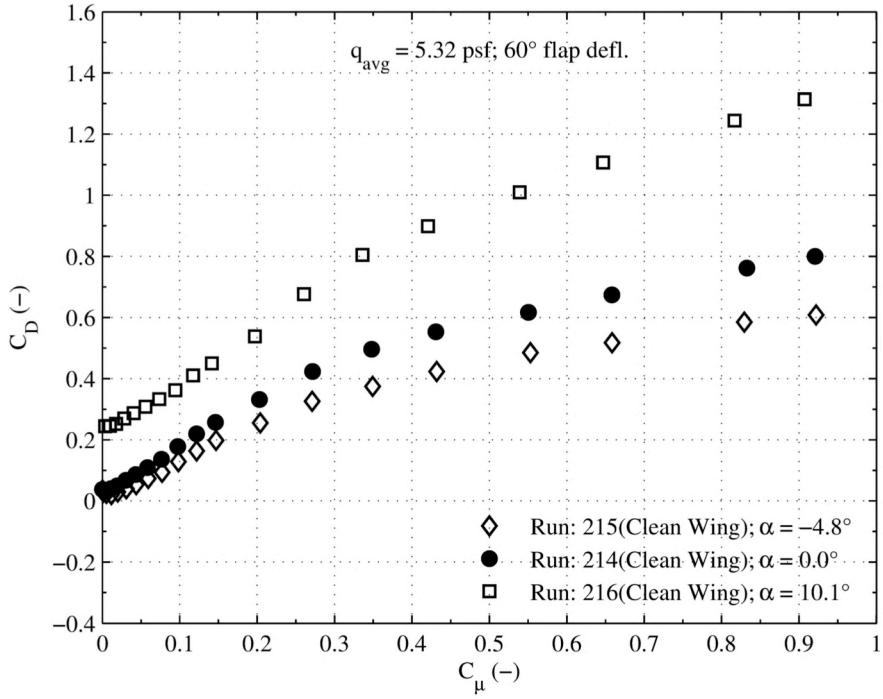

Figure 13.112. Clean wing plot set 11. ***(b) 40 KTS, 60° flap deflection, C_D vs. C_μ.***

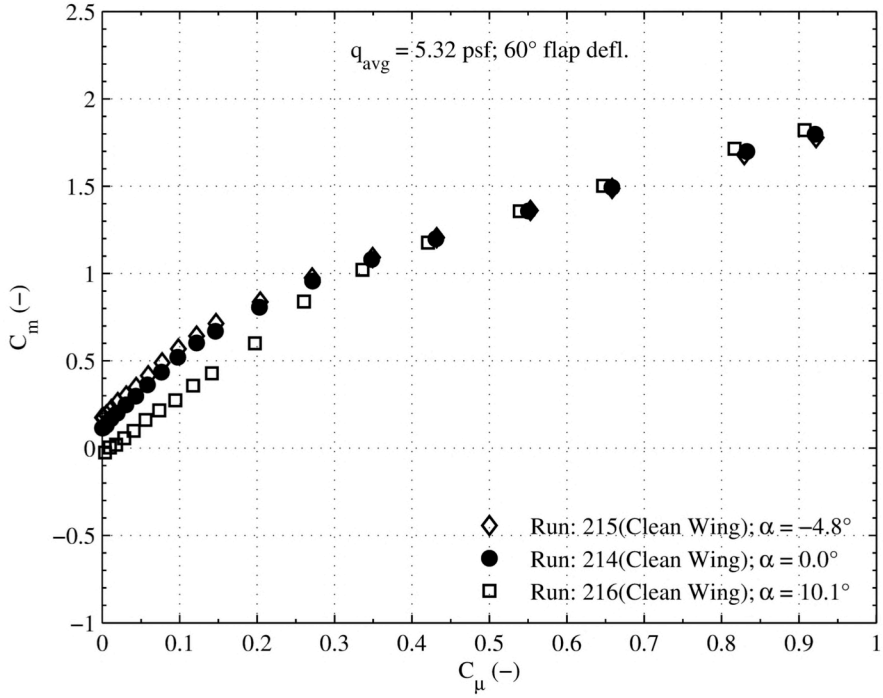

Figure 13.113. Clean wing plot set 11. ***(c) 40 KTS, 60° flap deflection, C_m vs. C_μ.***

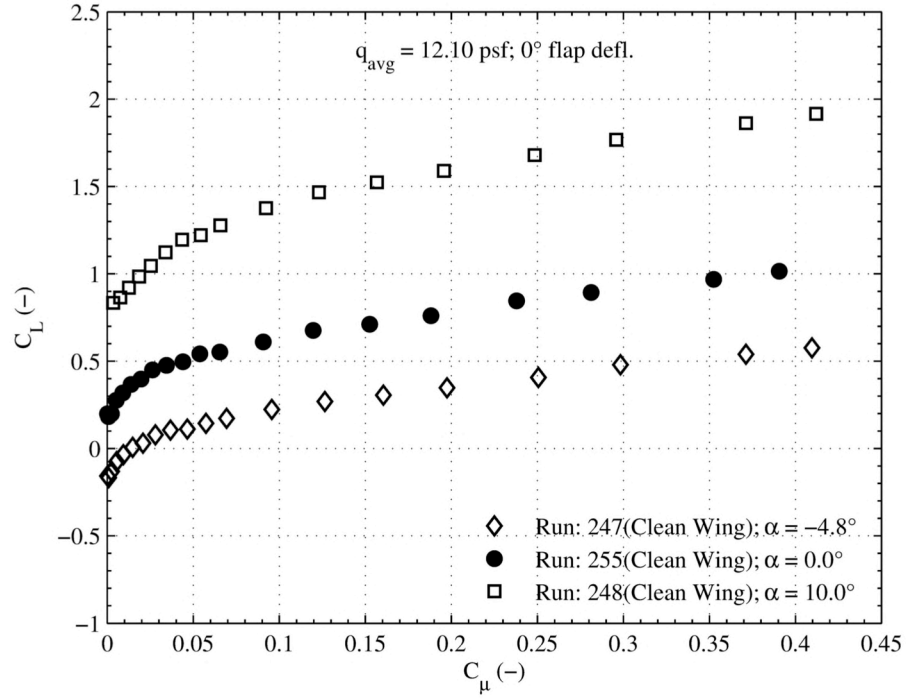

Figure 13.114. Clean wing plot set 12. ***(a) 60 KTS, 0° flap deflection, C_L vs. C_μ.***

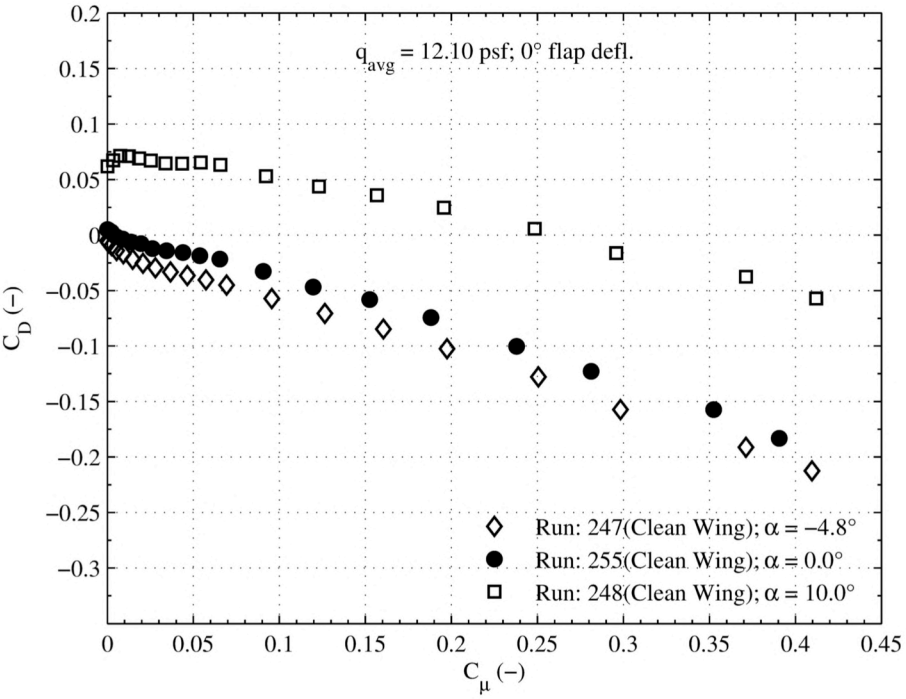

Figure 13.115. Clean wing plot set 12. ***(b) 60 KTS, 0° flap deflection, C_D vs. C_μ.***

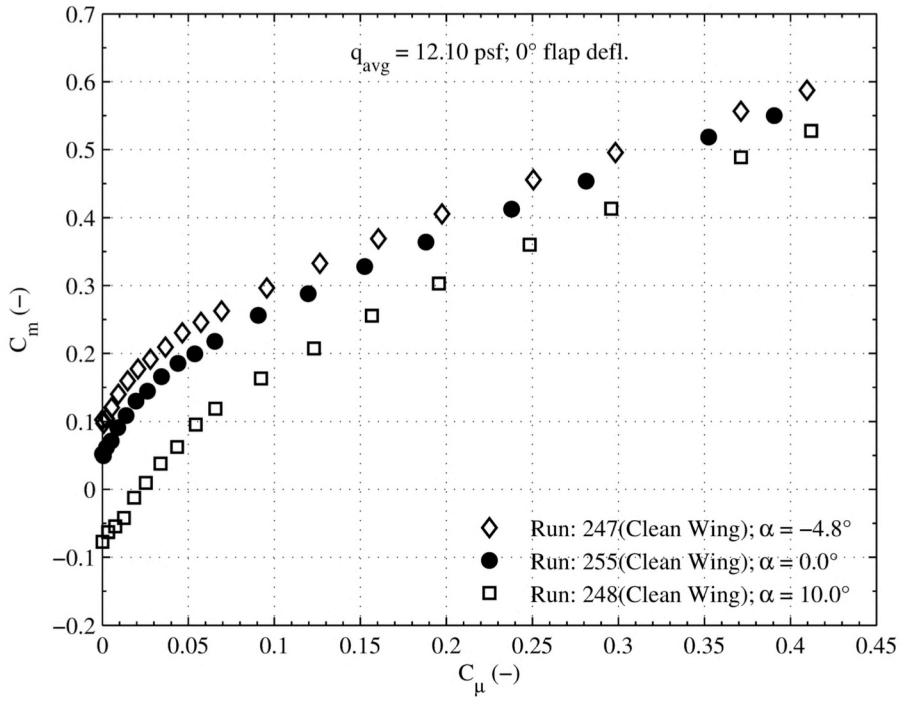

Figure 13.116. Clean wing plot set 12. ***(c) 60 KTS, 0° flap deflection, C_m vs. C_μ.***

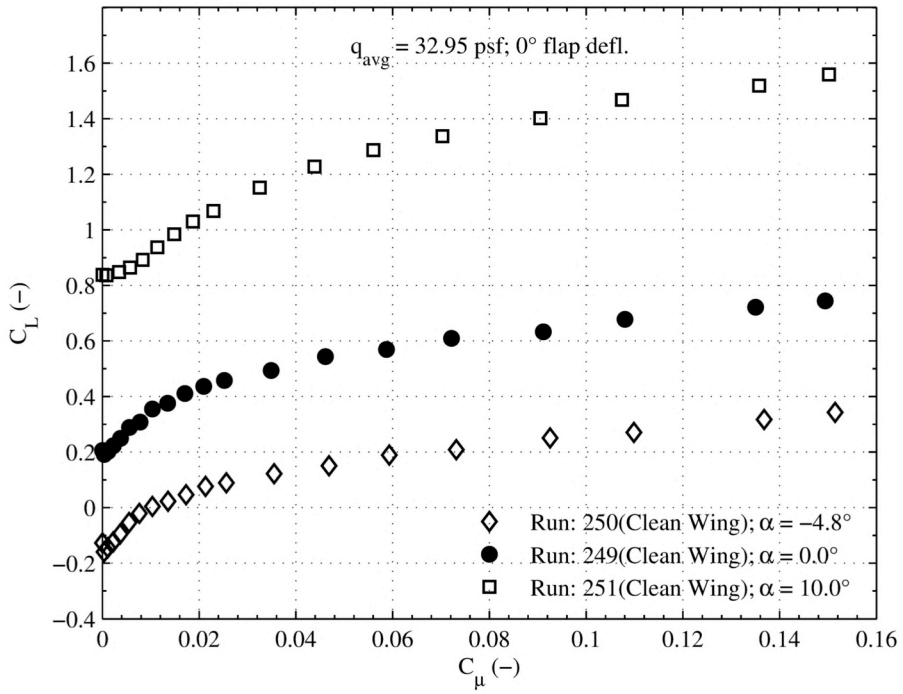

Figure 13.117. Clean wing plot set 13. ***(a) 100 KTS, 0° flap deflection, C_L vs. C_μ.***

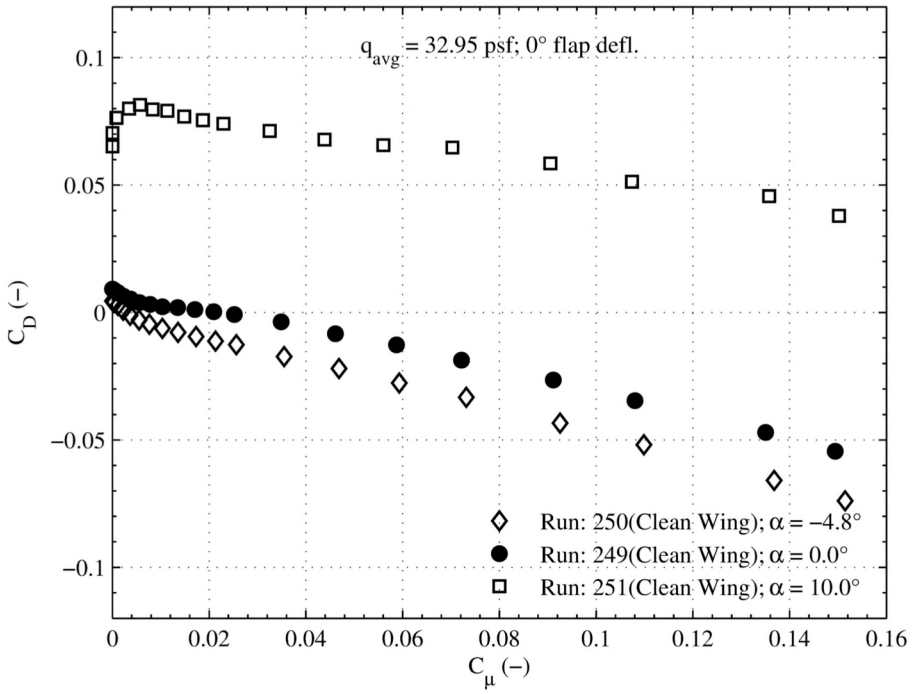

Figure 13.118. Clean wing plot set 13. ***(b) 100 KTS, 0° flap deflection, C_D vs. C_μ.***

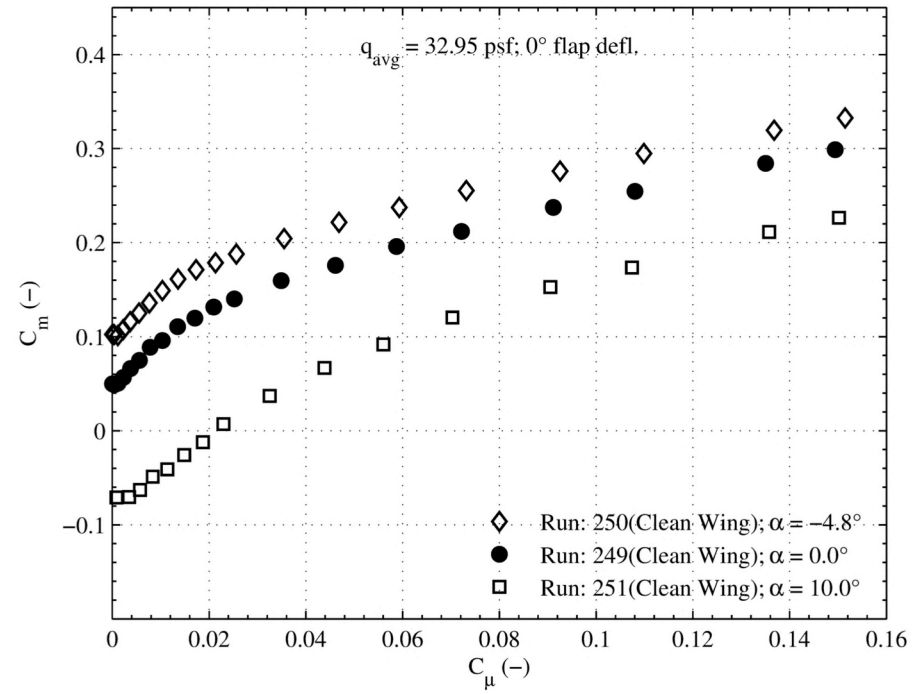

Figure 13.119. Clean wing plot set 13. ***(c) 100 KTS, 0° flap deflection, C_m vs. C_μ.***

13.5. Low Pylon Height

The low pylon configuration was the first configuration tested. Testing in this configuration lasted for a period of 20 wind-on days, wherein 151 useful data runs were acquired. Six critical test points, five oil flow visualization runs, and two smoke flow visualization runs were also completed in this configuration. The results from the oil flow and smoke flow runs are not presented here, but are available with the wind tunnel data set. For safety, the TPS were not in operation during the smoke flow runs.

Some general notes on the figures presented in this configuration. The data are left uncorrected, so the thrust component is present in the data. Because the aerodynamic data is presented in the wind axis-system and drag is aligned parallel to the local freestream, the majority of the thrust component from the TPS units is present in that axis and results in a negative value (often referred to as thrust recovery). The addition of the engine thrust increases the lift curve slope because it includes the thrust coefficient component, $C_T*\sin(\alpha+\delta_{jet})$. The increase in lift when the engine simulators are on is not so much due to the thrust deflection angle, but more due to the increased wing upper surface velocities and resulting increased negative static pressures. In general though, larger lift augmentation is achieved from increasing C_μ rather than increasing C_T. The data will show that even at high angles of attack, the addition of leading-edge blowing alone is not enough to prevent wing stall.

13.5.1. Block One

Low pylon block one plots are presented in Figure 13.120 through Figure 13.147. The plots present aerodynamic data for varying flap deflections at a fixed tunnel and power condition. Figure 13.120 through 13.123 and Figure 13.135 through 13.139 present un-powered data at 40 KTS and 100 KTS; the two figure sets show similar trends. The lift curve shows increased lift with flap deflection due to increased airfoil camber. The positive flap deflections show similar stall behavior, believed to be flap stall, which occurs around 10°-12° for the 40 KTS data, and 7° for the 100 KTS data. Drag polars show expected trends: increasing drag as flap deflection is increased. Pitching moment curves have a negative slope and pitching moment decreases as angle of attack increases.

Figures 23 and 26 present data from slots off, full TPS alpha-sweeps. Here, the lift benefit from the TPS can be seen at higher angles of attack, where the un-powered data showed stall. Drag data is negative because it is uncorrected and has the TPS thrust component in it. The TPS adds an almost constant offset to the pitching moment. At 40 KTS, the pitching moment caused by the TPS is greater than the restoring tendency of the model as angle of attack is increased. The model does not reach trim by $\alpha = 25°$, but does so at the 100 KTS case.

Figures 24 and 28 present full power alpha-sweeps at 40 KTS and 100 KTS. With the TPS on at high blowing and angle of attack, the 80° flap cannot maintain lift augmentation over the 60° flap. The low pylon doesn't appear overly strong at deflecting engine exhaust at high flap deflections. This is predominately seen at higher speeds where stall is seen in the 10°-12° range. For the 60° flap at 100 KTS, the addition of the TPS thrust delays stall from 7° to 13°. Slot thrust adds to the negative drag component for the 0° flap deflection. As seen with the clean wing configuration, drag and pitching moment increase as the flap deflection increases.

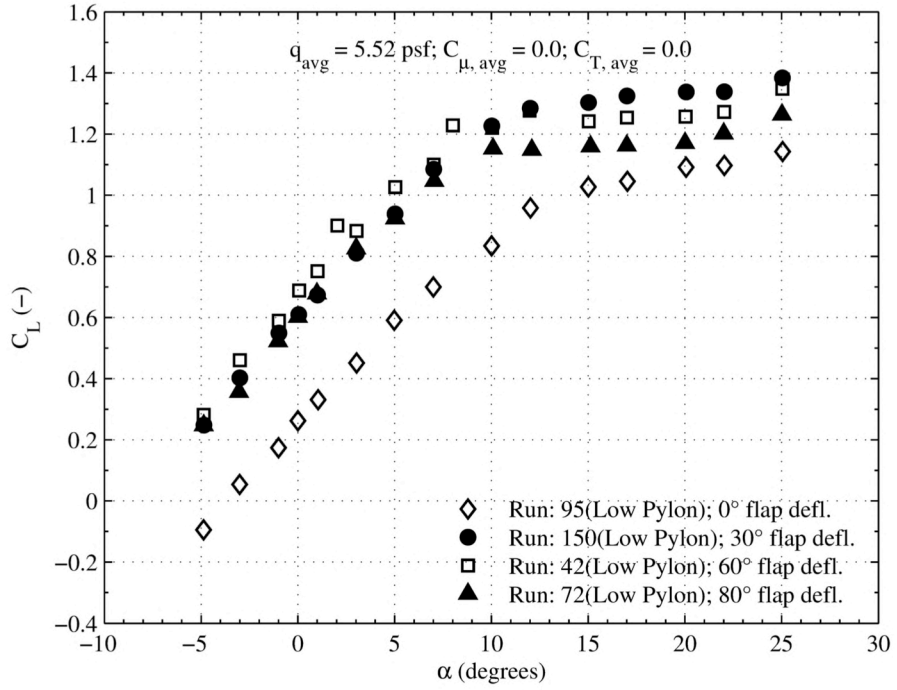

Figure 13.120. Low pylon plot set 1. ***(a) 40 KTS, no power, C_L vs. α.***

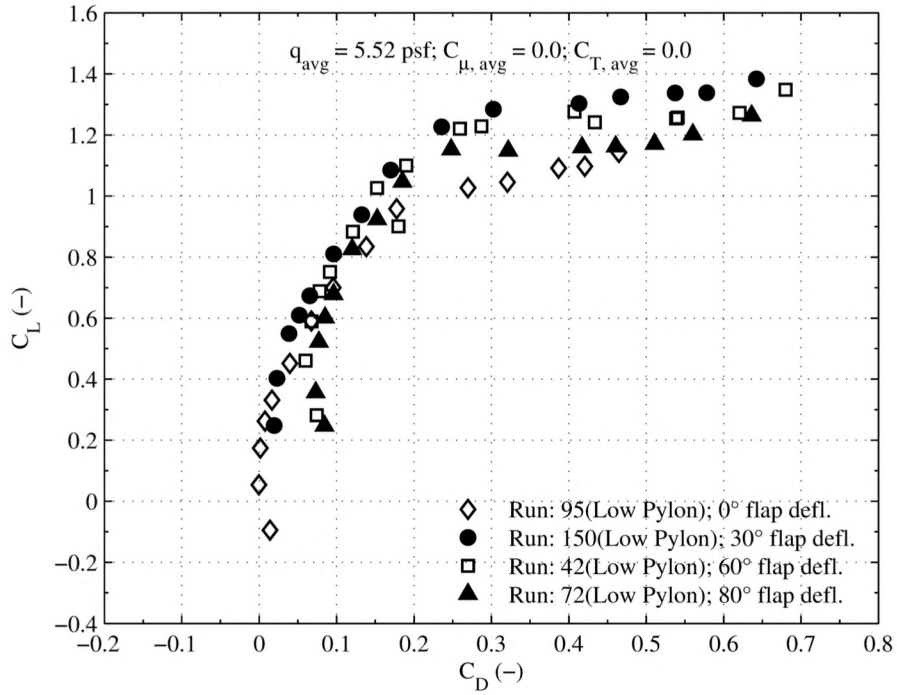

Figure 13.121. Low pylon plot set 1. ***(b) 40 KTS, no power, C_L vs. C_D.***

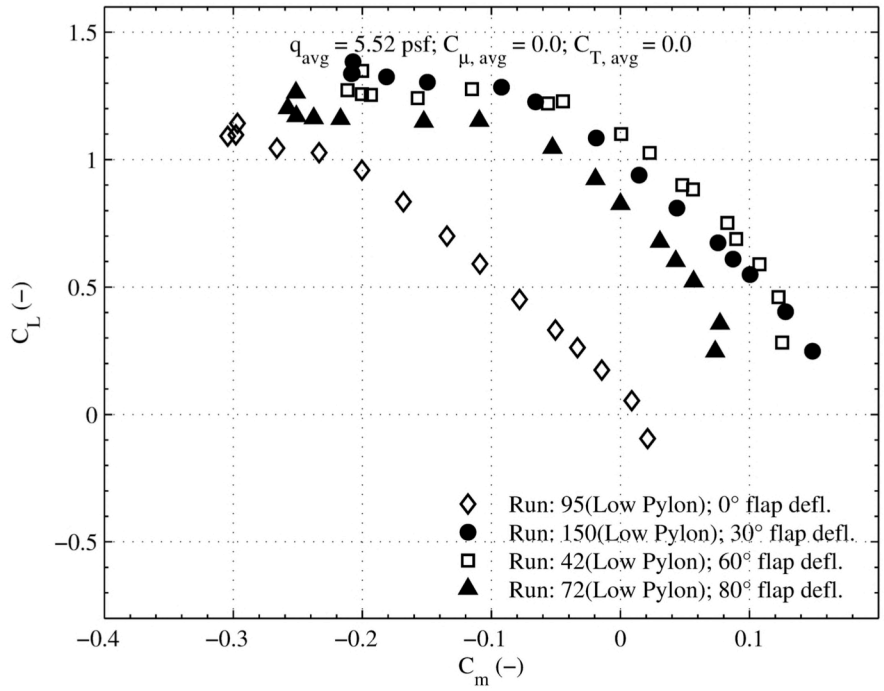

Figure 13.122. Low pylon plot set 1. ***(c) 40 KTS, no power, C_L vs. C_m.***

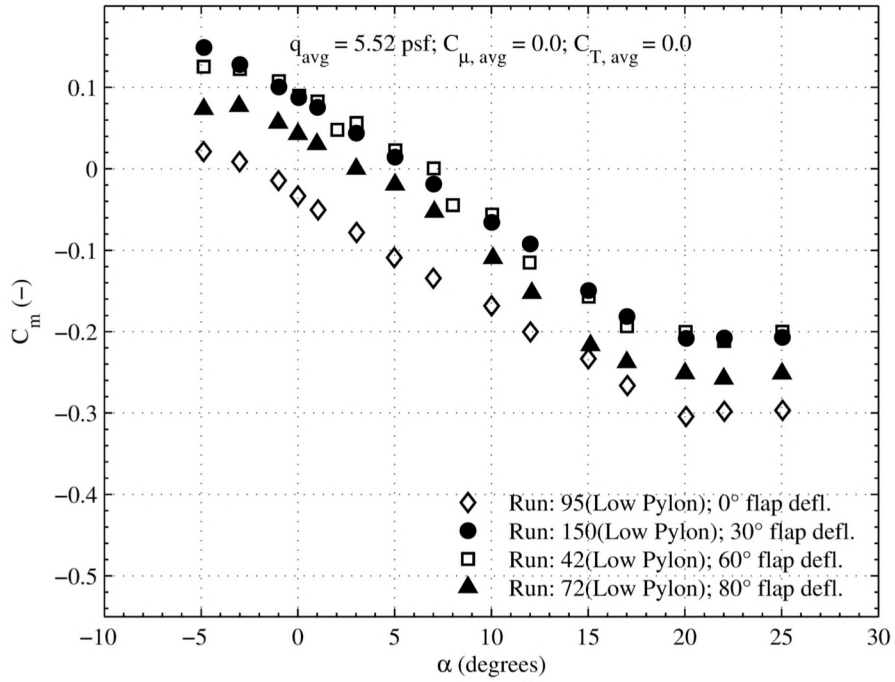

Figure 13.123. Low pylon plot set 1. ***(d) 40 KTS, no power, C_m vs. α.***

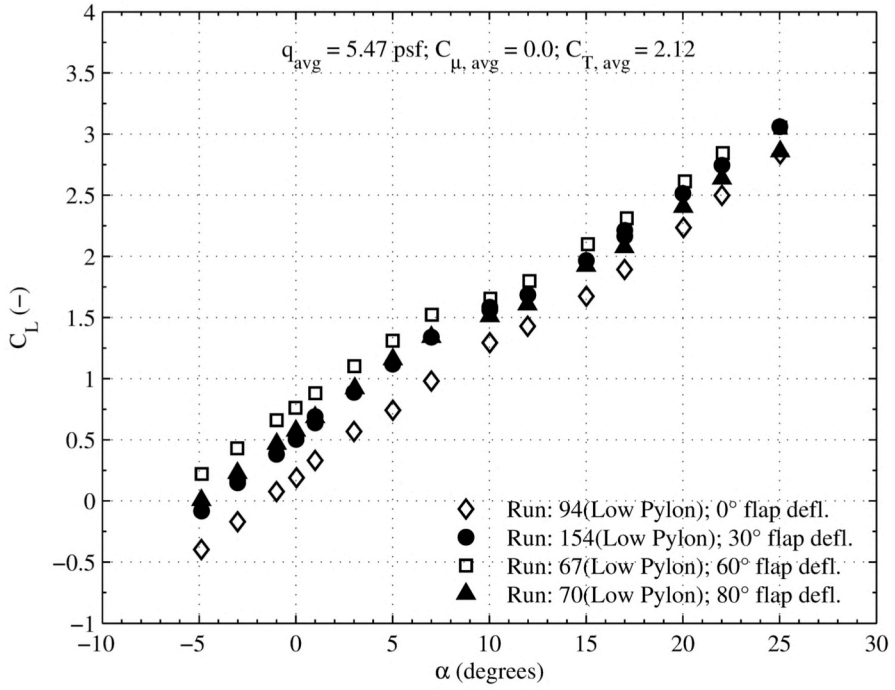

Figure 13.124. Low pylon plot set 2. ***(a) 40 KTS, no slots, full TPS, C_L vs. α.***

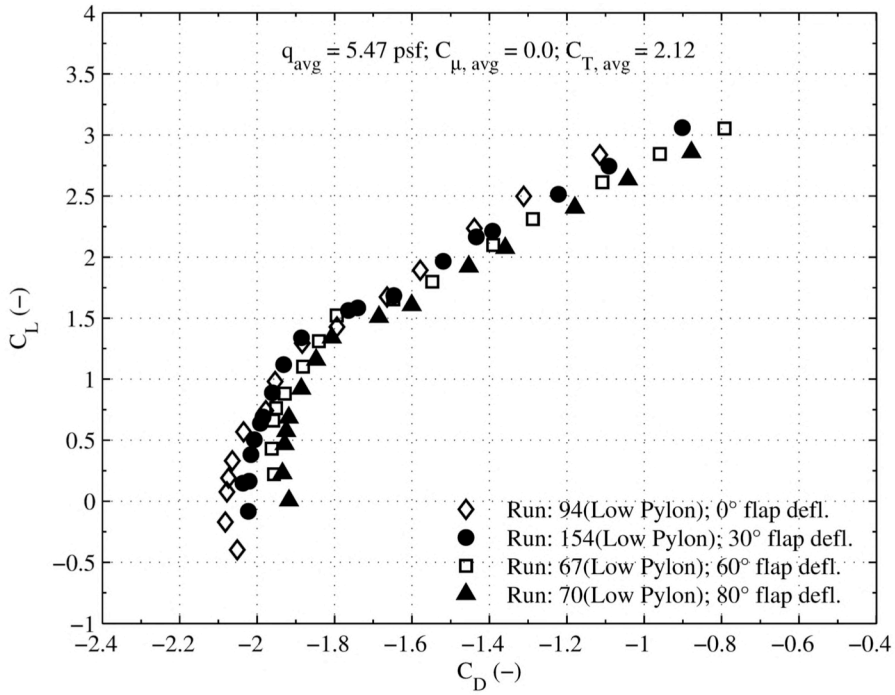

Figure 13.125. Low pylon plot set 2. ***(b) 40 KTS, no slots, full TPS, C_L vs. C_D.***

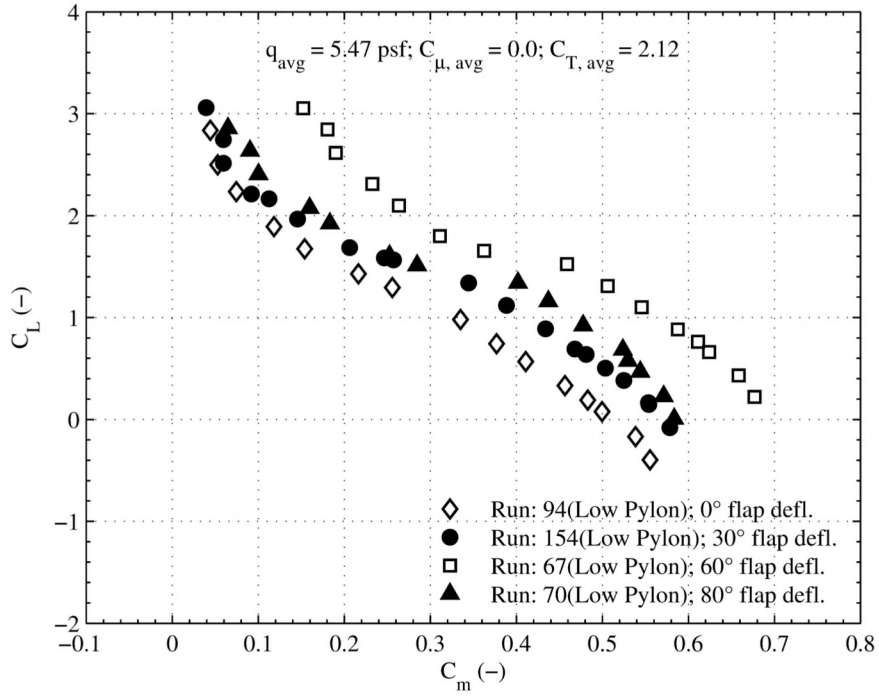

Figure 13.126. Low pylon plot set 2. ***(c) 40 KTS, no slots, full TPS, C_L vs. C_m.***

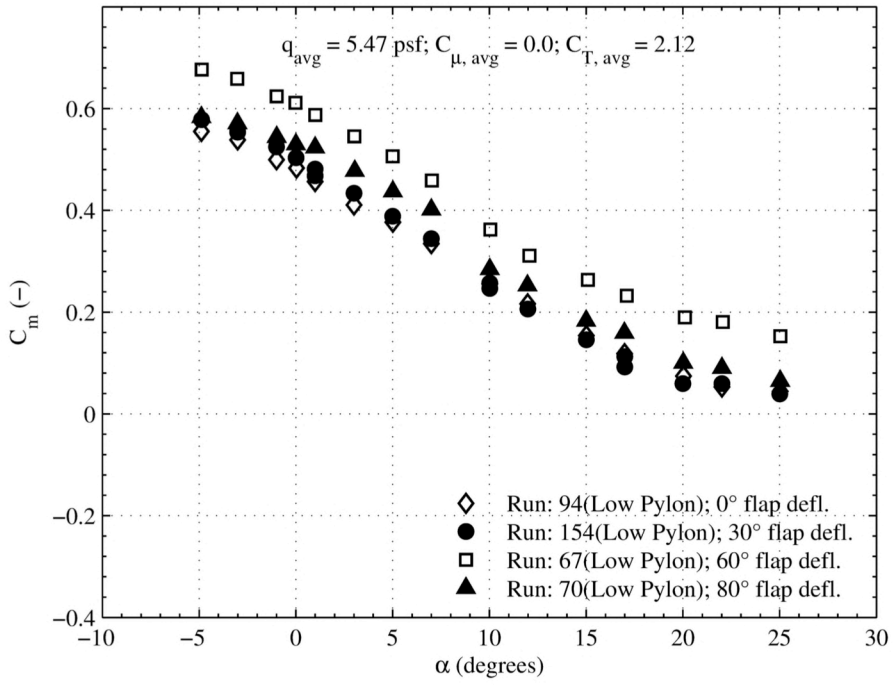

Figure 13.127. Low pylon plot set 2. ***(d) 40 KTS, no slots, full TPS, C_m vs. α.***

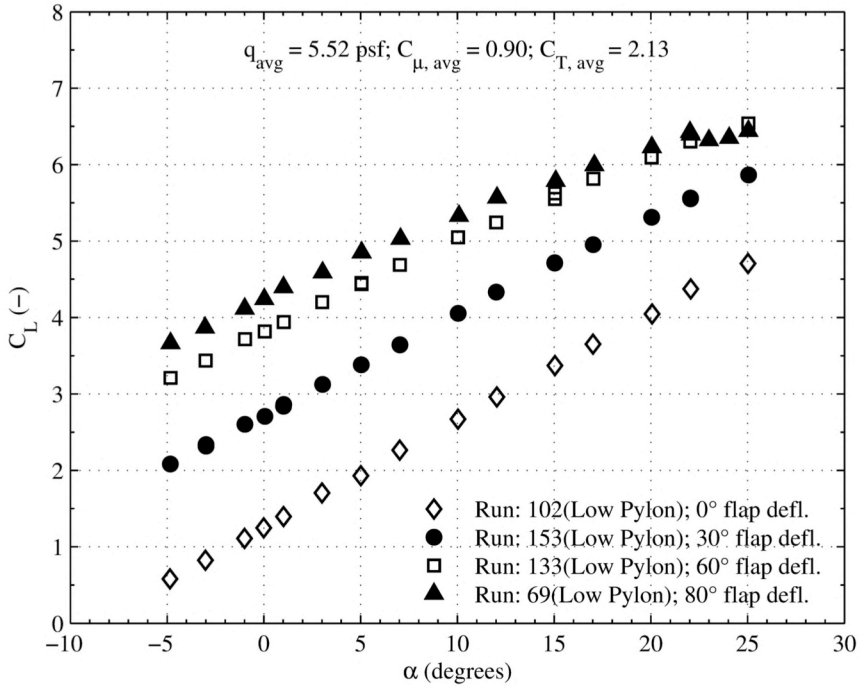

Figure 13.128. Low pylon plot set 3. ***(a) 40 KTS, full power, C_L vs. α.***

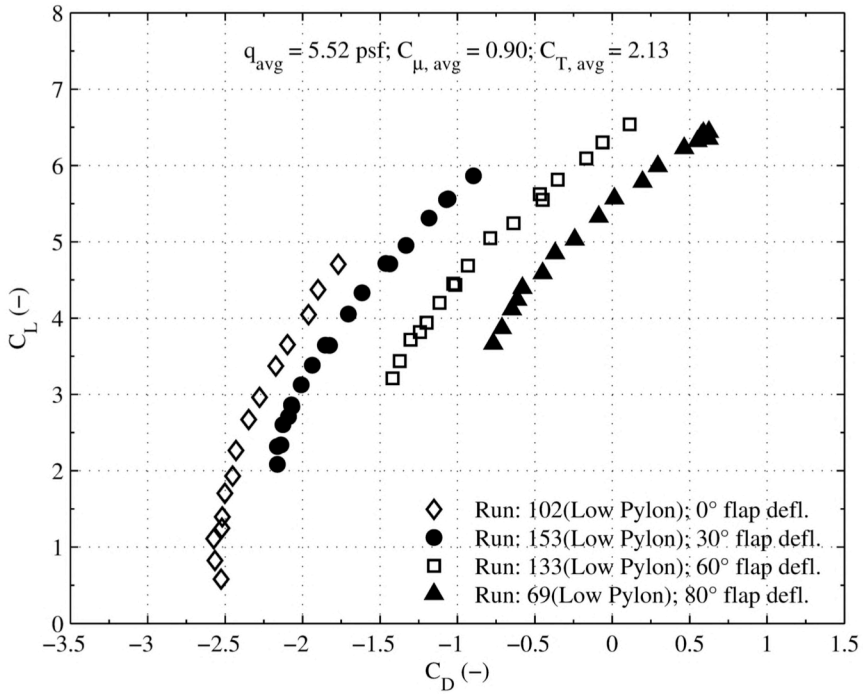

Figure 13.129. Low pylon plot set 3. ***(b) 40 KTS, full power, C_L vs. C_D.***

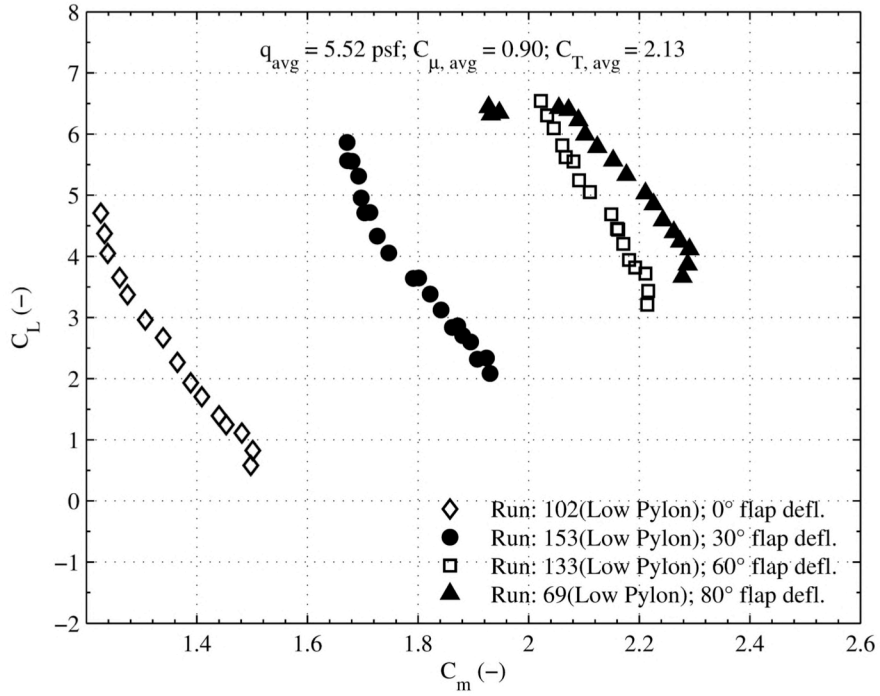

Figure 13.130. Low pylon plot set 3. ***(c) 40 KTS, full power, C_L vs. C_m.***

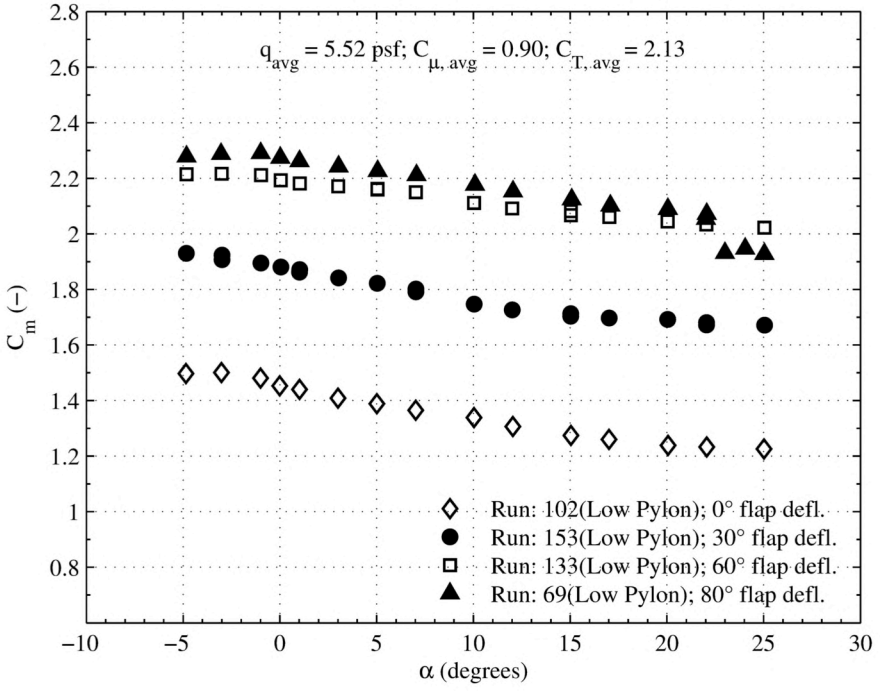

Figure 13.131. Low pylon plot set 3. ***(d) 40 KTS, full power, C_m vs. α.***

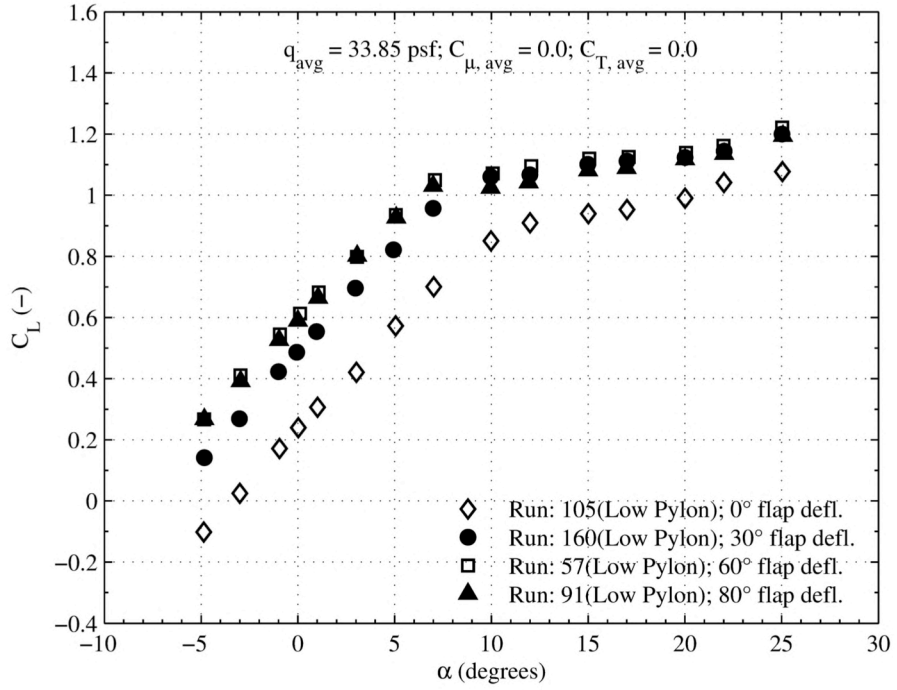

Figure 13.132. Low pylon plot set 4. ***(a) 100 KTS, no power, C_L vs. α.***

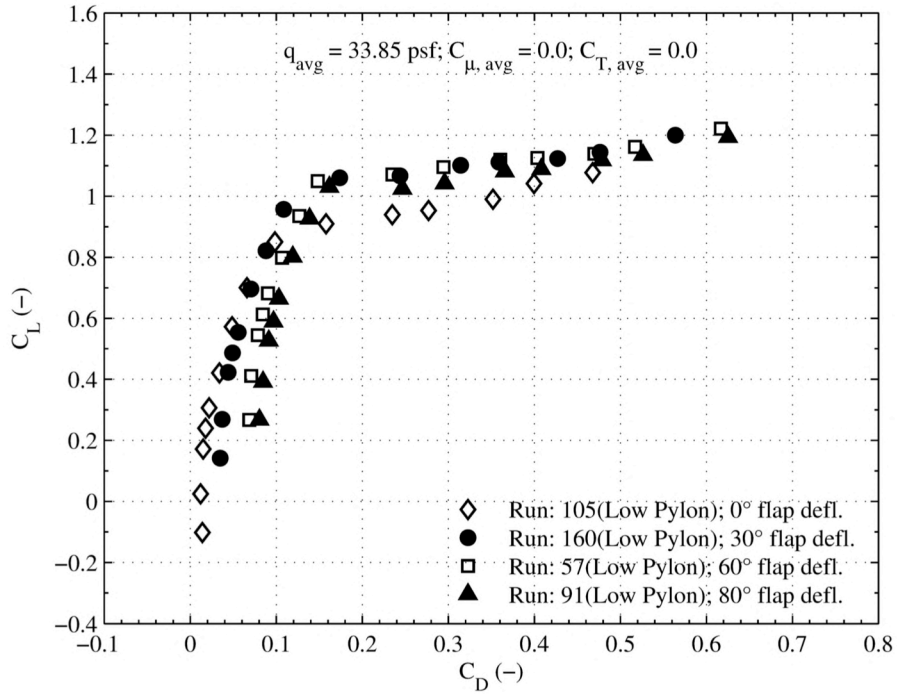

Figure 13.133. Low pylon plot set 4. ***(b) 100 KTS, no power, C_L vs. C_D.***

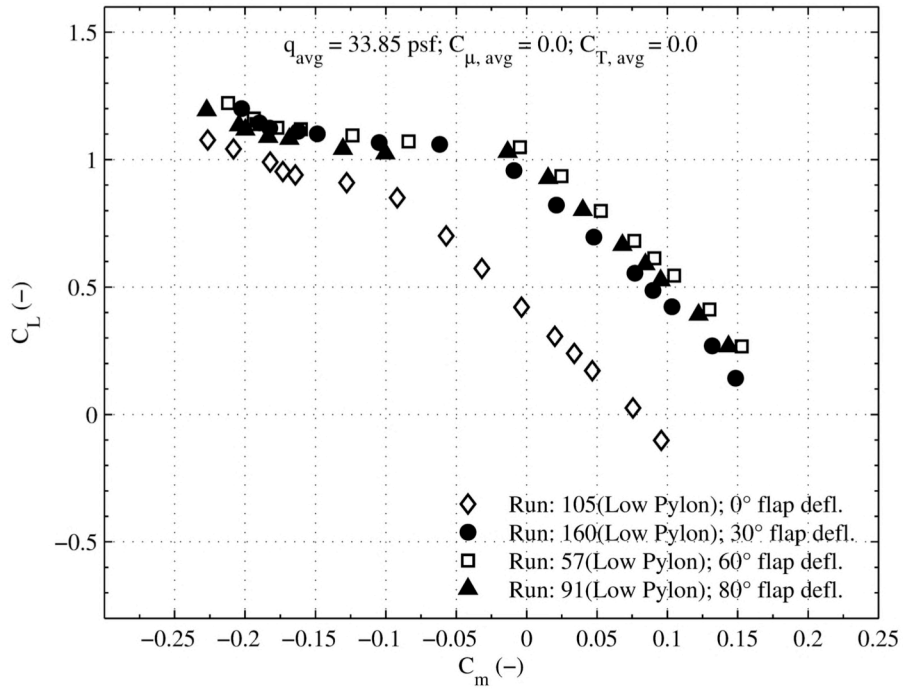

Figure 13.134. Low pylon plot set 4. ***(c) 100 KTS, no power, C_L vs. C_m.***

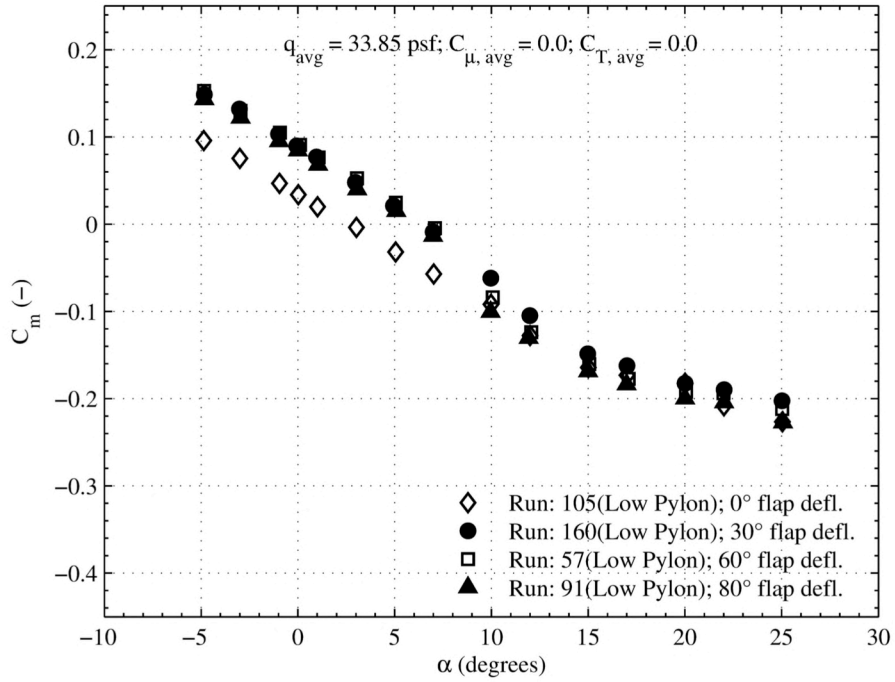

Figure 13.135. Low pylon plot set 4. ***(d) 100 KTS, no power, C_m vs. α.***

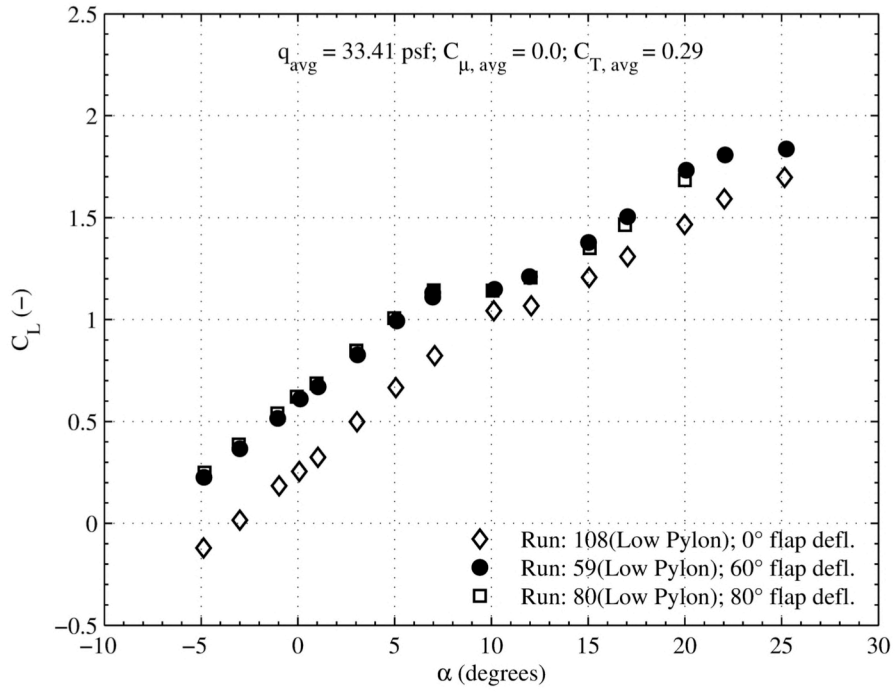

Figure 13.136. Low pylon plot set 5. ***(a) 100 KTS, no slots, full TPS, C_L vs. α.***

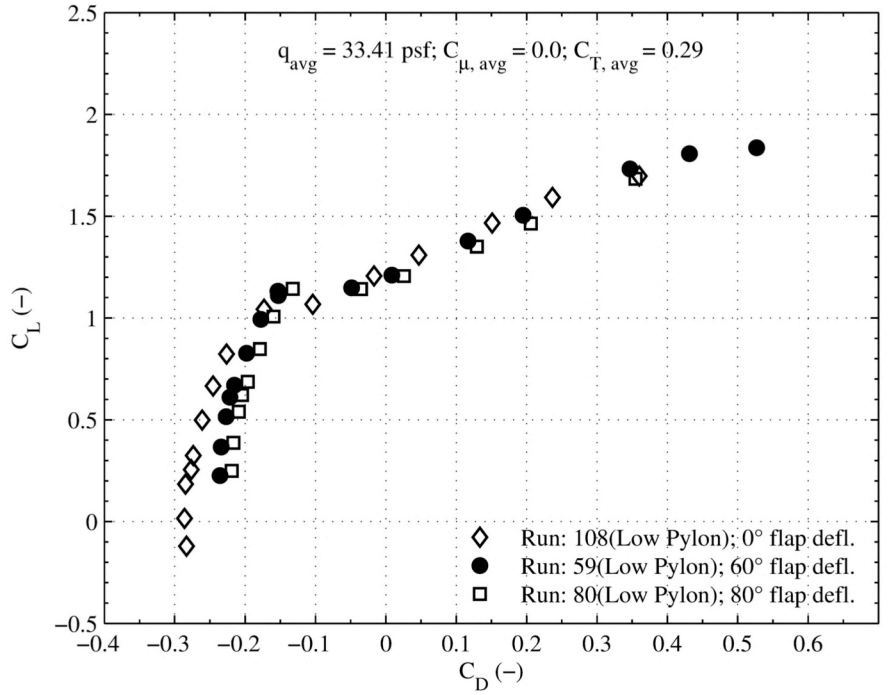

Figure 13.137. Low pylon plot set 5. ***(b) 100 KTS, no slots, full TPS, C_L vs. C_D.***

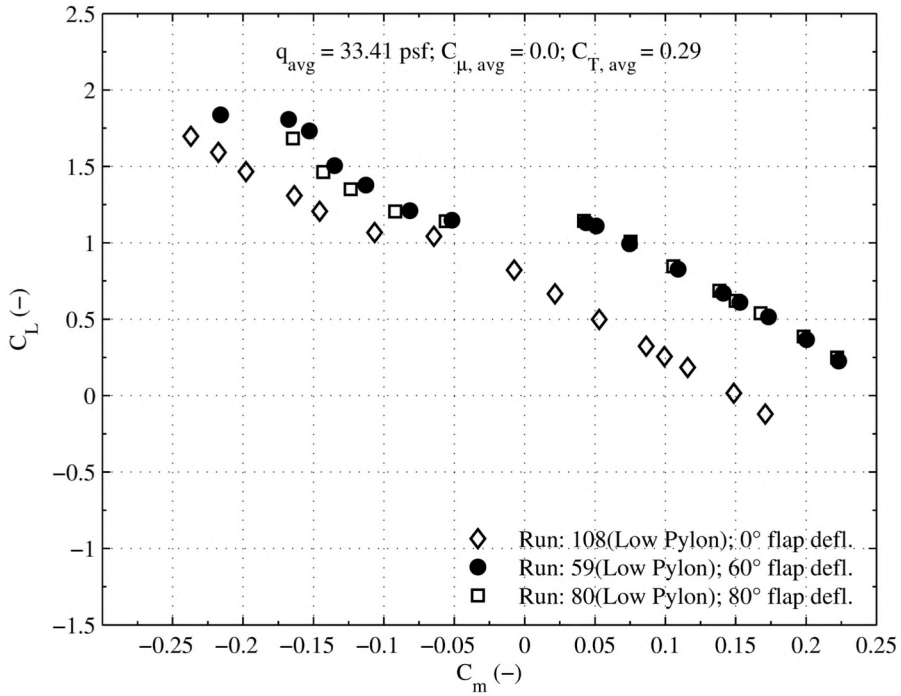

Figure 13.138. Low pylon plot set 5. ***(c) 100 KTS, no slots, full TPS, C_L vs. C_m.***

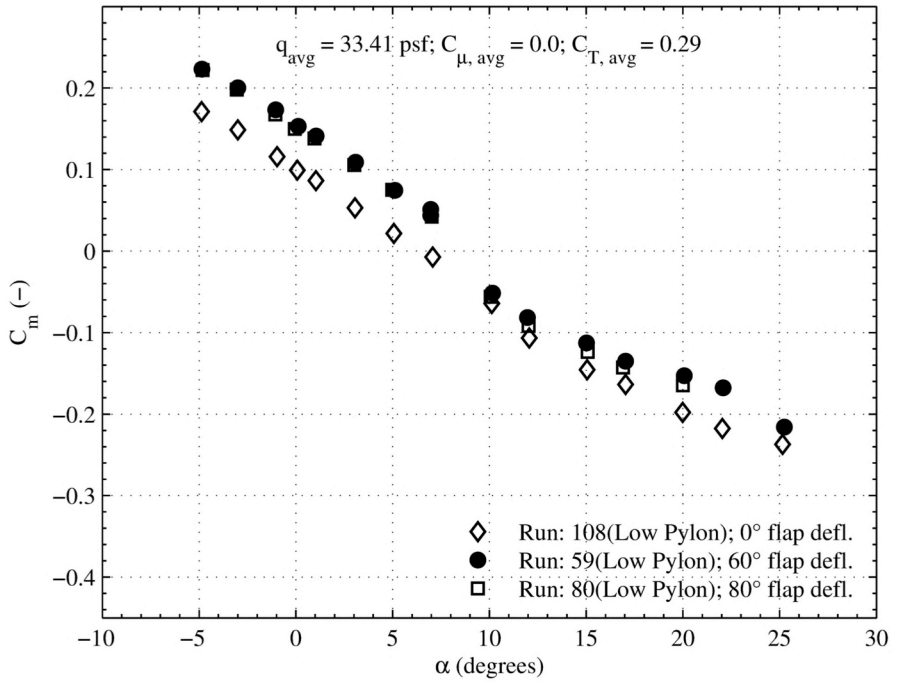

Figure 13.139. Low pylon plot set 5. ***(d) 100 KTS, no slots, full TPS, C_m vs. α.***

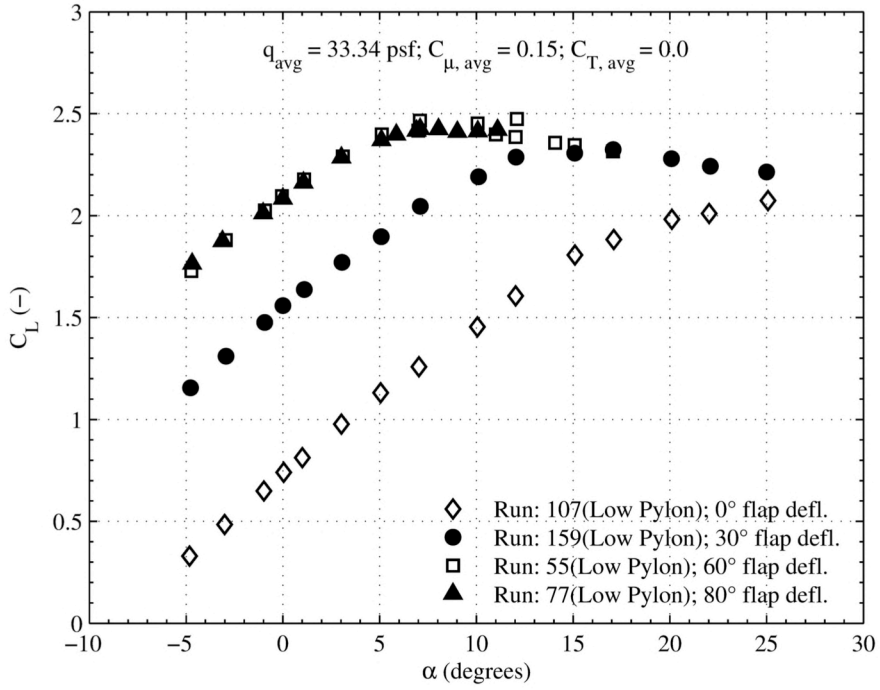

Figure 13.140. Low pylon plot set 6. ***(a) 100 KTS, full slots, no TPS, C_L vs. α.***

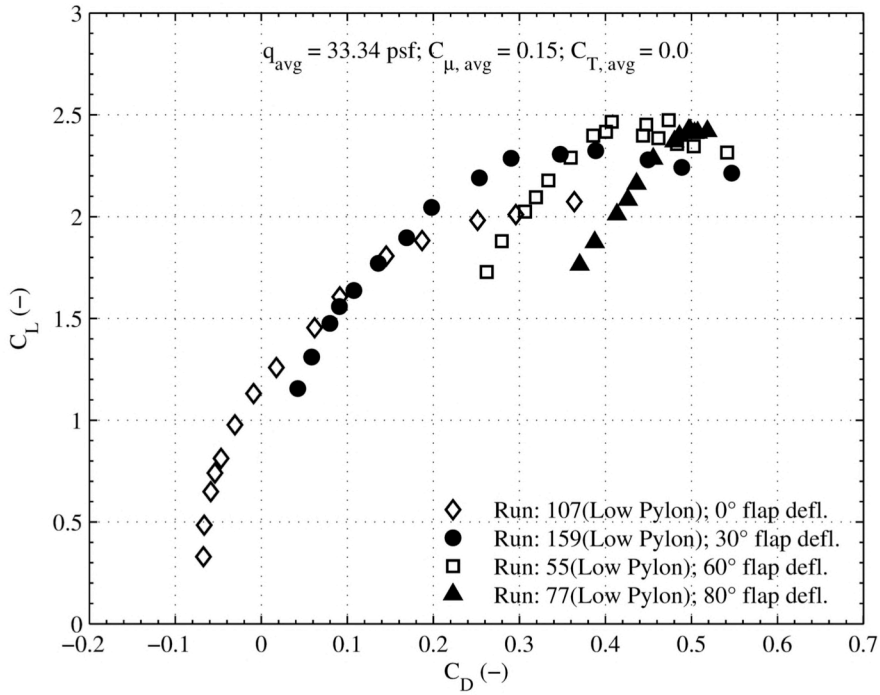

Figure 13.141. Low pylon plot set 6. ***(b) 100 KTS, full slots, no TPS, C_L vs. C_D.***

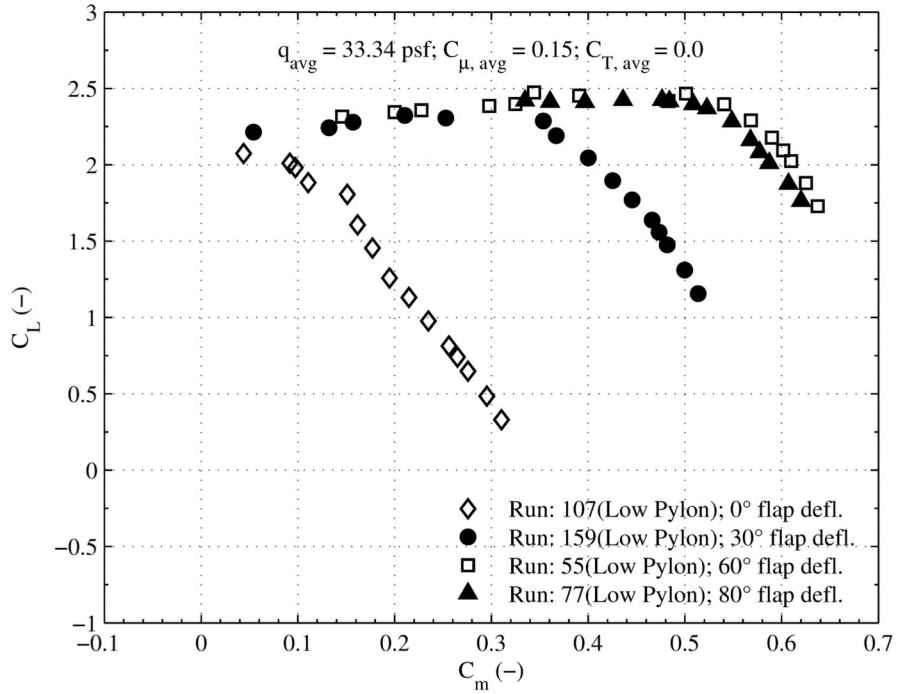

Figure 13.142. Low pylon plot set 6. ***(c) 100 KTS, full slots, no TPS, C_L vs. C_m.***

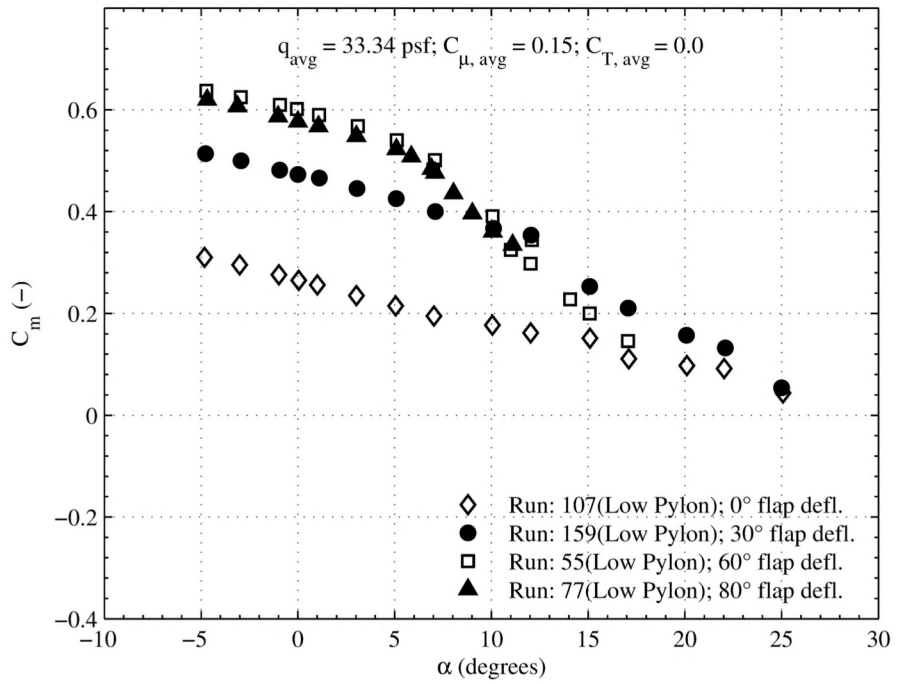

Figure 13.143. Low pylon plot set 6. ***(d) 100 KTS, full slots, no TPS, C_m vs. α.***

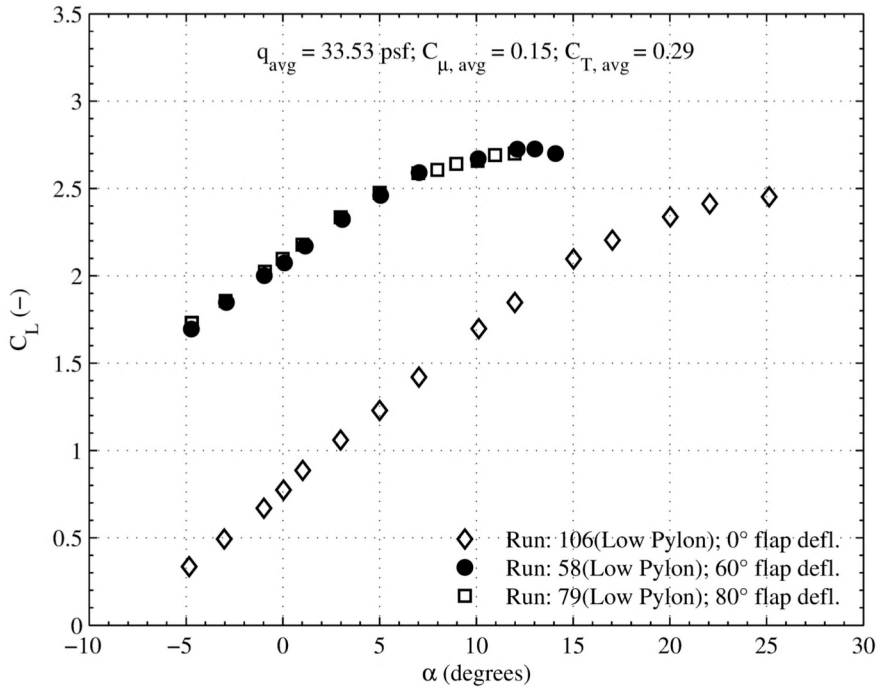

Figure 13.144. Low pylon plot set 7. ***(a) 100 KTS, full power, C_L vs. α.***

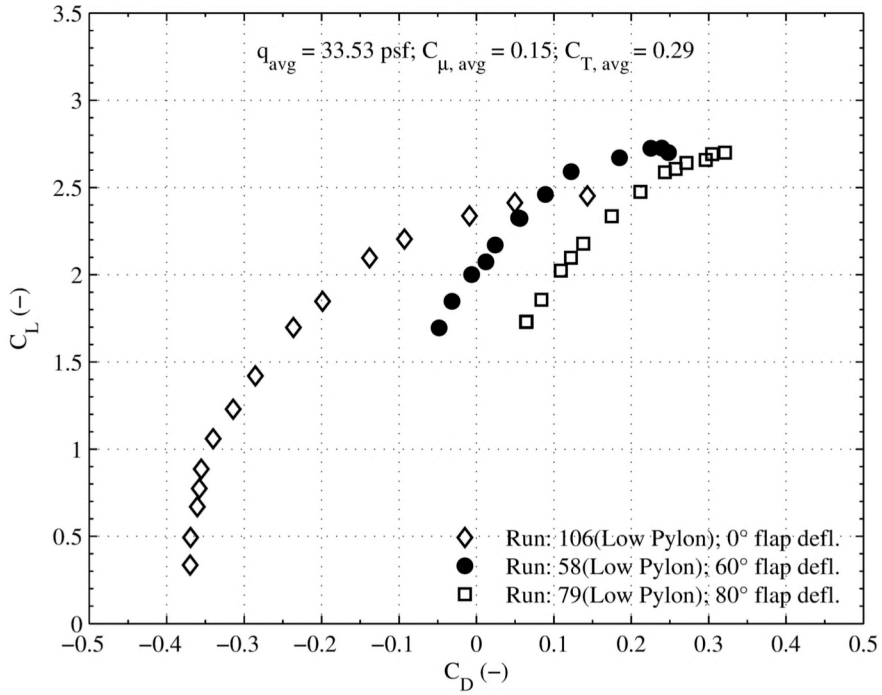

Figure 13.145. Low pylon plot set 7. ***(b) 100 KTS, full power, C_L vs. C_D.***

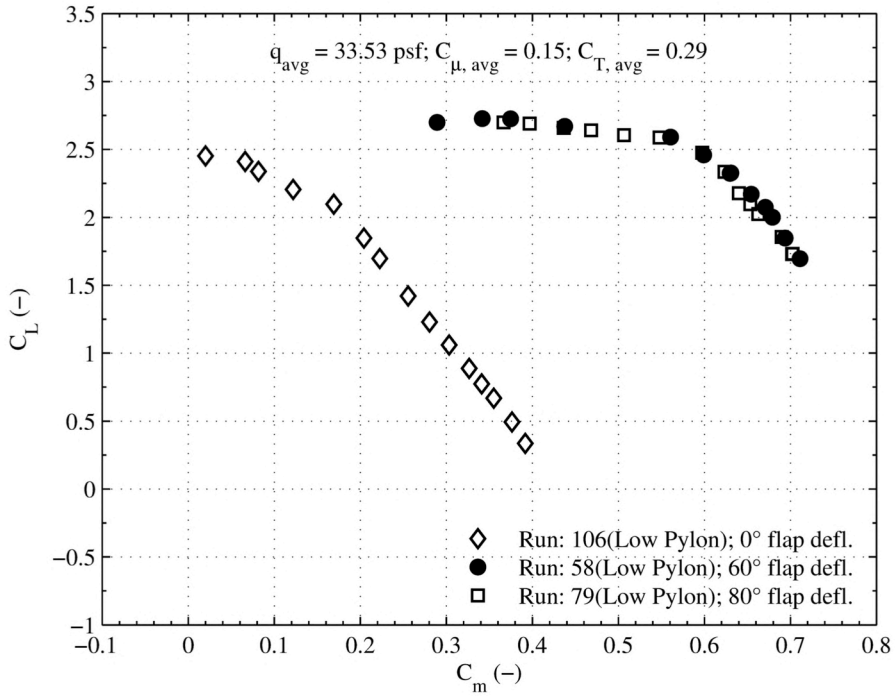

Figure 13.146. Low pylon plot set 7. ***(c) 100 KTS, full power, C_L vs. C_m.***

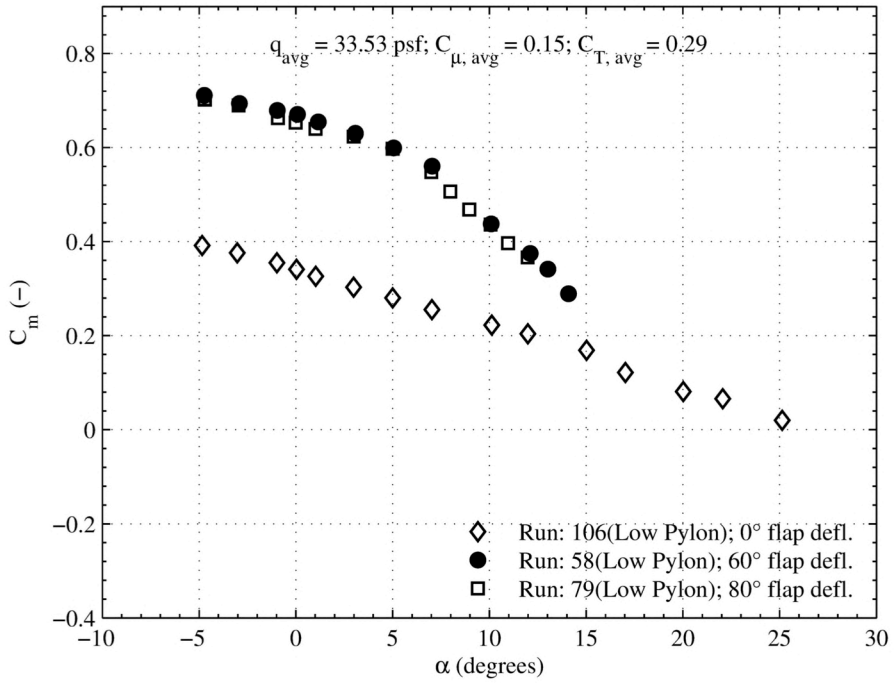

Figure 13.147. Low pylon plot set 7. ***(d) 100 KTS, full power, C_m vs. α.***

13.5.2. Block Two

Block two plots for the low pylon configuration are presented in Figure 13.148 through Figure 13.163. Data at fixed flap deflection and tunnel condition are presented as a function of slot/TPS power setting. At all speeds it is seen that the engine-on does contribute to higher lift. Performance benefits from engine exhaust deflection are primarily noticed at high angles of attack. The application of thrust increases the lift curve slope due to the $C_T*\sin(\alpha+\delta_{jet})$ in the test data. In the 80° flap deflection data at 60 KTS (Fig. 30), the application of engine thrust is responsible for a 3° increase in stall angle at an increase in the maximum lift coefficient of > 0.5. Note that this increase in lift is not so much due to the thrust deflection angle, but more so the increased upper surface velocities that result. Other general trends in the data sets are consistent with what has been reported: increased freestream speed and increased flap deflection contribute to earlier stall. Drag polars show a thrust recovery when the TPS is on. Recall this is because C_D, in the wind axis-system, is parallel to the local freestream vector and the majority of the TPS thrust component is present here. Pitching moment data shows similar trends to what was seen with the clean wing, application of both TPS thrust and slot flow are additive components to the total pitching moment.

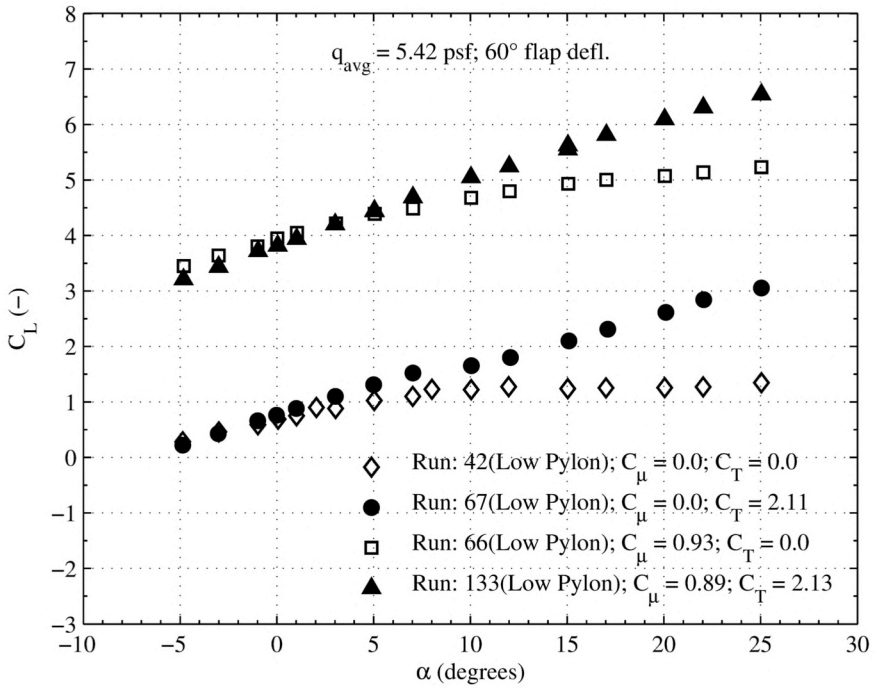

Figure 13.148. Low pylon plot set 8. ***(a) 40 KTS, 60° flap deflection, C_L vs. α.***

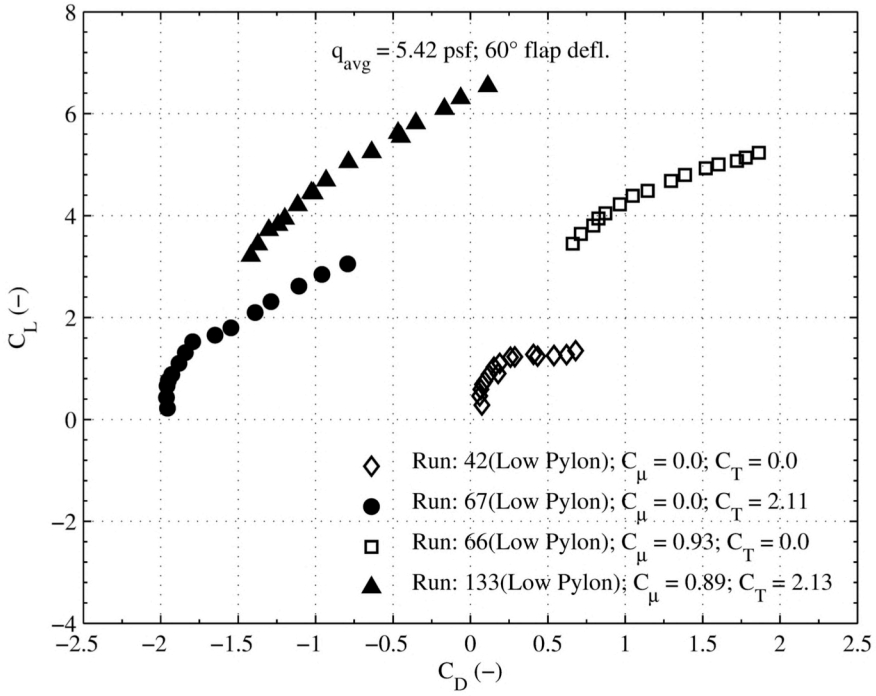

Figure 13.149. Low pylon plot set 8. ***(b) 40 KTS, 60° flap deflection, C_L vs. C_D.***

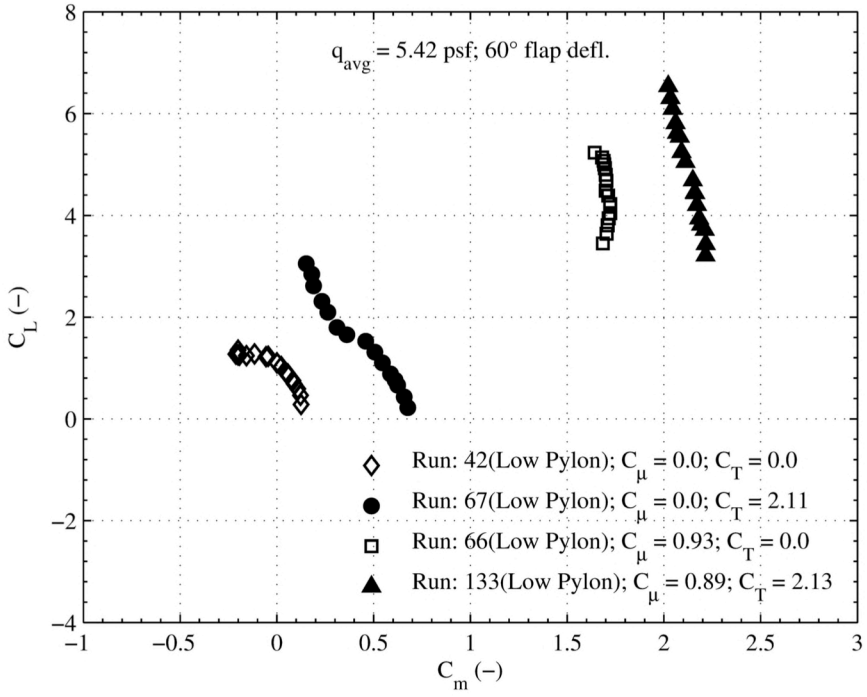

Figure 13.150. Low pylon plot set 8. ***(c) 40 KTS, 60° flap deflection, C_L vs. C_m.***

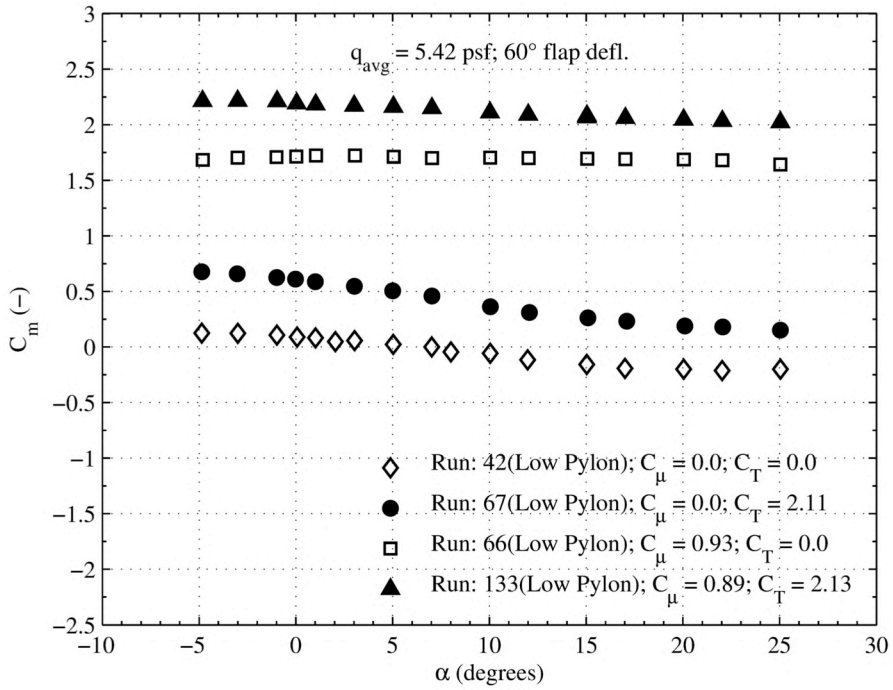

Figure 13.151. Low pylon plot set 8. ***(d) 40 KTS, 60° flap deflection, C_m vs. α.***

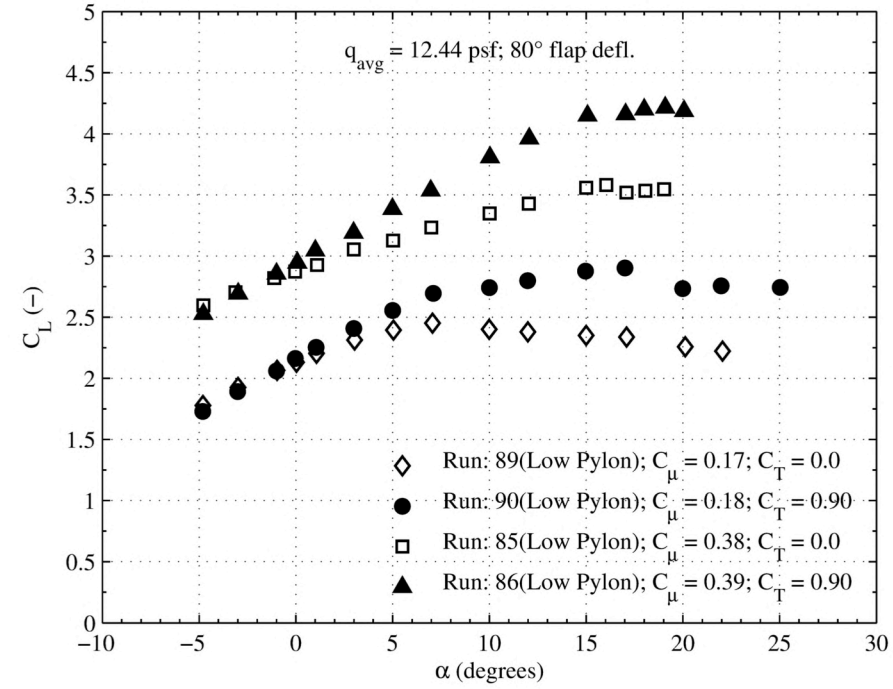

Figure 13.152. Low pylon plot set 9. ***(a) 60 KTS, 80° flap deflection, C_L vs. α.***

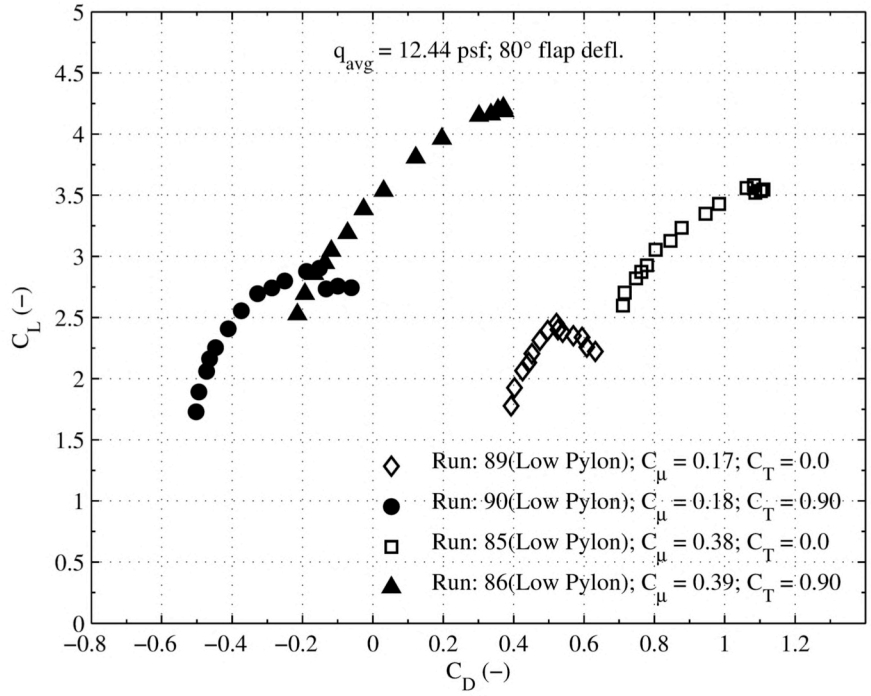

Figure 13.153. Low pylon plot set 9. ***(b) 60 KTS, 80° flap deflection, C_L vs. C_D.***

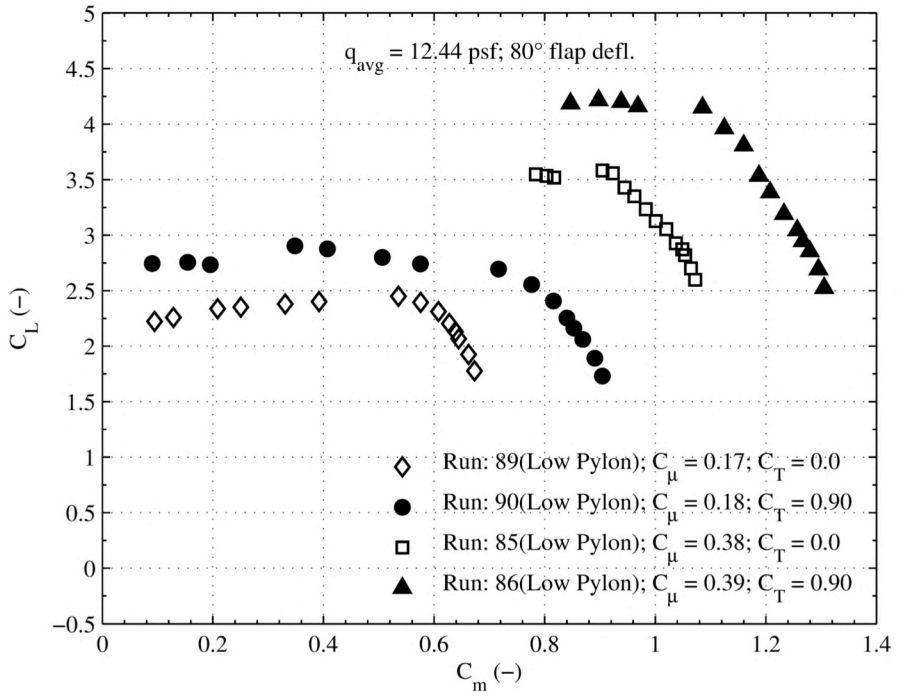

Figure 13.154. Low pylon plot set 9. ***(c) 60 KTS, 80° flap deflection, C_L vs. C_m.***

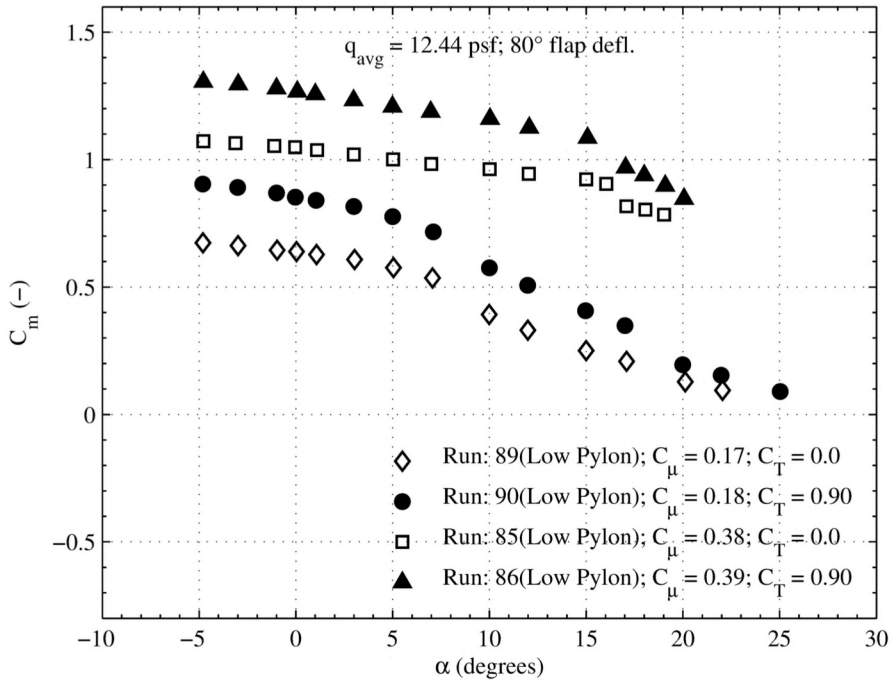

Figure 13.155. Low pylon plot set 9. ***(d) 60 KTS, 80° flap deflection, C_m vs. α.***

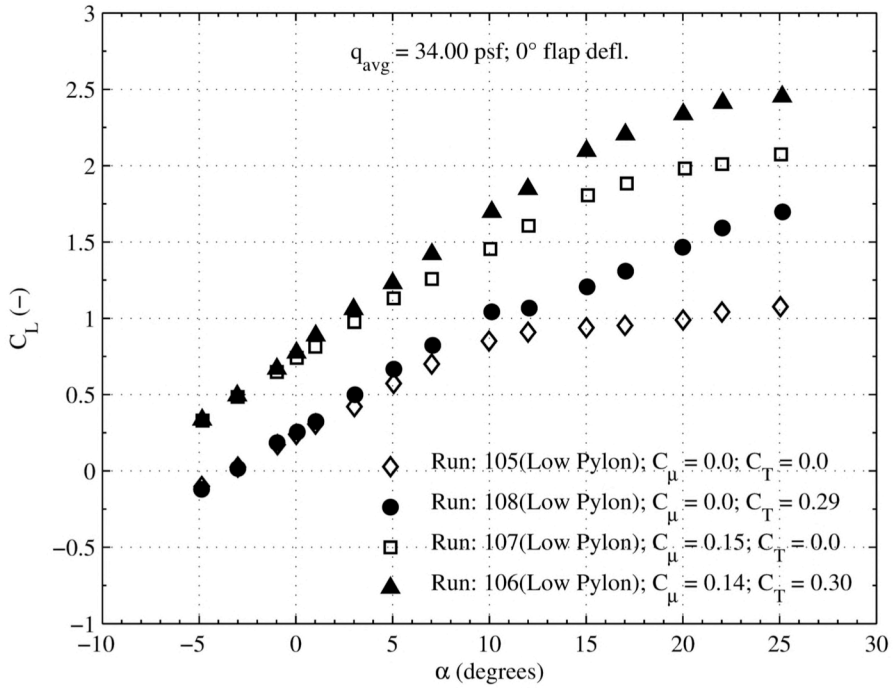

Figure 13.156. Low pylon plot set 10. ***(a) 100 KTS, 0° flap deflection, C_L vs. α.***

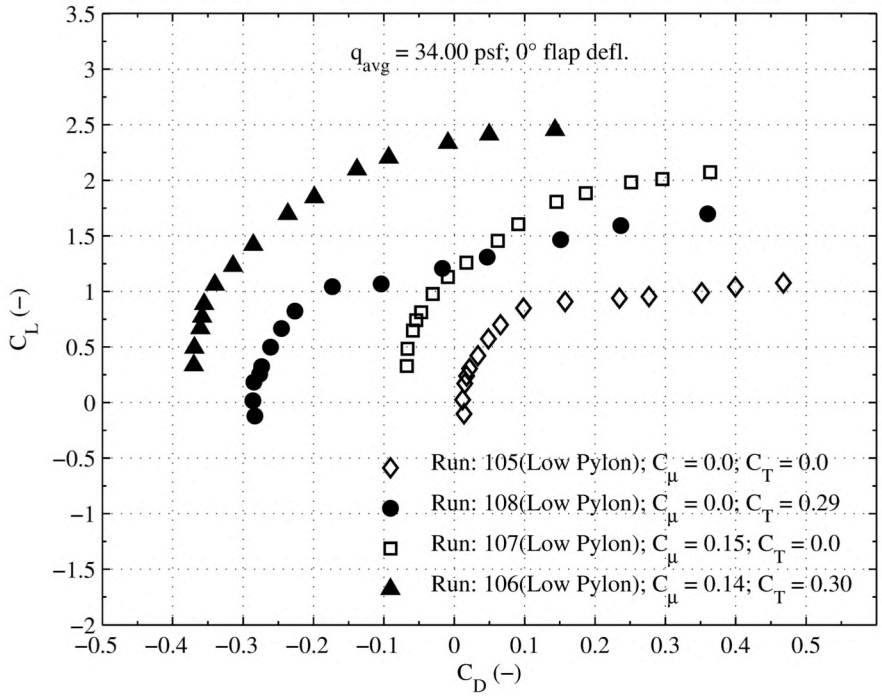

Figure 13.157. Low pylon plot set 10. ***(b) 100 KTS, 0° flap deflection, C_L vs. C_D.***

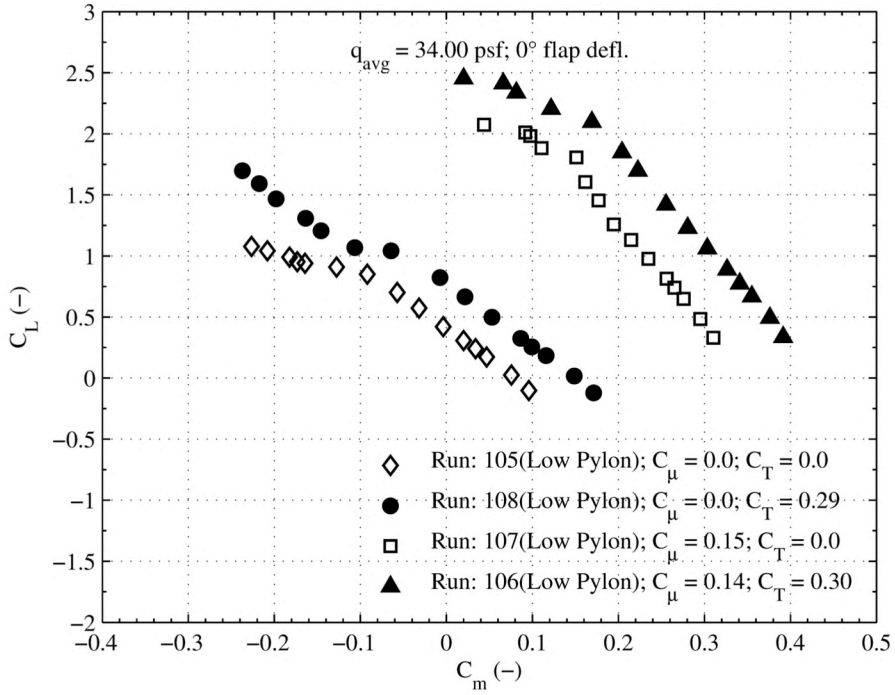

Figure 13.158. Low pylon plot set 10. ***(c) 100 KTS, 0° flap deflection, C_L vs. C_m.***

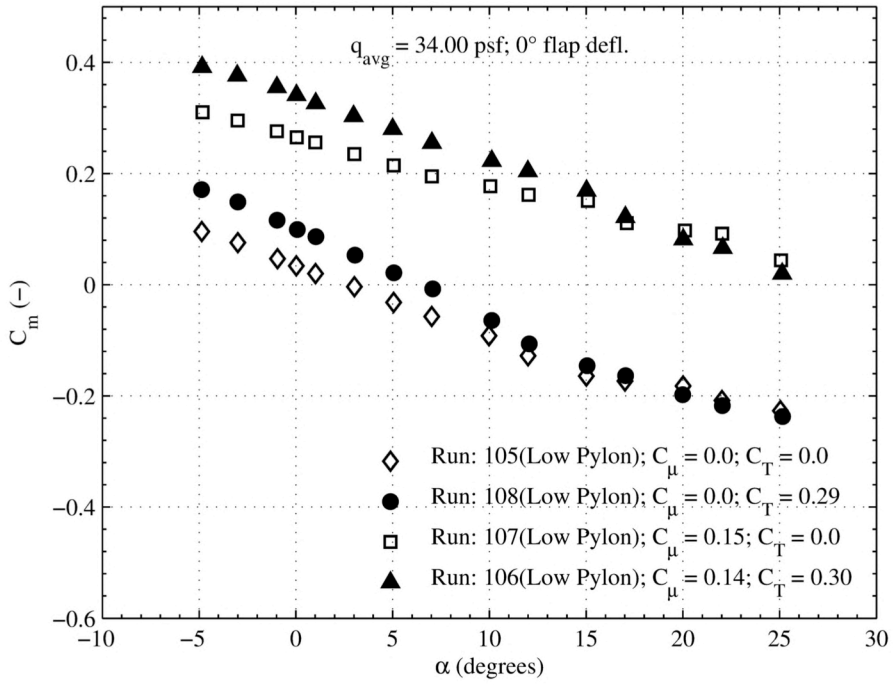

Figure 13.159. Low pylon plot set 10. ***(d) 100 KTS, 0° flap deflection, C_m vs. α.***

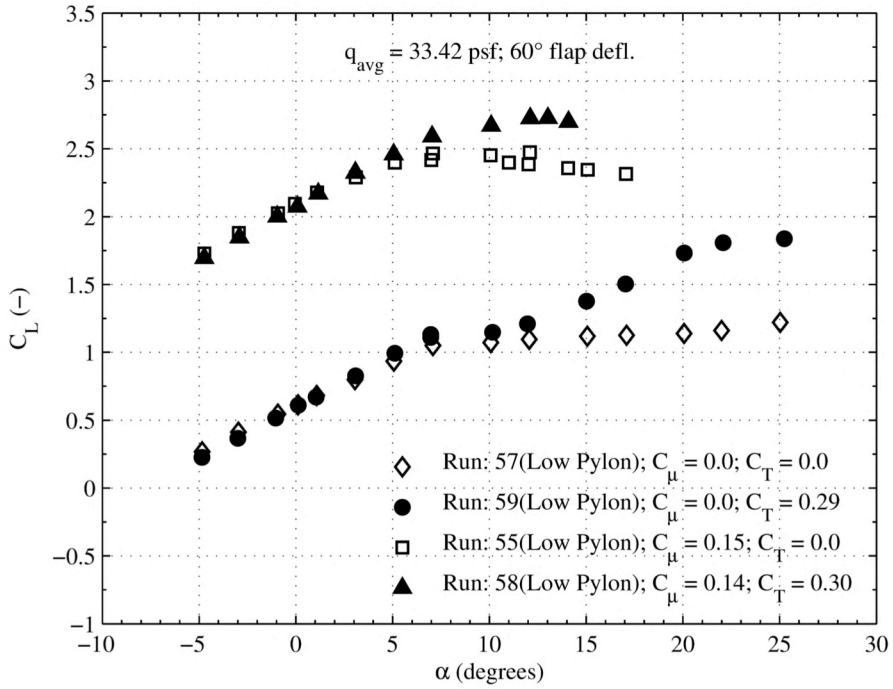

Figure 13.160. Low pylon plot set 11. ***(a) 100 KTS, 60° flap deflection, C_L vs. α.***

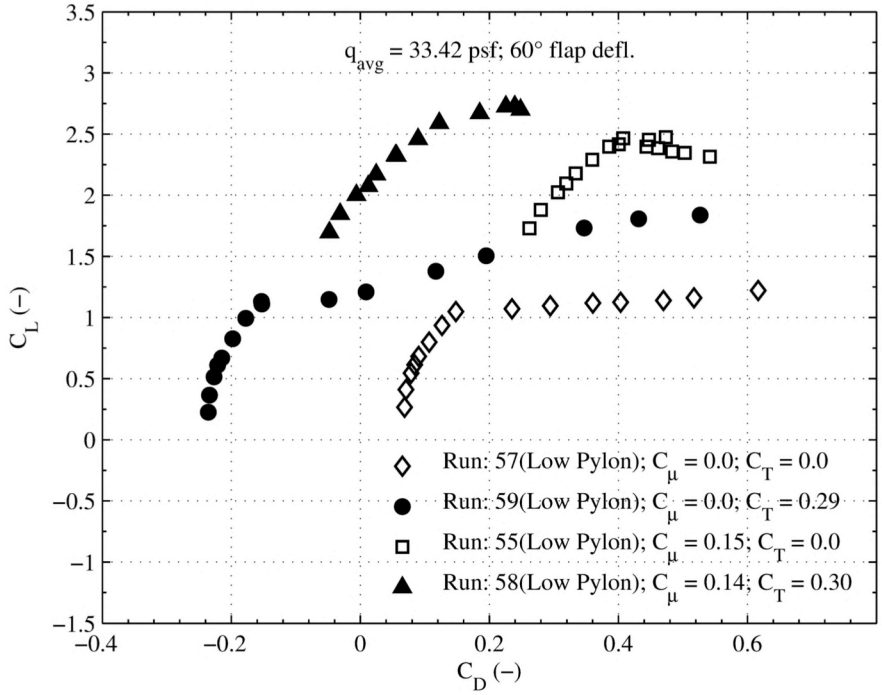

Figure 13.161. Low pylon plot set 11. ***(b) 100 KTS, 60° flap deflection, C_L vs. C_D.***

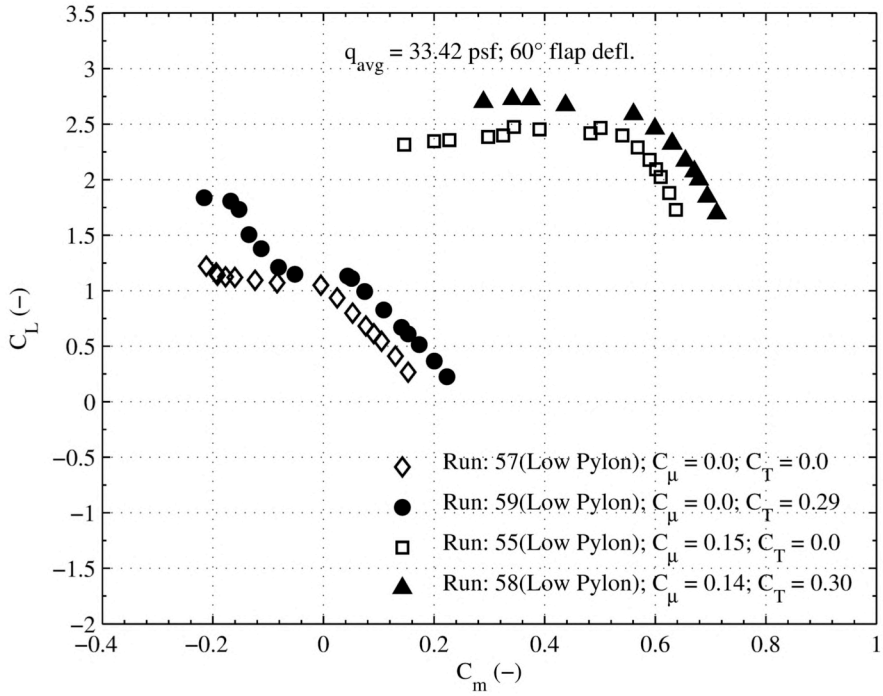

Figure 13.162. Low pylon plot set 11. ***(c) 100 KTS, 60° flap deflection, C_L vs. C_m.***

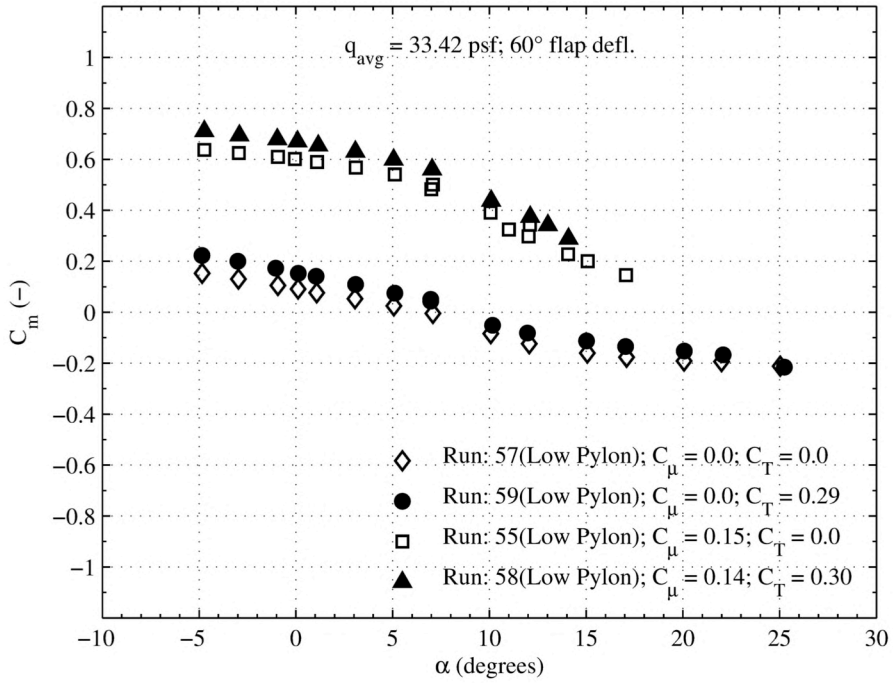

Figure 13.163. Low pylon plot set 11. ***(d) 100 KTS, 60° flap deflection, C_m vs. α.***

13.5.3. Block Three

Figure 13.164 through Figure 13.172 present the plot sets for block three data. The figures present slot sweep data for fixed angle of attack and tunnel condition; $C_T = 0$ for all figures presented. At 40 KTS, it is not expected that the 60° would be more effective than the 80° flap by α = 10°. Across all angle of attack, for a constant C_μ, it is seen that lift and pitching moment increase with flap deflection. Pitching moment magnitudes are similar for the 60° and 80° flap, at a fixed momentum coefficient. The 0° flap provides a slot thrust across all angles of attack; slot thrust is greater as C_μ increases. For positive flap deflections, drag increases with the flap angle and with increasing C_μ.

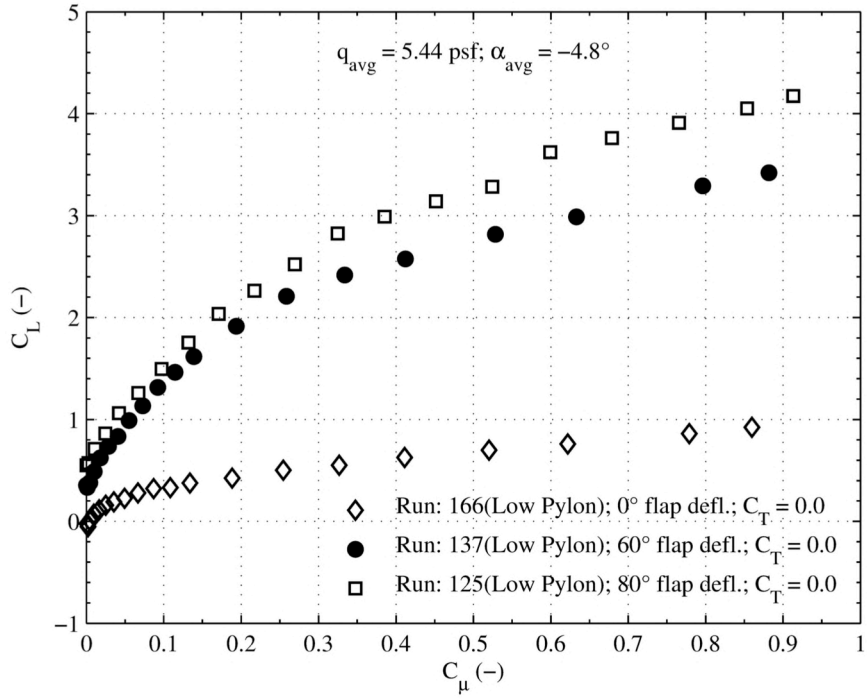

Figure 13.164. Low pylon plot set 12. ***(a) 40 KTS, -5° angle of attack, C_L vs. C_μ.***

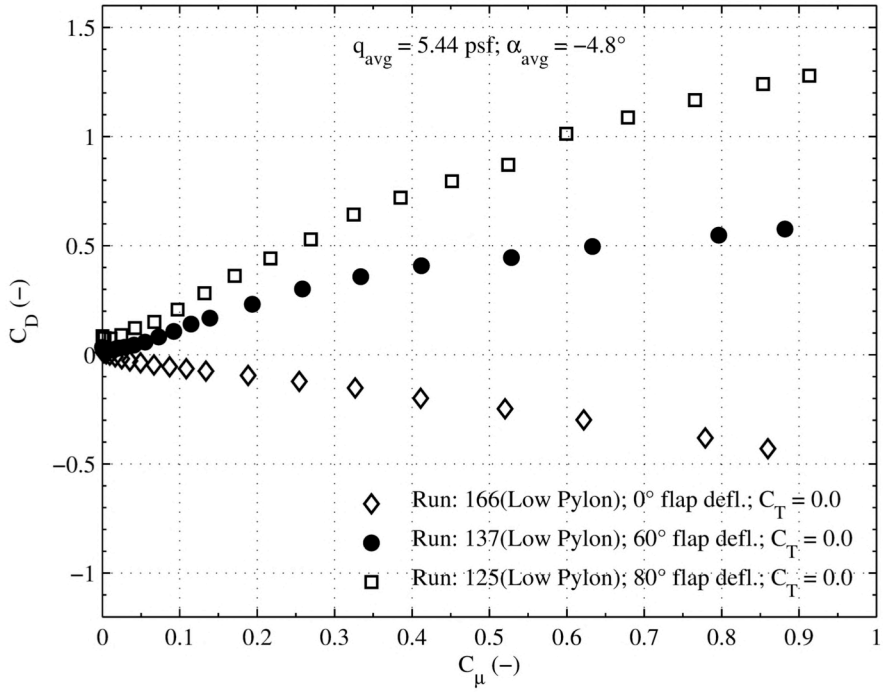

Figure 13.165. Low pylon plot set 12. ***(b) 40 KTS, -5° angle of attack, C_D vs. C_μ.***

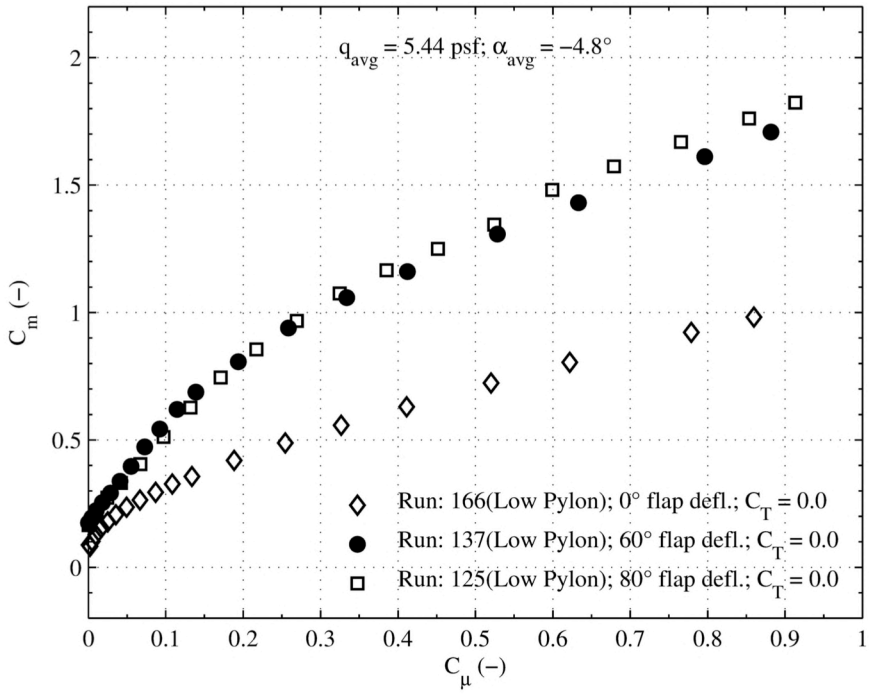

Figure 13.166. Low pylon plot set 12. ***(c) 40 KTS, -5° angle of attack, C_m vs. C_μ.***

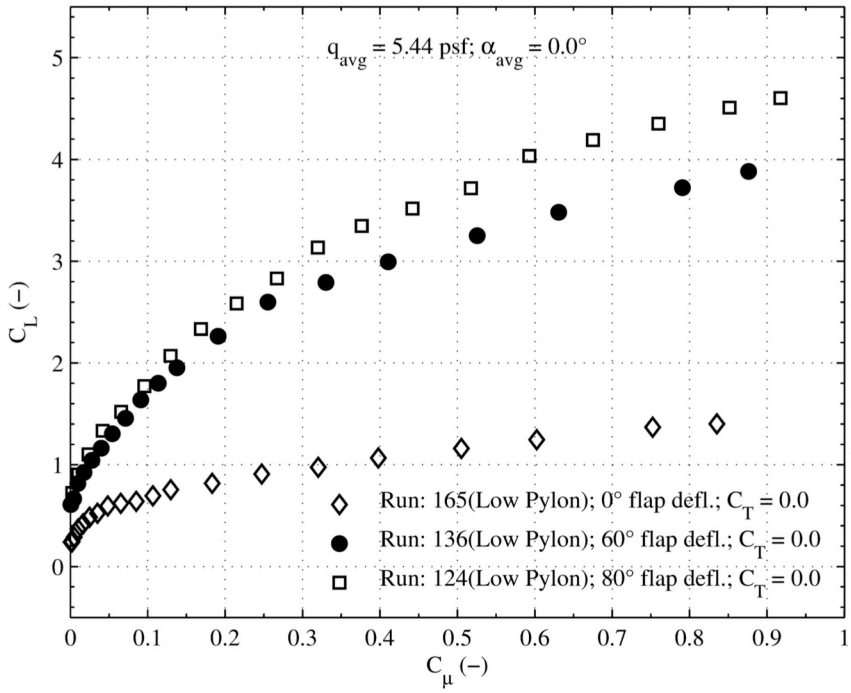

Figure 13.167. Low pylon plot set 13. ***(a) 40 KTS, 0° angle of attack, C_L vs. C_μ.***

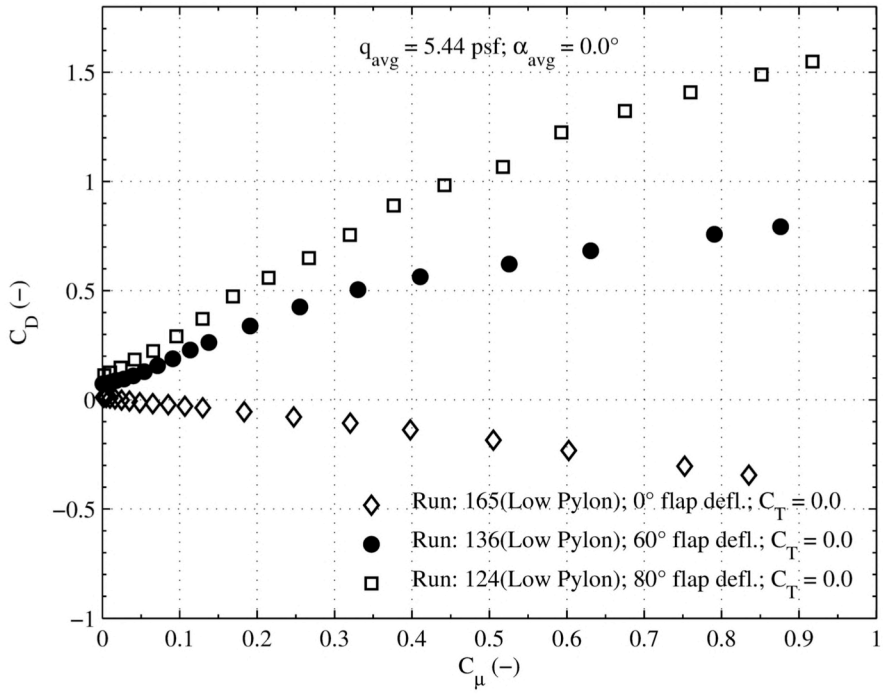

Figure 13.168. Low pylon plot set 13. ***(b) 40 KTS, 0° angle of attack, C_D vs. C_μ.***

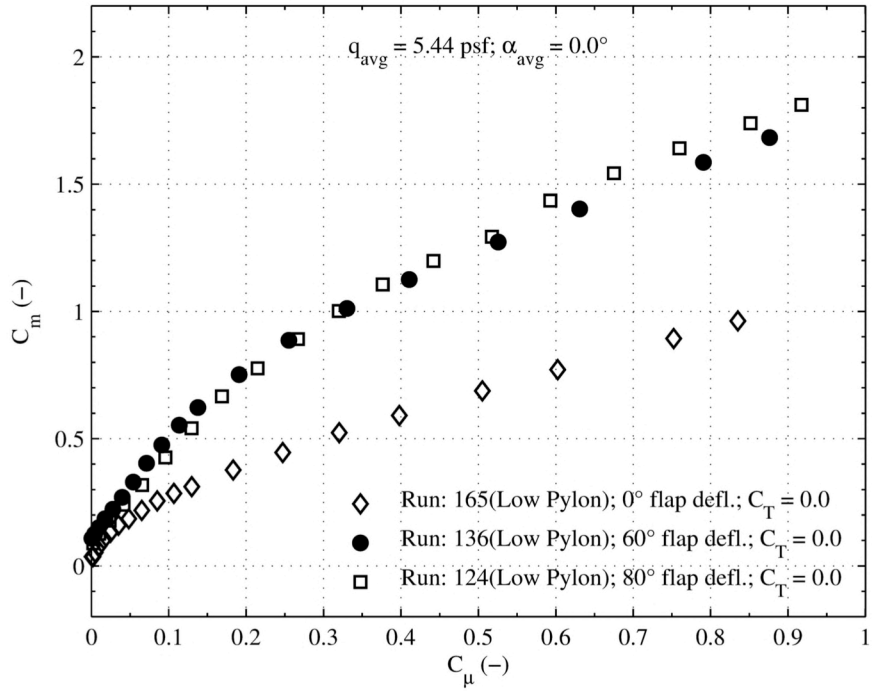

Figure 13.169. Low pylon plot set 13. ***(c) 40 KTS, 0° angle of attack, C_m vs. C_μ.***

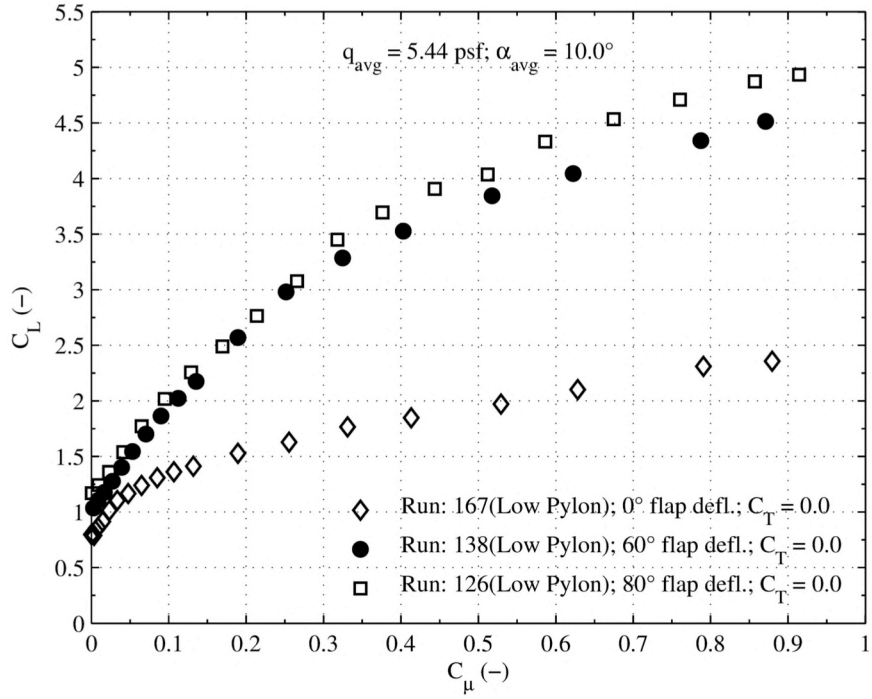

Figure 13.170. Low pylon plot set 14. ***(a) 40 KTS, 10° angle of attack, C_L vs. C_μ.***

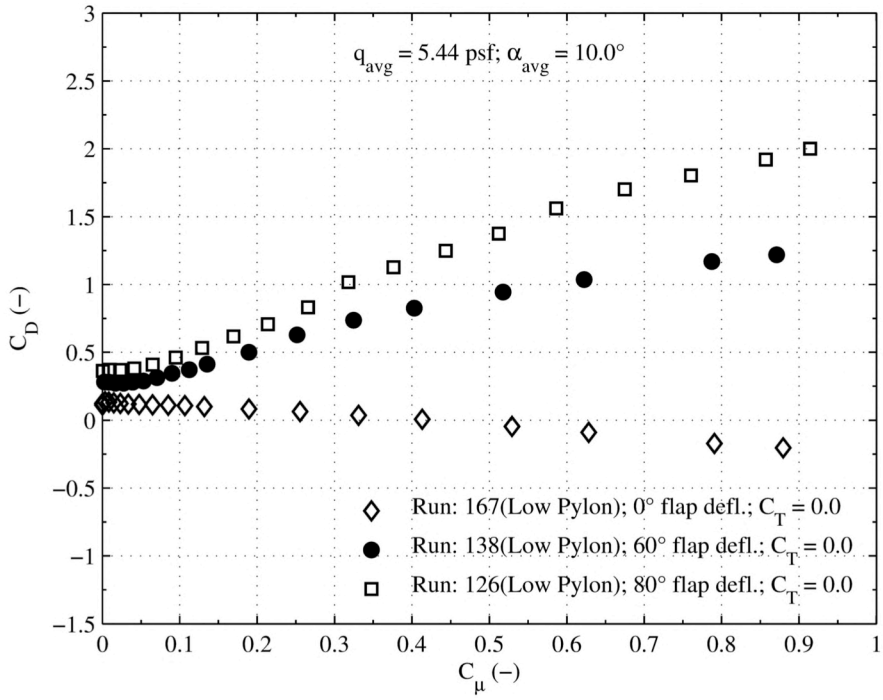

Figure 13.171. Low pylon plot set 14. ***(b) 40 KTS, 10° angle of attack, C_D vs. C_μ.***

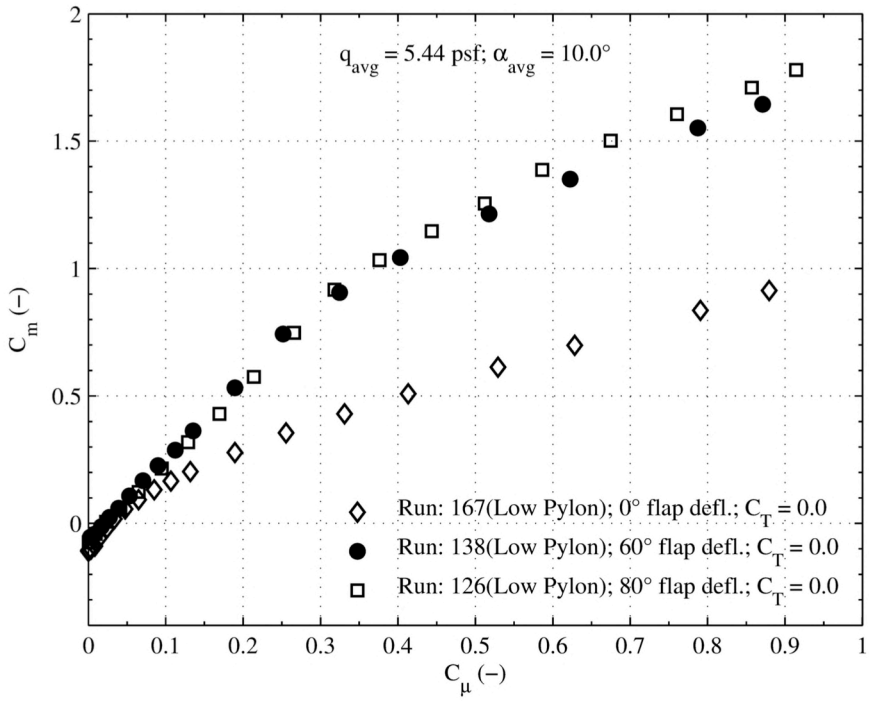

Figure 13.172. Low pylon plot set 14. ***(c) 40 KTS, 10° angle of attack, C_m vs. C_μ.***

13.5.4. Block Four

The plot set for block four data is presented in Figure 13.173 through Figure 13.177. The plot set presents data from a TPS sweep at a constant momentum coefficient. This sweep was conducted differently than others; in this sweep, the model was held at a fixed angle of attack and data points were taken at 3 different values of C_T before moving to the next angle and repeating. Thrust coefficients corresponding to 0, 2/3, and full conditions were investigated. In the figures it is seen that engine-on does contribute to higher lift. Again, the application of thrust increases the lift curve slope due to the C_T*sin(α+δ_{jet}) component. It is seen that going from the 2/3 to the full TPS setting provides only slightly better lift performance; ΔC_L = 0.35 for ΔC_T = 0.66. Higher thrust recovery, or more negative drag, is seen as C_T is increased. Pitching moment results show expected trends with increased thrust coefficient creating more pitching moment.

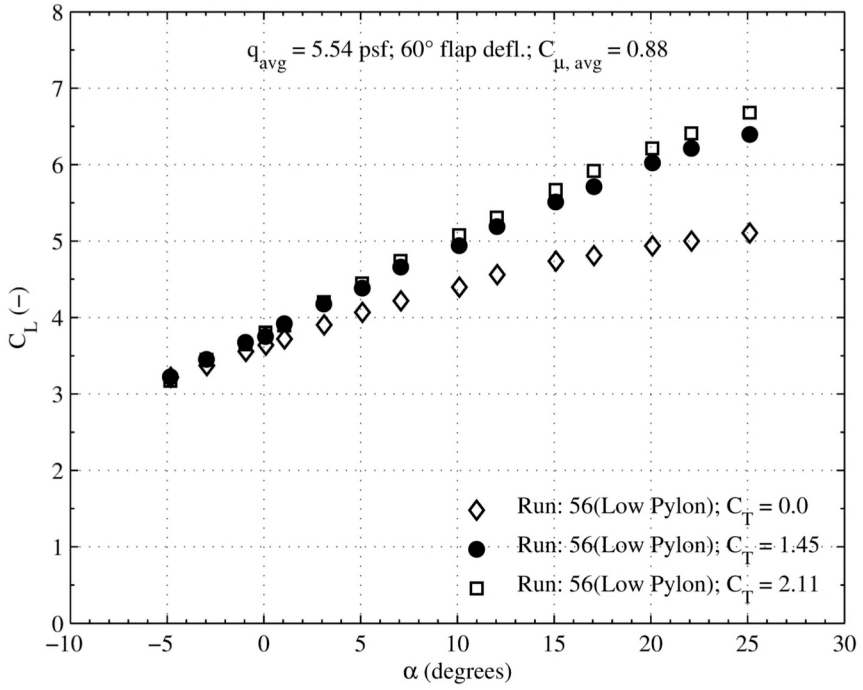

Figure 13.173. Low pylon plot set 15. ***(a) 40 KTS, 60° flap deflection, full slots, C_L vs. α.***

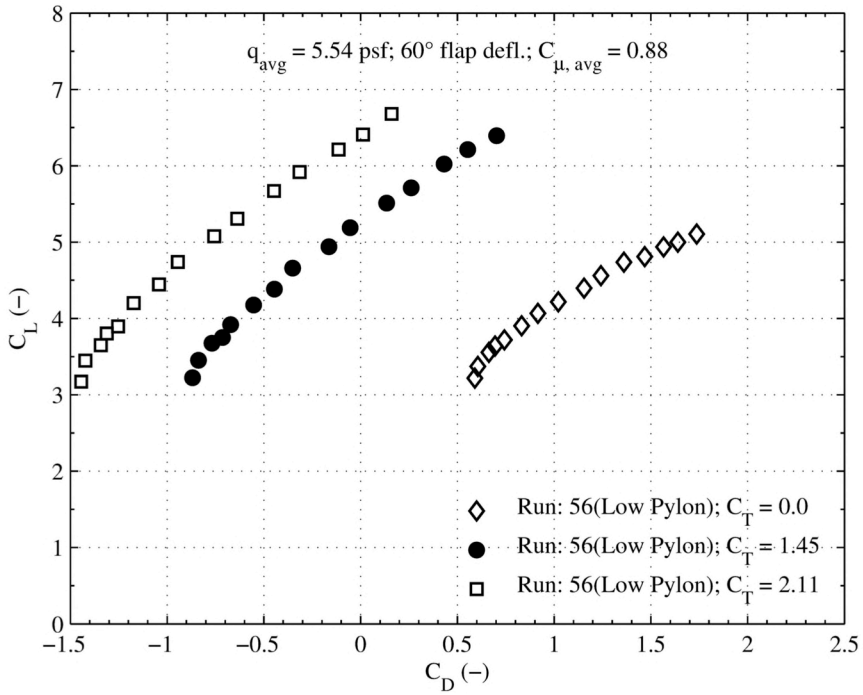

Figure 13.174. Low pylon plot set 15. ***(b) 40 KTS, 60° flap deflection, full slots, C_L vs. C_D.***

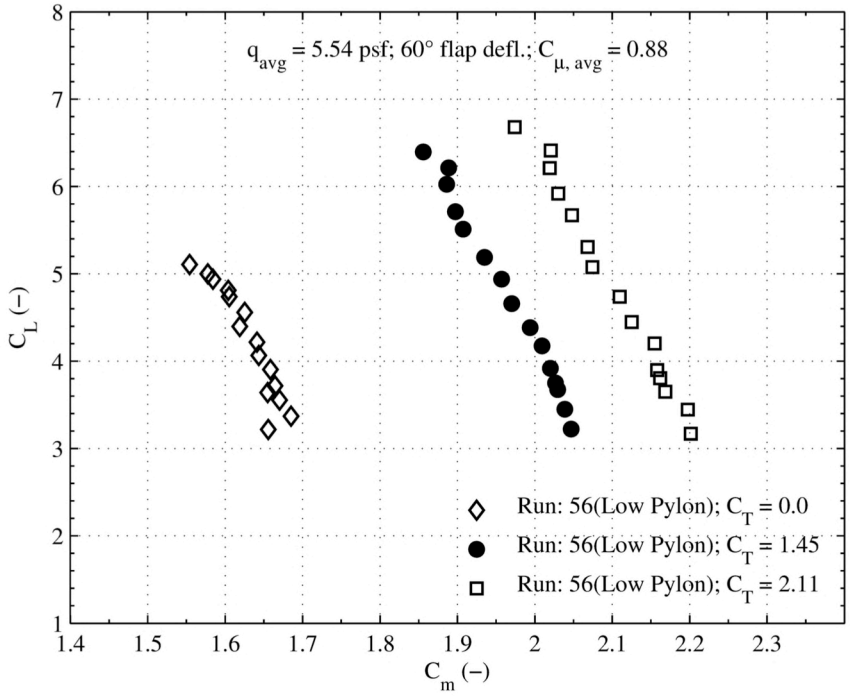

Figure 13.175. Low pylon plot set 15. ***(c) 40 KTS, 60° flap deflection, full slots, C_L vs. C_m.***

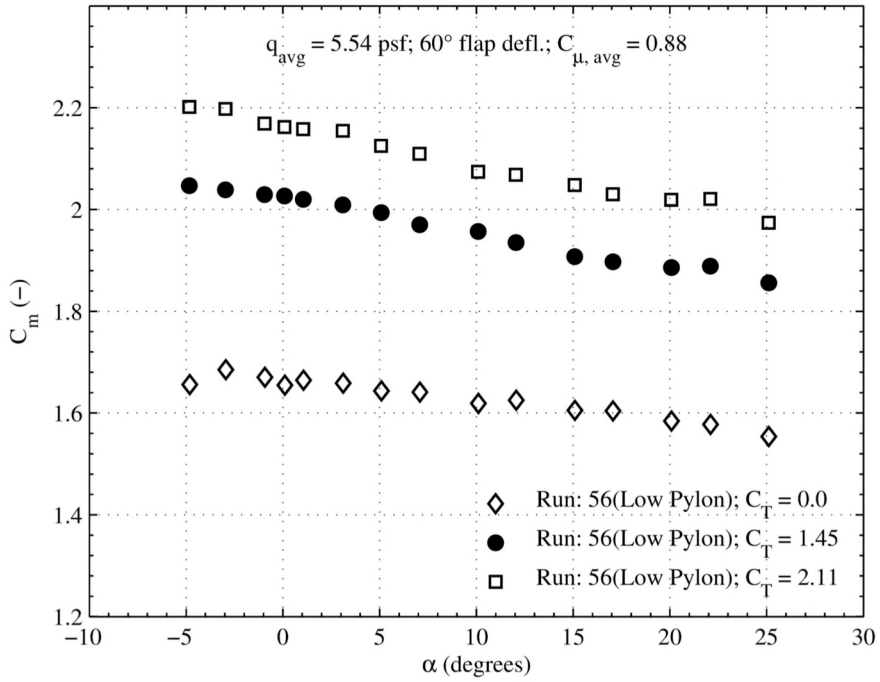

Figure 13.176. Low pylon plot set 15. ***(d) 40 KTS, 60° flap deflection, full slots, C_m vs. α.***

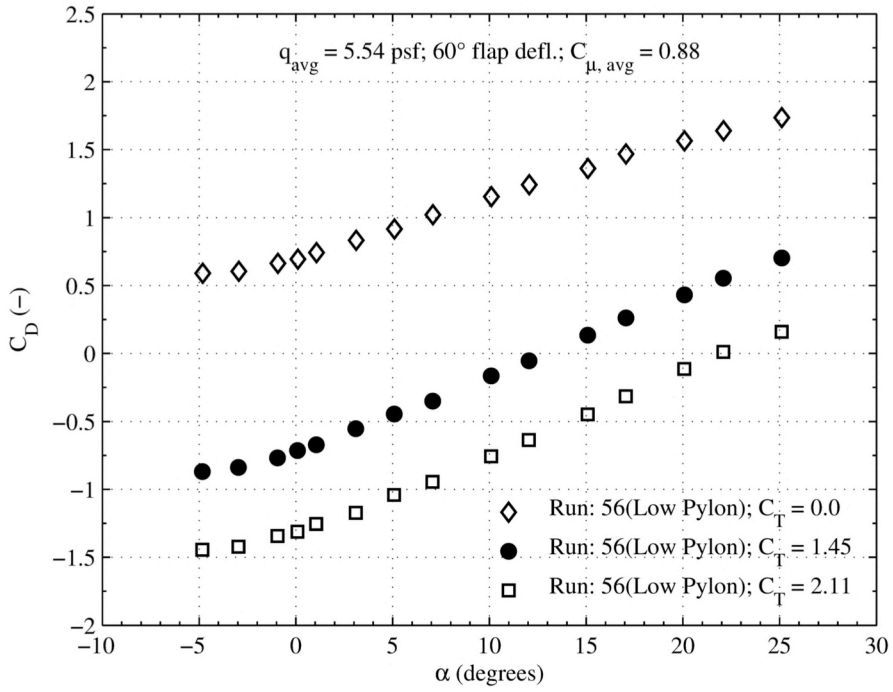

Figure 13.177. Low pylon plot set 15. ***(e) 40 KTS, 60° flap deflection, full slots, C_D vs. α.***

13.5.5. Sideslip Sweep

Alpha sweeps at 4 different angles of sideslip were conducted in the low pylon and clean wing configurations; data for both configurations is presented in Figure 13.178 through Figure 13.185. Model performance was evaluated for sideslip angles, β = -10°, -5°, 5°, and 10°. Relative wind from the pilots left is positive sideslip. Baseline performance, β = 0°, indicates a positive yawing moment slope, i.e. the model diverges from zero yawing moment with increasing angle of attack. The "fan" of sideslip angles is symmetric about the zero sideslip data, as expected. A positive side slip angle tends to restore the model to zero yaw with increasing angle of attack.

The differences in pitching moment and lift coefficient for the clean wing sideslip-sweep are due to temperature differences in the slot and TPS high pressure air lines from being the first run in the morning. HPA temperatures were consistently lower in the morning runs, as the air hadn't fully warmed up by the first run. This is consistent with what was seen during repeated runs that occur at the beginning and end of the day. The higher temperature air holds more energy and can be converted to produce more thrust out of the slots, resulting in higher lift and greater pitching moments compared to runs at lower temperatures. The differences are not seen with the low pylon beta-sweep as those runs were conducted back-to-back and temperature shifts between runs are small.

Overall, the results show that the relative wind direction is essentially negligible to the model performance for both the clean wing and low pylon configuration. As would be expected, the slope and magnitude of the yawing moment curve shows the sideslip disturbance and magnitudes needed for directional stability. The slot flow is the dominant flow feature and model performance is nearly insensitive to changes in the relative wind direction of up to 10°. This is

expected as the freestream dynamic pressure is up to 2 orders of magnitude less than the local dynamic pressure on the wing.

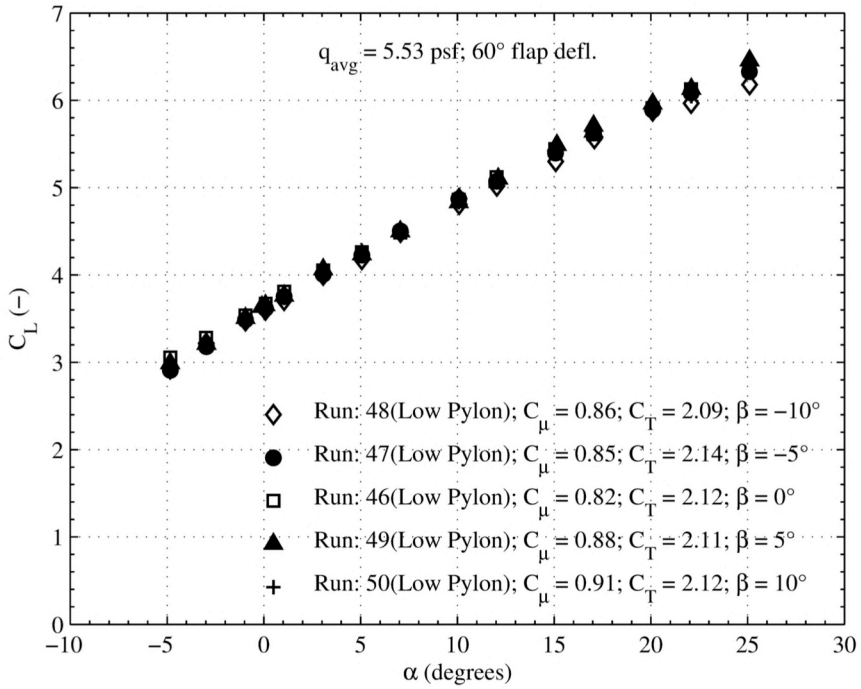

Figure 13.178. Sideslip plot set 1, low pylon. ***(a) 40 KTS, 60° flap deflection, full power, C_L vs. α.***

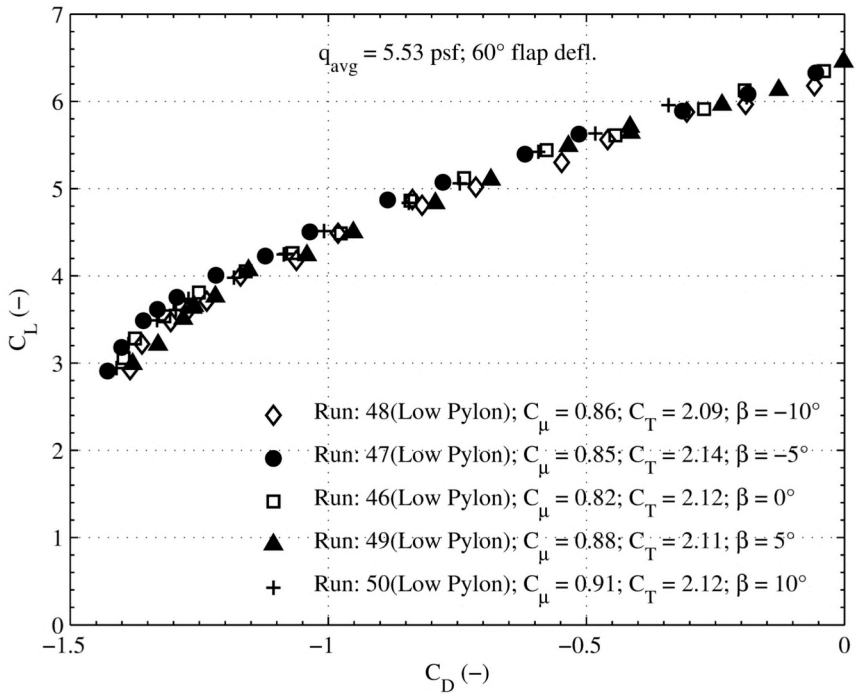

Figure 13.179. Sideslip plot set 1, low pylon. ***(b) 40 KTS, 60° flap deflection, full power, C_L vs. C_D.***

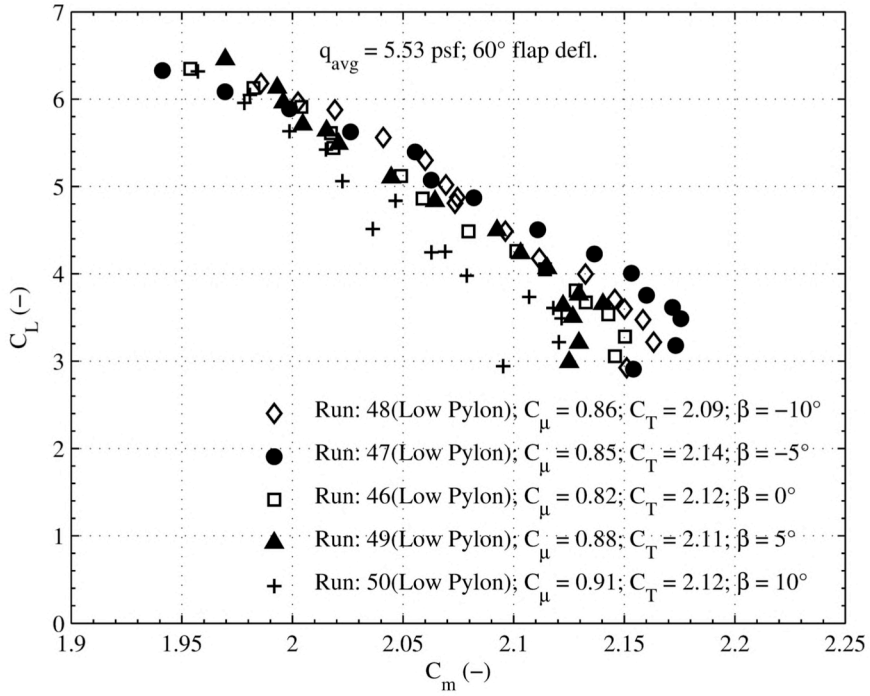

Figure 13.180. Sideslip plot set 1, low pylon. ***(c) 40 KTS, 60° flap deflection, full power, C_L vs. C_m.***

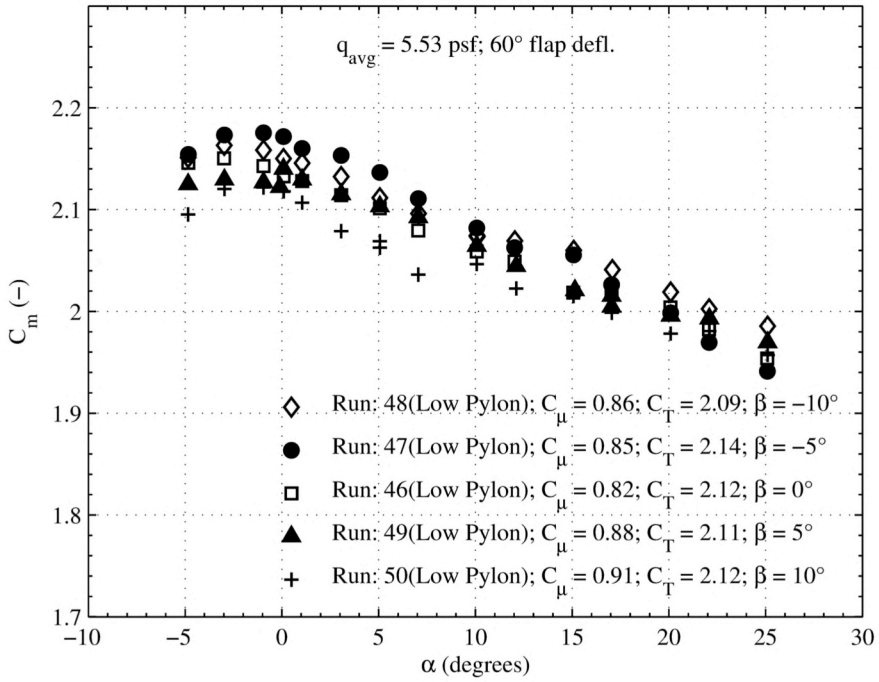

Figure 13.181. Sideslip plot set 1, low pylon. ***(d) 40 KTS, 60° flap deflection, full power, C_m vs. α.***

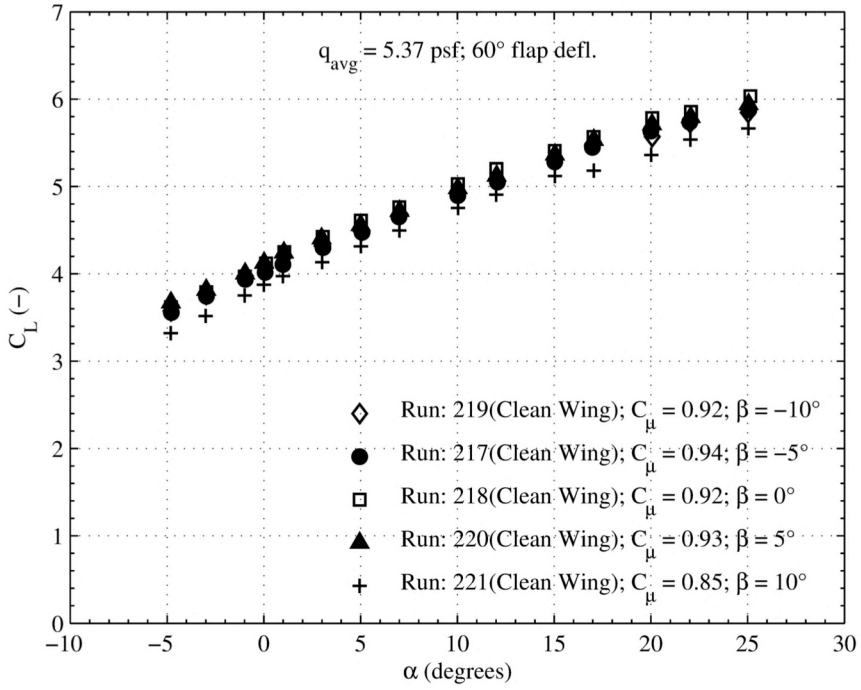

Figure 13.182. Sideslip plot set 2, clean wing. ***(a) 40 KTS, 60° flap deflection, full power, C_L vs. α.***

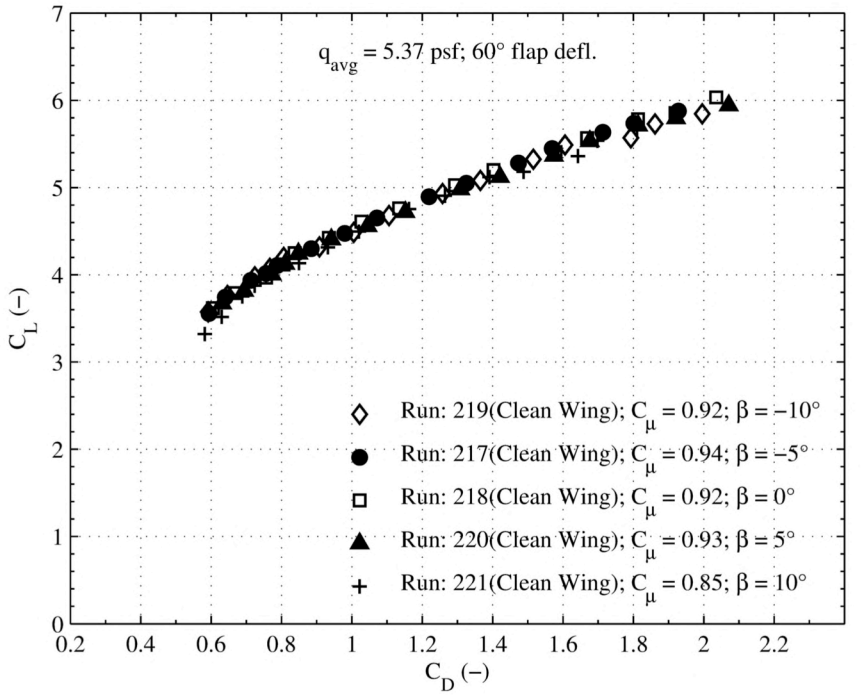

Figure 13.183. Sideslip plot set 2, clean wing. ***(b) 40 KTS, 60° flap deflection, full power, C_L vs. C_D.***

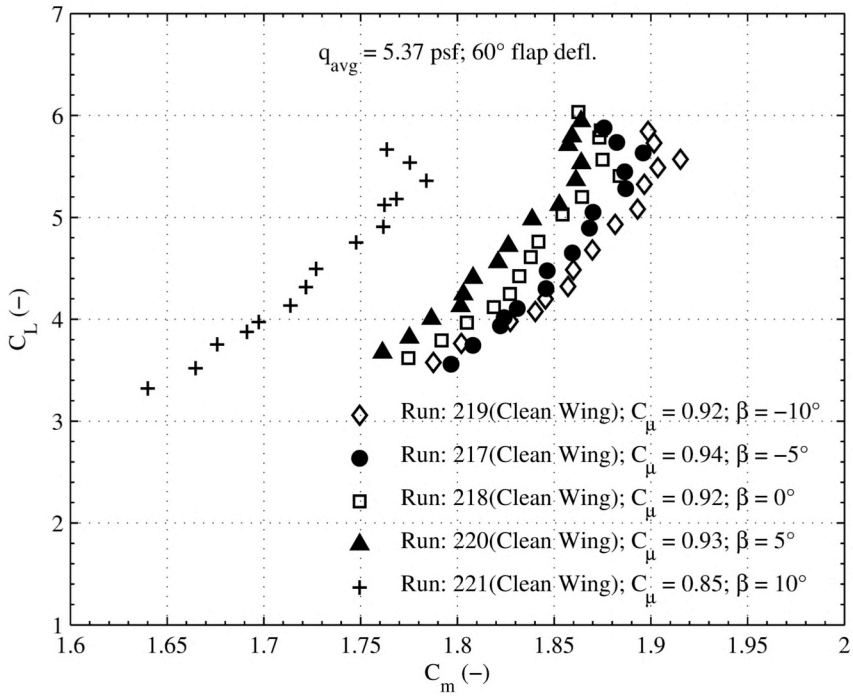

Figure 13.184. Sideslip plot set 2, clean wing. ***(c) 40 KTS, 60° flap deflection, full power, C_L vs. C_m.***

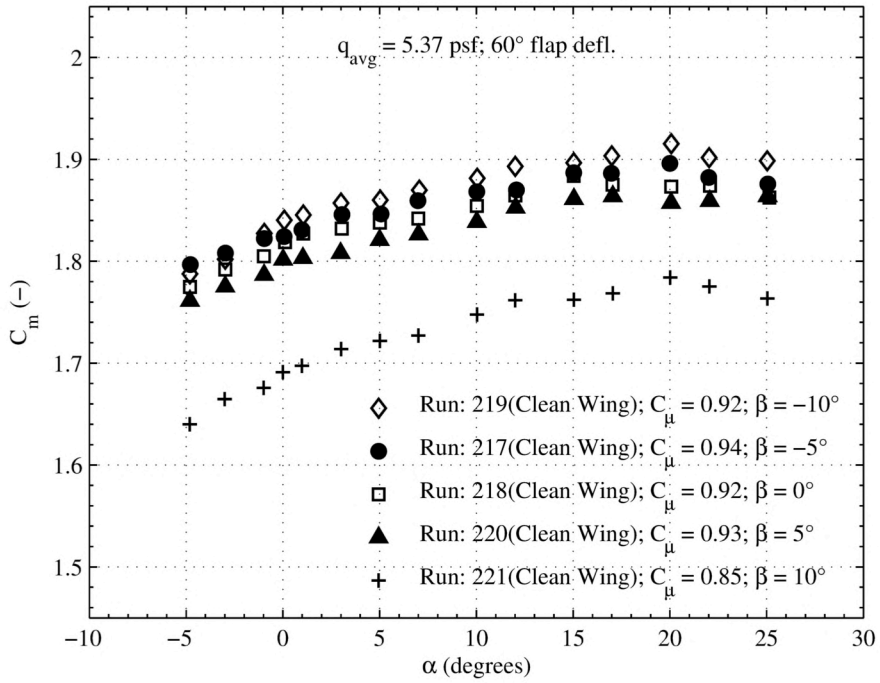

Figure 13.185. Sideslip plot set 2, clean wing. ***(d) 40 KTS, 60° flap deflection, full power, C_m vs. α.***

13.6. High Pylon Height

The model change from the low pylon to the high pylon took place over a day. There was minimal loss of instrumentation and testing was able to proceed with no down-time incurred. The model was in this configuration for a period of 5 wind-on days after which the TPS were removed and testing continued in the clean wing configuration. Within that span, 3 critical test points and 29 useful data runs at 3 different flap deflections were completed. No slot sweeps were conducted at the high pylon height. As a result, the plot sets for block three and block four are omitted. Block three will be substituted, instead, for a discussion on the aerodynamic differences between the low and high pylon heights.

The high pylon height measures 6.26 inches from the wing upper surface to the TPS centerline; the low pylon measures 4.21 inches along the same reference. Non-dimensionalizing by the fan diameter (D) of 5 inches, the high and low pylon heights correspond to a z/D of 1.25 and 0.84, respectively.

13.6.1. Block One

Block one figures show model performance as a function of flap deflection at 40 KTS freestream velocity and the full power setting (that is full slots and full TPS). The addition of the engine thrust provides increased lift augmentation due to increased negative pressures that result from the engine exhaust entrained onto the wing upper surface. As with the low pylon height though, the lift curve shows the 80° flap is not overly strong at entraining the engine thrust. As a result, the model stalls at $\alpha = 20°$ at a slightly lower maximum lift coefficient than the 60° flap deflection. Looking at the drag data, the thrust recovery provided by the TPS, and the slot thrust from the 0° flap are evident. Trends in pitching moment are consistent with what is seen at the low pylon height; pitch is increased with flap deflection.

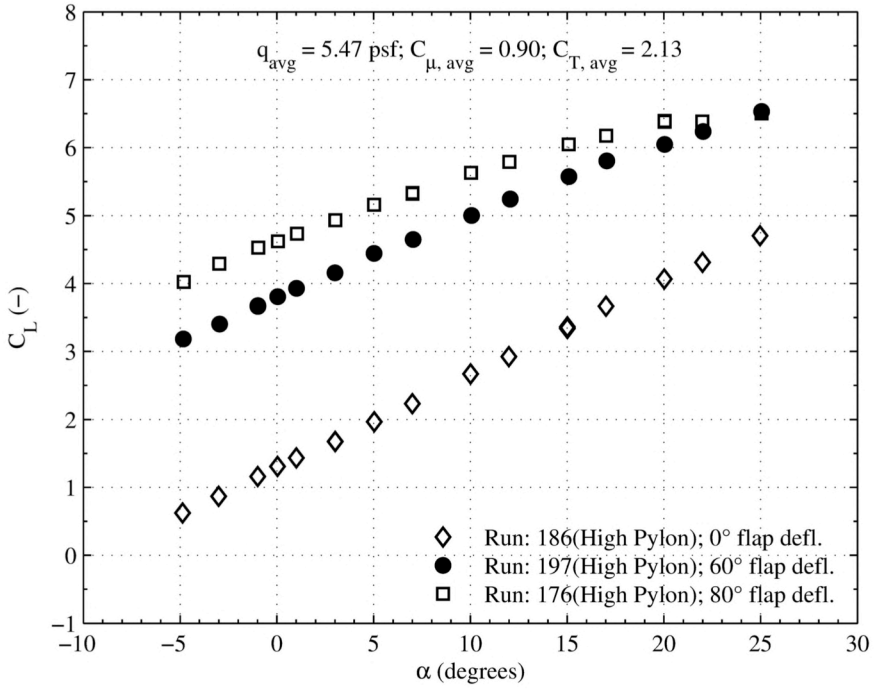

Figure 13.186. High pylon plot set 1. ***(a) 40 KTS, full power, C_L vs. α.***

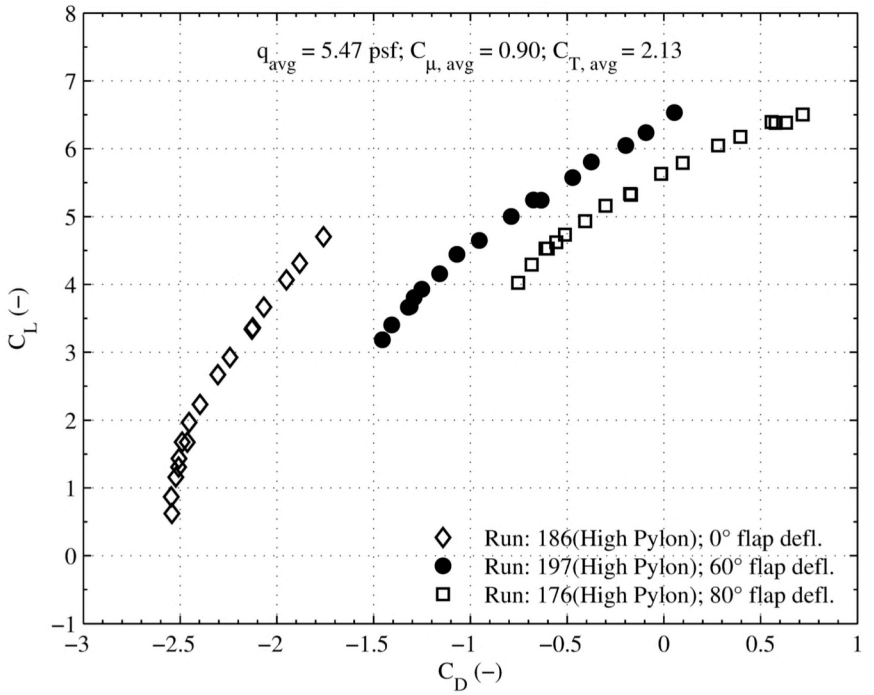

Figure 13.187. High pylon plot set 1. ***(b) 40 KTS, full power, C_L vs. C_D.***

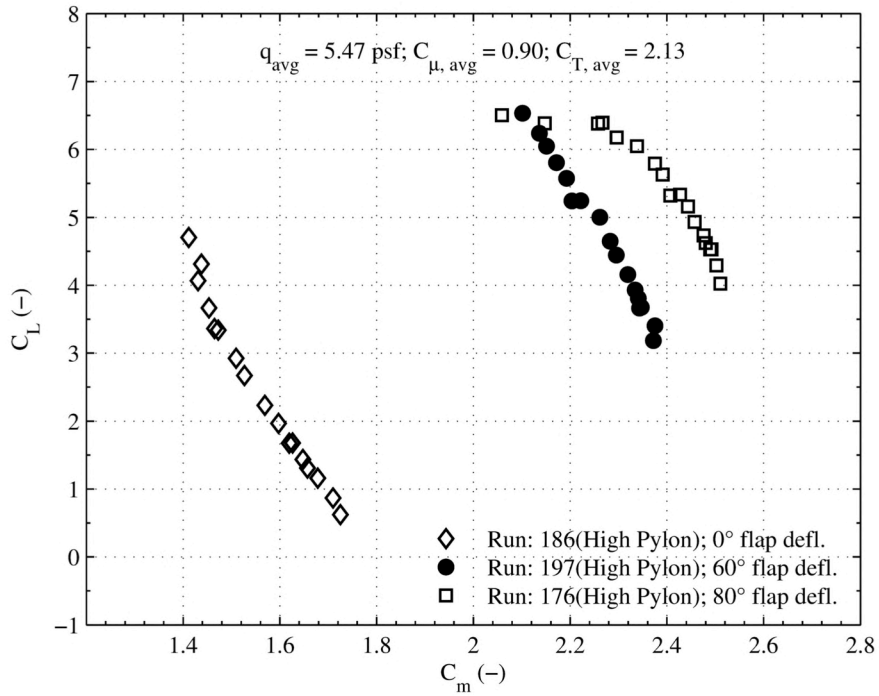

Figure 13.188. High pylon plot set 1. ***(c) 40 KTS, full power, C_L vs. C_m.***

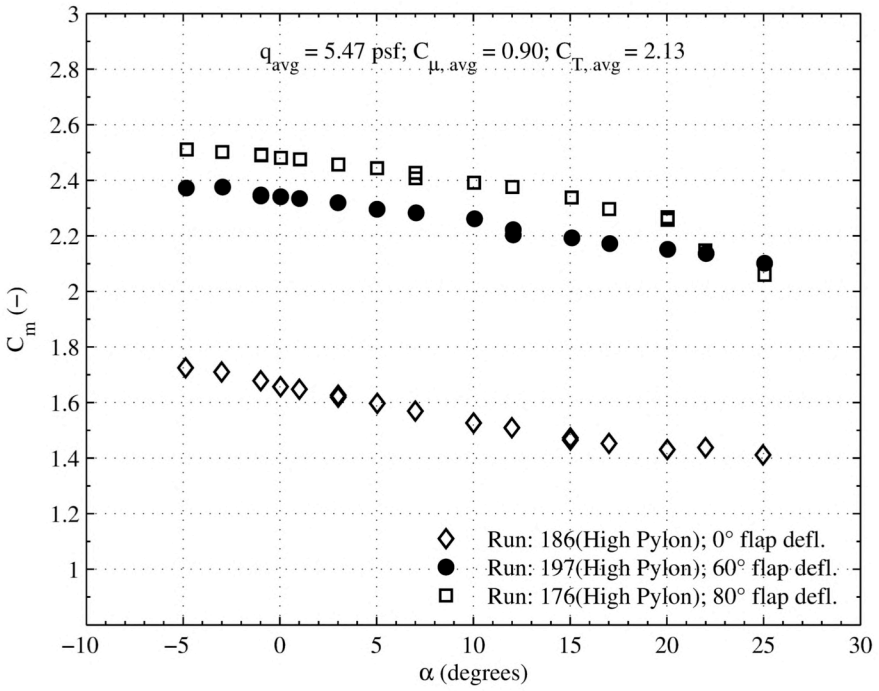

Figure 13.189. High pylon plot set 1. ***(d) 40 KTS, full power, C_m vs. α.***

13.6.2. Block Two

Figure 13.190 through Figure 13.193 presents block two plots for the high pylon configuration. The plots show alpha sweeps corresponding to the powered-lift matrix points at 40 KTS at the 80° flap deflection. The trends in the plot set are consistent with what is seen in the low pylon configuration. The performance benefits from deflecting the engine exhaust are seen, predominately, at higher angles of attack. Again, the lift curve slope is increased with the simulators turned on because the data are uncorrected and contain the $C_T*\sin(\alpha+\delta_{jet})$ component. As expected, each point in the powered-lift matrix is additive with respect to increasing the full powered lift coefficient. At $\alpha = 25°$, the maximum lift coefficient is increased by just over 1 to 6.5 with the engine simulators at the full set-point. The drag and pitching moment curves follow the expected trends. Pitching moment is increased with the points in the powered-lift matrix. Here, the positive flap deflection does not provide slot thrust, hence the larger (positive) drag when the slots are blowing.

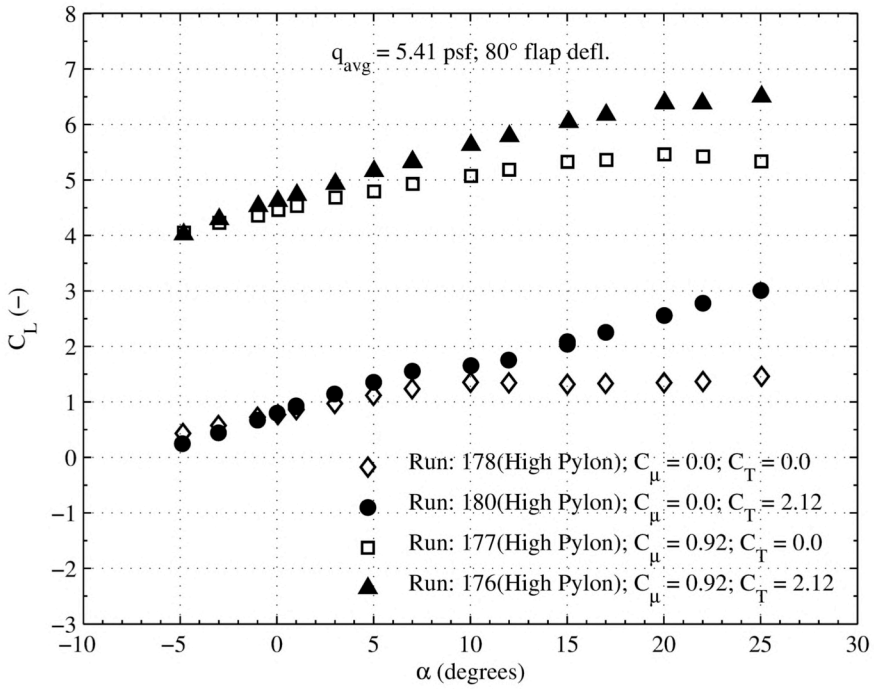

Figure 13.190. High pylon plot set 2. ***(a) 40 KTS, 80° flap deflection, C_L vs. α.***

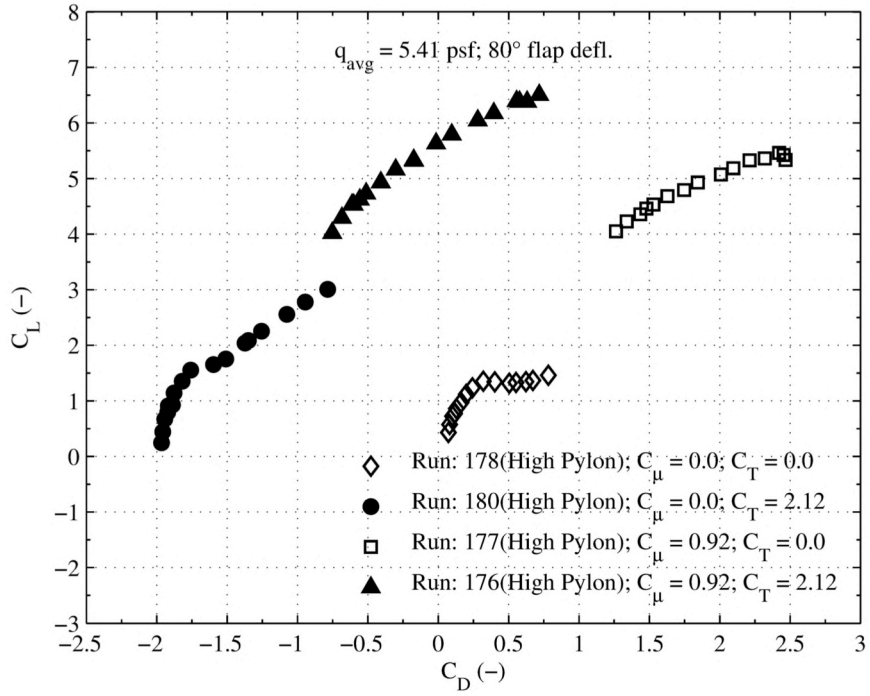

Figure 13.191. High pylon plot set 2. ***(b) 40 KTS, 80° flap deflection, C_L vs. C_D.***

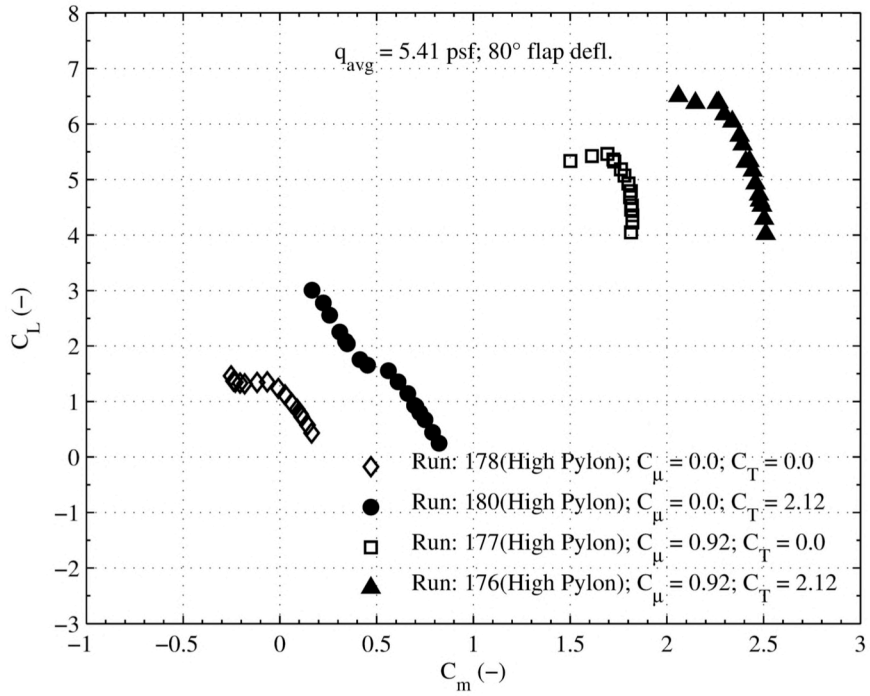

Figure 13.192. High pylon plot set 2. ***(c) 40 KTS, 80° flap deflection, C_L vs. C_m.***

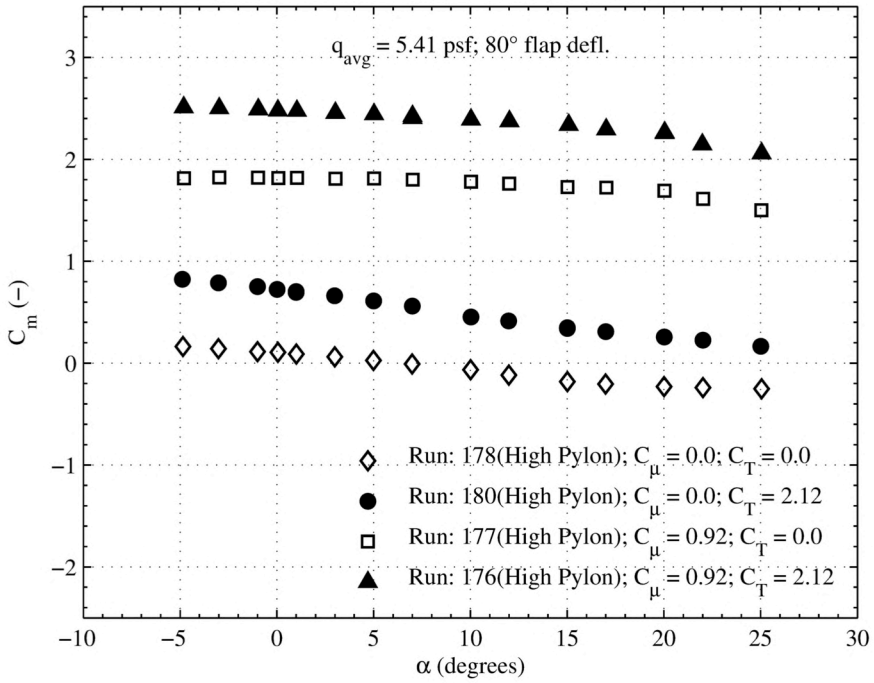

Figure 13.193. High pylon plot set 2. ***(d) 40 KTS, 80° flap deflection, C_m vs. α.***

13.6.3. Block Three

Block three plots directly compare data from the high and low pylon heights. The two pylon heights allowed for the highly coupled CCW and USB design to be characterized, both aerodynamically and acoustically. Figure set one presents un-powered data at 40 KTS and 0° flap deflection. Un-powered, the aero data tracks each other in both configurations, with only small noted differences. Lift coefficient magnitude is slightly offset (higher) in the high pylon configuration. With the TPS off, the pitching moment and drag data track each other. The drag differences in the pylon height are not discernible here, as the calibration showed the differences to be within the scatter of the balance uncertainty.

Figure set two presents full power data at 40 KTS and the 80° flap deflection. Here, the data shows higher lift across the angle of attack range in the high pylon configuration. This result goes against what is expected, that for a constant C_μ the low pylon height should deflect more engine exhaust, creating greater lift and better performance at high angles of attack. The greater lift curve slope for the low pylon height suggests there is a greater thrust component present in the lift data which would seem to support this expected result. The drag data, though, does not support this as there are negligible differences between the pylon heights. Higher drag in the low pylon would indicate more scrubbing drag due to increased engine deflection. Higher pithing moment at the higher pylon height is expected.

Figure sets three and four show similar data to figure set two; note figure set four shows the 60° flap deflection. Here though, as the speed is increased, the differences in the pylon height become less noticeable and the aerodynamic data tend to fall on top of each other. This can be expected as

the mass flow rate is fixed between the three speeds; as q_∞ increases, C_μ decreases. The relationship between increased engine deflection is tightly coupled to the value of C_μ. Without more mass flow rate or increased jet velocity, the expected trends are not seen at the lower values of C_μ.

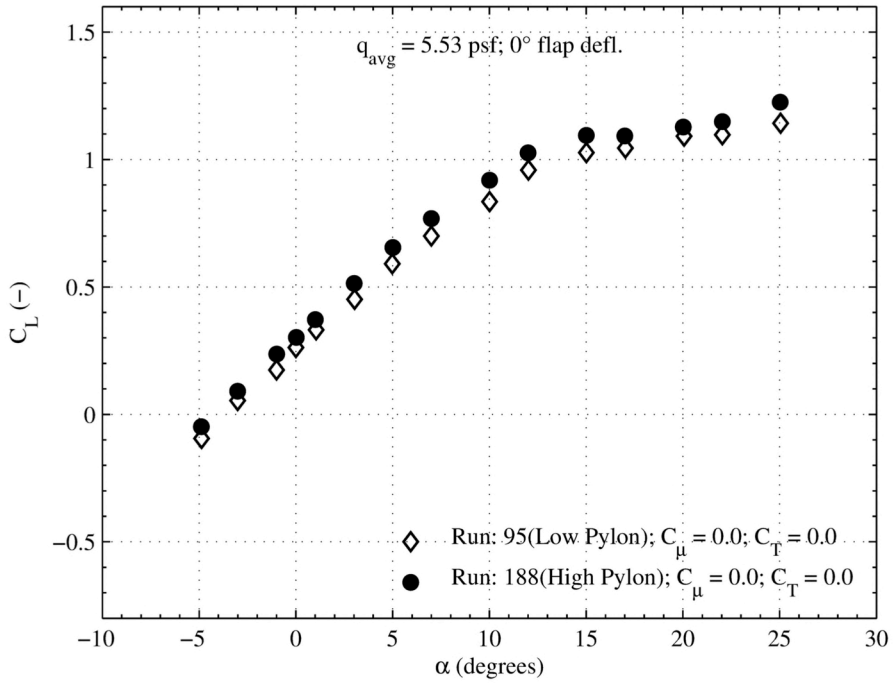

Figure 13.194. Low/High pylon plot set 1. ***(a) 40 KTS, no power, 0° flap deflection, C_L vs. α.***

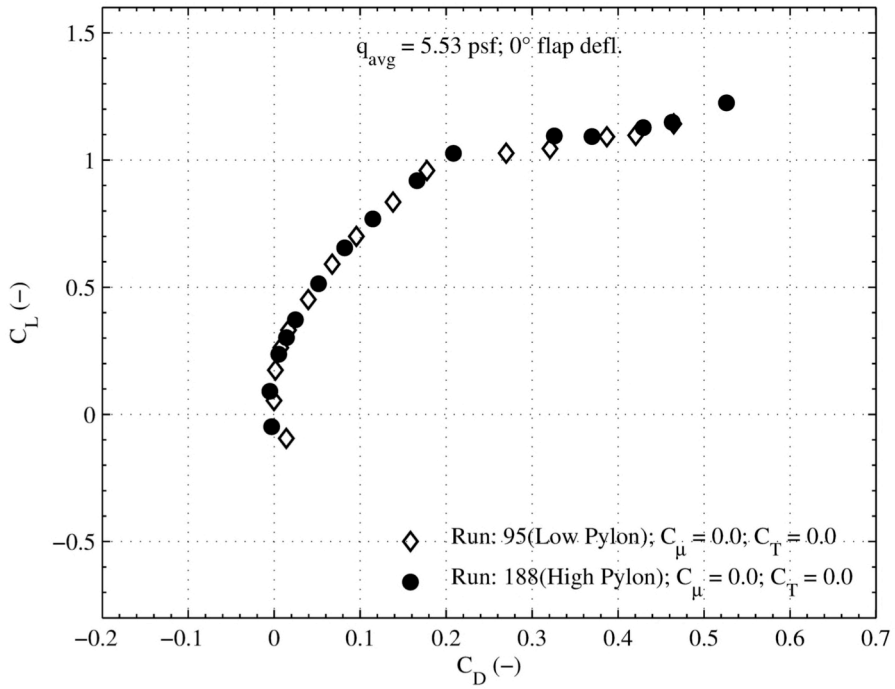

Figure 13.195. Low/High pylon plot set 1. ***(b) 40 KTS, no power, 0° flap deflection, C_L vs. C_D.***

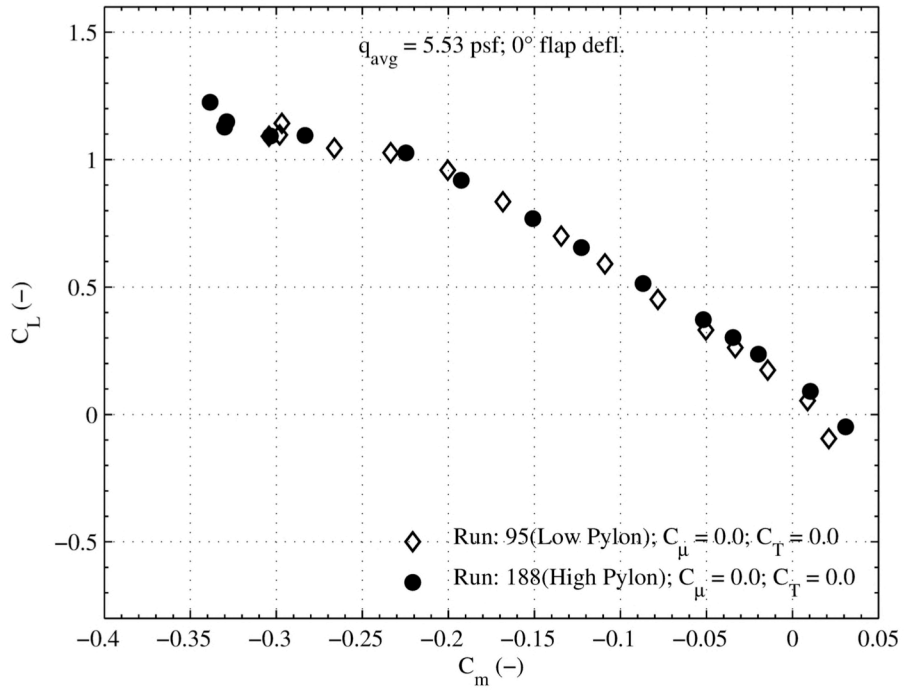

Figure 13.196. Low/High pylon plot set 1. ***(c) 40 KTS, no power, 0° flap deflection, C_L vs. C_m.***

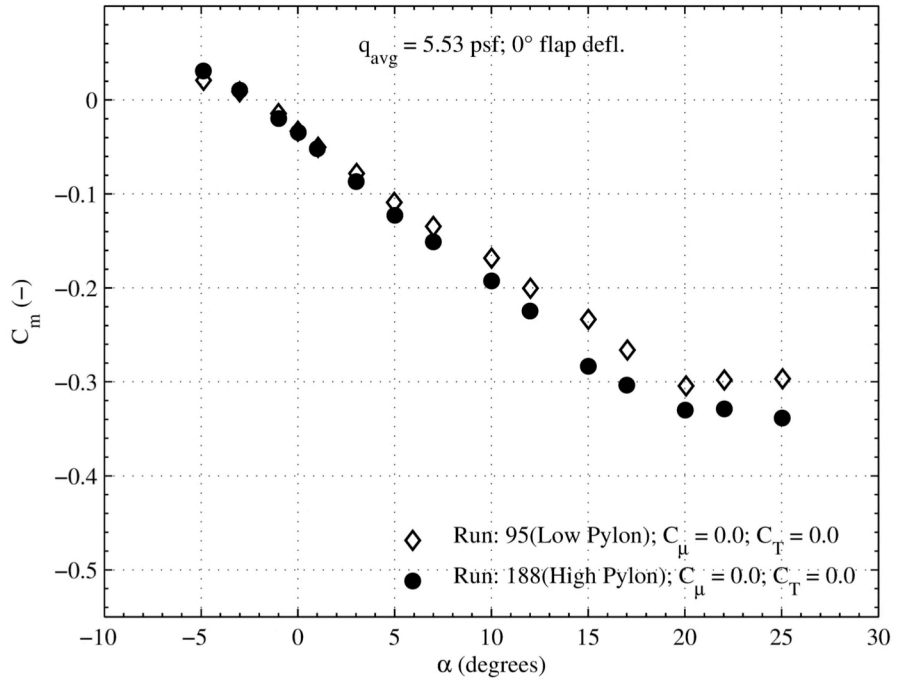

Figure 13.197. Low/High pylon plot set 1. ***(d) 40 KTS, no power, 0° flap deflection, C_m vs. α.***

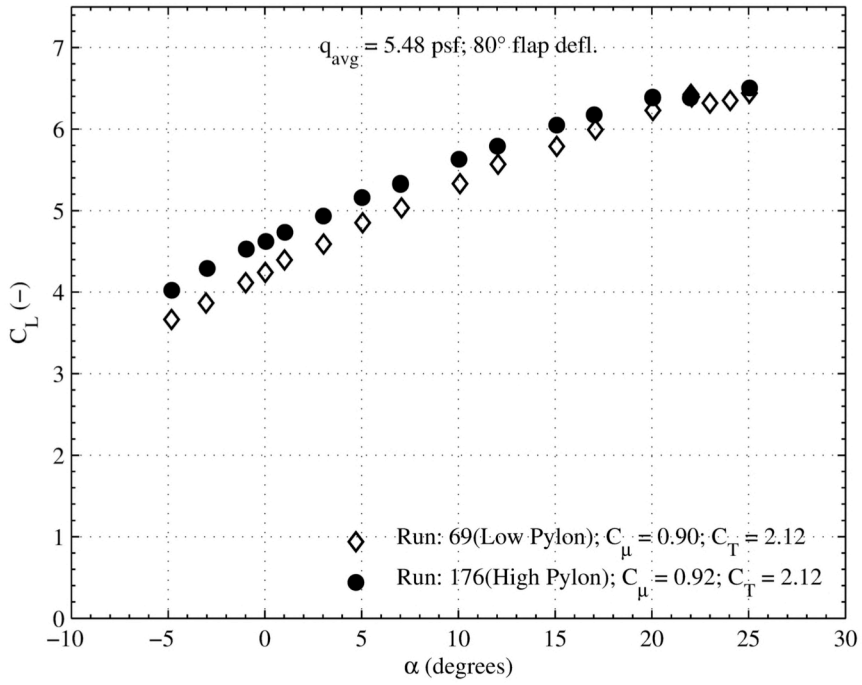

Figure 13.198. Low/High pylon plot set 2. ***(a) 40 KTS, full power, 80° flap deflection, C_L vs. α.***

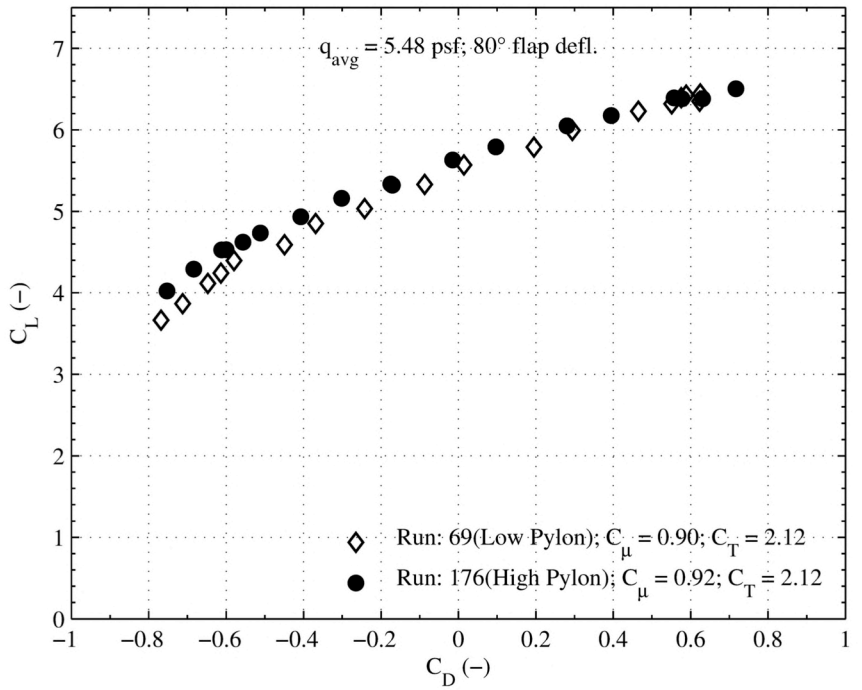

Figure 13.199. Low/High pylon plot set 2. ***(b) 40 KTS, full power, 80° flap deflection, C_L vs. C_D.***

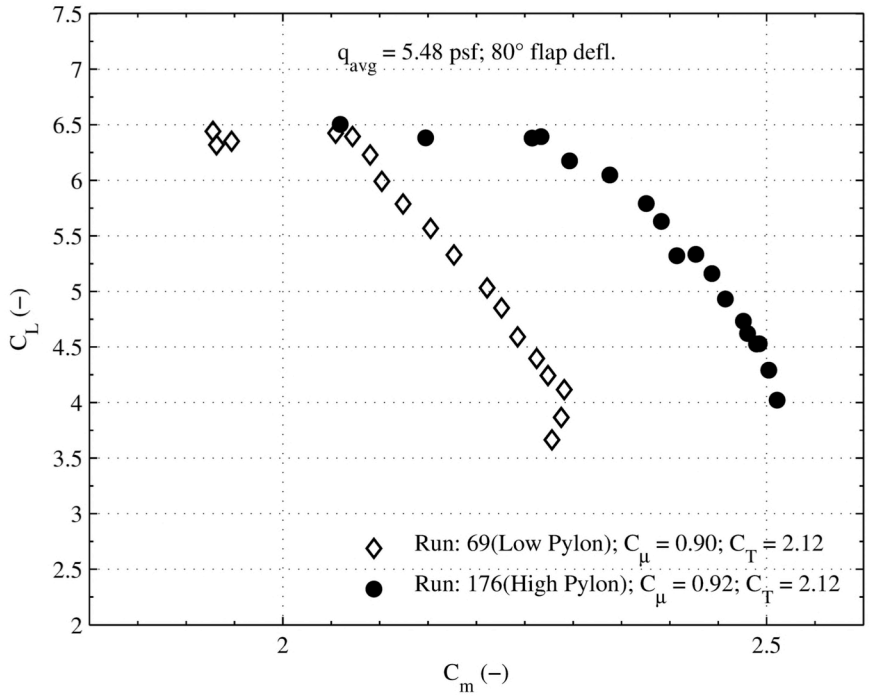

Figure 13.200. Low/High pylon plot set 2. ***(c) 40 KTS, full power, 80° flap deflection, C_L vs. C_m.***

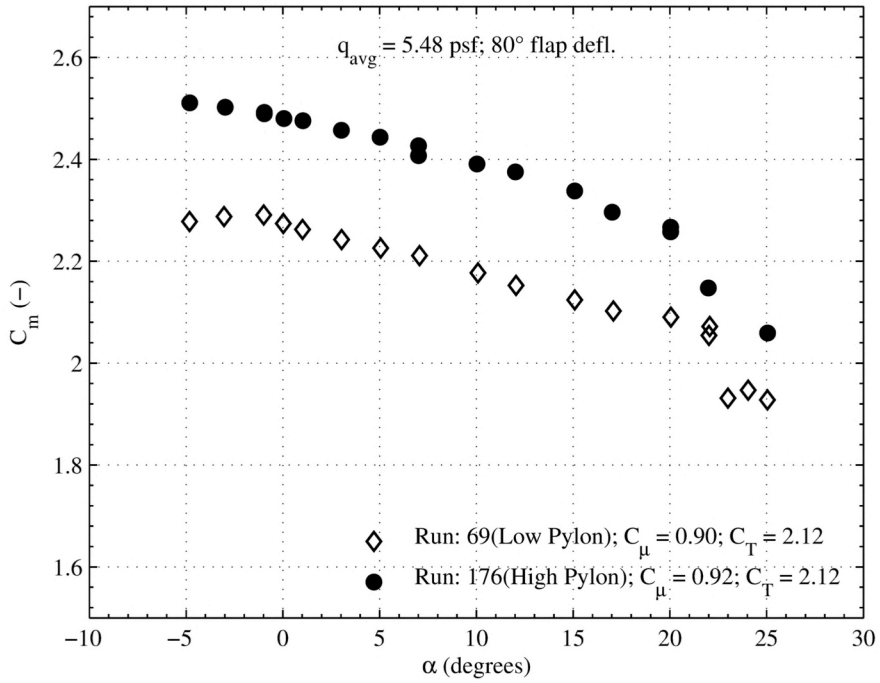

Figure 13.201. Low/High pylon plot set 2. ***(d) 40 KTS, full power, 80° flap deflection, C_m vs. α.***

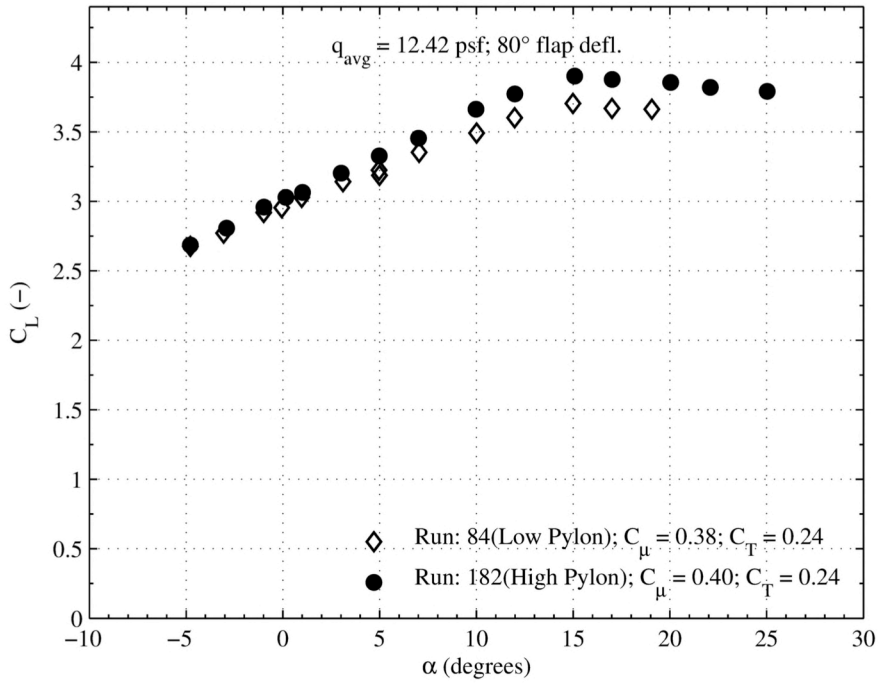

Figure 13.202. Low/High pylon plot set 3. ***(a) 60 KTS, full power, 80° flap deflection, C_L vs. α.***

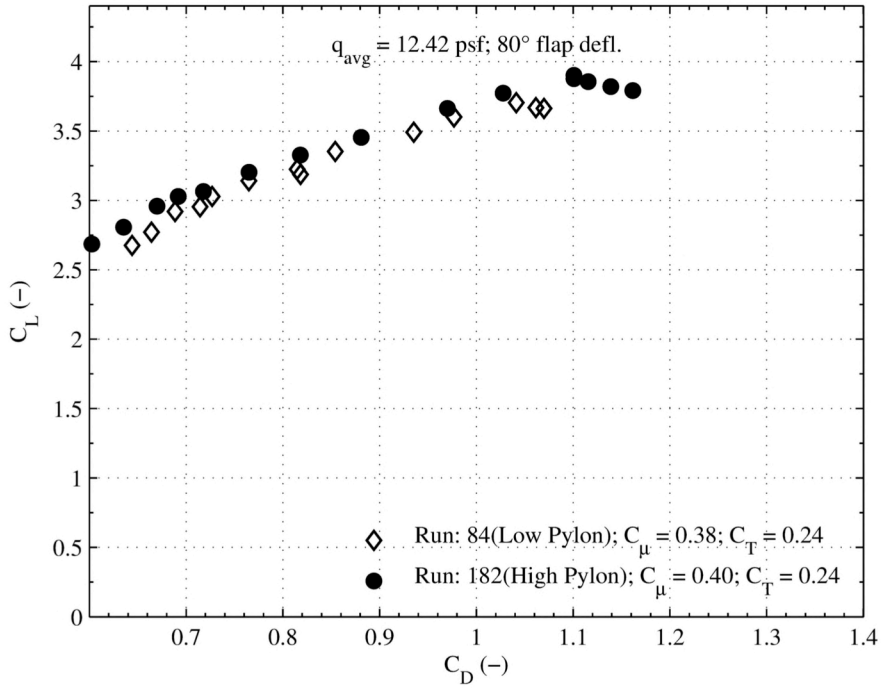

Figure 13.203. Low/High pylon plot set 3. ***(b) 60 KTS, full power, 80° flap deflection, C_L vs. C_D.***

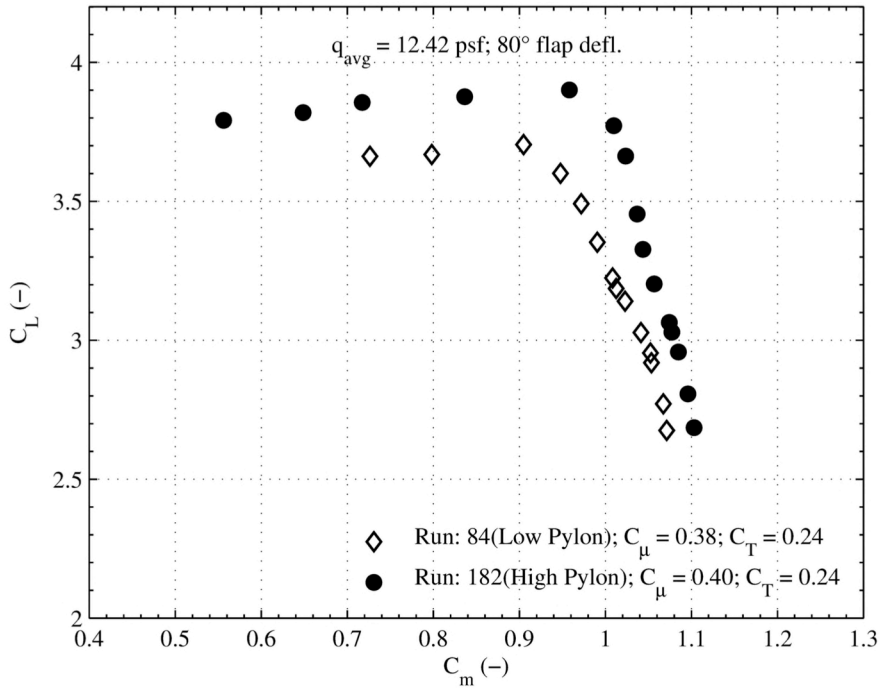

Figure 13.204. Low/High pylon plot set 3. ***(c) 60 KTS, full power, 80° flap deflection, C_L vs. C_m.***

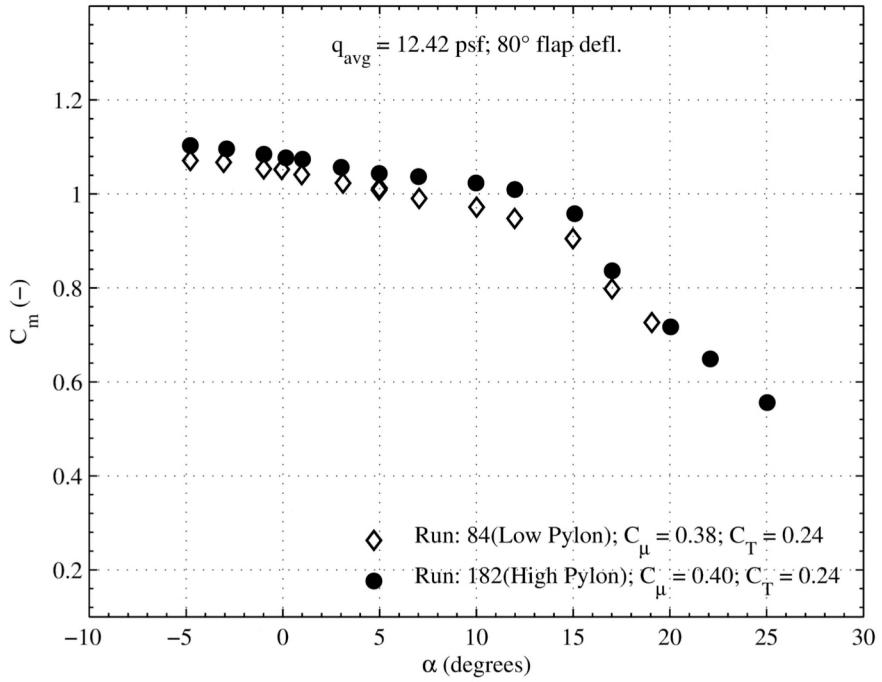

Figure 13.205. Low/High pylon plot set 3. ***(d) 60 KTS, full power, 80° flap deflection, C_m vs. α.***

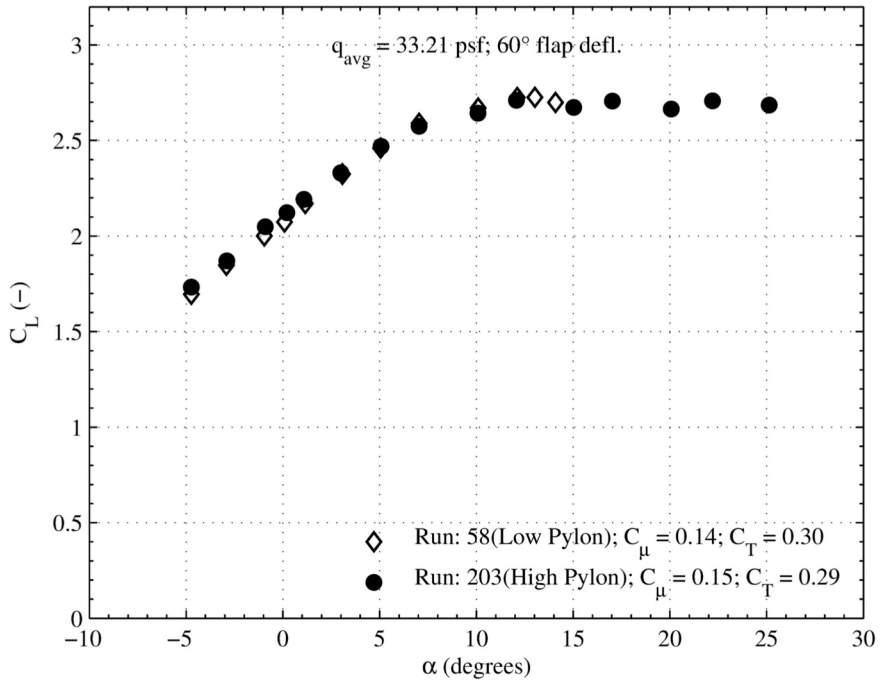

Figure 13.206. Low/High pylon plot set 4. ***(a) 100 KTS, full power, 60° flap deflection, C_L vs. α.***

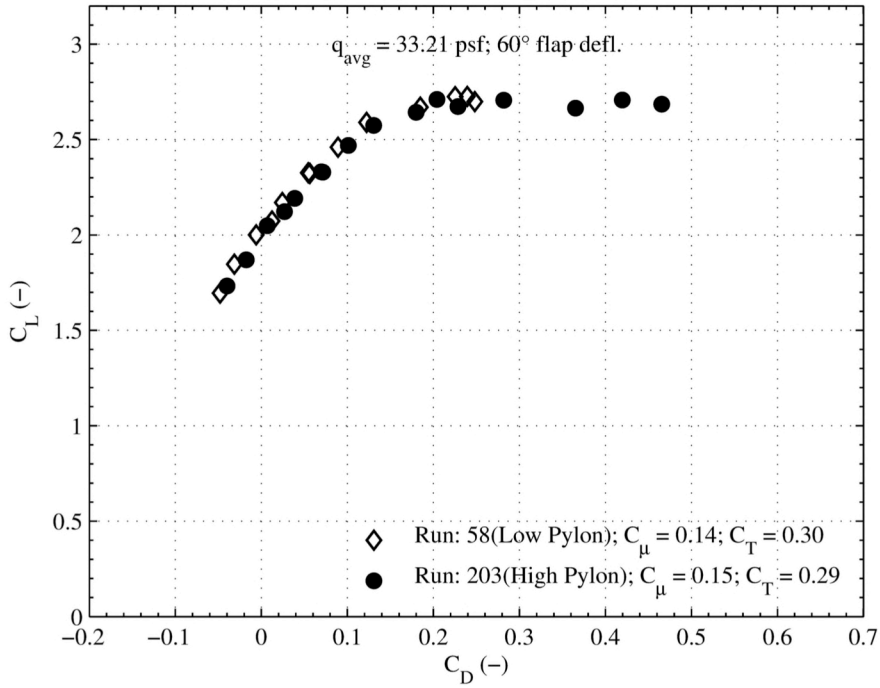

Figure 13.207. Low/High pylon plot set 4. ***(b) 100 KTS, full power, 60° flap deflection, C_L vs. C_D.***

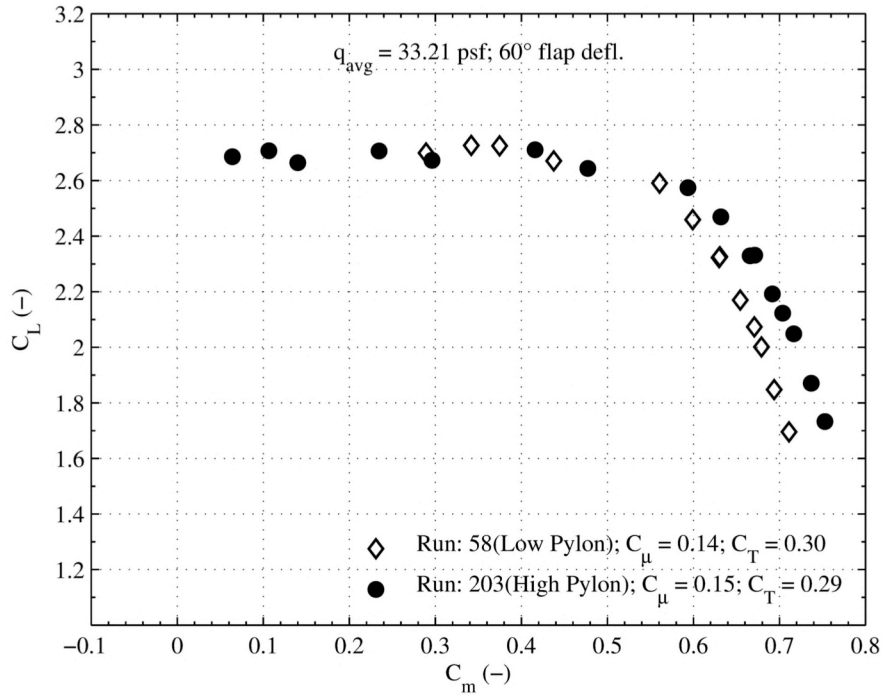

Figure 13.208. Low/High pylon plot set 4. ***(c) 100 KTS, full power, 60° flap deflection, C_L vs. C_m.***

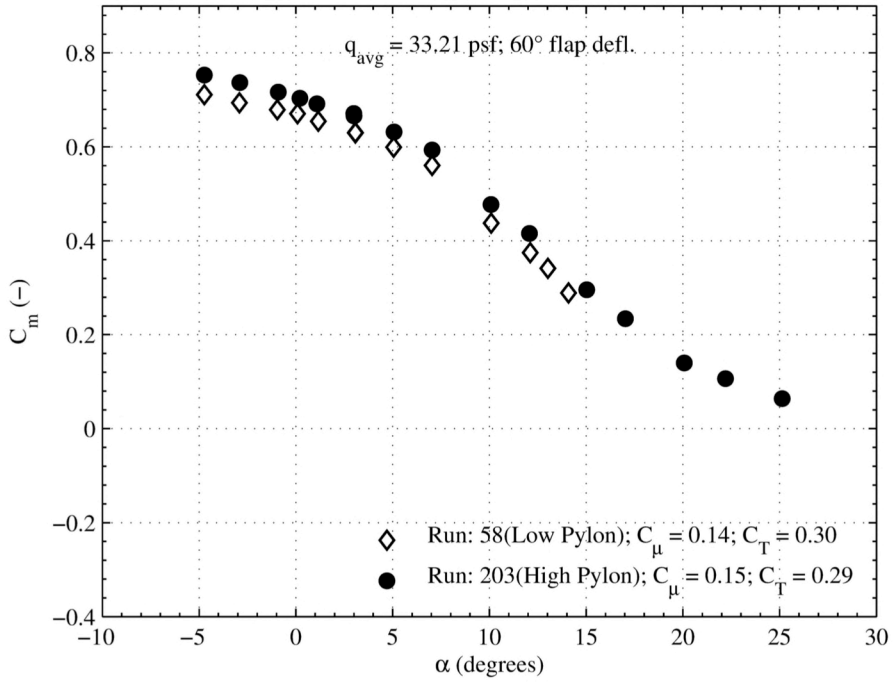

Figure 13.209. Low/High pylon plot set 4. ***(d) 100 KTS, full power, 60° flap deflection, C_m vs. α.***

14.Conclusions

This report has presented a thorough summary of the wind tunnel test of the advanced model for extreme lift and improved aeroacoustics, AMELIA, in the national full-scale aerodynamics complex, NFAC, 40 ft by 80 ft test section. An extensive description of the model, its components and the test facility was provided so that all geometric entities are sufficiently explained for future modeling efforts and so that a complete understanding of the model configuration can be obtained. The various test measurements, the techniques used to obtain the measurements and the data acquisition methods were described in sufficient detail to understand the fidelity of the measurements and to facilitate the reproduction of the measurements. Due to the sensitivity of the test results to the slot blowing fidelity, a detailed presentation of the slot blowing calibration and characterization was provided. Similarly for the turbofan propulsion simulator, TPS, performance, sufficient information was provided to document the calibration, configuration, control and usage of these devices. Finally, the test matrix, the test data and the corresponding results were presented to provide a complete presentation of the information collected. Issues such as the repeatability, balance calibration uncertainty, and other uncertainties were discussed so that the quality of the collected data can be determined and used in future analyses.

This test accomplished all of the pre-test objectives that were established by the test team. All 10 critical test points were performed with all relevant data collected. All Tier 1 and Tier 2 data was collected, and the complete test matrix was performed with any significant problems or delays. In addition to the pre-test determined activities, additional configurations were also tested. Tests were performed without the engine simulators, nacelles and pylons to obtain data for a more simple geometry as a starting point for computational modeling validation efforts. Also, tests were performed with only trailing edge slot blowing so that comparisons to existing trailing edge only blowing results could be done. The efficient operation of the test team made this possible.

This test is the first large scale, full-span wind tunnel test of its kind, and from the outset this test was intended to generate validation data for the CFD and acoustics modeling communities. The acoustics data was obtained concurrently with the aerodynamics data for better correlation between the flow conditions and measurements. The blended wing-body inspired design with circulation control wings and over-the-wing engine simulators are all unique design features that might become critical components of an N+2 aircraft design. The data presented in this report should provide a wealth of new data for modelers attempting to validate their tools on these types of configurations and to benchmark their model's improved ability to predict the performance of these types of configurations.

The test collected a wide variety of data using a number of techniques. Surface pressures were collected from over 200 pressure ports over the wing, flap and fuselage surfaces so that the local surface pressures can be compared. In addition, measurements were made for the TPS system to record the propulsion system performance so that the effects of the TPS on the aerodynamics and acoustics can be determined. Forces and moments were also measured for all tests using the internal balance.

In terms of the test data itself, there are a number of noteworthy observations to be made:

- The design of the plenum for the slot flow was critical to obtaining acceptable performance of the circulation control. It took significant efforts to achieve the desired flow uniformity, and this effort is well documented.

- In order to achieve significant lift augmentation from the circulation control wing, leading edge blowing was needed. Without leading edge blowing, stall occurred at low angles of attack and abruptly occurred with angle of attack variation. With leading edge blowing, there was no sudden lift loss noticed as angle of attack varied, and relatively large angles of attack would still yield some lift augmentation.
- Cases with leading edge blowing showed surface streamlines that followed the slot normal direction and not the freestream flow direction.
- The pitching moment increased with increased blowing. The circulation control phenomenon creates more lift aft of the original center of pressure. This has an impact on the aircraft design since this pitching moment needs to be balanced by other lifting surfaces (typically the tail) for stable flight.
- There was little lift benefit observed between the 80° flap deflection and the 60° flap deflection. It was expected that the larger flap deflection would result in higher lift and higher drag. Higher drag was observed, but no additional lift.
- It was expected that the lower engine height would impact the aerodynamic performance, (e.g. increased lift) but the tests demonstrated no significant impact on the aerodynamics. There were acoustic benefits, as expected.

While this test produced a number of significant datasets for future use and achieve a number of technical objectives, there are several suggestions for future work that can build of this test to produce even better data to be used by the aerodynamics and acoustics communities. These include:

- Specific tests to capture engine flow deflection. While there is some video documentation of it, this occurred because of the combination of high relative humidity and low engine flow temperatures and not because of a concerted effort by the experimental team. Also, the camera angles are not at the optimal location to capture the deflection.
- More detailed flow field measurement. This test focused on collecting surface properties in addition to the typical forces and moments that are collected in wind tunnel tests. The next step that would provide valuable to the validation community is local flow field quantities near and around the model. This could be accomplished with boundary layer and shear layer probes and with PIV measurements.
- Leading edge-only blowing data. The test data showed a strong coupling between blowing and pitching moment that cannot be fully investigated with the current data sets. A better understanding of the contribution the leading edge blowing has on the pitching moment would allow a more optimum blowing configuration to be assessed. The outcome of such an investigation would allow for a combination of leading- and trailing-edge blowing rates that would allow the airplane to optimize desired performance metrics while flying in a trimmed configuration.
- Improve the engine acoustics. One of the major limitations in the acoustics data is that the TPS do not accurately model the aircraft engine noise. To get a better understanding of how the engine noise contributes to the overall acoustic performance of this design, a more acoustically accurate model should be used.
- Enhanced Landing-gear Integration, ELI, test. While this test was focused at the low speeds associated with takeoff and landing, the impact that the landing gear would have on the performance was not part of this effort. It would be valuable to know how to efficiently integrate the landing gear into this design and what the penalties will be.
- Instrumented tail test. Now that the baseline configuration has been thoroughly tested, a test should be performed with a variety of candidate tails. Since the original design was created with the ability to instrument the tail and the tail section has existing off-blocks

for mounting, a new test could perform a wide variety of measurements on a number of tail designs relatively easily.

- Engine exhaust deflection. In smaller scale tests performed by GTRI for this contract, additional lift was obtained by using a mechanical device to deflect the engine exhaust. Similar deflections could be also achieved by pneumatic mechanisms, such as slots on the aft end of the engine nacelle. Understanding the performance capabilities of the mechanical and pneumatic devices in increasing lift and the associated acoustics results would be of benefit to the design community, and provide an additional validation dataset for the modeling community.

15.References

[1]Collier F, Zavala E, and Huff D. "Fundamental Aeronautics Program, Subsonic Fixed Wing Reference Guide". NASA.

[2]Jameson K. K., et al, "Design and Wind Tunnel Testing of Cal Poly's AMELIA 10 Foot Span Hybrid Wing-Body Low Noise CESTOL Aircraft", *27th International Congress of the Aeronautical Sciences*, Nice, France. September 2010.

[3]Marshall, D. M., et al, "NASA NRA End of Year One Progress Report" NASA.
[4]Booth D., Ulbrich N., "Calibration and Data Analysis of MC-130 Air Balance", *8th International Symposium on Strain Gauge Blances*, Lucerne, Switzerland, May 2012.

[5]Marshall, D.M., et al, "NASA NRA End of Year Two Progress Report" NASA.

[6]Golden, R. M., Marshall, D. D., "Design and Performance of Circulation Control Flap Systems", *48th AIAA Aerospace Sciences Meeting,* AIAA 2010-1053 Orlando, Florida.

[7]Zilliac, G. G., "Further Developments of the Fringe-Imaging Skin Friction Technique", Ames Research Center, Moffett Field CA, December 1996.

[8]National Full-Scale Aerodynamics Complex Interim Test Planning Guide for Experiments in the 40- by 80- Foot and 80- by 120- Foot Wind Tunnel Facilities, 22 January 2009/

[9]Scanners and Systems-DTC Initium (http://www.meas-spec.com/product/tm_product.aspx?id=9312).

[10] Zilliac, G. G., "Further Developments of the Fringe-Imaging Skin Friction Technique", NASA Ames Research Center, Moffett Field, CA, Dec. 1996.

[11]Personal Conversation with Theodore Garbeff, Aeronautical Engineer NASA Ames Research Center.

[12] Booth D., Ulbrich N., "Calibration and Data Analysis of MC-130 Air Balance", *8th International Symposium on Strain Gauge Blances*, Lucerne, Switzerland, May 2012.

[13]van Aken, J. M., and Yang, L., "Development of a new State-of-the-Art Data Acquisition System for the National Full-Scale Aerodynamics Complex Wind Tunnels", AIAA 2009-1346, American Institute of Aeronautics and Astronautics, January, 2009.

[14] Eppel J. C., Shovlin M. D., Jaynes D. N., Englar R. J., Nichols J. H., "Static Investigation of the Circulation-Control-Wing/Upper-Surface-Blowing Concept Applied to the Quiet Short-Haul Research Aircraft", NASA Technical Memorandum 84232, July 1982.

[15] Milholen W. E., Jones G. S., Cagle C. M., "NASA High-Reynolds Number Circulation Control Research – Overview of CFD and Planned Experiments (Invited)", AIAA 2010-344, AIAA Aerospace Sciences Meeting, Orlando Florida, January 2010.

[16] Englar R. J., Blaylock G. M., Gaeta R. J., Jones G. S., Milholen W. E., "Recent Experimental Development of Circulation Control Airfoils and Pneumatic Power-Lift Systems"

[17] Novak C. J., Cornelius K. C., "Investigations of a Circulation Control Airfoil Flowfield Using an Advanced Laser Velocimeter", NASA Conference Publication 2432, Proceedings of the Circulation Control Workshop, NASA Ames Research Center, Moffett Field CA, Feb. 1986.

[18] Englar R. J., "Subsonic Two-Dimensional Wind Tunnel INV of the High Lift Capability of Circulation Control Wing Sections", David W. Taylor Naval Ship R&D Center, April 1975.

[19] Englar R. J., "Two Dimensional Transonic Wind Tunnel Tests of Three 15-Percent Thick Circulation Control Airfoils", Naval Ship Research and Development Center, Washington DC, December 1970.

[20] Wood N., Nielsen J., "Circulation Control Airfoils Past, Present, Future", AIAA 23rd Aerospace Sciences Meeting, Reno Nevada, January 1985.

[21] Alley N. R., Steele J., Neidhoefer J. C., Englar R. J., Blaylock G., "Development of a Cruise-Efficient Extreme-STOL-Capable Demonstrator UAV", Atlanta Georgia, April 2010.

[22]Wetzel D., Griffin J., Liu F., Cattafesta L., "An Experimental Study of a Circulation Control Airfoil Trailing Edge Flow Field", 5th Flow Control Conference, Chicago Illinois, June-July 2010.

[23]Wahls, R. A., Adcock, J. B., Witkowski, D. P., and Wright, F. L., "A Longitudinal Aerodynamic Data Repeatability Study for a Commercial Transport Model Test in the National Transonic Facility," NASA TP-3522, 1995.

[24]"Assessment of Experimental Uncertainty With Application to Wind Tunnel Testing," AIAA Standard, S-071A-1999.

[25]"Guide to In-Flight Thrust Measurement of Turbojets and Fan Engines," AGARD-AG-237, 1979. (Also AD A065 939.)

[26]Zell, P. T., Flack, K., "Performance and Test Section Flow Characteristics of the National Full-Scale Aerodynamics Complex 40- by 80-Foot Wind Tunnel", NASA TM 101065, February, 1989.

[27]Milholen, W. E., II, Jones, G. S., Chan, D. T., and Goodliff, S. L., "High-Reynolds Number Circulation Control Testing in the National Transonic Facility (Invited)," AIAA 2012-0103.

[28]Englar, R. J., Jones, G. S., Allan, B. G., Lin, J. C., "2-D Circulation Control Airfoil Benchmark Experiments Intended for CFD Code Validation", AIAA 2009-902, American Institute of Aeronautics and Astronautics, January, 2009.

[29]Englar, R. J., Gaeta, R. J., Lee, W. J., Leone, V., "Development of Pneumatic Over-the-Wing Powered-Lift Technology; Part I: Aerodynamic/Propulsive", AIAA 2009-3942, American Institute of Aeronautics and Astronautics, January, 2009.

[30]Milholen, W. E., II, Jones, G. S., Chan, D. T., Goodliff, S. L., "High-Reynolds Number Circulation Control Testing in the National Transonic Facility", AIAA 2012-0103, American Institute of Aeronautics and Astronautics, January, 2012.

A1. Selected AMELIA Assembly Drawings

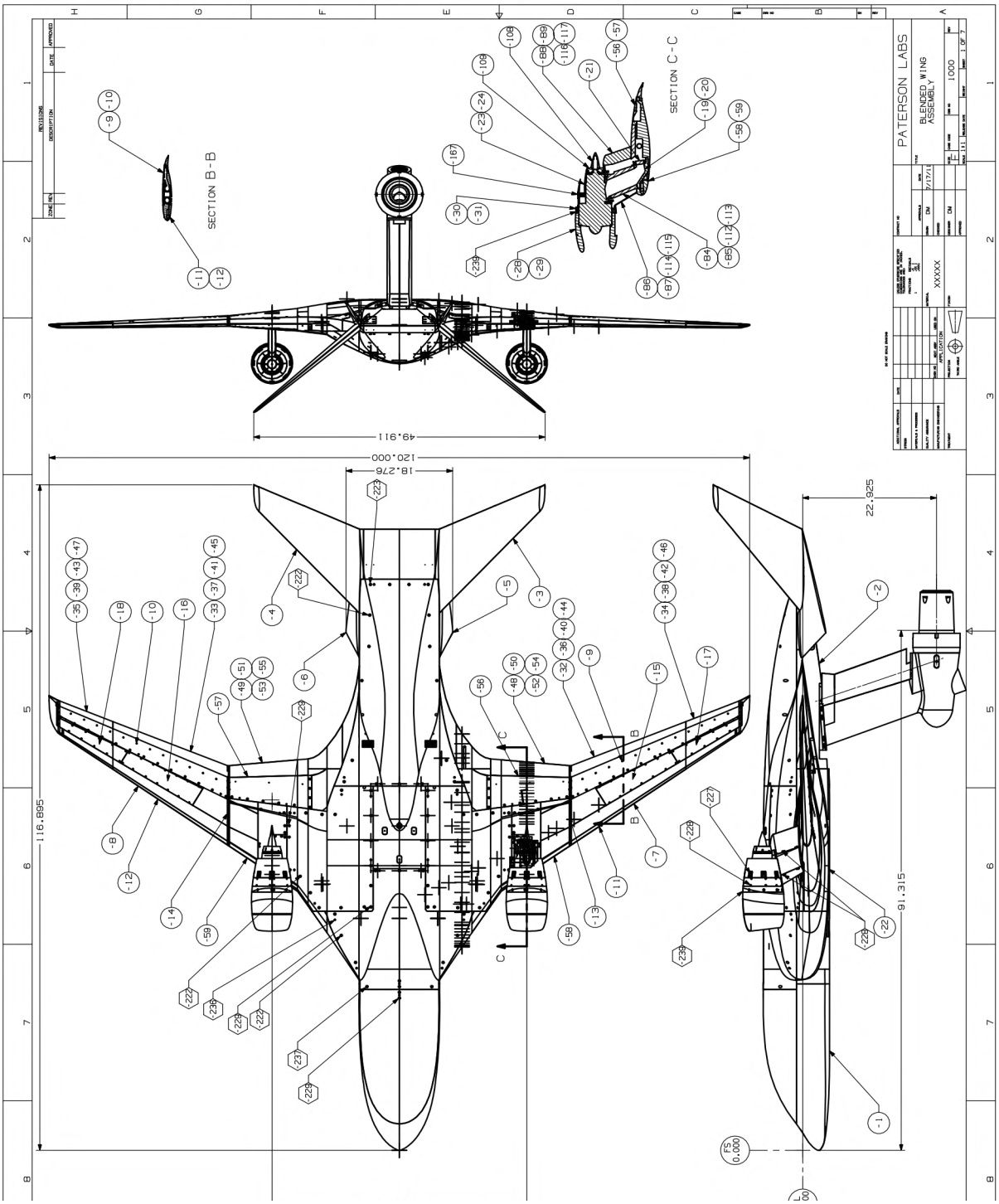

ITEM NO	PART OR IDENTIFYING NO	NOMENCLATURE OR DESCRIPTION	MATERIAL SPECIFICATION	QTY
-1	1001-3	LOWER NOSE		1
-2	1002-3	LOWER AFT FUSELAGE		1
-3	1003-3	LH VERTICAL		1
-4	1003-4	RH VERTICAL		1
-5	1004-3	LH DORSAL		1
-6	1004-4	RH DORSAL		1
-7	1006-3	LH OUTBOARD WING		1
-8	1006-4	RH OUTBOARD WING		1
-9	1007-3	LH TE OUTBD PLENUM COVER		1
-10	1007-4	RH TE OUTBD PLENUM COVER		1
-11	1007-5	LH LE OUTBD PLENUM COVER		1
-12	1007-6	RH LE OUTBD PLENUM COVER		1
-13	1008-3	LH WING BRACKET		1
-14	1008-4	RH WING BRACKET		1
-15	1009-3	LH OUTBD WING COVERPLATE		1
-16	1009-4	RH OUTBD WING COVERPLATE		1
-17	1009-5	LH OUTBD WING OUTBD COVERPLATE		1
-18	1009-6	RH OUTBD WING OUTBD COVERPLATE		1
-19	1011-3	LH TPS PLENUM		1
-20	1011-4	RH TPS PLENUM		1
-21	1011-5	AFT PLUG		1
-22	1013-3	CENTERBODY		1
-23	1014-3	LH TPS CORE FAIRING		1
-24	1014-4	RH TPS CORE FAIRING		1
-25	1014-5	LH TURBINE CORE		1
-26	1014-6	RH TURBINE CORE		1
-27	1014-7	TURBINE SUPPORT		1
-28	1015-3	LH FRWD NACELLE		1
-29	1015-4	RH FRWD NACELLE		1
-30	1015-5	LH AFT NACELLE		1
-31	1015-6	RH AFT NACELLE		1
-32	1020-3	0 DEG LH OUTBD FLAP		1
-33	1020-4	0 DEG RH OUTBD FLAP		1
-34	1020-5	0 DEG LH OUTBD OUTBD FLAP		1
-35	1020-6	0 DEG RH OUTBD OUTBD FLAP		1
-36	1020-7	30 DEG LH OUTBD FLAP		1
-37	1020-8	30 DEG RH OUTBD FLAP		1
-38	1020-9	30 DEG LH OUTBD OUTBD FLAP		1
-39	1020-10	30 DEG RH OUTBD OUTBD FLAP		1
-40	1020-11	60 DEG LH OUTBD FLAP		1
-41	1020-12	60 DEG RH OUTBD FLAP		1
-42	1020-13	60 DEG LH OUTBD OUTBD FLAP		1
-43	1020-14	60 DEG RH OUTBD OUTBD FLAP		1
-44	1020-15	80 DEG LH OUTBD FLAP		1
-45	1020-16	80 DEG RH OUTBD FLAP		1
-46	1020-17	80 DEG LH OUTBD OUTBD FLAP		1
-47	1020-18	80 DEG RH OUTBD OUTBD FLAP		1
-48	1021-3	0 DEG LH INBD FLAP		1
-49	1021-4	0 DEG RH INBD FLAP		1
-50	1021-5	30 DEG LH INBD FLAP		1
-51	1021-6	30 DEG RH INBD FLAP		1
-52	1021-7	60 DEG LH INBD FLAP		1
-53	1021-8	60 DEG RH INBD FLAP		1
-54	1021-9	80 DEG LH INBD FLAP		1
-55	1021-10	80 DEG RH INBD FLAP		1
-56	1022-3	LH TE INBD PLENUM COVER		1
-57	1022-4	RH TE INBD PLENUM COVER		1
-58	1022-5	LH LE INBD PLENUM COVER		1
-59	1022-6	RH LE INBD PLENUM COVER		1
-60	1023-3	BIN BALANCE BLOCK		1
-61	1024-3	UPPER TAPER ADAPTER		1
-62	1024-5	BLADE		1
-63	1024-7	LOWER TAPER ADAPTER		1
-64	1024-9	UPPER DRAWNUT		1
-65	1024-11	LOWER CLAMP		1
-66	1024-13	LH FAIRING		1
-67	1024-14	RH FAIRING		1
-68	1025-3	LH PLATE		1
-69	1025-4	RH PLATE		1
-70	1025-5	BULKHEAD		1
-71	1025-7	FLOW BLOCK		1

ITEM NO	PART OR IDENTIFYING NO	NOMENCLATURE OR DESCRIPTION	MATERIAL SPECIFICATION	QTY
-72	1025-9	TPS FEEDBLOCK		1
-73	1025-11	DRIVE ADAPTER		2
-74	1025-13	BEARING HOUSING		2
-75	1025-15	GEARHEAD MOUNT		2
-76	1025-17	UPPER LIMIT SWITCH ACTUATOR		1
-77	1025-18	LOWER LIMIT SWITCH ACTUATOR		1
-78	1025-19	UPPER POT MOUNT		2
-79	1025-20	LOWER POT MOUNT		2
-80	1025-21	POT STANDOFF		2
-81	1025-23	PLUG		2
-82	1025-25	ACME LEADSCREW		2
-83	1026-3	LOWER FORWARD FUSELAGE		1
-84	1027-3	LH SHORT PYLON		1
-85	1027-4	RH SHORT PYLON		1
-86	1027-5	LH FRWD SHORT PYLON FAIRING		1
-87	1027-6	RH FRWD SHORT PYLON FAIRING		1
-88	1027-7	LH AFT SHORT PYLON FAIRING		1
-89	1027-8	RH AFT SHORT PYLON FAIRING		1
-90	1027-9	LH SHORT PYLON SIDE FAIRING		1
-91	1027-10	RH SHORT PYLON SIDE FAIRING		1
-92	1028-3	LH LOW PRESSURE MANIFOLD		1
-93	1028-4	RH LOW PRESSURE MANIFOLD		1
-94	1029-3	LH INBD TE		1
-95	1029-4	RH INBD TE		1
-96	1030-3	FRWD FUSELAGE COVER		1
-97	1030-5	AFT FUSELAGE COVER		1
-98	1030-7	LH WING COVER		1
-99	1030-8	RH WING COVER		1
-100	1031-3	UPPER NOSE		1
-101	1032-3	LH INBD LE MANIFOLD		1
-102	1032-4	RH INBD LE MANIFOLD		1
-103	1032-5	LH OUTBD LE MANIFOLD		1
-104	1032-6	RH OUTBD LE MANIFOLD		1
-105	1032-7	LH OUTBD TE MANIFOLD		1
-106	1032-8	RH OUTBD TE MANIFOLD		1
-107	1034-3	CORE FAIRING		2
-108	1034-5	CONE		2
-109	1034-7	VANE		4
-110	1035-1	LH TPS FEED PIPE ASSY		1
-111	1035-2	RH TPS FEED PIPE ASSY		1
-112	1036-3	LH LONG PYLON		1
-113	1036-4	RH LONG PYLON		1
-114	1036-5	LH FRWD LONG PYLON FAIRING		1
-115	1036-6	RH FRWD LONG PYLON FAIRING		1
-116	1036-7	LH AFT LONG PYLON FAIRING		1
-117	1036-8	RH AFT LONG PYLON FAIRING		1
-118	1038-3	INBD FLAP MANIFOLD		1
-119	1040-3	LH OUTBD INBD WING COVER		1
-120	1040-4	RH OUTBD INBD WING COVER		1
-121	1040-5	LH OUTBD INBD WING COVER		1
-122	1040-6	RH OUTBD INBD WING COVER		1
-123	1041-3	LH PLENUM		1
-124	1041-4	RH PLENUM		1
-125	1041-5	LH PLENUM CAP		1
-126	1041-6	RH PLENUM CAP		1
-127	1041-7	LH DRIVE SUPPORT		4
-128	1041-8	RH DRIVE SUPPORT		4
-129	1041-9	SHAFT		8
-130	1041-11	COUPLING		8
-131	1041-13	LIMIT SWITCH MOUNT		2
-132	1041-15	LIMIT SWITCH MOUNT		2
-133	1041-17	LIMIT ARM		2
-134	1041-19	MOTOR MOUNT		8
-135	1041-21	HOSE FITTING		16
-136	1041-23	BEARING		16
-137	1041-25	WORM SDP P/N A 1C 5-N24		8
-138	1041-27	WORM GEAR SDP P/N A 1B 6-N24024		8
-139	1041-29	BOURNS POT P/N 3048-L-5-103		8
-140	1041-31	LIMIT SWITCH		16
-141	1041-33	CLAMP		8
-142	1041-35	19MM GEARMOTOR (149048+249990)		8

ITEM NO	PART OR IDENTIFYING NO	NOMENCLATURE OR DESCRIPTION	MATERIAL SPECIFICATION	QTY
-143	1041-37	LH INBD LE VALVE		1
-144	1041-38	RH LE INBD VALVE		1
-145	1041-39	LH OUTBD LE VALVE		1
-146	1041-40	RH OUTBD LE VALVE		1
-147	1041-41	LH OUTBD TE VALVE		1
-148	1041-42	RH OUTBD TE VALVE		1
-149	1041-43	LH INBD TE VALVE		1
-150	1041-44	RH INBD TE VALVE		1
-151	1041-45	POT ROD END		1
-152	1042-5	INBD FRWD PLENUM TUBE		1
-153	1042-7	INBD AFT PLENUM TUBE		1
-154	1042-9	LH OUTBD FRWD PLENUM TUBE		1
-155	1042-10	RH OUTBD FRWD PLENUM TUBE		1
-156	1042-11	LH OUTBD AFT PLENUM TUBE		1
-157	1042-12	RH OUTBD AFT PLENUM TUBE		1
-158	1043-13	PIPE		2
-159	1043-17	LH FRWD BELLOWS ASSY		1
-160	1043-18	RH FRWD BELLOWS ASSY		1
-161	1043-19	LH AFT BELLOWS ASSY		1
-162	1043-20	RH AFT BELLOWS ASSY		1
-163	1044-3	FRWD COVER TIEPLATE		1
-164	1044-5	LH WING COVER TIEPLATE		1
-165	1044-6	RH WING COVER TIEPLATE		1
-166	1045-3	AFT HIGH PRESSURE PLENUM		1
-167	1046-3	TPS RAKES		14
-168	1047-3	LH VERTICAL OFF BLOCK		1
-169	1047-4	RH VERTICAL OFF BLOCK		1
-170	1047-5	LH DORSAL OFFBLOCK		1
-171	1047-6	RH DORSAL OFFBLOCK		1
-172	1048-3	TPS PYLON FAIRING		1
-173	1051-3	BALANCE PIN		2
-174	1052-3	UPPER TAPER ADAPTER KEY		2
-175	1054-3	LH PLENUM SUPPORT BRACKET		1
-176	1054-4	RH PLENUM SUPPORT BRACKET		1
-177	1055-3	LOWER TAPER ADAPTER KEY		2
-178	1056-3	HIGH PRESSURE FEED PIPE		1
-179	1057-3	BLADE UPPER AFT COVER		1
-180	1057-5	BLADE LOWER AFT COVER		1
-181	2-029	O-RING		4
-182	2-037	O-RING		2
-183	2-036	O-RING		2
-184	2-032	O-RING		4
-185	2-152	O-RING		2
-186	2-222	O-RING		4
-187	2-145	O-RING		2
-188	2-040	O-RING		2
-189	2-030	O-RING		4
-190	.070 DIA	O-RING CORD		1
-191	2-031	O-RING		8
-192	2-161	O-RING		4
-193	2-017	O-RING		14
-194	2-050	O-RING		2
-195	2-024	O-RING		8
-196	2-135	O-RING		4
-197	2-158	O-RING		3
-198	2-155	O-RING		2
-199	2-156	O-RING		2
-200	2-143	O-RING		1
-201	2-156	O-RING		1
-202	2-118	O-RING		16

ITEM NO	PART OR IDENTIFYING NO	NOMENCLATURE OR DESCRIPTION	MATERIAL SPECIFICATION	QTY
-203	1/4-28 x 1.375	SHCS		16
-204	.25 x 1.25	PULL PIN		12
-205	1/4-28 x .75	SHCS		56
-206	M5 x 10MM	SHCS		8
-207	3/8-24 x 4.0	SHCS		8
-208	3/8-24 x 1.5	SHCS		8
-209	3/8 x 1.5	PULL PIN		4
-210	3/8-24 x 1.0	SHCS		8
-211	3/8 x 1.0	PULL PIN		2
-212	10-32 x .50	SHCS		36
-213	8-32 x .38	FHCS		20
-214	1/4-28 x 1.75	SHCS		6
-215	8-32 x .38	SHCS		74
-216	4-40 x .38	SHCS		8
-217	8-32 x .50	SHCS		32
-218	1/2-20 x 1.5	SHCS		8
-219	1/2-20 x 2.0	SHCS		2
-220	3/8-24 x 2.5	SHCS		6
-221	3/8 x 2.0	PIN		2
-222	1/4-28 x 1	SHCS		28
-223	1/4-28 x .50	SHCS		4
-224	1/4 x .75	PULL PIN		8
-225	4-40 x .25	SHCS		72
-226	2-56 x .19	SHCS		6
-227	2-56 x .19	FHCS		6
-228	4-40 x .25	FHCS		6
-229	10-32 x .38	SHCS		82
-230	2-56 x .375	SHCS		4
-231	3/8-24 x 2.0	SHCS		1
-232	3/8-24 x 2.50	SHCS		8
-233	10-32 x .63	SHCS		6
-234	.50 x 2.0	PULL PIN		4
-235	1/4 x .75	PULL PIN		2
-236	1/4 x 1.0	PULL PIN		2
-237	1/4-28 x 2.50	SHCS		2
-238	5/8-18 x 2.00	SHCS		8
-239	8-32 x .50	FHCS		14
-240	4-40 (CUT TO LENGTH	FHCS		1
-241	4-40 (CUT TO LENGTH)	SETSCREW		1
-242	6-32 (CUT TO LENGTH	FHCS		1
-243	6-32 (CUT TO LENGTH)	SETSCREW		1

DO NOT SCALE DRAWING

PARTS LIST

MATERIAL	XXXXX	CONTRACT NO	
FINISH		APPROVALS	DATE
DRAWN	DM	9/17/18	
CHECKED			
ENGINEER	DM		
APPROVED			

PATERSON LABS

TITLE: BLENDED WING ASSEMBLY

SIZE F | DWG CODE | DWG NO 1000 | REV

SCALE 1:1 | RELEASE DATE | SHEET 2 OF 7

APPLICATION

PROJECTION THIRD ANGLE

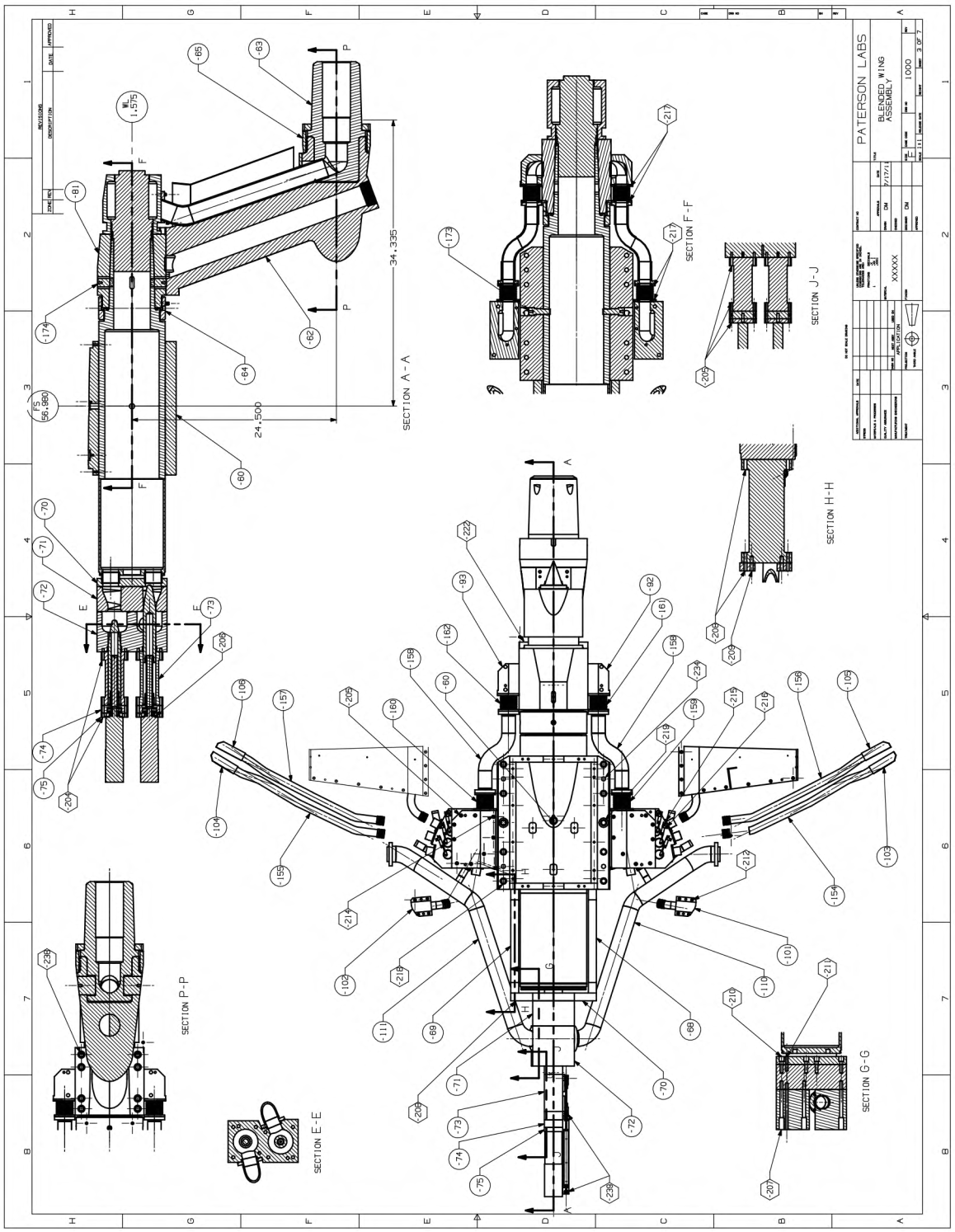
PATERSON LABS
BLENDED WING ASSEMBLY
XXXXX
1000
SECTION A - A
SECTION F - F
SECTION J - J
SECTION H - H
SECTION P - P
SECTION E - E
SECTION G - G

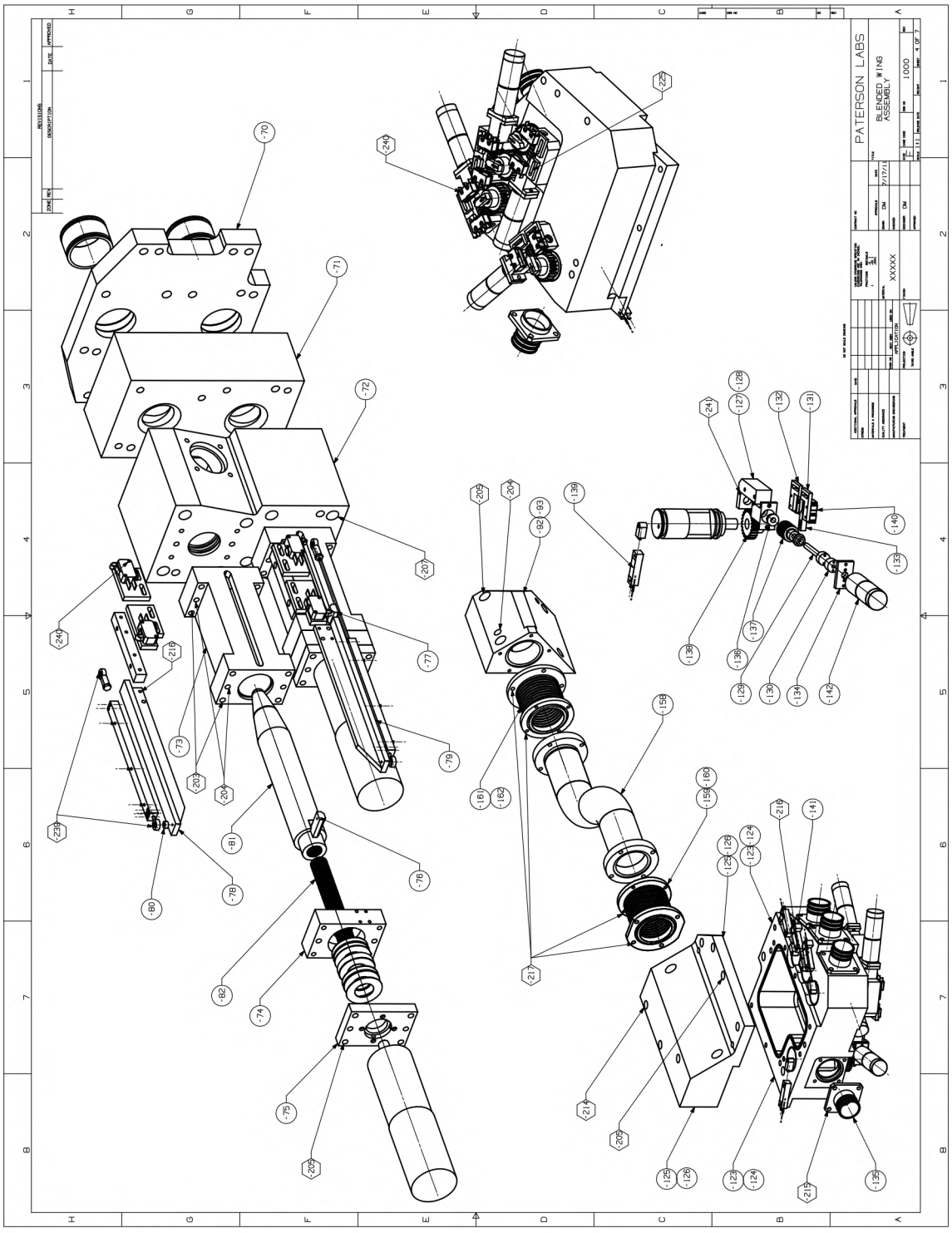
PATERSON LABS
BLENDED WING ASSEMBLY
XXXXX
1:000

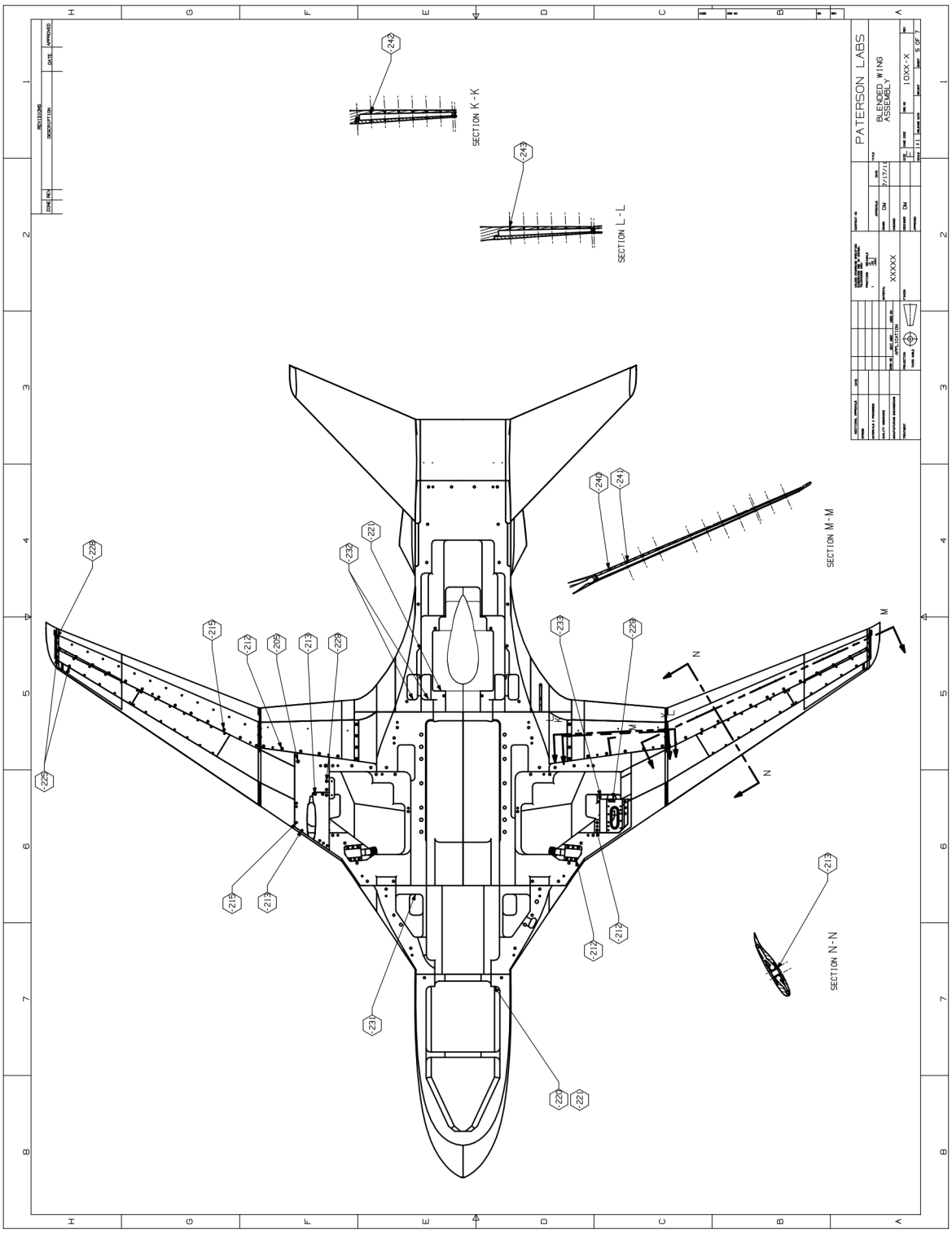
PATERSON LABS
BLENDED WING ASSEMBLY
10XX-X
SECTION K-K
SECTION L-L
SECTION M-M
SECTION N-N

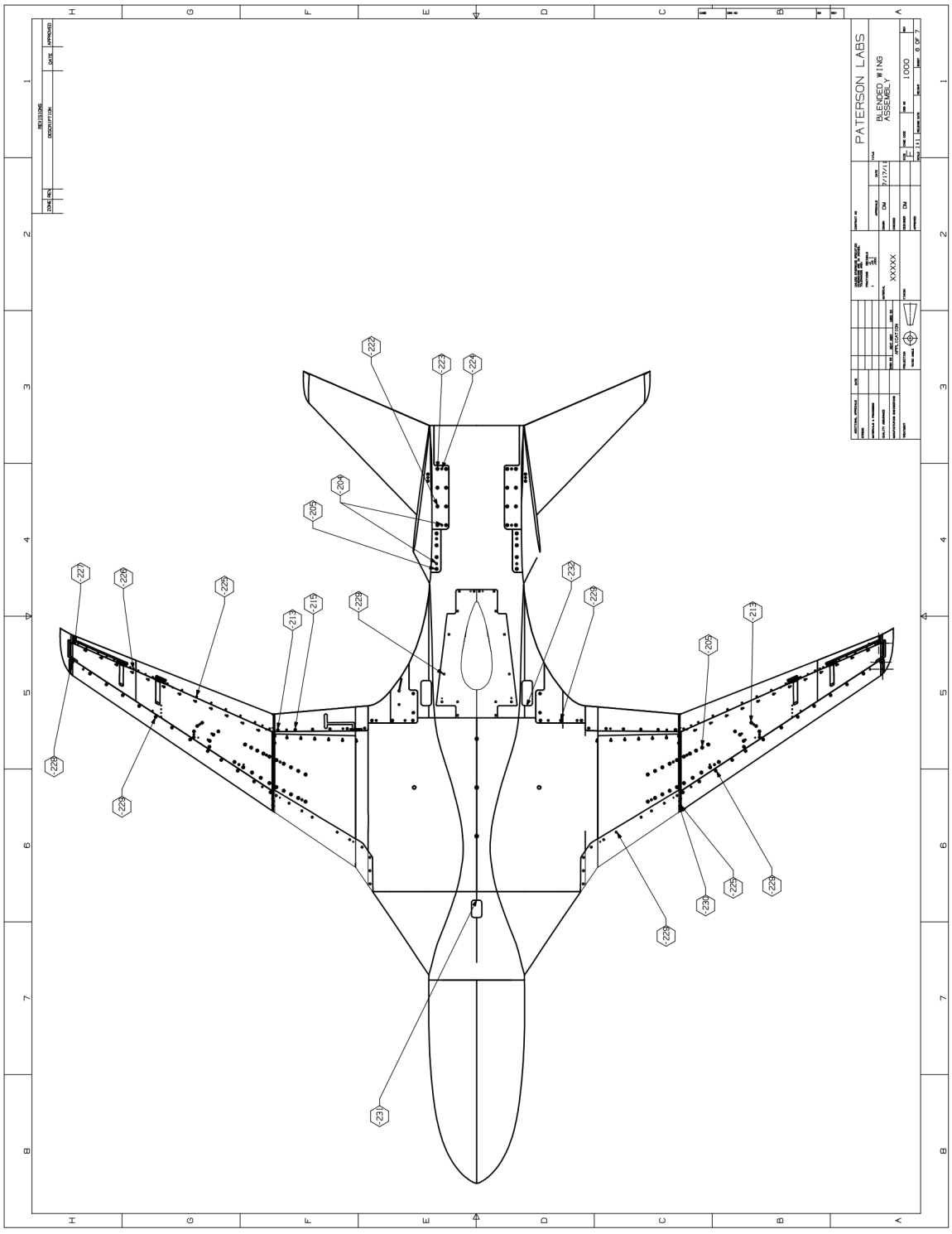
PATERSON LABS
BLENDED WING ASSEMBLY
1000
XXXXX
7/17/14
DM
DM
DM
REVISIONS
DESCRIPTION
DATE
APPROVED

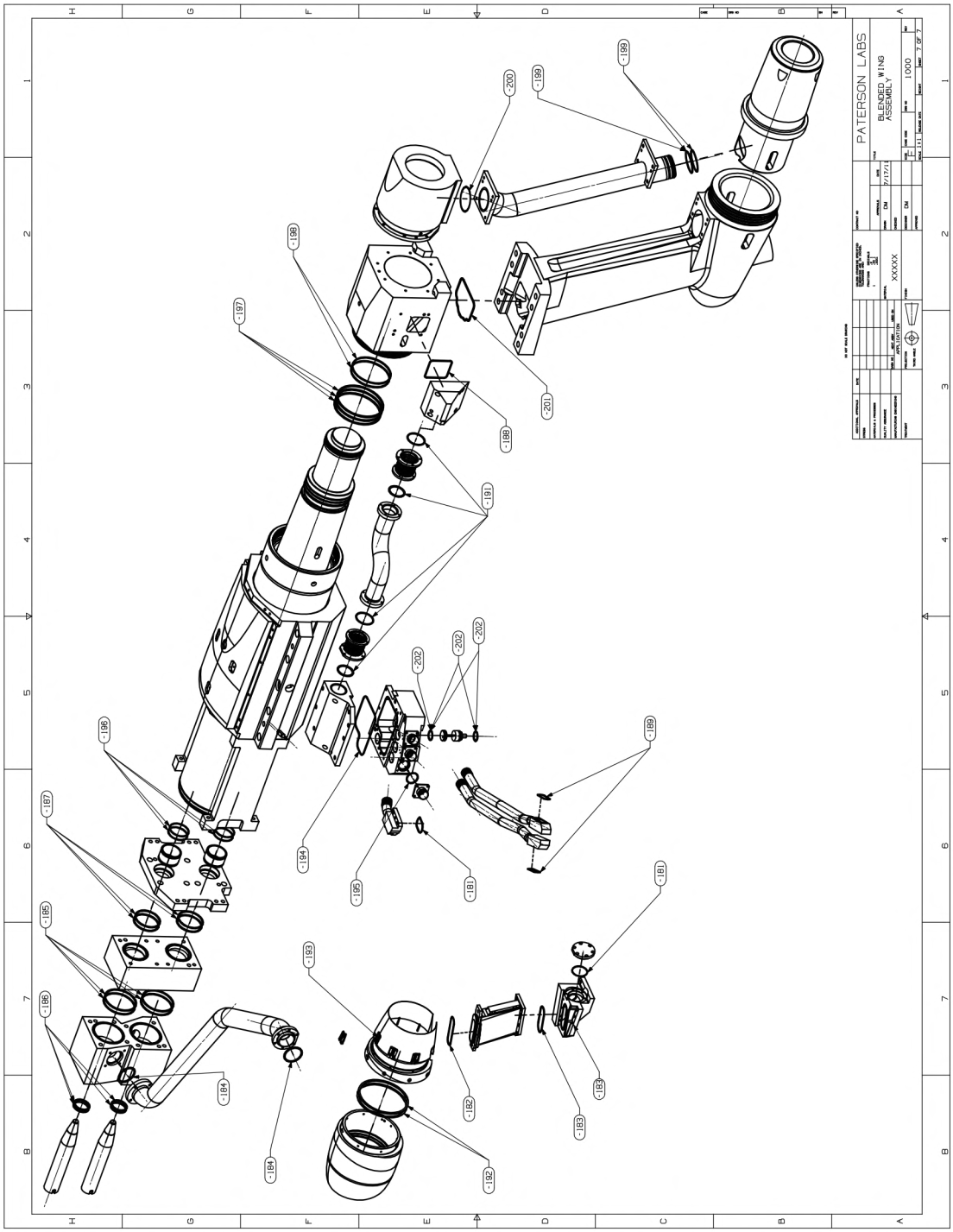
PATERSON LABS
BLENDED WING ASSEMBLY
XXXXX
1000
-181
-182
-183
-184
-185
-186
-187
-188
-189
-192
-193
-194
-195
-196
-197
-198
-199
-200
-201
-202

A2. Safety of Flight Operational Limits

Wind tunnel model loads were reviewed prior to testing to ensure they did not exceed the model and operational limits. Due to the large number of critical sub-systems and model components that can be impacted by operational loads, each system was individually reviewed to ensure sufficient margin exists between the component limit and the test operational loads. Operational margins were reviewed at test planning meetings with the NFAC staff, and if margins were deemed too small real-time monitoring was required.

The sub-systems reviewed for safety included the engine simulators, the model, the model balance system and the model support system.

A stress analysis was completed for the model using the loads documented in Appendix 7, Load Analysis, and summarized in Table 1. All model components were found to meet the NFAC model design requirement for factor safety of 3 on yield strength and a factor of safety of 4 on ultimate strength (Mason, David, PatersonLabs, " Cal Poly Model Stress Analysis", September 2011).

Table A2. 1. Comparison of Model Loads to Balance and Model Support Limits.

	Model Loads, Worst Case	Balance Limits	Model Support Limits
NF	2341 lbs	11,000 lbs	6250 lbs
AF	353.6 lbs	900 lbs	NA
SF	114.6 lbs	2000 lbs	1400 lbs
PM	600 ft-lbs	7563 ft-lbs	12600 ft-lbs
YM	319 ft-lbs	1375 ft-lbs	12600 ft-lbs
RM	684 ft-lbs	1667 ft-lbs	780 ft-lbs

- Balance limits provided by Triumph Aerospace Systems, Revised Load Envelope for CESTOL Test, Safety Factor 2.35. Load envelope is defined by a rhombus either full normal force or full pitch is allowable, %NF+%PM=100%, likewise for side force and yaw moment, %SF+%YM=100%
- Model support limits provided by NFAC June 2011

As seen in the expected model maximum model loads are within the balance operational envelope and deemed to have sufficient margin so that real time safety of flight monitoring of balance loads to protect the balance is not required. While expected model worst case loads are within the model support operational envelope, the margin was small enough to required real-time monitoring to protect the model support system from damage.

The TDI supplied the operational limits for the engine simulators. The engine simulator operational parameters monitored are the forward and aft bearing temperatures, the fan RPM, and acceleration. These parameters were monitored via real –time displays and by the engine simulator controller. If DO NOT EXCEED parameter values are reached the controller sends a signal to shut off high pressure air to the simulators. The controller also monitored the oiler state and pressure to provide indications that the oiler was operating. Table 2 lists the engine simulator parameters that were monitored.

Table A2. 2 Engine simulator operational limits .

Parameter	Warning Level	Do Not Exceed
RPM	45000 RPM	46000 RPM
Forward Shaft Bearing Temperature	169°F	225°F
Aft Shaft Bearing Temperature	94°F	125°F
Acceleration	0.7 G	1.0 G

A3. Fragmentation Analysis

AMELIA Fragmentation Analysis

The National Full-Scale Aerodynamics Complex (NFAC) required a fragmentation impact analysis to determine, in the event of an engine simulator failure, the risk of rotating components penetrating thru the engine simulator cowling. The NFAC provided the following analysis technique to determine the distance a given rotating component will travel, given its material.

$$t = (235.5/BHN)\ (W/A)\ (V/1000)^2$$

where:

t = computed material penetration thickness, in
BHN = material Brinell Hardness Number
W = fragment weight, lb
A = fragment minimum cross sectional area, sq in
V = fragment velocity at instant of separation, fps

Analysis indicated that the cowling has sufficient thickness to contain a blade in the event of a catastrophic engine simulator failure. The fragmentation analysis is included below.

Nov 1, 2011 | R Fong

Fragmentation Analysis for CalPoly Amelia

Fragmentation risk for operation of Turbofan Propulsion Simulators, (TPS)

TPS units are Model 4411 units loaned from LaRC.

TPS units have 2 stage fan driven by 3 stage turbine.

Greatest risk is from fragmentation of 1st stage fan

NFAC Fragmentation Calculation

$$t = \frac{235.5}{BHN} \cdot \frac{W}{A} \cdot \left(\frac{U}{1000}\right)^2$$

t = computed material penetration thickness, (in)

BHN = material Brinell Hardness

W = fragment weight (lbs)

A = fragment min. cross section area (sq in)

U = frag. velocity.

TPS Nominal Velocity = 36000 RPM

= 3769 $\frac{rad}{s}$

BHN

Fan shroud is stainless steel, unknown conditioning, assume annealed 304

$BHN_{304\ ann} = 185$

Fan Blade Dimension

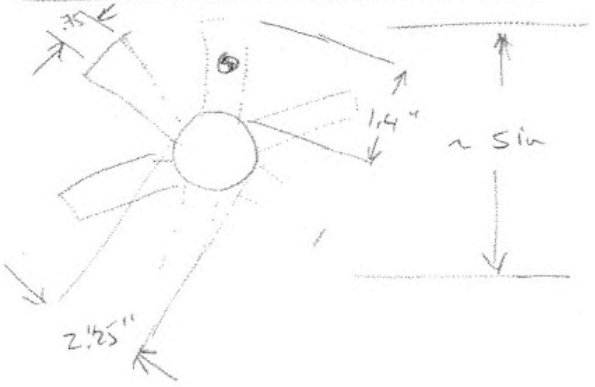

Not to scale; actual fan has more blades

Blade length = 1.41" (measd w/ calipers)

Blade width = .75" (measd)

Blade CG = $\frac{2.25}{2} + \frac{1.4}{2} = 1.825$"

Blade thickness < .04" could not directly measure but .04" is considerably thicker than actual blade

Fragment weight, W = Blade thickness x
Blade length x
Blade width x
Density of steel

$W = 1.41" (.75") (.04") \times .283 \frac{lb}{in^3}$

$W = .012\ lbs$ ⟸

Fragment cross section, A = Blade width x Blade Thickness

$A = .75(.04)$

$A = .03\ in^2$ ⟸

Fragment Velocity, V = Rotational Velocity x
CG of Blade

$\text{Rotational Velocity} = 3769 \frac{rad}{s}$

$V = 3769 \frac{rad}{s} (1.825in)$

$V = 6880\ in/s$

$= 573\ ft/s$ ⟸

$$t_{milled} = \frac{235.5}{BHN} \cdot \frac{W}{A}\left(\frac{U}{1000}\right)^2$$

$$\doteq \frac{235}{183} \cdot \frac{.0121 \text{ lbs}}{.031 \text{ in}^2}\left(\frac{573 \text{ ft/s}}{1000}\right)^2$$

$$= .168 \text{ inches}.$$

W/r to drawing of TPS it appears that there is at least 0.25" Thickness in fan Shroud.

TECH 441 TURBOFAN PROPULSION SIMULATOR

PRODUCT SPECIFICATION

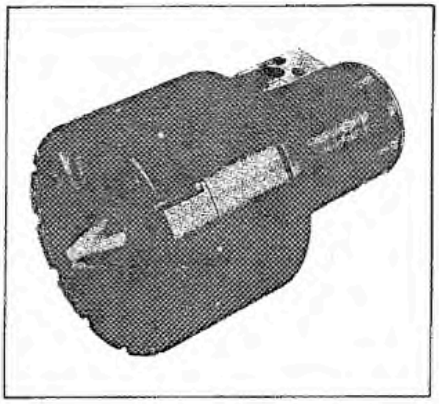

GENERAL INFORMATION

The use of Tech Development Inc Simulated Turbofan Engines* in wind tunnel aircraft models makes possible such studies as:

- High speed drag interference phenomena
- Effects of power on high and low speed stability and control parameters
- Effects of power on high lift parameters
- Thrust reverser aerodynamics
- Inlet and cowling development

The Model 441 Turbofan Simulator features a two stage fan driven by a three stage turbine. Corrosion resistant materials are used throughout. Bearing thermocouples and a magnetic speed pickup are provided.

*U.S. Patent 3434679

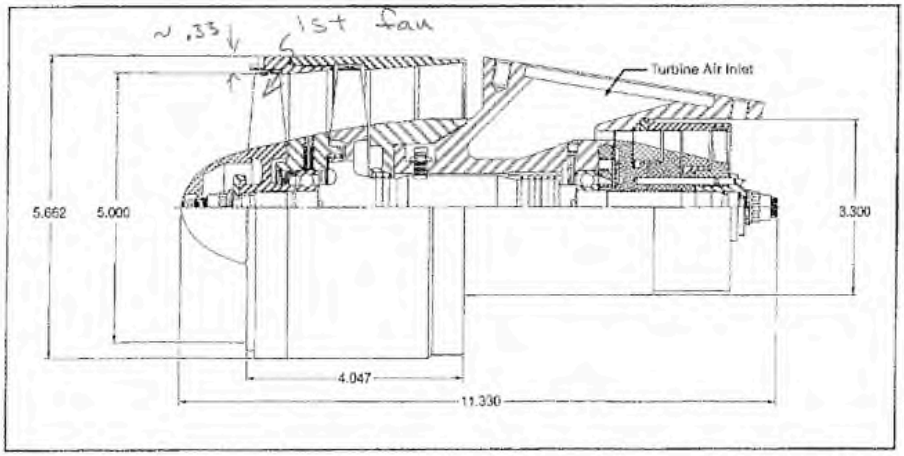

TECH DEVELOPMENT INC.
6800 Poe Ave. P.O. Box 14557, Dayton, Ohio 45414
Telephone: (513)898-9600 / TWX:810-472-2822

A4. Balance Calibration Report

The following table lists the Balance Data Reduction (Interaction) Matrix used for the AMELIA Wind Tunnel Test, based on the calibration of the MC-130 8.0 Air Balance conducted by Triumph Aerospace May 2011. Matrix excerpted from James, Kevin, "Data Reduction Matrix Calculation Report", Report Number 2011-1130-005541, November 2011. Unpublished report.

FILE_TYPE DATA_REDUCTION_MATRIX_IN_AMES_FORMAT								
BALANCE_NAME MC130 (3F3M)								
DESCRIPTION FMS calibration May 2011 (5V excitation)								
PREPARED_BY Kevin James								
REPORT_NO 2011-1130-005541								
ITERATION_METHOD Primary Load Iteration Method								
LOAD_NAME	NF	PM	SF	YM	RM	AF	PR1(i)	PR2(i)
LOAD_UNIT	lbs	in-lbs	lbs	in-lbs	in-lbs	lbs	psi	psi
LOAD_MINIMUM	-2.50E+03	-2.88E+04	-2.00E+03	-1.05E+04	-2.73E+04	-8.98E+02	-3.63E+00	-3.96E-01
LOAD_MAXIMUM	4.79E+03	2.52E+04	2.00E+03	1.05E+04	1.95E+04	9.98E+02	5.01E+02	1.25E+02
LOAD_CAPACITY	5.00E+03	2.90E+04	2.50E+03	1.05E+04	2.73E+04	1.20E+03	6.00E+02	6.00E+02
GAGE_OUT_NAME	R1	R2	R3	R4	R5	R6	PR1(d)	PR2(d)
GAGE_OUT_UNIT	microV/V	microV/V	microV/V	microV/V	microV/V	microV/V	psi	psi
GAGE_OUT_MINIMUM	-4.14E+02	-3.99E+02	-7.71E+02	-7.67E+02	-8.29E+02	-1.32E+03	-3.63E+00	-3.96E-01
GAGE_OUT_MAXIMUM	6.92E+02	7.63E+02	7.79E+02	7.66E+02	5.96E+02	1.31E+03	5.01E+02	1.25E+02
GAGE_SENSITIVITY	NOT_DEFINED	NOT_DEFINED	NOT_DEFINED	NOT_DEFINED	3.28E+01	NOT_DEFINED	1.00E+00	1.00E+00
NATURAL_ZERO	0.00E+00	0.00E+00	0.00E+00	0.00E+00	0.00E+00	0.00E+00	0.00E+00	0.00E+00
INTERCEPT	7.49E-03	9.80E-03	-6.55E-02	6.18E-02	-3.59E-01	3.26E-01	0.00E+00	0.00E+00
D0[C1INV] -								
R1	5.28E+00	4.27E+01	7.74E-02	1.42E+00	-2.64E-01	-2.14E-02	0.00E+00	0.00E+00
R2	5.37E+00	-4.48E+01	9.53E-02	-5.56E-01	8.26E-01	2.45E-02	0.00E+00	0.00E+00
R3	-6.25E-02	-2.88E-01	1.77E+00	1.47E+01	-1.82E-01	3.03E-02	0.00E+00	0.00E+00
R4	-7.27E-02	5.87E-01	1.79E+00	-1.50E+01	2.01E-02	4.94E-03	0.00E+00	0.00E+00
R5	-5.00E-02	4.93E-01	1.09E-02	-2.12E-01	3.28E+01	-2.88E-02	0.00E+00	0.00E+00
R6	1.55E-02	-1.07E+00	2.20E-02	-5.72E-01	1.28E-01	6.87E-01	0.00E+00	0.00E+00
PR1(d)	-3.59E-02	-4.94E-01	-6.01E-02	-7.54E-01	-1.68E-01	-5.37E-02	1.00E+00	0.00E+00
PR2(d)	-1.28E-02	1.72E+00	-2.70E-03	6.69E-01	8.37E-02	4.65E+00	0.00E+00	1.00E+00
D1[IGNORED] -								
NF	0.00E+00	0.00E+00	0.00E+00	0.00E+00	0.00E+00	0.00E+00	0.00E+00	0.00E+00
PM	0.00E+00	0.00E+00	0.00E+00	0.00E+00	0.00E+00	0.00E+00	0.00E+00	0.00E+00
SF	0.00E+00	0.00E+00	0.00E+00	0.00E+00	0.00E+00	0.00E+00	0.00E+00	0.00E+00
YM	0.00E+00	0.00E+00	0.00E+00	0.00E+00	0.00E+00	0.00E+00	0.00E+00	0.00E+00

RM	0.00E+00	0.00E+00	0.00E+00	0.00E+00	0.00E+00	0.00E+00	0.00E+00	0.00E+00
AF	0.00E+00	0.00E+00	0.00E+00	0.00E+00	0.00E+00	0.00E+00	0.00E+00	0.00E+00
PR1(i)	0.00E+00	0.00E+00	0.00E+00	0.00E+00	0.00E+00	0.00E+00	0.00E+00	0.00E+00
PR2(i)	0.00E+00	0.00E+00	0.00E+00	0.00E+00	0.00E+00	0.00E+00	0.00E+00	0.00E+00
D2[C1INVC2] -								
|NF|	-1.14E-03	-1.10E-02	-2.79E-03	-9.55E-03	-3.67E-02	2.01E-06	0.00E+00	0.00E+00
|PM|	-4.84E-05	5.53E-04	-1.35E-04	-1.04E-03	-6.42E-06	-6.72E-05	0.00E+00	0.00E+00
|SF|	-1.60E-04	1.57E-03	3.48E-05	-6.76E-04	1.05E-01	-9.19E-05	0.00E+00	0.00E+00
|YM|	6.19E-06	-5.00E-05	-1.53E-04	1.28E-03	-1.71E-06	-4.21E-07	0.00E+00	0.00E+00
|RM|	0.00E+00	0.00E+00	0.00E+00	0.00E+00	0.00E+00	0.00E+00	0.00E+00	0.00E+00
|AF|	0.00E+00	0.00E+00	0.00E+00	0.00E+00	0.00E+00	0.00E+00	0.00E+00	0.00E+00
|PR1(i)|	0.00E+00	0.00E+00	0.00E+00	0.00E+00	0.00E+00	0.00E+00	0.00E+00	0.00E+00
|PR2(i)|	0.00E+00	0.00E+00	0.00E+00	0.00E+00	0.00E+00	0.00E+00	0.00E+00	0.00E+00
NF*NF	-1.84E-07	1.51E-06	-6.23E-09	7.37E-08	-8.31E-06	6.37E-09	0.00E+00	0.00E+00
PM*PM	6.16E-09	4.99E-08	9.03E-11	1.66E-09	-3.08E-10	-2.50E-11	0.00E+00	0.00E+00
SF*SF	-1.51E-06	-2.95E-06	6.59E-07	-4.62E-06	-1.39E-04	-1.37E-06	0.00E+00	0.00E+00
YM*YM	-9.86E-10	-4.54E-09	2.79E-08	2.32E-07	-2.87E-09	4.79E-10	0.00E+00	0.00E+00
RM*RM	-1.69E-09	1.41E-08	-3.00E-11	1.75E-10	-2.60E-10	-7.71E-12	0.00E+00	0.00E+00
AF*AF	0.00E+00	0.00E+00	0.00E+00	0.00E+00	0.00E+00	0.00E+00	0.00E+00	0.00E+00
PR1(i)*PR1(i)	-9.38E-06	-5.80E-04	-7.77E-05	-9.09E-04	8.42E-07	-9.81E-05	0.00E+00	0.00E+00
PR2(i)*PR2(i)	0.00E+00	0.00E+00	0.00E+00	0.00E+00	0.00E+00	0.00E+00	0.00E+00	0.00E+00
NF*|NF|	0.00E+00	0.00E+00	0.00E+00	0.00E+00	0.00E+00	0.00E+00	0.00E+00	0.00E+00
PM*|PM|	0.00E+00	0.00E+00	0.00E+00	0.00E+00	0.00E+00	0.00E+00	0.00E+00	0.00E+00
SF*|SF|	0.00E+00	0.00E+00	0.00E+00	0.00E+00	0.00E+00	0.00E+00	0.00E+00	0.00E+00
YM*|YM|	0.00E+00	0.00E+00	0.00E+00	0.00E+00	0.00E+00	0.00E+00	0.00E+00	0.00E+00
RM*|RM|	0.00E+00	0.00E+00	0.00E+00	0.00E+00	0.00E+00	0.00E+00	0.00E+00	0.00E+00
AF*|AF|	0.00E+00	0.00E+00	0.00E+00	0.00E+00	0.00E+00	0.00E+00	0.00E+00	0.00E+00
PR1(i)*|PR1(i)|	0.00E+00	0.00E+00	0.00E+00	0.00E+00	0.00E+00	0.00E+00	0.00E+00	0.00E+00
PR2(i)*|PR2(i)|	0.00E+00	0.00E+00	0.00E+00	0.00E+00	0.00E+00	0.00E+00	0.00E+00	0.00E+00
NF*PM	-2.81E-08	-1.30E-06	-1.05E-07	-2.11E-06	3.42E-08	-2.13E-09	0.00E+00	0.00E+00
NF*SF	0.00E+00	0.00E+00	0.00E+00	0.00E+00	0.00E+00	0.00E+00	0.00E+00	0.00E+00
NF*YM	0.00E+00	0.00E+00	0.00E+00	0.00E+00	0.00E+00	0.00E+00	0.00E+00	0.00E+00
NF*RM	4.08E-08	9.51E-07	1.99E-09	-2.90E-09	4.19E-06	-4.14E-09	0.00E+00	0.00E+00
NF*AF	0.00E+00	0.00E+00	0.00E+00	0.00E+00	0.00E+00	0.00E+00	0.00E+00	0.00E+00
NF*PR1(i)	0.00E+00	0.00E+00	0.00E+00	0.00E+00	0.00E+00	0.00E+00	0.00E+00	0.00E+00
NF*PR2(i)	0.00E+00	0.00E+00	0.00E+00	0.00E+00	0.00E+00	0.00E+00	0.00E+00	0.00E+00
PM*SF	0.00E+00	0.00E+00	0.00E+00	0.00E+00	0.00E+00	0.00E+00	0.00E+00	0.00E+00
PM*YM	1.72E-09	2.07E-07	-1.24E-07	-2.33E-06	4.58E-09	-9.68E-08	0.00E+00	0.00E+00
PM*RM	1.12E-08	9.03E-08	1.64E-10	3.00E-09	-5.57E-10	-4.53E-11	0.00E+00	0.00E+00
PM*AF	-3.70E-07	2.66E-06	-2.24E-09	-1.12E-07	-1.32E-05	2.95E-07	0.00E+00	0.00E+00
PM*PR1(i)	0.00E+00	0.00E+00	0.00E+00	0.00E+00	0.00E+00	0.00E+00	0.00E+00	0.00E+00

PM*PR2(i)	0.00E+00	0.00E+00	0.00E+00	0.00E+00	0.00E+00	0.00E+00	0.00E+00	0.00E+00
SF*YM	-4.80E-08	-2.13E-06	1.20E-07	3.70E-06	-8.31E-09	5.49E-09	0.00E+00	0.00E+00
SF*RM	0.00E+00	0.00E+00	0.00E+00	0.00E+00	0.00E+00	0.00E+00	0.00E+00	0.00E+00
SF*AF	-3.61E-07	5.15E-07	9.60E-06	9.03E-06	-5.05E-07	1.04E-07	0.00E+00	0.00E+00
SF*PR1(i)	0.00E+00	0.00E+00	0.00E+00	0.00E+00	0.00E+00	0.00E+00	0.00E+00	0.00E+00
SF*PR2(i)	0.00E+00	0.00E+00	0.00E+00	0.00E+00	0.00E+00	0.00E+00	0.00E+00	0.00E+00
YM*RM	0.00E+00	0.00E+00	0.00E+00	0.00E+00	0.00E+00	0.00E+00	0.00E+00	0.00E+00
YM*AF	1.02E-07	4.71E-07	-2.89E-06	-2.40E-05	2.98E-07	-4.96E-08	0.00E+00	0.00E+00
YM*PR1(i)	-1.58E-07	3.04E-06	1.45E-06	-1.16E-05	4.69E-05	-1.22E-06	0.00E+00	0.00E+00
YM*PR2(i)	0.00E+00	0.00E+00	0.00E+00	0.00E+00	0.00E+00	0.00E+00	0.00E+00	0.00E+00
RM*AF	-4.02E-08	3.96E-07	8.74E-09	-1.70E-07	2.63E-05	-2.31E-08	0.00E+00	0.00E+00
RM*PR1(i)	0.00E+00	0.00E+00	0.00E+00	0.00E+00	0.00E+00	0.00E+00	0.00E+00	0.00E+00
RM*PR2(i)	0.00E+00	0.00E+00	0.00E+00	0.00E+00	0.00E+00	0.00E+00	0.00E+00	0.00E+00
AF*PR1(i)	1.84E-05	1.23E-04	9.67E-07	-1.26E-05	2.62E-04	1.88E-05	0.00E+00	0.00E+00
AF*PR2(i)	0.00E+00	0.00E+00	0.00E+00	0.00E+00	0.00E+00	0.00E+00	0.00E+00	0.00E+00
PR1(i)*PR2(i)	0.00E+00	0.00E+00	0.00E+00	0.00E+00	0.00E+00	0.00E+00	0.00E+00	0.00E+00
|NF*PM|	0.00E+00	0.00E+00	0.00E+00	0.00E+00	0.00E+00	0.00E+00	0.00E+00	0.00E+00
|NF*SF|	0.00E+00	0.00E+00	0.00E+00	0.00E+00	0.00E+00	0.00E+00	0.00E+00	0.00E+00
|NF*YM|	0.00E+00	0.00E+00	0.00E+00	0.00E+00	0.00E+00	0.00E+00	0.00E+00	0.00E+00
|NF*RM|	0.00E+00	0.00E+00	0.00E+00	0.00E+00	0.00E+00	0.00E+00	0.00E+00	0.00E+00
|NF*AF|	0.00E+00	0.00E+00	0.00E+00	0.00E+00	0.00E+00	0.00E+00	0.00E+00	0.00E+00
|NF*PR1(i)|	0.00E+00	0.00E+00	0.00E+00	0.00E+00	0.00E+00	0.00E+00	0.00E+00	0.00E+00
|NF*PR2(i)|	0.00E+00	0.00E+00	0.00E+00	0.00E+00	0.00E+00	0.00E+00	0.00E+00	0.00E+00
|PM*SF|	0.00E+00	0.00E+00	0.00E+00	0.00E+00	0.00E+00	0.00E+00	0.00E+00	0.00E+00
|PM*YM|	0.00E+00	0.00E+00	0.00E+00	0.00E+00	0.00E+00	0.00E+00	0.00E+00	0.00E+00
|PM*RM|	0.00E+00	0.00E+00	0.00E+00	0.00E+00	0.00E+00	0.00E+00	0.00E+00	0.00E+00
|PM*AF|	0.00E+00	0.00E+00	0.00E+00	0.00E+00	0.00E+00	0.00E+00	0.00E+00	0.00E+00
|PM*PR1(i)|	0.00E+00	0.00E+00	0.00E+00	0.00E+00	0.00E+00	0.00E+00	0.00E+00	0.00E+00
|PM*PR2(i)|	0.00E+00	0.00E+00	0.00E+00	0.00E+00	0.00E+00	0.00E+00	0.00E+00	0.00E+00
|SF*YM|	0.00E+00	0.00E+00	0.00E+00	0.00E+00	0.00E+00	0.00E+00	0.00E+00	0.00E+00
|SF*RM|	0.00E+00	0.00E+00	0.00E+00	0.00E+00	0.00E+00	0.00E+00	0.00E+00	0.00E+00
|SF*AF|	0.00E+00	0.00E+00	0.00E+00	0.00E+00	0.00E+00	0.00E+00	0.00E+00	0.00E+00
|SF*PR1(i)|	0.00E+00	0.00E+00	0.00E+00	0.00E+00	0.00E+00	0.00E+00	0.00E+00	0.00E+00
|SF*PR2(i)|	0.00E+00	0.00E+00	0.00E+00	0.00E+00	0.00E+00	0.00E+00	0.00E+00	0.00E+00
|YM*RM|	0.00E+00	0.00E+00	0.00E+00	0.00E+00	0.00E+00	0.00E+00	0.00E+00	0.00E+00
|YM*AF|	0.00E+00	0.00E+00	0.00E+00	0.00E+00	0.00E+00	0.00E+00	0.00E+00	0.00E+00
|YM*PR1(i)|	0.00E+00	0.00E+00	0.00E+00	0.00E+00	0.00E+00	0.00E+00	0.00E+00	0.00E+00
|YM*PR2(i)|	0.00E+00	0.00E+00	0.00E+00	0.00E+00	0.00E+00	0.00E+00	0.00E+00	0.00E+00
|RM*AF|	0.00E+00	0.00E+00	0.00E+00	0.00E+00	0.00E+00	0.00E+00	0.00E+00	0.00E+00
|RM*PR1(i)|	0.00E+00	0.00E+00	0.00E+00	0.00E+00	0.00E+00	0.00E+00	0.00E+00	0.00E+00
|RM*PR2(i)|	0.00E+00	0.00E+00	0.00E+00	0.00E+00	0.00E+00	0.00E+00	0.00E+00	0.00E+00

|AF*PR1(i)|	0.00E+00	0.00E+00	0.00E+00	0.00E+00	0.00E+00	0.00E+00	0.00E+00	0.00E+00
|AF*PR2(i)|	0.00E+00	0.00E+00	0.00E+00	0.00E+00	0.00E+00	0.00E+00	0.00E+00	0.00E+00
|PR1(i)*PR2(i)|	0.00E+00	0.00E+00	0.00E+00	0.00E+00	0.00E+00	0.00E+00	0.00E+00	0.00E+00
NF*|PM|	0.00E+00	0.00E+00	0.00E+00	0.00E+00	0.00E+00	0.00E+00	0.00E+00	0.00E+00
NF*|SF|	0.00E+00	0.00E+00	0.00E+00	0.00E+00	0.00E+00	0.00E+00	0.00E+00	0.00E+00
NF*|YM|	0.00E+00	0.00E+00	0.00E+00	0.00E+00	0.00E+00	0.00E+00	0.00E+00	0.00E+00
NF*|RM|	0.00E+00	0.00E+00	0.00E+00	0.00E+00	0.00E+00	0.00E+00	0.00E+00	0.00E+00
NF*|AF|	0.00E+00	0.00E+00	0.00E+00	0.00E+00	0.00E+00	0.00E+00	0.00E+00	0.00E+00
NF*|PR1(i)|	0.00E+00	0.00E+00	0.00E+00	0.00E+00	0.00E+00	0.00E+00	0.00E+00	0.00E+00
NF*|PR2(i)|	0.00E+00	0.00E+00	0.00E+00	0.00E+00	0.00E+00	0.00E+00	0.00E+00	0.00E+00
PM*|SF|	0.00E+00	0.00E+00	0.00E+00	0.00E+00	0.00E+00	0.00E+00	0.00E+00	0.00E+00
PM*|YM|	0.00E+00	0.00E+00	0.00E+00	0.00E+00	0.00E+00	0.00E+00	0.00E+00	0.00E+00
PM*|RM|	0.00E+00	0.00E+00	0.00E+00	0.00E+00	0.00E+00	0.00E+00	0.00E+00	0.00E+00
PM*|AF|	0.00E+00	0.00E+00	0.00E+00	0.00E+00	0.00E+00	0.00E+00	0.00E+00	0.00E+00
PM*|PR1(i)|	0.00E+00	0.00E+00	0.00E+00	0.00E+00	0.00E+00	0.00E+00	0.00E+00	0.00E+00
PM*|PR2(i)|	0.00E+00	0.00E+00	0.00E+00	0.00E+00	0.00E+00	0.00E+00	0.00E+00	0.00E+00
SF*|YM|	0.00E+00	0.00E+00	0.00E+00	0.00E+00	0.00E+00	0.00E+00	0.00E+00	0.00E+00
SF*|RM|	0.00E+00	0.00E+00	0.00E+00	0.00E+00	0.00E+00	0.00E+00	0.00E+00	0.00E+00
SF*|AF|	0.00E+00	0.00E+00	0.00E+00	0.00E+00	0.00E+00	0.00E+00	0.00E+00	0.00E+00
SF*|PR1(i)|	0.00E+00	0.00E+00	0.00E+00	0.00E+00	0.00E+00	0.00E+00	0.00E+00	0.00E+00
SF*|PR2(i)|	0.00E+00	0.00E+00	0.00E+00	0.00E+00	0.00E+00	0.00E+00	0.00E+00	0.00E+00
YM*|RM|	0.00E+00	0.00E+00	0.00E+00	0.00E+00	0.00E+00	0.00E+00	0.00E+00	0.00E+00
YM*|AF|	0.00E+00	0.00E+00	0.00E+00	0.00E+00	0.00E+00	0.00E+00	0.00E+00	0.00E+00
YM*|PR1(i)|	0.00E+00	0.00E+00	0.00E+00	0.00E+00	0.00E+00	0.00E+00	0.00E+00	0.00E+00
YM*|PR2(i)|	0.00E+00	0.00E+00	0.00E+00	0.00E+00	0.00E+00	0.00E+00	0.00E+00	0.00E+00
RM*|AF|	0.00E+00	0.00E+00	0.00E+00	0.00E+00	0.00E+00	0.00E+00	0.00E+00	0.00E+00
RM*|PR1(i)|	0.00E+00	0.00E+00	0.00E+00	0.00E+00	0.00E+00	0.00E+00	0.00E+00	0.00E+00
RM*|PR2(i)|	0.00E+00	0.00E+00	0.00E+00	0.00E+00	0.00E+00	0.00E+00	0.00E+00	0.00E+00
AF*|PR1(i)|	0.00E+00	0.00E+00	0.00E+00	0.00E+00	0.00E+00	0.00E+00	0.00E+00	0.00E+00
AF*|PR2(i)|	0.00E+00	0.00E+00	0.00E+00	0.00E+00	0.00E+00	0.00E+00	0.00E+00	0.00E+00
PR1(i)*|PR2(i)|	0.00E+00	0.00E+00	0.00E+00	0.00E+00	0.00E+00	0.00E+00	0.00E+00	0.00E+00
|NF|*PM	0.00E+00	0.00E+00	0.00E+00	0.00E+00	0.00E+00	0.00E+00	0.00E+00	0.00E+00
|NF|*SF	0.00E+00	0.00E+00	0.00E+00	0.00E+00	0.00E+00	0.00E+00	0.00E+00	0.00E+00
|NF|*YM	0.00E+00	0.00E+00	0.00E+00	0.00E+00	0.00E+00	0.00E+00	0.00E+00	0.00E+00
|NF|*RM	0.00E+00	0.00E+00	0.00E+00	0.00E+00	0.00E+00	0.00E+00	0.00E+00	0.00E+00
|NF|*AF	0.00E+00	0.00E+00	0.00E+00	0.00E+00	0.00E+00	0.00E+00	0.00E+00	0.00E+00
|NF|*PR1(i)	0.00E+00	0.00E+00	0.00E+00	0.00E+00	0.00E+00	0.00E+00	0.00E+00	0.00E+00
|NF|*PR2(i)	0.00E+00	0.00E+00	0.00E+00	0.00E+00	0.00E+00	0.00E+00	0.00E+00	0.00E+00
|PM|*SF	0.00E+00	0.00E+00	0.00E+00	0.00E+00	0.00E+00	0.00E+00	0.00E+00	0.00E+00
|PM|*YM	0.00E+00	0.00E+00	0.00E+00	0.00E+00	0.00E+00	0.00E+00	0.00E+00	0.00E+00
|PM|*RM	0.00E+00	0.00E+00	0.00E+00	0.00E+00	0.00E+00	0.00E+00	0.00E+00	0.00E+00

|PM|*AF	0.00E+00	0.00E+00	0.00E+00	0.00E+00	0.00E+00	0.00E+00	0.00E+00	0.00E+00
|PM|*PR1(i)	0.00E+00	0.00E+00	0.00E+00	0.00E+00	0.00E+00	0.00E+00	0.00E+00	0.00E+00
|PM|*PR2(i)	0.00E+00	0.00E+00	0.00E+00	0.00E+00	0.00E+00	0.00E+00	0.00E+00	0.00E+00
|SF|*YM	0.00E+00	0.00E+00	0.00E+00	0.00E+00	0.00E+00	0.00E+00	0.00E+00	0.00E+00
|SF|*RM	0.00E+00	0.00E+00	0.00E+00	0.00E+00	0.00E+00	0.00E+00	0.00E+00	0.00E+00
|SF|*AF	0.00E+00	0.00E+00	0.00E+00	0.00E+00	0.00E+00	0.00E+00	0.00E+00	0.00E+00
|SF|*PR1(i)	0.00E+00	0.00E+00	0.00E+00	0.00E+00	0.00E+00	0.00E+00	0.00E+00	0.00E+00
|SF|*PR2(i)	0.00E+00	0.00E+00	0.00E+00	0.00E+00	0.00E+00	0.00E+00	0.00E+00	0.00E+00
|YM|*RM	0.00E+00	0.00E+00	0.00E+00	0.00E+00	0.00E+00	0.00E+00	0.00E+00	0.00E+00
|YM|*AF	0.00E+00	0.00E+00	0.00E+00	0.00E+00	0.00E+00	0.00E+00	0.00E+00	0.00E+00
|YM|*PR1(i)	0.00E+00	0.00E+00	0.00E+00	0.00E+00	0.00E+00	0.00E+00	0.00E+00	0.00E+00
|YM|*PR2(i)	0.00E+00	0.00E+00	0.00E+00	0.00E+00	0.00E+00	0.00E+00	0.00E+00	0.00E+00
|RM|*AF	0.00E+00	0.00E+00	0.00E+00	0.00E+00	0.00E+00	0.00E+00	0.00E+00	0.00E+00
|RM|*PR1(i)	0.00E+00	0.00E+00	0.00E+00	0.00E+00	0.00E+00	0.00E+00	0.00E+00	0.00E+00
|RM|*PR2(i)	0.00E+00	0.00E+00	0.00E+00	0.00E+00	0.00E+00	0.00E+00	0.00E+00	0.00E+00
|AF|*PR1(i)	0.00E+00	0.00E+00	0.00E+00	0.00E+00	0.00E+00	0.00E+00	0.00E+00	0.00E+00
|AF|*PR2(i)	0.00E+00	0.00E+00	0.00E+00	0.00E+00	0.00E+00	0.00E+00	0.00E+00	0.00E+00
|PR1(i)|*PR2(i)	0.00E+00	0.00E+00	0.00E+00	0.00E+00	0.00E+00	0.00E+00	0.00E+00	0.00E+00
NF*NF*NF	0.00E+00	0.00E+00	0.00E+00	0.00E+00	0.00E+00	0.00E+00	0.00E+00	0.00E+00
PM*PM*PM	0.00E+00	0.00E+00	0.00E+00	0.00E+00	0.00E+00	0.00E+00	0.00E+00	0.00E+00
SF*SF*SF	0.00E+00	0.00E+00	0.00E+00	0.00E+00	0.00E+00	0.00E+00	0.00E+00	0.00E+00
YM*YM*YM	0.00E+00	0.00E+00	0.00E+00	0.00E+00	0.00E+00	0.00E+00	0.00E+00	0.00E+00
RM*RM*RM	0.00E+00	0.00E+00	0.00E+00	0.00E+00	0.00E+00	0.00E+00	0.00E+00	0.00E+00
AF*AF*AF	0.00E+00	0.00E+00	0.00E+00	0.00E+00	0.00E+00	0.00E+00	0.00E+00	0.00E+00
PR1(i)*PR1(i)*PR1(i)	0.00E+00	0.00E+00	0.00E+00	0.00E+00	0.00E+00	0.00E+00	0.00E+00	0.00E+00
PR2(i)*PR2(i)*PR2(i)	0.00E+00	0.00E+00	0.00E+00	0.00E+00	0.00E+00	0.00E+00	0.00E+00	0.00E+00
|NF*NF*NF|	0.00E+00	0.00E+00	0.00E+00	0.00E+00	0.00E+00	0.00E+00	0.00E+00	0.00E+00
|PM*PM*PM|	0.00E+00	0.00E+00	0.00E+00	0.00E+00	0.00E+00	0.00E+00	0.00E+00	0.00E+00
|SF*SF*SF|	0.00E+00	0.00E+00	0.00E+00	0.00E+00	0.00E+00	0.00E+00	0.00E+00	0.00E+00
|YM*YM*YM|	0.00E+00	0.00E+00	0.00E+00	0.00E+00	0.00E+00	0.00E+00	0.00E+00	0.00E+00
|RM*RM*RM|	0.00E+00	0.00E+00	0.00E+00	0.00E+00	0.00E+00	0.00E+00	0.00E+00	0.00E+00
|AF*AF*AF|	0.00E+00	0.00E+00	0.00E+00	0.00E+00	0.00E+00	0.00E+00	0.00E+00	0.00E+00
|PR1(i)*PR1(i)*PR1(i)|	0.00E+00	0.00E+00	0.00E+00	0.00E+00	0.00E+00	0.00E+00	0.00E+00	0.00E+00
|PR2(i)*PR2(i)*PR2(i)|	0.00E+00	0.00E+00	0.00E+00	0.00E+00	0.00E+00	0.00E+00	0.00E+00	0.00E+00

A5. Momentum Tare

High pressure air is used to power the AMELIA model's slot blowing circulation control system. The objective of the momentum tares was to quantify momentum effects of the slot blowing air flow within the model on the balance measurements. The slot blowing flow path was designed to flow the air across the balance's metric break via two s-pipe and bellows assemblies as shown in Figure A5.1. The balance was calibrated (as assembled in the photo shown in Figure A5.4) to account for the static pressure range of the slot blowing flow path, however, there was some concern that momentum flow effects may not cancel out between the split flow paths and that the residual momentum effects may show up in the test data.

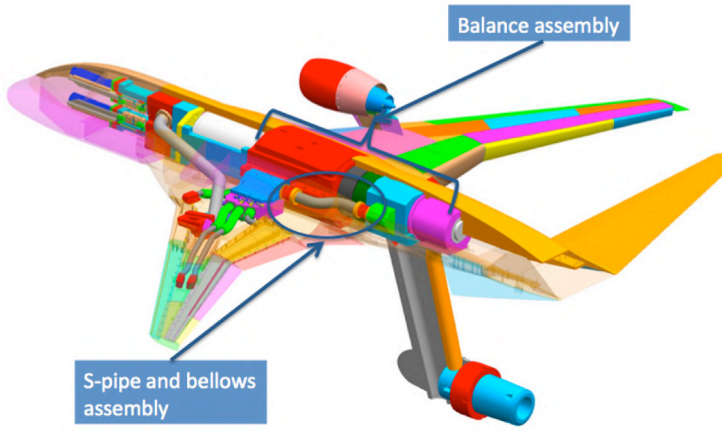

Figure A5.1. AMELIA Assembly showing slot blowing flow path w/r to the Balance Assembly.

Figure A5.2 is a schematic for the momentum tare set-up. A 1600 CFM compressor served as the pressurized air source. The air was flowed thru a critical flow venturi meter to measure the mass flow into the balance. The air is then split at the non-metric side of the balance assembly and flowed thru the left and right S-pipe and bellows assemblies to the respective left and right distribution plenums. From the plenums the air flows thru the zero thrust body. For the momentum tare effort he air can only flow to one side, since there is only one zero thrust body. Flow is blocked at the distribution plenum for the side not used. Pressure transducers are mounted to the left and right distribution plenums. The air flows from the zero thrust body to atmosphere.

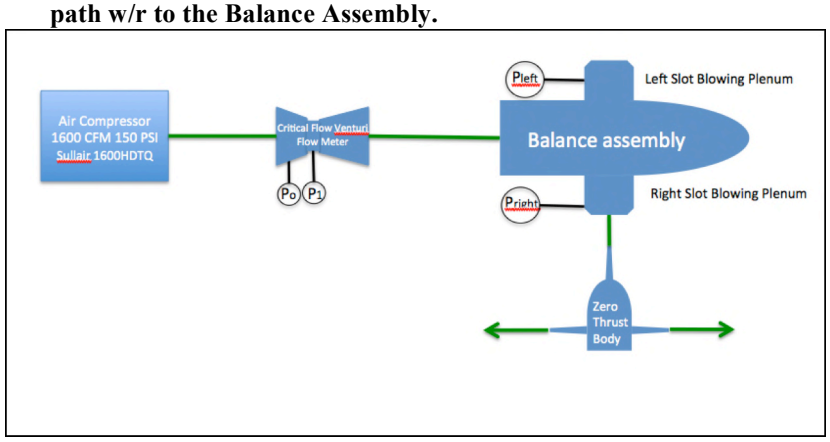

Figure A5.2. Schematic of Momentum Tare Set-up.

The AMELIA test team borrowed a zero thrust body (designed for another wind tunnel test that needed to quantify flow effects on balance measurements). The zero thrust body was designed to allow flow from the metric side of the balance to flow into a large plenum; from the plenum the air flows thru opposing nozzles to cancel the thrust effects of the flow, leaving only the momentum effects, if any, to influence any balance measurements.

Figure A5.3. Zero thrust body, assembled.

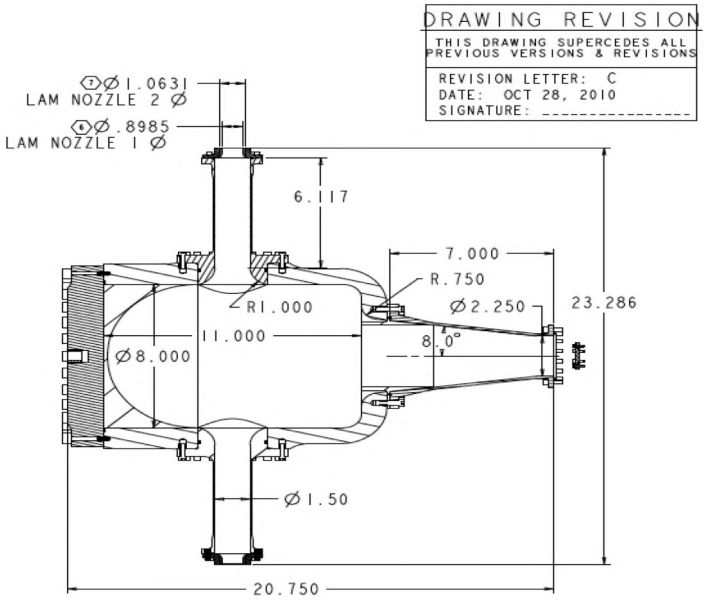

Figure A5.4. Zero thrust body, cross section view. Nozzle diameter for AMELIA was 0.94 in. Image courtesy of NASA.

The zero thrust body is shown in Figure A5.3 and Figure A5.4. An interface plate was fabricated to mate the zero thrust body to the AMELIA hardware, and 0.94" diameter nozzles were fabricated to simulate the appropriate back pressure in the balance air flow path. Figure A5.5 shows the zero thrust body mounted to the AMELIA's right slot blowing distribution plenum cover plate. Since we only possessed a single zero thrust body we could only mount the air on either the left or right slot blowing distribution plenum cover plate at a time. We performed momentum tare runs on both sides of the model. To verify the symmetry of the zero thrust body we also repeated each run with the zero thrust body rotated 180 degrees relative to the model.

Figure A5.5. Zero thrust body mounted to right side slot blowing plenum of balance assembly.

The run matrix for the momentum tare runs are shown in Table A5.1.

Table A5.1. Momentum Tare Run Matrix.

Run #	ZTB Mounting w/r to AMELIA	ZTB Orientation, degrees	Nozzle Size, inches
14	Right	0	0.94
15	Right	180	0.94
19	Left	0	0.94
20	Left	180	0.94

For the purposes of establishing a pressure dependent tare, the left and right plenum pressures are averaged and denoted as the plenum pressure, PL. The pressure range for the momentum tare runs was determined by the mass flow for the slot blowing system to achieve the required C_μ for the test. The desired mass flow for the test was nominally 2.8 lb_m/sec air which empirically correlates to approximately 55 psi at the both plenums. The critical flow venturi meter constrained the lowest mass flow to the plenums; when choked, the plenum pressure was 38 psi.

The momentum tare results are shown in Figure A5.6, Figure A5.7, Figure A5.8, and Figure A5.9.

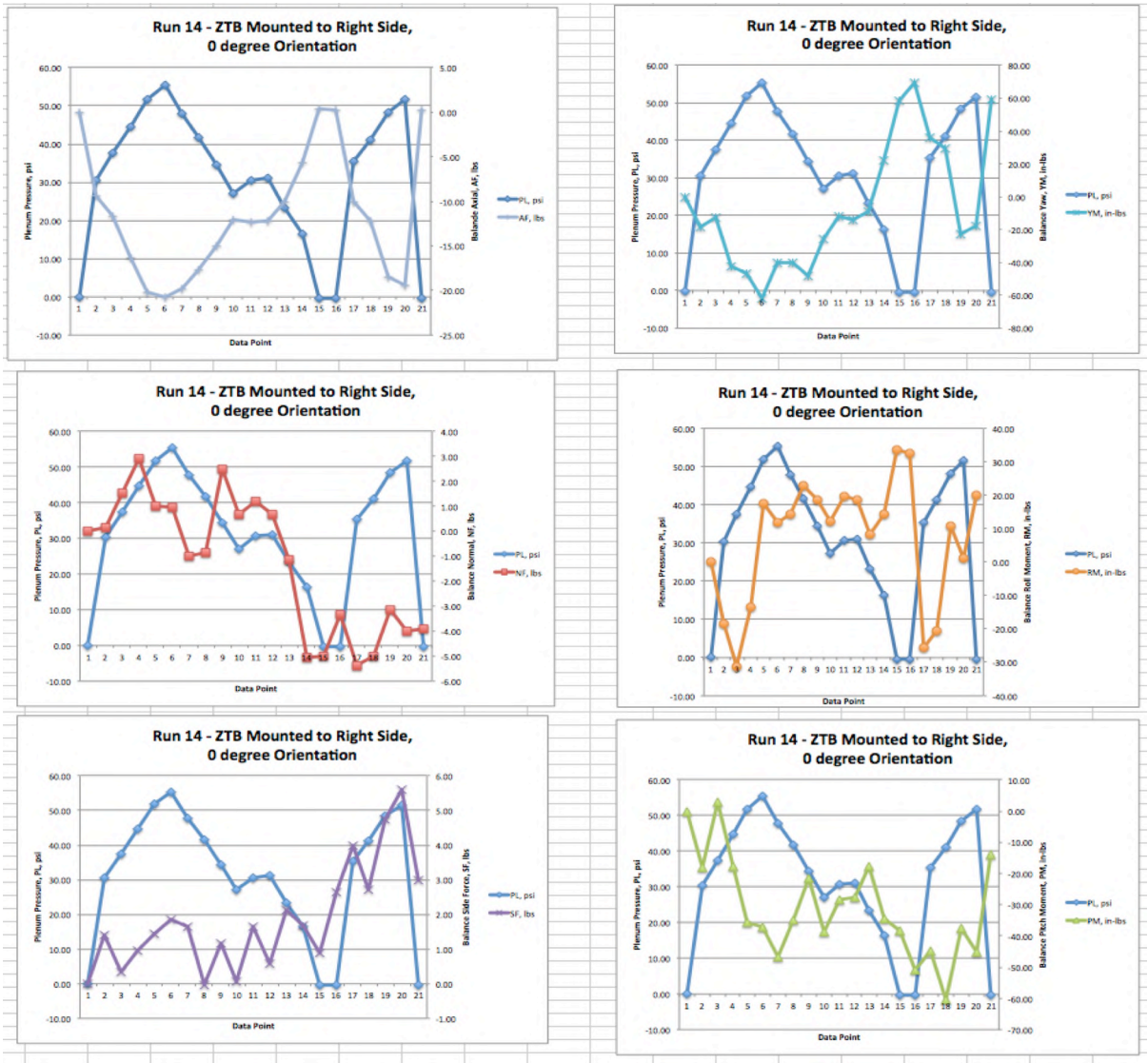

Figure A5.6. Run 14 Momentum Tare Results.

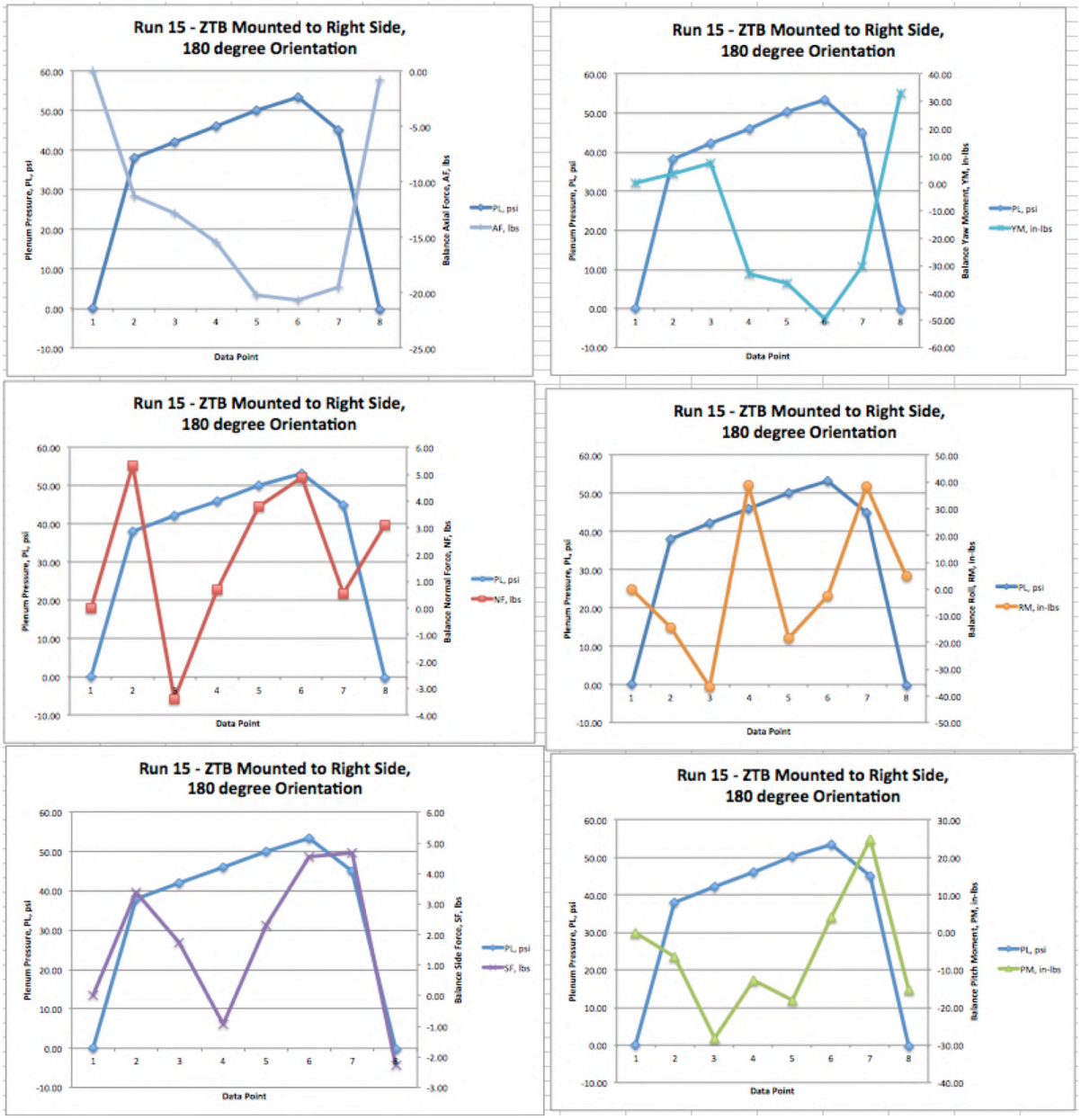

Figure A5.7. Run 15 Momentum Tare Results.

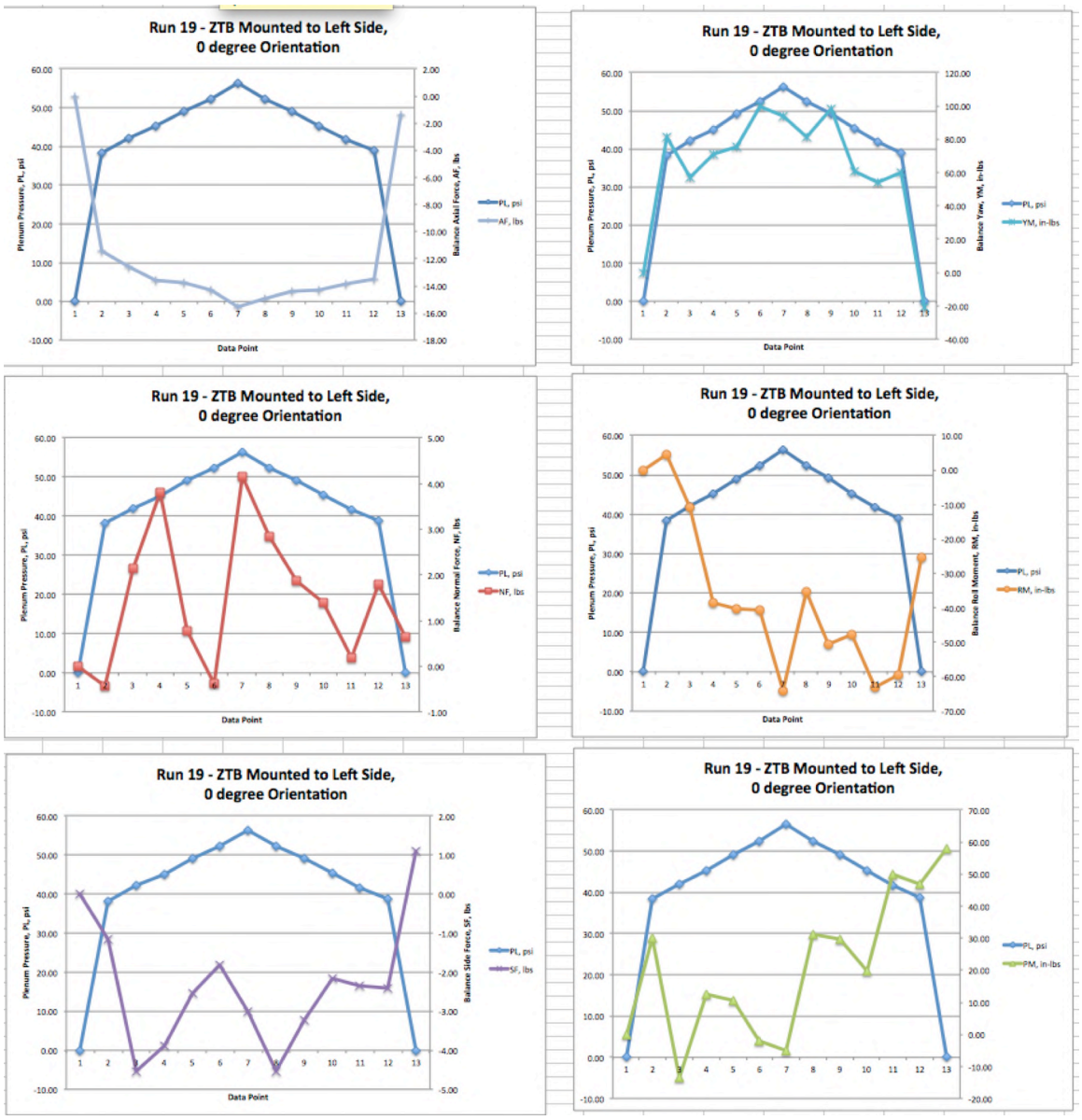

Figure A5.8. Run 19 Momentum Tare Results.

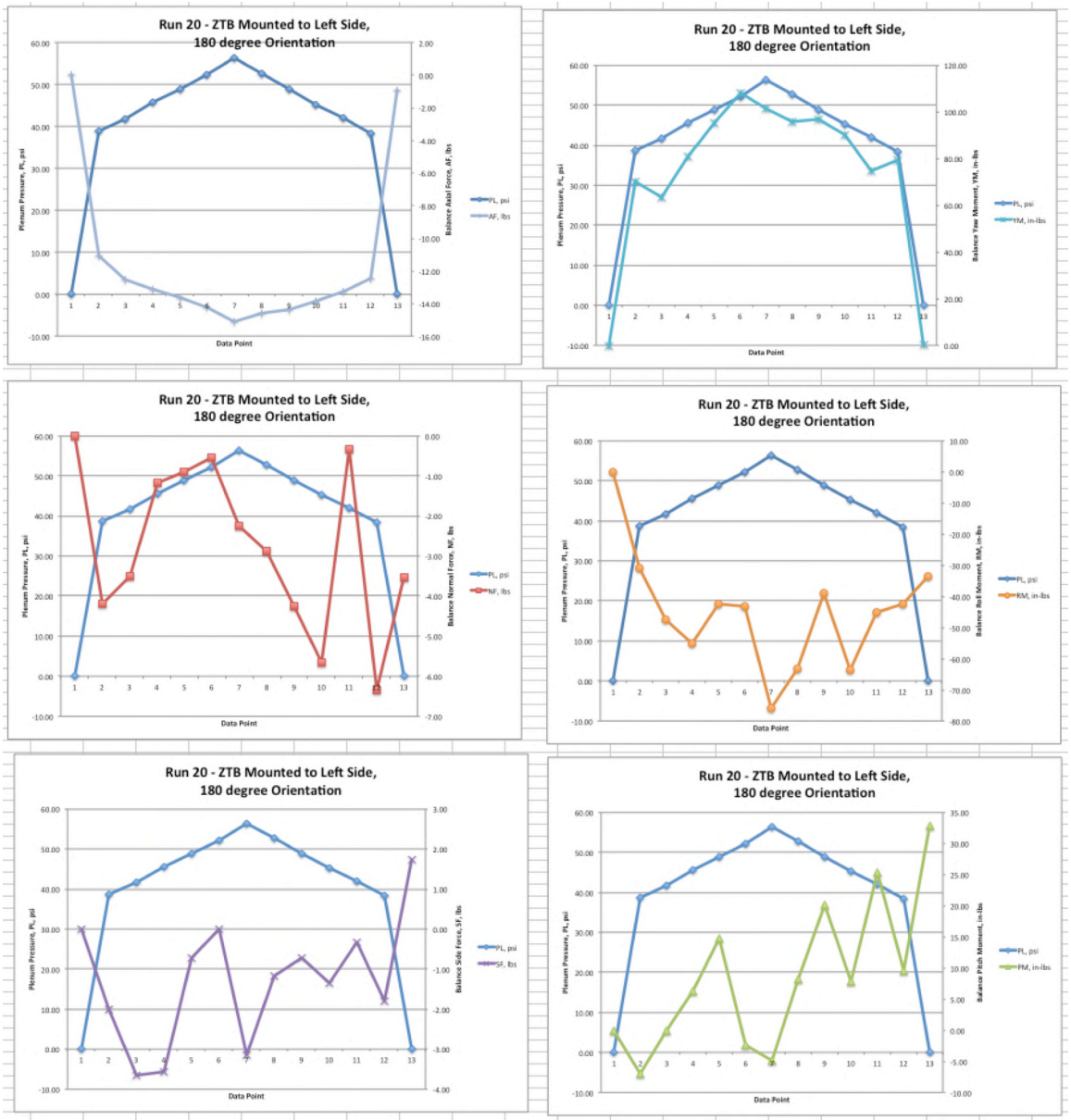

Figure A5.9. Run 20 Momentum Tare Results.

Discussion of momentum tare results

In reviewing the momentum tare runs, there is no correlation between balance side force (SF), normal force (NF), roll moment (RM), or pitch moment (PM) and increasing plenum pressure. No tares are necessary for SF, NF, RM, and PM

There is a correlation between balance yaw moment (YM) and axial force (AF) with increasing plenum pressure.

YM effects for the left blowing cases appear to correlate with plenum pressure oppositely from the right blowing cases. YM effects can be explained by fact that Pleft and Pright are not equal and the side that is blowing will have a higher pressure. Figure A5.6 shows Pleft and Pright for run 14, and clearly shows the difference in left and right plenum pressures, in this case the left side is blowing while the right side is not. The different pressures result in different area loads across the bellows. The bellows lie in the yaw plane, and the difference in plenum pressures, therefore area forces across the bellows, results in a yaw moment applied to the balance.

Figure A5.10 shows a direct comparison of YM effects for right and left blowing cases (Runs 15 and 19, respectively). In Run 15, at 52 psi plenum pressure the resulting YM is 100 lbs; In Run 19, at 52 lbs the resulting YM is -52 lbs. When left and right YM effects are combined the net YM is 48 lbs, about the same as the 2 standard deviation uncertainty of the YM balance calibration of 48.8 lbs and therefore no tare is recommended for YM.

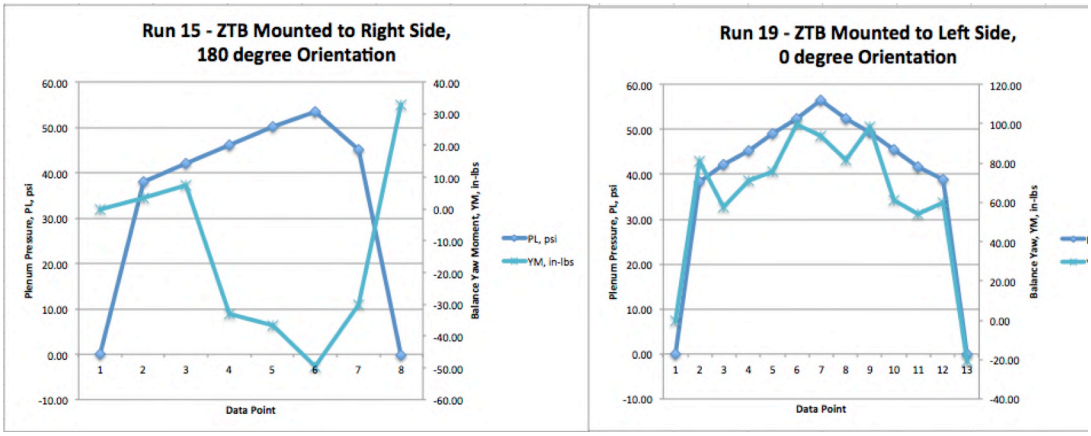

Figure A5.10. Comparison of Run 15 and Run 19 Yaw Moments.

Axial force for right side blowing at PL at 52 psi for Runs 14 and 15 are -20 lbs and -21 lbs, respectively. Axial force for left side blowing for PL at 52 psi are -14.7 and 15.0 lbs respectively. A tare correction for AF is recommended.

Table A5.2 summarizes the tare recommendations in a table format based on comparison of Run 15 and 19.

Table A5.2. Tare Recommendation Based on Comparison of Run 15 and Run 19.

	Units	Balance Calibration Uncertainty, 2 std dev	Momentum Tare Run 15, Left Blowing Max	Min	Momentum Tare Run 19, Right Blowing Max	Min	Tare Recommendation
DRAG AF	lbs	2.6	0.00	-20.63	0.00	-15.54	Drag correlates to pressure, need to add drag effects for both left and right blowing both sides flow air simultaneously during test operations.
SIDE, SFL	lbs	4.6	4.68	-2.28	1.10	-4.53	No correlation of side force w/r to pressure. No tare required
LIFT, NF	lbs	5.8	5.33	-3.40	4.16	-0.44	No correlation of lift force w/r to pressure. No tare required
ROLL, RM	in-lbs	107.3	38.85	-36.65	4.60	-63.93	No correlation roll w/r to pressure. No tare required
PITCH, PM	in-lbs	34.4	24.86	-28.17	57.80	-13.53	No correlation of pitch w/r to pressure. No tare required
YAW.YM	in-lbs	48.8	33.01	-49.52	99.55	-20.83	Yaw correlates to pressure. Left blowing appears to act in opposition to right blowing effects. Maximum left blowing effect combined with minimum right blowing effect yield 12.18 in-lbs, Maximum right blowing combined with minimum left blowning yields 50.03 in-lbs. The maximum yaw effects are slightly larger than the 2 std dev uncertainty of the balance calibration. No tare required.

Recommended Tare Corrections

Based on analysis of the momentum tare data axial force is the only balance measurement that requires a tare correction. The data show that the AF effects increase (negatively) with increasing pressure. In normal test operations the left and right plenums (Pleft and Pright, respectively) will be at the same pressure, unlike the momentum tare run, in which only one side is blowing (see Figure A5.11). A proper tare requires that the left and right momentum tare results be combined.

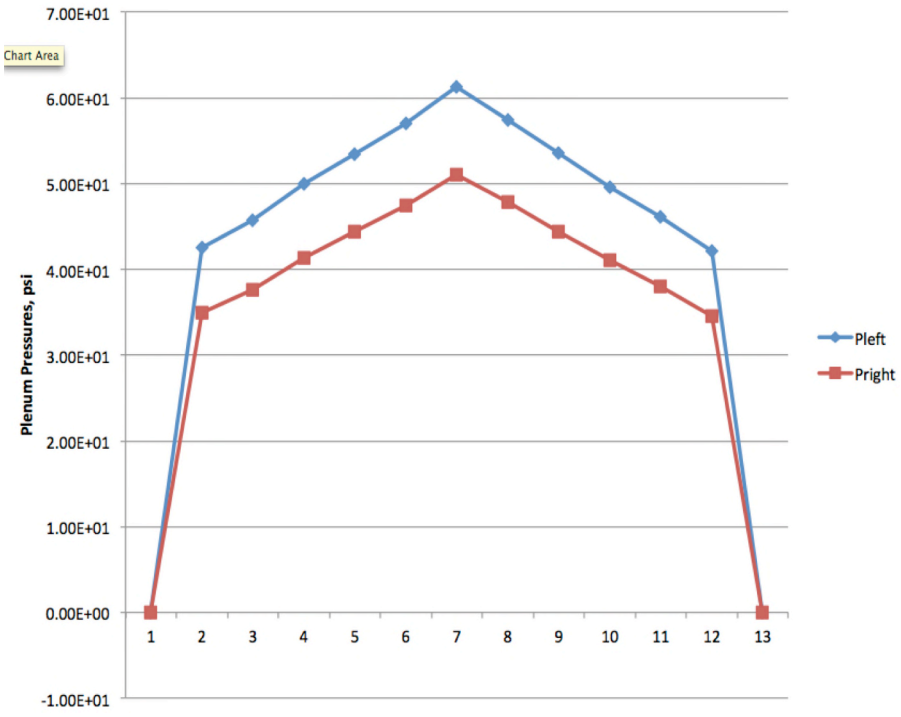

Figure A5.11. Comparison of Left and Right Plenum Pressures for Run 20, with left side blowing.

The combined result entails first determining the right side blowing sensitivity of AF w/r to PL using data from runs 14 and 15, secondly, determining the left side blowing sensitivity using data from runs 19 and 20, and finally, adding the left side sensitivity to the right side sensitivity to get the combined sensitivity. Figure A5.12 shows the Axial Force effects of increasing plenum pressure for all the momentum tare runs. Figure A5.13 shows the resultant left, right and combined blowing sensitivities.

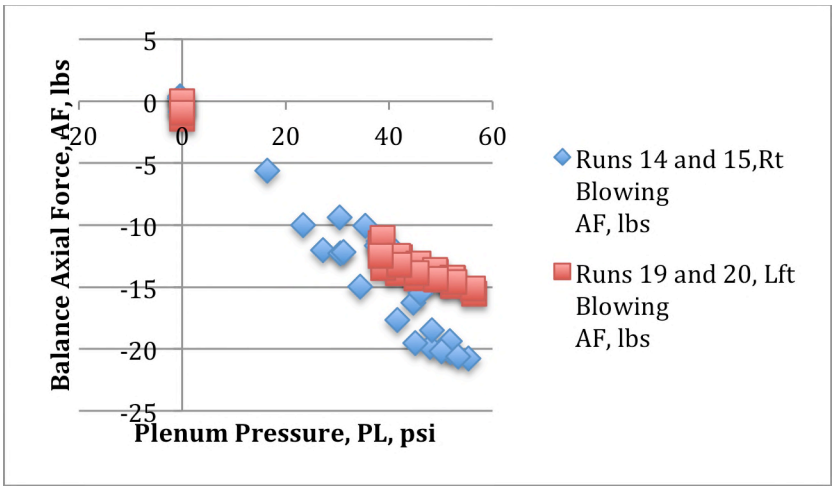

Figure A5.12. Axial Force Effects vs Plenum Pressure.

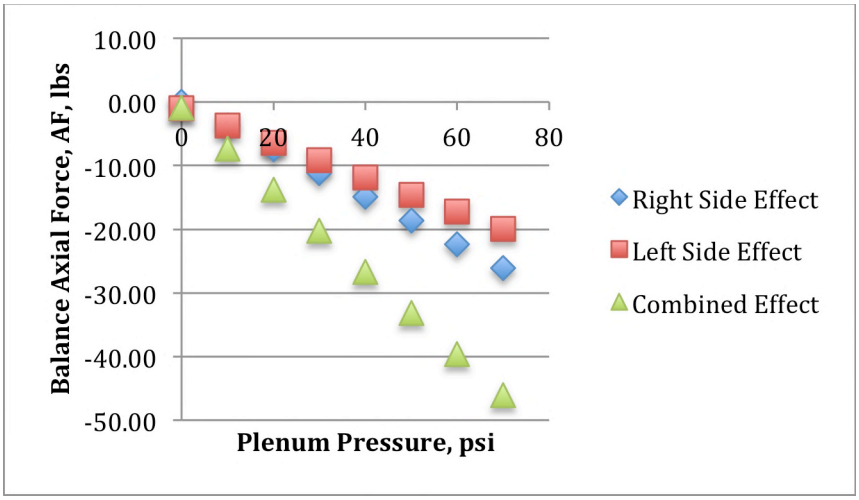

Figure A5.13. Plot of Left and Right Blowing Effects and Combined Blowing Effects on Axial Force.

The following equation provides the momentum tare correction to the balance axial force measurement. The tare correction is dependent on the average of the right and left, low pressure distribution plenum pressures. As the average plenum pressure increases there is a corresponding decrease in axial force (apparent increase in drag).

The sensitivity is -.646 lbs/psi.

$$AFcorrected = AF + .646 \times (\text{Pleft} + \text{Pright})/2$$

A6. Lifting Plan

The following is the NFAC generated lift plan for installing the AMELIA model into the 40x80 Wind Tunnel Test Section.

Cal Poly CESTOL Lift Plan

Rev0, October 4, 2011

Signature Approval

Title	Signature	Date
Originator	Charlie Rogers	
Peer Review	Chris Hartley	
Lift Director	Adam Walsh	
Mechanical Engineer	Dan Boyd	
System Safety	Scott DuBridge	
HSE	Jeff Law	
Chief Engineer	Rick Shinoda	
Site Manager	Jeff Johnson	

Revision History

Revision	Description	Date	Originator Initial
0	Initial Release	10/4/2011	

Overview

This document covers the lift plan for the installation of the Cal Poly CESTOL model in the 40' x 80' test section. The model is a hybrid blended wing-body, powered lift aircraft with Turbine Propulsion Simulators mounted above the wings, leading and trailing edge slot blowing, and a six component, flow through balance. The model will be mounted on the NFAC 13' sting support and pitch mechanism, as shown in Figure . The sting support and pitch mechanism will be installed in the test section prior to the model lift. A separate lift plan was made for the sting support and pitch mechanism installation.

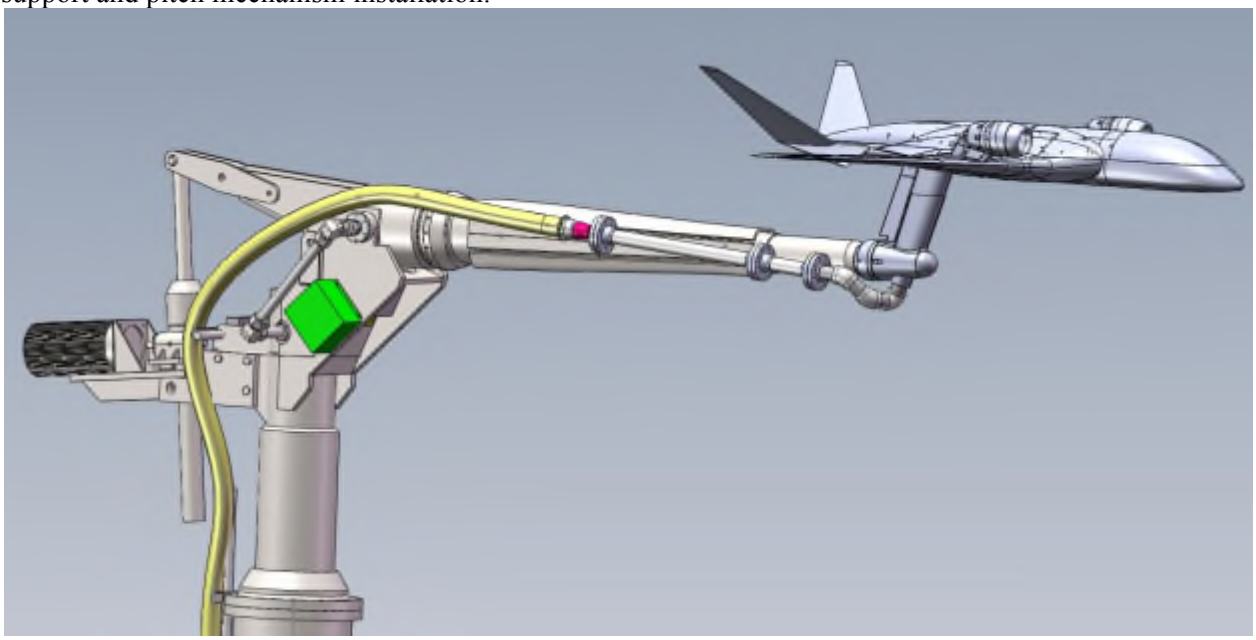

Figure 1. CESTOL Model Mounted on Sting Support.

The model is connected to the sting support by a modular blade adapter. The blade is an offset height adapter between the sting and the non-metric side of the model, raising the model centerline 24.4" above the sting's centerline. The blade will have two taper interfaces, one to the sting, and the other to the non-metric side of the model. The blade-to-sting tapered interface is pinned to restrain roll about the joint. The blade will be oriented level in roll and match-drilled to the sting keyway.

The upper component of the blade adapter, which connects to the non-metric side of the model, will be de-coupled from the blade and mated to the model prior to the lift. The combined weight of the model, balance, and upper blade adapter is 2560 lbs. The rest of the blade will be installed on the end of the sting pre-lift. The blade components that are captive on the model

will bolt onto the sting-mounted blade components during the lift. A schematic distinguishing between blade components is shown in Figure below.

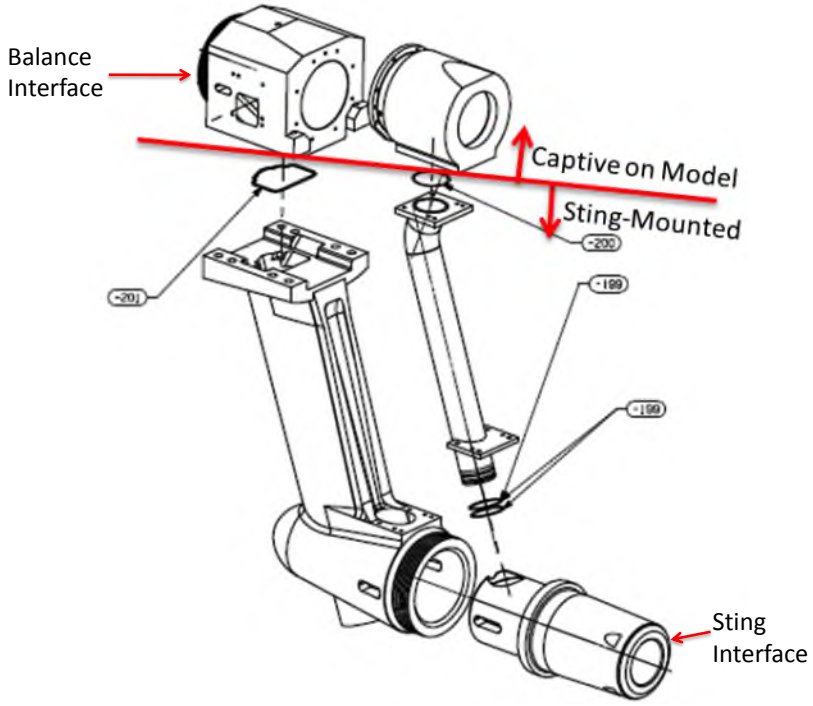

Figure 2. Blade Interface, Exploded View.

Rigging Schematic

The model has four lifting points with ½-13 threaded fixtures. The fixtures are labeled one through four in Figure and Figure below. Fixtures one and two are forward of the model CG and mirrored across the centerline, while three and four are aft.

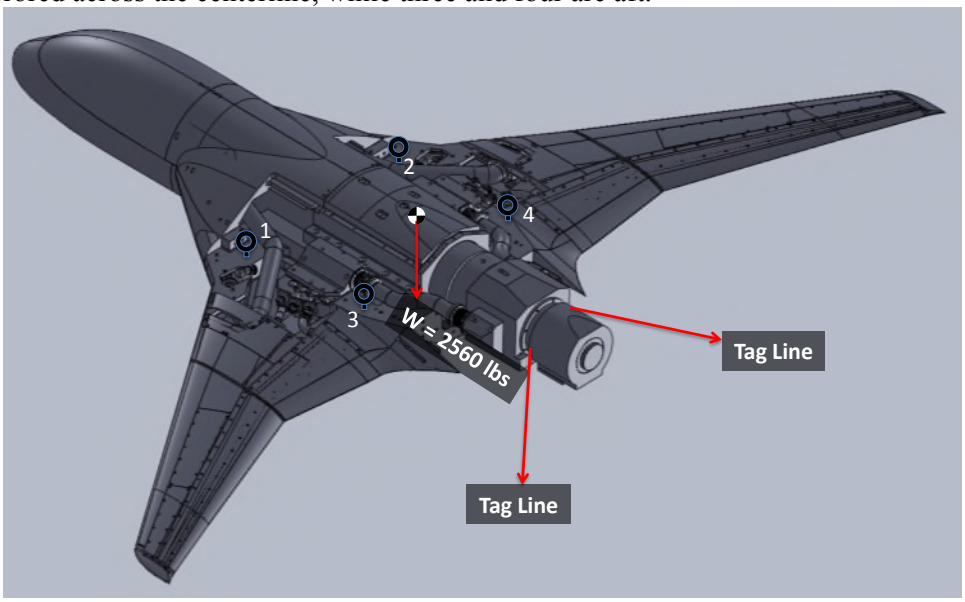

Figure 3. Model in Lift Configuration with Rigging Points, Isometric View.

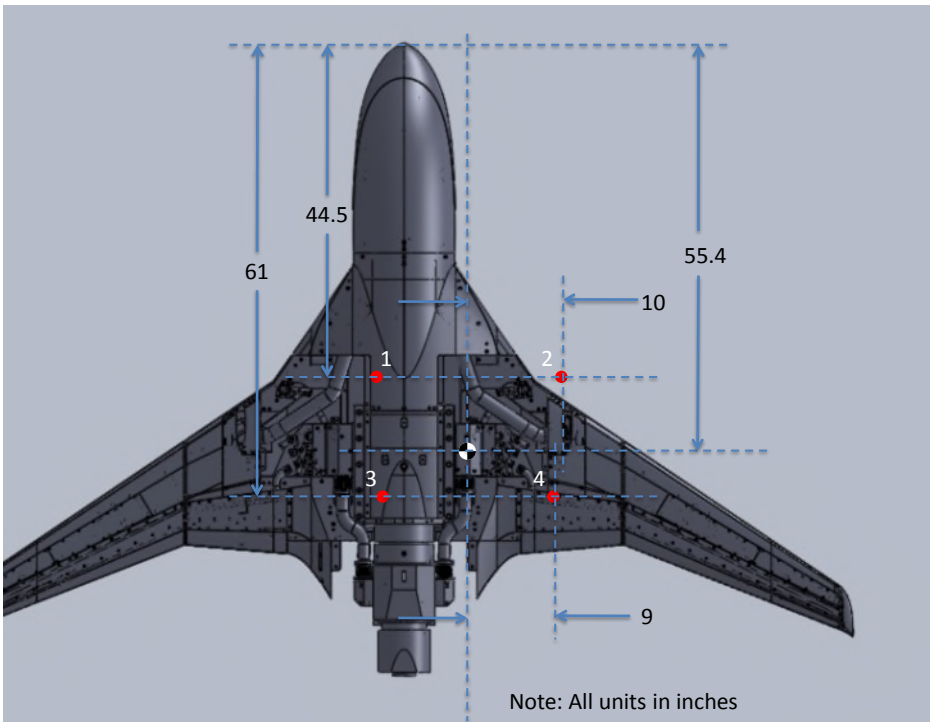

Figure 4. Model in Lift Configuration with Rigging Points, Top View with Dimensions.

Forward fixtures one and two will each be connected to the crane (from the bottom up) with a ½" hoist ring, ¾" shackle and 6' sling. Aft fixtures three and four will each connect to the crane with a ½" hoist ring, ¾-ton come-along, and 3' sling. Schematics of each rigging combination are shown in Figure .

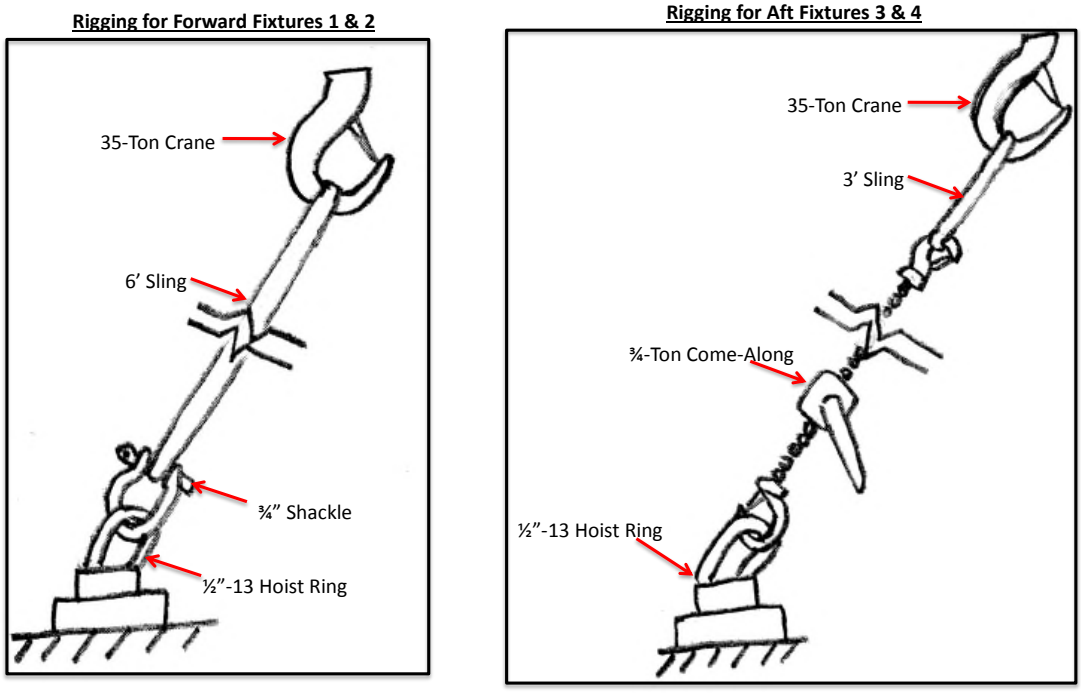

Figure 5. Rigging Diagrams for Forward and Aft Fixtures.

The working load limit and expected load for each hardware component is shown in Table 6.1 below. The calculations for the expected loads are shown in Section 4.

Table 6.1. Lifting Hardware and Ratings.

Component	Working Load Limit (lbs)	Max Expected Load (lbs)	% WLL
½" Hoist Ring	2500	870	34.8
¾" Shackle	9500	440	4.6
6' Sling	16800	440	2.6
3' Sling	10600	870	8.2
3/4 – Ton Come-Along	1500	870	58

Lift Procedure

Note: Personnel are not permitted to stand underneath the crane-suspended load unless it is necessary to perform installation duties. Time under a suspended load should be minimized or eliminated if possible.

1) **Stage model in high bay under crane loading zone.**
2) **Hold a pre-lift meeting to discuss roles and the sequence of events.**
3) **Make personnel assignments for the following roles: Lift director, certified crane operator, tag line operators.**
4) **Complete a SPA for the lift.**
5) **Secure lift area with appropriate warning tape. Only essential personnel allowed in secured area. All personnel in secured area must wear hard hats, safety glasses, and steel-toed shoes.**
6) **Perform pre-lift crane checkout.**
7) **Ensure model support system lifted off scales and resting on balance house wall pads.**
8) **Drive sting pitch mechanism to approximately level position.**
9) **Park scissor lift by tip of sting.**
10) **Gather and inspect all lifting hardware before attaching to model.**
11) **Open West clamshell door. Ensure East door is closed.**
12) **Connect lifting hardware to model and crane. Ensure some slack is still in each line.** *Be cautious with lifting hardware so as not to scratch the painted surface of the model.*
13) **Connect tag lines to aft end of model.** *Be cautious with lifting hardware so as not to scratch the painted surface of the model.*
14) **Disconnect model from transport cradle.**

15) **With crane hook roughly over model CG (ref Figure for approximate CG location), slowly raise crane until forward slings are taut.**

16) **Make adjustments to come-alongs until aft slings are taut.**

17) **Ensure slings are not tangled over crane hook.**

18) **Slowly lift model a few feet above cradle and verify visually model is level. Adjust come-alongs if necessary to level model.**

19) **Lift model above 4th floor catwalk and gather tag lines.**

20) **Transfer crane control to 5th floor.**

21) **Raise model over top of tunnel and drive over west side of test section, clear of East clamshell door.**

22) **Once clear, open East clamshell door.**

23) **Move model roughly over tunnel centerline, with tail end just south of sting support.**

24) **Lower model until it is within a few feet of the sting support.**

25) **Rotate model, using tag lines, so nose points south.**

26) **From scissor lift, guide crane operator to place aft end of model just over end of blade on sting support.**

27) **Adjust sting pitch angle and come-alongs to make mating planes parallel.**

28) **Slowly lower model to mate blade components and ensure mating surfaces are flush. Ensure o-rings are seated properly and are not pinched or dragged on mating surfaces.**

29) **Bolt blade components together. Use eight 5/8" – 18 x 2" SHCS with blue loctite. Torque to 204 ft*lbs. Ensure bolted connections are snug before unloading crane.**

30) **Unload lifting hardware and de-rig model.**

31) **Double check bolt torque once model is free of lifting hardware.**

32) **Close clamshell doors and return lifting hardware to storage.**

Calculations

C Rogers

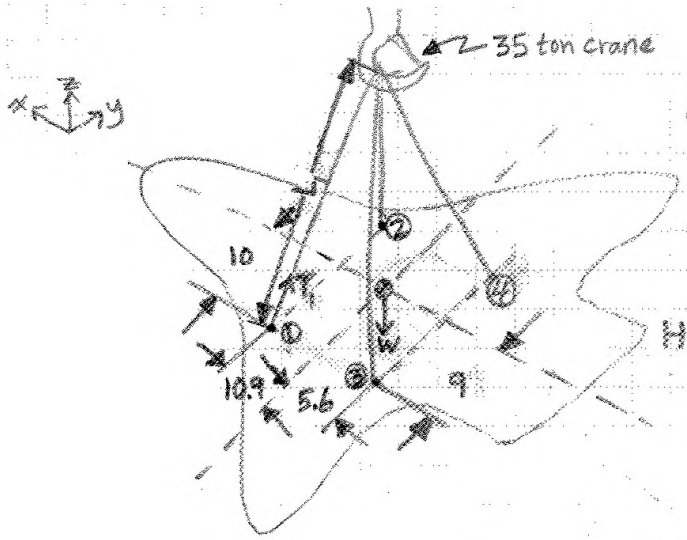

ALL DIMS IN INCHES

ALL FIXTURES ASSUMED COPLANAR.

HEIGHT OF HOOK ABOVE FIXTURES:

$H^2 = L_1^2 - (10^2 + 10.9^2)$

$L_1 = L_2 = 72 + 8 = 80$

(sling + hoist ring + shackle)

$H = 79$

$L_3 = L_4 = \sqrt{5.6^2 + 9^2 + 79^2}$

$= 79$

$T_1 = T_2,\ T_3 = T_4,\ W = 2560\ \text{lbf}$

$\vec{T}_1 = \frac{T_1}{L_1}(10.9\hat{i} - 10\hat{j} + 79\hat{k}) = T_1(0.14\hat{i} - 0.13\hat{j} + 0.98\hat{k})$

$\vec{T}_2 = \frac{T_2}{L_2}(10.9\hat{i} + 10\hat{j} + 79\hat{k}) = T_2(0.14\hat{i} + 0.13\hat{j} + 0.98\hat{k})$

$\vec{T}_3 = \frac{T_3}{L_3}(-5.6\hat{i} - 9\hat{j} + 79\hat{k}) = T_3(-0.07\hat{i} - 0.11\hat{j} + 0.99\hat{k})$

$\vec{T}_4 = \frac{T_4}{L_4}(-5.6\hat{i} + 9\hat{j} + 79\hat{k}) = T_4(-0.07\hat{i} + 0.11\hat{j} + 0.99\hat{k})$

$\Sigma F_x = 0,\ 0.27T_1 - 0.14T_3 = 0 \Rightarrow T_1 = 0.52T_3$

$\Sigma F_z = 0,\ 1.96T_1 + 1.98T_3 - W = 0 \Rightarrow T_1 = W/1.96 - T_3$

$= 1310 - T_3$

$0.52T_3 = 1310 - T_3 \Rightarrow$

$\boxed{T_3 = T_4 = 837\ \text{lbf}}$

$\boxed{T_1 = T_2 = 443\ \text{lbf}}$

A7. Instrumentation Listing

The instrumentation list that follows is an adaptation of the standard NFAC instrumentation list supplied to the NFAC Instrumentation Group. Three tables are used in this list to differentiate the tunnel's instrumentation (Table 1), the on-model pressure instrumentation (Table 2) and the on-model temperature instrumentation (Table 3).

The tunnel instrumentation list includes the tag name of each instrument, a description of the instrument, the units of measure, and the assigned data system. The PSI_Initium list is separated by pressure module. The list contains information for port number (within the module), the instrument's tag name, description, tubing label, and status according to leak/plugs check. The LXI tab, is separated into temperature modules (although only one is needed). The channel used by each instrument is listed (1-47), tag names are included, along with a description of the measurement, and the type of thermocouple used. Through all tables, malfunctioning instruments have been noted with *NR* or not responsive. Instruments that malfunctioned mid-test are noted with *NR* (written in red text) alongside the date that instrument began showing signs of malfunction.

For reference, all figures relevant to the instrumentation are repeated below.

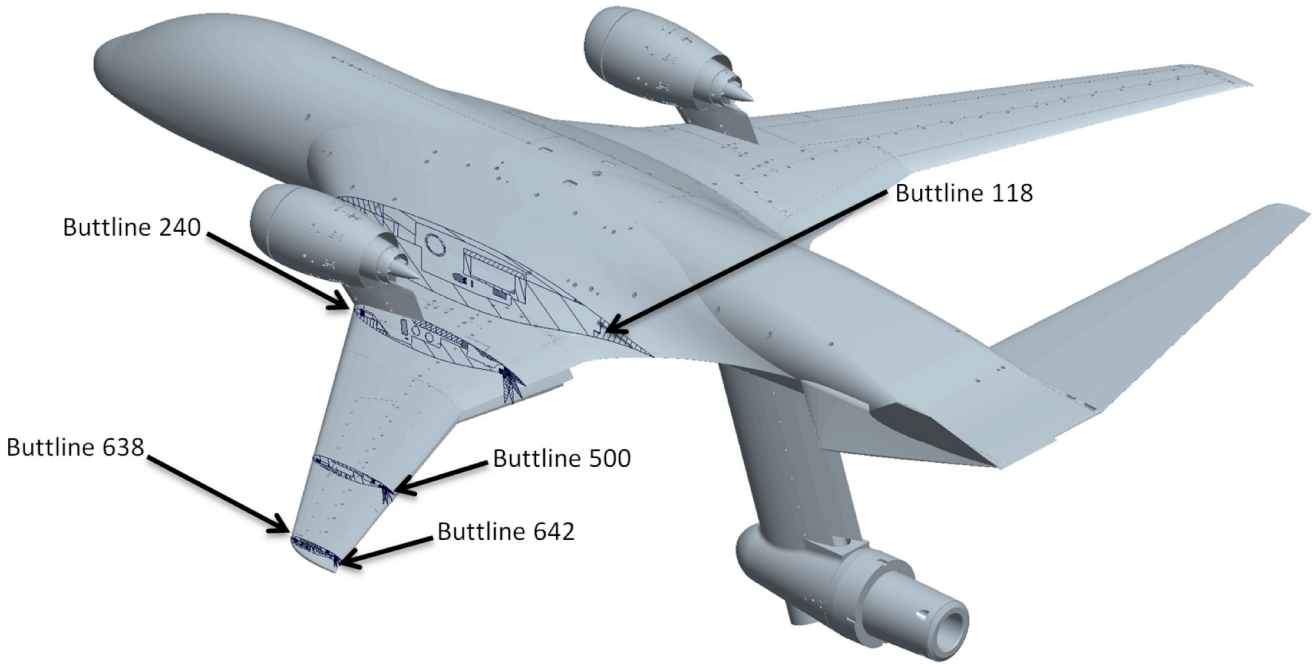

Figure A7.1. Pressure port chordwise groups.

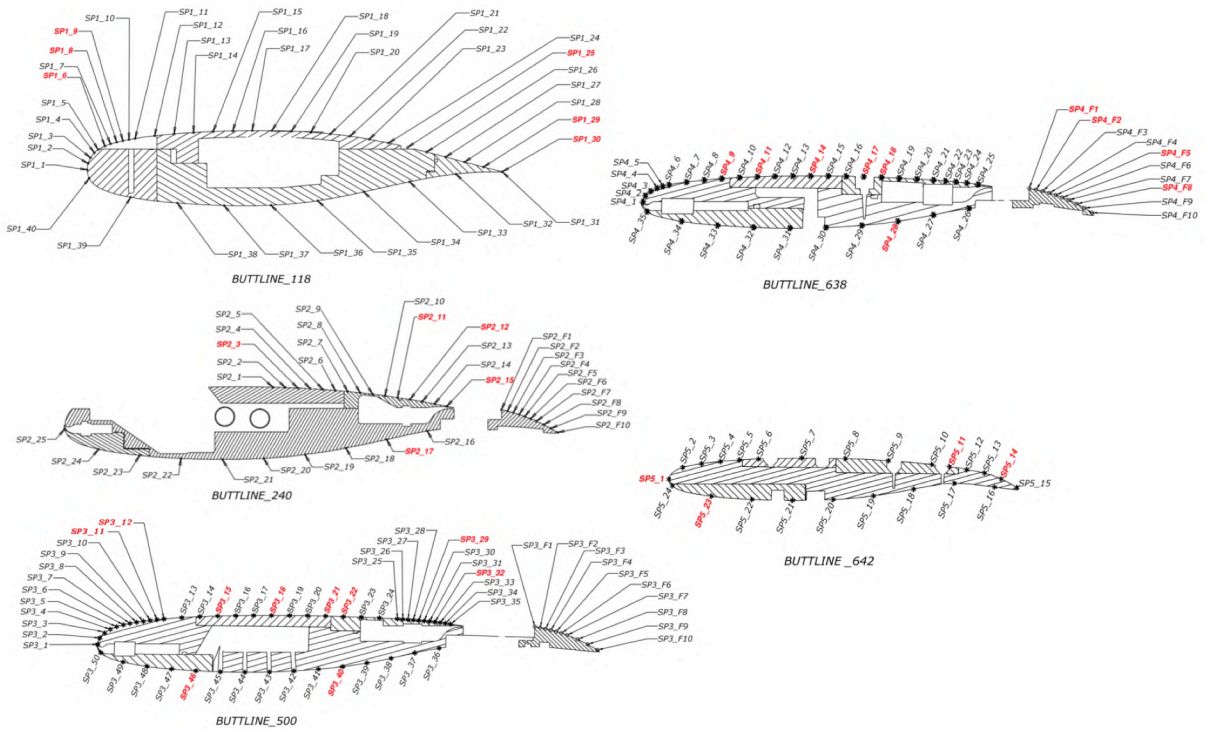

Figure A7.2. Pressure port layout of each chordwise group.

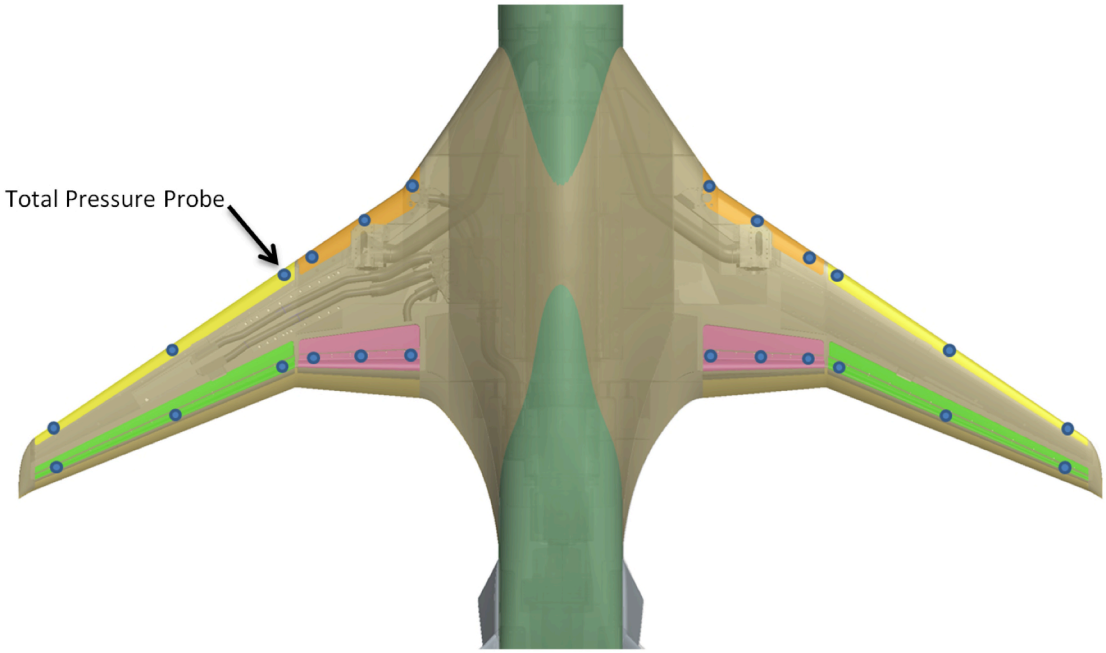

Figure A7.3. Total pressure probes inside each circulation control plenum.

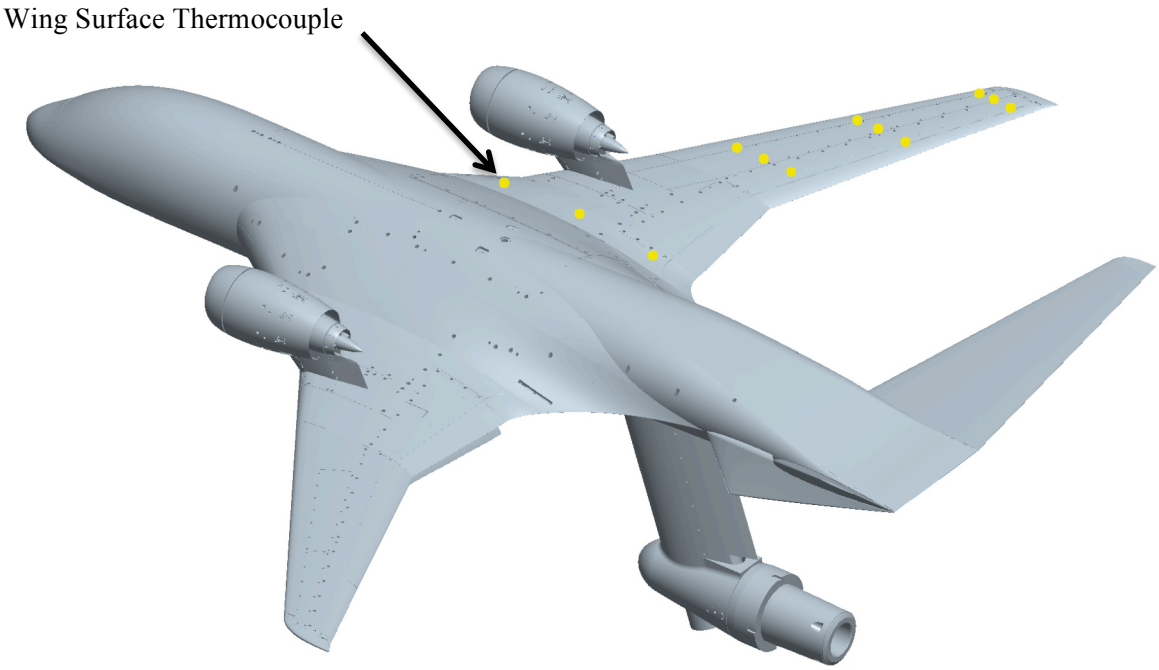

Figure A7.4. Wing surface thermocouples.

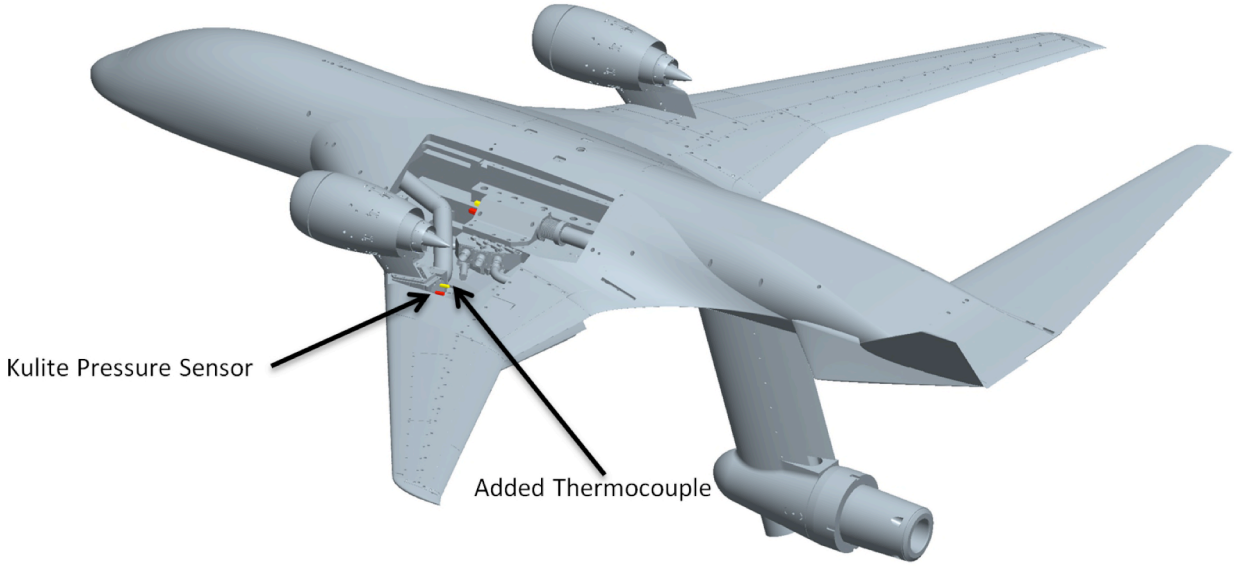

Figure A7.5. Low pressure distribution plenum and TPS pylon added thermocouples and pressure sensors.

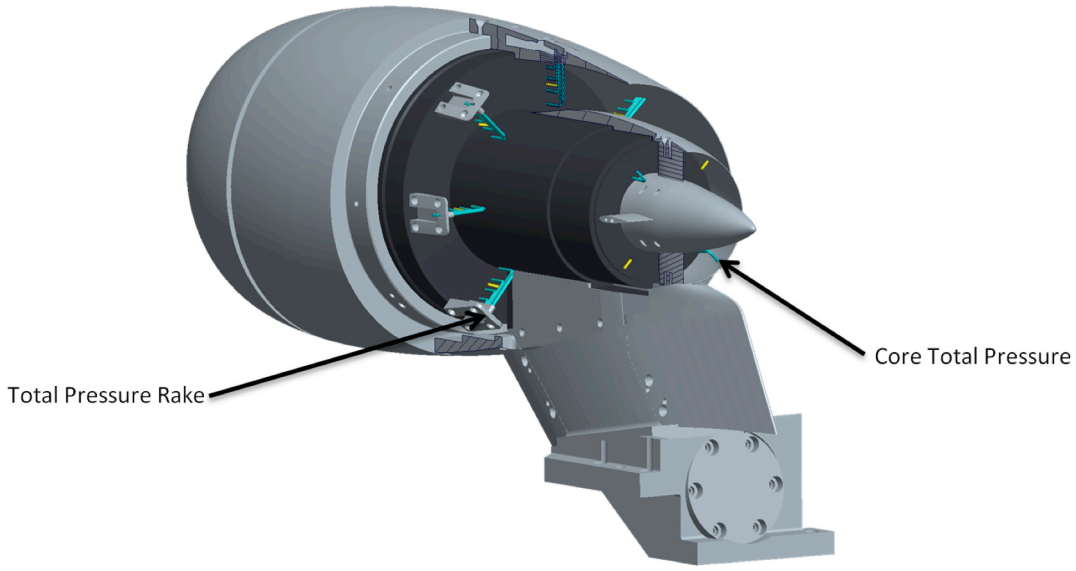

Figure A7.6. Rake layout in the fan, with core instrumentation (Thermocouple shown in yellow).

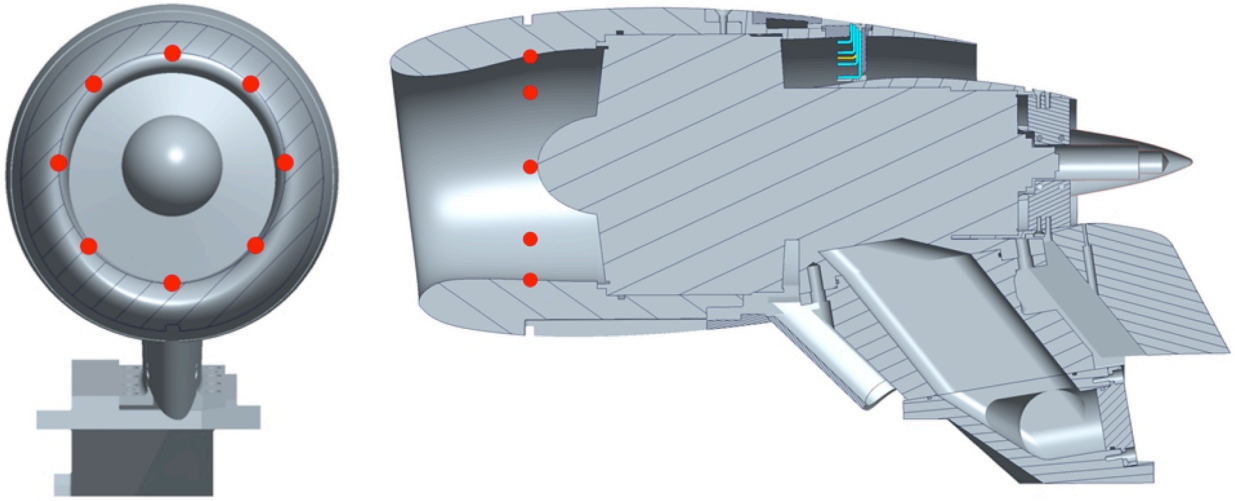

Figure A7.7. Front and side view of the TPS, each red dot represents the location of a static pressure tap.

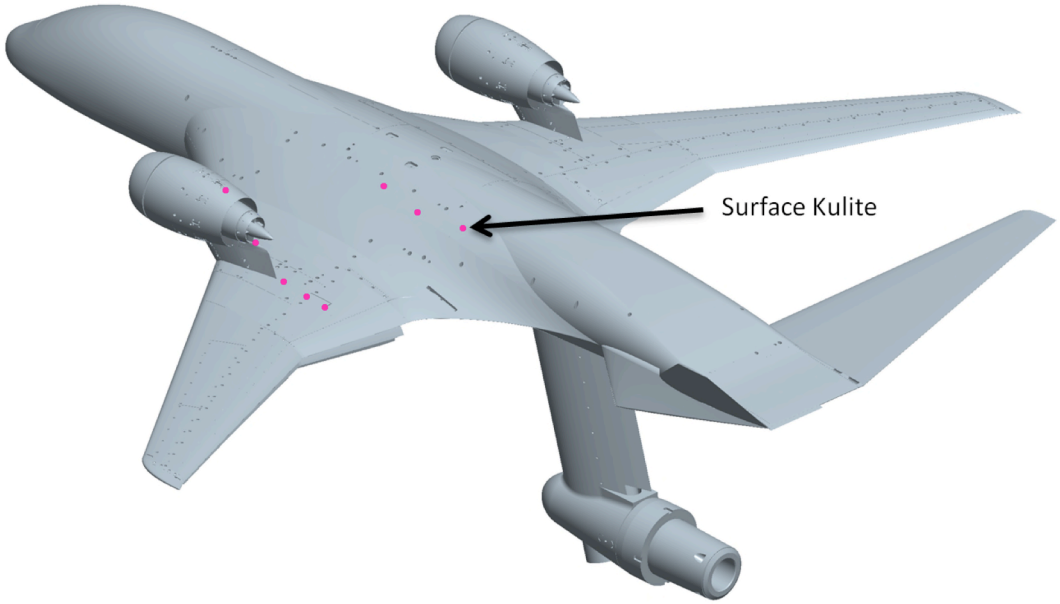

Figure A7.8. Surface unsteady pressure Kulites.

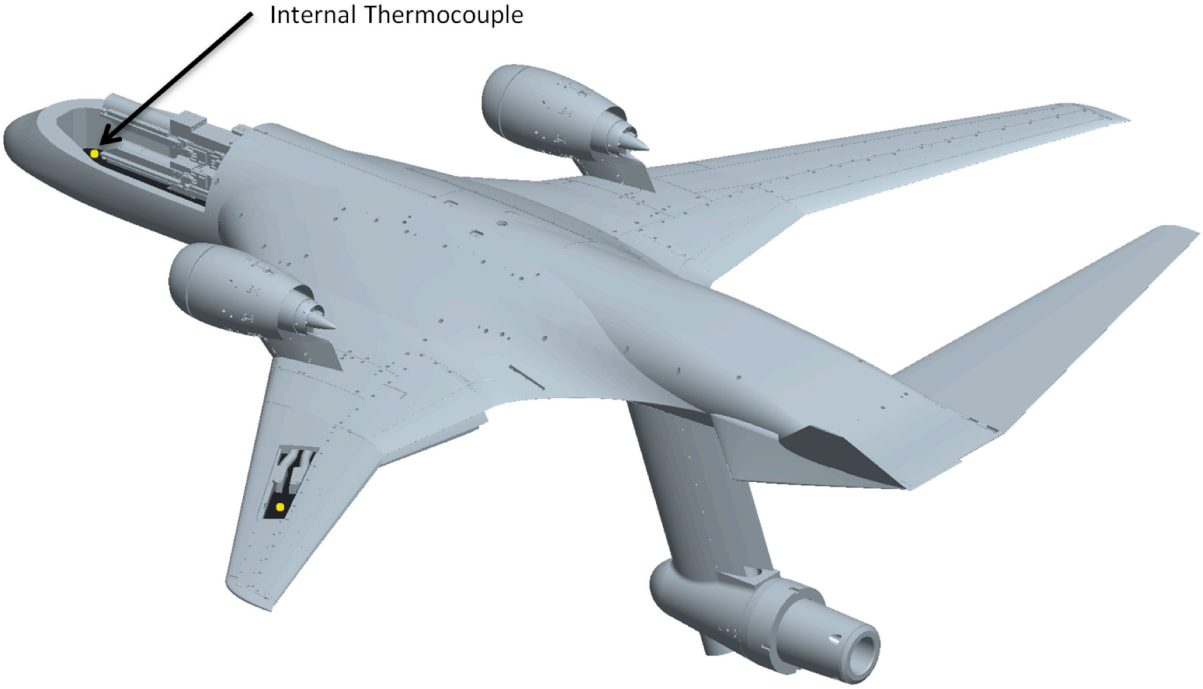

Figure A7.9. Internal thermocouples added to AMELIA.

Table A7. 1. Tunnel Instrumentation

	Last CONFIG update: 08/10/2011 12:05 EP		
Name	Description	Units	Customer
			0
BARO	Barometric Pressure		
PA	Atmospheric Pressure at tunnel centerline	PSF	
TTR	Tunnel total temperature	deg R	
QU	Uncorrected dynamic pressure	PSF	
QCLU	Centerline Q corrected for static plate errors	PSF	
DQSP	Static plate correction	PSF	
PT	Total pressure at tunnel centerline	PSF	
PS	Static pressure at tunnel centerline	PSF	
PSA	Absolute static pressure at tunnel centerline	PSIA	
MTUN	Tunnel Mach number	non_dim	
Q	Centerline corrected Q	PSF	
TSR	Tunnel static temperature	deg R	
TSF	Test section static temperature	deg F	
CSND	Tunnel speed of sound	ft/sec	
VPDB	Test section dry bulb vapor pressure	PSF	
VPDP	Test section dew point vapor pressure	PSF	
RH	Test section relative humidity	%	
RHO	Test section air density at static conditions	slug/ft^3	
VFPS	Test section velocity	ft/sec	
VKTS	Test section velocity	Knots	
VISC	Test section dynamic air viscosity	slug/ft-sec	
REYN	Reynolds number	millions/ft	
WP_A_04	40x80 Static Wall Pressure Tap Lower Half of Tunnel	PSF	
WP_D_04	40x80 Static Wall Pressure Tap Lower Half of Tunnel	PSF	
WP_E_04	40x80 Static Wall Pressure Tap Lower Half of Tunnel	PSF	
WP_F_04	40x80 Static Wall Pressure Tap Lower Half of Tunnel	PSF	
WP_G_04	40x80 Static Wall Pressure Tap Lower Half of Tunnel	PSF	
WP_H_04	40x80 Static Wall Pressure Tap Lower Half of Tunnel	PSF	
WP_J_04	40x80 Static Wall Pressure Tap Lower Half of Tunnel	PSF	
WP_K_04	40x80 Static Wall Pressure Tap Lower Half of Tunnel	PSF	
WP_L_04	40x80 Static Wall Pressure Tap Lower Half of Tunnel	PSF	
WP_M_04	40x80 Static Wall Pressure Tap Lower Half of Tunnel	PSF	
WP_N_05	40x80 Static Wall Pressure Tap Lower Half of Tunnel	PSF	
WP_P_05	40x80 Static Wall Pressure Tap Lower Half of Tunnel	PSF	
WP_R_04	40x80 Static Wall Pressure Tap Lower Half of Tunnel	PSF	
WP_T_04	40x80 Static Wall Pressure Tap Lower Half of Tunnel	PSF	
WP_V_04	40x80 Static Wall Pressure Tap Lower Half of Tunnel	PSF	
WP_X_04	40x80 Static Wall Pressure Tap Lower Half of Tunnel	PSF	
WP_A_09	40x80 Static Wall Pressure Tap Lower Half of Tunnel	PSF	
WP_D_09	40x80 Static Wall Pressure Tap Lower Half of Tunnel	PSF	
WP_E_09	40x80 Static Wall Pressure Tap Lower Half of Tunnel	PSF	
WP_F_09	40x80 Static Wall Pressure Tap Lower Half of Tunnel	PSF	

WP_G_09	40x80 Static Wall Pressure Tap Lower Half of Tunnel	PSF	
WP_H_09	40x80 Static Wall Pressure Tap Lower Half of Tunnel	PSF	
WP_J_09	40x80 Static Wall Pressure Tap Lower Half of Tunnel	PSF	
WP_K_09	40x80 Static Wall Pressure Tap Lower Half of Tunnel	PSF	
WP_L_09	40x80 Static Wall Pressure Tap Lower Half of Tunnel	PSF	
WP_M_09	40x80 Static Wall Pressure Tap Lower Half of Tunnel	PSF	
WP_N_09	40x80 Static Wall Pressure Tap Lower Half of Tunnel	PSF	
WP_P_09	40x80 Static Wall Pressure Tap Lower Half of Tunnel	PSF	
WP_R_09	40x80 Static Wall Pressure Tap Lower Half of Tunnel	PSF	
WP_T_09	40x80 Static Wall Pressure Tap Lower Half of Tunnel	PSF	
WP_V_09	40x80 Static Wall Pressure Tap Lower Half of Tunnel	PSF	
WP_X_09	40x80 Static Wall Pressure Tap Lower Half of Tunnel	PSF	
WP_A_12	40x80 Static Wall Pressure Tap Lower Half of Tunnel	PSF	
WP_D_12	40x80 Static Wall Pressure Tap Lower Half of Tunnel	PSF	
WP_E_12	40x80 Static Wall Pressure Tap Lower Half of Tunnel	PSF	
WP_F_12	40x80 Static Wall Pressure Tap Lower Half of Tunnel	PSF	
WP_G_12	40x80 Static Wall Pressure Tap Lower Half of Tunnel	PSF	
WP_H_12	40x80 Static Wall Pressure Tap Lower Half of Tunnel	PSF	
WP_J_12	40x80 Static Wall Pressure Tap Lower Half of Tunnel	PSF	
WP_K_12	40x80 Static Wall Pressure Tap Lower Half of Tunnel	PSF	
WP_L_12	40x80 Static Wall Pressure Tap Lower Half of Tunnel	PSF	
WP_N_12	40x80 Static Wall Pressure Tap Lower Half of Tunnel	PSF	
WP_P_12	40x80 Static Wall Pressure Tap Lower Half of Tunnel	PSF	
WP_R_12	40x80 Static Wall Pressure Tap Lower Half of Tunnel	PSF	
WP_T_12	40x80 Static Wall Pressure Tap Lower Half of Tunnel	PSF	
WP_V_12	40x80 Static Wall Pressure Tap Lower Half of Tunnel	PSF	
WP_X_12	40x80 Static Wall Pressure Tap Lower Half of Tunnel	PSF	
WP_A_15	40x80 Static Wall Pressure Tap Lower Half of Tunnel	PSF	
WP_C_15	40x80 Static Wall Pressure Tap Lower Half of Tunnel	PSF	
WP_D_15	40x80 Static Wall Pressure Tap Lower Half of Tunnel	PSF	
WP_E_15	40x80 Static Wall Pressure Tap Lower Half of Tunnel	PSF	
WP_F_15	40x80 Static Wall Pressure Tap Lower Half of Tunnel	PSF	
WP_G_15	40x80 Static Wall Pressure Tap Lower Half of Tunnel	PSF	
WP_H_14	40x80 Static Wall Pressure Tap Lower Half of Tunnel	PSF	
WP_J_15	40x80 Static Wall Pressure Tap Lower Half of Tunnel	PSF	
WP_K_15	40x80 Static Wall Pressure Tap Lower Half of Tunnel	PSF	
WP_L_15	40x80 Static Wall Pressure Tap Lower Half of Tunnel	PSF	
WP_N_15	40x80 Static Wall Pressure Tap Lower Half of Tunnel	PSF	
WP_P_15	40x80 Static Wall Pressure Tap Lower Half of Tunnel	PSF	
WP_R_15	40x80 Static Wall Pressure Tap Lower Half of Tunnel	PSF	
WP_T_15	40x80 Static Wall Pressure Tap Lower Half of Tunnel	PSF	
WP_V_15	40x80 Static Wall Pressure Tap Lower Half of Tunnel	PSF	
WP_X_15	40x80 Static Wall Pressure Tap Lower Half of Tunnel	PSF	
WP_A_18	40x80 Static Wall Pressure Tap Lower Half of Tunnel	PSF	
WP_C_18	40x80 Static Wall Pressure Tap Lower Half of Tunnel	PSF	
WP_D_18	40x80 Static Wall Pressure Tap Lower Half of Tunnel	PSF	
WP_E_18	40x80 Static Wall Pressure Tap Lower Half of Tunnel	PSF	
WP_F_18	40x80 Static Wall Pressure Tap Lower Half of Tunnel	PSF	
WP_G_18	40x80 Static Wall Pressure Tap Lower Half of Tunnel	PSF	
WP_H_18	40x80 Static Wall Pressure Tap Lower Half of Tunnel	PSF	
WP_J_18	40x80 Static Wall Pressure Tap Lower Half of Tunnel	PSF	

WP_K_18	40x80 Static Wall Pressure Tap Lower Half of Tunnel	PSF	
WP_L_18	40x80 Static Wall Pressure Tap Lower Half of Tunnel	PSF	
WP_M_18	40x80 Static Wall Pressure Tap Lower Half of Tunnel	PSF	
WP_N_18	40x80 Static Wall Pressure Tap Lower Half of Tunnel	PSF	
WP_P_18	40x80 Static Wall Pressure Tap Lower Half of Tunnel	PSF	
WP_R_18	40x80 Static Wall Pressure Tap Lower Half of Tunnel	PSF	
WP_T_18	40x80 Static Wall Pressure Tap Lower Half of Tunnel	PSF	
WP_V_18	40x80 Static Wall Pressure Tap Lower Half of Tunnel	PSF	
WP_X_18	40x80 Static Wall Pressure Tap Lower Half of Tunnel	PSF	
WP_C_23	40x80 Static Wall Pressure Tap Lower Half of Tunnel	PSF	
WP_D_23	40x80 Static Wall Pressure Tap Lower Half of Tunnel	PSF	
WP_F_23	40x80 Static Wall Pressure Tap Lower Half of Tunnel	PSF	
WP_G_23	40x80 Static Wall Pressure Tap Lower Half of Tunnel	PSF	
WP_H_23	40x80 Static Wall Pressure Tap Lower Half of Tunnel	PSF	
WP_J_23	40x80 Static Wall Pressure Tap Lower Half of Tunnel	PSF	
WP_K_23	40x80 Static Wall Pressure Tap Lower Half of Tunnel	PSF	
WP_L_23	40x80 Static Wall Pressure Tap Lower Half of Tunnel	PSF	
WP_M_23	40x80 Static Wall Pressure Tap Lower Half of Tunnel	PSF	
WP_N_23	40x80 Static Wall Pressure Tap Lower Half of Tunnel	PSF	
WP_P_23	40x80 Static Wall Pressure Tap Lower Half of Tunnel	PSF	
WP_R_23	40x80 Static Wall Pressure Tap Lower Half of Tunnel	PSF	
WP_T_23	40x80 Static Wall Pressure Tap Lower Half of Tunnel	PSF	
WP_V_23	40x80 Static Wall Pressure Tap Lower Half of Tunnel	PSF	
WP_X_23	40x80 Static Wall Pressure Tap Lower Half of Tunnel	PSF	
WP_A_25	40x80 Static Wall Pressure Tap Lower Half of Tunnel	PSF	
WP_C_30	40x80 Static Wall Pressure Tap Upper Half of Tunnel	PSF	
WP_D_30	40x80 Static Wall Pressure Tap Upper Half of Tunnel	PSF	
WP_E_30	40x80 Static Wall Pressure Tap Upper Half of Tunnel	PSF	
WP_F_30	40x80 Static Wall Pressure Tap Upper Half of Tunnel	PSF	
WP_G_30	40x80 Static Wall Pressure Tap Upper Half of Tunnel	PSF	
WP_H_30	40x80 Static Wall Pressure Tap Upper Half of Tunnel	PSF	
WP_J_30	40x80 Static Wall Pressure Tap Upper Half of Tunnel	PSF	
WP_K_30	40x80 Static Wall Pressure Tap Upper Half of Tunnel	PSF	
WP_L_30	40x80 Static Wall Pressure Tap Upper Half of Tunnel	PSF	
WP_M_30	40x80 Static Wall Pressure Tap Upper Half of Tunnel	PSF	
WP_N_30	40x80 Static Wall Pressure Tap Upper Half of Tunnel	PSF	
WP_P_30	40x80 Static Wall Pressure Tap Upper Half of Tunnel	PSF	
WP_S_30	40x80 Static Wall Pressure Tap Upper Half of Tunnel	PSF	
WP_V_30	40x80 Static Wall Pressure Tap Upper Half of Tunnel	PSF	
WP_X_30	40x80 Static Wall Pressure Tap Upper Half of Tunnel	PSF	
WP_A_31	40x80 Static Wall Pressure Tap Upper Half of Tunnel	PSF	
WP_A_35	40x80 Static Wall Pressure Tap Upper Half of Tunnel	PSF	
WP_C_35	40x80 Static Wall Pressure Tap Upper Half of Tunnel	PSF	
WP_D_35	40x80 Static Wall Pressure Tap Upper Half of Tunnel	PSF	
WP_E_35	40x80 Static Wall Pressure Tap Upper Half of Tunnel	PSF	
WP_G_35	40x80 Static Wall Pressure Tap Upper Half of Tunnel	PSF	
WP_H_35	40x80 Static Wall Pressure Tap Upper Half of Tunnel	PSF	
WP_J_35	40x80 Static Wall Pressure Tap Upper Half of Tunnel	PSF	
WP_K_35	40x80 Static Wall Pressure Tap Upper Half of Tunnel	PSF	
WP_L_35	40x80 Static Wall Pressure Tap Upper Half of Tunnel	PSF	

WP_M_35	40x80 Static Wall Pressure Tap Upper Half of Tunnel	PSF	
WP_N_35	40x80 Static Wall Pressure Tap Upper Half of Tunnel	PSF	
WP_P_35	40x80 Static Wall Pressure Tap Upper Half of Tunnel	PSF	
WP_R_35	40x80 Static Wall Pressure Tap Upper Half of Tunnel	PSF	
WP_S_35	40x80 Static Wall Pressure Tap Upper Half of Tunnel	PSF	
WP_V_35	40x80 Static Wall Pressure Tap Upper Half of Tunnel	PSF	
WP_X_35	40x80 Static Wall Pressure Tap Upper Half of Tunnel	PSF	
WP_A_38	40x80 Static Wall Pressure Tap Upper Half of Tunnel	PSF	
WP_C_38	40x80 Static Wall Pressure Tap Upper Half of Tunnel	PSF	
WP_D_38	40x80 Static Wall Pressure Tap Upper Half of Tunnel	PSF	
WP_E_38	40x80 Static Wall Pressure Tap Upper Half of Tunnel	PSF	
WP_F_38	40x80 Static Wall Pressure Tap Upper Half of Tunnel	PSF	
WP_G_38	40x80 Static Wall Pressure Tap Upper Half of Tunnel	PSF	
WP_H_38	40x80 Static Wall Pressure Tap Upper Half of Tunnel	PSF	
WP_J_38	40x80 Static Wall Pressure Tap Upper Half of Tunnel	PSF	
WP_K_38	40x80 Static Wall Pressure Tap Upper Half of Tunnel	PSF	
WP_L_38	40x80 Static Wall Pressure Tap Upper Half of Tunnel	PSF	
WP_M_38	40x80 Static Wall Pressure Tap Upper Half of Tunnel	PSF	
WP_N_38	40x80 Static Wall Pressure Tap Upper Half of Tunnel	PSF	
WP_P_38	40x80 Static Wall Pressure Tap Upper Half of Tunnel	PSF	
WP_R_38	40x80 Static Wall Pressure Tap Upper Half of Tunnel	PSF	
WP_S_38	40x80 Static Wall Pressure Tap Upper Half of Tunnel	PSF	
WP_V_38	40x80 Static Wall Pressure Tap Upper Half of Tunnel	PSF	
WP_X_38	40x80 Static Wall Pressure Tap Upper Half of Tunnel	PSF	
WP_A_41	40x80 Static Wall Pressure Tap Upper Half of Tunnel	PSF	
WP_C_41	40x80 Static Wall Pressure Tap Upper Half of Tunnel	PSF	
WP_D_41	40x80 Static Wall Pressure Tap Upper Half of Tunnel	PSF	
WP_E_41	40x80 Static Wall Pressure Tap Upper Half of Tunnel	PSF	
WP_F_41	40x80 Static Wall Pressure Tap Upper Half of Tunnel	PSF	
WP_G_41	40x80 Static Wall Pressure Tap Upper Half of Tunnel	PSF	
WP_H_41	40x80 Static Wall Pressure Tap Upper Half of Tunnel	PSF	
WP_J_41	40x80 Static Wall Pressure Tap Upper Half of Tunnel	PSF	
WP_K_41	40x80 Static Wall Pressure Tap Upper Half of Tunnel	PSF	
WP_L_41	40x80 Static Wall Pressure Tap Upper Half of Tunnel	PSF	
WP_M_41	40x80 Static Wall Pressure Tap Upper Half of Tunnel	PSF	
WP_N_41	40x80 Static Wall Pressure Tap Upper Half of Tunnel	PSF	
WP_P_41	40x80 Static Wall Pressure Tap Upper Half of Tunnel	PSF	
WP_R_41	40x80 Static Wall Pressure Tap Upper Half of Tunnel	PSF	
WP_S_41	40x80 Static Wall Pressure Tap Upper Half of Tunnel	PSF	
WP_V_41	40x80 Static Wall Pressure Tap Upper Half of Tunnel	PSF	
WP_X_41	40x80 Static Wall Pressure Tap Upper Half of Tunnel	PSF	
WP_A_44	40x80 Static Wall Pressure Tap Upper Half of Tunnel	PSF	
WP_C_44	40x80 Static Wall Pressure Tap Upper Half of Tunnel	PSF	
WP_D_44	40x80 Static Wall Pressure Tap Upper Half of Tunnel	PSF	
WP_E_44	40x80 Static Wall Pressure Tap Upper Half of Tunnel	PSF	
WP_G_44	40x80 Static Wall Pressure Tap Upper Half of Tunnel	PSF	
WP_H_44	40x80 Static Wall Pressure Tap Upper Half of Tunnel	PSF	
WP_J_44	40x80 Static Wall Pressure Tap Upper Half of Tunnel	PSF	
WP_K_44	40x80 Static Wall Pressure Tap Upper Half of Tunnel	PSF	
WP_L_44	40x80 Static Wall Pressure Tap Upper Half of Tunnel	PSF	
WP_M_44	40x80 Static Wall Pressure Tap Upper Half of Tunnel	PSF	

WP_N_44	40x80 Static Wall Pressure Tap Upper Half of Tunnel	PSF	
WP_P_44	40x80 Static Wall Pressure Tap Upper Half of Tunnel	PSF	
WP_S_44	40x80 Static Wall Pressure Tap Upper Half of Tunnel	PSF	
WP_V_44	40x80 Static Wall Pressure Tap Upper Half of Tunnel	PSF	
WP_X_44	40x80 Static Wall Pressure Tap Upper Half of Tunnel	PSF	
WP_A_48	40x80 Static Wall Pressure Tap Upper Half of Tunnel	PSF	
WP_C_49	40x80 Static Wall Pressure Tap Upper Half of Tunnel	PSF	
WP_E_49	40x80 Static Wall Pressure Tap Upper Half of Tunnel	PSF	
WP_F_49	40x80 Static Wall Pressure Tap Upper Half of Tunnel	PSF	
WP_G_49	40x80 Static Wall Pressure Tap Upper Half of Tunnel	PSF	
WP_H_49	40x80 Static Wall Pressure Tap Upper Half of Tunnel	PSF	
WP_J_49	40x80 Static Wall Pressure Tap Upper Half of Tunnel	PSF	
WP_K_49	40x80 Static Wall Pressure Tap Upper Half of Tunnel	PSF	
WP_L_49	40x80 Static Wall Pressure Tap Upper Half of Tunnel	PSF	
WP_M_49	40x80 Static Wall Pressure Tap Upper Half of Tunnel	PSF	
WP_N_49	40x80 Static Wall Pressure Tap Upper Half of Tunnel	PSF	
WP_P_49	40x80 Static Wall Pressure Tap Upper Half of Tunnel	PSF	
WP_S_49	40x80 Static Wall Pressure Tap Upper Half of Tunnel	PSF	
WP_V_49	40x80 Static Wall Pressure Tap Upper Half of Tunnel	PSF	
WP_X_49	40x80 Static Wall Pressure Tap Upper Half of Tunnel	PSF	
N1_V_B1	Raw N1 Bridge zero corrected and rcal-scaled	Volts	
N2_V_B1	Raw N2 Bridge zero corrected and rcal-scaled	Volts	
AX_V_B1	Raw AX Bridge zero corrected and rcal-scaled	Volts	
S1_V_B1	Raw S1 Bridge zero corrected and rcal-scaled	Volts	
S2_V_B1	Raw S2 Bridge zero corrected and rcal-scaled	Volts	
RM_V_B1	Raw RM Bridge zero corrected and rcal-scaled	Volts	
N1_BIAS_V_B1	Bridge voltage converted to equivalent calibration voltage	mV/V	
N2_BIAS_V_B1	Bridge voltage converted to equivalent calibration voltage	mV/V	
AX_BIAS_V_B1	Bridge voltage converted to equivalent calibration voltage	mV/V	
S1_BIAS_V_B1	Bridge voltage converted to equivalent calibration voltage	mV/V	
S2_BIAS_V_B1	Bridge voltage converted to equivalent calibration voltage	mV/V	
RM_BIAS_V_B1	Bridge voltage converted to equivalent calibration voltage	mV/V	
N1_EU_B1	Corrected Gage reading in Engineering Units	LBF	
N2_EU_B1	Corrected Gage reading in Engineering Units	LBF	
AX_EU_B1	Corrected Gage reading in Engineering Units	LBF	
S1_EU_B1	Corrected Gage reading in Engineering Units	LBF	
S2_EU_B1	Corrected Gage reading in Engineering Units	LBF	
RM_EU_B1	Corrected Gage reading in Engineering Units	IN-LBS	
AF_UNC_B1	Converted Gage Readings into Force and Moments	LBF	
SF_UNC_B1	Converted Gage Readings into Force and Moments	LBF	
NF_UNC_B1	Converted Gage Readings into Force and Moments	LBF	
RM_UNC_B1	Converted Gage Readings into Force and Moments	IN-LBS	
PM_UNC_B1	Converted Gage Readings into Force and Moments	IN-LBS	
YM_UNC_B1	Converted Gage Readings into Force and Moments	IN-LBS	
AF_BAL_B1	Force and Moments Corrected for Weight Tares	LBF	

SF_BAL_B1	Force and Moments Corrected for Weight Tares	LBF	
NF_BAL_B1	Force and Moments Corrected for Weight Tares	LBF	
RM_BAL_B1	Force and Moments Corrected for Weight Tares	IN-LBS	
PM_BAL_B1	Force and Moments Corrected for Weight Tares	IN-LBS	
YM_BAL_B1	Force and Moments Corrected for Weight Tares	IN-LBS	
AF_BD_B1	Force and Moments in Body Axis	LBF	
SF_BD_B1	Force and Moments in Body Axis	LBF	
NF_BD_B1	Force and Moments in Body Axis	LBF	
RM_BD_B1	Force and Moments in Body Axis	IN-LBS	
PM_BD_B1	Force and Moments in Body Axis	IN-LBS	
YM_BD_B1	Force and Moments in Body Axis	IN-LBS	
CA_BD_B1	Force and Moment Coefficient in Body Axis	nondim	
CY_BD_B1	Force and Moment Coefficient in Body Axis	nondim	
CN_BD_B1	Force and Moment Coefficient in Body Axis	nondim	
CMX_BD_B1	Force and Moment Coefficient in Body Axis	nondim	
CMY_BD_B1	Force and Moment Coefficient in Body Axis	nondim	
CMZ_BD_B1	Force and Moment Coefficient in Body Axis	nondim	
DRAG_ST_B1	Force and Moments in Stability Axis	LBF	
SIDE_ST_B1	Force and Moments in Stability Axis	LBF	
LIFT_ST_B1	Force and Moments in Stability Axis	LBF	
ROLL_ST_B1	Force and Moments in Stability Axis	IN-LBS	
PITCH_ST_B1	Force and Moments in Stability Axis	IN-LBS	
YAW_ST_B1	Force and Moments in Stability Axis	IN-LBS	
CD_ST_B1	Force and Moment Coefficient in Stability Axis	nondim	
CY_ST_B1	Force and Moment Coefficient in Stability Axis	nondim	
CL_ST_B1	Force and Moment Coefficient in Stability Axis	nondim	
CMX_ST_B1	Force and Moment Coefficient in Stability Axis	nondim	
CMY_ST_B1	Force and Moment Coefficient in Stability Axis	nondim	
CMZ_ST_B1	Force and Moment Coefficient in Stability Axis	nondim	
DRAG_W_B1	Force and Moments in Wind Axis	LBF	
SIDE_W_B1	Force and Moments in Wind Axis	LBF	
LIFT_W_B1	Force and Moments in Wind Axis	LBF	
ROLL_W_B1	Force and Moments in Wind Axis	IN-LBS	
PITCH_W_B1	Force and Moments in Wind Axis	IN-LBS	
YAW_W_B1	Force and Moments in Wind Axis	IN-LBS	
CD_W_B1	Force and Moment Coefficient in Wind Axis	nondim	
CY_W_B1	Force and Moment Coefficient in Wind Axis	nondim	
CL_W_B1	Force and Moment Coefficient in Wind Axis	nondim	
CMX_W_B1	Force and Moment Coefficient in Wind Axis	nondim	
CMY_W_B1	Force and Moment Coefficient in Wind Axis	nondim	
CMY_W_B1	Force and Moment Coefficient in Wind Axis	nondim	
DRAG_WE_B1	Force and Moments in Wind Axis Corrected for Wall Effect	LBF	
SIDE_WE_B1	Force and Moments in Wind Axis Corrected for Wall Effect	LBF	
LIFT_WE_B1	Force and Moments in Wind Axis Corrected for Wall Effect	LBF	
ROLL_WE_B1	Force and Moments in Wind Axis Corrected for Wall Effect	IN-LBS	
PITCH_WE_B1	Force and Moments in Wind Axis Corrected for Wall Effect	IN-LBS	
YAW_WE_B1	Force and Moments in Wind Axis Corrected for Wall Effect	IN-LBS	

CD_WE_B1	Force and Moment Coefficient in Wind Axis Corrected for Wall Effect	nondim	
CY_WE_B1	Force and Moment Coefficient in Wind Axis Corrected for Wall Effect	nondim	
CL_WE_B1	Force and Moment Coefficient in Wind Axis Corrected for Wall Effect	nondim	
CMX_WE_B1	Force and Moment Coefficient in Wind Axis Corrected for Wall Effect	nondim	
CMY_WE_B1	Force and Moment Coefficient in Wind Axis Corrected for Wall Effect	nondim	
CMZ_WE_B1	Force and Moment Coefficient in Wind Axis Corrected for Wall Effect	nondim	
DP_001	Dynamic Model Pressures (Kulites)		
DP_002	Dynamic Model Pressures (Kulites)		**NR**
DP_003	Dynamic Model Pressures (Kulites)		
DP_004	Dynamic Model Pressures (Kulites)		**NR**
DP_005	Dynamic Model Pressures (Kulites)		
DP_006	Dynamic Model Pressures (Kulites)		**NR**
DP_007	Dynamic Model Pressures (Kulites)		
DP_008	Dynamic Model Pressures (Kulites)		
MIC_001	Microphone Measurement (raw voltage only)	Volts	
MIC_002	Microphone Measurement (raw voltage only)	Volts	
MIC_003	Microphone Measurement (raw voltage only)	Volts	
MIC_004	Microphone Measurement (raw voltage only)	Volts	
MIC_005	Microphone Measurement (raw voltage only)	Volts	
MIC_006	Microphone Measurement (raw voltage only)	Volts	
MIC_007	Microphone Measurement (raw voltage only)	Volts	
MIC_008	Microphone Measurement (raw voltage only)	Volts	
MIC_009	Microphone Measurement (raw voltage only)	Volts	
MIC_010	Microphone Measurement (raw voltage only)	Volts	
MIC_011	Microphone Measurement (raw voltage only)	Volts	
MIC_101	Microphone Measurement 48 element array (raw voltage only)	Volts	
MIC_102	Microphone Measurement 48 element array (raw voltage only)	Volts	
MIC_103	Microphone Measurement 48 element array (raw voltage only)	Volts	
MIC_104	Microphone Measurement 48 element array (raw voltage only)	Volts	
MIC_105	Microphone Measurement 48 element array (raw voltage only)	Volts	
MIC_106	Microphone Measurement 48 element array (raw voltage only)	Volts	
MIC_107	Microphone Measurement 48 element array (raw voltage only)	Volts	
MIC_108	Microphone Measurement 48 element array (raw voltage only)	Volts	
MIC_109	Microphone Measurement 48 element array (raw voltage only)	Volts	
MIC_110	Microphone Measurement 48 element array (raw voltage	Volts	

	only)		
MIC_111	Microphone Measurement 48 element array (raw voltage only)	Volts	
MIC_112	Microphone Measurement 48 element array (raw voltage only)	Volts	
MIC_113	Microphone Measurement 48 element array (raw voltage only)	Volts	
MIC_114	Microphone Measurement 48 element array (raw voltage only)	Volts	
MIC_115	Microphone Measurement 48 element array (raw voltage only)	Volts	
MIC_116	Microphone Measurement 48 element array (raw voltage only)	Volts	
MIC_117	Microphone Measurement 48 element array (raw voltage only)	Volts	
MIC_118	Microphone Measurement 48 element array (raw voltage only)	Volts	
MIC_119	Microphone Measurement 48 element array (raw voltage only)	Volts	
MIC_120	Microphone Measurement 48 element array (raw voltage only)	Volts	
MIC_121	Microphone Measurement 48 element array (raw voltage only)	Volts	
MIC_122	Microphone Measurement 48 element array (raw voltage only)	Volts	
MIC_123	Microphone Measurement 48 element array (raw voltage only)	Volts	
MIC_124	Microphone Measurement 48 element array (raw voltage only)	Volts	
MIC_125	Microphone Measurement 48 element array (raw voltage only)	Volts	
MIC_126	Microphone Measurement 48 element array (raw voltage only)	Volts	
MIC_127	Microphone Measurement 48 element array (raw voltage only)	Volts	
MIC_128	Microphone Measurement 48 element array (raw voltage only)	Volts	
MIC_129	Microphone Measurement 48 element array (raw voltage only)	Volts	
MIC_130	Microphone Measurement 48 element array (raw voltage only)	Volts	
MIC_131	Microphone Measurement 48 element array (raw voltage only)	Volts	
MIC_132	Microphone Measurement 48 element array (raw voltage only)	Volts	
MIC_133	Microphone Measurement 48 element array (raw voltage only)	Volts	
MIC_134	Microphone Measurement 48 element array (raw voltage only)	Volts	
MIC_135	Microphone Measurement 48 element array (raw voltage only)	Volts	
MIC_136	Microphone Measurement 48 element array (raw voltage only)	Volts	
MIC_137	Microphone Measurement 48 element array (raw voltage only)	Volts	
MIC_138	Microphone Measurement 48 element array (raw voltage only)	Volts	
MIC_139	Microphone Measurement 48 element array (raw voltage only)	Volts	
MIC_140	Microphone Measurement 48 element array (raw voltage	Volts	

	only)		
MIC_141	Microphone Measurement 48 element array (raw voltage only)	Volts	
MIC_142	Microphone Measurement 48 element array (raw voltage only)	Volts	
MIC_143	Microphone Measurement 48 element array (raw voltage only)	Volts	
MIC_144	Microphone Measurement 48 element array (raw voltage only)	Volts	
MIC_145	Microphone Measurement 48 element array (raw voltage only)	Volts	
MIC_146	Microphone Measurement 48 element array (raw voltage only)	Volts	
MIC_147	Microphone Measurement 48 element array (raw voltage only)	Volts	
MIC_148	Microphone Measurement 48 element array (raw voltage only)	Volts	
TPS_RPM_L1	LH TPS RPM 1	volts (0-10 out)	
TPS_RPM_L2	LH TPS RPM 2	volts (0-10 out)	
TPS_RPM_R1	RH TPS RPM 1	volts (0-10 out)	
TPS_RPM_R2	RH TPS RPM 2	volts (0-10 out)	
TPS_ACCL_L1	LH TPS accelerometer 1	voltage	
TPS_ACCL_L2	LH TPS accelerometer 2	voltage	
TPS_ACCL_R1	RH TPS accelerometer 1	voltage	
TPS_ACCL_R2	RH TPS accelerometer 2	voltage	
INCL_1	Inclinometer 1	voltage	
INCL_2	Inclinometer 2		
TPS_OIL_ON	TPS Oiler On Indication		
LTPSFB_1	Left TPS Forward Bearing 1	milivolts	
LTPSFB_2	Left TPS Forward Bearing 2	milivolts	
LTPSMB_1	Left TPS Mid Bearing 1	milivolts	
LTPSAB_1	Left TPS Aft Bearing 1	milivolts	
LTPSAB_2	Left TPS Aft Bearing 2	milivolts	
RTPSFB_1	Right TPS Forward Bearing 1	milivolts	
RTPSFB_2	Right TPS Forward Bearing 2	milivolts	
RTPSMB_1	Right TPS Mid Bearing 1	milivolts	
RTPSAB_1	Right TPS Aft Bearing 1	milivolts	
RTPSAB_2	Right TPS Aft Bearing 2	milivolts	
		volts (0-5 out)	
Bal_P1	Balance Pressure 1	volts (0-5 out)	
Bal_P2	Balance Pressure 2	volts (0-5 out)	
Bal_P3	Balance Pressure 3	volts (0-5 out)	
Bal_P4	Balance Pressure 4	volts (0-5 out)	
Bal_P5	Balance Pressure 5	volts (0-5 out)	
Bal_P6	Balance Pressure 6	volts (0-5 out)	

OPU_P1	Oriface Plate upstream pressure 1	volts	
OPU_P2	Orifice Plate upstream pressure 2	volts	
OPD_P1	Oriface Plate upstream pressure 1	volts	
OPD_P2	Orifice Plate downstream pressure 2	volts	
LLPDPP_1	Left Low Presure Distribution Plenum pressure	volts	
RLPDPP_1	Right Low Presure Distribution Plenum pressure	volts	
LPP_1	Left Pylon upstream pressure	volts	
RPP_1	Right Pylon upstream pressure	volts	

Table A7. 2. Tunnel Instrumentation

Module #1		**Module range: 15 PSID**		
Port Number	Model Orifice	Description	Tubing labeled as:	a = good, NA = not accessible, NR = no response
1	SP1_1	BL_118 leading edge	SP1_1	A
2	SP1_2	BL_118 leading edge	SP1_2	A
3	SP1_3	BL_118 leading edge	SP1_3	A
4	SP1_4	BL_118 leading edge	SP1_4	A
5	SP1_5	BL_118 leading edge	SP1_5	A
6	NSPL_1	BL_118 leading edge	NSPL_1	A--Reassigned(1/5/2012)
7	SP1_7	BL_118 leading edge	SP1_7	A
8	NSPL_2	BL_118 leading edge	NSPL_2	A--Reassigned(1/5/2012)
9	NSPL_3	BL_118 leading edge	NSPL_3	A--Reassigned(1/5/2012)
10	SP1_10	BL_118 leading edge	SP1_10	A
11	SP1_11	BL_118 leading edge	SP1_11	A
12	NSPL_4	BL_240 Wing Upper Surface at slot	NSPL_4	A--Reassigned(1/5/2012)
13	SP2_13	BL_240 Wing Upper Surface at slot	SP2_13	A
14	SP2_14	BL_240 Wing Upper Surface at slot	SP2_14	A
15	NSPL_5	BL_240 Wing Upper Surface at slot	NSPL_5	A--Reassigned(1/5/2012)
16	PMON1_16m	PSI module monitoring pressure, module 1, port 16		
17	SP2_F1	BL_240 Flap	SP2_F1	A
18	SP2_F2	BL_240 Flap	SP2_F2	A
19	SP2_F3	BL_240 Flap	SP2_F3	A
20	SP2_F4	BL_240 Flap	SP2_F4	A
21	SP2_F5	BL_240 Flap	SP2_F5	A
22	SP2_F6	BL_240 Flap	SP2_F6	A
23	SP2_F7	BL_240 Flap	SP2_F7	A
24	SP2_F8	BL_240 Flap	SP2_F8	A
25	SP2_F9	BL_240 Flap	SP2_F9	A
26	SP2_F10	BL_240 Flap	SP2_F10	A
27	SP3_1	BL_500 Leading Edge	SP3_1	A
28	SP3_2	BL_500 Leading Edge	SP3_2	A
29	SP3_3	BL_500 Leading Edge	SP3_3	A
30	SP3_4	BL_500 Leading Edge	SP3_4	A
31	SP3_5	BL_500 Leading Edge	SP3_5	A
32	PMON1_32m	PSI module monitoring pressure, module		

		1, port 32		
33	SP3_6	BL_500 Leading Edge	SP3_6	A
34	SP3_7	BL_500 Leading Edge	SP3_7	A
35	SP3_8	BL_500 Leading Edge	SP3_8	A
36	SP3_9	BL_500 Leading Edge	SP3_9	A
37	SP3_10	BL_500 Leading Edge	SP3_10	A
38	SP3_25	BL_500 Upper Surface at slot	SP3_25	A
39	SP3_26	BL_500 Upper Surface at slot	SP3_26	A
40	SP3_27	BL_500 Upper Surface at slot	SP3_27	A
41	SP3_28	BL_500 Upper Surface at slot	SP3_28	A
42	NSPL_6	BL_500 Upper Surface at slot	NSPL_6	A--Reassigned(1/5/2012)
43	SP3_30	BL_500 Upper Surface at slot	SP3_30	A
44	SP3_31	BL_500 Upper Surface at slot	SP3_31	A
45	NSPL_7	BL_500 Upper Surface at slot	NSPL_7	A--Reassigned(1/5/2012)
46	SP3_33	BL_500 Upper Surface at slot	SP3_33	A
47	SP3_34	BL_500 Upper Surface at slot	SP3_34	A
48	PMON1_48m	PSI module monitoring pressure, module 1, port 48		
49	SP3_35	BL_500 Upper Surface at slot	SP3_35	A
50	SP3_F1	BL_500 Flap	SP3_F1	A
51	SP3_F2	BL_500 Flap	SP3_F2	A
52	SP3_F3	BL_500 Flap	SP3_F3	A
53	SP3_F4	BL_500 Flap	SP3_F4	A
54	SP3_F5	BL_500 Flap	SP3_F5	A
55	SP3_F6	BL_500 Flap	SP3_F6	A
56	SP3_F7	BL_500 Flap	SP3_F7	A
57	SP3_F8	BL_500 Flap	SP3_F8	A
58	SP3_F9	BL_500 Flap	SP3_F9	A
59	SP3_F10	BL_500 Flap	SP3_F10	A
60	SP4_1	BL_638 Leading Edge	SP4_1	A
61	SP4_2	BL_638 Leading Edge	SP4_2	A
62	SP4_3	BL_638 Leading Edge	SP4_3	A
63	SP4_4	BL_638 Leading Edge	SP4_4	A
64	PMON1_64m	PSI module monitoring pressure, module 1, port 64		
Module #2		**Module range: 15 PSID**		
Port Number	Model Orifice	Description	Tubing labeled as:	a = good, NA = not accessible, NR = no response
1	SP4_5	BL_638 Leading Edge	SP4_5	A

2	SP4_6	BL_638 Leading Edge	SP4_6	A
3	SP4_21	BL_638 Upper Surface at Slot	SP4_21	A
4	SP4_22	BL_638 Upper Surface at Slot	SP4_22	A
5	SP4_23	BL_638 Upper Surface at Slot	SP4_23	A
6	SP4_24	BL_638 Upper Surface at Slot	SP4_24	A
7	SP4_25	BL_638 Upper Surface at Slot	SP4_25	A
8	NSPR_1	BL_638 Flap	NSPR-1	A--Reassigned(1/5/2012)
9	NSPR_2	BL_638 Flap	NSPR_2	A--Reassigned(1/5/2012)
10	SP4_F3	BL_638 Flap	SP4_F3	A
11	SP4_F4	BL_638 Flap	SP4_F4	A
12	NSPR_3	BL_638 Flap	NSPR_3	A--Reassigned(1/5/2012)
13	SP4_F6	BL_638 Flap	SP4_F6	A
14	SP4_F7	BL_638 Flap	SP4_F7	A
15	NSPR_4	BL_638 Flap	NSPR_4	A--Reassigned(1/5/2012)
16	PMON2_16m	PSI module monitoring pressure, module 2, port 16		
17	SP4_F9	BL_638 Flap	SP4_F9	A
18	SP4_F10	BL_638 Flap	SP4_F10	A
19	NSPR_5	BL_642 Leading Edge	NSPR_5	A--Reassigned(1/5/2012)
20	SP5_2	BL_642 Leading Edge	SP5_2	A
21	SP5_3	BL_642 Leading Edge	SP5_3	A
22	SP5_4	BL_642 Leading Edge	SP5_4	A
23	NSPR_6	BL_642 Trailing Edge	NSPR_6	A--Reassigned(1/5/2012)
24	SP5_12	BL_642 Trailing Edge	SP5_12	A
25	SP5_13	BL_642 Trailing Edge	SP5_13	A
26	NSPR_7	BL_642 Trailing Edge	NSPR_7	A--Reassigned(1/5/2012)
27	SP5_15	BL_642 Trailing Edge	SP5_15	A
28	SP2_7R	Right Wing Port Mirroring 2_7	SP2_7R	A
29	SP2_15R	Right Wing Port Mirroring 2_15	SP2_15R	A
30	SP4_10R	Right Wing Port Mirroring 4_10	SP4_10R	A
31	SP4_22R	Right Wing Port Mirroring 4_22	SP4_22R	A
32	PMON2_32m	PSI module monitoring pressure, module 2, port 32		
33	PTP_1L_1	Plenum Total Pressure	PTP_1L_1	NA
34	PTP_1L_2	Plenum Total Pressure	PTP_1L_2	NA
35	PTP_1L_3	Plenum Total Pressure	PTP_1L_3	NA
36	PTP_2L_1	Plenum Total Pressure	PTP_2L_1	NA
37	PTP_2L_2	Plenum Total Pressure	PTP_2L_2	NA

38	PTP_2L_3	Plenum Total Pressure	PTP_2L_3	NA
39	PTP_3L_1	Plenum Total Pressure	PTP_3L_1	NA
40	PTP_3L_2	Plenum Total Pressure	PTP_3L_2	NA
41	PTP_3L_3	Plenum Total Pressure	PTP_3L_3	NA
42	PTP_4L_1	Plenum Total Pressure	PTP_4L_1	NA
43	PTP_4L_2	Plenum Total Pressure	PTP_4L_2	NA
44	PTP_4L_3	Plenum Total Pressure	PTP_4L_3	NA
45	PTP_1R_1	Plenum Total Pressure	PTP_1R_1	NA
46	PTP_1R_2	Plenum Total Pressure	PTP_1R_2	NA
47	PTP_1R_3	Plenum Total Pressure	PTP_1R_3	NA
48	PMON2_48m	PSI module monitoring pressure, module 2, port 48		
49	PTP_2R_1	Plenum Total Pressure	PTP_2R_1	NA
50	PTP_2R_2	Plenum Total Pressure	PTP_2R_2	NA
51	PTP_2R_3	Plenum Total Pressure	PTP_2R_3	NA
52	PTP_3R_1	Plenum Total Pressure	PTP_3R_1	NA
53	PTP_3R_2	Plenum Total Pressure	PTP_3R_2	NA
54	PTP_3R_3	Plenum Total Pressure	PTP_3R_3	NA
55	PTP_4R_1	Plenum Total Pressure	PTP_4R_1	NA
56	PTP_4R_2	Plenum Total Pressure	PTP_4R_2	NA
57	PTP_4R_3	Plenum Total Pressure	PTP_4R_3	NA
58	NTPL_1_1	Left TPS Nacelle Total Pressure Rake 1	1_1: NTPL_1_1	NA
59	NTPL_1_2	Left TPS Nacelle Total Pressure Rake 1	1_2: NTPL_1_2	NA
60	NTPL_1_3	Left TPS Nacelle Total Pressure Rake 1	1_3: NTPL_1_3	NA
61	NTPL_1_4	Left TPS Nacelle Total Pressure Rake 1	1_4: NTPL_1_4	NA
62	NTPL_2_1	Left TPS Nacelle Total Pressure Rake 2	1_5: NTPL_2_1	NA
63	NTPL_2_2	Left TPS Nacelle Total Pressure Rake 2	1_6: NTPL_2_2	NA
64	PMON2_64m	PSI module monitoring pressure, module 2, port 64		
Module #3		**Module range: 15 PSID**		
Port Number	Model Orifice	Description	Tubing labeled as:	a = good, NA = not accessible, NR = no response
1	NTPL_2_3	Left TPS Nacelle Total Pressure Rake 2	1_7: NTPL_2_3	NA
2	NTPL_2_4	Left TPS Nacelle Total Pressure Rake 2	1_8: NTPL_2_4	NA
3	NTPL_3_1	Left TPS Nacelle Total Pressure Rake 3	1_9: NTPL_3_1	NA
4	NTPL_3_2	Left TPS Nacelle Total Pressure Rake 3	1_10: NTPL_3_2	NA
5	NTPL_3_3	Left TPS Nacelle Total Pressure Rake 3	1_11: NTPL_3_3	NA
6	NTPL_3_4	Left TPS Nacelle Total Pressure Rake 3	1_12: NTPL_3_4	NA
7	NTPL_4_1	Left TPS Nacelle Total Pressure Rake 4	1_13: NTPL_4_1	NA
8	NTPL_4_2	Left TPS Nacelle Total Pressure Rake 4	1_14: NTPL_4_2	NA
9	NTPL_4_3	Left TPS Nacelle Total Pressure Rake 4	1_15: NTPL_4_3	NA

10	NTPL_4_4	Left TPS Nacelle Total Pressure Rake 4	1_16: NTPL_4_4	NA
11	NTPL_5_1	Left TPS Nacelle Total Pressure Rake 5	1_17: NTPL_5_1	NA
12	NTPL_5_2	Left TPS Nacelle Total Pressure Rake 5	1_18: NTPL_5_2	NA
13	NTPL_5_3	Left TPS Nacelle Total Pressure Rake 5	1_19: NTPL_5_3	NA
14	NTPL_5_4	Left TPS Nacelle Total Pressure Rake 5	1_20: NTPL_5_4	NA
15	NTPL_6_1	Left TPS Nacelle Total Pressure Rake 6	1_21: NTPL_6_1	NA
16	PMON3_16m	PSI module monitoring pressure, module 3, port 16		
17	NTPL_6_2	Left TPS Nacelle Total Pressure Rake 6	1_22: NTPL_6_2	NA
18	NTPL_6_3	Left TPS Nacelle Total Pressure Rake 6	1_23: NTPL_6_3	NA
19	NTPL_6_4	Left TPS Nacelle Total Pressure Rake 6	1_24: NTPL_6_4	NA
20	NTPL_7_1	Left TPS Nacelle Total Pressure Rake 7	1_25: NTPL_7_1	NA
21	NTPL_7_2	Left TPS Nacelle Total Pressure Rake 7	1_26: NTPL_7_2	NA
22	NTPL_7_3	Left TPS Nacelle Total Pressure Rake 7	1_27: NTPL_7_3	NA
23	NTPL_7_4	Left TPS Nacelle Total Pressure Rake 7	1_28: NTPL_7_4	NA
24	NTPR_1_1	Right TPS Nacelle Total Pressure Rake 1	2_1: NTPR_1_1	NA
25	NTPR_1_2	Right TPS Nacelle Total Pressure Rake 2	2_2 : NTPR_1_2	NA
26	NTPR_1_3	Right TPS Nacelle Total Pressure Rake 3	2_3: NTPR_1_3	NA
27	NTPR_1_4	Right TPS Nacelle Total Pressure Rake 4	2_4: NTPR_1_4	NA
28	NTPR_2_1	Right TPS Nacelle Total Pressure Rake 2	2_5: NTPR_2_1	NA
29	NTPR_2_2	Right TPS Nacelle Total Pressure Rake 3	2_6: NTPR_2_2	NA
30	NTPR_2_3	Right TPS Nacelle Total Pressure Rake 2	2_7: NTPR_2_3	NA
31	NTPR_2_4	Right TPS Nacelle Total Pressure Rake 2	2_8: NTPR_2_4	NA
32	PMON3_32m	PSI module monitoring pressure, module 3, port 32		
33	NTPR_3_1	Right TPS Nacelle Total Pressure Rake 3	2_9: NTPR_3_1	NA
34	NTPR_3_2	Right TPS Nacelle Total Pressure Rake 3	2_10: NTPR_3_2	NA
35	NTPR_3_3	Right TPS Nacelle Total Pressure Rake 3	2_11: NTPR_3_3	NA
36	NTPR_3_4	Right TPS Nacelle Total Pressure Rake 3	2_12: NTPR_3_4	NA
37	NTPR_4_1	Right TPS Nacelle Total Pressure Rake 4	2_13L NTPR_4_1	NA
38	NTPR_4_2	Right TPS Nacelle Total Pressure Rake 4	2_14: NTPR_4_2	NA
39	NTPR_4_3	Right TPS Nacelle Total Pressure Rake 4	2_15: NTPR_4_3	NA
40	NTPR_4_4	Right TPS Nacelle Total Pressure Rake 4	2_16: NTPR_4_4	NA
41	NTPR_5_1	Right TPS Nacelle Total Pressure Rake 5	2_17: NTPR_5_1	NA
42	NTPR_5_2	Right TPS Nacelle Total Pressure Rake 5	2_18: NTPR_5_2	NA
43	NTPR_5_3	Right TPS Nacelle Total Pressure Rake 5	2_19: NTPR_5_3	NA
44	NTPR_5_4	Right TPS Nacelle Total Pressure Rake 5	2_20: NTPR_5_4	NA
45	NTPR_6_1	Right TPS Nacelle Total Pressure Rake 6	2_21: NTPR_6_1	NA
46	NTPR_6_2	Right TPS Nacelle Total Pressure Rake 6	2_22: NTPR_6_2	NA
47	NTPR_6_3	Right TPS Nacelle Total Pressure Rake 6	2_23: NTPR_6_3	NA
48	PMON3_48m	PSI module monitoring pressure, module 3, port 48		
49	NTPR_6_4	Right TPS Nacelle Total Pressure Rake 6	2_24: NTPR_6_4	NA
50	NTPR_7_1	Right TPS Nacelle Total Pressure Rake 7	2_25: NTPR_7_1	NA
51	NTPR_7_2	Right TPS Nacelle Total Pressure Rake 7	2_26: NTPR_7_2	NA

52	NTPR_7_3	Right TPS Nacelle Total Pressure Rake 7	2_27: NTPR_7_3	NA
53	NTPR_7_4	Right TPS Nacelle Total Pressure Rake 7	2_28: NTPR_7_4	NA
54	CTPL_1	Left TPS Core Total Pressure	1_29: CTPL_1	NA
55	CTPL_2	Left TPS Core Total Pressure	1_30: CTPL_2	NA
56	CTPR_1	Right TPS Core Total Pressure	2_29: CTPR_1	NA
57	CTPR_2	Right TPS Core Total Pressure	2_30: CTPR_2	NA
58	SP3_11	BL_500 Leading Edge Upper Surface		NR
59	SP3_12	BL_500 Leading Edge Upper Surface		NR
60				
61				
62				
63				
64	PMON3_64m	PSI module monitoring pressure, module 3, port 64		
Module #4		**Module range: 2.5 PSID**		
Port Number	Model Orifice	Description	Tubing labeled as:	a = good, NA = not accessible, NR = no response
1	SP1_12	BL_118 Upper Surface	SP1_12	A
2	SP1_13	BL_118 Upper Surface	SP1_13	A
3	SP1_14	BL_118 Upper Surface	SP1_14	A
4	SP1_15	BL_118 Upper Surface	SP1_15	A
5	SP1_16	BL_118 Upper Surface	SP1_16	A
6	SP1_17	BL_118 Upper Surface	SP1_17	A
7	SP1_18	BL_118 Upper Surface	SP1_18	A
8	SP1_19	BL_118 Upper Surface	SP1_19	A
9	SP1_20	BL_118 Upper Surface	SP1_20	A
10	SP1_21	BL_118 Upper Surface	SP1_21	A
11	SP1_22	BL_118 Upper Surface	SP1_22	A
12	SP1_23	BL_118 Upper Surface	SP1_23	A
13	SP1_24	BL_118 Upper Surface	SP1_24	A
14	SP1_25	BL_118 Upper Surface	SP1_25	NR
15	SP1_26	BL_118 Upper Surface	SP1_26	A
16	PMON4_16m	PSI module monitoring pressure, module 4, port 16		
17	SP1_27	BL_118 Trailing Edge	SP1_27	A
18	SP1_28	BL_118 Trailing Edge	SP1_28	A
19	SP1_29	BL_118 Trailing Edge	SP1_29	NR
20	SP1_30	BL_118 Trailing Edge	SP1_30	NR
21	SP1_31	BL_118 Lower Surface/Trailing Edge	SP1_31	A
22	SP1_32	BL_118 Lower Surface	SP1_32	A
23	SP1_33	BL_118 Lower Surface	SP1_33	A

24	SP1_34	BL_118 Lower Surface	SP1_34	A
25	SP1_35	BL_118 Lower Surface	SP1_35	A
26	SP1_36	BL_118 Lower Surface	SP1_36	A
27	SP1_37	BL_118 Lower Surface	SP1_37	A
28	SP1_38	BL_118 Lower Surface	SP1_38	A
29	SP1_39	BL_118 Lower Surface	SP1_39	A
30	SP1_40	BL_118 Lower Surface	SP1_40	A
31	SP2_1	BL_240 Upper Surface (Behind TPS)	SP2_1	A
32	PMON4_32m	PSI module monitoring pressure, module 4, port 32		
33	SP2_2	BL_240 Upper Surface	SP2_2	A
34	SP2_3	BL_240 Upper Surface	SP2_3	NR
35	SP2_4	BL_240 Upper Surface	SP2_4	A
36	SP2_5	BL_240 Upper Surface	SP2_5	A
37	SP2_6	BL_240 Upper Surface	SP2_6	A
38	SP2_7	BL_240 Upper Surface	SP2_7	A
39	SP2_8	BL_240 Upper Surface	SP2_8	A
40	SP2_9	BL_240 Upper Surface	SP2_9	A
41	SP2_10	BL_240 Upper Surface	SP2_10	A
42	SP2_11	BL_240 Upper Surface	SP2_11	NR
43	SP2_16	BL_240 Lower Surface	SP2_16	A
44	SP2_17	BL_240 Lower Surface	SP2_17	NR
45	SP2_18	BL_240 Lower Surface	SP2_18	A
46	SP2_19	BL_240 Lower Surface	SP2_19	A
47	SP2_20	BL_240 Lower Surface	SP2_20	A
48	PMON4_48m	PSI module monitoring pressure, module 4, port 48		
49	SP2_21	BL_240 Lower Surface	SP2_21	A
50	SP2_22	BL_240 Lower Surface	SP2_22	A
51	SP2_23	BL_240 Lower Surface	SP2_23	A
52	SP2_24	BL_240 Lower Surface	SP2_24	A
53	SP2_25	BL_240 Lower Surface (Leading Edge at Slot Lip)	SP2_25	A
54	SP3_13	BL_500 Upper Surface	SP3_13	A
55	SP3_14	BL_500 Upper Surface	SP3_14	A
56	SP3_15	BL_500 Upper Surface	SP3_15	NR
57	SP3_16	BL_500 Upper Surface	SP3_16	A
58	SP3_17	BL_500 Upper Surface	SP3_17	A
59	SP3_18	BL_500 Upper Surface	SP3_18	NR
60	SP3_19	BL_500 Upper Surface	SP3_19	A
61	SP3_20	BL_500 Upper Surface	SP3_20	A
62	SP3_21	BL_500 Upper Surface	SP3_21	NR
63	SP3_22	BL_500 Upper Surface	SP3_22	NR
64	PMON4_64m	PSI module monitoring pressure, module 4, port 64		

Module #5		**Module range: 2.5 PSID**		
Port Number	Model Orifice	Description	Tubing labeled as:	a = good, NA = not accessible, NR = no response
1	SP3_23	BL_500 Upper Surface	SP3_23	A
2	SP3_24	BL_500 Upper Surface	SP3_24	A
3	SP3_36	BL_500 Lower Surface	SP3_36	A
4	SP3_37	BL_500 Lower Surface	SP3_37	A
5	SP3_38	BL_500 Lower Surface	SP3_38	A
6	SP3_39	BL_500 Lower Surface	SP3_39	A
7	~~*SP3_40*~~	~~*BL_500 Lower Surface*~~	~~*SP3_40*~~	~~*NR*~~ *NR(1/3/2012)*
8	SP3_41	BL_500 Lower Surface	SP3_41	A
9	SP3_42	BL_500 Lower Surface	SP3_42	A
10	SP3_43	BL_500 Lower Surface	SP3_43	A
11	SP3_44	BL_500 Lower Surface	SP3_44	A
12	SP3_45	BL_500 Lower Surface	SP3_45	A
13	SP3_46	BL_500 Lower Surface	SP3_46	NR
14	SP3_47	BL_500 Lower Surface	SP3_47	A
15	SP3_48	BL_500 Lower Surface	SP3_48	A
16	PMON5_16m	PSI module monitoring pressure, module 5, port 16		
17	SP3_50	BL_500 Upper Surface	SP3_50	A
18	SP4_7	BL_638 Upper Surface	SP4_7	A
19	SP4_8	BL_638 Upper Surface	SP4_8	A
20	SP4_9	BL_638 Upper Surface	SP4_9	r
21	SP4_10	BL_638 Upper Surface	SP4_10	A
22	SP4_11	BL_638 Upper Surface	SP4_11	NR
23	SP4_12	BL_638 Upper Surface	SP4_12	A
24	SP4_13	BL_638 Upper Surface	SP4_13	A
25	SP4_14	BL_638 Upper Surface	SP4_14	NR
26	SP4_15	BL_638 Upper Surface	SP4_15	A
27	SP4_16	BL_638 Upper Surface	SP4_16	A
28	SP4_17	BL_638 Upper Surface	SP4_17	NR
29	SP4_18	BL_638 Upper Surface	SP4_18	NR
30	SP4_19	BL_638 Upper Surface	SP4_19	A
31	SP4_20	BL_638 Upper Surface	SP4_20	A
32	PMON5_32m	PSI module monitoring pressure, module 5, port 32		
33	SP4_26	BL_638 Lower Surface	SP4_26	A
34	SP4_27	BL_638 Lower Surface	SP4_27	A
35	SP4_28	BL_638 Lower Surface	SP4_28	NR
36	SP4_29	BL_638 Lower Surface	SP4_29	A
37	SP4_30	BL_638 Lower Surface	SP4_30	A

38	SP4_31	BL_638 Lower Surface	SP4_31	A
39	SP4_32	BL_638 Lower Surface	SP4_32	A
40	SP4_33	BL_638 Lower Surface	SP4_33	A
41	SP4_34	BL_638 Lower Surface	SP4_34	A
42	SP4_35	BL_638 Lower Surface	SP4_35	A
43	SP5_5	BL_642 Upper Surface	SP5_5	A
44	SP5_6	BL_642 Upper Surface	SP5_6	A
~~*45*~~	~~*SP5_7*~~	~~*BL_642 Upper Surface*~~	~~*SP5_7*~~	~~*A NR (1/3/2012)*~~
46	SP5_8	BL_642 Upper Surface	SP5_8	A
47	SP5_9	BL_642 Upper Surface	SP5_9	A
48	PMON5_48m	PSI module monitoring pressure, module 5, port 48		
49	SP5_10	BL_642 Upper Surface	SP5_10	A
50	SP5_16	BL_642 Lower Surface	SP5_16	A
51	SP5_17	BL_642 Lower Surface	SP5_17	A
52	SP5_18	BL_642 Lower Surface	SP5_18	A
53	SP5_19	BL_642 Lower Surface	SP5_19	A
54	SP5_20	BL_642 Lower Surface	SP5_20	A
55	SP5_21	BL_642 Lower Surface	SP5_21	A
56	SP5_22	BL_642 Lower Surface	SP5_22	A
57	SP5_23	BL_642 Lower Surface	SP5_23	NA
58	SP5_24	BL_642 Lower Surface	SP5_24	A
59	SPS_1	Spanwise Group	SPS_1	NR
60	SPS_2	Spanwise Group	SPS_2	NR
61	SPS_3	Spanwise Group	SPS_3	A
62	SPS_4	Spanwise Group	SPS_4	A
63	SPS_5	Spanwise Group	SPS_5	NR
64	PMON5_64m	PSI module monitoring pressure, module 5, port 64		
Module #6		**Module range: 2.5 PSID**		
Port Number	Model Orifice	Description	Tubing labeled as:	a = good, NA = not accessible, NR = no response
1	SPS_6	Spanwise Group	SPS_6	NR
2	SPS_7	Spanwise Group	SPS_7	NR
3	SPS_8	Spanwise Group	SPS_8	A
4	SPS_9	Spanwise Group	SPS_9	A
5	SPS_10	Spanwise Group	SPS_10	NR
6	SPS_11	Spanwise Group	SPS_11	A
7	SPS_12	Spanwise Group	SPS_12	A
8	SPS_13	Spanwise Group	SPS_13	A
9	SPS_14	Spanwise Group	SPS_14	A

10	SPS_15	Spanwise Group	SPS_15	NR
11	SPS_16	Spanwise Group	SPS_16	A
12	SPS_17	Spanwise Group	SPS_17	A
13	SPS_18	Spanwise Group	SPS_18	A
14	SPS_19	Spanwise Group	SPS_19	A
15	SPS_20	Spanwise Group	SPS_20	A
16	PMON6_16m	PSI module monitoring pressure, module 6, port 16		
17	SPS_21	Spanwise Group	SPS_21	A
18	SPS_22	Spanwise Group	SPS_22	A
19	SPS_23	Spanwise Group	SPS_23	A
20	SPS_24	Spanwise Group	SPS_24	NR
21	SP3_18R	Right Wing Port Mirroring 3_18	SP3_18R	A
22	ISPL_1	Left TPS Inlet Static Pressure	1_32: ISPL_1	NA
23	ISPL_2	Left TPS Inlet Static Pressure	1_33: ISPL_2	NA
24	ISPL_3	Left TPS Inlet Static Pressure	1_34: ISPL_3	NA
25	ISPL_4	Left TPS Inlet Static Pressure	1_35: ISPL_4	NA
26	ISPL_5	Left TPS Inlet Static Pressure	1_36: ISPL_5	NA
27	ISPL_6	Left TPS Inlet Static Pressure	1_37: ISPL_6	NA
28	ISPL_7	Left TPS Inlet Static Pressure	1_38: ISPL_7	NA
29	ISPL_8	Left TPS Inlet Static Pressure	1_39: ISPL_8	NA
30	~~*ISPR_1*~~	~~*Right TPS Inlet Static Pressure*~~	~~*2_32: ISPR_1*~~	*NR*
31	ISPR_2	Right TPS Inlet Static Pressure	2_33: ISPR_2	NA
32	PMON6_32m	PSI module monitoring pressure, module 6, port 32		
33	ISPR_3	Right TPS Inlet Static Pressure	2_34: ISPR_3	NA
34	ISPR_4	Right TPS Inlet Static Pressure	2_35: ISPR_4	NA
35	~~*ISPR_5*~~	~~*Right TPS Inlet Static Pressure*~~	~~*2_36: ISPR_5*~~	*NR*
36	ISPR_6	Right TPS Inlet Static Pressure	2_37: ISPR_6	NA
37	ISPR_7	Right TPS Inlet Static Pressure	2_38: ISPR_7	NA
38	ISPR_8	Right TPS Inlet Static Pressure	2_39: ISPR_8	NA
39	~~*NSPL_1*~~	~~*Left TPS Nacelle Static Pressure Rake 1*~~	~~*1_40: NSPL_1*~~	*Moved to 15 psi modules*
40	~~*NSPL_2*~~	~~*Left TPS Nacelle Static Pressure Rake 2*~~	~~*1_41: NSPL_2*~~	*Moved to 15 psi modules*
41	~~*NSPL_3*~~	~~*Left TPS Nacelle Static Pressure Rake 3*~~	~~*1_42: NSPL_3*~~	*Moved to 15 psi modules*
42	~~*NSPL_4*~~	~~*Left TPS Nacelle Static Pressure Rake 4*~~	~~*1_43: NSPL_4*~~	*Moved to 15 psi modules*
43	~~*NSPL_5*~~	~~*Left TPS Nacelle Static Pressure Rake 5*~~	~~*1_44: NSPL_5*~~	*Moved to 15 psi modules*
44	~~*NSPL_6*~~	~~*Left TPS Nacelle Static Pressure Rake 6*~~	~~*1_45: NSPL_6*~~	*Moved to 15 psi modules*
45	~~*NSPL_7*~~	~~*Left TPS Nacelle Static Pressure Rake 7*~~	~~*1_46: NSPL_7*~~	*Moved to 15 psi modules*
46	~~*NSPR_1*~~	~~*Right TPS Nacelle Static Pressure Rake 1*~~	~~*2_40: NSPR_1*~~	*Moved to 15 psi modules*
47	~~*NSPR_2*~~	~~*Right TPS Nacelle Static Pressure Rake 2*~~	~~*2_41: NSPR_2*~~	*Moved to 15 psi modules*
48	~~*PMON6_48m*~~	~~*PSI module monitoring pressure, module 6, port 48*~~	-	
49	~~*NSPR_3*~~	~~*Right TPS Nacelle Static Pressure Rake 3*~~	~~*2_42: NSPR_3*~~	*Moved to 15 psi*

				modules
50	~~*NSPR_4*~~	~~*Right TPS Nacelle Static Pressure Rake 4*~~	~~*2_43: NSPR_4*~~	*Moved to 15 psi modules*
51	~~*NSPR_5*~~	~~*Right TPS Nacelle Static Pressure Rake 5*~~	~~*2_44: NSPR_5*~~	*Moved to 15 psi modules*
52	~~*NSPR_6*~~	~~*Right TPS Nacelle Static Pressure Rake 6*~~	~~*2_45: NSPR_6*~~	*Moved to 15 psi modules*
53	~~*NSPR_7*~~	~~*Right TPS Nacelle Static Pressure Rake 7*~~	~~*2_46: NSPR_7*~~	*Moved to 15 psi modules*
54	CSPL_1	Left TPS Core Static Pressure	1_47: CSPL_1	NA
55	CSPL_2	Left TPS Core Static Pressure	1_48: CSPL_2	NA
56	CSPR_1	Right TPS Core Static Pressure	2_47: CSPR_1	NA
57	CSPR_2	Right TPS Core Static Pressure	2_48: CSPR_1	NA
58				
59				
60				
61				
62				
63				
64	PMON6_64m	PSI module monitoring pressure, module 6, port 64		

LXI Channel	Tagname Channel	Description	T/C Type (J/K/T/E/S/R/B/N)
0	RWTC_1	RH Wing Surface	J
1	RWTC_2	RH Wing Surface	J
2	RWTC_3	RH Wing Surface	J
3	RWTC_4	RH Wing Surface	J
4	RWTC_5	RH Wing Surface	J
5	RWTC_6	RH Wing Surface	J
6	RWTC_7	RH Wing Surface	J
7	RWTC_8	RH Wing Surface	J
8	RWTC_9	RH Wing Surface	J
9	RWTC_10	RH Wing Surface	J
10	RWTC_11	RH Wing Surface	J
11	RWTC_12	RH Wing Surface	J
12	LTPSR_1	Left TPS Rake 1	J
13	LTPSR_2	Left TPS Rake 2	J
14	LTPSR_3	Left TPS Rake 3	J
15	LTPSR_4	Left TPS Rake 4	J
16	LTPSR_5	Left TPS Rake 5	J
17	LTPSR_6	Left TPS Rake 6	J
18	LTPSR_7	Left TPS Rake 7	J

19	LTPSC_1	Left TPS Core 1	J
20	LTPSC_2	Left TPS Core 2	J
21	RTPSR_1	Right TPS Rake 1	J
22	RTPSR_2	Right TPS Rake 2	J
23	RTPSR_3	Right TPS Rake 3	J
24	RTPSR_4	Right TPS Rake 4	J
25	RTPSR_5	Right TPS Rake 5	J
26	RTPSR_6	Right TPS Rake 6	J
27	RTPSR_7	Right TPS Rake 7	J
28	RTPSC_1	Right TPS Core 1	J
29	RTPSC_2	Right TPS Core 2	J
30	BSTC_1	Balance Surface 1	J
31	BSTC_2	Balance Surface 2	J
32	BITC_1	Balance Internal Air Heater 1	J
33	BITC_2	Balance Internal Air Heater 2	J
34	LLPDP_1	Left Low Presure Distribution Plenum	J
35	RLPDP_1	Right Low Presure Distribution Plenum	J
36	LPTC_1	Left Pylon	J
37	RPTC_1	Right Pylon	J
38	OP_T1	Orifice Plate	J
39	WING TC	Additional Wing TC for instrumentation	J
40	NOSE	Additional Nose TC for instrumentation	J

A8. Load analysis

In order to ensure the maximum loadings generated by the model do not compromise the integrity of both the balance and the model (sting) support system, a complete loads analysis was conducted for the assumed worst case loading conditions. The balance has 6-degrees of sensitivity for which a maximum loading condition is analyzed: normal force, axial force, side force, rolling moment, pitching moment, and yawing moment. CFD simulations are used to analyze the loadings for each of the loading conditions, except where noted; computation details are provided in a subsequent section. Loads and limits are presented in the body-axis system. It should be noted that the loads reflect a certain amount of conservatism in the analyses as the purpose is to create an encompassing operational envelope for the model, less so a prediction.

Normal Force

The maximum loading condition for the normal force is the result of the model pitched to its maximum lift coefficient. Predicting the angle of attack at which this occurs is not trivial; the results of three CFD simulations at several angles of attack (0°, 10°, 25°) were used to estimate the maximum lift force generated by the model. The results of the simulations showed that at 10° the model was subject to the highest lift force, corresponding to a C_L of 7.7. Dimensionalizing the coefficient at the highest dynamic pressure (33.7 psf @ 100 KTS) yields a force of 2341 lb_f.

Axial Force

In the same way the normal force is evaluated, the highest drag from CFD simulations at 0°, 10°, and 25° is assumed to be the maximum axial force the model generates. At 25° angle of attack, the drag coefficient is 3.76. Dimensionalizing this at 33.7 psf yields a force of 353.6 lb_f.

Side Force

Ideally, the only time the model will experience a pronounced side force is when the relative wind vector is no longer in line with the model centerline, i.e. the model is yawed. To analyze this condition, the side force is assumed to be the product of the projected side area of the model facing the wind and the dynamic pressure. The model is yawed to 10° in testing, but 20° is assumed for conservatism. At this angle, the projected model area is 3.4 ft^2; the total side area is approximately 10 ft^2. The resulting side force is 114.6 lb_f at 33.7 psf.

Rolling Moment

During normal test conditions where most forces act symmetrically on the model, rolling moment should be a small load. It is assumed the maximum loading would occur under the inadvertent stoppage of flow to one slot plenum at the highest lifting condition. The difference in wing loading on one side is estimated to be a 30% reduction in lift. To get the net lift contribution from the slots, the un-blown lift created by the model is subtracted from the blown lift at 10°. Using aircraft performance methods outlined in *Aircraft Design* by Dan Raymer[1], the un-blown lift is calculated to be 517.4 lb_f. Subtracting from the maximum lift, the total lift contribution due to slot flow is 1824 lb_f (both wings). The lift produced by one wing with flow stopped in one plenum is then calculated as (2341-1824*0.30)/2 = 897 lb_f. The resultant asymmetric loading is then the lift of the semi-span less the contribution of the stopped flow, or (2341/2)-897 = 274 lb_f. Assuming the integration of the resultant asymmetric load acts at half of the semi-span, i.e. 2.5 ft from the model centerline, the rolling moment is 684 ft-lb_f.

Pitching Moment

The model loading in the pitch axis is predicted greatest at -5° angle of attack, by way of CFD. The pitching moment coefficient, relative to the balance center, is 0.6. The balance center is 56.73 inches from the nose and the reference chord used in the analysis is 3.281 ft. At 100 KTS, the pitching moment load is 600.1 ft-lb_f.

Yawing Moment

The one engine inoperative (OEI) case presents the highest yawing load on the model. The ideal gross thrust produced by a single TPS unit spinning at the maximum rated RPM is 175 lb_f. The distance from the engine centerline to the model centerline is 1.82 ft. Assuming one TPS is producing maximum thrust and the other is producing no thrust, the yawing moment is 318.5 ft-lb_f; this analysis neglects any contribution from the slots and from drag.

Analysis/CFD Solution Strategy

The solution strategy for each of the 6 load components is described above. For the loads predicted via CFD, the solution strategy follows. As analysis was required for multiple tunnel speeds with short turnaround, solutions were computed for one freestream and predictions were scaled to the other freestream conditions. The commercially available code, FLUENT[2], is used to generate all the numerical solutions. Within FLUENT, specifically version 12.1, the 3-D RANS equations are solved with their implicit density based solver and the *SST* formulation of the k-ω turbulence model. The grid is a hybrid type; unstructured tetrahedral fill the near-field, while the far-field boundaries are meshed with structured hexahedral elements. Boundary layer and wall effects are captured with prisms built-up from triangular surface elements. Meshes are generated using ICEM CFD[3], version 12.1. A few simplifications are made to the computational model to aid the mesh generation process and limit the computational resources required to generate solutions. The pylon is removed, creating a "floating" engine; the pylon presents several issues in the mesh generation process, like poor cell quality, and has little contribution to the overall flow field, so it is removed, creating a "floating" engine. The main fuselage is also removed as its contribution is negligible[4]. The resulting geometry and some of the flow features of a representative solution are shown in Figure A8.1. The computational boundary for the slot blowing plenums starts at the downstream end of the metal foam. A pressure inlet boundary condition is enforced with inputs of flow total pressure and temperature. The total pressure and temperature inputs are averages based on known operating conditions to match the experimental C_μ. The engine boundaries are at the fan inlet/outlet and the core outlet. A pressure outlet boundary condition is enforced at the fan inlet. Static pressure and total temperature are inputted with values representative of typical operational conditions. The fan and core outlets are enforced with a mass flow outlet boundary condition. Inputs of mass flow rate and total temperature based on calibration data are supplied to match the experimental C_T.

Comparison of Predicted Loads and Limits

Table A8.1 presents a comparison of the predicted maximum loads against the limits for both the Triumph 8 inch air balance and the NFAC 13.3 foot sting model support system in each of the 6 components. Balance limit information was provided by Triumph Force Measurement Systems and model support system information was provided by the NFAC, June 2011. The load envelope for the balance is defined by a rhombus where either the full normal force or full pitching moment force is allowable; the capacity is defined by the summation of the percent loading for both components, %NF+%PM = 100%. Likewise for side force and yawing moment, %SF+%YM = 100%. The model support load is limited to 6250 lb_f normal force due to the butt taper at the sting/pitch interface. No analysis was provided for the axial limit on the model support, but the balance total capacity of 1200 lb_f proved to be within the limits. Rolling moment is also limited to 780 ft-lb_f, under the balance limit of 2275 ft-lb_f, for roll pin failure at the model/sting interface. Overall, estimated maximum model loads in all 6 components fall within the limits of both the balance and model support system with conservative margin.

Table A8. 1. Comparison of maximum model loads and balance/model support system limits.

Force Component	Maximum Model Loads	Balance Limits	Model Support Limits
Normal Force	2341 lb_f	±5000 lb_f	6250 lb_f
Axial Force	353.6 lb_f	±1200 lb_f	N/A
Side Force	114.6 lb_f	±2500 lb_f	1400 lb_f
Rolling Moment	684 ft-lb_f	±2275 ft-lb_f	780 ft-lb_f
Pitching Moment	600.1 ft-lb_f	±2417 ft-lb_f	12,600 ft-lb_f
Yawing Moment	318.5 ft-lb_f	±875 ft-lb_f	12,600 ft-lb_f

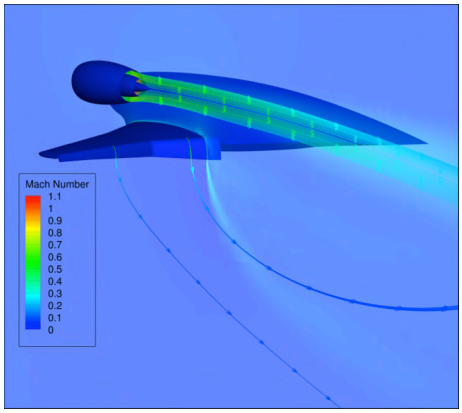

Figure A8.1. CFD solution showing relevant model and flow features; streamlines and contours colored by Mach number.

References

[1]Raymer, D. P., *Aircraft Design: A Conceptual Approach*, 4th Ed., AIAA Education Series, 2006.
[2]ANSYS FLUENT, Software Package, Ver. 12.1, ANSYS, Inc., Canonsburg, PA, 2009.
[3]ANSYS ICEM CFD, Software Package, Ver. 12.1, ANSYS, Inc., Canonsburg, PA, 2009.
[4]Blessing, B. H., "A Computational Study of Engine Deflection Using a Circulation Control Wing", Master's Thesis, California Polytechnic State University, May, 2011.

A9. Transient Balance Data

The Triumph MC-130 8.0 inch diameter Air Balance is equipped with a heater. The heater serves to heat soak the balance, keeping it at a constant temperature to avoid any temperature dependent data anomalies. To check for temperature dependent trends in the balance readings, periodic balance data were acquired on two separate occasions with the heater turned off and then on. The runs were conducted over holiday downtime; the model was mounted and static for this period. 10 second data points were acquired every 10 minutes. The heating run acquired a total of 257 data points over 42.5 hours. The cooling run acquired a total of 551 data points over 92.6 hours. The wind tunnel test section temperature, °F, variance over the time is shown in Figure A10.1. The dashed vertical lines represent a span of 24 hours. Figures A10.2-A10.7 show the balance measurements over time for each of the 6 components. As can be seen from the plots, the data variance when the heater is turned off (cooling run) is significant. Periodic balance measurements are sensitive to tunnel temperature trends for the cooling run and data values are shifted from those when the balance heater is turned on. The heating runs do not show the same correlation to

tunnel temperature, except in the axial force measurement, and appear to also not be effected by the cycling on and off of the heaters thermostat. After review, it was determined that the heater was to be turned on for the duration of testing to minimize ambient temperature effects on the balance data.

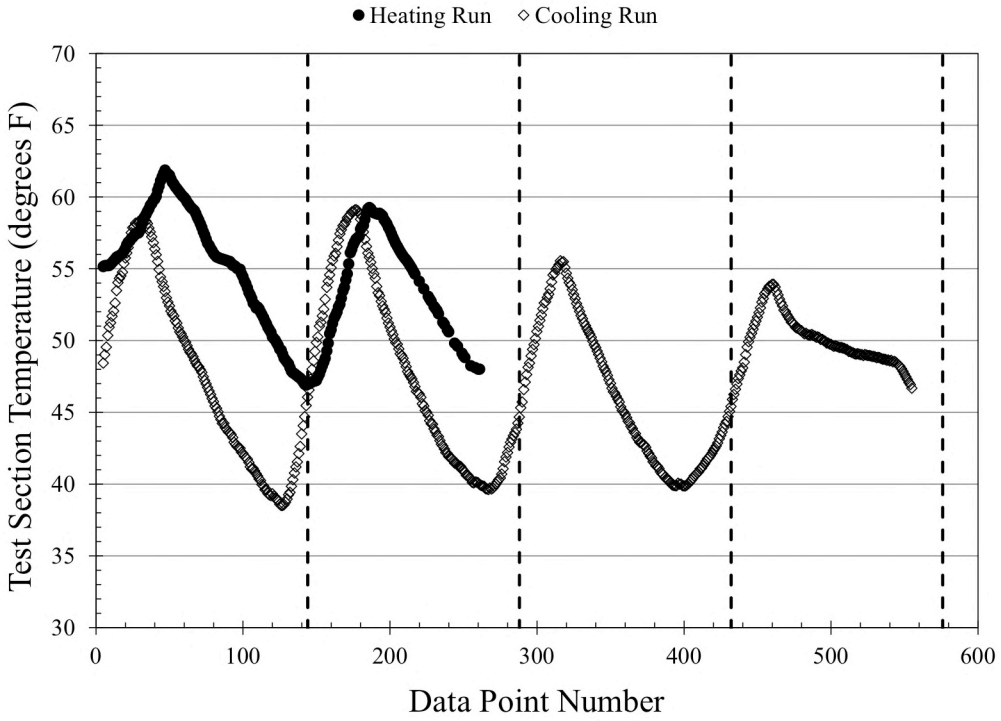

Figure A9.1. Test section temperature profiles versus time for balance heater on and off runs.

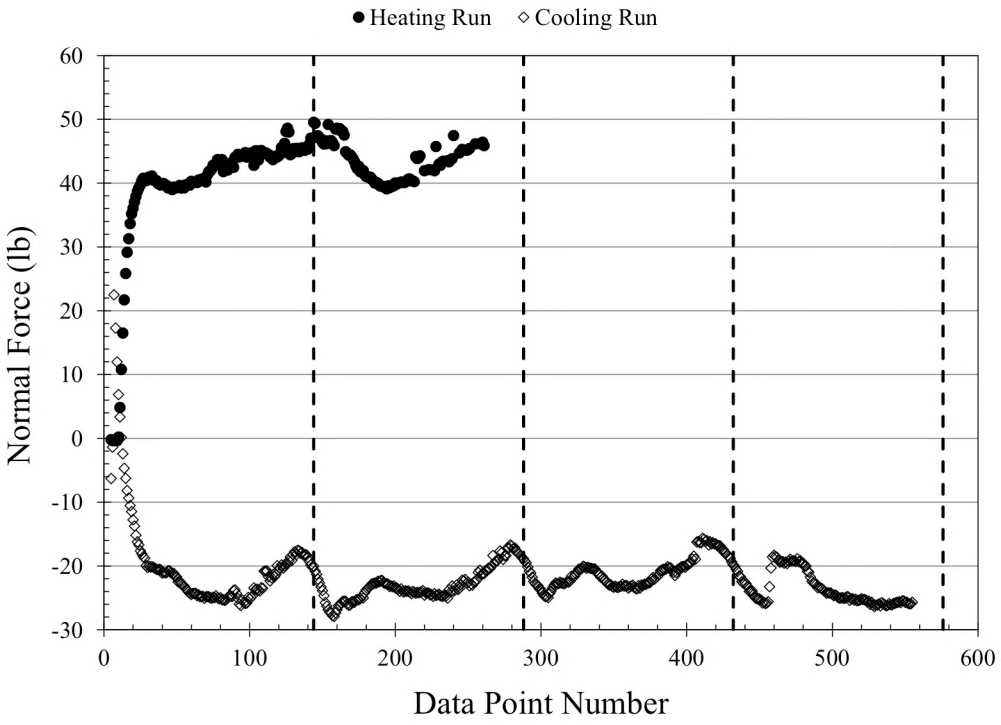

Figure A9.2. Normal force variation for balance heater on and off runs.

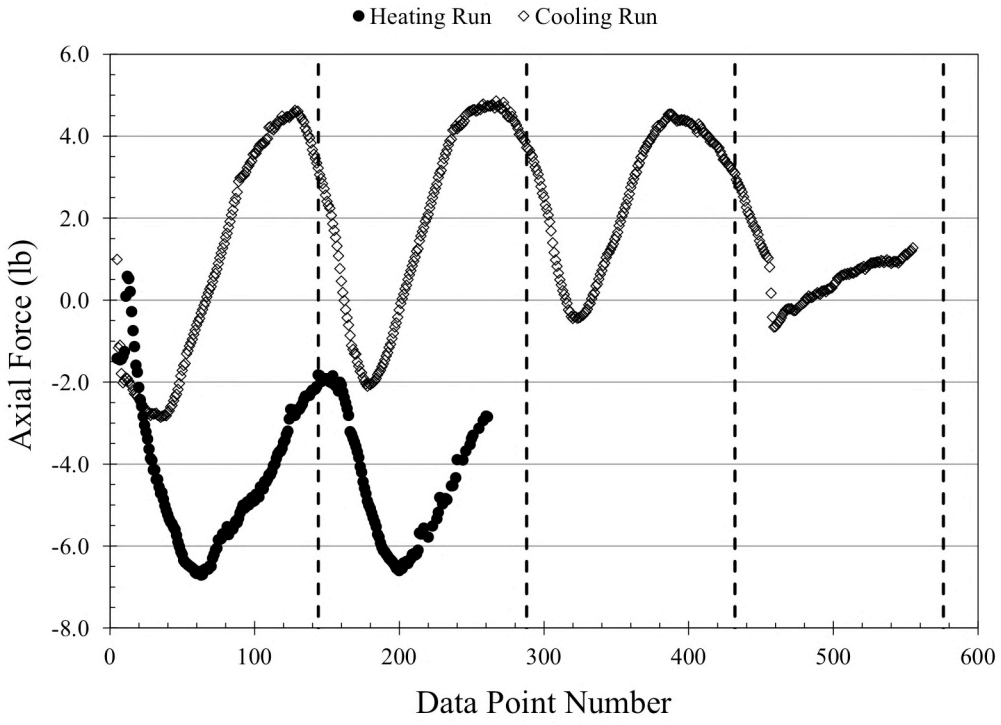

Figure A9.3. Axial force variation for balance heater on and off runs.

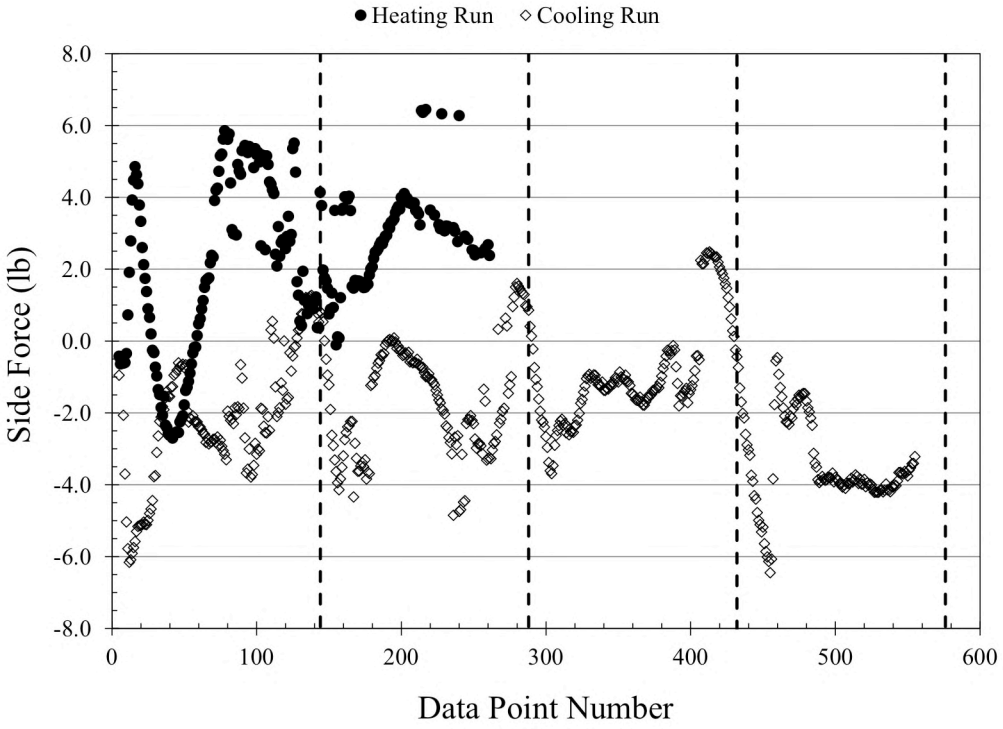

Figure A9.4. Side force variation for balance heater on and off runs.

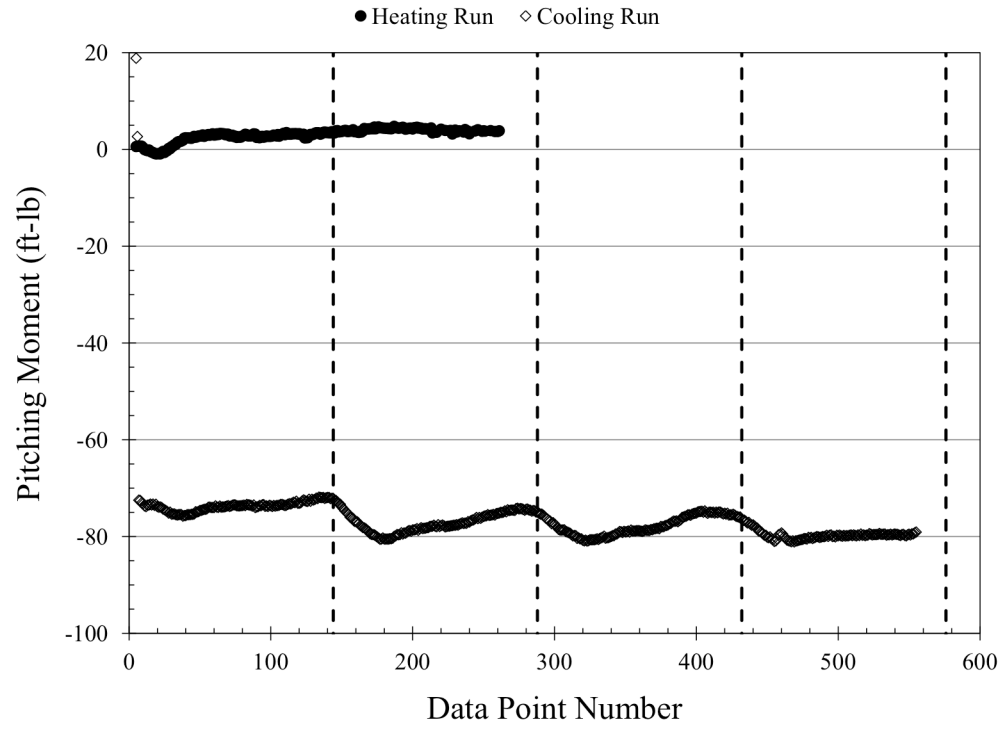

Figure A9.5. Pitching moment variation for balance heater on and off runs.

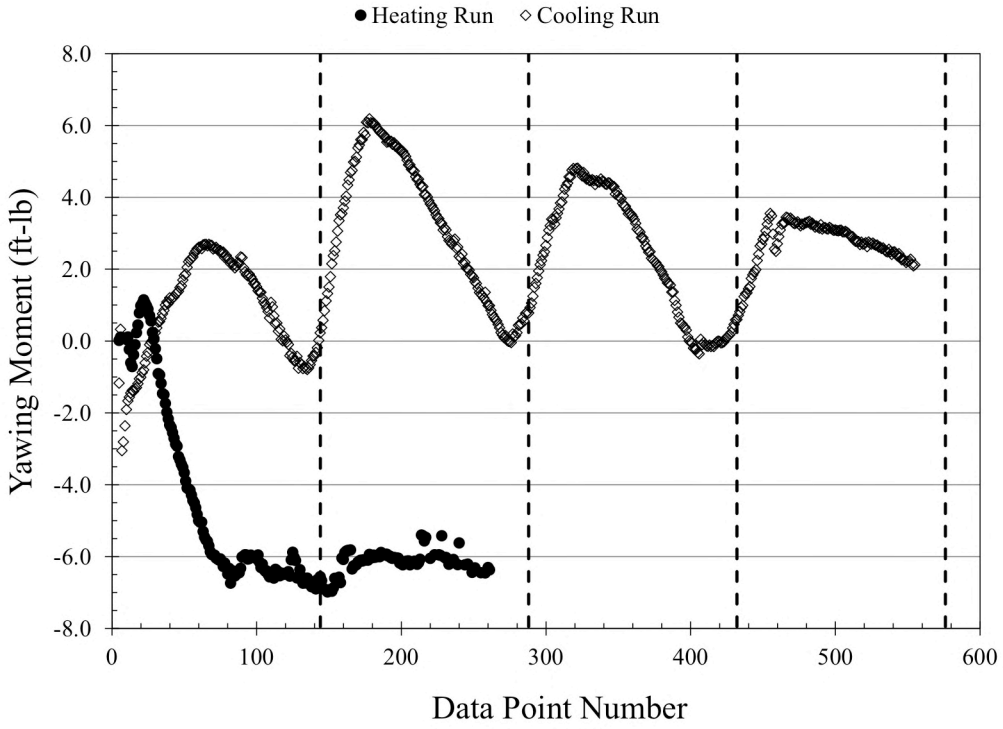

Figure A9.6. Yawing moment variation for balance heater on and off runs.

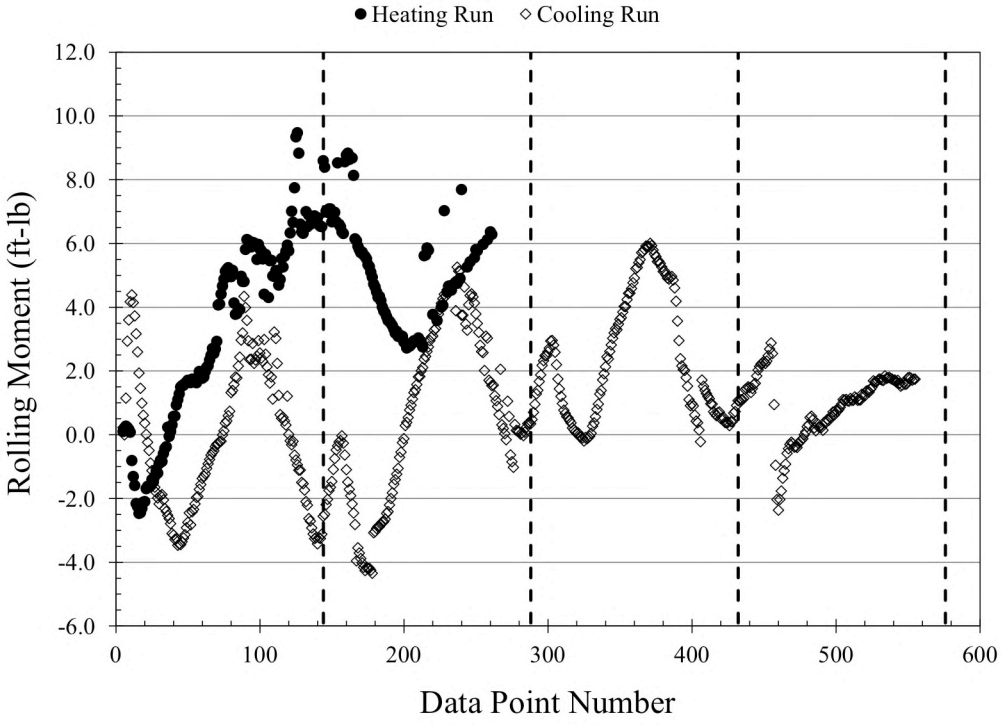

Figure A9.7. Rolling moment variation for balance heater on and off runs.

A10. Lessons Learned

The late model redesign mentioned in Section 2.4.2 came as a big surprise to most of the test team. Although it was required to assure force and moment isolation on the balance,

A11. Discrepancy Listing

Discrepancy Listing (in no particular order)

1. Run 39 data points are anomalous. Repeat sweeps at runs 69, 81, 82, and 128 have better repeatability and trends are in agreement with one another. Run 39 data showed a loss in $C_{L,max}$ and stall at a lower angle of attack than those from runs 69,81,82, and 128. Upon examination of the high pressure air leg, no appreciable difference was seen in air being supplied to the TPS units between the four runs (this can be seen mostly from the matching of the uncorrected drag data). The low pressure line, however, showed large temperature gradients during R39 that are believed to be the cause of the faulty run.

    a. Figures:

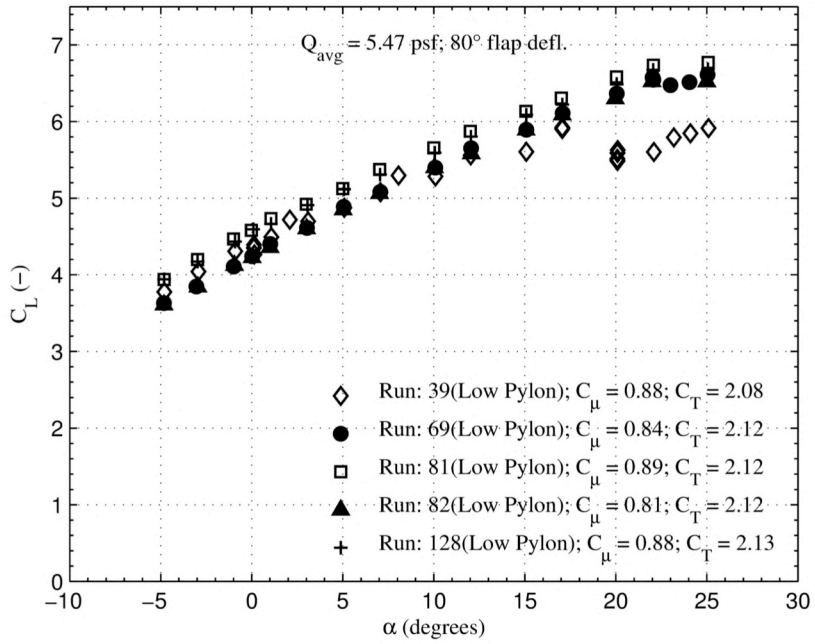

Figure A11.1. Lift curve showing the anomalous high angle of attack behavior during R39.

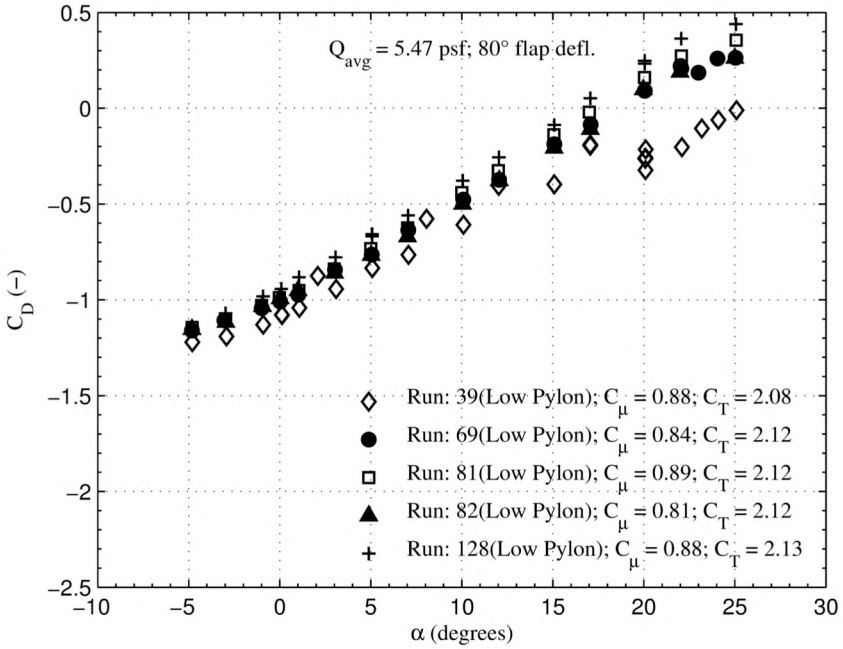

Figure A11.2. Drag curve showing thrust matching for repeated runs.

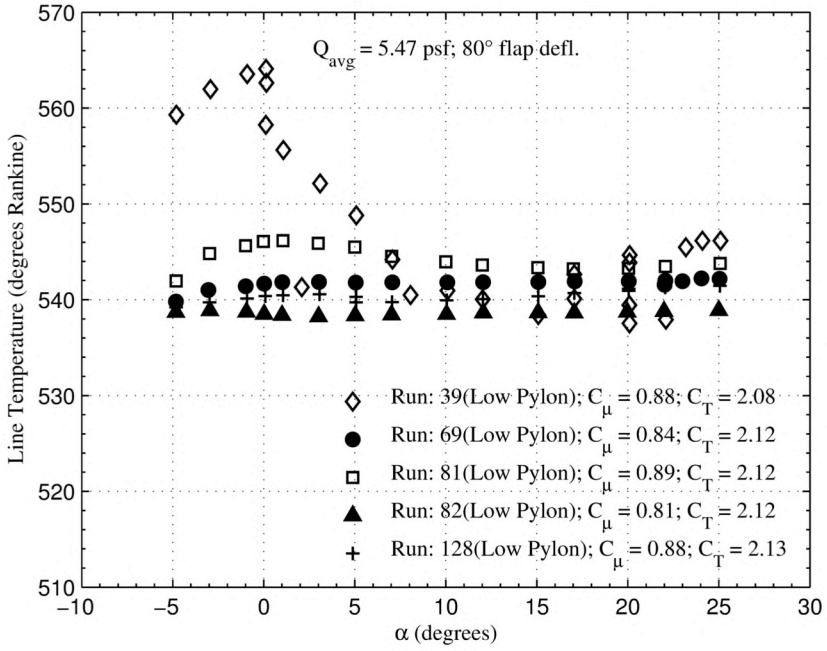

Figure A11.3. Low pressure line temperature. Note the large temperature gradients at low angles of attack for R39.

2. The inboard most tie-down on the left wing trailing edge outboard plenum was compromised during installation. As such, the slot cannot be secured in tension or set

to the proper height. The result of this can be seen in the slot height measurements as well as the plenum pressure measurements. The local shift in slot height creates an imbalance in the pressure distribution across the slot that is not seen in the right wing.

a. Figures:

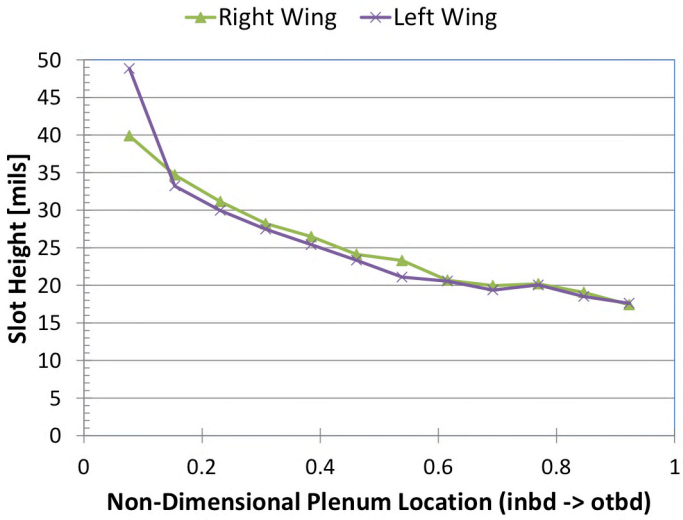

Figure A11.4. Trailing-edge outboard plenum slot height differences between left and right wings.

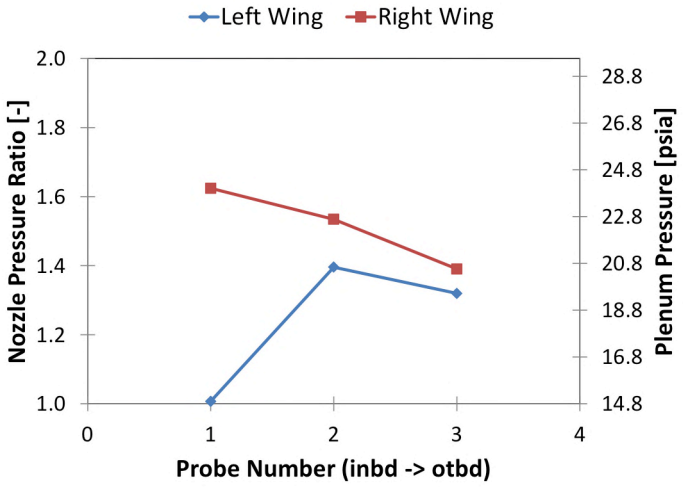

Figure A11.5. Trailing-edge outboard plenum pressure differences. Run 69, test conditions: 40 KTS, 80° flap, C_μ = 0.84, C_T = 2.12.

3. The redundant mass flow rate measurements, on the low pressure line, showed a discrepancy in their readings for the extent of the test. At the nominal slot blowing condition, the digital valve regulated flow at a measured 2.8 lb_m/sec, whereas the orifice plate measured 1.9 lb_m/sec. The digital valve measurement was used to set on mass flow rate for the entirety of the test. The digital valve was last calibrated in

1992 and the orifice plate was not calibrated. A post-test calibration was performed on the orifice plate and the results are provided in the report and summarized here. During testing, the orifice plate was run at conditions outside the typical operating range for an orifice plate of its diameter ratio. Consequently, the data reduction routine for calculating mass flow rate from the instrumentation yielded faulty results. The calibration confirmed the readings of the digital valve to within 5% across the entire mass flow range. Mass flow rate data were corrected to account for the results of the calibration and all mass flow data presented herein reflect the correction. The data files contain all mass flow measurements, corrected and uncorrected.

4. For a given tunnel speed, the left and right TPS units windmill at different RPMs. The left TPS unit spins freer than the right TPS and without any stickiness or binding sounds. At 100 KTS, the left and right TPS units windmill at approx. 4000 RPM and 3700 RPM, respectively. What thrust is produced by the simulators at such a small RPM (on the order of a few pounds) is unlikely to cause any discrepancy in any aerodynamic data and is also within the uncertainty of the balance measurements.

5. When the model did seem to stall, the stall was mostly asymmetric. This was marked by large, negative in sign, rolling moments at high angles of attack. The likely cause is an imbalance in the slot flow strength between the left and right wings in the LEOB plenum.

6. Due to relative humidity in the tunnel circuit, and high pressure line temperature, small amounts of icing did occur on the back end of the TPS core. At points where appreciable ice accumulation was observed, ice was shed. The TPS units were brought down to idle (~9000 RPM) to let the accumulated ice melt and then brought back up on-condition for a repeat point. This procedure could have been repeated as much as 4 times during a run. There were a small number of occurrences where the repeat point was not taken; run sheets are annotated to reflect this. To avoid any non-linear aerodynamic interactions, deicing points were avoided whenever possible at higher angles of attack. There seems to be no indicated performance difference caused by icing on the back end of the TPS.

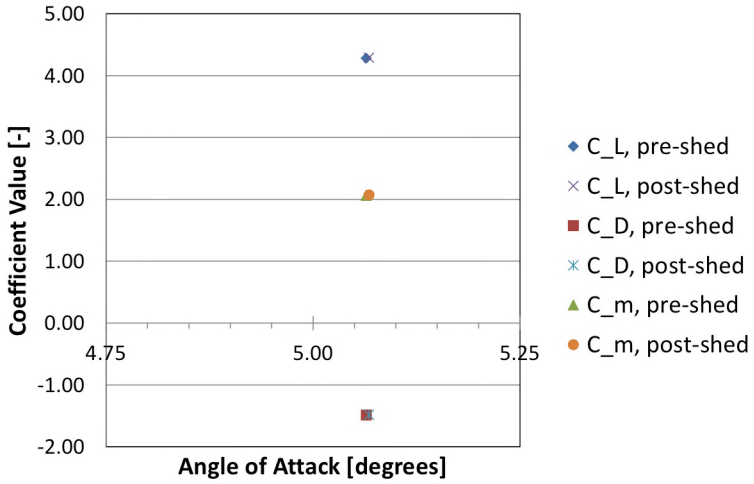

Figure A11.6. Pre- and post-icing aerodynamic coefficient repeatability. Run 50, test conditions: 40 KTS, 60° flap, β = 10°, C_μ = 0.85, C_T = 2.12.

7. Flap fastener holes for flap deflections other than 0° were not plastered. The only exception being the 60° flap for the first set of matrix runs with the low pylon height (R40-67). The reason was to create as little down-time as possible; flap changes, which nominally take under 1 hour to complete, were twice as time consuming when plastering fastener holes. This decision was justified because at flap deflections greater than 0°, the flow cannot maintain attachment as far back as the fastener holes and separates further upstream.

8. Wind tunnel personnel access door (PAD) seals were not inflated for CTP#7, Run 190 (100 KTS freestream) to reduce model access time once fringes have formed. The PAD is located downstream of the sting support system on the right wall (pilot's right).

9. Traditionally, the drive air supplied to TPS units is heated to preclude exposure of the aft bearing to excessively low temperatures, resulting from the expansion through the turbine, causing a failure. Upon operation of the model 441 units, however, an increase in drive air temperature resulted in increased aft bearing temperatures despite the nearly -110°F flow temperature exiting the last turbine stage. Regulating the drive air temperature to 150°F resulted in aft bearing temperatures nearly reaching the SOF limit at 125°F. This necessitated the change to lower the maximum operating condition from 80% to 77%, or 36,000 RPM to 34,500 RPM, respectively. Drive air temperature was regulated at 110°F. At 40 KTS, this represents a reduction in thrust of 9.9 lb_f, ~10%.

10. Four model angle of attack measurements were recorded during testing. They are defined, by tagname, as:

    a. ALPHA_MODEL_1 – derived from Schaevitz sensor

    b. QANGLE – derived from Qflex sensor and Unitary Plan Wind Tunnel (UPWT) equation set

    c. ALT_QANGLE – derived from Qflex sensor and alternative UPWT equation set

    d. ALPHA_OPC – derived from the sting pitch resolver

    The Schaevitz sensor was used for data computations, and was the reference for angle of attack set points. The two Qflex measurements were taken from the same analog inputs, but calculated from a different set of equations. It is believed that the QANGLE measurement is more accurate than ALT_QANGLE, but bench tests indicated otherwise. There also appeared to be scaling issues associated with the QANGLE measurement, whereas the ALT_QANGLE measurement consistently tracked both the calibration reference and Schaevitz sensor. In the interest of time and measurement priority, the discrepancy in the QANGLE channel was not investigated further.
    Another issue was the unsteadiness in model alpha readings. The Schaevitz and Qflex sensors were mounted in the nose of the model, which experienced varying levels of vibration depending on the test condition. For high speed, high lift test points, the variation in angle of attack reading reached as high as 0.3° peak-to-peak. This made it difficult for operators to consistently set angle of attack, and may explain minor variations in balance data run-to-run.

A12. NRA Announcement

Excerpt from NASA Research Announcement NNH06ZEA001Ncontaining original solicitation that resulted in the AMELIA research effort. Cal Poly's effort supports subtopic A2.4.1 of the Fundamental Aeronautics Program's Sub-sonic Fixed Wing Project.

OMB Approval Number 2700-0087

NATIONAL AERONAUTICS AND SPACE ADMINISTRATION (NASA) HEADQUARTERS
AERONAUTICS RESEARCH MISSION DIRECTORATE
300 E STREET, SW
WASHINGTON, DC 20546-0001

RESEARCH OPPORTUNITIES IN AERONAUTICS – 2006
(ROA-2006)

NASA RESEARCH ANNOUNCEMENT (NRA): NNH06ZEA001N

SOLICITING BASIC AND APPLIED RESEARCH PROPOSALS

CATALOG OF FEDERAL DOMESTIC ASSISTANCE (CFDA) NUMBER: 00.000

ISSUED: May 23, 2006

PROPOSALS DUE
STARTING July 7, 2006
THROUGH July 6, 2007

RESEARCH OPPORTUNITIES IN AERONAUTICS (ROA) – 2006

EXECUTIVE SUMMARY

This NASA Research Announcement (NRA), entitled *RESEARCH OPPORTUNITIES IN AERONAUTICS (ROA) – 2006*, solicits foundational research in support of the Aeronautics Research Mission Directorate (ARMD), National Aeronautics and Space Administration (NASA). This NRA covers a variety of topics in aeronautics foundational research that are being pursued by NASA personnel. Specific research thrusts are outlined in the Appendices. A major focus of this NRA is to encourage collaboration between other organizations and NASA to help achieve specific goals in a variety of foundational aeronautics research programs.

Details for award scope are provided for each project task area listed in the Appendices. Awards will be made as grants, cooperative agreements or contracts, depending on the nature of the proposing organization and/or program requirements. It is anticipated that the majority of awards will be cooperative agreements or contracts due to the expected collaborative nature of the work specified in the technical appendices. Section D of the *NASA Guidebook for Proposers* provides a discussion regarding funding mechanisms. The typical period of performance for an award is three years, although a few programs may specify shorter or longer (maximum of five years) periods. Note that it is NASA policy that all programs involving non-U.S. participants will be conducted on the basis of no exchange of funds. Details of the solicited program elements along with any changes or modifications to any of these guidelines will be specified in the descriptions in the Appendices of this solicitation. Proposal due dates are given in Tables 2 and 3 which are located at the end of this NRA.

APPENDIX A: Fundamental Aeronautics Program

A.1 Program Overview

The top-level goal of this program is the development of system-level, multi-disciplinary capabilities for both civilian and military applications. This program provides long-term investment in research to support and sustain expert competency in critical core areas of aeronautics technology.

The Fundamental Aeronautics Program encompasses core capabilities in the four (4) thrust areas of Subsonic Fixed Wing, Subsonic Rotary Wing, Supersonics and Hypersonics. It also supports NASA's Vision for Space Exploration by providing key aeronautical capabilities that can be adapted for high-speed vehicles exiting and entering the atmosphere of our planet as well as operating throughout the atmospheres of other planetary bodies such as Mars.

The Fundamental Aeronautics Program is dedicated to the mastery and intellectual stewardship of the core competencies of Aeronautics for the Nation across all flight regimes. NASA will focus the research in areas that are appropriate to our unique capabilities. The research is long-term and is both focused and integrated across disciplines. NASA will invest broadly and deeply in the core competencies of aeronautics, producing knowledge, technology, and tools that are applicable across a broad range of air vehicles.

NASA has defined a four-level approach to technology development: (1) conduct foundational research to further our fundamental understanding of the underlying physics and our ability to model that physics, (2) leverage the foundational research to develop technologies and analytical tools focused on discipline-based solutions, (3) integrate methods and technologies to develop multi-disciplinary solutions, and (4) solve the aeronautics challenges for a broad range of air vehicles with system-level optimization, assessment and technology integration.

Interaction with the aeronautics community aligns with the four levels: (1) NASA will advance the state of knowledge of the underlying physics and its modeling by partnering with universities and companies engaged in foundational research where that partnership supplements NASA capabilities, (2) NASA will investigate discipline-related challenges and will interact with the aeronautics community through published reports and direct technology transfer, (3) NASA will develop multi-disciplinary methods and technologies, and disseminate them in published reports and direct technology transfer, and (4) NASA will collaborate with industry by means of non-reimbursable cooperative agreements to address system-level challenges at the pre-competitive level.

The awards from this NRA will support U.S. leadership in aerospace through its commitment to identify and advance innovative ideas, concepts, technologies, and approaches to the aeronautics challenges described below for each of the four Fundamental Aeronautics thrust areas.

Milestone references are provided in the sections below under the heading "NASA Milestones" so that it is possible to see how the NRA topics fit into the NASA Aeronautics research plan. These milestones are listed on project roadmaps that are available on the ARMD website (www.aeronautics.nasa.gov, under the Programs link).

Evaluation Criteria and Basis for Award

The evaluation criteria in Appendix B, part (i) and Appendix C, paragraph C.2 of the "Guidebook for Proposers Responding to a NASA Research Announcement (NRA), January 2006" are superseded by the following.

The principal elements considered in evaluating a proposal are its relevance to NASA's objectives, technical merit, effectiveness of the proposed work plan, and its cost.

The following evaluation factors will be used to evaluate proposals. Every proposal will be evaluated on its own merits and not compared with other proposals. Failure of a proposal to be highly rated in any one of the following elements is sufficient cause for the proposal to not be selected.

(1) Relevance (weight 30%):

- Evaluation of a proposal's relevance to NASA's objectives includes the consideration of the potential contribution of the effort to NASA's mission as expressed in the 2006 NASA Strategic Plan available at http://www.nasa.gov and the specific objectives and goals given in the solicitation to which the proposal is submitted.
- The proposer is required to identify the specific area (Program, Project, Topic, and Subtopic selected from Appendix A.2, A.3, A.4, or A.5) that is being addressed.
- The evaluation process will also consider the importance of the work to the primary project objectives of advancing knowledge and understanding of the fundamental principles of flight unique to the proposed flight regime, contributing to the development of a validated physics-based multidisciplinary design and analysis tool(s) for enabling air vehicles with innovative capabilities to fly as designed.

(2) Technical Merit (weight 40%):

- Overall scientific or technical merit of the proposal, including unique and innovative methods, approaches, or concepts.
- Evaluation will also include: credibility of technical approach, including a clear assessment of primary risks and a means to address them; proposer's capabilities, related experience, facilities, techniques, or unique combination of these which are integral factors for achieving the proposal's objectives; and qualifications, capabilities, and experience of the proposed principal investigator, team leader, or key personnel critical in achieving the proposal objectives.
- The selection process will also assess the proposal against the state-of-the-art.

(3) Effectiveness of the Proposed Work Plan (weight: 25%):

- Comprehensiveness of work plan, effective use of resources, management approach, and proposed schedule for meeting the objectives.
- Milestones with measurable metrics toward achieving the proposer's goal must be provided, with a minimum of one metric per year.
- Proof-of-concept demonstrations are encouraged.
- Annual oral presentations made as part of an open Technical Exchange Meeting for purposes of technology transfer and knowledge dissemination will be expected.
- Documentation of approach and results in the form of final written technical reports is required.
- A clear statement of what intellectual property is expected to be publicly available at the conclusion of the work is required. It is our intent to share all knowledge developed under this solicitation, thus, any restrictions to that objective will cause a lower score in this area.
- Collaboration with NASA researchers (including joint use of facilities, visits by faculty, graduate students, and researchers to NASA facilities for significant exchanges, sharing of materials, development of computer code modules compatible with NASA's software, and synergistic research goals) is desirable, with the objective of enhancing knowledge transfer and the long term value of the proposed work.

(4) Proposed Cost (weight: 5%)

- Evaluation of the cost of a proposed effort shall include the realism and reasonableness of the proposed cost, and the comparison of that proposed cost to available funds.
- Low cost, while desirable, does not offset the importance of realism and reasonableness of the proposed budget.

A.2: Subsonic Fixed Wing

1. Project Overview

A major focus of the Subsonic Fixed Wing (SFW) project is to develop improved prediction methods and technologies for lower noise, lower emissions, and higher performance for subsonic aircraft. Increased performance requires increased energy efficiency and operability for advanced airframe and engine systems and subsystems. The ten-year strategy includes providing novel test methods and validated prediction tools that can be used to improve system trades for advanced concepts capable of meeting longer-term noise, emissions, and performance targets. The following objectives address the overall project goals, not all of which are within the scope of this solicitation.

- Improvements in prediction tools and new experimental methods that provide fundamental properties and establish validation data
- Noise prediction and reduction technologies for airframe and propulsion systems
- Emissions reduction technologies, alternative fuels, and particulate measurement methods
- Improved vehicle performance through design and development of lightweight, multifunctional and durable structural components, high lift aerodynamics, and higher bypass ratio engines with efficient power plants.

The Project will invest a significant portion of its allocated budget to NASA Research Announcement (NRA) solicitations. Approximately ~$16M is anticipated to be invested in this solicitation over the next 3 years; at about $5.2M for year 1, $6.2M for year 2, and $4.7M for year 3. In this solicitation (Second Round) we are releasing the second set of topics, which emphasizes technologies for future generation hybrid wing/body vehicles (referred to "N+2", or two generations beyond current aircraft, or aircraft that may be introduced around 2020) that are described in the Subsonic Fixed Wing project plans (*http://www.aeronautics.nasa.gov/programs_fap.htm*). NASA started this work over fifteen years ago with the Blended Wing Body (BWB) concept and intends to continue research for a broader class of hybrid wing/body aircraft. Hybrid wing/body refers to a basic vehicle concept from small aircraft through transport aircraft including piloted aircraft and Unmanned Air Vehicles (UAV). It includes platforms such as a BWB with podded or embedded engines, and Cruise Efficient Short Takeoff and Landing (CESTOL) vehicles that depend on effective integration of the propulsion and airframe systems. Combined fuel burn, noise and emissions reduction are achievable for hybrid wing/body vehicles that are significantly better than today's "tube-and-wing" subsonic aircraft.

This solicitation encompasses the full range of hybrid wing/body vehicles and it is assumed that much of the fundamental analysis and design methodology for hybrid wing/body aircraft will be applicable or adaptable, for a wide range of vehicles. However, one of the key thrusts of the Subsonic Fixed Wing Project is the advancement of "N+2" hybrid wing/body large transport vehicles that cruise at Mach .8, or greater, with payloads ranging from 12,000 to 75,000 lbs or 50 to 300 passengers and runway

lengths of less than 3000 feet for CESTOL aircraft. This range of aircraft will have the greatest impact on the environment, fuel consumption and air space capacity over the next 20 years. As a reference, Table 1 indicates the performance expected for the next generation of vehicles and technology targets for future "N+2" vehicles.

	"N+1" Generation Conventional 2012-2014	"N+2" Generation Hybrid Wing 2018-2020
Noise (cum below Stage 3)	- 42 dB	- 52 dB
Emissions (LTO NOx) (below CAEP/2)	- 70%	- 80%
Performance: Aircraft Fuel Burn (relative to 737/CFM56)	- 15%	- 25%

Table 1

The topics in Round 2 are aimed at providing critical long-term, multi-disciplinary technologies needed to enable hybrid wing/body vehicles. The approaches should have broad applications across vehicle classes, and should address the following areas:

- Focused research efforts on hybrid wing/body vehicles and propulsion systems
- Prediction of the benefits from the advanced technologies to the project goals in Table 1
- Verification of the new technologies through component or multi-component testing
- Analysis of the test results with comparisons to pre-test predictions and uncertainty analysis

NASA anticipates participation of multidisciplinary teams of educational institutions, small businesses, and companies. NASA has no responsibility for the formation of teaming arrangements. However, in order to facilitate teaming, NASA will post a list of Notices of Intent (NOI) received in response to this call, including Title, Organization, and Principal Investigator. Any prospective proposer who submits an NOI will have the option to decline the publication of their information. The hardware developed from these investments is expected to be NASA property, and the developed models, design, analysis and test results are expected to be publicly available. The objective of this investment is to stimulate innovation, and create an environment for collaboration with NASA researchers and among members of the aeronautics research community. All proposals should include detailed work plans including specific quantifiable metrics that can be used by NASA to evaluate progress.

2. Description of Solicited Research

The topics and subtopics, originally covered in the Appendix A-2, released on May 24, 2006, are not covered in this call. These are:

Topic A.2.1 - Noise Reduction (***Not covered in this call***)
- Subtopic A2.1.1 High-Fidelity Numerical Simulations
- Subtopic A2.1.2 Fundamental Diagnostic Experiments
- Subtopic A2.1.3 Aircraft Noise Prediction Tools

Topic A.2.2 - Emissions Reduction (***Not covered in this call***)
- Subtopic A.2.2.1 Physics Based Modeling
- Subtopic A.2.2.2 Fundamental Experiments
- Subtopic A2.2.3 Alternative Fuels

Topic A.2.3 - Improved Performance (***Not covered in this call***)
- Subtopic A.2.3.1 Turbomachinery Flow Control
- Subtopic A.2.3.2 Turbulence Model Development for Flow Separation
- Subtopic A.2.3.3 Innovative Aerodynamic Concepts for Vehicle Efficiency
- Subtopic A.2.3.4 Physics-based, Multi-Scale Modeling Tools for Materials

Topic A.2.4 – Hybrid wing/body Technologies

High performance, environmentally compatible flight has at its foundation highly integrated technologies addressing aerodynamic performance, vehicle weight, and propulsion system efficiency. To meet future performance, noise and emissions goals, new configuration concepts with highly integrated airframe and propulsion systems will be required. The notion of a hybrid wing/body concept used in this solicitation encompasses several ideas: 1) a very closely-coupled aero-structure for blending traditional aircraft components, 2) very closely-coupled propulsion/airframe integration, 3) a very closely-coupled airframe/propulsion/flight controls system, and 4) ideally some combination of the three. The resulting hybrid wing/body vehicle should offer efficient high-speed cruise with quiet takeoff and landing, and sufficient stability and control characteristics throughout the flight envelope. Note that a hybrid wing/body vehicle is not limited to a tailless vehicle.

NASA anticipates investing approximately $10M in this topic over the next three years; at about $3M for year 1, $4M for year 2, and $3M for year 3. NASA plans to award between 4 and 8 proposals for this topic for the first phase, with a period of performance of one year. There will be a down select to 1-3 proposals for the second phase, which should take an additional two years. NASA anticipates awarding contracts for this topic that will be structured with a base year for the first phase and an option for two years for the second phase. Proposals submitted under this topic must cover both the first and second phases. The down-select decision at the end of the first phase will be based on:

- NASA's judgment of the progress made during the first year relative to quantifiable metrics defined in the proposal and agreed to by the NASA Technical Monitor at the onset of the contract.
- NASA's judgment of the impact the technologies being developed will have on the goals of the SFW project.
- NASA's judgment of the ability to extend and validate prediction tools to model physics associated with advanced hybrid wing/body technologies.

- The availability of resources to support the proposed work for the second and third years.

The underlying challenge towards the end-goal of enabling new vehicle or component concepts and capability is high-confidence, preflight prediction of all aspects of flight. The introduction of new technologies and configurations is too often limited by insufficient confidence in the eventual performance of a concept in flight. As such, this topic seeks to develop and validate improved prediction capabilities applicable to a range of subsonic fixed wing aircraft, but with validation for advanced hybrid wing vehicle enabling technologies at conditions relevant to flight. Work plans for all sub-topics within this topic should be structured as follows:

Phase 1 (1 year):

a) Investigate vehicle concept(s) offering revolutionary capability to meet the "N+2" project goals and determine what advances in analysis codes are needed to realize these concepts.
b) Establish the current state of the art for prediction methods and begin to extend their capabilities toward assessing key technologies that enable the new vehicle concept(s).
c) For each key technology identified in (b), obtain data at the component or sub-component level (either existing or new) that provide sufficient validation of the prediction methods. At the conclusion of the first year, there should be clear evidence that the prediction methods can be used to evaluate the key technologies needed to enable the concept(s) identified in (a).

Phase 2 (2 years) (if selected):

d) Refine prediction capabilities for evaluating the most promising enabling technologies.
e) Design, fabricate, and test concepts at the subcomponent, component, integrated components, and/or configuration level to provide validation data for the advanced prediction methods in a relevant environment and quantify the benefit of the enabling technologies applied to the advanced concept.
f) Document the results including an assessment of the prediction accuracy.

In order to support the down-select decision before Phase 2, proposers should plan to submit a summary report at the end of the first year that describes the capabilities of the predictive method developed in Phase 1 along with justification of what further developments are needed to test an advanced configuration in Phase 2.

It is reasonable, but not required, to propose use of NASA facilities for testing. If NASA facilities are proposed, the cost will be covered by NASA internal resources pending negotiations on cost and schedule, but the proposer is required to account for the cost of design and fabrication for wind tunnel models, support hardware, or advanced measurement capabilities in the proposal. The cost must be included in the proposal for any non-NASA facilities that are proposed. Information on NASA facilities can be found at the web sites listed in Section 5 of this solicitation.

Each proposal shall address one of the four subtopics listed below; multiple proposals may be submitted from a principal investigator (PI). Additional subtopics may be released in subsequent solicitations.

Subtopic A.2.4.1 Low Speed, High Lift, and Low Noise Technologies

Objective

The objective of this subtopic is to develop and validate predictive capabilities for the key low-speed, high-lift advanced technologies related to the performance of hybrid wing/body vehicles with high cruise efficiency and low-noise takeoff and landing characteristics. For CESTOL vehicles, the hybrid wing/body should also include enabling technologies for short takeoff and landing. Specifically, proposals are sought to provide prediction methods, design and fabrication of test hardware for advanced hybrid wing/body concepts, test data, and analysis of test data for:

- Low-speed aerodynamic characteristics up to and beyond the maximum lift of a hybrid wing/body system, component, or subcomponent.
- Acoustic characteristics of a low-noise hybrid wing/body system, component, or subcomponent.
- Stability and control characteristics of a hybrid wing/body system, component, or subcomponent throughout the flight envelope.

Relevant SFW Milestones

SFW.1.11.05 - Experimental data for low-speed separation onset and control
SFW.2.04.22 - Develop/Improve & Validate Next Generation Multi-Fidelity Component & Aircraft Noise Prediction Capability
SFW.2.04.32 - Predict & Validate Advanced Low-Noise Airframe Configuration Benefits
SFW.2.04.33 - Design, Predict & Validate Noise Reduction Concepts for Aircraft
SFW.2.06.02 - Low-speed high-lift prediction to maximum lift
SFW.2.09.03 - Demonstrate Improved Phased Microphone Array for Noise Model Validation

Approach

Integrated vehicle efficiency has significantly improved over the decades, but further advances are yet to be realized. Hybrid wing/body concepts seek to revolutionize the coupling of aerodynamic, structural, propulsion, controls, and other systems to the benefit of the overall vehicle system. In order to realize the potential benefits, predictive tools must accurately predict the characteristics of the new hybrid wing/body applied technologies to provide sufficient confidence for the eventual end-users to implement in the design of practical new vehicles.

Proposals are sought which include the development of improved prediction methods, and the development of hardware to test and validate the improved predictive tools as applied to hybrid wing/body configurations. The first step in the process is to validate the predictive tools with the best available data, but in order to fully understand their

capabilities, there is an expectation that additional testing will be needed with unconventional configurations (for subcomponent, component, or integrated components). This second validation will be the focus of the second phase of this effort. Development of new measurement and/or experimental techniques necessary to validate prediction methods or advanced technologies/concepts may be incorporated in the proposals. In addition to validating the capabilities of the predictive tool, it is desired that proposers use this opportunity to further investigate the potential advantages and limitations of the new configurations being tested to better understand how they may someday contribute to enabling the "N+2" project goals identified in Table 1 of Section 1. Multi-partner proposals are envisioned to develop advanced computational analysis, modeling and design techniques, and experimental measurement of airframe components in a flow environment relevant to hybrid/wing body vehicles.

Advanced technology areas relevant to this subtopic include low-speed high-lift aerodynamic concepts, low-noise propulsion/airframe acoustic concepts, and stability and control characteristics throughout the flight envelope. Proposals addressing multiple approaches are of particular interest. In the high-lift performance area, concepts of interest could include variable geometry, powered-lift, circulation control, and separation control concepts with an emphasis on the accurate prediction of separation onset and progression. In the propulsion/airframe acoustics area, emphasis is on advanced acoustic prediction with the objective of including the complex effects from the highly integrated configuration; concepts of interest include engine noise shielding, noise generation and propagation from the complex shear layer developed on the fuselage and from control surfaces, and airframe component noise such as drooped leading edges with variable geometry, landing gear, and continuous mold line (CML) flaps/elevons. In the stability and control area, the emphasis is on simulation of flight control characteristics using elevons, wing tip rudders, thrust vectoring, distributed propulsion controls, drooped leading edge with variable geometry, and CML flaps/elevons.

It is reasonable, but not required, to propose use of NASA facilities for testing. If NASA facilities are proposed, the cost will be covered by NASA internal resources pending negotiations on cost and schedule, but the proposer is required to account for the cost of design and fabrication for wind tunnel models, support hardware, or advanced measurement capabilities in the proposal. The cost must be included in the proposal for any non-NASA facilities that are proposed. Information on NASA facilities can be found at the web sites listed in Section 5 of this solicitation.

Outcome (Note for this subtopic a contract is expected with deliverables)
Prediction tools for the prediction of low-speed performance of cruise efficient hybrid wing/body vehicles with low noise and flight-worthy stability and control characteristics will be developed and validated. Documentation will be available summarizing benefits and the uncertainty of the predictive tools based on post-test analysis. Test databases will be documented for future validation of further improvements to predictive tools. Analysis will be conducted to better understand the advantages and limitations of the advanced concepts that are tested. Test hardware, including new measurement

techniques, will be available for future modification and test. Test articles developed as a part of this work shall be delivered to NASA.

Subtopic A.2.4.2 – Integrated Embedded Propulsion Systems

Objective

The objective of this subtopic is to develop verified analysis capabilities for the key technical issues related to integrating embedded propulsion systems for "N+2" hybrid wing/body configurations. These key technical issues include: inlet technologies for distorted engine inflows related to embedded engines with boundary layer ingestion; fan-face flow distortion and its effects on fan efficiency and operability, noise, flutter stability and aeromechanical stress and life; wide operability of the fan and core with a variable area nozzle; issues related to the implementation of a thrust vectoring variable area nozzle; and duct losses related to long flow paths associated with embedded engines. Specifically, proposals are sought to provide prediction methods, design and fabrication of test hardware for advanced hybrid wing/body concepts, test data, and analysis of test data for one or more of the following areas:

- Analysis and verification of inlet distortion expected for embedded engines in a hybrid wing/body vehicle due to boundary layer ingestion from the vehicle body. The levels and types of inflow distortion should be assessed for embedded engine inflows typical of what might be encountered in hybrid wing/body applications. Management techniques for this distortion (such as inlet guide vanes, inlet lip virtual shaping and/or inlet passive or active flow control) should be assessed.
- Analysis and verification of the effects of fan-face distortion propagated through the inlet on the embedded engines in a hybrid wing/body vehicle. The levels and types of fan-face distortion should be assessed for embedded engine inflows typical of what might be encountered in hybrid wing/body applications. Management techniques for this distortion (such as advanced fan design techniques) should be assessed. Fan noise, aeromechanical stress and life, aerodynamic performance, and stall margin should be considered in the presence of the flow distortion typical of highly-integrated propulsion systems.
- Analysis and verification of fan and compressor flutter stability, forced response vibrations, and non-synchronous vibrations due to large inlet distortions, variable geometry and wide variations in operating conditions. Work should cover efficient approaches to fan/compressor aeroelastic analysis and identify design-oriented methods to screen for aeroelastic vibrations. The effects of turbulence, unsteady separation and highly separated flows on aeroelastic vibrations should be assessed.
- Analysis and verification of fan aerodynamic performance subjected to wide incidence angle changes resulting from variable area nozzles associated with embedded engines for potential hybrid wing/body vehicles. Methods for designing fans and exit guide vanes with higher incidence angle variation (through variable geometry and/or with passive or active flow control) should be assessed.
- Analysis and verification of duct losses and thrust vectoring variable area nozzle thrust losses associated with embedded engines for potential hybrid wing/body

A13. TDI Refurbishment Report

Turbine Propulsion Simulator Information

Prior to using the installing the engine simulators in the AMELIA model the TPS units were refurbished and operationally checked out by Tech Development Inc (TDI). The materials in this section include the 441 TPS Units manufacturer specifications and the two TDI refurbishment and check out reports.

TECH DEVELOPMENT INC.

TPS SUMMARY PERFORMANCE CHARACTERISTICS

	MODEL NUMBER											
	441	460	800	1079	1200	1300	1400	1410	1500	2601	2700	2701
Year Introduced	1965	1966	1972	1977	1978	1979	1982	1983	1983	1995	1996	1997
Inlet Diameter (In.)	5.00	4.10	2.81	3.45	2.81	4.20	9.09	16.14	5.00	8.70	6.00	4.80
Overall Diameter (In.)	5.66	4.29	3.15	3.95	3.33	4.75	9.92	17.61	5.50	10.38	6.83	5.20
Overall Length (In.)	11.33	6.57	6.00	7.12	6.04	8.13	15.96	27.64	8.56	10.98	12.04	6.65
RPM	45000	80000	86500	70500	80000	59000	35500	20000	64600	33000	51200	59300
Pressure Ratio	1.55	1.60	1.65	1.65	1.55	1.65	1.75	1.75	1.75	1.44	1.7	1.56
Flow (Lbm/Sec)	4.48	2.72	1.35	2.03	1.40	3.02	13.40	42.20	4.05	14.37	5.61	4.21
Stages	2	1	2	2	2	2	1	1	1	1	1	1
Annulus Flow*		36.53					39.89			39.5		
Hub/Tip Ratio		.43					.50	.50	.50	.34	.50	.34
Aspect Ratio**		1.48					1.24			1.90		1.90
Tip Solidity***		1.06					1.46			1.34		1.34
Specific Flow****	32.82	29.7	31.3	31.3	32.5	31.3	29.7	29.7	29.7	34.8		33.5
Tip Speed (Ft/Sec)		1430					1400			1250		1242
Blade Count		18					25			22	25	22

* Weight Flow Per Unit Annulus Area, LBM/SEC/FT^2
** Average Length Over Root Chord
*** Ratio of Chord to Spacing
**** Weight Flow Per Unit Frontal Area, LBM/SEC/FT^2

TECH DEVELOPMENT INC.

6800 Poe Avenue • P.O. Box 13557 • Dayton, Ohio 45413-0557

PRICE LIST
PROPULSION SIMULATION EQUIPMENT

POWERED HIGH-BYPASS FANJET ENGINE SIMULATORS*				
MODEL NO.	(1)	(2)	(3)	NOTE
441	235,950	225,167	219,127	1, 2
800	152,944	145,422	141,209	1, 2
1079	163,008	154,998	150,478	1, 2
1200	157,983	150,217	145,850	1, 2
1300	175,707	167,052	162,182	1, 2
1400	383,812	366,271	356,446	1, 3
1410	767,624	732,544	712,892	1, 3
1500	216,828	205,997	199,905	1, 3
2600	369,578	351,099	343,228	1, 3
2601	539,000	512,050	496,958	1, 3
2700	518,100	492,195	477,688	1, 10

434,262

TIP TURBINE FAN SIMULATORS*				
MODEL NO.	(1)	(2)	(3)	NOTE
292-1C	84,436	80,577	78,417	1
292-1L	84,436	80,577	78,417	1
457	58,050	55,147	53,493	1, 4
897	44,044	42,032	40,905	1
1109	126,654	120,866	117,624	1, 4

EJECTOR TYPE ENGINE SIMULATORS*				
MODEL NO.	(1)	(2)	(3)	NOTE
350	27,685	26,421	25,710	1
405	15,788	15,067	14,663	1
530	15,540	14,762	14,315	1
870	15,238	14,543	14,154	1
898	14,115	13,423	13,020	1
1666	22,579	21,643	21,062	1
1900	38,166	36,423	35,444	1
2008	28,718	27,407	26,673	1
2691	15,400	14,630	14,199	1

TURBINE POWERED AIR MOTORS*				
MODEL NO.	(1)	(2)	(3)	NOTE
646	77,000	73,150	70,994	1, 8
666E	77,000	73,150	70,994	1,2,7,8
666H	77,000	73,150	70,994	1,2,7,8
845A	54,479	51,755	50,203	1, 8,
866A	38,500	36,575	35,882	1, 4, 8
1234	586,278	556,970	540,507	1, 3, 8
1277	586,278	556,970	540,507	1, 3, 8
1555A	220,000	209,000	202,840	1, 3, 8
1700A	267,410	255,190	248,344	1, 5, 8
1724	642,562	610,445	592,400	1, 8
1999	72,416	68,785	66,755	1,2,6,8
2000	280,656	268,820	262,182	1, 5, 9
2100	367,925	349,528	339,042	1, 6, 8

NOTES:
1. All prices listed are in U.S. Dollars and include packing for export.
2. Pulse lubrication systems included.
3. Circulating oil lubrication system included.
4. Oil mist lubrication system included.
5. Two (2) pulse lubrication systems included.
6. Exit guide vane assembly included.
7. Exit guide vane assemblies available at $10,696 each in purchase quantity of one (1).
8. Special motor output shaft configurations are available at additional cost.
9. Special hub contours and blade attachments available at additional cost.
10. Circulating lube system included first unit only

* Unit Prices Based Upon the Quantities Shown

Telephone: (937) 898-9600
Engineering Fax: (937) 898-6846
Marketing/Order Entry Fax: (937) 898-8431
www.tdiairstarters.com

AN00-416 Issued JULY 14, 2000

A Smiths Industries Company

TURBOFAN PROPULSION SIMULATOR

PRODUCT SPECIFICATION

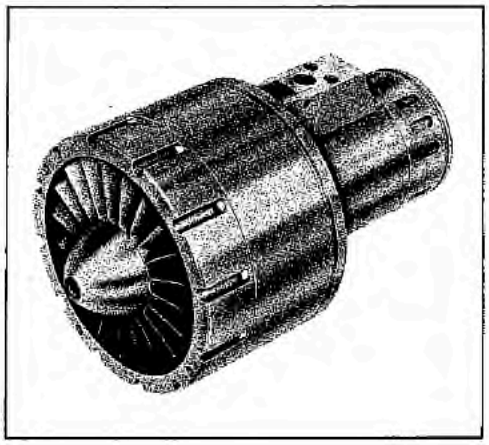

GENERAL INFORMATION

The use of Tech Development Inc Simulated Turbofan Engines* in wind tunnel aircraft models makes possible such studies as:

- High speed drag interference phenomena
- Effects of power on high and low speed stability and control parameters
- Effects of power on high lift parameters
- Thrust reverser aerodynamics
- Inlet and cowling development

The Model 441 Turbofan Simulator features a two stage fan driven by a three stage turbine. Corrosion resistant materials are used throughout. Bearing thermocouples and a magnetic speed pickup are provided.

*U.S. Patent 3434679

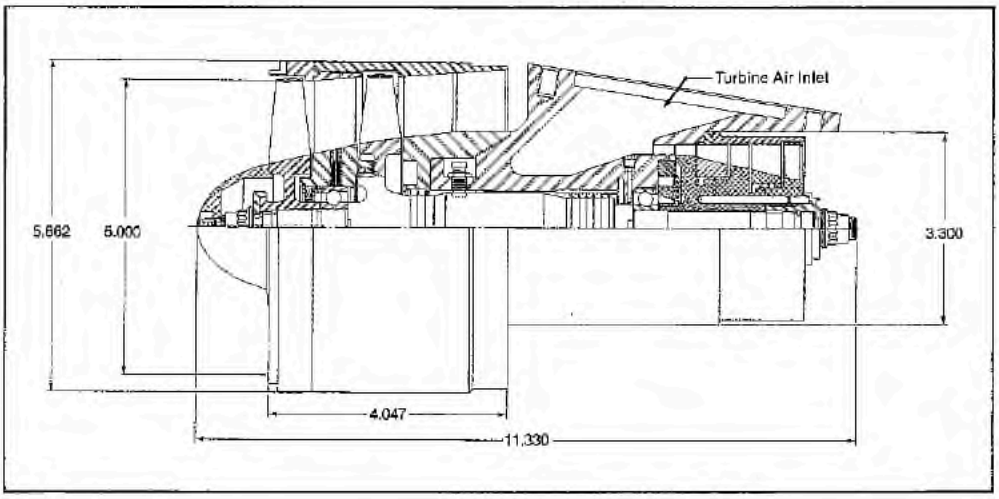

TECH DEVELOPMENT INC.

8800 Poe Ave., P.O. Box 14557, Dayton, Ohio 45414
Telephone: (513)898-9600 / TWX:810-472-2822

MODEL 441
Turbofan Propulsion Simulator

TECH DEVELOPMENT INC.
6800 Poe Ave., P.O. Box 14567, Dayton, Ohio 45414
Telephone: (513)898-9600 / TWX:810-472-2822

OPERATION

The two adjacent graphs show the Model 441 performance data. A typical operating point is a fan pressure ratio of 1.55 at 45,000 rpm, with a fan airflow of 4.48 lbm/sec. The corresponding turbine drive gas requirements are an inlet pressure of 425 psig, with a flow of 2.08 lbm/sec at 60°F.

INSTALLATION

The drawing on the reverse side shows the Model 441 envelope dimensions. The model is attached by means of two bolts to a suitable mount incorporating an air inlet passage. Please contact TDI for more specific information on the Model 441 performance and installation requirements.

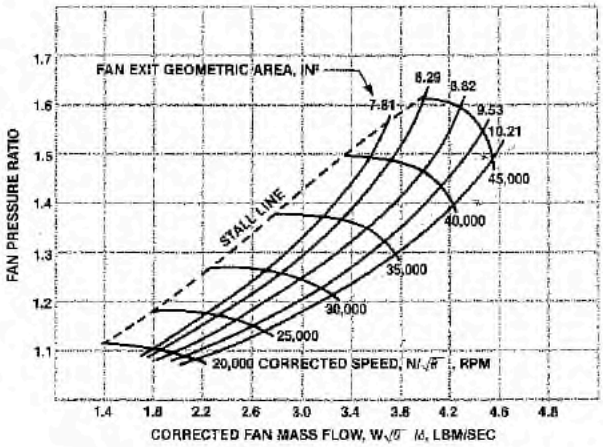

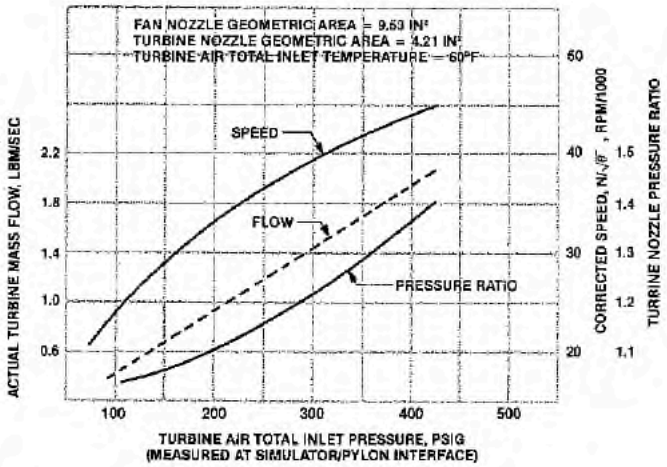

AN85-534

TECH DEVELOPMENT

TDI MEMO

DATE: 10 October 2009

TO: W.O. 3082 Engineering File

FROM: Brian C. Kemp

SUBJECT: Checkout Run of Model 441 Simulator – S/N's 1, 3 and 4

COPY: Bob Montgomery

I. INTRODUCTION

Model 441 serial number 1, 3 and 4 were manufactured in 1966 for NASA LaRC under Tech Development's work order 441 along with (2) additional units (S\N's 2 and 5). S/N's 2 and 5 were not refurbished under this effort.

All units were returned to TDI for an upgrade in 1971. The grease lubricated rear bearing was change to oil wick and the turbine section was weight reduced under work order 772. Numerous refurbishments of the subject TPS units have been completed since the 1972 rework. No additional modifications have been recorded.

Mechanical checkout tests were conducted between 23 and 25 June 2009.

TDI
TECH DEVELOPMENT

II. MODEL AND TEST APPARATUS

The Model 441's were mounted to a TDI-provided pylon block that interfaces with the simulator Model B. This part also contains the turbine air supply port. The test inlet for mounting the air supply hose was sandwiched between the pylon block and a mounting plate. The mounting plate was mounted to a phenolic block which in turn is mounted to the test bench plate, D-21602.

All test runs were completed with the inlet cowl and the exit cowl. The exit cowl created a 9.86 in^2 exit area (REF: Figures 1 and 2).

Figure 3 shows a drawing of the fan exit cowl used in the check-out test.

III. INSTRUMENTATION

The turbine supply air conditions (at the venturi flow meter) and cell temperatures were read out on the panel mounted Omega Model 660 thermal meter (J calibration).

Each set of forward and aft bearing thermocouples were connected to separate Omega DPS-3204 T/C Scanning indicators. The devices were adjusted for type K thermocouples for runs 1 thru 4. A single forward and a single aft thermocouple were used as an emergency trip. The forward bearing temperature trip was set at 225°F. The aft bearing temperature trip was set at 125°F for all runs.

An accelerometer (Endevco Model 256HX-10, S/N) was mounted on the simulator fan case (REF: Figure 1). The accelerometer signal was fed into a Data Physics Quattro Ace dynamic signal analyzer. Only the 1/rev peak frequencies were manually recorded.

Each of the two magnetic pickups in the simulator read 6 counts per revolution. One signal was read by a DIGITEC frequency meter and overspeed trip with the gate set at 1 sec. This, therefore, displayed rpm divided by 10. The second pickup signal was fed to a Tektronix Oscilloscope Model T935A, S/N T935A B022698, for measurement of its output voltage level.

The airflow rates supplied to the simulator turbine were determined using the facility venturi flow meter.

Plenum pressure was measured using the pressure tube embedded in the test unit inlet plenum.

The aft bearing position was supplied with lubrication using a pulse oiler system (REF: Figure 4). The units were originally configured for a fixed volume fill of lubricant that is to be checked and refilled at a specific interval. All of the units were tested using pulse oil distribution at a rate of 10 cc/hr. The drain tube that was utilized in the fixed lube volume operational approach was capped off for the testing.

TECH DEVELOPMENT

IV. TEST PROGRAM

The tests were conducted for the purpose of demonstrating the mechanical integrity of the overhauled units.

These simulators were run at the following approximate speeds and cumulative durations,

SN 1

Operating Speed (rpm)	Cumulative Duration @ Speed (min)
10,000	1
15,400	2
20,100	2
35,300	4
40,000	2
44,000	5
TOTAL	16 minutes

SN 3

Operating Speed (rpm)	Cumulative Duration @ Speed (min)
10,000	2
15,400	2
20,500	2
35,200	5
40,000	3
44,000	5
TOTAL	19 minutes

SN 4

Operating Speed (rpm)	Cumulative Duration @ Speed (min)
10,600	2
15,200	3
20,300	3
24,300	7
35,200	4
40,000	5
44,000	6
TOTAL	30 minutes

Data was recorded by hand on data sheet forms during the steady state periods. The bearing temperature thermocouple pairs, fed to temperature meters, were read to verify consistent output with their mates.

V. RESULTS

Supply pressure was measured using the plenum pressure tap in the air supply pipe to the simulator. The following table shows the favorable performance of the tested units (S/N 1, 3 and 4).

	CORRECTED SPEED [RPM]	PLENUM PRESSURE [PSIG]	TURBINE MASS FLOW [LBM/SEC]	FWD BRG TEMP Δ [°F]	AFT BRG TEMP Δ [°F]	VIBRATION (peak G's) 1P
TEST DATE-25 JUNE 2009	34833	160	1.05	75	1	.5
UNIT S/N-001	39471	220	1.40	71	-6	2.2
	43418	270	1.70	76	10	1.8
TEST DATE 24 JUNE 2009	34734	175	1.00	54	-4	.2
UNIT S/N-003	39471	245	1.38	55	0	1.0
	43517	305	1.71	102	19	.8
TEST DATE 23 JUNE 2009	34537	175	1.01	64	9	.2
UNIT S/N-004	39471	240	1.38	58	13	.4
	43418	300	1.68	83	14	.6

Fwd bearing temperature rise is the thermocouple reading as measured with the digital meter reading minus the cell temperature (°F). The aft bearing temperature difference is the supply air temperature minus the rear bearing temperature.

The data reduction program M441 output and test data, taken both in reduced and unreduced format, are included in this report as reference material.

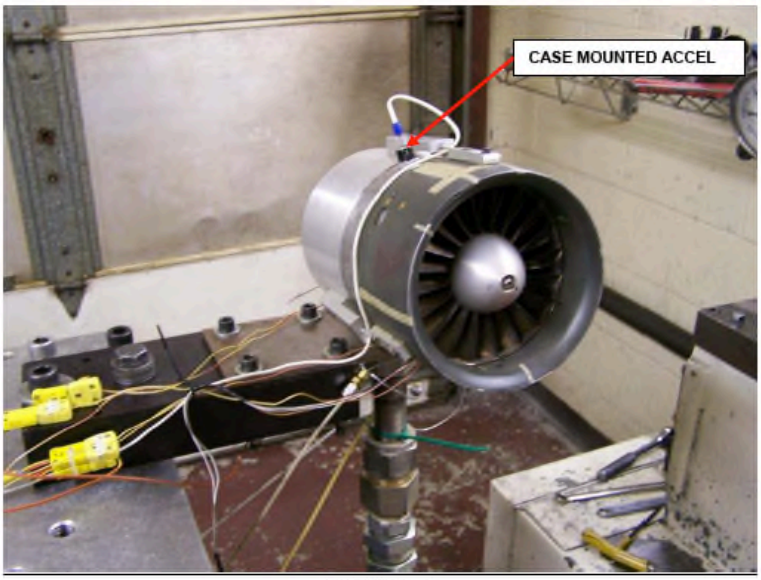

FIGURE 1

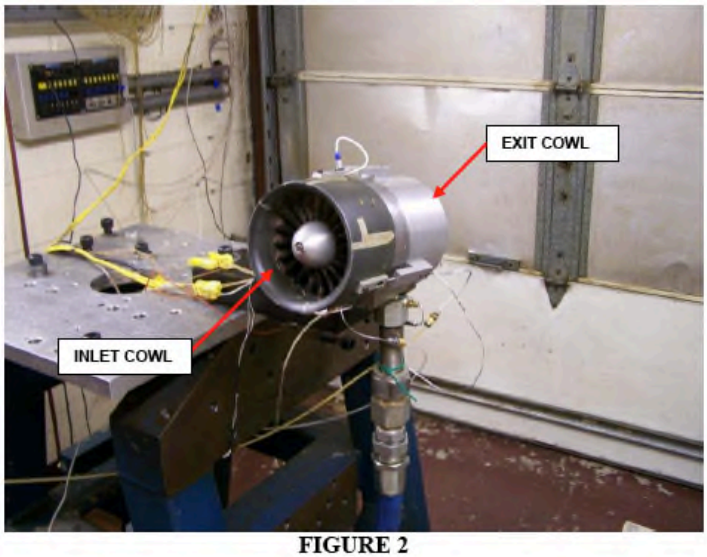

FIGURE 2

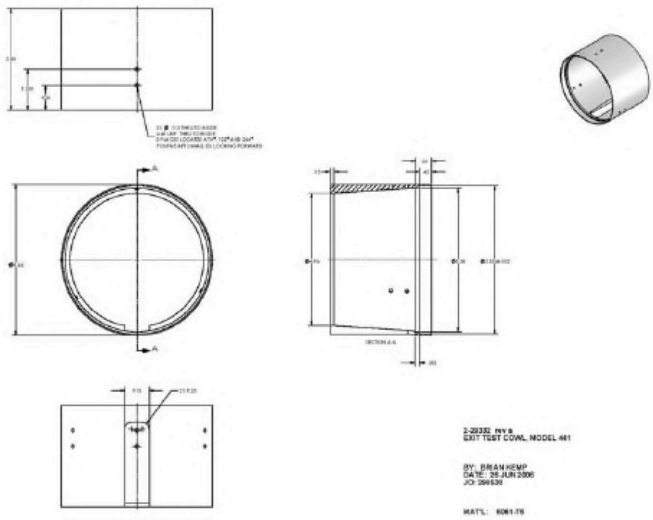

FIGURE 3

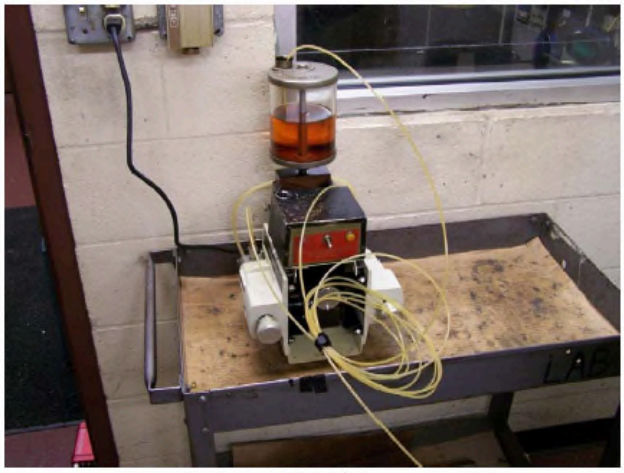

FIGURE 4

TECH DEVELOPMENT

REDUCED TEST DATA

08-18-2009 16:14:59

MODEL 441 TURBOFAN SIMULATOR
PROJECT NO. W0308230
TEST DATE 06-25-09
S/N 1

VENTURI THROAT = .7492 INCH
VENTURI SIZE = 1.275 INCH

T E S T D A T A

RUN	PT	TURB T DEG F	BAROM IN HG	CELL T DEG F	SPEED RPM	PLENUM P PSIG
1	1	73	30.02	73	10000	9
1	2	68	30.02	73	15400	30
1	3	66	30.02	73	20100	50

RUN	PT	TIME OF DAY	FR BRG (F) (610)	FR BRG (F) (611)	AFT BRG (F) (612)	AFT BRG (F) (613)	VIBRATION RMS (G'S)	SPEED PICK UP VOLTAGE (VOLTS)
1	1	10	83	82	73	73	0.0	1.4
1	2	10	124	122	74	76	0.1	2.1
1	3	10	129	127	72	70	0.2	2.6

RUN	PT	N(COR) RPM	FWD BRG TEMP RISE (F)	AFT BRG DELTA TEMP (F)
1	1	9868	10	0
1	2	15196	50	7
1	3	19834	55	5

RUN	PT	DRIV.AIR Pt PSIG	PLENUM T-DEGF	T-AMB F	P-AMB IN-HG
1	1	9.0	73	73	30.02
1	2	30.0	68	73	30.02
1	3	50.0	66	73	30.02

RUN	PT	VENTURI INLET Ps	FLOW-PSIG DEL-P	FLOW TEMP (F)
1	1	18	1.10	72
1	2	43	2.00	69
1	3	71	3.06	67

P E R F O R M A N C E D A T A

RUN	PT	TURBINE W #/SEC
1	1	0.13
1	2	0.23
1	3	0.35

RUN	PT	PLENUM P PSIG (CORR)	TURBINE W #/SEC (CORR)
1	1	9	0.13
1	2	30	0.24
1	3	50	0.36

08-18-2009 16:17:29 MODEL 441 TURBOFAN SIMULATOR

PROJECT NO. WO308230
TEST DATE 06-25-09
S/N 1

VENTURI THROAT = .7492 INCH
VENTURI SIZE = 1.275 INCH

T E S T D A T A

RUN	PT	TURB T DEG F	BAROM IN HG	CELL T DEG F	SPEED RPM	PLENUM P PSIG
1	4	64	30.02	73	35300	160
1	5	69	30.02	73	40000	220
1	6	75	30.02	73	44000	270
1	7	78	30.02	73	43000	265

RUN	PT	TIME OF DAY	FR BRG (F) (610)	FR BRG (F) (611)	AFT BRG (F) (612)	AFT BRG (F) (613)	VIBRATION RMS (G'S)	SPEED PICK UP VOLTAGE (VOLTS)
1	4	10	148	148	65	65	0.5	4.2
1	5	10	144	143	62	64	2.2	4.7
1	6	10	149	149	82	87	1.8	5.1
1	7	10	130	132	82	86	1.4	5.0

RUN	PT	N(COR) RPM	FWD BRG TEMP RISE (F)	APT BRG DELTA TEMP (F)
1	4	34833	75	1
1	5	39471	71	-6
1	6	43418	76	10
1	7	42431	58	6

RUN	PT	DRIV.AIR Pt PSIG	PLENUM T-DEGF	T-AMB F	P-AMB IN-HG
1	4	160.0	64	73	30.02
1	5	220.0	69	73	30.02
1	6	270.0	75	73	30.02
1	7	265.0	78	73	30.02

RUN	PT	VENTURI INLET Ps	FLOW-PSIG DEL-P	FLOW TEMP (F)
1	4	238	9.20	65
1	5	324	12.39	71
1	6	399	15.10	78
1	7	386	14.57	82

P E R F O R M A N C E D A T A

RUN	PT	TURBINE W #/SEC
1	4	1.05
1	5	1.40
1	6	1.70
1	7	1.63

RUN	PT	PLENUM P PSIG (CORR)	TURBINE W #/SEC (CORR)
1	4	161	1.06
1	5	222	1.43
1	6	274	1.75
1	7	270	1.69

TECH DEVELOPMENT

08-18-2009 16:19:54 MODEL 441 TURBOFAN SIMULATOR

PROJECT NO. WO308230
TEST DATE 06-24-09
S/N 3

VENTURI THROAT = .7492 INCH
VENTURI SIZE = 1.275 INCH

T E S T D A T A

RUN	PT	TURB T DEG F	BAROM IN HG	CELL T DEG F	SPEED RPM	PLENUM P PSIG
1	1	70	30.09	73	10000	10
1	2	67	30.09	73	15400	35
1	3	65	30.09	73	20500	55

RUN	PT	TIME OF DAY	FR BRG (F) (610)	FR BRG (F) (611)	AFT BRG (F) (612)	AFT BRG (F) (613)	VIBRATION RMS (G'S)	SPEED PICK UP VOLTAGE (VOLTS)
1	1	10	88	88	78	78	0.1	1.6
1	2	10	96	96	82	78	0.0	2.2
1	3	10	112	114	84	82	0.1	2.8

RUN	PT	N(COR) RPM	FWD BRG TEMP RISE (F)	AFT BRG DELTA TEMP (F)
1	1	9868	15	8
1	2	15196	23	13
1	3	20229	40	18

RUN	PT	DRIV.AIR Pt PSIG	PLENUM T-DEGF	T-AMB F	P-AMB IN-HG
1	1	10.0	70	73	30.09
1	2	35.0	67	73	30.09
1	3	55.0	65	73	30.09

RUN	PT	VENTURI INLET Ps	FLOW-PSIG DEL-P	FLOW TEMP (F)
1	1	19	1.09	72
1	2	42	1.90	68
1	3	73	3.00	66

P E R F O R M A N C E D A T A

RUN	PT	TURBINE W #/SEC
1	1	0.13
1	2	0.23
1	3	0.35

RUN	PT	PLENUM P PSIG (CORR)	TURBINE W #/SEC (CORR)
1	1	10	0.13
1	2	35	0.23
1	3	55	0.36

TECH DEVELOPMENT

08-18-2009 16:21:06 MODEL 441 TURBOFAN SIMULATOR

PROJECT NO. W0308230
TEST DATE 06-24-09
S/N 3

VENTURI THROAT = .7492 INCH
VENTURI SIZE = 1.275 INCH

T E S T D A T A

RUN	PT	TURB T DEG F	BAROM IN HG	CELL T DEG F	SPEED RPM	PLENUM P PSIG
1	4	65	30.09	73	35200	175
1	5	71	30.09	73	40000	245
1	6	76	30.09	73	44100	305
1	7	79	30.09	73	43400	300

RUN	PT	TIME OF DAY	FR BRG (F) (610)	FR BRG (F) (611)	AFT BRG (F) (612)	AFT BRG (F) (613)	VIBRATION RMS (G'S)	SPEED PICK UP VOLTAGE (VOLTS)
1	4	11	128	126	64	59	0.2	3.0
1	5	11	128	128	74	68	1.0	3.4
1	6	11	176	174	98	92	0.8	3.7
1	7	11	151	150	93	88	2.2	3.6

RUN	PT	N(COR) RPM	FWD BRG TEMP RISE (F)	AFT BRG DELTA TEMP (F)
1	4	34734	54	-4
1	5	39471	55	0
1	6	43517	102	19
1	7	42826	78	12

RUN	PT	DRIV.AIR Pt PSIG	PLENUM T-DEGF	T-AMB F	P-AMB IN-HG
1	4	175.0	65	73	30.09
1	5	245.0	71	73	30.09
1	6	305.0	76	73	30.09
1	7	300.0	79	73	30.09

RUN	PT	VENTURI INLET Ps	FLOW-PSIG DEL-P	FLOW TEMP (F)
1	4	233	8.64	67
1	5	328	11.96	74
1	6	412	14.93	80
1	7	390	14.10	84

P E R F O R M A N C E D A T A

RUN	PT	TURBINE W #/SEC
1	4	1.00
1	5	1.38
1	6	1.71
1	7	1.61

RUN	PT	PLENUM P PSIG (CORR)	TURBINE W #/SEC (CORR)
1	4	176	1.02
1	5	248	1.41
1	6	310	1.77
1	7	306	1.68

TDI TECH DEVELOPMENT

08-18-2009 16:22:54 MODEL 441 TURBOFAN SIMULATOR

PROJECT NO. WO308230
TEST DATE 06-23-09
S/N 4

VENTURI THROAT = .7492 INCH
VENTURI SIZE = 1.275 INCH

T E S T D A T A

RUN	PT	TURB T DEG F	BAROM IN HG	CELL T DEG F	SPEED RPM	PLENUM P PSIG
1	1	69	30.05	73	10600	10
1	2	66	30.05	73	15200	23
1	3	65	30.05	73	20300	55
1	4	65	30.05	73	24300	80

RUN	PT	TIME OF DAY	FR BRG (F) (610)	FR BRG (F) (611)	AFT BRG (F) (612)	AFT BRG (F) (613)	VIBRATION RMS (G'S)	SPEED PICK UP VOLTAGE (VOLTS)
1	1	11	97	88	75	74	0.1	0.2
1	2	11	94	92	71	71	0.1	0.3
1	3	11	142	123	66	67	0.0	0.4
1	4	11	150	129	70	70	0.1	0.4

RUN	PT	N(COR) RPM	FWD BRG TEMP RISE (F)	AFT BRG DELTA TEMP (F)
1	1	10460	20	6
1	2	14999	20	5
1	3	20031	60	2
1	4	23979	67	5

RUN	PT	DRIV.AIR Pt PSIG	PLENUM T-DEGF	T-AMB F	P-AMB IN-HG
1	1	10.0	69	73	30.05
1	2	23.0	66	73	30.05
1	3	55.0	65	73	30.05
1	4	80.0	65	73	30.05

RUN	PT	VENTURI INLET Ps	FLOW-PSIG DEL-P	FLOW TEMP (F)
1	1	20	1.17	67
1	2	42	1.91	64
1	3	73	2.99	62
1	4	105	4.10	63

P E R F O R M A N C E D A T A

RUN	PT	TURBINE W #/SEC
1	1	0.14
1	2	0.23
1	3	0.35
1	4	0.48

RUN	PT	PLENUM P PSIG (CORR)	TURBINE W #/SEC (CORR)
1	1	10	0.14
1	2	23	0.23
1	3	55	0.36
1	4	81	0.49

TECH DEVELOPMENT

08-18-2009 16:29:15 MODEL 441 TURBOFAN SIMULATOR

PROJECT NO. WO308230
TEST DATE 06-23-09
S/N 4

VENTURI THROAT = .7492 INCH
VENTURI SIZE = 1.275 INCH

T E S T D A T A

RUN	PT	TURB T DEG F	BAROM IN HG	CELL T DEG F	SPEED RPM	PLENUM P PSIG
2	1	69	30.05	73	25100	80
2	2	68	30.05	73	35000	175

RUN	PT	TIME OF DAY	FR BRG (F) (610)	(611)	AFT BRG (F) (612)	(613)	VIBRATION RMS (G'S)	SPEED PICK UP VOLTAGE (VOLTS)
2	1	13	105	103	70	70	0.2	0.5
2	2	13	138	135	77	76	0.2	0.6

RUN	PT	N(COR) RPM	FWD BRG TEMP RISE (F)	AFT BRG DELTA TEMP (F)
2	1	24768	31	1
2	2	34537	64	9

RUN	PT	DRIV.AIR Pt PSIG	PLENUM T-DEGF	T-AMB F	P-AMB IN-HG
2	1	80.0	69	73	30.05
2	2	175.0	68	73	30.05

RUN	PT	VENTURI INLET Ps	FLOW-PSIG DEL-P	FLOW TEMP (F)
2	1	111	4.36	68
2	2	235	8.77	68

P E R F O R M A N C E D A T A

RUN	PT	TURBINE W #/SEC
2	1	0.51
2	2	1.01

RUN	PT	PLENUM P PSIG (CORR)	TURBINE W #/SEC (CORR)
2	1	81	0.52
2	2	177	1.03

TECH DEVELOPMENT

08-18-2009 16:30:43 MODEL 441 TURBOFAN SIMULATOR

PROJECT NO. WO308230
TEST DATE 06-23-09
S/N 4

VENTURI THROAT = .7492 INCH
VENTURI SIZE = 1.275 INCH

T E S T D A T A

RUN	PT	TURB T DEG F	BAROM IN HG	CELL T DEG F	SPEED RPM	PLENUM P PSIG
3	1	74	30.05	73	40000	240
4	1	83	30.05	73	44000	300
4	2	89	30.05	73	42000	280

RUN	PT	TIME OF DAY	FR BRG (F) (610)	FR BRG (F) (611)	AFT BRG (F) (612)	AFT BRG (F) (613)	VIBRATION RMS (G'S)	SPEED PICK UP VOLTAGE (VOLTS)
3	1	14	129	133	88	86	0.4	0.8
4	1	14	138	174	98	95	0.6	0.9
4	2	14	139	143	106	104	0.7	0.9

RUN	PT	N(COR) RPM	FWD BRG TEMP RISE (F)	AFT BRG DELTA TEMP (F)
3	1	39471	58	13
4	1	43418	83	14
4	2	41444	68	16

RUN	PT	DRIV.AIR Pt PSIG	PLENUM T-DEGF	T-AMB F	P-AMB IN-HG
3	1	240.0	74	73	30.05
4	1	300.0	83	73	30.05
4	2	280.0	89	73	30.05

RUN	PT	VENTURI INLET Ps	FLOW-PSIG DEL-P	FLOW TEMP (F)
3	1	327	12.03	75
4	1	406	14.83	87
4	2	369	13.43	95

P E R F O R M A N C E D A T A

RUN	PT	TURBINE W #/SEC
3	1	1.38
4	1	1.68
4	2	1.52

RUN	PT	PLENUM P PSIG (CORR)	TURBINE W #/SEC (CORR)
3	1	244	1.42
4	1	307	1.76
4	2	288	1.60

TECH DEVELOPMENT

MODEL 441B SIMULATOR CHECKOUT

DATE 6-25-09 (1) CELL TEMP 73 °F (4) RECORDER B. MONTGOMERY

NO. OF DATA POINTS (2) BAROMETER 30.02 IN HG (5) (S/N) 1 (7)

VENTURI INLET SIZE 1.275 (3) VENTURI THROAT .7492 (6) W.O. 308230 (8)

RUN (9)	PT (10)	TIME OF DAY	DRIVE PRESS PSIG	PLENUM PRESS PSIG (11)	VENTURI INLET STATIC PSIG (12)	VENTURI Δ P PSI (13)	VENTURI FLOW TEMP (°F) (14)	DRIVE TEMP (°F) (15)	PLENUM TEMP (°F)	FRONT BRG TEMP (°F) (16)	REAR BRG TEMP (°F) (17)	FRONT BRG TEMP (°F) (18)	REAR BRG TEMP (°F) (19)	ROTOR SPEED (RPM) (20)	VERT. ACCEL (G'S) RMS (21)	SPU VOLTAGE (VOLTS) P-P (22)
1	00	10:21	0	0	0	.104	75	75	75	70	72	69	71	0	0	0
10:22	01	10:24	8	9	18.4	1.10	72	70	73	83	73	82	73	10,000	.04	1.4
	02	10:26	24	30	42.5	2.00	69	68	70	124	74	122	76	15,400	.06	2.1
	03	10:27	44	50	71.3	3.06	67	66	67	129	72	127	70	20,100	.15	2.6
	04	10:31	158	160	238.3	9.20	65	64	64	148	65	148	65	35,300	.46	4.2
	05	10:33	218	220	324.2	12.39	71	69	69	144	67	143	64	40,000	2.2	4.7
	06	10:36	270	270	399.2	15.10	78	75	76	149	82	149	87	44,000	1.8	5.1
	07	10:38	264	265	386.2	14.57	82	78	80	130	82	132	86	43,000	1.4	5.0

Model 441B Simulator Checkout.xls

FM09-1126

RAW TEST DATA

TECH DEVELOPMENT

TECH DEVELOPMENT

MODEL 441B SIMULATOR CHECKOUT

DATE 6-24-09 (1) CELL TEMP 73 °F (4) RECORDER B. MONTGOMERY

NO. OF DATA POINTS _____ (2) BAROMETER 30.09 IN HG (5) (S/N) 3 (7)

VENTURI INLET SIZE 1.275" (3) VENTURI THROAT .7492 (6) W.O. 308230 (8)

RUN (9)	PT (10)	TIME OF DAY	DRIVE PRESS PSIG	PLENUM PRESS PSIG (11)	VENTURI INLET STATIC PSIG (12)	VENTURI Δ P PSI (13)	VENTURI FLOW TEMP (°F) (14)	DRIVE TEMP (°F) (15)	PLENUM TEMP (°F)	FRONT BRG TEMP (°F) (16)	REAR BRG TEMP (°F) (17)	FRONT BRG TEMP (°F) (18)	REAR BRG TEMP (°F) (19)	ROTOR SPEED (RPM) (20)	VERT. ACCEL (G'S) RMS (21)	SPU VOLTAGE (VOLTS) P-P (22)
1	00	10:32	0	0	0	0	73	74	74	68	71	68	72	0	0	0
	01	10:53	8	10	18.9	1.09	72	70	72	88	78	88	78	10,000	.05	1.6
	02	10:55	22	35	43.3	1.90	68	67	69	96	82	96	78	15400	.08	2.2
	03	10:57	45	55	73.4	3.00	66	65	67	112	84	114	82	20,500	.05	2.8
	04	11:02	150	175	233.4	8.64	67	65	66	128	64	126	59	35,200	.2	3.0
	05	11:05	218	245	329.2	11,96	74	71	73	128	74	128	68	46,000	1	3.4
	06	11:07	272	305	412.0	14,93	80	76	77	176	98	174	92	49,100	.75	3.7
	07	11:10	261	300	390.2	14,10	84	79	82	151	93	150	88	47,400	2.2	3.6

Model 441B Simulator Checkout.xls

TECH DEVELOPMENT

TECH DEVELOPMENT

MODEL 441B SIMULATOR CHECKOUT

DATE 6-23-09 (1) CELL TEMP 73 °F (4) RECORDER B. Mohammed

NO. OF DATA POINTS _____ (2) BAROMETER 30.05 IN HG (5) (S/N) 4 (7)

VENTURI INLET SIZE 1.275 (3) VENTURI THROAT .7492 (6) W.O. 308220 (8)

RUN (9)	PT (10)	TIME OF DAY	DRIVE PRESS PSIG	PLENUM PRESS PSIG (11)	VENTURI INLET STATIC PSIG (12)	VENTURI Δ P PSI (13)	VENTURI FLOW TEMP (°F) (14)	DRIVE TEMP (°F) (15)	PLENUM TEMP (°F)	FRONT BRG TEMP (°F) (16)	REAR BRG TEMP (°F) (17)	FRONT BRG TEMP (°F) (18)	REAR BRG TEMP (°F) (19)	ROTOR SPEED (RPM) (20)	VERT. ACCEL (G'S) RMS (21)	SPU VOLTAGE (VOLTS) P-P (22)
1	00	11:26	0	0	.2	0	72	73	73	68	72	68	71	0	0	0
	01	11:32	8	10	20.4	1.17	87	69	64	97	75	88	74	10,600	.05	.2
	02	11:35	22	23	41.6	1.91	64	66	61	94	71	92	71	15,200	.05	.3
	03	11:38	43	55	72.9	2.99	62	65	59	142	86	123	67	20,300	.04	.38
1:42	04	11:42	66	80	104.6	4.10	63	65	60	150	70	129	70	24,300	.1	.44
3:46	2	01	12:48	70	80	110.7	4.36	68	69	65	105	70	103	70	25,100	.16	.45
3:53		02	13:52	150	175	236.0	8.77	68	68	64	138	77	135	76	35,00	.*	.62
		ACCELEROMETER CAME LOOSE														.23	
4:20	3	01	14:24	215	240	327.2	12.03	75	74	72	129	88	133	96	40,000	.35	.8
4:27		AFT BEARING TEMP TRIP															
4:32	4	01	14:35	270	300	406	14.83	87	83	84	134	98	141	95	44,000	.6	.9
4:38		02	14:38	250	260	369	13.43	95	82	92	139	106	143	104	42,000	.7	.9

Model 441B Simulator Checkout.xls

TECH DEVELOPMENT

TDI MEMO

DATE: 02 March 2011

TO: W.O. 3128 Engineering File

FROM: Brian C. Kemp

SUBJECT: Checkout Run of Model 441 Simulator – S/N's 1, 3 and 4

COPY: Bob Montgomery

I. INTRODUCTION

Model 441 serial number 1, 3 and 4 were manufactured in 1966 for NASA LaRC under Tech Development's work order 441 along with (2) additional units (S\N's 2 and 5). S/N's 2 and 5 were not refurbished under this effort.

All units were returned to TDI for an upgrade in 1971. The grease lubricated rear bearing was change to oil wick and the turbine section was weight reduced under work order 772. Numerous refurbishments of the subject TPS units have been completed since the 1972 rework. No additional modifications have been recorded.

Mechanical checkout tests were conducted between 22 and 24 February 2011. These were follow-up checkouts to those performed after the original refurbishment in June 2009 (WO 3082).

TECH DEVELOPMENT

II. MODEL AND TEST APPARATUS

The Model 441's were mounted to a TDI-provided pylon block that interfaces with the simulator Model B. This part also contains the turbine air supply port. The test inlet for mounting the air supply hose was sandwiched between the pylon block and a mounting plate. The mounting plate was mounted to a phenolic block which in turn is mounted to the test bench plate, D-21602.

All test runs were completed with the inlet cowl and the exit cowl. The exit cowl created a 9.86 in^2 exit area (REF: Figures 1 and 2).

Figure 3 shows a drawing of the fan exit cowl used in the check-out test.

III. INSTRUMENTATION

The turbine supply air conditions (at the venturi flow meter) and cell temperatures were read out on the panel mounted Omega Model 660 thermal meter (J calibration).

Each set of forward and aft bearing thermocouples were connected to separate Omega DPS-3204 T/C Scanning indicators. The devices were adjusted for type K thermocouples for runs 1 thru 4. A single forward and a single aft thermocouple were used as an emergency trip. The forward bearing temperature trip was set at 225°F. The aft bearing temperature trip was set at 125°F for all runs.

An accelerometer (Endevco Model 256HX-10, S/N) was mounted on the simulator fan case (REF: Figure 1). The accelerometer signal was fed into a Data Physics Quattro Ace dynamic signal analyzer. Only the 1/rev peak frequencies were manually recorded. Vibration information for the entire data run was stored electronically.

Each of the two magnetic pickups in the simulator read 6 counts per revolution. One signal was read by a DIGITEC frequency meter and overspeed trip with the gate set at 1 sec. This, therefore, displayed rpm divided by 10. The second pickup signal was fed to a Tektronix Oscilloscope Model T935A, S/N T935A B022698, for measurement of its output voltage level.

The airflow rates supplied to the simulator turbine were determined using the facility venturi flow meter.

Plenum pressure was measured using the pressure tube embedded in the test unit inlet plenum.

The aft bearing position was supplied with lubrication using a pulse oiler system (REF: Figure 4). The units were originally configured for a fixed volume fill of lubricant that is to be checked and refilled at a specific interval. All of the units were tested using pulse oil distribution at a rate of 10 cc/hr. The drain tube that was utilized in the fixed lube volume operational approach was capped off for the testing.

IV. TEST PROGRAM

The tests were conducted for the purpose of demonstrating the mechanical integrity of the overhauled units.

These simulators were run at the following approximate speeds and cumulative durations,

SN 1

Operating Speed (rpm)	Cumulative Duration @ Speed (min)
10,000	2
20,000	3
30,000	3
40,000	2
44,000	1
TOTAL	11 minutes

SN 3

Operating Speed (rpm)	Cumulative Duration @ Speed (min)
10,000	3
20,000	3
35,000	2
40,000	2
44,000	2
TOTAL	19 minutes

SN 4

Operating Speed (rpm)	Cumulative Duration @ Speed (min)
10,000	2
20,000	3
30,000	2
40,000	4
44,000	2
TOTAL	13 minutes

Data was recorded by hand on data sheet forms during the steady state periods. The bearing temperature thermocouple pairs, fed to temperature meters, were manually read to verify consistent output with their mates.

V. RESULTS

Supply pressure was measured using the plenum pressure tap in the air supply pipe to the simulator. The following table shows the favorable performance of the tested units (S/N 1, 3 and 4).

	CORRECTED SPEED [RPM]	PLENUM PRESSURE [PSIG]	TURBINE MASS FLOW [LBM/SEC]	FWD BRG TEMP Δ [°F]	AFT BRG TEMP Δ [°F]	VIBRATION (peak G's) 1P
TEST DATE 23FEB2011	29914	122	.53	-3	-3	.3
UNIT S/N-001	39885	251	1.49	12	3	1.9
	44172	299	1.85	28	24	2.7
TEST DATE 22FEB2011	30217	135	.78	43	-4	.1
UNIT S/N-003	40055	264	1.49	39	14	.8
	43669	308	1.72	38	51	2.2
TEST DATE 24FEB2011	30175	137	.79	4	11	.2
UNIT S/N-004	40334	260	1.51	23	32	1.5
	44257	327	1.86	44	34	3.0

Post test review of one of the aft bearing T/C's resulted in identification of wire sheath damage to lead wire extension. Sheath exposed both leads and created TC joint exposed to ambient conditions. T/C was returned to normal operational status after repair.

Fwd bearing temperature rise is the thermocouple reading as measured with the digital meter reading minus the cell temperature (°F). The aft bearing temperature difference is the supply air temperature minus the rear bearing temperature.

The data reduction program M441 output and test data, taken both in reduced and unreduced format, are included in this report as reference material.

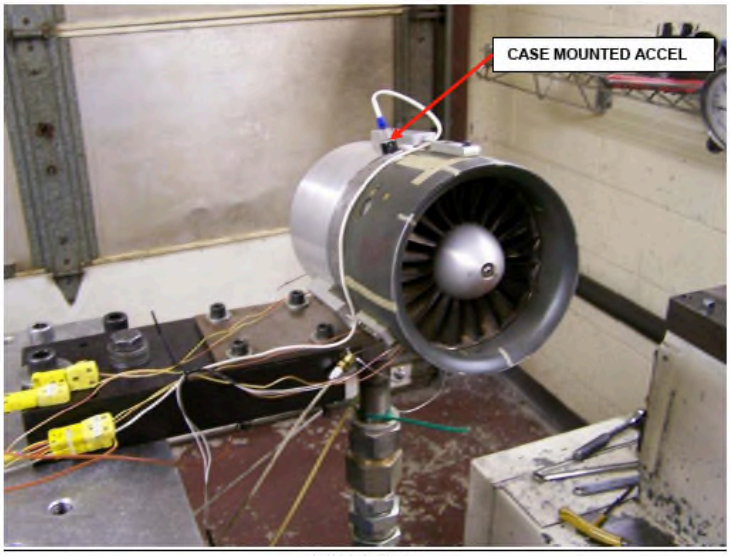

FIGURE 1

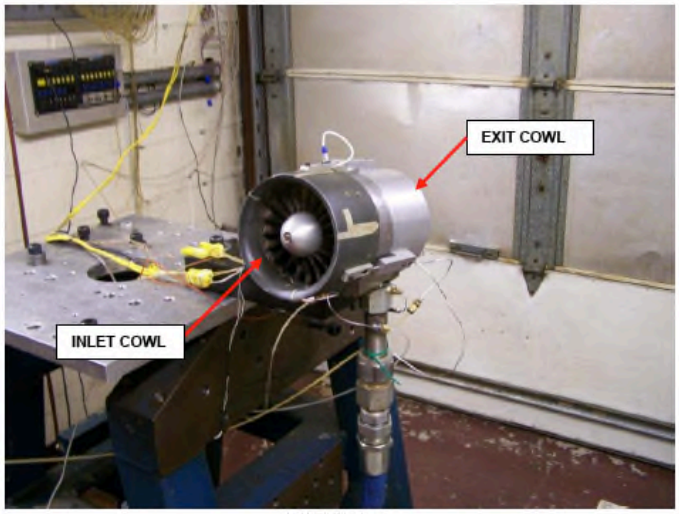

FIGURE 2

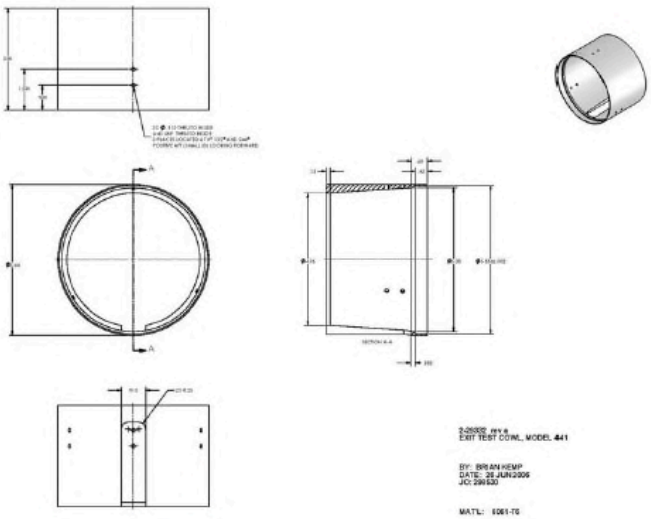

FIGURE 3

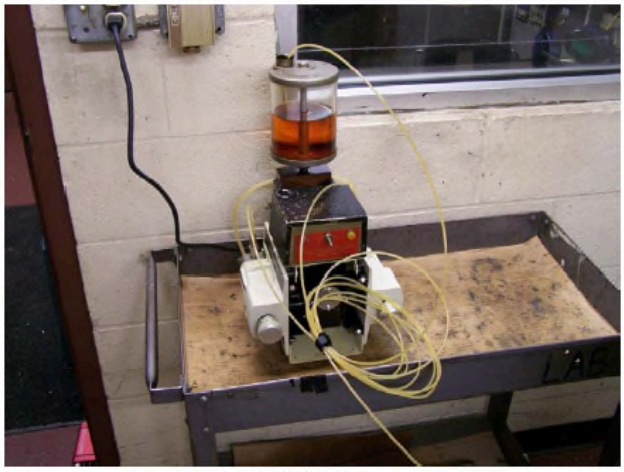

FIGURE 4

TECH DEVELOPMENT

REDUCED TEST DATA

03-02-2011 07:49:52 MODEL 441 TURBOFAN SIMULATOR

PROJECT NO. WO312830
TEST DATE 02-24-2011
S/N 1

VENTURI THROAT = .7492 INCH
VENTURI SIZE = 1.275 INCH

T E S T D A T A

RUN	PT	TURB T DEG F	BAROM IN HG	CELL T DEG F	SPEED RPM	PLENUM P PSIG
1	1	56	29.98	62	10400	10
1	2	51	29.98	62	20100	60

RUN	PT	TIME OF DAY	FR BRG (F) (610)	FR BRG (F) (611)	AFT BRG (F) (612)	AFT BRG (F) (613)	VIBRATION RMS (G'S)	SPEED PICK UP VOLTAGE (VOLTS)
1	1	11	50	48	50	50	0.0	1.8
1	2	11	52	52	44	46	0.3	3.3

RUN	PT	N(COR) RPM	FWD BRG TEMP RISE (F)	AFT BRG DELTA TEMP (F)
1	1	10370	-13	-6
1	2	20042	-10	-6

RUN	PT	DRIV.AIR Pt PSIG	PLENUM T-DEGF	T-AMB F	P-AMB IN-HG
1	1	10.0	56	62	29.98
1	2	60.0	51	62	29.98

RUN	PT	VENTURI INLET Ps	FLOW-PSIG DEL-P	FLOW TEMP (F)
1	1	22	1.52	57
1	2	77	3.50	51

P E R F O R M A N C E D A T A

RUN	PT	TURBINE W #/SEC
1	1	0.16
1	2	0.39

RUN	PT	PLENUM P PSIG (CORR)	TURBINE W #/SEC (CORR)
1	1	10	0.16
1	2	59	0.39

TECH DEVELOPMENT

03-02-2011 07:51:18

MODEL 441 TURBOFAN SIMULATOR
PROJECT NO. WO312830
TEST DATE 02-24-2011
S/N 1

VENTURI THROAT = .7492 INCH
VENTURI SIZE = 1.275 INCH

T E S T D A T A

RUN	PT	TURB T DEG F	BAROM IN HG	CELL T DEG F	SPEED RPM	PLENUM P PSIG
1	3	38	29.98	62	30000	125
1	4	26	29.98	62	40000	260
1	5	24	29.98	62	44300	310

RUN	PT	TIME OF DAY	FR BRG (F) (610)	FR BRG (F) (611)	AFT BRG (F) (612)	AFT BRG (F) (613)	VIBRATION RMS (G'S)	SPEED PICK UP VOLTAGE (VOLTS)
1	3	11	60	58	35	36	0.3	4.8
1	4	11	76	72	26	32	1.9	5.9
1	5	11	93	86	42	53	2.7	6.5

RUN	PT	N(COR) RPM	FWD BRG TEMP RISE (F)	AFT BRG DELTA TEMP (F)
1	3	29914	-3	-3
1	4	39885	12	3
1	5	44172	28	24

RUN	PT	DRIV.AIR Pt PSIG	PLENUM T-DEGF	T-AMB F	P-AMB IN-HG
1	3	125.0	38	62	29.98
1	4	260.0	26	62	29.98
1	5	310.0	24	62	29.98

RUN	PT	VENTURI INLET Ps	FLOW-PSIG DEL-P	FLOW TEMP (F)
1	3	75	7.23	40
1	4	350	13.63	29
1	5	439	16.91	27

P E R F O R M A N C E D A T A

RUN	PT	TURBINE W #/SEC
1	3	0.55
1	4	1.59
1	5	1.98

RUN	PT	PLENUM P PSIG (CORR)	TURBINE W #/SEC (CORR)
1	3	122	0.53
1	4	251	1.49
1	5	299	1.85

TECH DEVELOPMENT

03-02-2011 07:52:48 MODEL 441 TURBOFAN SIMULATOR

PROJECT NO. WO312830
TEST DATE 02-22-2011
S/N 3

VENTURI THROAT = .7492 INCH
VENTURI SIZE = 1.275 INCH

T E S T D A T A

RUN	PT	TURB T DEG F	BAROM IN HG	CELL T DEG F	SPEED RPM	PLENUM P PSIG
1	1	49	30.05	55	10300	10
1	2	39	30.05	55	20300	60

RUN	PT	TIME OF DAY	FR BRG (F) (610)	FR BRG (F) (611)	AFT BRG (F) (612)	AFT BRG (F) (613)	VIBRATION RMS (G'S)	SPEED PICK UP VOLTAGE (VOLTS)
1	1	11	48	48	58	56	0.0	2.0
1	2	11	57	56	59	56	0.1	3.2

RUN	PT	N(COR) RPM	FWD BRG TEMP RISE (F)	AFT BRG DELTA TEMP (F)
1	1	10340	-7	8
1	2	20379	2	19

RUN	PT	DRIV.AIR Pt PSIG	PLENUM T-DEGF	T-AMB F	P-AMB IN-HG
1	1	10.0	49	55	30.05
1	2	60.0	39	55	30.05

RUN	PT	VENTURI INLET Ps	FLOW-PSIG DEL-P	FLOW TEMP (F)
1	1	22	1.20	51
1	2	79	3.18	41

P E R F O R M A N C E D A T A

RUN	PT	TURBINE W #/SEC
1	1	0.15
1	2	0.38

RUN	PT	PLENUM P PSIG (CORR)	TURBINE W #/SEC (CORR)
1	1	10	0.14
1	2	59	0.37

TECH DEVELOPMENT

03-02-2011 07:53:46

MODEL 441 TURBOFAN SIMULATOR
PROJECT NO. WO312830
TEST DATE 02-22-2011
S/N 3

VENTURI THROAT = .7492 INCH
VENTURI SIZE = 1.275 INCH

T E S T D A T A

RUN	PT	TURB T DEG F	BAROM IN HG	CELL T DEG F	SPEED RPM	PLENUM P PSIG
1	3	29	30.05	55	30100	140
1	4	22	30.05	55	39900	275
1	5	22	30.05	55	43500	320

RUN	PT	TIME OF DAY	FR BRG (F) (610)	(611)	AFT BRG (F) (612)	(613)	VIBRATION RMS (G'S)	SPEED PICK UP VOLTAGE (VOLTS)
1	3	11	98	98	24	26	0.1	4.5
1	4	11	93	94	34	38	0.8	5.4
1	5	11	94	91	72	74	2.2	5.7

RUN	PT	N(COR) RPM	FWD BRG TEMP RISE (F)	AFT BRG DELTA TEMP (F)
1	3	30217	43	-4
1	4	40055	39	14
1	5	43669	38	51

RUN	PT	DRIV.AIR Pt PSIG	PLENUM T-DEGF	T-AMB F	P-AMB IN-HG
1	3	140.0	29	55	30.05
1	4	275.0	22	55	30.05
1	5	320.0	22	55	30.05

RUN	PT	VENTURI INLET Ps	FLOW-PSIG DEL-P	FLOW TEMP (F)
1	3	182	6.85	31
1	4	363	13.23	25
1	5	422	15.28	25

P E R F O R M A N C E D A T A

RUN	PT	TURBINE W #/SEC
1	3	0.83
1	4	1.60
1	5	1.85

RUN	PT	PLENUM P PSIG (CORR)	TURBINE W #/SEC (CORR)
1	3	135	0.78
1	4	264	1.49
1	5	308	1.72

TECH DEVELOPMENT

03-02-2011 07:59:48 MODEL 441 TURBOFAN SIMULATOR

PROJECT NO. WO312830
TEST DATE 02-23-2011
S/N 4

VENTURI THROAT = .7492 INCH
VENTURI SIZE = 1.275 INCH

T E S T D A T A

RUN	PT	TURB T DEG F	BAROM IN HG	CELL T DEG F	SPEED RPM	PLENUM P PSIG
1	1	54	30.27	53	10400	10
1	2	48	30.27	53	20300	60

RUN	PT	TIME OF DAY	FR BRG (F) (610)	(611)	AFT BRG (F) (612)	(613)	VIBRATION RMS (G'S)	SPEED PICK UP VOLTAGE (VOLTS)
1	1	11	44	40	44	53	0.1	0.5
1	2	11	48	49	46	46	0.1	0.6

RUN	PT	N(COR) RPM	FWD BRG TEMP RISE (F)	AFT BRG DELTA TEMP (F)
1	1	10461	-11	-6
1	2	20418	-5	-2

RUN	PT	DRIV.AIR Pt PSIG	PLENUM T-DEGF	T-AMB F	P-AMB IN-HG
1	1	10.0	54	53	30.27
1	2	60.0	48	53	30.27

RUN	PT	VENTURI INLET Ps	FLOW-PSIG DEL-P	FLOW TEMP (F)
1	1	22	1.28	55
1	2	80	3.27	50

P E R F O R M A N C E D A T A

RUN	PT	TURBINE W #/SEC
1	1	0.15
1	2	0.39

RUN	PT	PLENUM P PSIG (CORR)	TURBINE W #/SEC (CORR)
1	1	10	0.15
1	2	59	0.38

TECH DEVELOPMENT

03-02-2011 07:54:57 MODEL 441 TURBOFAN SIMULATOR

PROJECT NO. WO312830
TEST DATE 02-23-2011
S/N 4

VENTURI THROAT = .7492 INCH
VENTURI SIZE = 1.275 INCH

T E S T D A T A

RUN	PT	TURB T DEG F	BAROM IN HG	CELL T DEG F	SPEED RPM	PLENUM P PSIG
1	3	36	30.27	53	30000	140
1	4	24	30.27	53	40100	270
1	5	21	30.27	53	44000	340

RUN	PT	TIME OF DAY	FR BRG (F) (610)	FR BRG (F) (611)	AFT BRG (F) (612)	AFT BRG (F) (613)	VIBRATION RMS (G'S)	SPEED PICK UP VOLTAGE (VOLTS)
1	3	11	56	58	52	42	0.2	0.8
1	4	11	70	82	64	48	1.5	1.0
1	5	11	84	110	69	41	3.0	1.1

RUN	PT	N(COR) RPM	FWD BRG TEMP RISE (F)	AFT BRG DELTA TEMP (F)
1	3	30175	4	11
1	4	40334	23	32
1	5	44257	44	34

RUN	PT	DRIV.AIR Pt PSIG	PLENUM T-DEGF	T-AMB F	P-AMB IN-HG
1	3	140.0	36	53	30.27
1	4	270.0	24	53	30.27
1	5	340.0	21	53	30.27

RUN	PT	VENTURI INLET Ps	FLOW-PSIG DEL-P	FLOW TEMP (F)
1	3	183	6.98	39
1	4	366	13.49	28
1	5	454	16.69	25

P E R F O R M A N C E D A T A

RUN	PT	TURBINE W #/SEC
1	3	0.83
1	4	1.62
1	5	2.01

RUN	PT	PLENUM P PSIG (CORR)	TURBINE W #/SEC (CORR)
1	3	137	0.79
1	4	260	1.51
1	5	327	1.86

TDI
TECH DEVELOPMENT

RAW TEST DATA

TDI
TECH DEVELOPMENT

MODEL 441B SIMULATOR CHECKOUT

DATE 2-24-11 (1) CELL TEMP 62 °F (4) RECORDER B. MONTGOMERY

NO. OF DATA POINTS _____ (2) BAROMETER 29.98 IN HG (5) (S/N) 1 (7)

VENTURI INLET SIZE 1.375" (3) VENTURI THROAT .7492 (6) W.O. 312870 (8)

RUN (9)	PT (10)	TIME OF DAY	DRIVE PRESS PSIG	PLENUM PRESS PSIG (11)	VENTURI INLET STATIC PSIG (12)	VENTURI Δ P PSI (13)	VENTURI FLOW TEMP (°F) (14)	DRIVE TEMP (°F) (15)	PLENUM TEMP (°F)	FRONT BRG TEMP (°F) (16)	REAR BRG TEMP (°F) (17)	FRONT BRG TEMP (°F) (18)	REAR BRG TEMP (°F) (19)	ROTOR SPEED (RPM) (20)	VERT. ACCEL (G'S) RMS (21)	SPU VOLTAGE (VOLTS) P-P (22)
1	00	10:59	0	0	0	0	56	58	60	47	50	47	50	0	0	0
	01	11:02	10	10	22	1.52	57	56	54	50	50	48	50	10,400	.04	1.8
	02	11:04	45	60	77	3.50	51	51	48	52	48	52	46	20,100	.33	3.3
	03	11:07	110	125	175	7.23	40	38	35	60	35	58	36	30,000	.26	4.8
	04	11:10	235	260	350	13.63	29	26	25	76	26	72	32	40,000	1.9	5.9
	05	11:12	280	310	439	16.91	32	24	24	93	42	86	53	44,300	3.7	6.5

Model 441B Simulator Checkout.xls PM09-T126

TECH DEVELOPMENT

TECH DEVELOPMENT

MODEL 441B SIMULATOR CHECKOUT

DATE 2-22-11 (1) CELL TEMP 55 °F (4) RECORDER B. Montgomery

NO. OF DATA POINTS _____ (2) BAROMETER 30.05 IN HG (5) (S/N) 3 (7)

VENTURI INLET SIZE 1.375 (3) VENTURI THROAT .7492 (6) W.O. 312830 (8)

RUN (9)	PT (10)	TIME OF DAY	DRIVE PRESS PSIG	PLENUM PRESS PSIG (11)	VENTURI INLET STATIC PSIG (12)	VENTURI Δ P PSI (13)	VENTURI FLOW TEMP (°F) (14)	DRIVE TEMP (°F) (15)	PLENUM TEMP (°F)	FRONT BRG TEMP (°F) (16)	REAR BRG TEMP (°F) (17)	FRONT BRG TEMP (°F) (18)	REAR BRG TEMP (°F) (19)	ROTOR SPEED (RPM) (20)	VERT. ACCEL (G'S) RMS (21)	SPU VOLTAGE (VOLTS) P-P (22)
1	00	11:12	0	0	0	0	53	53	54	50	52	49	57	0	0	0
	01	11:24	16	10	12	1.20	51	49	47	48	58	43	56	10,300	.02	2.0
	02	11:27	50	60	79	7.18	41	39	36	57	59	56	56	20,700	.06	3.2
	03	11:31	118	140	192	6.85	31	29	27	98	74	98	76	30,100	.075	4.5
	04	11:33	245	275	363	13.23	25	22	21	93	74	94	76	39,900	.8	5.4
11:37	05	11:36	285	320	422	15.24	25	22	21	94	72	91	74	43,560	2.2	5.7

Model 441B Simulator Checkout.xls FM09-1126

TECH DEVELOPMENT

TECH DEVELOPMENT

MODEL 441B SIMULATOR CHECKOUT

DATE 2-23-11 (1) CELL TEMP 53 °F (4) RECORDER B. HOUTSONEAU

NO. OF DATA POINTS (2) BAROMETER 30.27 IN HG (5) (S/N) 4 (7)

VENTURI INLET SIZE 1.275 (3) VENTURI THROAT .7492 (6) W.O. 312830 (8)

RUN (9)	PT (10)	TIME OF DAY	DRIVE PRESS PSIG	PLENUM PRESS PSIG (11)	VENTURI INLET STATIC PSIG (12)	VENTURI Δ P PSI (13)	VENTURI FLOW TEMP (°F) (14)	DRIVE TEMP (°F) (15)	PLENUM TEMP (°F)	FRONT BRG TEMP (°F) (16)	REAR BRG TEMP (°F) (17)	FRONT BRG TEMP (°F) (18)	REAR BRG TEMP (°F) (19)	ROTOR SPEED (RPM) (20)	VERT. ACCEL (G'S) RMS (21)	SPU VOLTAGE (VOLTS) P-P (22)
1	00	11:36	0	0	1	0.00	56	57	55	51	52	50	52	0	0	0
11:37	01	11:39	10	10	12	1.38	55	54	53	44	44	40	53	10,400	.05	.5
	02	11:42	50	40	80	3.27	50	48	46	48	46	49	46	20,300	.08	.6
	03	11:45	170	140	183	6.08	39	36	34	56	52	56	42	30,000	.23	.8
	04	11:49	245	220	266	13.49	28	24	23	70	64	82	48	38,100	1.5	1.0
11:52	05	11:50	300	340	454	Max 9	39	21	21	84	69	110	41	44 80	3.0	1.1
11:53 11:58	2 01	11:55	7	5	13	0.88	24	27	23	45	34	43	24	8,077	.0	.4

Model 441B Simulator Checkout.xls FM09-1126

A14. Calibration Report for Q-Flex

Angle of Attack Sensor Calibrations

The following is a report of the calibration and check of the AMELIA angle of attack sensors performed December 14, 2011 before the start of testing.

Calibration and check of angle-of-attack sensors

J.M. van Aken

Dec 14, 2011

Introduction

Calibration of the model angle-of-attack sensor, ALPHA_MODEL_1, was performed on Dec 12, 2011.

IE: Dan Pruyn

Data Tech: Sandee Ruiz

TE: Charlie Rogers

Calibration data were acquired in TR021, RN002 and RN003. The applied angle was measured with a hand-held angle sensor (DINC) and the value was inserted into the numerical input ALPHA_INP. Run RN003 is used for the analysis to obtain calibration coefficients. The amplifier gain was set to 1.

At the same time data were acquired for ALPHA_OPC (angle of attack from sting encoder), and from the QA-2000 sensors (QANGLE and ALT_QANGLE). These data are presented as well.

Analysis of ALPHA_MODEL_1

The curve fit utility in review_TS_data was used to analysis the data and to obtain the coefficients. The following table summarizes the computed coefficients.

Tagname	ifit	c0	c1	c2	c3
ALPHA_MODEL_1	3	1.2422	-5.6615	0.13331	0.022043

The remaining pages show the curve fit results in graphical format with ALPHA_INP=applied angle along the x-axis and the voltage measurement of the sensor along the y-axis.

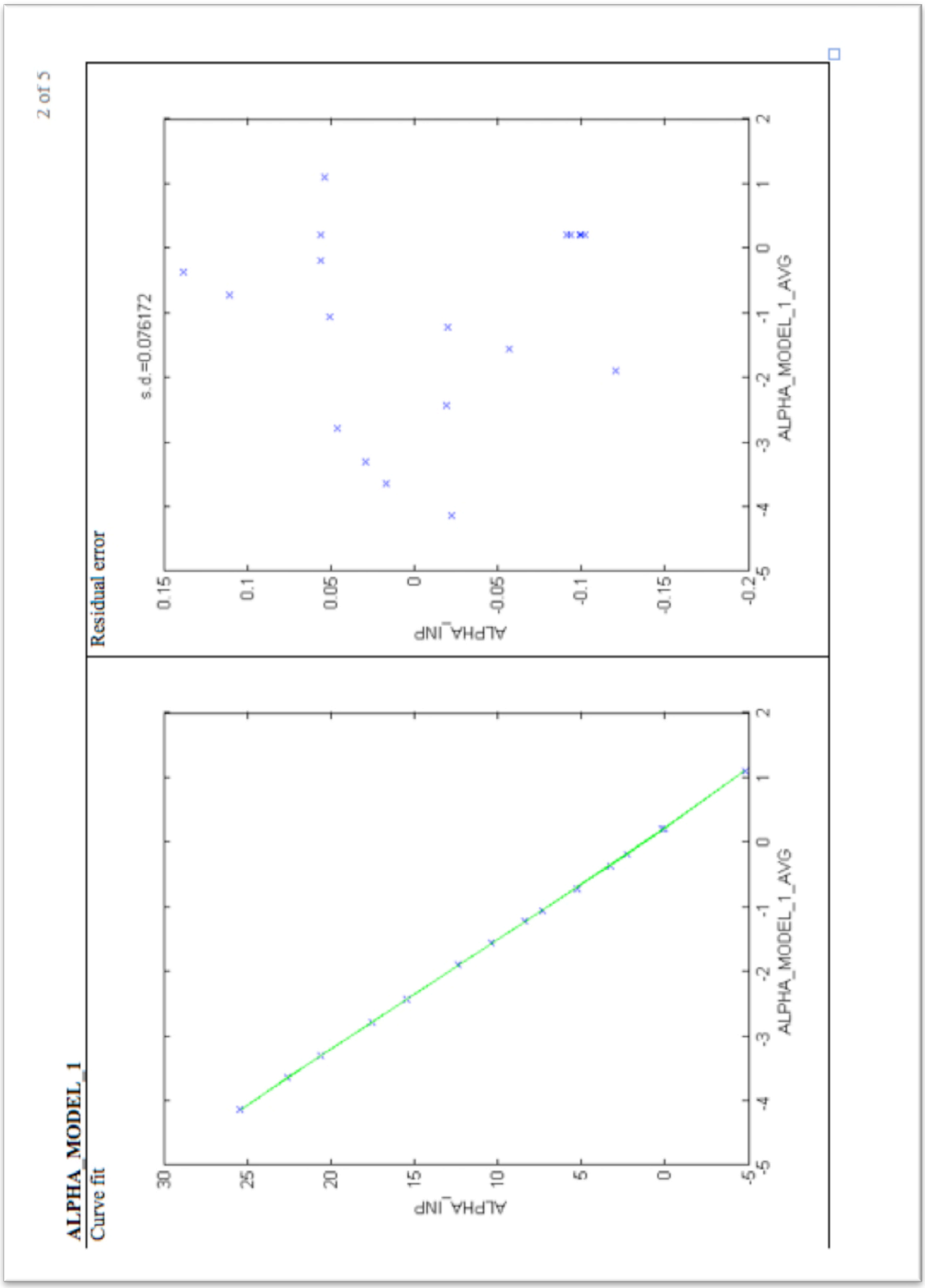
2 of 5
ALPHA_MODEL_1
Curve fit
ALPHA_INP
ALPHA_MODEL_1_AVG
Residual error
s.d.=0.076172
ALPHA_INP
ALPHA_MODEL_1_AVG

ALPHA_OPC versus ALPHA_INP

Curve fit

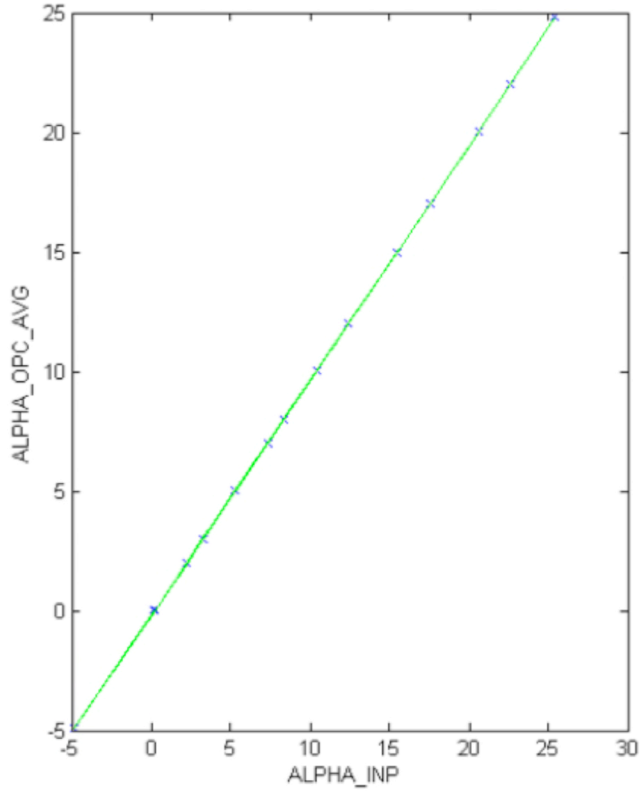

Residual error

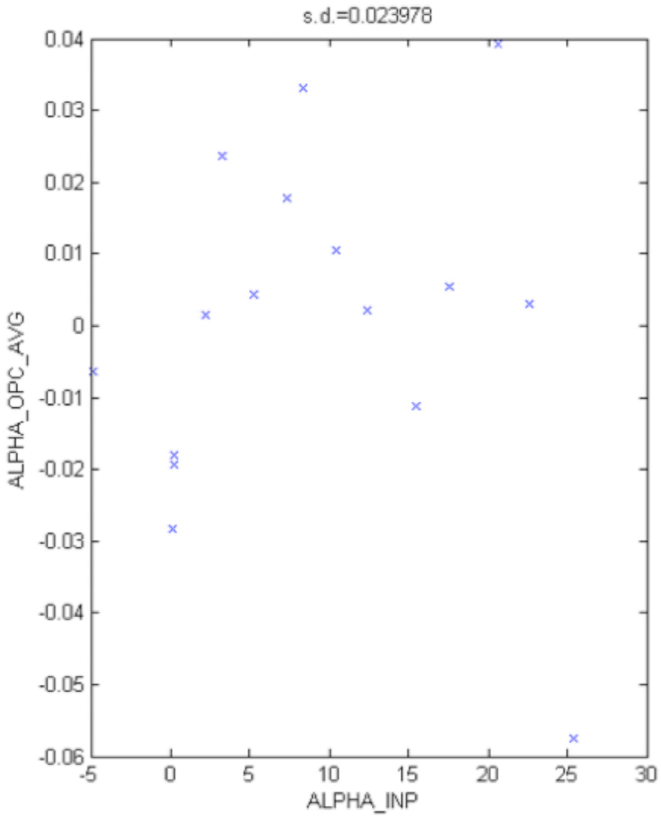

Curve fit coefficients:

c0= -0.173, c1= 0.981 (if using estat files)

ALPHA_INP versus ALT_QANGLE

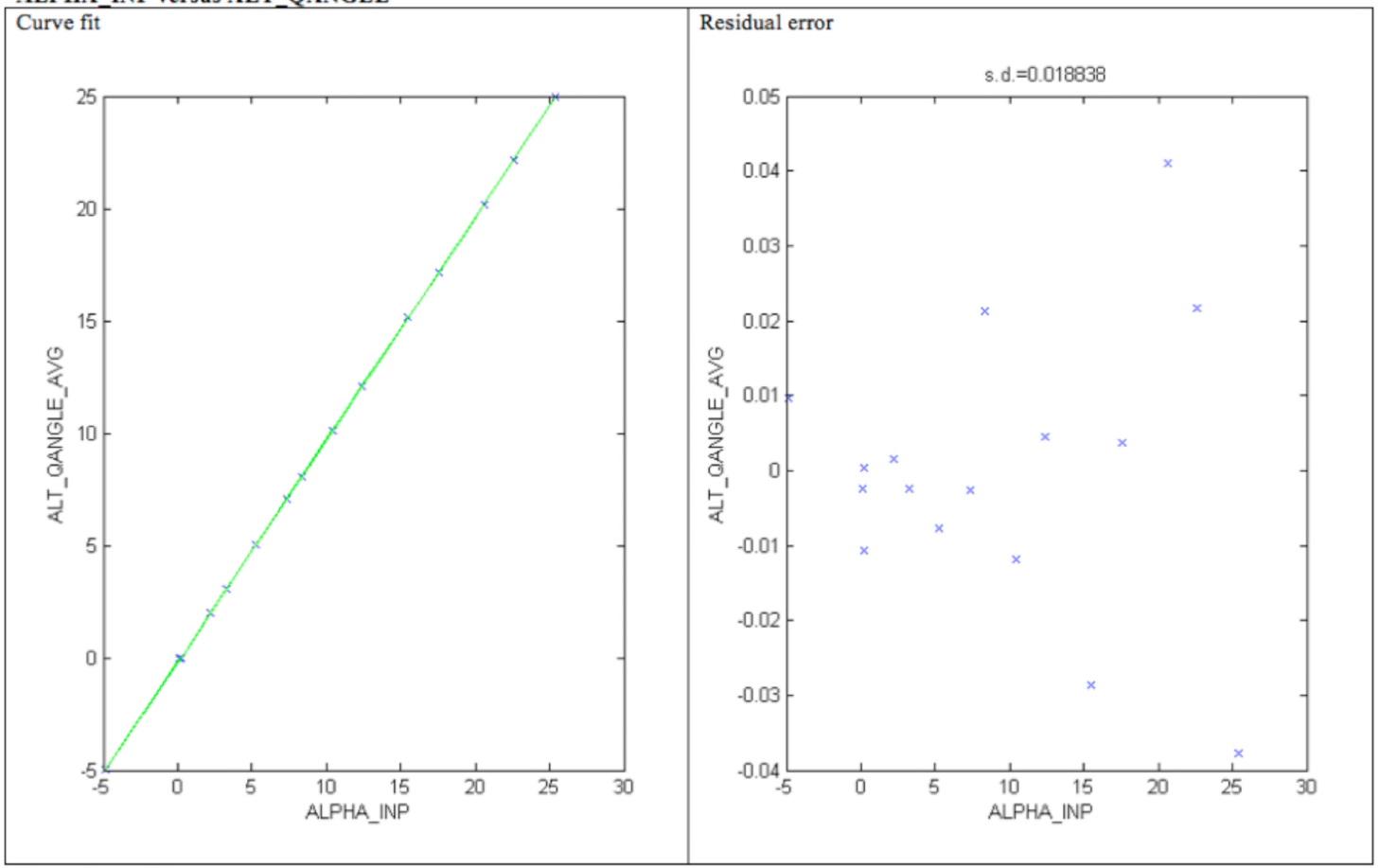

Curve fit coefficients:

c0= -.171, c1= 0.989 (if using estat files)

ALPHA_INP versus QANGLE

Curve fit

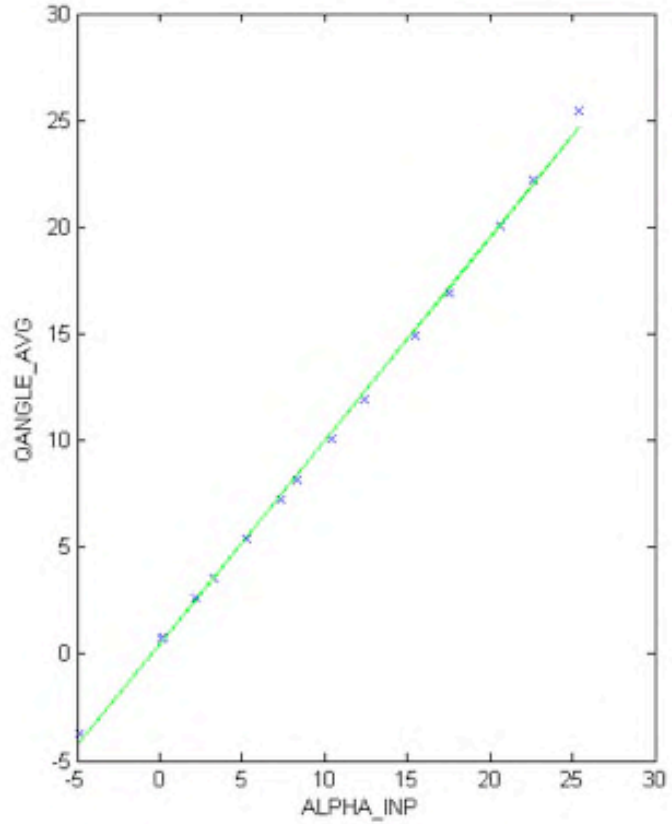

Residual error

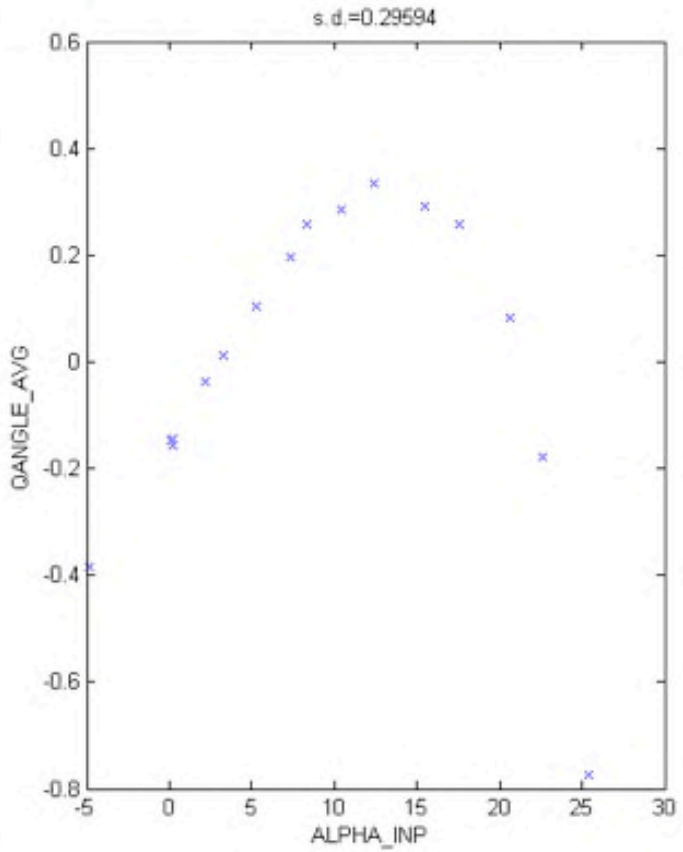

Curve fit coefficients:

c0= 0.459, c1= 0.954 (if using estat files)